

**Accepted papers (original version)
for ICPST-39**

English Symposia

- The accepted papers are published in Journal of Photopolymer Science and Technology Vol. 35, No. 1-5 (2022).
- Publication work on journal of Photopolymer Science and Technology, Vol. 35, No. 1-5 (2022) has been delayed. We sincerely apologize for any inconvenience.
- Please be careful when handling the file.

Contact:

Dr. Hiroyuki Mayama, Editor-in-Chief of Journal of Photopolymer Science and Technology

e-mail: mayama@asahikawa-med.ac.jp

Dependence of Dissolution Kinetics of Main-Chain Scission Type Resists on Molecular Weight

Akihiro Konda¹, Hiroki Yamamoto², Shusuke Yoshitake³, and Takahiro Kozawa^{1*}

¹ *The Institute of Scientific and Industrial Research, Osaka University,
8-1 Mihogaoka, Ibaraki, Osaka, 567-0047, Japan*

² *Takasaki Advanced Radiation Research Institute, National Institutes for Quantum
Science and Technology (QST),
1233 Watanuki, Takasaki, Gunma 370-1292, Japan*

³ *Nuflare Technology, 8-1 Shinsugita, Isogo, Yokohama, Kanagawa 235-8522, Japan
kozawa@sanken.osaka-u.ac.jp

The dissolution kinetics and molecular weight in main-chain scission type resists such as poly(methyl methacrylate) (PMMA) and ZEP520A were investigated using a quartz crystal microbalance (QCM) method and a Gel Permeation Chromatography (GPC) to clarify the effects of the molecular weight after polymer degradation on the dissolution kinetics. G-values of main chain scissions in PMMA and ZEP520A are estimated using GPC measurement. The G-value of ZEP520A showed higher G-values than that of PMMA. There are three molecular weight regions in PMMA, whereas there are only two molecular weight regions in ZEP 520A. The dissolution behavior depends on molecular weight after polymer degradation in both PMMA and ZEP 520A. These results indicate that ZEP520A is better to be better lithographic performance.

Keywords: lithography, main-chain scission type resist, extreme ultraviolet (EUV), electron beam (EB), development process

1. Introduction

Lithography is a major method to fabricate ultrafine feature size patterning of circuits to produce semiconductor devices. The miniaturization of them has been achieved by using shorter wavelength exposure source according to Rayleigh's formula. Further miniaturization is required to increase processing speed and reduce power consumption. Recently, ArF immersion lithography (193 nm) has reached the limit of nanofabrication. Therefore, extreme ultraviolet (EUV) lithography with 13.5 nm wavelength has been adopted by the semiconductor industry as the advanced lithography technology to achieve further device scaling. EUV lithography are used for nanofabrication with the highest resolution.

The deployment of EUV had a great impact on the resist design because the energy of exposure tools first exceeds the ionization potential of resist

materials for mass production. It has been reported that the acid generation mechanism changes above the ionization potential of resist materials (typically around 10 eV) [1, 2]. Therefore, the ionization process preferentially occurs in the acid generation processes in EUV lithography [3].

It is challenging to continue to implement EUV lithography for mass production because the demand for the EUV resist materials is very strict. Chemically amplified resist has been used for the purpose of both high sensitivity and high resolution. In the development of EUV chemically amplified resist, the trade-off relationships among sensitivity, resolution and line width roughness (LWR) are the most serious problem. In order to overcome this trade-off problem concurrently, it is essential to understand the basic chemistry of resist matrices in each resist processes.

With the progress of miniaturization, the

Received April 30, 2022

Accepted June 24, 2022

diffusion of acids used as a catalyst becomes an obstacle to the improvement of resist performance such as resolution. Also, chemically amplified resists are irradiated and give secondary electrons. These secondary electrons become thermalized electrons by losing energy and react with acid generator. After that, acid is generated and deprotection reactions occur. Therefore, irradiation site and reaction site differ due to the reaction mechanism. This resolution blur induces the degradation of resolution and the cause of LWR. Therefore, it is difficult for chemically amplified resists to obtain sub-10 nm patterning. On the other hand, main chain scission type resist such as poly(methyl methacrylate) and ZEP520A induces main chain scissions after EB or EUV irradiation. Therefore, irradiation site and main chain scission site is same. That's why it is considered to improve resolution and LWR due to the resolution blur. Therefore, main-chain-scission-type resists have recently attracted much attention [4-6].

Main chain scission type resists have been widely used for the fabrication of nano-devices because they could fabricate in principle ultrafine structures to the dimensions of the monomers they consist of. Among them, poly(methyl methacrylate) (PMMA) and ZEP520A (a copolymer consisting of methyl α -chloroacrylate and α -methylstyrene) are a typical main chain scission type resist [7-13]. PMMA and ZEP520A has the capability for fabricating sub-10 nm half-pitch [12-15]. The reaction mechanism of PMMA and ZEP 520A upon exposure to radiation and electron beam has been reported [16-21].

The development process is a key process among resist processes in fine patterning [22]. The development processes for resist materials have been investigated using tetramethylammonium hydroxide (TMAH) aqueous solutions [22-28]. Backbone polymers such as poly(4-hydroxystyrene) (PHS) and polyacrylic acid typically show the dissolution kinetics with Case II diffusion in 2.38% TMAH aqueous solution [27, 28]. These backbone polymers typically hardly change the molecular weight before and after exposure to radiation such as EB or EUV. On the other hand, main chain scission type resists decrease the molecular weight upon exposure to radiation. The solubility of resist films in organic developers increases with decreasing molecular weight [29, 30]. It has been reported that the ZEP series sufficiently irradiated by EB dissolves with Case II diffusion [31]. Also, it has been reported that the low-molecular-weight components were preferentially

dissolved in the developer and high-molecular-weight components remained when the resist was irradiated by EB at a moderate dose [32]. However, the details of the dissolution kinetics in main chain scission type resists still remains unclear in organic solvent. In this study, the dissolution kinetics and molecular weight in main chain scission type resists such as PMMA and ZEP520A were investigated using a quartz crystal microbalance (QCM) method and a Gel Permeation Chromatography (GPC) to clarify the effects of the molecular weight after polymer degradation on the dissolution kinetics.

2. Experimental

As resist materials, PMMA ($M_w=50,000$) from Aldrich and ZEP520A ($M_w=56,000$) from ZEON were used, respectively. In PMMA, Propylene glycol monomethyl ether acetate (PGMEA, Tokyo Ohka Kogyo Co. Ltd) was used as a casting solvent. The resist solutions were prepared by dissolving PMMA in PGMEA to carry out the evaluation of resist performance and QCM measurement. The irradiated samples of PMMA were developed in a developer (methyl isobutyl ketone (MIBK): isopropyl alcohol (IPA) 1:3 mixed solvent) for 60 s at room temperature (21 °C). On the other hand, ZED-N50 (N-amyl acetate) was used as a developer of ZEP520A.

– In the sample preparation for the evaluation of resist performance, Si wafers were primed with hexamethyldisilazane (HMDS). The resist solutions were filtered through a 0.20 μm PTFE syringe filter prior to spin-coating to silicon wafers. Resist solutions were spin-coated onto silicon substrates at 3000 rpm for 30 s to form thin films on a silicon wafer. Then, spin-coated PMMA films were pre-baked at 130 °C for 90 s, whereas spin-coated ZEP 520A films were prebaked at 180 °C for 180 s. The film thickness was adjusted to be around 100 nm. The films were exposed to EUV (Energetic, EQ-10M) [32]. EB irradiation was carried out using EB-ENGINE[®] (Hamamatsu Photonics) in N₂ gas flow (monitored O₂ < 100 ppm) at 25 °C. The exposed area was approximately 1 \times 1 cm². These films were developed by dipping in MIBK: IPA= 1:3 mixed solvent for PMMA and by dipping in ZED-N50 for ZEP520A for 60s. And then, they rinsed in 2-propanol for PMMA and ZMD-B for ZEP520A for 15 s before drying. Resist film thickness was measured with an ET200 surface profiler to make sensitivity curves.

In the sample preparation for GPC measurement, the resist solutions were filtered through a 0.20 μm

PTFE syringe filter prior to spin-coating to 4-inch silicon substrates. Resist films of approximately 400 nm thickness were prepared by spin-coating on 4-inch Si substrates, followed by prebaking at 180 °C for 180 s. We used EB irradiation tool instead of EUV exposure tool because EUV exposure system cannot expose large area all at once. The molecular weight distribution of PMMA and ZEP 520A degraded using a EB shower (EB-ENGINE[®] (Hamamatsu Photonics)) was estimated using a GPC system (Shodex GPC-104). A 75 kV EB shower was chosen as the irradiation source, which can irradiate large area once at all and uniformly. The EB irradiation was carried out in N₂ gas flow (monitored O₂ < 100 ppm) at 25 °C. After EB exposure to PMMA and ZEP520A, the exposed films were scraped from Si substrates and were dissolved in THF. They were analyzed by GPC.

In the sample preparation for QCM measurement, the resist solutions were filtered through a 0.20 μm PTFE syringe filter prior to spin-coating to QCM wafers. The quartz crystal substrates (frequency of 5 MHz) were used. The resist solutions were spin-coated onto at 3000 rpm for 30 s QCM substrate to form thin film with c.a. 100 nm thickness. They were exposed to EUV radiation. The exposed area was approximately 1 × 1 cm². The exposure doses ranged from 0 to 15 mJ/cm² for ZEP520A, while they ranged from 0 to 50 mJ/cm² for PMMA. Dissolution behaviors of PMMA and ZEP520A films were investigated by the QCM-based analyzer (RDA-Qz3) [33]. The exposed films were subjected to QCM analysis in MIBK: IPA= 1:3 mixed solvent and ZED-N50. They were developed by dipping in their solutions for 60 s at 21 °C. After development, they were rinsed in 2-propanol and ZMD-B before drying. Resist film thickness was measured with spectroscopic ellipsometry (UVISEL (Horiba)).

3. Results and discussion

In order to convert to EB irradiation dose to EUV exposure dose, the sensitivity of PMMA and ZEP 520A was investigated. Fig. 1 shows the sensitivity curves of PMMA and ZEP upon exposure to (a) EUV and (b) EB, respectively. The sensitivity and contrast of PMMA is 30 mJ/cm² and 2.3 for EUV exposure and 240 μC/cm² and 2.2 for EB irradiation. On the other hand, the sensitivity and contrast of ZEP520A is 16 mJ/cm² and 3.3 for EUV exposure and 120 μC/cm² and 2.7 for EB irradiation. It was clarified that the sensitivity and contrast of ZEP520A is better than those of PMMA. EUV exposure dose of 1 mJ/cm² is equivalent to EB

irradiation dose of 8 μC/cm².

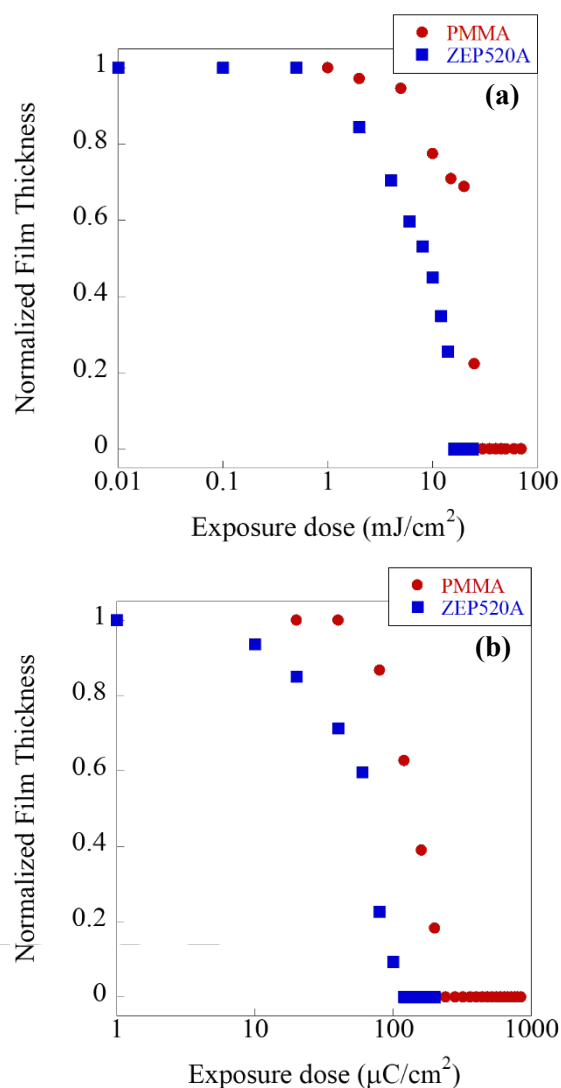


Fig. 1. Sensitivity curves of PMMA and ZEP520A upon exposure to (a) EUV and (b) EB, respectively.

In order to know the change in molecular weight after EB irradiation, GPC measurement was conducted. Fig.2 shows the GPC charts of (a) PMMA and (b) ZEP520A films after EB irradiation, respectively. The peak intensity was normalized to 1 for each sample. In both PMMA and ZEP520A GPC chromatograms, the retention time of chromatograms become longer with the increase of EB irradiation dose. The molecular weight of both PMMA and ZEP 520A becomes smaller because of main chain scissions. The initial rise of chromatograms overlap in PMMA at low exposure dose, whereas the initial rise of chromatograms hardly overlaps in ZEP520A. Longer fragment of PMMA remains after EB irradiation. On the other hand, longer fragments of ZEP520A hardly remains

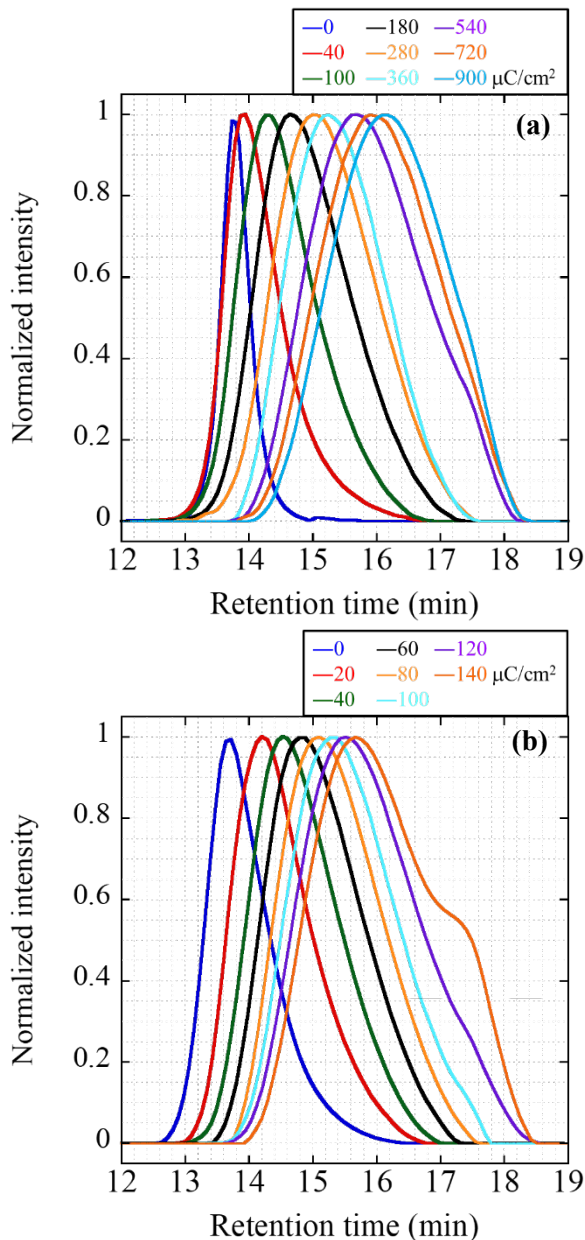


Fig. 2. GPC charts of (a) PMMA and (b) ZEP520A films after EB irradiation, respectively.

compared to PMMA. These results indicate that the reaction mechanism of PMMA is different from that of ZEP520A.

The number of average M_n , and weight average, M_w , molecular weights of all samples tested, both irradiated and unexposed, were calculated. Fig. 3 shows the relationship between molecular weights (M_n and M_w) of all samples with and without irradiation and exposure dose in ZEP 520A. As expected, as the irradiation dose increased both M_n and M_w decreased drastically. For example, a eight-fold decrease from 54000 to 6700 was observed as the irradiation dose increased from 20 to 140 $\mu\text{C}/\text{cm}^2$. In all cases, the irradiation led to polymer

degradation.

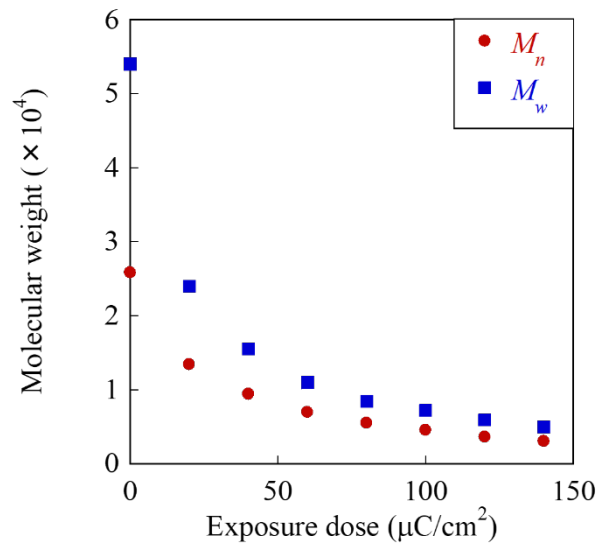
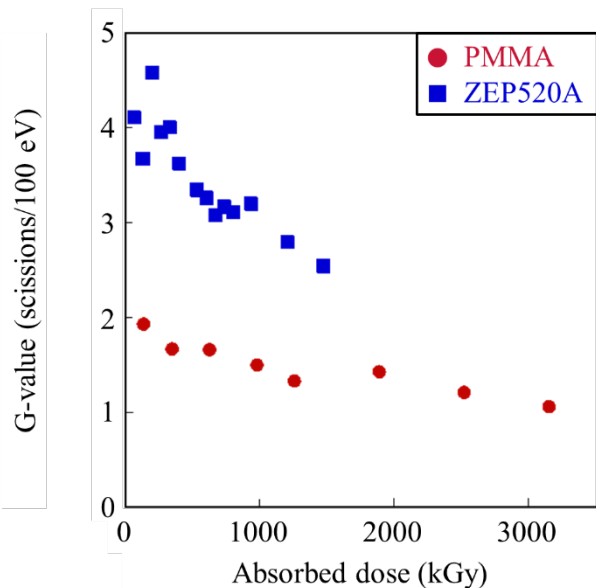


Fig. 3. Relationship between molecular weights (M_n and M_w) of all samples with and without irradiation and exposure dose in ZEP 520A.

The parameter used to compare the suitability of polymers as positive resists is G-value, that is the number of chain scissions per 100 eV of absorbed energy. G-value can be estimated from Alexander Charlesby Ross equation by using number average molecular weight before and after EB irradiation [34]. Fig. 4 shows relationship between absorbed dose and G-values in PMMA and ZEP520A. G-values was estimated to be approximately from 1 to 2 in PMMA, while G-values was approximately



from 2 to 5 in ZEP520A. Both results have a similar Fig. 4. Relationship between absorbed dose and G-values in PMMA and ZEP520A.

tendency to decrease G-values with the increasing of absorbed dose. G-values of ZEP520A are higher than that of PMMA. A high G-value indicates a large difference in molecular weight between the exposed and unexposed regions of the resist, so that the difference in dissolution rates between the two regions increases. As a result, ZEP520A showed better sensitivity and contrast than PMMA. Also, G-values of PMMA and ZEP520A are considerably different. This result also indicates that reaction mechanism of PMMA and ZEP520A is different.

The reaction mechanism of PMMA upon exposure to radiation and electron beam has been reported as follows [16-18]. Upon exposure to radiation such as EUV and electron beam, PMMA molecules are ionized and their radical cations results in. After the detachment of side chains from the radical cations, β -scission of PMMA molecules occurs. On the other hand, the reaction mechanism of ZEP520A upon exposure to radiation and electron beam has been reported as follows [20]. In ZEP520A, two reaction mechanisms can be plausible. Firstly, chloride ions are eliminated by dissociative electron attachment. Then main chain scissions occur by electron transfer. Radical recombination can easily occur in PMMA, whereas there are two pathway of main chain scission in ZEP520A, so that it is difficult to occur radical recombination in ZEP520A. These results lead to the difference of GPC chromatogram and G-values. Dissolution behavior of PMMA and ZEP520A were investigated using QCM. Fig. 5 shows the QCM graphs of (a) ZEP520A and (b) PMMA obtained upon EUV exposure. Dissolution rates were calculated from QCM results. The difference in dissolution kinetics between PMMA and ZEP 520 A clearly was observed. In PMMA, dissolution rate shows negative value when exposure dose become less than 10 mJ/cm². Without exposure, 20 nm swelling was observed. In the case of low exposure dose, PMMA firstly swells and then dissolved into developer. By GPC measurement, we revealed that longer fragment of PMMA remains. It is considered that slight swelling is caused by long fragment of PMMA. The dependence of dissolution rate on MW of polymer could be attributable to penetration of the solvent, disentanglement of polymer chains, or transport of disentangled chains into the bulk solvent (external mass transfer). Higher MW chains are anchored deeper into the polymer, and consequently the thickness of the swollen layer must be greater to release them. When exposure

dose exceeds 10 mJ/cm², only dissolution was

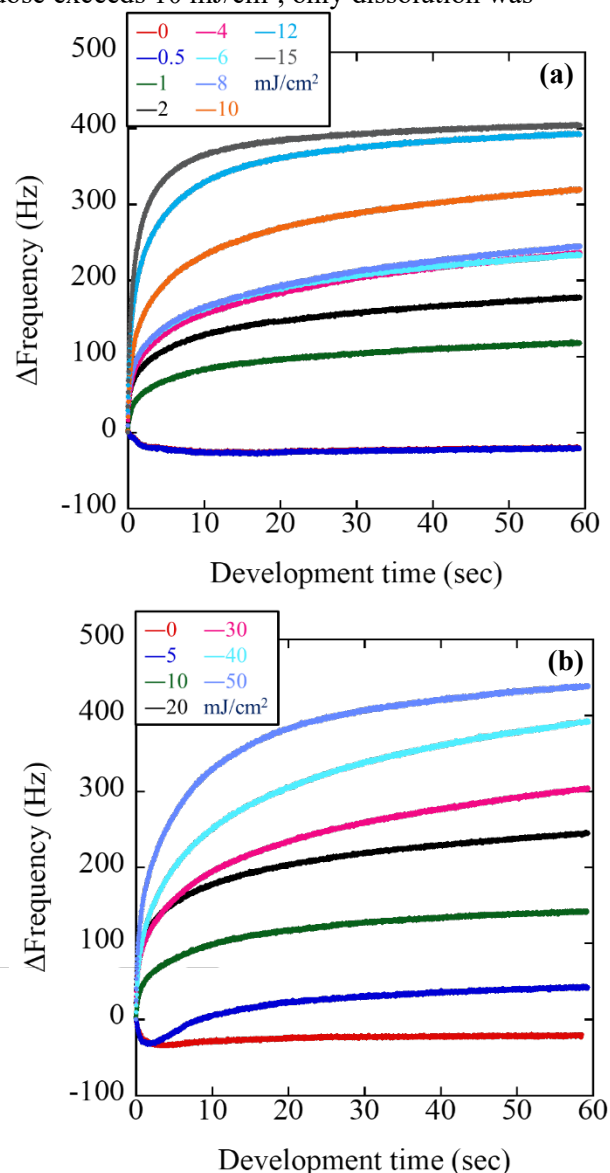
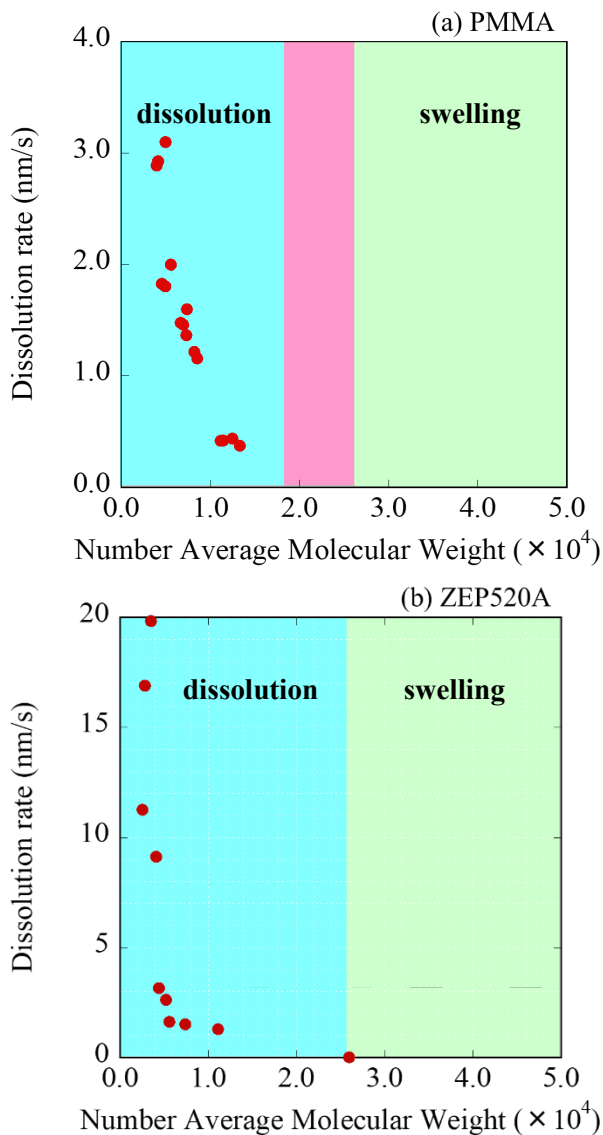


Fig. 5 QCM graphs of (a) ZEP520A and (b) PMMA obtained upon EUV exposure. Horizontal axis: time (s). Vertical axis: frequency (Hz).

observed. On the other hand, this indicates resist swelling. Dissolution rates increase in proportion to exposure doses. Without exposure, 10 nm swelling was observed. Exposure dose exceeds 0.5 mJ/cm², only dissolution can be observed. We couldn't observe resist swelling after EUV exposure. In case of ZEP, dissolution rate doesn't show negative value after EUV exposure.

Fig.6 shows the relationship between dissolution rate and number average molecular weight in (a) PMMA and (b) ZEP520A. Dissolution rates were calculated from QCM results and number average molecular weights were calculated by GPC. The dissolution kinetics of PMMA and ZEP520A are



compared. Dissolution rate of PMMA and ZEP 520A. Fig. 6 Relationship between dissolution rate and number average molecular weight in (a) PMMA and (b) ZEP520A.

520A depend on molecular weight after main chain scission. There are three molecular weight regions in case of PMMA. In small molecular weight region, only dissolution occurs. In middle molecular weight region, PMMA firstly swells and then dissolved into developer. In large molecular weight region, only swellings are observed. By these results, dissolution kinetics of PMMA depends on its molecular weight after irradiation. On the other hand, there are two molecular weight regions in ZEP520A. Small molecular weight region, only dissolution occurs. Large molecular weight region, only swellings are observed. We couldn't observe the middle molecular weight region, where swelling and dissolution occur simultaneously. This region

affects lithographic performance. When EUV and EB are irradiated to resist, exposure dose has special distribution. At development process, resist swelling leads to non-resolvable for sub-10 nm fabrication, and induces pattern defects such as bridge pattern. As for roughness formation, the middle molecular weight region is important. When the resist films are exposed to EUV or EB, exposure dose of pattern edge become low. Therefore, molecular weight of edge area corresponds to this region. Dissolution kinetics of edge part of pattern is complex involving with swelling and dissolution. That's why LWR might increase. Thus, it is important to reduce the middle molecular weight region to improve LWR.

4. Conclusion

The dissolution kinetics and molecular weight in main-chain scission type resists such as PMMA and ZEP520A were investigated using a QCM and GPC to clarify the effects of the molecular weight after polymer degradation on the dissolution kinetics. The G-value of ZEP520A showed higher G-values than that of PMMA. There are three molecular weight regions in PMMA, whereas there are only two molecular weight regions in ZEP520A. The dissolution behavior depends on molecular weight after polymer degradation in both PMMA and ZEP 520A. These results indicate that ZEP520A is better to be better lithographic performance.

References

1. S. Tagawa, S. Nagahara, T. Iwamoto, M. Wakita, T. Kozawa, Y. Yamamoto, D. Werst, and A. D. Trifunac, *Proc. SPIE* **3999**, (2000) 204.
2. T. Kozawa, Y. Yoshida, M. Uesaka, S. Tagawa, *Jpn. J. Appl. Phys.*, **31** (1992) 4301.
3. H. Yamamoto, T. Kozawa, S. Tagawa, H. B. Cao, H. Deng and M. J. Leeson *Jpn. J. Appl. Phys.*, **46** (2007) L142.
4. A. Nakajima, M. Hoshino, M. Hashimoto, and T. Kozawa, *Jpn. J. Appl. Phys.*, **58**, 020909 (2019).
5. A. Nakajima, M. Hoshino, K. Taguchi, and T. Kozawa, *Proc. SPIE*, **11148** 1114814 (2019).
6. A. Shirotori, Y. Vesters, M. Hoshino, A. Rathoreb, D. De Simone, G. Vandenberghe, and H. Matsumoto, *Proc. SPIE*, **11147** 111470J (2019).
7. S. Yasin, D. G. Hasko, and H. Ahmed, *Appl. Phys. Lett.*, **78** (2001) 2760.
8. E. A. Dobisz, S. L. Brandow, R. Bass, and J. Mitterender, *J. Vac. Sci. Technol. B*, **18** (2000) 107.

9. D. R. S. Cumming, S. Thoms, S. P. Beaumont, and J. M. R. Weaver, *Appl. Phys. Lett.*, **68** (1996) 322.
10. M. Khoury and D. K. Ferry, *J. Vac. Sci. Technol., B* **14** (1996) 75.
11. W. Chen and H. Ahmed, *Appl. Phys. Lett.*, **62** (1993) 1499.
12. T. Nishida, M. Notomi, R. Iga, and T. Tamamura., *Jpn. J. Appl. Phys.* **31** (1992) 4508.
13. T. G. Oyama, A. Oshima, H. Yamamoto, S. Tagawa, and M. Washio: *Appl. Phys. Express* **4** (2011) 076501.
14. W. C. Hu, K. Sarveswaran, M. Lieberman, and G. H. Bernstein, *J. Vac. Sci. Technol. B*, **22** (2004) 1711.
15. D. R. S. Cumming, S. Thoms, J. M. R. Weaver, and S. P. Beaumont, *Microelectron. Eng.*, **30** (1996) 423.
16. T. Kozawa, S. Tagawa, T. Kai, and T. Shimokawa, *J. Photopolym. Sci. Technol.*, **20** (2007) 577.
17. T. Ichikawa and H. Yoshida, *J. Polym. Sci. A*, **28** (1990) 1185.
18. G. Geuskens and C. David, *Makromol. Chem.*, **165** (1973) 273.
19. T. Yamaguchi and H. Namatsu, *J. Vac. Sci. Technol. B*, **22** (2004) 1037.
20. T. G. Oyama, K. Enomoto, Y. Hosaka, A. Oshima, M. Washio, and S. Tagawa, *Appl. Phys. Express* **5** (2012) 036501.
21. Y. Hosaka, T. G. Oyama, A. Oshima, S. Enomoto, M. Washio, and S. Tagawa, *J. Photopolym. Sci. Technol.*, **26** (2013) 745.
22. H. Ito, *IBM J. Res. Dev.* **45**, (2001) 683.
23. S. Burns, G. Schmid, B. Trinqué, J. Willson, J. Wunderlich, P. Tsiartas, J. C. Taylor, R. Burns, and C. G. Willson, *Proc. SPIE*, **5039** (2003) 1063.
24. M. Toriumi, J. Santillan, T. Itani, T. Kozawa, and S. Tagawa, *J. Vac. Sci. Technol. B*, **25** (2007) 2486.
25. P. R. Varanasi et al., *Proc. SPIE*, **5753** (2005) 131.
26. T. Itani and J. J. Santillan, *Appl. Phys. Express*, **3** (2010) 061601.
27. A. Tsuneishi, S. Uchiyama, and T. Kozawa, *Jpn. J. Appl. Phys.*, **57** (2018) 046501.
28. A. Nakajima, K. Watanabe, K. Matsuoka, T. Kozawa, Y. Komuro, D. Kawana, and A. Yamazaki, *Proc. SPIE*, **10957** (2019) 109571R.
29. A. C. Ouano, *Polym. Eng. Sci.*, **18** (1978) 306.
30. E. Gipstein, A. C. Ouano, D. E. Johnson, and O. U. Need III, *IBM. J. Res. Dev.*, **21** (1977) 143.
31. A. Nakajima, K. Matsuo, and T. Kozawa, *Appl. Phys. Express.*, **14** (2021) 026501.
32. S. F. Horne, M. M. Besen, D. K. Smith, P. A. Blackborow, R. D'Agostino, *Proc. SPIE*, **6151** (2006) 61510P.
33. A. Sekiguchi, *J. Photopolym. Sci. Technol.* **23** (2010)421.
34. A. Charlesby, *Atomic Radiation and Polymers*, (Pergamon, New York.) (1960).

Designing Er³⁺/Ho³⁺-Doped Near-Infrared (NIR-II) Fluorescent Ceramic Particles for Avoiding Optical Absorption by Water

Masakazu Umezawa,^{1,*} Hiroyuki Kurahashi,¹ Karina Nigoghossian,^{1,2}
Kyohei Okubo,¹ and Kohei Soga¹

¹ *Department of Materials Science and Technology, Faculty of Advanced Engineering, Tokyo University of Science, Katsushika, Tokyo, Japan*

² *Present Affiliation: School of Chemistry, University College Dublin, Belfield, Dublin, Ireland*

**masa-ume@rs.tus.ac.jp*

Rare-earth-doped ceramics, which are near-infrared (NIR) fluorescent materials, have applications as photonic materials in various fields, including medical biology. The NIR wavelength range in which these rare-earth-based materials function is highly transparent in biological tissues and is suitable for deep-tissue imaging. However, the most commonly used 980-nm excitation light is partially absorbed by the water involved in the observation system. In the present study, we focused on the wavelength bands of 800-nm excitation and 1150-nm emission, where no water absorption exists, and investigated the rare-earth doping composition to obtain a ceramic material, NaYF₄, with the above excitation and emission wavelengths. NaYF₄ particles co-doped with rare-earth ions Er³⁺ (sensitizer to 800 nm) and Ho³⁺ (emitter at 1150 nm) were designed for over-1000 nm NIR fluorescent probes. The fluorescence intensity at 1150 nm was maximum at a rare-earth composition of Y³⁺: Er³⁺: Ho³⁺ = 82:14:4 (mol%). The obtained fluorescent Er³⁺/Ho³⁺-doped NaYF₄ particles exhibited a long fluorescence lifetime (3300 ± 120 μs at 25°C), which is characteristic of rare-earth elements. Er³⁺/Ho³⁺-doped NaYF₄ is expected to have applications as a long-lifetime NIR-II fluorescent material with the highest transparency in biological tissues.

Keywords: NIR-II, Fluorescence lifetime, Rare-earth-doped ceramics, 800-nm excitation, Second biological window, Time-gated imaging

1. Introduction

Fluorescence lifetime is a time constant calculated as the decay rate unaffected by the optical loss or fluctuation of the intensity of excitation light. Because the lifetime of a phosphor changes in response to the surrounding environment, such as temperature [1–5] and pH [6–9], it is used for contactless sensing in various applications, including biological tissues. In particular, long-wavelength near-infrared (NIR) light, of wavelengths over-1000 nm (over thousand nanometers (OTN)), is less scattered by biological tissues when compared with ultraviolet (UV), visible, and shorter wavelength NIR lights [10]. Therefore, OTN-NIR light expands the observation depth from several millimeters in UV and visible ranges to 1–2 cm [11]. OTN-NIR has been attracting increasing attention and is called the second biological

window in NIR (NIR-II) [12] to realize biosensing and bioimaging of deep targets in tissues [13]. Various OTN-NIR fluorescent probes have been reported, including organic dyes [14–23], quantum dots [24–28], single-walled carbon nanotubes [29–36], and rare-earth-doped ceramic nanoparticles [5, 37–45]. Among these fluorophores, rare-earth-doped ceramics have the advantages of non-blinking, non-bleaching, and long lifetimes [46,47]

The long fluorescence lifetime of rare-earth-based phosphors can be imaged using time-gated imaging (TGI), a synchronized system of a pulsed laser and detector, in which the fluorescence decay rates are determined for each pixel from a series of decay images [48]. TGI for long-lifetime fluorescent probes can

Received	April 19, 2022
Accepted	June 20, 2022

separate autofluorescence signals and enhance target contrast during imaging [49]. Previous studies have indicated that lifetime-based temperature measurements can be performed using the fluorescence of Nd^{3+} and Yb^{3+} -doped NaYF_4 at 1000 nm under 808-nm excitation with a pulsed laser [5]. However, fluorescence at the wavelength of 1150 nm from Ho^{3+} [38] has not yet been fully utilized, although the OTN-NIR emissions of Ho^{3+} (1150 nm) and Er^{3+} (1550 nm) applicable to luminescent ratiometric thermometers can be obtained by 980-nm excitation [39]. The OTN-NIR light of 1150 nm is useful for deep-tissue imaging in small animals because it is absorbed less by water when compared with the light of 1550-nm wavelength; therefore, sample immersion in an aqueous solution is possible [50]. In addition, because light of 980-nm wavelength is weakly absorbed by water, the temperature of the samples containing water increases when it is irradiated as excitation light. In contrast, the 800-nm wavelength is known as a “heating-free” wavelength because it is not absorbed by water. Therefore, a probe that can emit NIR fluorescence under the 800-nm excitation is expected to be a powerful tool for *in vivo* deep imaging. The objective of this study was to design a rare-earth-based phosphor containing Ho^{3+} that emits fluorescence at 1150 nm upon excitation at 808 nm instead of 980 nm. To achieve this, we investigated the use of Er^{3+} and Nd^{3+} as photosensitizers excited in the 800-nm band [51] to transfer energy to Ho^{3+} .

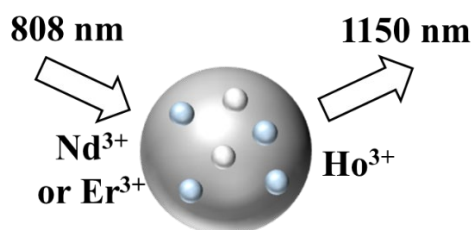


Fig. 1. Rare-earth ions investigated in this study as dopants into NaYF_4 particles. Nd^{3+} and Er^{3+} are used as sensitizers to the 808-nm light. Energy should be transferred to Ho^{3+} to yield the emission of OTN-NIR fluorescence at 1150 nm.

2. Experimental

2.1 Materials

Yttrium(III) nitrate hexahydrate ($\text{Y}(\text{NO}_3)_3 \cdot 6\text{H}_2\text{O}$), neodymium(III) nitrate hexahydrate ($\text{Nd}(\text{NO}_3)_3 \cdot 6\text{H}_2\text{O}$), ytterbium(III) nitrate heptahydrate ($\text{Yb}(\text{NO}_3)_3 \cdot 5\text{H}_2\text{O}$), erbium(III) nitrate heptahydrate ($\text{Er}(\text{NO}_3)_3 \cdot 5\text{H}_2\text{O}$), holmium(III) nitrate heptahydrate ($\text{Ho}(\text{NO}_3)_3 \cdot 5\text{H}_2\text{O}$), and oleic acid were purchased from Sigma-Aldrich Co. (MO, USA). Sodium fluoride (NaF), ammonium fluoride (NH_4F), and decahydronaphthalene (cis/trans isomer mixture) were purchased from Fujifilm Wako Pure Chemical Industries (Tokyo, Japan). All reagents were used without further purification.

2.2 Synthesis and characterization of rare-earth-doped NaYF_4 particles with various dopant concentration ratios

Rare-earth-doped NaYF_4 was synthesized via the coprecipitation method [5,52] to yield hundreds of milligrams of crystals simultaneously. A mixture of $\text{Y}(\text{NO}_3)_3$, $\text{Nd}(\text{NO}_3)_3$, $\text{Yb}(\text{NO}_3)_3$, $\text{Er}(\text{NO}_3)_3$, and $\text{Ho}(\text{NO}_3)_3$ dissolved at the indicated ratios (Table 1, 10 mmol) in 10 mL of distilled water was added to 40 mL of an aqueous solution of NaF (80 mmol) and stirred at 75°C for 60 min. After stirring, the precipitate was collected and washed via centrifugation (20000 g, 10 min, $\times 3$). The precursor samples were dried at 80°C for 24 h and calcined with NH_4F (0.8 g) for 1 h at 550°C under a nitrogen atmosphere. The crystalline phase of the synthesized particles was analyzed by X-ray diffraction (XRD) using RINT-ULTIMA (Rigaku Co., Tokyo, Japan).

2.3 Near-infrared fluorescence spectroscopy

The fluorescence spectra of samples dispersed in a 3:1 (volume ratio) mixture of decahydronaphthalene and oleic acid were analyzed using a spectrometer (NIRQuest; Ocean Optics Inc., FL, USA) under irradiation with 808-nm light from a fiber-coupled laser diode (FL-FCSE08-7-808-200; Focuslight Technologies Inc., Xi'an, China). A long-pass filter (cut-on wavelength 850 nm; #86-452, Edmund Optics Inc., NJ, USA) was placed between the sample and spectrometer to remove the excitation light.

Table 1. Nominal concentrations of rare-earth ions doped into NaYF₄ particles.

	Nd ³⁺ (mol %)	Er ³⁺ (mol %)	Yb ³⁺ (mol %)	Ho ³⁺ (mol %)	Y ³⁺ (mol %)
Nd-Ho Particles	1.5	0	0	2.0	96.5
	3.0	0	0	2.0	95.0
	4.0	0	0	2.0	94.0
Nd-Yb-Ho Particles	1.5	0	28.5	0.5	69.5
	1.5	0	28.5	2.0	68.0
	1.5	0	28.5	4.0	66.0
	1.5	0	28.5	6.0	64.0
Er-Ho _{0.02} Particles	0	3.5	0	2.0	94.5
	0	7.0	0	2.0	91.0
	0	10.5	0	2.0	87.5
	0	14.0	0	2.0	84.0
	0	17.5	0	2.0	80.5
	0	21.0	0	2.0	77.0
	0	21.0	0	2.0	77.0
Er-Ho _{0.04} Particles	0	3.5	0	4.0	92.5
	0	7.0	0	4.0	89.0
	0	10.5	0	4.0	85.5
	0	14.0	0	4.0	82.0
	0	17.5	0	4.0	78.5
	0	21.0	0	4.0	75.0
	0	21.0	0	4.0	75.0
Er-Ho _{0.06} Particles	0	3.5	0	6.0	90.5
	0	7.0	0	6.0	87.0
	0	10.5	0	6.0	83.5
	0	14.0	0	6.0	80.0
	0	17.5	0	6.0	76.5
	0	21.0	0	6.0	73.0
	0	21.0	0	6.0	73.0

2.4 Analysis of fluorescence lifetime

The fluorescence lifetimes of the samples were determined by analyzing their fluorescence decay using an infrared photomultiplier (H10330C; Hamamatsu Photonics Co., Ltd., Shizuoka, Japan) coupled with a spectrometer (CT-25GD; JASCO Co., Tokyo, Japan), connected to a digital oscilloscope (TDS2024C; Tektronix Inc., OR, USA), and excited by pulsed laser light of 808 nm pumped from a laser diode (K808D02FN; BWT Beijing Ltd., Beijing, China). Fluorescence decay images were

acquired using an NIR TGI system composed of synchronized pulsed laser diodes and an NIR camera (ARTCAM-0016TNIR; Artray Co., Ltd., Tokyo, Japan), as described previously [5]. A band-pass filter (1150 ± 50 nm; #85-907, Edmund Optics) was placed between the sample and NIR camera to collect fluorescence decay images at a wavelength of 1150 nm.

3. Results

3.1 Crystalline phase of rare-earth-doped NaYF₄ particle samples

First, the crystalline phase of rare-earth-doped

NaYF₄ synthesized via the coprecipitation method was analyzed using XRD. Of the α and β phases of NaYF₄, the β -phase generally exhibited a higher fluorescence intensity [53] probably because of its lower phonon energy than that of the α -phase crystal [54]. The XRD results indicated that β -NaYF₄ was mainly obtained by calcination at 550°C from the α -NaYF₄ precursors (Fig. 2a), regardless of the

doping concentrations of rare-earth ions, Nd³⁺, Yb³⁺, Er³⁺, and Ho³⁺ (Fig. 2a-c). NaYF₄ with a high concentration of Ho³⁺ (4–6 mol%) and Yb³⁺ (28.5 mol%) tended to contain the α -phase. This is because the crystal lattice is disrupted by doping with rare-earth ions with slightly different ionic radii, making the phase transitions from α -NaYF₄ to β -NaYF₄ less likely to occur during calcination.

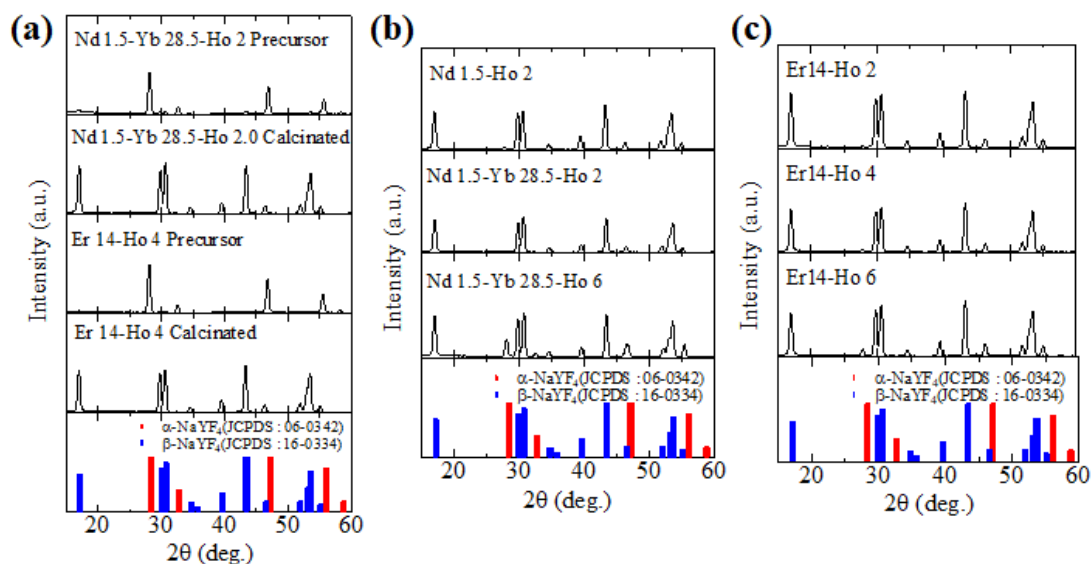


Fig. 2. Typical XRD patterns of rare-earth-doped NaYF₄ particles synthesized via coprecipitation method. (a) Fluoride precursor and calcinated NaYF₄ particles. Calcinated NaYF₄ particles doped with (b) Nd³⁺ and Ho³⁺ with and without Yb³⁺ and (c) Er³⁺ and Ho³⁺ majorly exhibited crystalline structure of hexagonal β -phase (JCPDS 16-0334) with minor signals of cubic α -phase (JCPDS 06-0342).

3.2 Near-infrared fluorescence of rare-earth-doped NaYF₄ particle samples obtained using Nd³⁺ as a photosensitizer to 808-nm light

The β -NaYF₄ doped with Nd³⁺ and Ho³⁺ (NaYF₄:Nd³⁺/Ho³⁺) emitted fluorescence at wavelengths of 1060 nm (Nd³⁺: ⁴F_{3/2} → ⁴I_{11/2}), 1150 nm (Ho³⁺: ⁵I₆ → ⁵I₈), and 1330 nm (Nd³⁺: ⁴F_{3/2} → ⁴I_{13/2}) (Fig. 3a); NaYF₄ doped with Nd³⁺, Yb³⁺, and Ho³⁺ (NaYF₄:Nd³⁺/Yb³⁺/Ho³⁺) emitted fluorescence at wavelengths of 980 nm (Yb³⁺: ²F_{5/2} → ²F_{7/2}) and 1150 nm (Ho³⁺: ⁵I₆ → ⁵I₈) (Fig. 3b) under 808-nm laser excitation (Nd³⁺: ⁴I_{9/2} → ⁴F_{5/2}) based on the energy diagram (Fig. 3c). Comparing NaYF₄ co-doped with Nd³⁺ at 1.5 mol% and Ho³⁺ at 2.0 mol% with and without Yb³⁺ at 28.5 mol%, (NaY_{0.68}F₄: Nd³⁺_{0.015}/Yb³⁺_{0.285}/Ho³⁺_{0.02} and NaY_{0.965}F₄: Nd³⁺_{0.015}/Ho³⁺_{0.02}), the intensity of Ho³⁺-derived

fluorescence (1150 nm) was 3.7 times higher in the sample with Yb³⁺ (Fig. 3b, Table 2) when compared with the sample without Yb³⁺ (Fig. 3a, Table 2). This result indicates that Yb³⁺ bridges the energy transfer from Nd³⁺ excited by 808-nm light to Ho³⁺. Therefore, Nd³⁺/Yb³⁺/Ho³⁺ instead of Nd³⁺/Ho³⁺ is a more appropriate combination of rare-earth ions to obtain fluorescence at 1150 nm. In this tri-doped sample, the fluorescence intensity at 1150 nm was the highest when Ho³⁺ was doped at 2.0 mol% and decreased with higher concentrations of Ho³⁺ probably owing to concentration quenching (Fig. 3a, Table 2). Therefore, doping of Ho³⁺ at 2.0 mol% is optimal for NaYF₄ with Nd³⁺ (1.5 mol%) and Yb³⁺ (28.5 mol%). However, because the concentration combinations to be investigated for the tri-doped samples were complex, NaYF₄:Er³⁺/Ho³⁺ was used instead of NaYF₄:Nd³⁺/Yb³⁺/Ho³⁺ in the experiments.

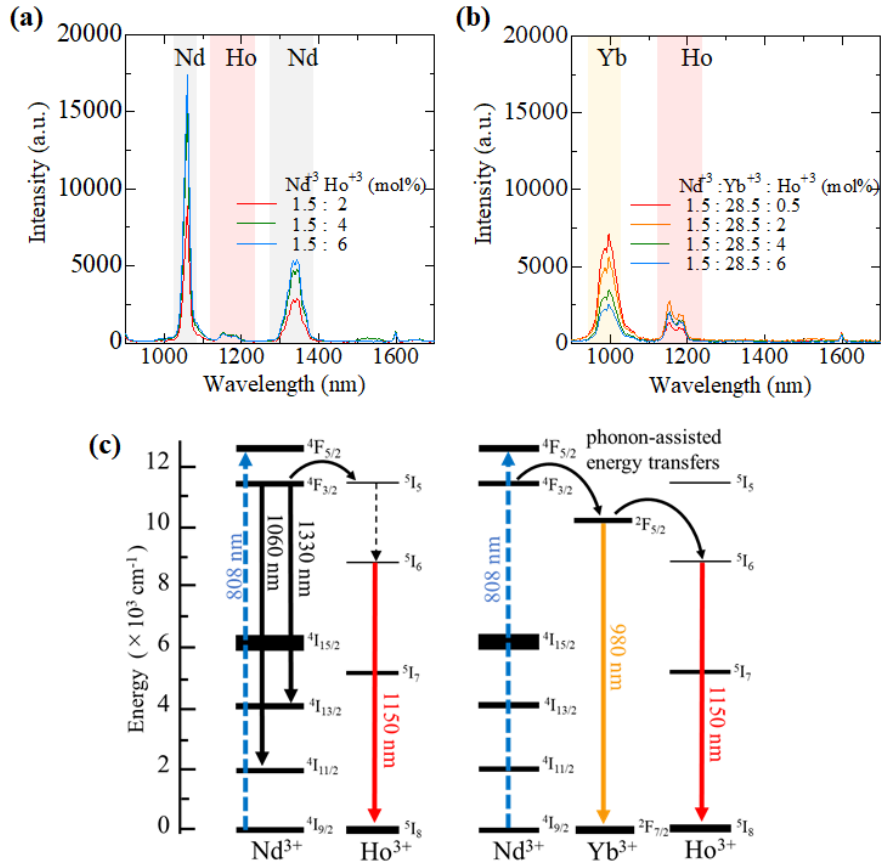


Fig. 3. Near-infrared fluorescence spectra of (a) NaYF₄:Nd³⁺/Ho³⁺, (b) NaYF₄:Nd³⁺/Yb³⁺/Ho³⁺, and (c) their energy diagrams. Fluorescence spectra were collected under optical excitation (wavelength 808 nm, power density 60 W/cm²).

Table 2. Relation between concentrations of doping of Nd³⁺, Yb³⁺, and Ho³⁺ to NaYF₄ and fluorescence intensity at 1150 nm.

	Nd ³⁺ (mol %)	Yb ³⁺ (mol %)	Ho ³⁺ (mol %)	Fluorescence intensity at 1150 nm (a. u.)
Nd-Ho	1.5	0	2.0	65
	3.0	0	2.0	71
	4.0	0	2.0	62
Nd-Yb-Ho	1.5	28.5	0.5	136
	1.5	28.5	2.0	243
	1.5	28.5	4.0	202
	1.5	28.5	6.0	178

The fluorescence intensity was obtained by integration within the range of 1129–1207 nm.

3.3 Near-infrared fluorescence of rare-earth-doped NaYF₄ particle samples obtained using Er³⁺ as photosensitizer to 808-nm light

β -NaYF₄ doped with Er³⁺ and Ho³⁺ (NaYF₄:

Er³⁺/Ho³⁺) emitted OTN-NIR fluorescence at wavelengths of 1150 nm (Ho³⁺: ⁵I₆→⁵I₈) and 1550 nm (⁴I_{13/2}→⁴I_{15/2}) with a minor peak at 980 nm (Er³⁺: ⁴I_{11/2}→⁴I_{15/2}) under 808-nm laser excitation (Er³⁺: ⁴I_{15/2}→⁴I_{9/2}) based on the energy diagram (Fig. 4). While the emission intensities of both 1150- and 1550-nm wavelengths varied with the doping concentrations of Er³⁺ and Ho³⁺, the emission at 1150 nm was the highest when Er³⁺ and Ho³⁺ were doped at 14 and 4 mol%, respectively, into NaYF₄ (Table 3).

In the NaYF₄:Er³⁺/Ho³⁺ particles, Er³⁺ acts as a photosensitizer absorbing the energy of 808-nm light. Therefore, up to a certain Er³⁺ concentration (10.5–14.0 mol%), the fluorescence intensity at both 1150- and 1550-nm wavelengths increased with an increase in its doping concentration (Fig. 4b, Table 3). The fluorescence intensity at 1150 nm (Ho³⁺) decreased at higher Er³⁺ concentrations because the emission at 1550 nm (Er³⁺) became more dominant than that at 1150 nm (Fig. 4, Table 3). An increase in the Ho³⁺ doping concentration

decreased the emission not only at 1550 nm (Er^{3+}) of $\text{NaYF}_4:\text{Er}^{3+}/\text{Ho}^{3+}$ but also at 1150 nm (Ho^{3+}) at 6 mol% of Ho^{3+} (Table 3), probably because of concentration quenching. This is similar to the case of $\text{NaYF}_4:\text{Nd}^{3+}/\text{Yb}^{3+}/\text{Ho}^{3+}$. Therefore, the optimal doping concentrations of Er^{3+} and Ho^{3+} were 14 and 4 mol% to obtain the highest fluorescence at 1150 nm (Ho^{3+}) from $\text{NaYF}_4:\text{Er}^{3+}/\text{Ho}^{3+}$ under optical excitation by 808-nm light. The upconversion emission of $\text{Er}^{3+}/\text{Ho}^{3+}$ -doped fluoride ceramic nanoparticles has been previously reported [55]. $\text{NaErF}_4:\text{Ho}@\text{NaYF}_4$ core-shell nanoparticles (Ho^{3+} 0.1-0.5 mol%) emit 1150-nm light under 1530-nm excitation via upconversion. $\text{NaErF}_4:\text{Ho}@\text{NaYF}_4$ also emits red upconversion emission at 660 nm under 808-nm excitation [55]. Instead of upconversion emissions, we found that a biologically more transparent OTN-NIR emission at 1150 nm can be obtained under 808-nm excitation by co-doping Er^{3+} and

Ho^{3+} without a core-shell nanostructure.

Table 3. Relation between concentrations of doping of Er^{3+} and Ho^{3+} to NaYF_4 and fluorescence intensity at 1150 nm (Ho^{3+}) and 1550 nm (Er^{3+}).

Fluorescence		Er^{3+} (mol %)					
(1150 nm)		3.5	7.0	10.5	14.0	17.5	21.0
Ho^{3+} (mol %)	2.0	79	446	387	575	655	625
	4.0	166	405	403	669	471	286
	6.0	264	429	517	485	460	460
Fluorescence		Er^{3+} (mol %)					
(1550 nm) ($\times 10$)		3.5	7.0	10.5	14.0	17.5	21.0
Ho^{3+} (mol %)	2.0	266	489	651	921	833	1210
	4.0	99	270	270	366	333	393
	6.0	56	147	246	212	254	365

The fluorescence intensities at 1150 and 1550 nm were obtained by integration within the ranges of 1129–1207 nm and 1469–1589 nm, respectively.

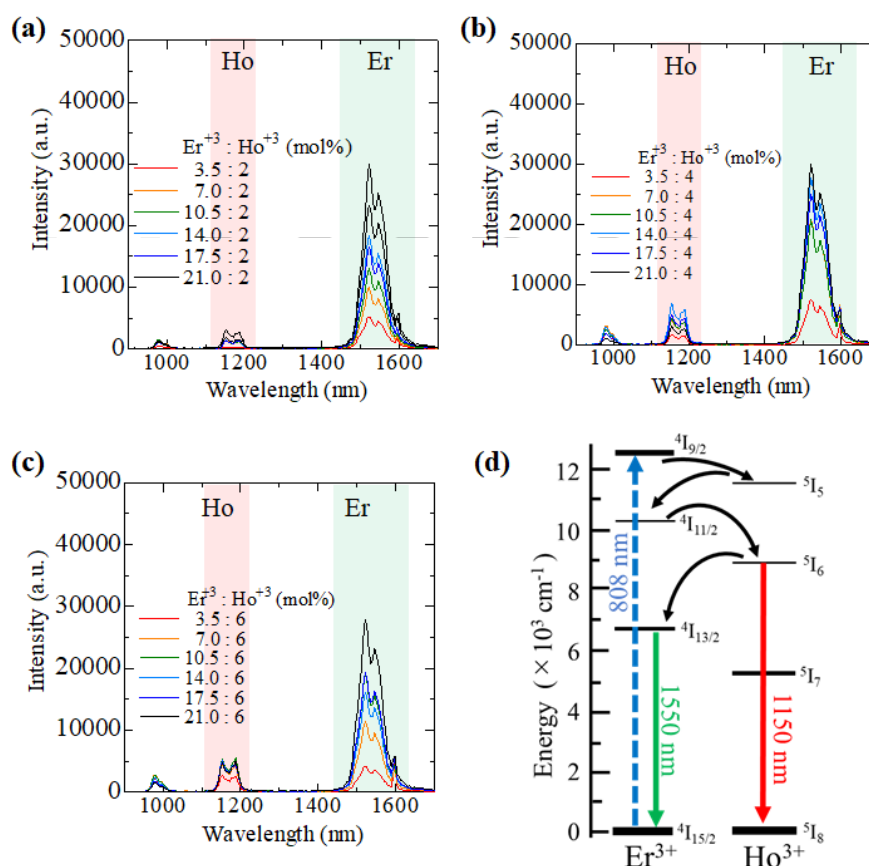


Fig. 4. Near-infrared fluorescence spectra of $\text{NaYF}_4:\text{Er}^{3+}/\text{Ho}^{3+}$. Fluorescence of samples doped with Ho^{3+} at (a) 2.0 mol%, (b) 4.0 mol%, and (c) 6.0 mol%, and (d) related energy diagrams. Fluorescence spectra were collected under optical excitation (wavelength 808 nm, power density 47 W/cm^2).

3.4 Fluorescence lifetime of Er^{3+} and Ho^{3+} -doped NaYF_4 particles

Finally, the fluorescence lifetime of the emission of $\text{NaYF}_4:\text{Er}^{3+}/\text{Ho}^{3+}$ ($\text{Y}^{3+}:\text{Er}^{3+}:\text{Ho}^{3+} = 82:14:4$ mol%) at 1150 nm ($\text{Ho}^{3+}:^5\text{I}_6 \rightarrow ^5\text{I}_8$) was analyzed at 25°C under optical irradiation with 808-nm light. As depicted in Fig. 5a, the fluorescence lifetime of $\text{NaYF}_4:\text{Er}^{3+}/\text{Ho}^{3+}$ is 3.26 μs , which is a characteristic typical of rare-earth-doped ceramics. This fluorescence decay was also observed using the NIR camera in the TGI system (Fig. 5b,c). The TGI data also indicated a fluorescence lifetime of 3.30 ± 0.12 ms for the $\text{NaYF}_4:\text{Er}^{3+}/\text{Ho}^{3+}$. Its lifetime was

longer than previously reported rare-earth-doped ceramics, several hundreds of microseconds to 1.5 ms of $\text{NaYF}_4:\text{Nd}^{3+}/\text{Yb}^{3+}$ [5,40] and $\text{NaGdF}_4:\text{Yb}^{3+}/\text{Ho}^{3+}$ [56]. The long fluorescence lifetime of $\text{NaYF}_4:\text{Er}^{3+}/\text{Ho}^{3+}$ was attributed to multiple phonon-assisted energy transfers between Er^{3+} and Ho^{3+} (Fig. 4d), which emitted fluorescence at 1150 nm under optical excitation at 808 nm. Such a long lifetime (several milliseconds) has also been reported for multi-core/shell NaGdF_4 nanoparticles doped with Nd^{3+} , Yb^{3+} , and Er^{3+} emitting fluorescence at 1550 nm via relayed energy transfer [56].

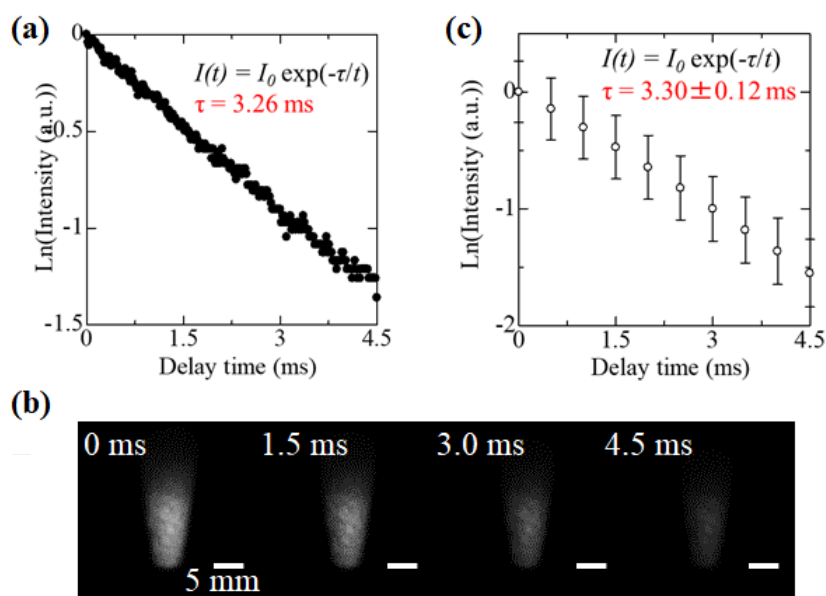


Fig. 5. Fluorescence decay of the emission of $\text{NaY}_{0.82}\text{F}_4:\text{Er}^{3+}_{0.14}/\text{Ho}^{3+}_{0.04}$ to determine its fluorescence lifetime at 25°C. (a) Fluorescence decay detected by photomultiplier coupled with spectrometer to obtain data on the light of wavelength 1150 nm. (b) Typical images of fluorescence decay acquired at indicated time (delay time) after cutting off the pulsed laser light of 808 nm for excitation in a time-gated imaging (TGI) system for near-infrared (NIR) fluorescence. (c) Fluorescence decay profile observed by the NIR fluorescence TGI.

4. Conclusion

NaYF_4 particles co-doped with the rare-earth ions Er^{3+} and Ho^{3+} were designed as OTN-NIR fluorescent probes emitting 1150 nm under excitation at 808 nm, which is less absorbed by water in biological tissues when compared with the light at 980 nm and 1420–1500 nm. NaYF_4 doped with Nd^{3+} , Yb^{3+} , and Ho^{3+} also emits 1150-nm fluorescence under excitation by 808-nm light; however, a core-shell structure separating the sensitizer in the shell and emissive ions in the core is usually required to

obtain highly emissive fluorescent nanomaterials. In this study, we proposed the use of Er^{3+} as a sensitizer at 800 nm and found that the fluorescence intensity at 1150 nm was maximized at a rare-earth $\text{Y}^{3+}:\text{Er}^{3+}:\text{Ho}^{3+}$ concentration of 82:14:4 (mol%) without complex core-shell structures. The obtained fluorescent material $\text{NaYF}_4:\text{Er}^{3+}/\text{Ho}^{3+}$ exhibited a long fluorescence lifetime (3.3 ms, 25°C) owing to the presence of multiple phonon-assisted energy transfers within the process of 1150-nm emission following 808-nm excitation. Therefore, while the Nd^{3+} energy

levels of electrons are not resonant with those of Ho^{3+} or Er^{3+} , energy is transferred from Er^{3+} , which can be excited by 800-nm light, to Ho^{3+} . $\text{Er}^{3+}/\text{Ho}^{3+}$ -doped NaYF_4 is expected to be used as a long-lifetime NIR-II fluorescent material with the highest transparency in biological tissues.

Acknowledgement

This work was supported by Japan Society for the Promotion of Science through KAKENHI (Grant numbers: 19H01179, 22K06565).

References

1. K. Okabe et al., *Nat. Commun.*, **3** (2012) 705.
2. H. Li et al., *J. Mater. Chem. B*, **6** (2018) 5078.
3. S. Gharouel et al., *J. Lumin.*, **201** (2018) 372.
4. M. Back et al., *ACS Appl. Mater. Interfaces*, **10** (2018) 41512.
5. T. Chihara et al., *Sci. Rep.*, **9** (2019) 12806.
6. H. J. Lin et al., *Cytometry*, **52A** (2003) 77.
7. M. Y. Berezin et al., *Biophys. J.*, **100** (2011) P2063.
8. R. Tang et al., *J. Am. Chem. Soc.*, **134** (2012) 4545.
9. L. Jin et al., *Analyst*, **144** (2019) 3533.
10. R. R. Anderson et al., *J. Invest. Dermatol.*, **77** (1981) 13.
11. Zako T, et al., *Biomater. Sci.*, **3** (2015) 59.
12. A. M. Smith et al., *Nat. Nanotechnol.*, **4** (2010) 710.
13. K. Soga, M. Umezawa, K. Okubo (eds), *Transparency in Biology: Making Invisible Visible*. Springer (2021).
14. Z. Tao et al., *Angew. Chem. Int. Ed.*, **52** (2013) 13002.
15. L. Antaris et al., *Nat. Mater.*, **15** (2016) 235.
16. X. D. Zhang et al., *Adv. Mater.*, **28** (2016) 6872.
17. M. Kamimura et al., *Polym. J.*, **49** (2017) 799.
18. M. Kamimura et al., *J. Photopolym. Sci. Technol.*, **32** (2019) 93.
19. M. Umezawa et al., *ACS Omega*, **7** (2022) 5817.
20. Y. Ueya et al., *ACS Nanosci. Au*, **1** (2021) 68.
21. K. Ichihashi et al., *RSC Adv.*, **12** (2022) 710.
22. M. Umezawa et al., *ACS Omega*, **7** (2022) 5817.
23. Y. Ueya et al., *Anal. Sci.*, **38** (2022) 199.
24. X. Michalet et al., *Science*, **307** (2005) 538.
25. A. Sasaki et al., *Nanoscale*, **7** (2015) 5115.
26. T. Kameyama et al., *Nanoscale*, **8** (2016) 5435.
27. H. Yukawa et al., *Anal. Sci.*, **34** (2018) 525.
28. D. H. Ortgies et al., *Nano Res.*, **12** (2019) 749.
29. S. M. Bachilo et al., *Science*, **298** (2002) 2361.
30. S. Ghosh et al., *Science*, **330** (2010) 1656.
31. K. Welsher et al., *PNAS*, **108** (2011) 8943.
32. G. Hong et al., *Nat. Photonics*, **8** (2014) 723.
33. Y. Yomogida et al., *Nat. Commun.*, **7** (2016) 12056.
34. M. Yudasaka et al., *Sci. Rep.*, **7** (2017) 44760.
35. Y. Iizumi et al., *Sci. Rep.*, **8** (2018) 6272.
36. S. Sekiyama et al., *Langmuir*, **35** (2019) 831.
37. E. Hemmer et al., *Nanoscale*, **5** (2013) 11339.
38. D. J. Naczynski et al., *Nat. Commun.*, **4** (2013) 2199.
39. M. Kamimura et al., *J. Mater. Chem. B*, **5** (2017) 1917.
40. D. H. Ortgies et al., *ACS Nano*, **12** (2018) 4362.
41. S. Sekiyama et al., *Sci. Rep.*, **8** (2018) 16979.
42. T. Kuchimaru et al., *Nat. Commun.*, **9** (2018) 2981.
43. Y. Ren et al., *Nanoscale*, **12** (2020) 11510.
44. G. Yeroslavsky et al., *J. Photopolym. Sci. Technol.*, **33** (2020) 129.
45. K. Okubo et al., *Sci. Technol. Adv. Mater.*, **21** (2021) 160.
46. D. Jaque et al., *Adv. Opt. Photon.*, **8** (2016) 1-103.
47. K. Soga et al., *J. Imaging Soc. Jpn.*, **58** (2019) 602.
48. L. Gu et al., *Nat. Commun.*, **4** (2013) 2326.
49. B. D. Rosal et al., *Adv. Mater.*, **28** (2016) 10118.
50. M. Umezawa et al., *J. Biophotonics*, **13** (2020) e202000071.
51. Z. Wang, B. Zing, *Chem. Asian J.*, **15** (2020) 2076.
52. Y. Yao et al., *J. Mater. Sci.*, **51** (2016) 5460.
53. F. Wang et al., *Nature*, **463** (2010) 1061.
54. K. Okubo et al., *ECS J. Solid State Sci. Technol.*, **10** (2021) 096006.
55. L. Yan et al., *Nanoscale*, **10** (2018) 17949.
56. Y. Fan et al., *Nat. Nanotechnol.*, **13** (2018) 941.

Effect of Modified Chemical Junction of a Diblock Copolymer on the Microphase Separation Behavior

Yoshihiro Agata¹, Yuta Nabae¹, Toshiaki Ougizawa¹, and Teruaki Hayakawa^{1*}

¹ Department of Materials Science and Engineering, School of Materials and Chemical Technology, Tokyo Institute of Technology, 2-12-1 Ookayama, Meguro-ku, Tokyo 152-8552, Japan
*hayakawa.t.ac@m.titech.ac.jp

A polystyrene-*b*-poly(methylmethacrylate) (PS-*b*-PMMA) modified with a fluorine-containing functional group at its chemical junction was designed to study the effect of the modified chemical junction on the microphase separation behavior. Various molecular weights of modified and unmodified PS-*b*-PMMA were synthesized, and effective χ parameter for them were estimated by small-angle X-ray scattering. The effect of the modified chemical junction was clearly observed in the measured effective χ parameters for the block copolymers below 200 of degree of polymerization. In contrast, the modified PS-*b*-PMMA over 200 of degree of polymerization showed quite similar behavior to the unmodified PS-*b*-PMMA.

Keywords: Chemical junction, Block copolymer, χ parameter

1. Introduction

The microphase separation of block copolymer (BCP) has been of interest to many scientists, because it has a wide range of potential applications such as BCP lithography and porous materials [1-5]. Many BCPs have been designed and synthesized, and various microphase-separated structures such as lamella, cylinder, sphere and double-gyroid have been reported [6,7]. Such microphase separation behavior of BCP is often characterized with the Flory-Huggins interaction parameter, χ [8,9]. For the BCP lithography, BCPs with high χ parameters are particularly desired to provide a lamellar structure with a small domain spacing [10-12]. If one desired a complex structure such as double-gyroid, predicting and measuring the χ parameter of newly designed BCP are essential to focus the narrow window of volume fraction in the phase diagram. In this context, understanding the correlation between the molecular design and χ parameter of BCP is extremely important.

For actual discussion regarding the χ parameter for a synthesized BCP, effective χ parameter, χ_{eff} , is often estimated by the random phase approximation (RPA) method, which analyzes scattering data obtained by small-angle X-ray scattering (SAXS) or

small-angle neutron scattering [13,14]. The RPA method for polymer melts is derived from the Landau type mean-field theory developed by Leibler, and the scattering intensity is given as

$$I(q) = A_0 / (S(q) / W(q) - 2\chi_{\text{eff}}) \quad (1)$$

where $I(q)$ is scattering intensity, A_0 is constant, and $S(q)$ and $W(q)$ are scattering functions. While the theoretical χ parameters for BCP are independent of their molecular weights, the effect of functional groups at the chain ends on the physical property cannot be neglected in actual BCP [15,16], and measured χ_{eff} can be affected by their molecular weight, especially in the range of low molecular weights. Besides, if the nature of the chemical junction is different from that of the

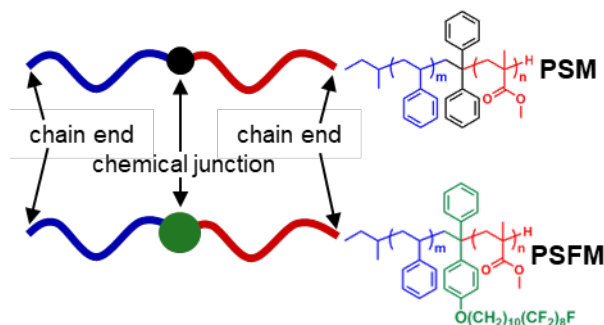
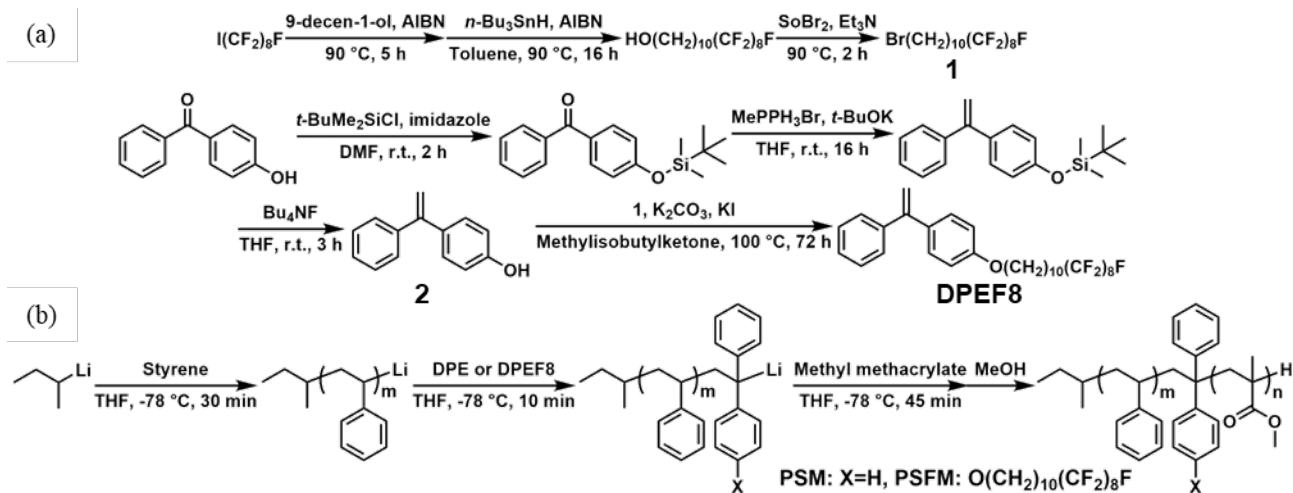


Fig. 1. Schematic image of polymers in this study.

Received March 31, 2022

Accepted June 25, 2022



Scheme 1. Synthetic routes of (a) DPEF8 and (b) diblock copolymers, PSM and PSFM.

polymer chains, it might also affect their measured χ_{eff} . Indeed, some studies have reported that the interfacial width and line edge roughness for lamellar structure decreased by modifying the chemical junctions of BCP [17-20].

In this context, our research group is interested in how a slight difference at the chemical junction of a BCP affects its microphase separation behavior. In this study, we have designed and synthesized a polystyrene-*b*-poly(methyl methacrylate) (PS-*b*-PMMA) modified with a fluorine-containing functional group at the chemical junction (Fig. 1), with various molecular weights below 28,000 of number average molecular weight (M_n) via the route shown in Scheme 1. The effect of the chemical modification on the microphase separation behavior is discussed by investigating χ_{eff} of the synthesized polymers.

2. Experimental

2.1. Materials

Two precursors, 11,11,12,12,13,13,14,14,15,15,16,16,17,17,18,18,18-heptafluorooctadecanol (**1**) and 1-(4-hydroxyphenyl)-1-phenyl ethylene (**2**), were synthesized according to the procedure described by Obers and Summers respectively [21,22]. Styrene was purchased from Tokyo Chemical Industry (TCI), distilled over CaH_2 under reduced pressure, degassed by freeze-pump-thaw cycling, and further distilled over di-*n*-butylmagnesium. Methyl methacrylate (MMA) was purchased from TCI, distilled over CaH_2 under reduced pressure, degassed by freeze-pump-thaw cycling, and further distilled over trioctylaluminum. 1,1-diphenyl ethylene (DPE) was purchased from TCI and distilled over *n*-butyllithium under reduced pressure. Azobisisobutyronitrile (AIBN) was

purchased from TCI and recrystallized from methanol. *Sec*-butyllithium (*s*-BuLi), tetrahydrofuran (THF), lithium chloride (LiCl), and all the other chemicals were reagent grade and used as received unless otherwise stated.

2.2. Measurement

Nuclear magnetic resonance (NMR) spectra were recorded with a JEOL ECS400 spectrometer (400 MHz). Size-exclusion chromatography (SEC) was performed with THF as the eluent, using a Shimadzu Prominence501 system equipped with a Shodex RI-501 detector and a Shodex LF-804 column. The number-average molecular weight (M_n) and polydispersity index (D) were determined relative to polystyrene standards. Small-angle X-ray scattering (SAXS) was recorded with a Bruker NanoSTAR (50 kV/50 mA) equipped with a Vantec500 detector at 1055 mm of camera length.

2.3. Synthesis of 1-(4-(11,11,12,12,13,13,14,14,15,15,16,16,17,17,18,18,18-heptafluorooctadecyloxy)phenyl)-1-phenyl ethylene (DPEF8)

In a 100 mL flask, 2.13 g of **1** (3.33 mmol), 0.81 g of **2** (4.11 mmol), 0.55 g of potassium carbonate (4.00 mmol), and 0.033 g of potassium iodide (0.20 mmol) were stirred with 5.7 mL of methylisobutylketone at 100 °C for 72 hours (Scheme 1a). The product was poured into 100 mL of 1:1 water/methanol solution, and the precipitate was collected by filtration. The obtained yellow solid was purified by silica gel column chromatography with *n*-hexane, and recrystallized from toluene to obtain a white solid (0.30 g, 12 % yield). TLC (SiO_2 , hexane): $R_f = 0.30$. ^1H NMR (400 MHz, CDCl_3 , δ , ppm): 7.34-7.31, 7.27-7.25, 6.86, 6.84 (m; aromatic CH), 5.39, 5.34 (d; =CH₂),

3.98, 3.97, 3.95 (t; OCH₂), 2.12-1.98 (m; CF₂CH₂), 1.82, 1.81, 1.79, 1.77, 1.75 (q; OCH₂CH₂), 1.64, 1.62, 1.60, 1.58, 1.56 (q; CF₂CH₂CH₂), 1.50-1.25 (m; CH₂). ¹³C NMR (100 MHz, CDCl₃, δ, ppm): 149.52, 141.85, 133.73, 129.35, 128.33, 128.11, 127.63, 114.02, 112.86, 67.96, 30.86, 29.47-29.10, 26.05, 20.08. ¹⁹F NMR (400 MHz, C₆F₆, δ, ppm): -81.87, -115.55, -122.80, -123.01, -123.81, -124.61, -127.22.

2.4. Synthesis of block copolymers

The synthetic manner for a typical BCP is as follows (Scheme 1b). The polymerization was performed under an argon atmosphere. To a round bottom flask sealed with a stopcock and septum was added 21.0 mg of LiCl (0.495 mmol) and 10 mL of THF. The flask was chilled to -78 °C. 0.50 mL of *s*-BuLi was added, changing the color to yellow, and stirred for a few minutes. The flask was then allowed to warm to room temperature and kept until the solution became colorless. After returning the flask to -78 °C, 0.044 mL of *s*-BuLi (0.055 mmol) was added followed immediately by 0.50 mL of styrene (4.4 mmol), changing the color to orange, and stirred for 30 minutes. 82 mg of DPEF8 (0.11 mmol) in 10 mL of THF was added, changing the color to dark red, and stirred for 10 minutes. 0.45 mL of MMA (4.3 mmol) was added, changing the color to colorless, and stirred for 45 minutes before being terminated by adding 5 mL of argon bubbled methanol. The product was precipitated into 400 mL of methanol, filtered, washed by Soxhlet extraction with a 1:1 hexane/cyclohexane solution for 16 hours, and dried under reduced pressure at 40 °C to obtain block copolymers (PSFM14) as a white powder (0.49 g, 56 % yield). M_n : 14.4 kg mol⁻¹, D : 1.04,

f_{PS} : 0.50. ¹H NMR (400 MHz, CDCl₃, δ, ppm): 7.22-6.82 (br; m-, p-aromatic), 6.73-6.23 (br; o-aromatic), 3.60 (s; -(C=O)O-CH₃), 2.23-1.65, 1.52-1.24, 1.07-0.95, 0.93-0.73 (br; backbones). ¹⁹F NMR (400 MHz, C₆F₆, δ, ppm): -81.87, -115.58, -122.89, -123.07, -123.87, -124.67, -127.25.

Other BCPs (PSFM16, PSFM18, and PSFM28) were synthesized in a similar manner but changed the monomer/initiator ratio.

Unmodified PS-*b*-PMMA samples (PSM15, PSM21, PSM25 and PSM27) were also synthesized from DPE instead of DPEF8 in THF.

2.5. Effective χ parameter estimation

χ_{eff} was estimated by the RPA method [14]. Polymer powder was filled into a quartz capillary and heated at 200 °C for 1 hour. Temperature-controlled SAXS measurements for a polymer were carried out above the highest T_g (around 120 °C) of the BCP under reduced pressure. The temperatures were held for 30 minutes, and then the spectra were recorded during the following 30 minutes. The obtained spectra were fitted by equation (1) to evaluate χ_{eff} of the measured polymer. The degree of polymerization (N) of each segment was normalized with respect to a common reference volume ($v_0 = 118 \text{ \AA}^3$).

3. Results and discussion

3.1. Synthesis and characterization of BCP

The designed BCPs were synthesized by living anionic polymerization with DPEF8 under an argon atmosphere. The results of characterization are summarized in Table 1. The crude BCPs after the polymerization showed bimodal SEC curves,

Table 1. Results of the characterization for the synthesized polymers.

samples	M_n^a (kg mol ⁻¹)	D^a	N_{total}^b	f_{PS}^c (vol%)	f_{junction}^c (vol%)	α^d	β^d	χ_{eff}^e at 250 °C	χ_{eff}^e at 200 °C	χ_{eff}^e at 150 °C
PSFM14	14.4	1.04	134	48	4	-0.065	47.1	0.026	0.035	0.047
PSFM16	16.0	1.05	148	48	4	-0.029	30.9	0.030	0.036	0.044
PSFM18	18.3	1.03	171	53	3	-0.0013	18.8	0.035	0.039	0.043
PSFM28	27.5	1.02	263	36	2	0.026	4.11	0.034	0.035	0.036
PSM15	14.6	1.04	140	53	1	-0.0080	21.5	0.033	0.037	0.043
PSM21	20.7	1.04	201	48	1	0.015	9.92	0.034	0.036	0.038
PSM25	25.1	1.04	245	41	1	0.019	7.69	0.034	0.035	0.037
PSM27	26.6	1.03	259	43	1	0.024	3.21	0.031	0.031	0.032

^a Determined by SEC. ^b Calculated from M_n , f_{PS} and f_{junction} . ^c Determined by ¹H NMR. ^d Determined by the RPA method. ^e Calculated by $\chi = \alpha + \beta/T$.

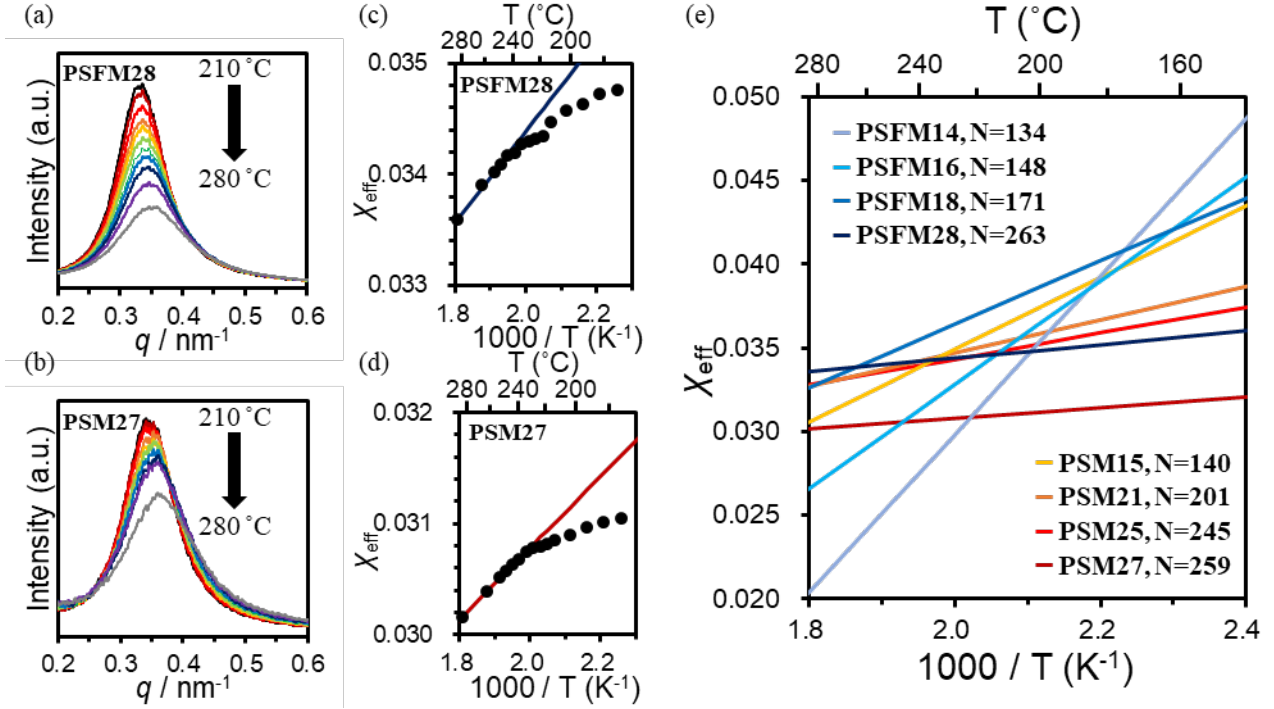


Fig. 2. SAXS profiles of (a) PSFM28 and (b) PSM27, and plots of χ_{eff} against temperature of (c) PSFM28 and (d) PSM27. Temperature dependencies of each sample are summarized in (e).

suggesting the formation of PS homopolymer end-capped by DPEF8 or terminated by impurities, such as air or water. Therefore, we performed the Soxhlet extraction for purification, and the D for all the purified polymers were found to be below 1.05, accompanied by unimodal SEC curves. Control samples with unmodified PS-*b*-PMMA were also successfully prepared, as shown in Table 1. The RPA method requires relatively low molecular weights of BCPs because the SAXS spectra needs to be recorded in the mean-field region. Therefore, this study investigated BCPs with M_n below 28000.

3.2. Estimation of effective χ parameter

The results of temperature-controlled SAXS measurement for PSFM28 and PSM27 are shown in Fig. 2a and Fig. 2b, respectively. These SAXS profiles were fitted by equation (1), and the evaluated χ_{eff} against temperature (Fig. 2c and Fig. 2d.) As the plots above 250 °C showed good linearity and seem to be in the mean-field region, linear regression for the plots over 250 °C was performed, and α and β for $\chi = \alpha + \beta/T$ were

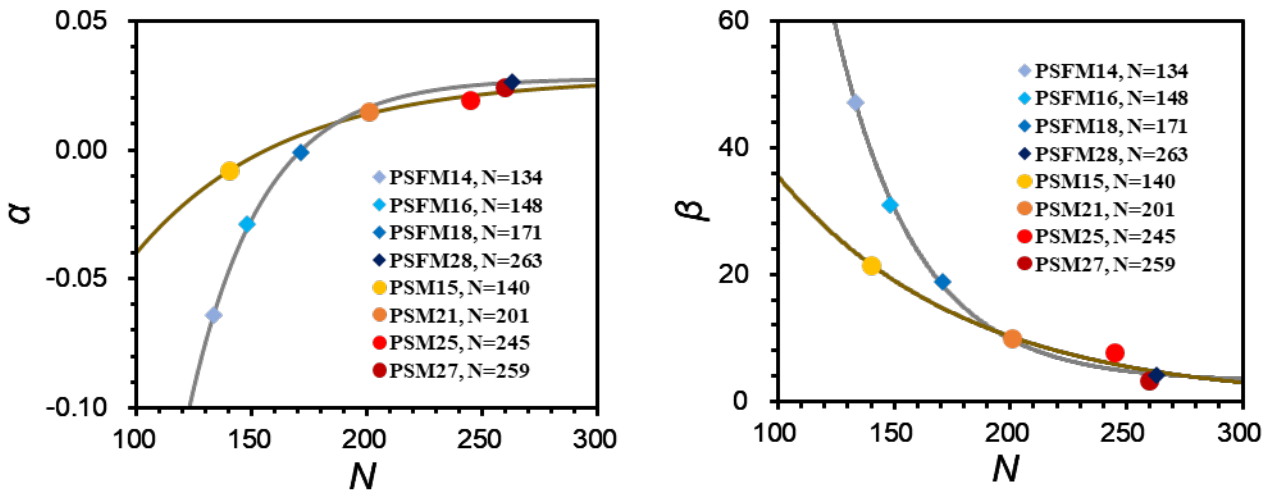


Fig 3. Total degree of polymerization dependence of (a) α and (b) β . Squares and dots are PSFM and PSM respectively. The silver and gold line are coming from the exponential fitting of PSFM and PSM respectively.

determined. The evaluated coefficients are summarized in Fig. 3 and Table 1.

The results in Fig. 3 suggest that α and β of PSM and PSFM over 200 of N are independent on N , and close to the reported value for PS-*b*-PMMA, 0.028 and 3.9, respectively [23]. In contrast, these parameters below 200 of N are dependent on N . Moreover, α with PSFM is much lower than that with PSM, whereas β is much larger than that with PSM in the low molecular weights. One might wonder if this tendency is reasonable, because theoretical χ is regarded as independent of molecular weights. However, this tendency is understandable by considering that χ_{eff} was experimentally determined by the RPA method and can be actually affected by the chain end, especially in the range of low molecular weights. It is also understandable to observe a significant difference between the parameters of PSM and PSFM in the range of low molecular weights, by considering the concentration of chemical junction.

The results in Fig. 3 suggest that α and β of PSM and PSFM are independent on N over 200 of N , despite that these of them are dependent on N in the low molecular weights. Moreover,

The present findings suggest that a small difference at the chemical junction can affect the microphase separation behavior of BCPs. If this sort of property could be wisely utilized, the development of more promising materials for the next generation lithography will be possible, by affecting the line-edge roughness and/or correlation length of lamella. While this study focused BCPs with low molecular weights to demonstrate the effect of modified chemical junction, a clear microphase-separated structure such as lamella could be studied with higher molecular weights of BCPs. In that case, increasing the fluorine content and changing the functional groups for modification will be required for strengthening the effect of the modified chemical junction.

4. Conclusion

In this study, we synthesized novel BCPs modified with fluoroalkane at the chemical junction. The results of temperature-controlled SAXS measurements have revealed that χ_{eff} depends on molecular weights, in the range of low molecular weights. This tendency probably caused by the influence of chain ends on the microphase separation behavior. Besides, the effect of the modified chemical junction was clearly observed in χ_{eff} for the BCPs below 200 of N . In contrast, the

modified PS-*b*-PMMA over 200 of N showed quite similar behavior to the unmodified PS-*b*-PMMA. Further studies will be done for developing more attracting BCPs by effectively modifying the chemical junction.

Acknowledgement

This work was supported by JSPS KAKENHI grant numbers 20H02785.

References

1. S. O. Kim, H. H. Solak, M. P. Stoykovich, N. J. Ferrier, J. J. de Pablo, and P. F. Nealey, *Nature*, 424 (2003) 411.
2. R. Ruiz, H. Kang, F. A. Detcheverry, E. Dobisz, D. S. Kercher, T. R. Albrecht, J. J. de Pablo, and P. F. Nealey, *Science*, 31 (2008) 936.
3. E. A. Jackson and M. A. Hillmyer, *ACS Nano*, 4 (2010) 3548.
4. S. Y. Yang, J.-A. Yang, E.-S. Kim, G. Jeon, E. J. Oh, K. Y. Choi, S. K. Hahn, and J. K. Kim, *ACS Nano*, 4 (2010) 3817.
5. C. M. Bates, M. J. Maher, D. W. Janes, C. J. Ellison, and C. G. Willson, *Macromolecules*, 47 (2014) 2.
6. F. S. Bates and G. H. Fredrickson, *Annu. Rev. Phys. Chem.*, 41 (1990) 525.
7. F. S. Bates and G. H. Fredrickson, *Phys Today*, 52 (1999) 32.
8. P. J. Flory, *J. Chem. Phys.*, 10 (1942) 51.
9. M. L. Huggins, *J. Phys. Chem.*, 46 (1942) 151.
10. C. Sinturel, F. S. Bates, and M. A. Hillmyer, *ACS Macro Lett.*, 4 (2015) 1044.
11. D. F. Sunday, M. J. Maher, A. F. Hannon, C. D. Liman, S. Tein, G. Blachut, Y. Asano, C. J. Ellison, C. G. Willson, and R. J. Kline, *Macromolecules*, 51 (2018) 173.
12. K. Azuma, J. Sun, Y. Choo, Y. Rokhlenko, J. H. Dwyer, B. Schwitzer, T. Hayakawa, C. O. Osuji, and P. Gopalan, *Macromolecules*, 51 (2018) 6460.
13. L. Leibler, *Macromolecules*, 13 (1980) 1602.
14. K. Mori, A. Okawara, and T. Hashimoto, *J. Chem. Phys.*, 104 (1996) 7765.
15. G. T. Dee, T. Ougizawa, D. J. Walsh, *Polymer*, 33 (1992) 3462.
16. W.-C. Lai, W.-B. Liao, T.-T. Lin, *Polymer*, 45 (2004) 3073.
17. S. Woo, S. Jo, D. Y. Ryu, S.-H. Choi, Y. Choe, A. Khan, J. Huh, and J. Bang, *ACS Macro. Lett.*, 6 (2017) 1386.
18. K. S. Lee, J. Lee, J. Kwak, H. C. Moon, J. K. Kim, *ACS Appl. Mater. Interfaces*, 9 (2017)

- 31245.
19. K. Wylie, L. Dong, A. Chandra, Y. Nabaе, and T. Hayakawa, *Macromolecules*, 53 (2020), 1293.
 20. T. Yoshimura, T. Morishita, Y. Agata, K. Nagashima, K. Wylie, Y. Nabaе, T. Hayakawa, and M. Ouchi, *Macromolecules*, published online.
 21. J. Wang and C. K. Ober, *Liquid Crystals*, 26 (1999), 637.
 22. G. J. Summers, M. G. Kasiama, and C. A. Summers, *Polymer International*, 65 (2016) 798.
 23. T. P. Russell, R. P. Hjelm, and P. A. Serger, *Macromolecules*, 23 (1990) 890.

Substitution Effect on Self-Assembly and the Resulting Fluorescence Efficiency of Triangular Azo Chromophores

Pyae Thu^{1,2} and Mina Han²

¹Department of Chemistry, ²Department of Chemistry Education,
Kongju National University, 56 Gongjudaehak-ro, Gongju-si, Chungnam 32588, Korea
hanmin@kongju.ac.kr

To investigate the effect of substituents and substitution positions on absorption and fluorescence spectroscopic properties, and self-assembled structures, we designed triangular azo chromophores (**1–3**) in which three azo groups are connected to a central ring. **1** and **2** where electron-donating methoxy (MeO) groups are attached to *para* and *meta* positions, respectively, had different melting temperatures and colors. A dilute *para*-MeO (**1**) solution was redder than **3** with electron-withdrawing bromo (Br) groups and liquefied at lower temperatures. The elongated structure formed as a result of the one-dimensional (1D) assembly of **1** showed little fluorescence, whereas the chopstick-shaped structure and the entangled fiber assembled from **2** and **3**, respectively, were brightly red fluorescent. Our investigation suggest that the molecular geometry and steric effects play important roles in self-assembly and the resulting fluorescence characteristics.

Keywords: substituent and substitution position, AIEE, triangular azo chromophore, 1D structure

1. Introduction

The fluorescent organic molecules have received widespread attention because of their extensive applications in organic light emitting diodes (OLEDs), optoelectronic devices, fluorescent probes, and so on [1-4]. However, the fabrication of the organic materials which are fluorescent in concentrated solution and aggregated state is still a challenge due of aggregation caused quenching (ACQ) phenomenon of traditional organic chromophores. On the other hand, the aggregation-induced emission enhancement (AIEE) is the reverse phenomenon, which shows high fluorescence efficiency in aggregated states. To synthesize such AIEE-active organic chromophores, several design strategies have been proposed [5], such as, the restriction of intramolecular motion (RIM) [6], excited-state intramolecular proton transfer (ESIPT) [7], twisted intramolecular charge transfer (TICT) [8], J-aggregate formation [9], and the effect of position difference of the bulky group called regioisomerization [10].

Azobenzene is one of the photochromic compounds which undergo reversible *trans*↔*cis* isomerization by the irradiation of different wavelength of light. However, in general, because azobenzene does not fluoresce at ambient temperature, it is limited in its application as information storage, optical sensors, and molecular devices [11-14]. Although fluorescent azobenzene-containing compounds known so far are very limited, light driven self-assemblies of azobenzene derivatives were reported by Han et al. [15,16]. Apart from photoisomerization, the fluorescence and photophysical properties of the chromophores could vary by controlling the substituent, and position of the substituent [17-20]. Moreover, Liu et al. presented the influence of substitution position on fluorescence of 9, 10-bis (alkoxystyryl)-anthracenes. Compared with *ortho* and *para* positions, *meta*-substituted compound showed the highest fluorescence because of the inhibition of intramolecular torsion motion which is induced by

Received March 31, 2022
Accepted June 10, 2022

the introduction of the substituent unsymmetrically [21].

To understand the effect of substituent and the substitution position on molecular assembly and the resulting fluorescence property, we prepared three triangular azo chromophores (**1–3**, Fig. 1). **1** and **2** contain electron-donating methoxy (MeO) group at *para* and *meta* positions, respectively, whereas *ortho*-diethylated azo chromophore (**3**) has electron-withdrawing bromo (Br) at three *para* positions [22]. Their absorption and fluorescence spectroscopic properties were investigated, and the respective self-assembled structures were fabricated in chloroform/methanol (CHCl₃/MeOH) and chloroform/hexane (CHCl₃/hexane) mixtures. Their morphology and fluorescence characteristics were investigated by using optical microscopy (OM), fluorescence optical microscopy (FOM) and field-emission scanning electron microscopy (FE-SEM) observations.

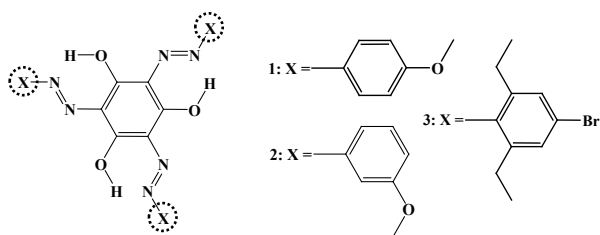


Fig. 1. Chemical structures of **1**, **2** and **3**

2. Experimental

2.1. Synthesis

Compounds **1** and **2** are synthesized in the following azo coupling reaction.

1 ($X = \textit{para}$ -MeO) A solution of NaNO₂ (1.09 g, 15.9 mmol) in H₂O (15 mL) was added to a solution of *p*-anisidine (1.65 g, 13.4 mmol) and HCl (30 mL) at 0–5 °C. A solution of 1,3,5-trihydroxybenzene (0.71 g, 4.40 mmol), NaOH (0.64 g, 15.9 mmol), and Na₂CO₃ (1.69 g, 15.9 mmol) in water (20 mL) was added to the diazonium salt solution. The mixture was stirred for two hours at 0–5 °C and water and chloroform were added to collect the organic layer. The crude compound was purified by silica gel column chromatography using the eluent (CHCl₃: acetone, v/v=60:1). Dark grey colored solid was collected (yield: 17 %). ¹H NMR (400 MHz, CDCl₃) δ 7.60 (*d*, 2H, ArH, J= 9.06 Hz), 6.99 (*d*, 2H, ArH, J= 9.05 Hz), 3.88 (*s*, 3H, Ar-OCH₃). ¹³C NMR (400 MHz, CDCl₃) δ 178.43, 159.26, 134.97, 128.20, 119.07, 115.12, 55.66. FAB-HRMS (*m/z*): [M+H] Found: 529.1833 (= M+1), Calcd for C₂₇H₂₅N₆O₆ = 529.1836.

2 ($X = \textit{meta}$ -MeO) (yield: 27 %). ¹H NMR (400

MHz, CDCl₃) δ 7.36 (*t*, 1H, ArH), 7.19–7.23 (*m*, 2H, ArH), 6.84–6.87 (*dd*, 1H, ArH), 3.90 (*s*, 3H, Ar-OCH₃). ¹³C NMR (400 MHz, CDCl₃) δ 178.63, 160.99, 142.51, 130.61, 128.85, 113.94, 110.37, 102.55, 55.59. FAB-HRMS (*m/z*): [M+H] Found: 529.1834 (= M+1), Calcd for C₂₇H₂₅N₆O₆ = 529.1836.

2.2. Instrumentation

Spectroscopic grade chloroform, methanol and hexane were used to prepare mixture solutions of **1**, **2** and **3**. Screw-cap quartz cuvette containing azobenzene solution sealed with Parafilm was purged nitrogen gas for 30 s and took UV-visible absorption and fluorescence spectra by using Shimadzu UV-2600 spectrophotometer and Horiba FluoroMax-4 spectrofluorometer, respectively. ¹H and ¹³C NMR measurements were carried out by Bruker 400 MHz, and optical and fluorescence optical microscopic measurements were recorded by using Olympus BX53 microscope after placing a few drops of mixture solutions on a clean glass substrate and fully dried the sample. Field-emission scanning electron microscopy (FE-SEM) images were taken by using TESCAN VEGA3 SBH after preparing the sample by dropping the mixed solution on a clean glass substrate and fully removed the solvent. The melting temperature was investigated by using heating and freezing microscope stage (Linkham THMS 600). Fourier transform infrared (FT-IR) spectra were taken by using Perkinelmer (Spectrum 1000) after placing aggregates on a pre-cleaned CaF₂ glass slide and fully dried under vacuum pump.

3. Results and discussion

The melting temperatures of **1–3** were determined by combining an optical microscope (OM) and a temperature control stage, and are summarized in Table 1. **3** containing Br group (*para*-Br) melted at temperatures of 260–270 °C [22], and **1** (*para*-MeO) with electron-donating MeO groups at the *para* position began to melt at 247 °C and was fully liquefied at 251 °C. Notably, a triangular azo chromophore (**2**, *meta*-MeO) in which three MeO groups were substituted at the *meta* position turned into a liquid at higher temperature in the range of 278–280 °C. Such differences in melting temperatures are considered because the electronic nature of the substituent and substitution position would affect their molecular geometry and three-dimensional molecular arrangement [23,24].

Comparing **1** and **3**, **1** containing three *para*-MeO groups has stronger absorption bands at longer wavelengths (405.5 and 524.0 nm, Fig. 2 and 3). Even when comparing **2** and **3**, it could be seen that the greater the electron-donating strength, the longer the maximum absorption wavelength (Table 1). The red-shift of these absorption bands was in the order (**1** > **2** > **3**), which is likely due to the relatively increased planarization of the molecules

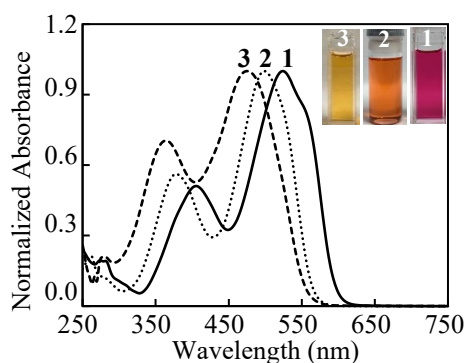


Fig. 2. Absorption spectra of **1**, **2** and **3** in 20 μM CHCl_3 solution

as a result of the substitution of the electron-donating group.

To produce self-assembled structures, poor solvent (such as MeOH or *n*-hexane) was slowly dropped in chloroform solution and left in the dark. The morphology of the obtained aggregates was characterized by OM and scanning electron microscopy (SEM) measurements, and their fluorescence properties were monitored with fluorescence spectroscopy and fluorescence optical microscopy (FOM) observations. Fig. 3 (c) and Table 1 show that **1** tended to assemble into thin and long fibers of 10 micrometers or more regardless of the type of mixed solution ($\text{CHCl}_3/\text{MeOH}$ and $\text{CHCl}_3/\text{hexane}$). Two strong absorption bands were blue-shifted (Table 1) after the one-dimensional (1D) self-assembly. At the same time, the fluorescence intensity was considerably reduced. That is, **1** is not AIEE-active.

Contrastively, the *ortho*-diethylated azo chromophore (**3**) having *para*-Br groups formed

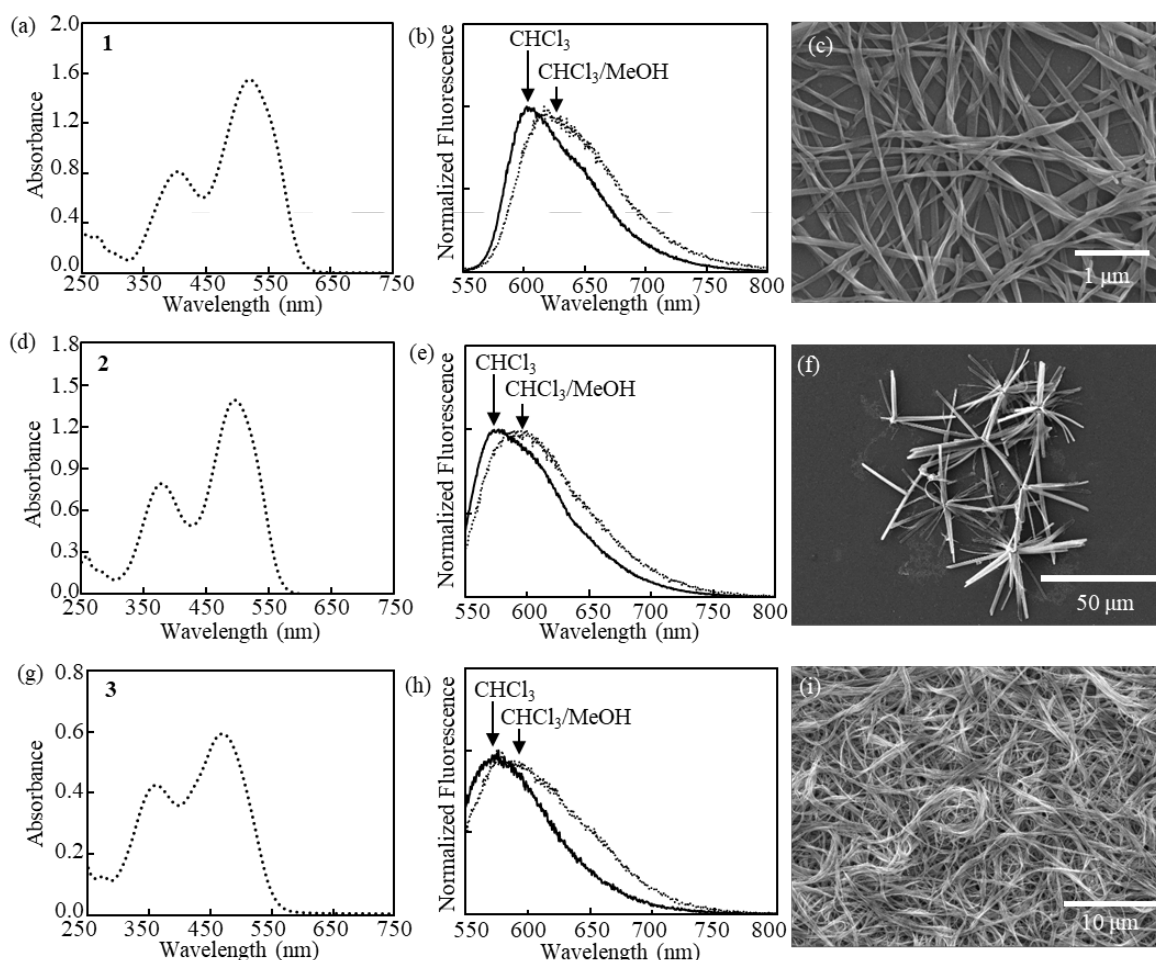


Fig. 3. (a), (d) and (g) Absorption spectra of **1-3** in 20 μM of $\text{CHCl}_3/\text{MeOH}$ (1/9, v/v), (b), (e) and (h) fluorescence spectra of **1-3** in 20 μM of CHCl_3 and $\text{CHCl}_3/\text{MeOH}$ (1/9, v/v). SEM images of **1** (c), **2** (f) and **3** (i).

much longer fibrous structures. They intertwined with each other to form visible agglomerates and slowly separated from the solution. In marked contrast to **1**, the entangled structure had stronger fluorescence intensity compared to that of the corresponding dilute solution. The fluorescence quantum efficiency increased to approximately 0.01.

The FOM images and the inset white line profiles in Fig. 4 display the relative fluorescence intensity changes of the respective 1D structures. The entangled fibers in Fig. 4 (f) were brightly fluorescent, whereas fluorescence from the assembled structure of **1** in Fig. 4 (b) was hardly detected.

Table 1. Melting temperature, absorption, fluorescence spectral data and self-assembled structures of **1**, **2** and **3**

Compound	Melting temperature	Solvent	λ_{max}^{abs} (nm)	λ_{max}^{em} (nm)	Aggregate morphology	AIEE property
1	247-251 °C	CHCl ₃	405.5, 524.0	602.0	-	
		CHCl ₃ /MeOH	405.0, 520.5	616.5	≥ 10 μm, elongated	×
		CHCl ₃ /hexane	399.5, 515.5	593.5	fibrous structure	
2	278-280 °C	CHCl ₃	378.0, 498.5	577.5	-	
		CHCl ₃ /MeOH	378.0, 495.0	589.5	> 20 μm, chopstick-shaped structure	○
3	260-270 °C	CHCl ₃	364.0, 475.5	576.0	-	
		CHCl ₃ /MeOH	362.5, 470.0	580.0	entangled fibrous structure	○

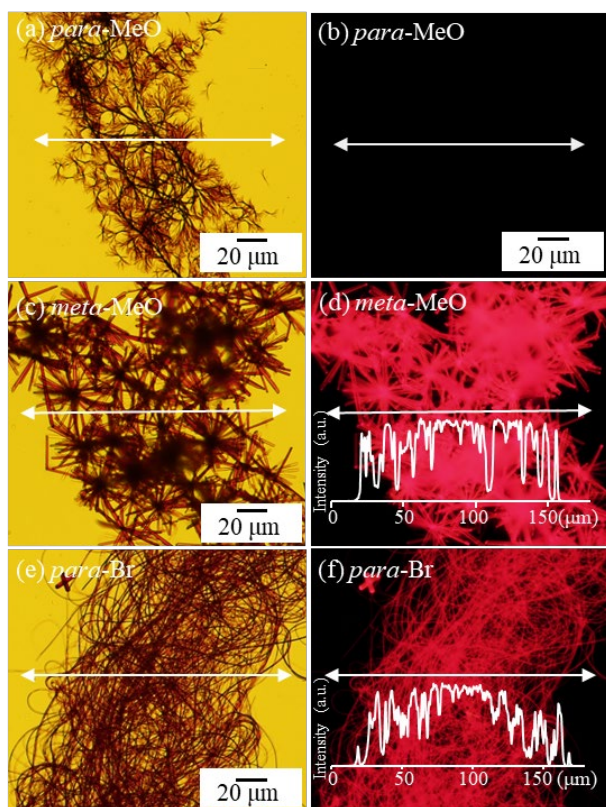


Fig. 4. OM and FOM images of 1D structures obtained from 20 μM CHCl₃/MeOH (1/9, v/v) mixtures

The observation of the noticeable difference in fluorescence intensity before and after the formation of 1D structures can be interpreted as follows. The substitution of *para*-MeO group at the three terminals would improve the planarization of triangular chromophore by increasing the extension of the conjugation system. Considering that the maximum absorption wavelengths were blue-shifted after the 1D assembly, **1** seems to form H-aggregates in a relatively parallel molecular packing mode. By contrast, the *ortho*-diethylated azo chromophore (**3**) is more sterically crowded and has a significantly twisted structure [22]. Therefore, the 1D assembly proceeds through the intermolecular interactions between the twisted molecules (**3**), and the resulting entangled fibers would significantly inhibit intramolecular motion. That is, molecular geometry and steric effects originating from substituents and their substitution position determine three-dimensional molecular packing and as a result are responsible for the fluorescence characteristics of the produced structures.

Intriguingly, **2** substituted with *meta*-MeO groups asymmetrically formed a chopstick-shaped structure with the thickness and length of ~2 micrometers and 20-50 micrometers, respectively,

in CHCl₃/MeOH mixed solution (Fig. 3f and Table 1). The straight morphology was in contrast to flexible fibrous structures formed from **1** and **3**. In addition, the crystalline structure showed quite strong red fluorescence (Fig. 4d) and its fluorescence efficiency was estimated to be approximately >1%. The evident differences in absorption and fluorescence characteristics of symmetric **1** and asymmetric **2** is closely associated with the steric effect resulting from the variation in the substitution position of the MeO group [25,26].

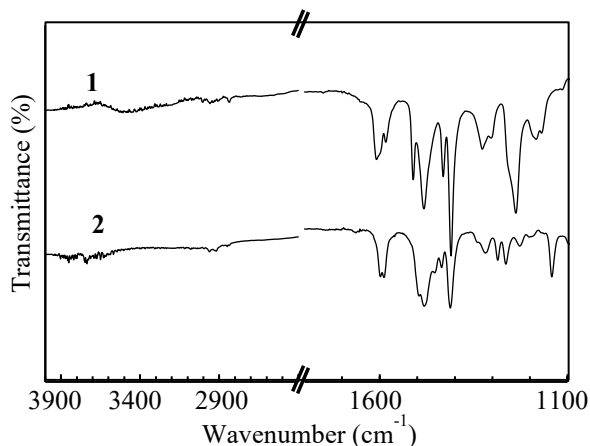


Fig. 5. FT-IR spectra of 1D structures

Quite strong absorption bands at around 1600 and 1480 cm⁻¹ (aromatic C=C stretching) and weak bands at around 3015 cm⁻¹ (aromatic C-H stretching) appeared in the FT-IR spectra of the fibrous and chopstick-shaped structures (Fig. 5). However, unlike **2** with asymmetric *meta*-MeO groups, the fiber assembled from symmetric **1** had a broad absorption band around 3150-3600 cm⁻¹. It can be attributed to intramolecular and/or intermolecular hydrogen bonding. Our IR, absorption and fluorescence spectroscopic results support that symmetric **1** tends to assemble into fibrous structure without AIEE property through hydrogen bonding and parallel molecular stacking, which is in contrast to AIEE-active **2** and **3**.

4. Conclusion

The electronic nature of the substituent and the change in the substitution position affected the molecular structure and three-dimensional molecular stacking of the triangular azo molecules, determining the melting point, the color of the solution, self-assembly, and the resulting fluorescence characteristics. The symmetric azo chromophore substituted with electron-donating *para*-MeO had a planar structure and assembled

into elongated fibrous structure with little fluorescence through hydrogen bonding and H-aggregation. In contrast, the sterically crowded and asymmetric molecules showed relatively weaker absorption bands at shorter wavelengths, and formed 1D structures with AIEE characteristics.

Acknowledgement

This work was supported by National Research Foundation (NRF) of Korea (2018R1A2B6009315) and the framework of bilateral international cooperation program managed by the NRF-Japan Society for the Promotion of Science (2018K2A9A2A08000191).

References

1. D. Knapton, M. Burnworth, S. J. Rowan, and C. Weder, *Angew. Chem. Int. Ed.*, **45** (2006) 5825.
2. P. Bosch, F. Catalina, T. Corrales, and C. Peinado, *Chem. Eur. J.*, **11** (2005) 4314.
3. S. R. Forrest, *Nature.*, **428** (2004) 911.
4. A. P. de Silva, H. Q. N. Gunaratne, T. Gunnlaugsson, A. J. M. Huxley, C. P. McCoy, J. T. Rademacher, and T. E. Rice, *Chem. Rev.*, **97** (1997)
5. M. M. Islam, Z. Hu, Q. Wang, C. Redshaw, and X. Feng, *Mater. Chem. Front.*, **3** (2019) 762.
6. Y. Hong, J. W. Y. Lam, and B. Z. Tang, *Chem. Soc. Rev.*, **40** (2011) 5361.
7. P. Gayathri, M. Pannipara, A. Al-Sehemi, and S. P. Anthony, *CrystEngComm.*, **23** (2021) 3771.
8. S. Sasaki, G. P. C. Drummen, and G. Konishi, *J. Mater. Chem. C.*, **4** (2016) 2731.
9. F. Würthner, T. E. Kaiser, and C. R. Saha-Möller, *Angew. Chem. Int. Ed.*, **50** (2011) 3376.
10. X. Wang, X. Lin, R. Li, Z. Wang, W. Liu, L. Chen, N. Chen, T. Dai, S. Sun, Z. Li, J. Hao, B. Lin, and L. Xie, *MOLEFW.*, **27** (2022).
11. H. Rau, *Angew. Chem. Int. Ed Engl.*, **12** (1973) 224.
12. B. Tsai, C. Chen, C. Hung, V. K. S. Hsiao, and C. Chu, *J. Mater. Chem.*, **22** (2012) 20874.
13. W. Xu, S. Sun, and S. Wu, *Angew. Chem. Int. Ed.*, **58** (2019) 9712.
14. L. Xue, Y. Pan, S. Zhang, Y. Chen, H. Yu, Y. Yang, L. Mo, Z. Sun, L. Li, and H. Yang, *Crystals.*, **11** (2021).
15. M. R. Han, Y. Hirayama, and M. Hara, *Chem. Mater.*, **18** (2006) 2784.
16. M. Han, Y. Norikane, K. Onda, Y. Matsuzawa, M. Yoshida, and M. Hara, *New J. Chem.*, **34** (2010) 2892.
17. Y. Xiong, X. Yan, Y. Ma, Y. Li, G. Yin, and L.

- Chen, *Chem. Commun.*, **51** (2015) 3403.
18. N. K. Ramya, C. Femina, S. Suresh, D. S. Mohanakumari, R. Krishnan, and R. Thomas, *New J. Chem.*, **46** (2022) 1339.
19. V. Montes, G. Li, R. Pohl, J. Shinar, and P. Anzenbacher Jr., *Adv Mater.*, **16** (2004) 2001.
20. R. Pohl, V. A. Montes, J. Shinar, and P. Anzenbacher, *J. Org. Chem.*, **69** (2004) 1723.
21. W. Liu, Y. Wang, M. Sun, D. Zhang, M. Zheng, and W. Yang, *Chem. Commun.*, **49** (2013) 6042.
22. M. Han, S. J. Cho, Y. Norikane, M. Shimizu, A. Kimura, T. Tamagawa, and T. Seki, *Chem. Commun.*, **50** (2014) 15815.
23. B. Roy, P. Bairi, A. Saha, and A. K. Nandi, *Soft Matter.*, **7** (2011) 8067.
24. Monika, A. Verma, M. K. Tiwari, B. Show, and S. Saha, *ACS Omega.*, **5** (2020) 448.
25. T. Yang, S. Pu, B. Chen, and J. Xu, *Can. J. Chem.*, **85** (2007) 12.
26. S. Pu, C. Fan, W. Miao, and G. Liu, *Dyes Pigm.*, **84** (2010) 25.

Recent status of the stochastic issues of photoresist materials in EUV lithography

Toru Fujimori

*Electronic Materials Research Laboratories, Electronic Materials Business Div.
FUJIFILM Corporation
4000 Kawashiri, Yoshida-Cho, Haibara-Gun, Shizuoka 421-0396, Japan
toru.fujimori@fujifilm.com*

In 2019, finally, extreme ultraviolet (EUV) lithography has been applied to high volume manufacturing (HVM) for preparing advanced semiconductor devices. That was very important year for EUV enthusiasts and semiconductor industry. Because it takes for a long time, more than 30 years, to study EUV lithography for realizing HVM. With recent rapid progress on the source power improvement, EUV lithography development including photoresist materials has been achieved HVM requirements. However, the performance of EUV resist materials are still not enough for the expected HVM requirements, even by using the latest qualifying EUV resist materials. One of the critical issues is the stochastic issues, which will be become ‘defectivity’, like a nano-bridge or a nano-pinching.

The analyzing summary of the stochastic factors in EUV lithography, and their improvement status are described in this paper. 2 (two) major stochastic issues, which are photon stochastic and chemical stochastic, were observed in the lithography steps. And the improvement status of each stochastic issues including lithographic results are also described.

Keywords: Extreme ultraviolet, Photoresist, Stochastic, Lithography, Defectivity

1. Introduction

In 2019, finally, EUV lithography has been applied to HVM for preparing advanced semiconductor devices, like 5 nm technology node and beyond. That was very important year for EUV enthusiasts and semiconductor industry. Because it takes for a long time, more than 30 years, to study EUV lithography for realizing HVM. In fact, the 1st paper of EUV lithography was published in 1986 by prof. Kinoshita’s group [1]. However, it had been so difficult to realizing EUV lithography for a long time. Figure 1 showed focus area of EUV lithography development, which was from the closing remarks in EUVL symposium in 2017, the key factors for EUV lithography realization were light source, mask defectivity and inspection, and photo resist materials. The most critical issue was light source until 2016 [2]. With recent rapid progress on source power improvement [3], photo resist materials and processes explorations are more and more accelerated to achieve HVM requirements. A key factor for the realization of

EUV lithography is the choice of EUV resist materials that is capable to resolving below 15 nm half pitch with high sensitivity [4].

Figure 1. Focus Area (EUVL symposium 2017):
EUVL extension including High NA



Unfortunately, the performance of EUV resist is still NOT enough for the true HVM requirements, even by using the qualified EUV resist materials for the 1st generation. One critical issue is ‘stochastic issues’, which will be become

Received	May 8, 2022
Accepted	June 24, 2022

‘defectivity’ [5]. The understanding of the status of the stochastic issues of EUV lithography and their improvement procedure were described in this paper.

2. Experimental

2.1. Materials

Each polymer materials were synthesized according to the conventional polymerization methods [6]. A series of photoresist were prepared by mixing organic solvents, the protected co-polymers, optimized amount of PAG and organic quencher or the related compounds. The resulting solution was filtered using 0.03 or 0.02 μm polyethylene filter or other filter before lithographic performance evaluation.

2.2. Lithography performance evaluation

The photoresist solution was spin-coated on a silicon wafer that was treated with an organic under layer (UL) or spin on glass (SOG) stacked with spin on carbon (SOC), and the resulting film was pre-baked at appropriate temperature for 60 sec to give a specific film thickness for each

patterning features. The wafer was exposed with EUV light (13.5 nm) from an ASML NXE:3300 series with 0.33 NA or Small Field Exposure Tools (SFET) with 0.33 NA. After exposure, the wafer was baked (PEB) at moderate temperature for 60 sec. and developed with 2.38% TMAH aq. or organic solvent developer for moderate time. CD-SEM measurements were performed with a Hitachi CG4100 or CG5000.

3. Results and discussion

Analyzing of the stochastic issues

In the past, speaking of the stochastic issue of EUV lithography was basically considered from poor photon number from EUV light source, which means ‘photon shot noise’. It was still critical concerning point of the stochastic issue, even with recent progress on source power improvement. However, the stochastic issue is not only from them but also from EUV materials and processes, called ‘Chemical Stochastic’ [7]. The ‘Chemical stochastic’ means caused from resist materials and processes for lithography,

Figure 2. The analyzing summary of stochastic factors in lithography

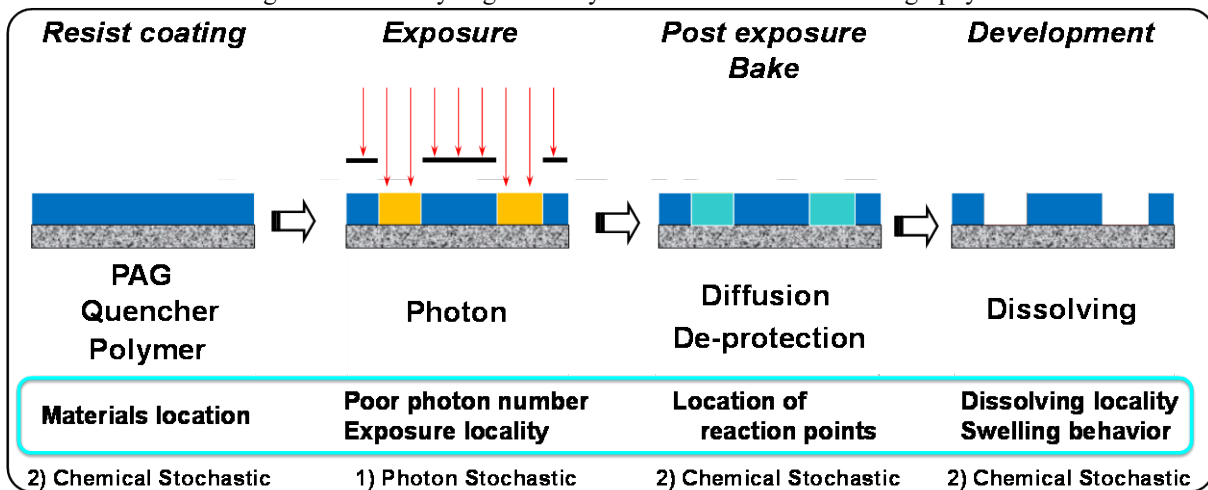


Figure 3. Photon stochastic and chemical stochastic, issues and improvement strategy

1) Photon Stochastic (photon shot noise)

< Cause : light source > Poor photon number.

=> The resist materials can help it.

Introduce the function of ‘catch more photon’.

2) Chemical Stochastic

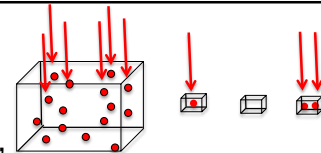
< Cause : resist materials and processes >

The materials location randomness, the reaction randomness in the film.

=> The **functionalized materials** are effective.

The dissolving randomness during the development process.

=> **Organic solvent development** is effective.



materials uniformity in the film, catch the photon efficiency, reactive uniformity in the film, and dissolving behavior with the developer (Figure 2). Each step must be reduced each stochastic issue to improve the quality of lithographic performance, photon stochastic and chemical stochastic (Figure 3).

3.2. To reduce the photon stochastic

Photon stochastic, photon shot noise effect, on EUV lithography was well-known issue and various studies have emphasized its impact on LWR performance [8-10]. As well as LWR, the

photon shot noise effect on defectivity must be considered to obtain pattern quality satisfying HVM requirements. To reduce the photon stochastic effect, EUV resist must catch more photon effectively, because of their poor photon numbers. By simulation study, using the high absorption material observed higher image contrast than standard one [11]. So, the high absorption materials should be effective for improving the lithographic performance. According to the study of the absorption coefficient, a wide variety of atoms, like halogen atoms, observed stronger absorption coefficient than carbon and hydrogen [12]. ‘Organic high

Figure 4. The simulation study of high EUV absorption materials and design concept of ‘Organic high EUV absorption materials’.

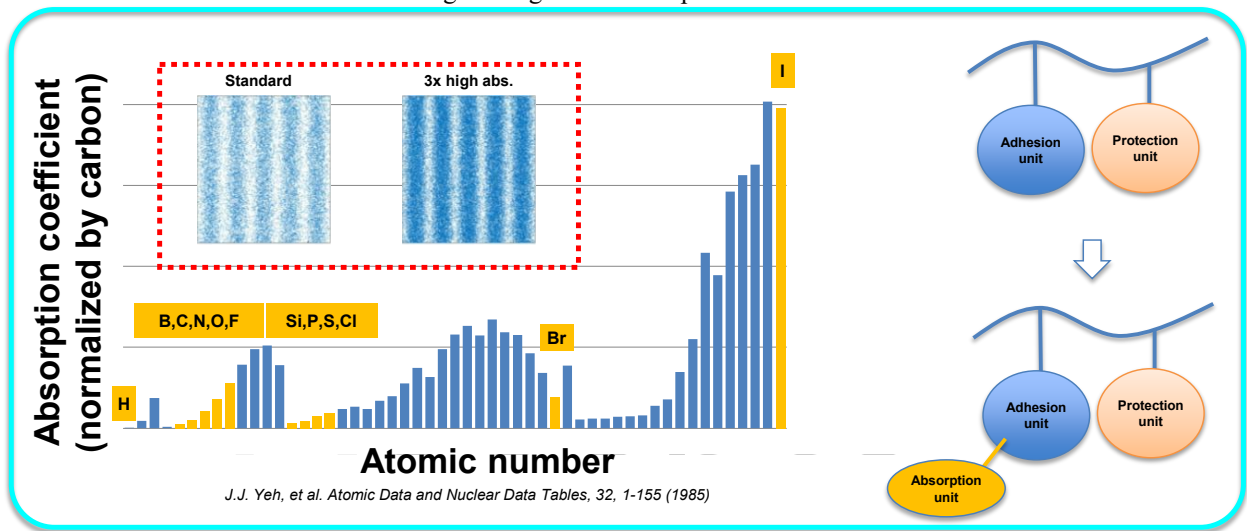
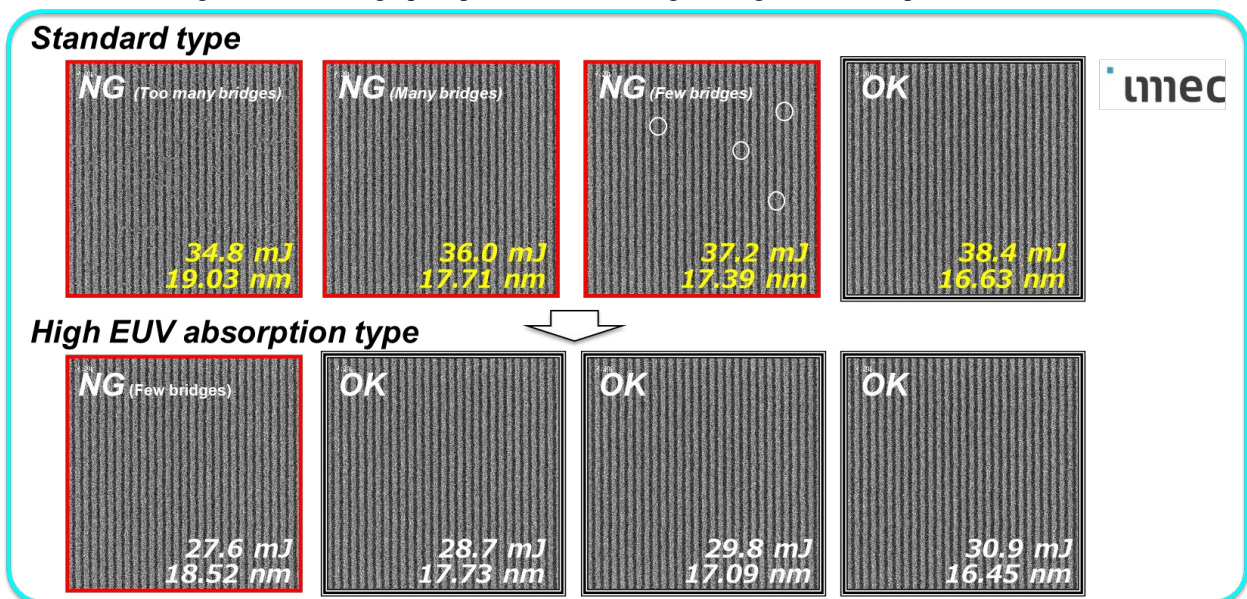


Figure 5. The lithographic performance of ‘Organic high EUV absorption materials’.



EUV absorption materials' was newly designed and synthesized, which expected to be able to catch photon more efficiency from the source (Fig. 4). As a result of the lithographic performance, 'Organic high EUV absorption materials', showed 20% dose reduction with keeping its LWR value. Besides that, nano-bridge is clearly decrease on the high absorption resist (Fig. 5).

3.3. To reduce the chemical stochastic, materials location in the film

The other hand, 'Chemical stochastic', the materials location randomness, could be observed in the film. A traditional CAR material is mainly composed from polymers, PAGs (Photo Acid

Generator) and quenchers, which located variously in the film. The location locality of the materials in the film induced solubility randomness during the development process, which observed worse LWR and defectivity, like nano-bridge and nano-pinching. One of the famous methods to reduce the chemical stochastic is higher PAG loading formulation (Fig. 6) (Fig. 7) [7]. However, even introduced higher loading technology, it still remained the fluctuation, like unexpected repulsion, interaction and aggregation. To reduce such an unexpected behavior and expected to control of the materials location in the films, 'The novel functionalized materials' was designed and synthesized to introduce connection unit, interaction, or bounded. 'The novel functionalized materials' observed

Figure 6. Simulation study of PAG loading effect

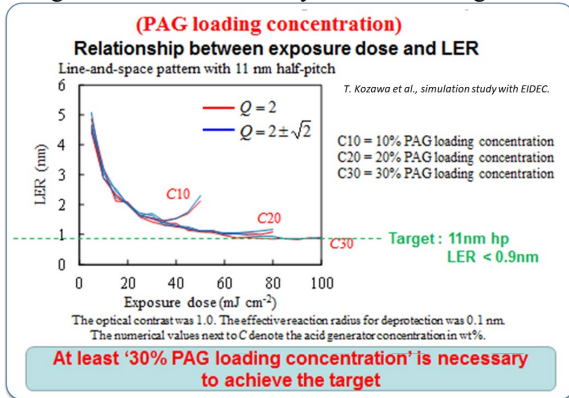


Figure 7. Experimental results of PAG/protecting group effect

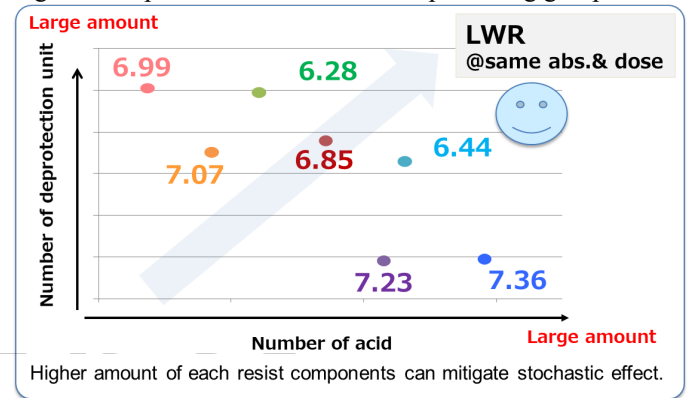
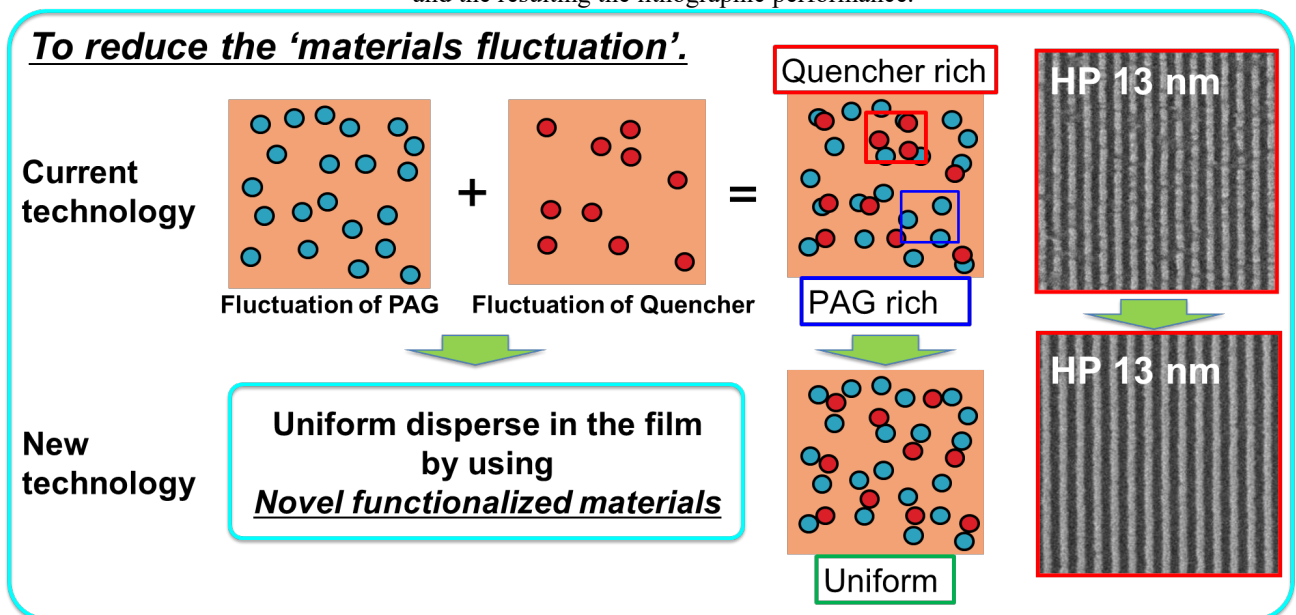


Figure 8. The concept of the novel functionalized materials to control of the materials location in the film, and the resulting the lithographic performance.



excellent lithographic performance on 13 nm half pitch without pinching and bridging (Fig. 8) [13] [14].

3.4. To reduce the chemical stochastic, dissolving behavior control

The dissolving stochastic with developer, a kind of ‘Chemical Stochastic’, could be observed during the development process due to their swelling behavior. One of the key items to improve them was Negative-tone imaging (NTI, using organic solvent-based developer) process.

Negative-tone imaging (NTI) process has been developed to expand ArF immersion lithography by FUJIFILM [15]. Previously, negative-tone system means crosslink system with conventional TMAH developer. However, the crosslink system with TMAH developer observed huge swelling, so it does not suit for preparing the small CD patterns. NTI process is a different idea, which is

developed with organic solvent to prepare the negative images (Fig. 9) [16][17][18].

NTI process provided lower swelling and smoother dissolving behavior than Positive-tone imaging (PTI) process, which reduced the dissolving stochastic. Therefore, negative-tone imaging with EUV exposure (EUV-NTI) has huge advantages for the performance, especially for improving LWR, which will be expected to resolve RLS trade off. Also, NTI system has already introduced to manufacturing with ArF exposure. So, it seems not so difficult to use EUV-NTI for manufacturing. Comparison of dissolving behavior between positive-tone and negative-tone by using in-situ high speed AFM, NTI process observed less swelling than PTI process. The lithographic performance of NTI process observed 60% better LWR performance than PTI process under the same exposure dose owing to their smooth-dissolving behavior and non-swelling properties (Fig. 10) [19][20].

Figure 9. The process flow of the lithography, PTI (Positive-tone imaging) and NTI (Negative-tone imaging).

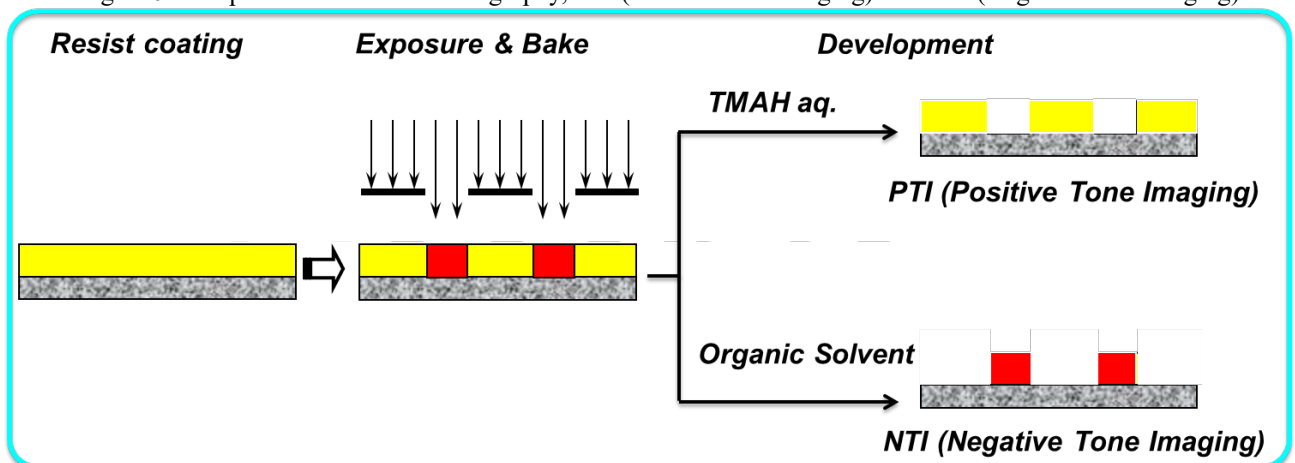


Figure10. The dissolution behavior comparison between PTI and NTI by using in-situ high speed AFM (HS AFM), and their resulting lithographic performance with Small Field Exposure Tools (SFET).

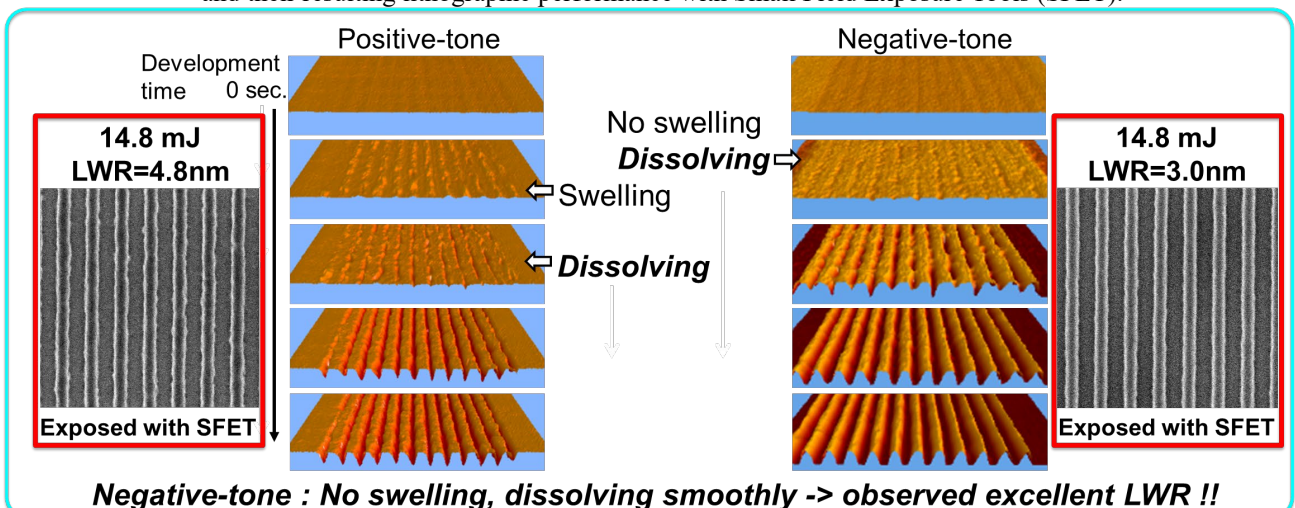
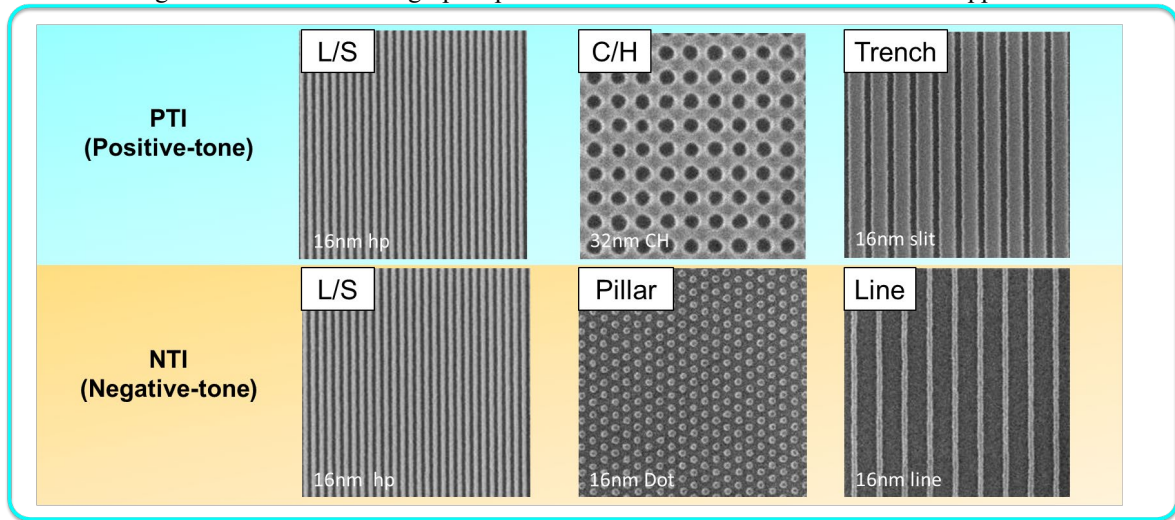


Figure 11. The latest lithographic performance of both PTI and NTI for each application.



4. Conclusion

The latest lithographic performances of both PTI and NTI were introduced, which observed brilliant performance for each application (Fig. 11).

This study hereby showed excellent improving the lithographic performance due to reduce the stochastic issue, ‘Photon stochastic’ and ‘Chemical stochastic’. ‘Organic EUV high absorption materials’, ‘The novel functionalized materials’, and ‘Negative-tone imaging with EUV exposure (EUV-NTI)’ were very effective to reduce the stochastic effect. The most critical issue is how to apply each item. These technologies were expected to apply the real EUV lithography HVM.

References

1. H. Kinoshita, et.al., *The Japan Society of Applied Physics*, **28-ZF-15** (1986).
2. P. Naulleau and P. Gargini, *International Symposium on Extreme Ultraviolet Lithography, closing remarks*, (2017).
3. A. Schafgans, D. Brown, I. Fomenkov, Y. Tao, M. Purvis, S. Rokitski, G. Vaschenko, R. Rafac, D. Brandt, *Proc. SPIE*, **10143** (2017) 101431I.
4. T. Fujimori, *International Microprocesses and Nanotechnology Conference, the 34th, MNC* (2021).
5. P. De Bisschop, J. Van de Kerckhove, J. Mailfert, A. Vaglio Pret, J. Biafore, *Proc. SPIE*, **9048** (2014) 904809.
6. G. Odian, “Principles of polymerization” *John Wiley* (2004).
7. T. Fujimori, *International Symposium on extreme ultraviolet lithography*, **11147** (2019).
8. R. L. Brainard, P. Trefonas, J. H. Lammers, C. A. Cutler, J. F. Mackevich, A. Trefonas, and S. A. Robertson, *Proc. SPIE*, **5374** (2004) .
9. J. M. Hutchinson, *Proc. SPIE*, **3331** (1998)
10. S. Bhattarai, W. Chao, S. Aloni, A. R. Neureuther, P. Naulleau, *Proc. SPIE*, **9422** (2015) 942209
11. H. Furutani, M. Shirakawa, W. Nishashi, K. Sakita, H. Oka, M. Fujita, T. Omatsu, T. Tsuchihashi, N. Fujimaki, and T. Fujimori, *J. Photopolym. Sci. Technol.*, **31** (2018) 201.
12. J. J. Yeh, et al., *Atomic Data and Nuclear Data Tables*, **32** (1985) 1-155
13. T. Fujimori, *China Semiconductor Technology International Conference (CSTIC)*, (2020).
14. T. Fujimori, *International Workshop on Advanced Patterning Solutions (IWAPS)*, (2020).
15. S. Tarutani, S. Kanna, H. Tsubaki, *Proc. SPIE*, **6923** (2008) 69230G.
16. H. Tsubaki, *International Symposium on Extreme Ultraviolet Lithography* (2014).
17. T. Fujimori, J. J. Santillan, T. Takahashi, E. Shiobara, T. Itani, and S. Inoue, *International Symposium on Extreme Ultraviolet Lithography* (2014).
18. T. Fujimori, *International Workshop on Advanced Patterning Solutions (IWAPS)*, (2021).
19. T. Fujimori, 2-7, *Advanced Technologies for Functional Materials and Process Optimization*, CMC books (2017).
20. T. Fujimori, T. Tsuchihashi and T. Itani, *J. Photopolym. Sci. Technol.*, **28** (2015) 485.

Synthesis and resist sensitive property of iodine-containing materials using extreme ultraviolet (EUV) exposure tool

Yutaro Iwashige¹, Hiroto Kudo^{1*}, Kazumasa Okamoto², and Takahiro Kozawa²

¹ *Department of Chemistry and Materials Engineering, Faculty of Chemistry, Materials and Bioengineering, Kansai University, 3-3-35, Yamate-cho, Suita-shi, Osaka, 564-8680, Japan*

² *Institute of Scientific and Industrial Research, Osaka University, 8-1 Mihogaoka, Ibaraki, Osaka 567-0047, Japan*

**kudoh@kansai-u.ac.jp*

We examined the synthesis, physical properties, and resist properties of various iodine-containing molecules and polymers as resist materials. By condensation reaction of 2,6-dimethylphenol (DMP) with 4-iodobenzaldehyde (IBA), 3,5-diiodosalicylaldehyde (DISA) and 4-hydroxy-3,5-diiodobenzaldehyde (HDIA), the corresponding iodine containing compounds DIPM, 2-DIPM, and 4-DIPM were synthesized. The reaction of these compounds with adamantyl bromo acetate, yielding corresponding compounds with adamantyl ester groups DIPM-AD, 2-DIPM-AD, and 4-DIPM-AD. The polyaddition of 4-DIPM with divinyl ethers such as diethylene glycol divinyl ether (DGDE), 1,4-bis(allyloxymethyl)cyclohexane (BAC), 2,2'-bis(4-vinyloxyethoxyphenyl)perfluoropropane (BVFP) was investigated to give iodine containing hyperbranched polyacetals poly(4-DIPM-co-DGDE), poly(4-DIPM-co-BAC), poly(4-DIPM-co-BVFP). In the same way, tri(4-hydroxyphenyl)methane (THM) was used instead of 4-DIPM, the corresponding hyperbranched polyacetals poly(THM-co-DGDE), poly(THM-co-BAC), and poly(THM-co-BVFP) were also synthesized. Almost all resist materials had good physical properties (solubility, film formation, high thermal stability,) and excellent thickness loss property. The resist sensitivity in the extreme ultraviolet (EUV) exposure tool showed that these resist materials were good candidate to offer higher resolution resist pattern, i.e., $E_0 = 7.0 \text{ mJ/cm}^2$ for DIPM-AD, $E_0 = 7.0 \text{ mJ/cm}^2$ for 2-DIPM-AD, $E_0 = 2.0 \text{ mJ/cm}^2$ for 4-DIPM-AD, poly(THM-co-DGDE) and poly(THM-co-BAC), $E_0 = 1.0 \text{ mJ/cm}^2$ for poly(4-DIPM-co-DGDE) and poly(4-DIPM-co-BVFP).

Keywords: Iodine, Molecular resist, Hyperbranched polyacetal, Extreme ultraviolet

1. Introduction

Very recently, extreme ultraviolet (EUV) lithography has been put to practical use, and sub 10 nm of resist pattern is expected to be applied to next generation large-scale integration (LSIs). However, there are three key properties to be solved, i.e., the relationship among resolution, sensitivity with exposure system, and line-edge roughness (LER) is called as a trade-off issue and would make it difficult to reduce the size of resist pattern. Then, it is necessary to develop a new resist material [1-6].

The first challenge to overcome the trade-off issue is to increase the resist-sensitivity. At the

present time, a chemically amplified resist (CAR) system is considered to increase sensitivity [7, 8]. Furthermore, instead of conventional polymer-based resist materials, molecular resists have been considered in terms of material uniformity and small size for sub 20 nm of resist patterns [9-12]. Our research group has also reported molecular resists based on ladder cyclic oligomer noria ("noria" = water wheel in Latin) [13-19], which could show higher sensitivity in the EUV exposure dose, presumably because of that noria has fixed hole in it, which might reduce the density of the resist material and eventually achieve higher

Received March 30, 2022

Accepted June 24, 2022

sensitivity[20]. Recently, we have also reported that hyperbranched polyacetal (HBPA) could show higher sensitivity on EUV exposure tool due to their structural features, i.e., HBPA has branched structures and lower density in the comparison of linear polymer. Furthermore, acetal bond of HBPA would be decomposed easily by an acid to offer main-chain scission type photoresist material [21-23].

While, mechanism of CAR using EUV exposure tool is different from those of KrF and ArF exposure tools [15, 16]. The resist material would absorb EUV light and generating secondary electron would decompose PAG to afford the acids applying CAR. Then metal-containing resist materials could show higher resist-sensitivity, anticipating that they can show good etching property and higher resolution resist property using EUV resist system [24 - 31]. We also reported the tellurium-containing polymer and low molecular resists with pendant adamantly ester groups, showing higher resist sensitivity in EUV exposure tool [32].

In this paper, we designed the iodine-containing resist materials, focusing that iodine has high absorption efficiency of EUV light [3,33]. The synthesis and property of certain iodine-containing molecules and hyperbranched polyacetals were examined, and their resist sensitivities were investigated using EUV exposure tool.

2. Experimental

2.1. Materials

N,N-Dimethylformamide (DMF) and *N*-methylpyrrolidone (NMP) were dried with calcium hydride (CaH₂) and purified by distillation under reduced pressure. Tetrahydrofuran (THF) was dried with sodium and purified by distillation under reduced pressure. Chloroform (CHCl₃), hexane, ethanol, ethyl acetate, hydrochloric acid (HCl), pyridinium *p*-toluenesulfonate (PPTS), tetrabutylammonium bromide (TBAB), 2,6-dimethylphenol (DMP), 4-iodobenzaldehyde (IBA), 3,5-diiodosalicylaldehyde (DISA), 4-hydroxy-3,5-diiodobenzaldehyde (HDIA), diethylene glycol divinyl ether (DGDE), 1,4-bis(allyloxymethyl)cyclohexane (BAC), propylene glycol monomethyl ether (PGME), propylene glycol methyl ether acetate (PGMEA), and triphenylsulfonium nonaflate (TPS-Nf) were used as commercially available. Tetramethylammonium hydroxide (TMAH) was a commercial product diluted with water to 2.38wt%. Adamantyl bromo acetate (ADBAc) and 2,2'-bis(4-

binyloxyethoxyphenyl)perfluoropropane (BVFP) were synthesized according to the previous report[22]

2.2. Measurements

Infrared (IR) spectra were taken with a JASCO FT/IR4200. The ¹H-NMR spectra were recorded on JEOL ECS-400K (400 MHz for ¹H-NMR) instruments in DMSO-*d*₆ and CDCl₃ with Me₄Si (TMS) as an internal standard. Thermal analysis was performed on a Shimadzu thermogravimetric analyzer (TGA) TGA-50/50H at a heating rate of 10 °C/min under nitrogen.

2.3. Condensation reaction of 4-iodobenzaldehyde (IBA) and DMP [Synthesis of di(3,5-dimethyl-4-hydroxy)phenyl(4-iodophenyl) methane (DIPM)].

Typical procedure: A solution of IBA (2.90 g, 12.5 mmol), DMP (3.05 g, 25 mmol), HCl (1mL) and ethanol (15mL) was stirred at 90 °C for 24 h. After that, K₂CO₃ aq. was added to the resulting mixture and stirred at r.t. for 30 min. The organic phase was dried over anhydrous magnesium sulfate and concentrated in a rotary evaporator. The resulting residue was dropped into large amount of hexane to precipitate the solid DIPM. Its structure was confirmed by IR and ¹H-NMR spectroscopy. Yield = 4.79 g (84%). IR (KBr, cm⁻¹); 3450(v O-H), 2922(v C-H), 1484(v aromatics), 1209(v C-O). ¹H-NMR (400MHz, DMSO-*d*₆, TMS); δ(ppm): 7.91(s, 2.0H, -OH), 7.48-7.46(d, *J* = 8.0Hz, 2.0H, aromatic), 6.65-6.62 (d, *J* = 8.0Hz, 2.0H, aromatic), 6.40(s, 4.0H, aromatic), 5.03(s, 1.0 H, -CH), 1.99(s, 12.0H, -CH₃).

2.4. Condensation reaction of DISA and DMP [synthesis of di(3,5-dimethyl-4-hydroxy)phenyl(3,5-diiodo-2-hydroxyphenyl)methane (2-DIPM)].

Typical procedure: Reaction of DISA (0.748g, 2mmol) and DMP (0.488g, 4mmol) was performed in the same way for the synthesis of DIPM. Yield = 0.96 g (80%). IR (KBr, cm⁻¹); 3499(v O-H), 2946(v C-H), 1496(v aromatics), 1245(v C-O). ¹H-NMR (400MHz, DMSO-*d*₆, TMS): δ(ppm): 9.08(s, 1.0 H, -OH), 8.05(s, 2.0 H, -OH), 7.90(s, 1.0 H, aromatic), 6.94(s, 1.0 H, aromatic), 6.49(s, 8.0 H, aromatic), 5.53(s, 1.0 H, -CH), 2.03(s, 12.0 H, -CH₃).

2.5. Condensation reaction of HDIA and DMP [synthesis of di(3,5-dimethyl-4-hydroxy)phenyl(3,5-diiodo-4-hydroxyphenyl)methane (4-DIPM)].

Typical procedure: Reaction of HDIA (3.74g, 10mmol) and

DMP (2.44g, 20mmol) was performed in the same way for the synthesis of DIPM. Yield = 3.34 g (56%). IR (KBr, cm^{-1}): 3526(v O-H), 2915(v C-H), 1485(v aromatics), 1194(v C-O). $^1\text{H NMR}$ (400MHz, $\text{DMSO-}d_6$, TMS): δ (ppm): 9.43 s, 1.0H, -OH), 8.07 s, 2.0 H, -OH), 7.47 (s, 2.0 H, aromatic), 6.61(s, 4.0 H, aromatic), 5.08 (s, 1.0 H, -CH), 2.02 s, 12.0 H, - CH_3).

2.6. Synthesis of DIPM, 2-DIPM, and 4-DIPM derivatives with pendant adamanty ester groups (DIPM-AD, 2-DIPM-AD, and 4-DIPM-AD). Reaction of DIPM (2.47g, 5mmol) and ADBAc (5.746g, 20 mmol) was carried out in the presence of K_2CO_3 (1.73g, 12.5mmol) and TBAB (0.322g, 10mmol) in NMP (10mL) at 80°C for 24 h. After that the resulting mixture was precipitated dropwise into 1N-HCl aq. The residue was purified by silica gel column chromatography eluted with mixture of ethyl acetate and hexane (4/1), followed by concentration using rotary evaporator to obtain DIPM derivative with pendant adamanty ester groups (DIPM-AD). Yield = 1.25 g (28%). IR (KBr, cm^{-1}): 2901(v C-H), 1705(v C=O of ester), 1448(v aromatics), 1195(v C-O of ester). $^1\text{H NMR}$ (400MHz, $\text{DMSO-}d_6$, TMS): δ (ppm) : 7.19(d, $J = 8.0$, 2.0H, aromatic), 6.51(d, $J = 8.0\text{Hz}$, 2.0H, aromatic), 6.45(s, 4.0 H, aromatic), 5.03(s, 1.0H, -CH), 4.07(s, 1.0 H, - CH_2 -), 2.03(s, 12.0H, $>\text{CH}_3$), 2.09-1.22(m, 34.0 H, - CH_2 - of ADBAc).

In the same way for the synthesis of 2-DIPM-AD and 4-DIPM-AD were synthesized.

2-DIPM-AD (yield = 18%). IR (KBr, cm^{-1}): 2903(v C-H), 1700(v C=O of ester), 1478(v aromatics), 1195(v C-O of ester). $^1\text{H NMR}$ (400MHz, $\text{DMSO-}d_6$, TMS): δ (ppm): 8.01(s, 1.0H, aromatic protons), 7.56(s, 1.0H, aromatic protons), 6.38(s, 4.0 H, aromatic protons), 5.57(s, 1.0 H, $>\text{CH}$), 4.07(s, 12.0 H, - CH_3), 2.21-1.23(m, 51.0 H, - CH_2 -ADBAc).

4-DIPM-AD (yield = 25%). IR (KBr, cm^{-1}): 2915(v C-H), 1725(v C=O of ester), 1442(v aromatics), 1100(v C-O of ester). $^1\text{H NMR}$ (400MHz, $\text{DMSO-}d_6$, TMS): δ (ppm) : 7.59 (s, 2.0 H, aromatic), 6.92 (s, 4.0 H, aromatic), 5.43 (s, 1.0 H, $>\text{CH}$), 4.43 (s, 4.0 H, - CH_2 -), 2.10 (s, 12.0 H, - CH_3), 2.09-1.52 (m, 51.0 H, - CH_2 - of ADBAc).

2.7. Polyaddition of phenols (4-DIPM, THM) and divinyl ethers [diethylene glycol divinyl ether (DGDE), BAC, BVFP]

(Synthesis of hyperbranched polyacetals)

Typical procedure for the synthesis of poly(4-DIPM-*co*-DGDE): A solution of 4-DIPM (2.1g,

3.5mmol) and DGDE (0.64g, 4.2mmol) was stirred in the presence of PPTS (0.21g, 2.1mmol) in THF (20mL) at r.t. for 6 h. After that, triethylamine was added and the resulting mixture and stirred at r.t. for 30 min. The organic phase was dried over anhydrous magnesium sulfate and was concentrated in a rotary evaporator. The resulting residue was dropped into large amount of hexane to precipitate the solid poly(4-DIPM-*co*-DGDE). Yield = 2.1 g (91%). IR(KBr, cm^{-1}): 3486(v O-H), 2815(v C-H), 1495(v aromatic), 1194(v C-O). $^1\text{H NMR}$ (400MHz, $\text{DMSO-}d_6$, TMS): δ (ppm): 9.35-8.02(m, -OH), 7.50-6.32(m, aromatic), 6.2-6.02(m, vinyl), 5.52-4.96(m, -CH), 4.65-4.53(m, - CH_2), 1.56-1.23(m, 12.0 H, - CH_3).

Poly(4-DIPM-*co*-BAC) was obtained by the polyaddition of 4-DIPM and BAC. Yield = 75%. IR (KBr, cm^{-1}): 3456(v O-H), 2915(v C-H), 1485(v aromatics), 1194(v C-O). $^1\text{H NMR}$ (400MHz, $\text{DMSO-}d_6$, TMS): δ (ppm) : 8.05(s, -OH), 7.34-7.02(m, aromatic), 6.60-6.40(m, vinyl), 5.12-5.03(m, -CH), 2.93-2.01(m, - CH_2), 1.62-1.23(m, - CH_3).

Poly(4-DIPM-*co*-BVFP) was obtained by the polyaddition of 4-DIPM and 2,2'-bis(4-binyloxyethoxyphenyl)perfluoropropane (BVFP). Yield = 43%. IR (KBr, cm^{-1}): 3426(v O-H), 2915(v C-H), 1485(v aromatics), 1194(v C-O). $^1\text{H NMR}$ (400MHz, $\text{DMSO-}d_6$, TMS): δ (ppm): 8.12(s, -OH), 7.31-6.72(m, aromatic), 5.20-4.92(m, CH), 4.02-3.51(m, - CH_2), 2.21-1.89(m, - CH_3).

Poly(THM-*co*-DGDE) was obtained by the polyaddition of THM and DGDE. Yield = 65%. IR (KBr, cm^{-1}): 3486(v O-H), 2815(v C-H), 1495(v aromatics), 1194(v C-O). $^1\text{H NMR}$ (400MHz, $\text{DMSO-}d_6$, TMS): δ (ppm): 9.35-9.02(m, -OH), 6.91-6.62(m, aromatic), 5.42-5.16(m, $>\text{CH}$), 4.65-3.53(m, - CH_2 -, vinyl), 1.32-1.02(- CH_3).

Poly(THM-*co*-BAC) was obtained by the polyaddition of THM and BAC. Yield = 42%. IR (KBr, cm^{-1}): 3480(v O-H), 2823(v C-H), 1491(v aromatics), 1180(v C-O). $^1\text{H NMR}$ (400MHz, $\text{DMSO-}d_6$, TMS): δ (ppm): 8.08-7.95(m, -OH), 7.52-6.45(m, aromatic), 5.62-5.02(m, $>\text{CH}$), 2.94-2.01(m, - CH_2 -, vinyl), 1.95-1.02(- CH_3).

Poly(THM-*co*-BVFP) was obtained by the polyaddition of THM and BVFP. Yield = 48%. IR (KBr, cm^{-1}): 3468(v O-H), 2950(v C-H), 1501(v aromatics), 1210(v C-O). $^1\text{H NMR}$ (400MHz, $\text{DMSO-}d_6$, TMS): δ (ppm): 8.08-8.01(m, -OH), 7.51-6.62(m, aromatic), 5.58-4.82(m, CH), 4.22-3.58(m, - CH_2), 2.21-1.29(m, - CH_3).

2.8. Film forming ability and thickness loss property on silicon wafer in tetramethylammonium hydroxide (TMAH) aq.

The solutions of resist materials in propylene glycol monomethyl ether acetate (PGMEA) were spin-coated on the silicon wafer which were primed with hexamethyldisilazane (HMDS). The value of thickness of the films was determined by ellipsometry before and after soaking in 2.38wt% tetramethylammonium hydroxide (TMAH) aq. for 30 sec.

2.9. Thermal stability

The thermal properties of the resist materials were examined by means of TGA (TGA-50/50H at a heating rate of 10 °C/min under nitrogen).

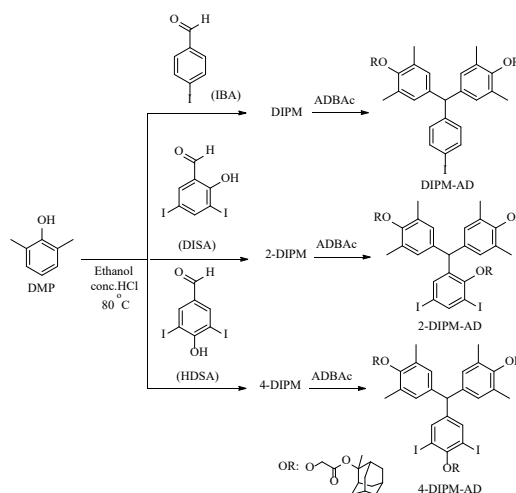
2.10. Resist sensitivity

The resist solutions were filtered through a 0.20 μm PTFE syringe filter prior to spin-coating on silicon wafers which were primed with hexamethyldisilazane (HMDS). Spin-coating was performed at 2800 rpm for 30 s to form films on the silicon wafers. Then these spin-coated films were prebaked at 90 or 110 °C for 60s. The resulting films were exposed to EUV lithography (energetic EQ10M). The area of exposure was approximately 1 × 1 cm². After the exposure, they were developed by dipping in TMAH solution at for 30s and then rinsed in deionized water before drying. The resist film thickness was measured to obtain sensitivity curves.

3. Results and discussion

3.1. Synthesis of iodine-containing compounds containing adamantly ester group (DIPM-AD, 2-DIPM-AD, 4-DIPM-AD).

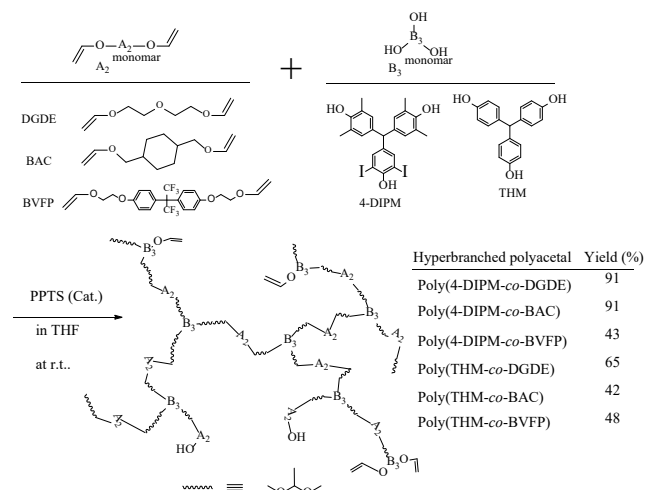
Condensation reaction of IBA and DMP was carried out using HCl in ethanol at 90 °C for 24 h to give a corresponding compound DIPM in a 84 % yield. Its structure was confirmed by ¹H NMR and IR spectroscopy. In the same way, the reaction of benzaldehydes (DISA, HDSA) and DMP was performed, yielding corresponding compounds 2-DIPM and 4-DIPM in 56 and 80% yields, respectively. Next, the reaction of IMDP and ADBAc was carried out using K₂CO₃ as a base in NMP at 80°C for 24 h in the presence of TBAB as a catalyst, to obtain a corresponding compound DIPM-AD in 28% yield. In the same way, 2-DIPM-AD, 4-DIPM-AD were synthesized in 18~25% yields. These synthetic procedures are illustrated in Scheme 1.



Scheme 1. Synthesis of molecular resists DIPM-AD, 2-DIPM-AD, 4-DIPM-AD

3.2. Synthesis of hyperbranched polyacetals by the polyaddition of divinyl ethers (A₂ type monomer) and phenols (B₃ type monomer).

The polyaddition of divinyl ethers DGDE, BAC and BVFP as (A₂ type monomers) and 4-DIPM (B₃ type monomer) was performed, to give corresponding hyperbranched polyacetals poly(4-DIPM-co-DGDE), poly(4-DIPM-co-BAC), poly(4-DIPM-co-BVFP), poly(THM-co-DGDE), poly(THM-co-BAC), and poly(THM-co-BVFP) $M_n = 3,610\sim 7,020$, $M_w/M_n = 1.56\sim 2.71$ in 42~91% yields (Scheme 2). Their structures were confirmed by ¹H NMR and IR spectroscopy.



Scheme 2. Synthesis of hyperbranched polyacetals

3.3. Physical properties (solubility, film-forming ability, thickness loss and thermal stability)

Physical properties relevant to their applicability as EUV resist materials were examined.

Solubility and Film-forming ability. The synthesized resists materials were soluble in

common organic solvents. Then 2 wt% solution of resist materials in PGMEA was prepared and spin coated onto the silicon wafer. As the results, all synthesized resist materials could show good film-forming ability.

Thickness loss property. The solutions of resist materials in PEGMEA were spin-coated on the silicon wafer to prepare corresponding films with about 30 nm thickness. The value of thickness of the films was determined by ellipsometry before and after soaking in 2.38wt%TMAH aq. for 30 sec. The ratios of decrease of the thickness of poly(4-DIPM-co-BAC) were 100% respectively. On the other hand, almost resist materials were 10% or less respectively. These results mean these DIPM-AD, 2-DIPM-AD, 4-DIPM-AD, Poly(4-DIPM-co-DGDE), Poly(4-DIPM-co-BAC) and Poly(4-DIPM-co-BVFP) can be used as positive resist materials with 2.38 wt% TMAH aq. as the developer. These results are summarized in Table1.

Table 1 Film-forming ability and thickness loss property of resist materials.

Resist material	Film forming ability	Thickness loss(%)
DIPM-AD	good	9
2-DIPM-AD	good	5
4-DIPM-AD	good	9
Poly(4-DIPM-co-DGDE)	good	10
Poly(4-DIPM-co-BAC)	good	100
Poly(4-DIPM-co-BVFP)	good	<1
Poly(THM-co-DGDE)	good	15
Poly(THM-co-BAC)	good	13
Poly(THM-co-BVFP)	good	<1

Thermal stability. The thermal stability of the synthesized resist materials was determined by TGA. The initial decomposition temperatures (T_d^i) of molecular resists (DIPM-AD, 2-DIPM-AD, and 4-DIPM-AD) were in the range between 168 and 197 °C (Figure 1[A]), those of hyperbranched polyacetals [poly(4-DIPM-co-DGDE), poly(4-DIPM-co-BAC), poly(4-DIPM-co-BVFP)] were in the range between 123 and 193 °C (Figure 1[B]), and those of hyper branched polyacetals [poly(THM-co-DGDE), poly(THM-co-BVC), and poly(THM-co-BVFP)] were in the range between 110 and 228 °C (Figure 1[C]). These mean that the synthesized resist materials have sufficient thermal stability which can be applied as resist materials withstand high temperatures of nearly 100°C in

prebake and postexposure bake.

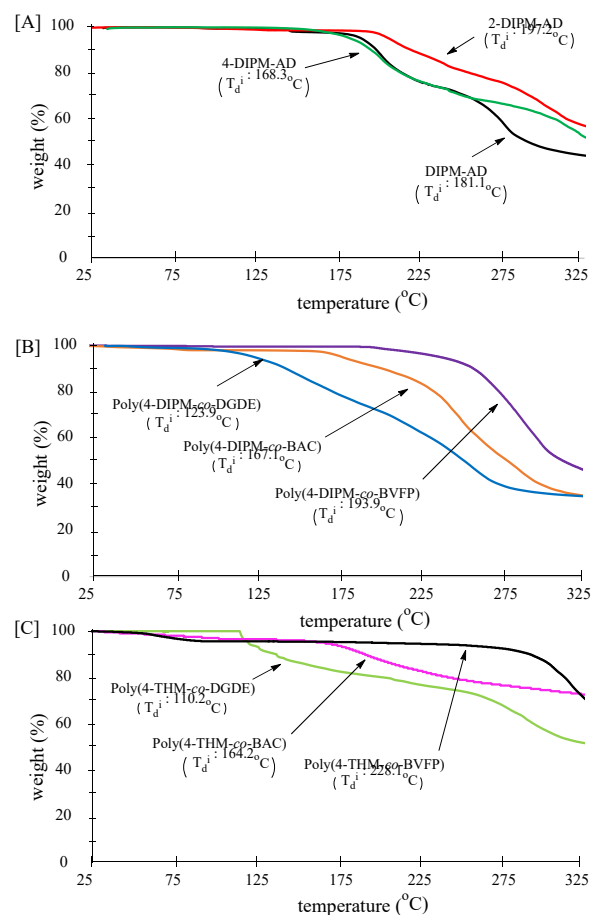


Figure 1. TGA curves of resist materials. [A]: Low molecular resist materials. [B]: Hyperbranched polyacetals (compound iodine). [C]: Hyperbranched polyacetals.

We have synthesized certain low molecular compounds and hyperbranched polyacetals, and their basic physical properties were examined for the application of resist materials. Consequently, only poly(4-DIPM-co-BAC) could not have good thickness loss property.

3.4. Resist sensitivity

The resist sensitivity of resist materials except poly(4-DIPM-co-BAC) were examined using EUV exposure tool. Solutions of the resist materials in the presence of 10 wt% of TPS-Nf as a PAG in PGMEA were spin coated on silicon wafers to prepare corresponding thin films of about 30 nm thickness. The postexposure baking (PEB) temperature and time were 90~110 °C and 60s. The thickness of the remind films was measured with ellipsometry after the lithography process (soaking in 2.38wt%TMAH aq. and water for 30 sec).

In the case of molecular resists, E_0 of DIPM-AD, 2-DIPM-AD, and 4-DIPM-AD showed $E_0 = 2.0, 7.0,$ and 9.0 mJ/cm^2 , respectively, i.e., the resist sensitivity was consistent of the structures and its order was DIPM-AD > 2-DIPM-AD > 4-DIPM-AD (Figure 2[A]).

Furthermore, in the case of hyperbranched polyacetals, poly(THM-co-BVFP) not show resist sensitivity, but poly(THM-co-DGDE) and poly(THM-co-BAC) showed $E_0 = 2.0 \text{ J/cm}^2$, and poly(4-DIPM-co-DGDE) and poly(4-DIPM-co-BVFP) showed $E_0 = 1.0 \text{ J/cm}^2$. Generally, an E_0 value of less than 10 mJ/cm^2 is required for EUV lithography. Then, the present resist materials could appear to have adequate resist sensitivity for application as EUV photoresist systems. Especially, iodine containing hyperbranched polyacetals poly(4-DIPM-co-DGDE) and poly(4-DIPM-co-BVFP) could show higher sensitivity. Presumably because of that these polymers are main-chain scission type and contain iodine in the polymers.

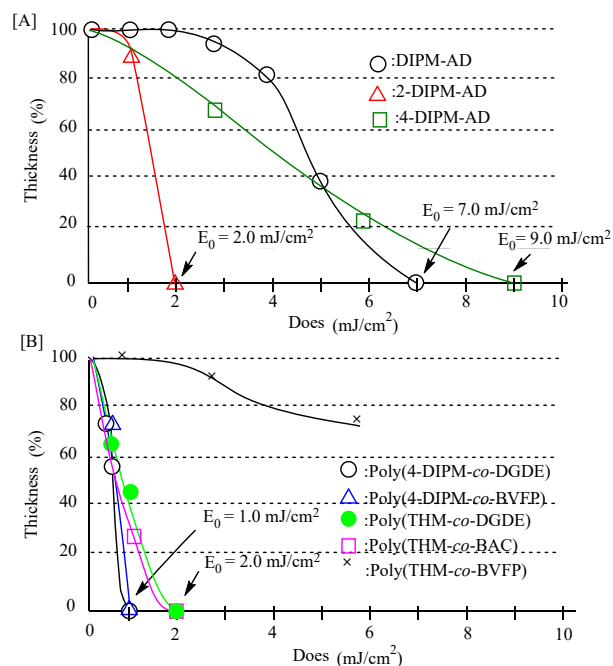


Figure 2. Resist sensitivity of resist materials using EUV exposure tool. [A]: Low molecular type resist. [B]: Hyperbranched polyacetals.

4. Conclusion

In summary, we examined the synthesis of iodine-containing molecular resists with pendant adamanty ester groups (DIPM-AD, 2-DIPM-AD, and 4-DIPM-AD). Further, the hyperbranched polyacetals [poly(THM-co-DGDE), poly(THM-co-BAC), and poly(THM-co-BVFP)] and iodine-containing hyperbranched polyacetals [poly(4-

DIPM-co-DGDE), poly(4-DIPM-co-BAC), and poly(4-DIPM-co-BVFP)] could be obtained by the polyaddition of divinyl ethers (A_2 type) and triphenols (B_3 type). The physical properties (solubility, film-forming ability, thermal stability) and thickness loss property soaking in 2.38wt%TMAH aq. were examined. As the result, almost all resist materials except poly(4-DIPM-co-BAC) could show good basic property which can be applicable as posi-type resist materials.

Furthermore, the resist sensitivity of the synthesized low molecule and hyperbranched polyacetals applicable to resist materials was examined using EUV exposure tool. These resist materials showed high resist sensitivity E_0 in the range between 1.0 and 9.0 mJ/cm^2 . Among them, poly(4-DIPM-co-DGDE) and poly(4-DIPM-co-BVFP) could show higher sensitivity. This is due to that hyperbranched skeleton linked by acetal bonds forms main-chain scission type and inclusion of iodine might further improve the absorption of EUV to increase the resist sensitivity.

Acknowledgement

This work was partly supported by Cooperative Research Program "Network Joint Research Center for Materials and Devices".

References

1. B. Wu, A. Kumar, *Journal of Vacuum Science & Technology B : Microelectronics and Nanometer Structures Processing, Measurement, and Phenomena* **25**, (2007), 1473.
2. V. Bakshi, *EUV Lithography*, John Wiley & Sons, Inc., (2009).
3. L. Li, X. Liu, S. Pal, S. Wang, C. K. Ober, E. Giannelis, *P. Chem. Soc. Rev.*, **46**, (2017), 4855–4866
4. A. Narasimhan, L. Wisehart, S. Grzeskowiak, L. E. Ocola, G. Denbeaux, R. L. Brainard, *Journal of Photopolymer Science and Technology*, **30** (2017), 113–120.
5. T. Manouras, P. Argitis, *Nanomaterials*, **10** (2020), 1593.
6. T. Kozawa, S. Tagawa, *Jpn. J. Appl. Phys.* **49**, (2013)
7. T. Kozawa, A. Saeki, S. Tagawa, *J. Vac. Sci. Technol. B*, **22** (2004), 3489.

8. A. Saeki, S. Tagawa, *Pure appl. Chem.*, **81** (2009), 45-60.
9. S. W. Chang, R. Ayothi, D. Bratton, D. Yang, N. Felix, H. B. Cao, H. Dengb, C. K. Ober, *J. Mater. Chem.*, **16** (2006), 1470–1474.
10. J. Chen, Q. Hao, S. Wang, S. Li, T. Yu, Y. Zeng, J. Zhao, S. Yang, Y. Wu, C. Xue, G. Yang, and Y. Li, *ACS Appl. Polym. Mater.*, **1** (2019), 526–534.
11. X. Peng, Y. Wang, J. Xu, H. Yuan, L. Wang, T. Zhang, X. Guo, S. Wang, Yi. Li, and G. Yang, *Macromol. Mater. Eng.*, **303** (2018), 1700654.
12. H. Kudo, S. Ohori, H. Takeda, H. Ogawa, T. Watanabe, H. Yamamoto, T. Kozawa, *J. Photopolym. Sci. Technol.*, **28** (2018) 221.
13. H. Kudo, D. Watanabe, T. Nishikubo, K. Maruyama, D. Shimiu, T. Kai, T. Shimokawa, C.K. Ober, *J.Mater.Chem.*, **18** (2008), 3588-3592.
14. X. André, J.K. Lee, A. Desilva, C.K. Ober, H.B. Cao, H. Deng, H. Kudo, D. Watanabe, T. Nishikubo, *Proc.SPIE*, **6519** (2007), 65194B
15. T. Nishikubo, H. Kudo, Y. Suyama, H. Oizumi, T. Itani, *J. Photopolym. Sci. Technol.*, **22** (2009), 73-76.
16. H. Kudo, Y. Suyama, H. Oizumi, T. Itani, T. Nishikubo, *J. Mater. Chem.*, **20** (2010), 4445-4450.
17. N. Niina, H. Kudo, H. Oizumi, T. Itani, T. Nishikubo, *Thin Solid Films*, **534** (2013), 459-464.
18. H. Kudo, M. Jinguji, T. Nishikubo, H. Oizumi, T. Itani, *J. Photopolym. Sci. Technol.*, **23** (2010), 657-664.
19. H. Seki, Y. Kato, H. Kudo, H. Oizumi, T. Itani, T. Nishikubo, *Jpn. J. Appl. Phys.*, **49** (2010).
20. H. Yamamoto, H. Kudo, T. Kozawa, *Microelectronic Eng.*, **133** (2015), 16-22.
21. H. Kudo, S. Matsubara, H. Yamamoto, T. Kozawa, *Journal of photopolymer Science and Technology.*, **28** (2015), 125-129.
22. H. Kudo, M. Fukunaga, K. Shiotsuki, H. Takeda, H. Yamamoto, T. Kozawa, T. Watanabe, *Reac.&Func. Polym.* **131** (2018) 361.
23. R. Fallica, D. Kazazis *Journal of Vacuum Science & Technology B*, **35**, (2017) 061603.
24. H. Ito, C. G. Willson, J. H. J. Frechet, *Digest of Technical Papers. VLSI Technology*, **86** (1982).
25. T. Kozawa, S. Tagawa, *Jpn. J. Appl. Phys.* **49** (2010) 030001.
26. R. Lescouëzec, *Inorganica Chimica Acta*, **350** (2003), 131.
27. H. Kudo, M. Fukunaga, K. Shiotsuki, H. Takeda, H. Yamamoto, T. Kozawa, T. Watanabe, *Reac. & Func. Polym.* **131** (2018) 361.
28. J. R. Strahan, J. R. Adams, W.-L. Jen, A. Vanleenhove, C. C. Neikirk, T. Rochelle, R. Gronheid, C. G. Willson, *Proc. SPIE*, **7373** (2009), 72733G.
29. S. Enomoto et al, *Jpn. J. Appl. Phys.* **58** (2019) 016504.
30. J. Peter, M. G. Moinuddin, S. Ghosh, S. K. Sharma, K. E. Gonsalves, *ACS Appl. Polym. Mater.*, **2** (2020), 1790–1799.
31. J. R. Gomez, H. Kuan Ng, P. Kumar, A. Suwardi, M. Zheng, M. Asbahi, S. Tripathy, I. Nandhakumar, M. S. M. Saifullah, and K. Hippalgaonkar, *ACS Appl. Mater.* **12** (2020), 33647–33655.
32. L. Wu, M. F. Hilbers, O. Lugier, N. Thakur, M. Vockenhuber, Y. Ekinici, A. M. Brouwer, and S. Castellanos, *ACS Appl. Mater.*, **13** (2021), 51790–51798.
33. M. Yogesh, M. G. Moinuddin, M. Chauhan, S.

K. Sharma, S. Ghosh, and K. E. Gonsalves,
ACS Appl. Electron. Mater., **3** (2021), 1996–
2004

Comparison of photoresist sensitivity between KrF, EB and EUV exposure

Yosuke Ohta^{1*}, Atsushi Sekiguchi¹, Shinji Yamakawa², Tetsuo Harada²,
Takeo Watanabe², and Hiroki Yamamoto³

¹ *Litho Tech Japan Co., Ltd., 2-6-6 Namiki, Kawaguchi, Saitama 332-0034, Japan*

² *Center for EUV Lithography, Laboratory of Advanced Science and Technology for Industry, University of Hyogo, 1-1-2 Kouto, Kamigori, Ako-gun, Hyogo 678-1205, Japan*

³ *Takasaki Advanced Radiation Research, National Institutes for Quantum Science and Technology, 1233 Watanuki-machi, Takasaki, Gunma 370-1292, Japan*

*ohta.yosuke@ltj.co.jp

It has been reported that the good correlation in sensitivity and resolution between EUV exposure and EB exposure because of the similar mechanism of the photochemical-reaction in photoresists during exposure. However, in the early stages of EUV resist development, there are problems on the points of the cost and time-consuming to evaluate all EUV resist materials by EB exposure. Therefore, we investigated the possibility of using KrF exposure as the initial screening of EUV resists. If the correlation between KrF exposure, EB exposure and EUV exposure can be found, it will be possible to evaluate photoresists in a step-by-step manner, such as screening with KrF exposure first, followed by EB exposure, and finally EUV exposure in the initial evaluation stage. In this paper, we report on our investigations in the case of novolac resists, PHS chemically amplified resists, acrylic chemically amplified resists, and EUV polymer resists.

Keywords: KrF exposure, EB exposure, EUV exposure, novolac resist, PHS resist, Acrylic resist, EUV resist and resist sensitivity-evaluation — —

1. Introduction

EUVL (Extreme Ultra Violet Lithography) technology has begun to be used for fabrication of 7-nm logic devices, and has been used for a mass-production technology since 2020 [1-10]. Furthermore, EUVL technology is about to be used for the fabrication of 1.5nm device patterns. However, EUV still has various problems in photoresist development. For example, it is well known a trade-off between resolution, LER (Line Edge Roughness) and sensitivity, so-called RLS Trade-off [11-15]. Until now, the development of EUV photoresist has been carried out by EB exposure [16]. This is because EUV exposure equipment is not available in Japan and EUV exposure equipment is very expensive. However, the EB exposure equipment was expensive too, and it was difficult to use it conveniently for evaluation of the EUV photoresist, because it took long time for EB drawing. Especially in the early stage, the use of EB exposure needs to take much time and

large cost. It does not seem to be efficient for the EUV photoresist development. Therefore, we examined whether the simple KrF exposure could be used for the screening of the EUV photoresist in the early stage of the development.

KrF exposure sensitivity, EB exposure sensitivity and EUV exposure sensitivity of novolac resist, PHS type resist, acrylic type resist, and main chain cutting type resist were compared, and the correlation of the sensitivity was examined for what kind of material system.

2. Experimental

2.1. Materials

The resists and conditions used in this experiment are shown in Table 1.

The resist was spin-coated on a 6-inch silicon substrate at a specified rotation speed. Prebaking was performed at specified temperature and time after spin coating.

Received	April 15, 2022
Accepted	May 20, 2022

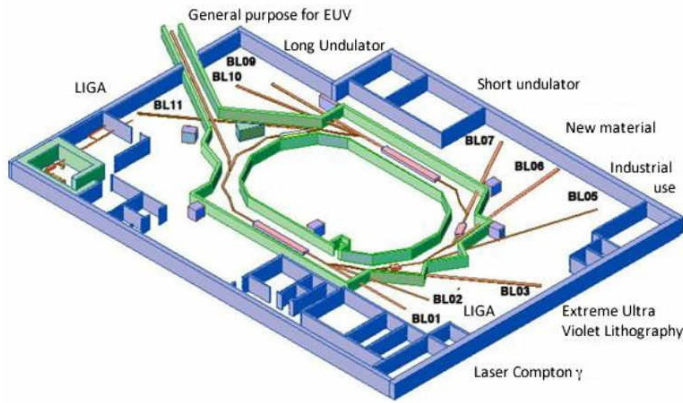


Fig. 1. NewSUBARU synchrotron radiation facility.



Fig. 2. Appearance of BL3 exposure system.

Table 1. Experimental condition.

Photoresist	Type	Wavelength	Film thickness [nm]	Pre-Bake		PEB		Development time [s]	Developer
				Temp. [deg.C]	Time [s]	Temp. [deg.C]	Time [s]		
ZEP520A	NCAP	EB	50	180	180	-	-	30	nBA
UV-135G0.4	ESCAP	KrF	50	120	60	130	60	10	TMAH
TDUR-P036	Acetal	KrF	50	90	90	110	90	10	TMAH
TArF-P6111	Acrylic	ArF	50	130	90	130	90	60	TMAH
EUVJ854	Acetal	EUV	50	130	60	120	60	60	TMAH
SEVR-140	Acetal	EUV	50	105	60	95	60	30	TMAH
FEVS-P1245A	Acetal	EUV	50	120	90	110	90	30	TMAH
OFPR-800	Novolac	g-line	50	100	60	110	60	60	TMAH
PFI	Novolac	i-line	50	90	60	110	60	60	TMAH

2.2. Apparatus and exposure

In this experiment, three kinds of exposures, KrF, EB and EUV, were carried out.

KrF exposure was performed by UVES-2000 (Litho Tech Japan) with the open frame exposure of 10x10mm. EB exposure was performed by ELS-G100 (Elionix) with drawing the area of 40x40um. EUV exposure was performed at NewSUBARU cyclotron facility Beam-line 3 (University of Hyogo) with open frame exposure. A schematic diagram of NewSUBARU cyclotron facility and an external view of BL3 exposure equipment are shown in Figs. 1 and 2, respectively [17, 18].

2.3. Measurements

After exposure, development was performed under the process conditions in Table 1. In KrF exposure and EUV exposure, the film thickness at the exposure area was measured by an ellipsometer, and the sensitivity curve was plotted. Since the exposure area is too small in the EB exposure to measure film thickness by an ellipsometer, the probe type step profiler Dektak XT (Bruker) was used, and then the sensitivity curve was plotted. In each exposure, we calculated the exposure dose at which film thickness became 0 in sensitivity curve and then we defined it as so-called E_{th} which generally means sensitivity of photoresist.

Figure 3 (a) and (b) show pictures of the substrate after KrF, EUV exposure and development respectively. Figure 3 (c) shows a picture of zoom up image by laser microscope after EB exposure and development.

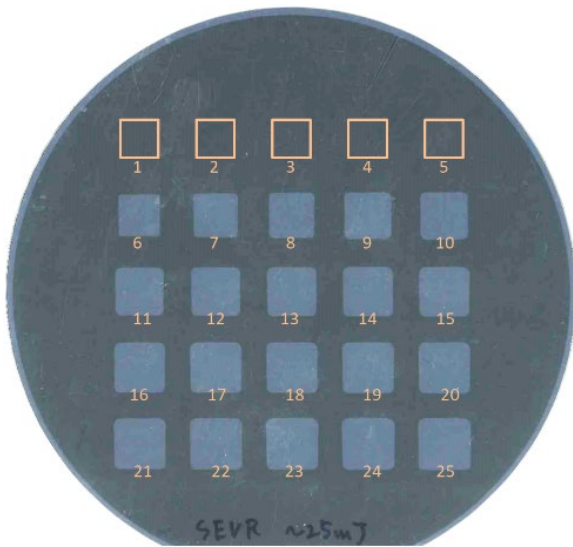
3. Experimental result

Figure 4 shows the sensitivity curves at each exposure, and the obtained E_{th} are shown in Table 2.

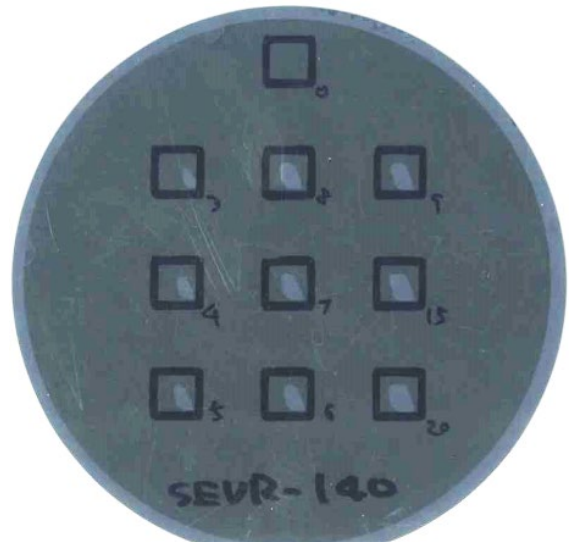
At first, we found that novolac resists don't have contrast by KrF, EB and EUV exposure at all. Therefore, we considered the sensitivity comparison between KrF, EB and EUV exposure by using photoresist other than novolac resists.

Figure 5(a) shows a correlation of E_{th} between KrF and EB exposures from each photoresist, Fig. 5(b) shows a correlation of E_{th} between KrF and EB exposures, and Fig. 5(c) shows a correlation of E_{th} between EB and EUV exposures. In addition, the correlating equations for each graph are shown in (1), (2) and (3).

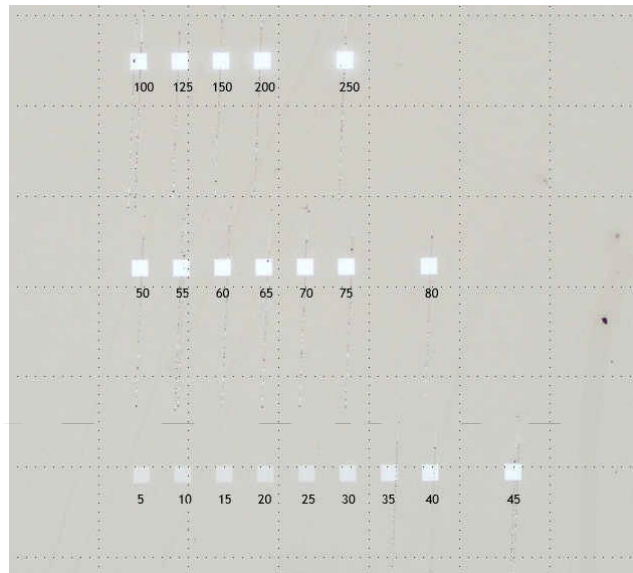
As a result, it was found that there is a correlation of the sensitivity of each exposure in the chemically amplified resist.



(a) KrF exposure



(b) EUV exposure



(c) EB exposure

Fig. 3. Wafers after exposure and development (a) and (b),
Laser microscope image of patterns after exposure and development (c).

- KrF-EB: $15.6x-55.2$ (1)
 KrF-EUV: $1.28x-4.19$ (2)
 EB-EUV: $0.0719x+1.00$ (3)

relationships.

$$E = \alpha F \quad (4)$$

Thus, the sensitivity in EUV can be predicted from the sensitivity in EB exposure.

4. Results and discussion

4.1. Correlation between EB exposure and EUV exposure

It is generally known that there is a correlation of sensitivity between EB exposure and EUV exposure because the mechanisms of EB exposure and EUV exposure are similar.

Basically, units of UV exposure are expressed in mJ/cm^2 , and units of EB exposure are expressed in $\mu C/cm^2$. When the accelerating voltage of EB is defined as α , it is known that the UV exposure dose E and the EB exposure dose F have the following

relationships. However, the slope of the fitting equation (3) between EB and EUV exposure obtained in this experiment is 0.0719. Considering from the equation (4), the theoretical value is 100.0 for the acceleration-voltage 100KeV, then there is a large difference from the experimental result. This is because, in EB exposure, when the accelerating voltage increases, electrons will pass through the resist film and all electrons cannot be absorbed in the resist film. In other words, the resist does not absorb 100% of the energy. Therefore, it is considered that the relationship between the UV

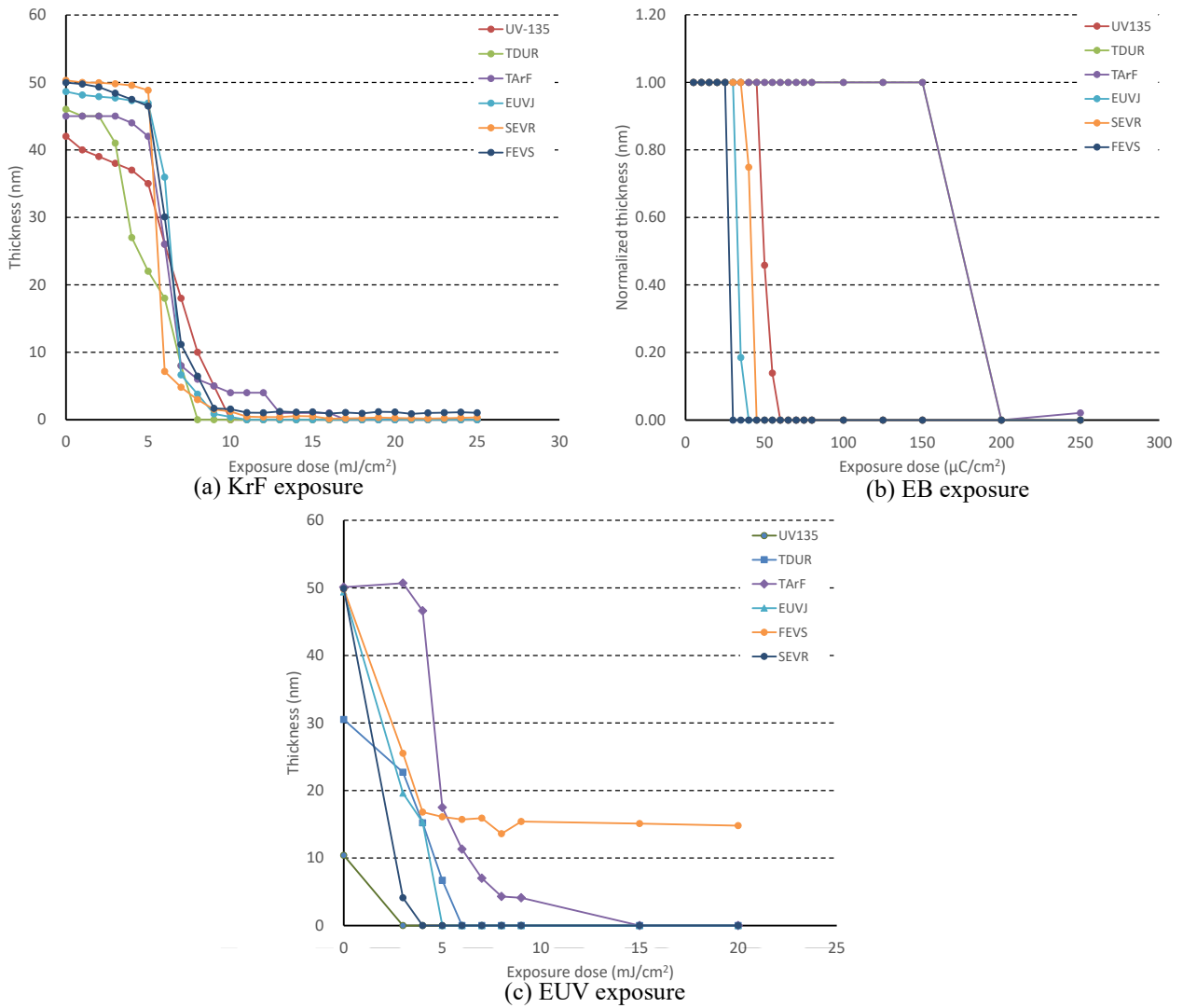


Fig. 4. Sensitivity curve.

Table 2. Result of Eth.

Photoresist	Type	Wavelength	KrF [mJ/cm ²]	EB [µC/cm ²]	EUV [mJ/cm ²]
ZEP520A	NCAP	EB	371.5	100	10
UV-135G0.4	ESCAP	KrF	9.58	60	3
TDUR-P036	Acetal	KrF	8.09	200	6
TArF-P6111	Acrylic	ArF	14.9	200	15
EUVJ854	Acetal	EUV	7.2	40	5
SEVR-140	Acetal	EUV	6.2	45	4
FEVS-P1245A	Acetal	EUV	3.8	30	20
OFPR-800	Novolac	g-line	-	-	-
PFI	Novolac	i-line	-	-	-

exposure dose E and the EB exposure dose F is much lower than the theoretical value (about 1/1000 in this experiment).

4.2. Correlation between KrF exposure and EUV exposure

Table 3 shows the photon absorptions, acid

generation numbers and quantum efficiencies for KrF exposure and EUV exposure, respectively, calculated by PROLITH [19, 20]. Figure 6 is a schematic representation of acid evolution.

The acid generation number of KrF exposure is about 1.2 times larger than that of EUV exposure. In other words, in order to obtain the same exposure

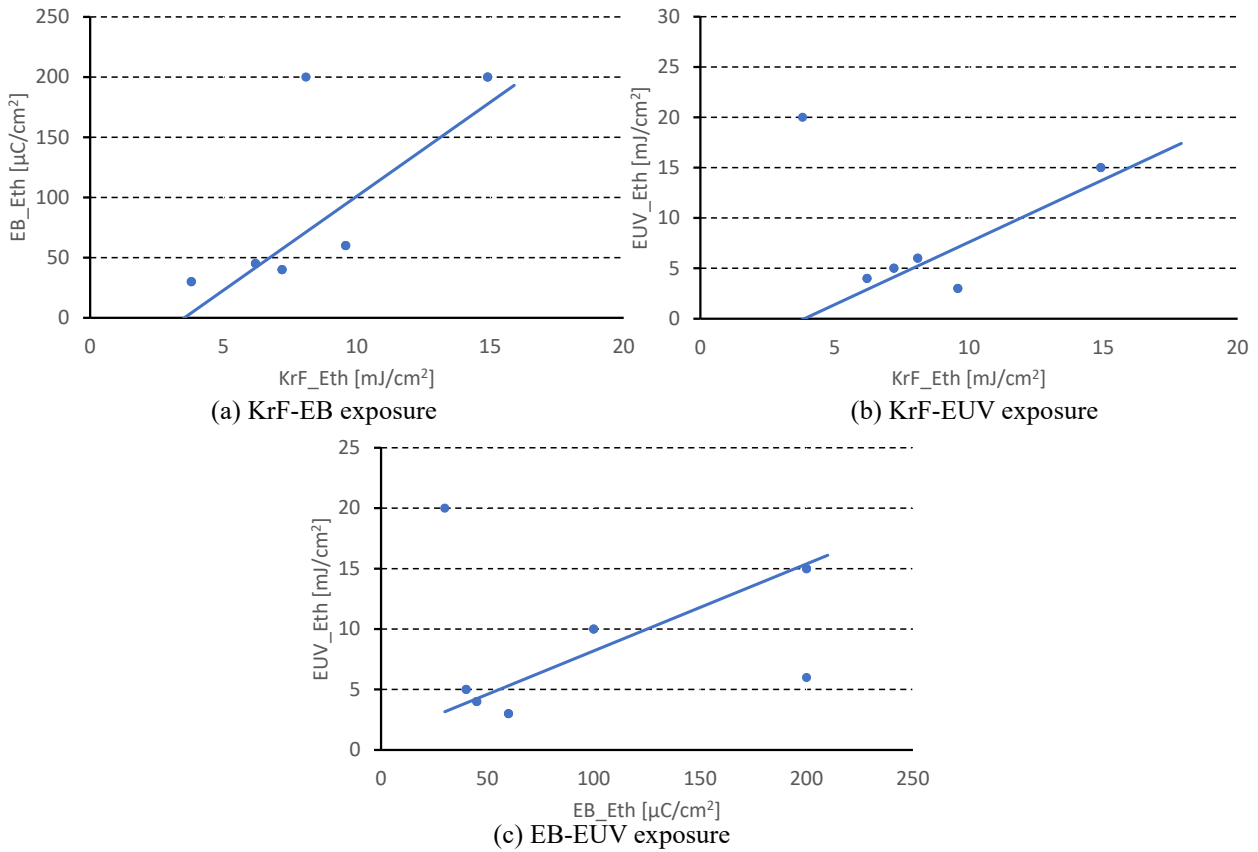


Fig. 5. Correlation of sensitivity.

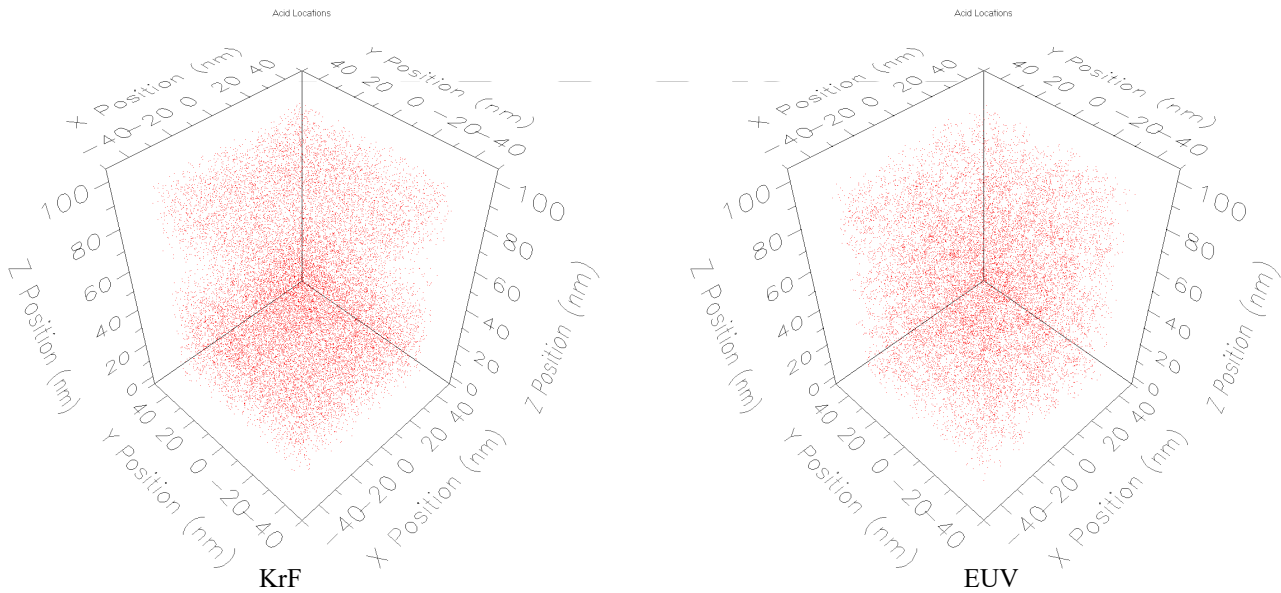


Fig. 6. Distribution of acid generation.

effect, the exposure dose of the EUV should be 1.2 times larger than the exposure dose of KrF. The correlation coefficient of the equation (2) is about 1.28, and the theoretical value agrees well with the experimental value.

4.3. The main chain scission type resist

Besides chemically amplified resist, three kinds

of exposure were also carried out in main chain scission type resist (ZEP-520), and then Eth were compared. As a result, it was found that very large exposure dose was necessary only for KrF exposure.

KrF exposure mainly cause chemical reaction, generation of acid from PAG (Photo Acid Generator), and the effect of physical reaction is small. On the contrary, EB exposure and EUV

Table 3. Calculation result of absorbed photon and acid generation.

	Absorbed Photons	Generated Acid	Acid Quantum Yield
KrF	155,929	20,452	0.131
EUV	8,852	16,943	1.914
Ratio (KrF/EUV)	17.615	1.2071	

exposure mainly cause physical reactions by secondary electrons. Therefore, it is considered that a very large exposure energy is required to cut the main chain of the main chain scission type resist using KrF exposure.

5. Summary

Using various kind of photoresists, we measured sensitivity of photoresists by KrF, EB and EUV exposure, and calculated the correlation between each exposure. As a result, it was found that there was some correlation between KrF, EB and EUV exposure in photoresist except for the main chain scission type. Especially the correlation between KrF and EUV agree well with the number of acid generation calculated by the simulation. It was shown KrF exposure is experimentally meaningful as an initial evaluation of chemically amplified resist for EUV.

Acknowledgements

We here highly appreciate TOKYO OHKA KOGYO Co., Ltd, JSR Corporation, FUJIFILM Corporation, ROHM AND HAAS ELECTRONIC MATERIALS K. K. and Zeon Corporation for supply of photoresists.

References

1. H. Kinoshita, T. Kaneko, H. Takei, N. Takeuchi, and S. Ishihara, *47th Autumn Meeting of the Japan Society of Applied Physics*, **28-ZF-15** (1986) 332 (in Japanese).
2. H. Kinoshita, K. Kurihara, T. Mizota, T. Haga, H. Takenaka, and Y. Torii, *Appl. Opt.*, **32** (1993) 7079.
3. T. Haga, M. Tinone, H. Takenaka, and H. Kinoshita, *Microelectron Eng.*, **30** (1996) 179.
4. Y. Ekinci, M. Vockenhuber, M. Hojeij, L. Wang, and N. Mojarad, *Proc. SPIE*, **8679** (2013) 867910.
5. W. J. Bae, M. Trikeriotis, R. Rodriguez, M. F. Zettel, E. Piscani, C. K. Ober, E. P. Giannelis, and P. Zimmerman, *Proc. SPIE*, **7273** (2009) 727326.
6. M. E. Krysak, J. M. Blackwell, S. E. Putna, M. J. Leeson, T. R. Younkin, S. Harlson, K. Frasure, and F. Gstrein, *Proc. SPIE*, **9048** (2014) 904805.
7. C. J. Brinker and G. W. Scherer, "Sol-Gel Science", Academic Press (1990).
8. S. Chakrabarty, C. Sarma, L. Li, E. P. Giannelis, and C. K. Ober, *Proc. SPIE*, **9048** (2014) 90481C.
9. M. Trikeriotis, M. Krysak, Y. S. Chung, C. Ouyang, B. Cardineau, R. Brainard, C. K. Ober, E. P. Giannelis, and K. Cho, *Proc. SPIE*, **8322** (2012) 83220U.
10. C. Y. Ouyang, Y. S. Chung, L. Li, M. Neisser, K. Cho, E. P. Giannelis, and C. K. Ober, *Proc. SPIE*, **8682** (2013) 86820R.
11. A. Sekiguchi, T. Watanabe, and H. Kinoshita, *J. Pohotopolym. Sci. Technol.*, **27** (2014) 623.
12. Y. Fukushima, T. Watanabe, T. Harada, and H. Kinoshita, *J. Pohotopolym. Sci. Technol.*, **22** (2009) 85.
13. T. Ishiguro, J. Tanaka, T. Harada, and T. Watanabe, *J. Pohotopolym. Sci. Technol.*, **32** (2019) 333.
14. A. Sekiguchi, T. Harada, and T. Watanabe, *Proc. SPIE*, **10143** (2017) 1014322.
15. A. Sekiguchi, Y. Matsumoto, M. Isono, M. Naito, Y. Utsumi, T. Harada, and T. Watanabe, *Proc. SPIE*, **10583** (2018) 1058320.
16. Y. Ohta, A. Sekiguchi, A. Voigt, and N. Taksatorn, *J. Pohotopolym. Sci. Technol.*, **33** (2020) 221.
17. Laboratory of Advanced Science and Technology for Industry, University of Hyogo <https://www.lasti.u-hyogo.ac.jp/NS-en/facility/bl03/>
18. Y. Ohta, A. Sekiguchi, T. Harada, and T. Watanabe, *J. Pohotopolym. Sci. Technol.*, **34** (2021) 105.
19. J. J. Biafore, M. D. Smith, C. A. Mack, J. W. Thackeray, R. Gronheid, S. A. Robertson, T. Graves, and D. Blankenship, *Proc. SPIE*, **7273** (2009) 727343.
20. J. J. Biafore, M. D. Smith, S. A. Robertson, and T. Graves, *Proc. SPIE*, **6519** (2007) 65190Y

Development of Selenonium PAGs in EUV Lithography toward High Sensitivity Achievement

Tomohito Kizu^{1*}, Shinji Yamakawa², Takeo Watanabe²,
Seiji Yasui¹, and Tomoyuki Shibagaki¹

¹ San-Apro Ltd., 1-40, Goryo-Ohara, Nishikyo-ku, Kyoto 615-8245, Japan

² Center for EUV Lithography, Laboratory of Advanced Science and Technology for Industry, University of Hyogo, 1-1-2 NewSUBARU, Kouto, Kamigori, Ako-gun, Hyogo 678-1205, Japan

*kizu@sanyo-chemical.group

Extreme ultraviolet (EUV) lithography at 13.5 nm has become an essential technology for the mass production of state-of-the-art semiconductor integrated circuits for use in devices such as smartphones. Chemically amplified resists (CARs) are primarily used for their production, and several performance requirements have to be met to achieve fine patterning. The requirements are known for simultaneous achievement of resolution, low line edge roughness (LER), high sensitivity, and low outgassing. As photoacid generators (PAGs) are ingredients for determine CARs sensitivity, high absorption of EUV light, acceptability of the secondary electron from matrix polymer, and high decomposability (high acid generation efficiency) are required in EUV lithography. Most onium-salt structures that have been proposed for use as EUV PAGs possess a sulfur atom at its center of cation. In this study, we focus on selenonium salts possessing selenium atoms at its center of cation, which exhibit strong absorption of EUV light, and evaluate their utility in EUV lithography.

Keywords: EUV lithography, Photoacid generators, Selenonium, Selenium, Sensitivity

1. Introduction

Extreme ultraviolet (EUV) lithography is an essential technology introduced from 7 nm node process for the mass production of micro-processing units, which are used in compact high-performance devices such as smartphones and tablet PCs. Chemically amplified resists (CARs) [1] have been utilized in EUV lithography to transfer circuit patterns from masks to substrates. To improve the performance of these devices, manufacturers are attempting to feasibly produce more high-performance resists. However, such resists have the technical issue called RLS trade-off [2]. Namely 1) high resolution, 2) decreased line edge roughness (LER), and 3) high sensitivity conflict with each other. Therefore, development of resists satisfying all the performance requirements is crucial [3]. In the performance, it is widely known that sensitivity is strongly influenced by photoacid generators (PAGs), which initiate reactions during EUV irradiation. And it is

desired to develop highly sensitive PAGs to overcome the trade-off.

Similar to conventional UV-PAGs, ionic sulfonium salts, iodonium salts, and nonionic molecular phthalimide derivatives have been investigated for the application to EUV lithography. Particularly, sulfonium salts are preferred owing to their thermal stability and various structures of their counter anion. However, for further miniaturization of the process, the sensitivity of PAGs is insufficient and requires further investigation.

To improve sensitivity, it is important to focus on acid generation mechanisms in EUV lithography [4]. The energy of photons at the exposure wavelength of 13.5 nm is 91.8 eV, which is approximately 14 times higher than that of conventional ArF excimer laser lithography. This implies that the EUV absorption of materials does not depend on the molecular structure but on the constituent elements and density. Because conventional sulfonium

Received	April 12, 2022
Accepted	June 25, 2022

PAGs are composed of low absorbance elements like carbon, oxygen, and sulfur, acid generation efficiency of PAGs under EUV irradiation is related to electron affinity of sulfonium [5]. This indicates that the decomposition of PAGs is primarily induced by the absorption of the secondary electron from the polymer matrix, and further improvement in electron acceptability is difficult to achieve owing to structural limitations. However, other approaches have attempted to add EUV high absorbance elements as sensitizers [6]. Furthermore, some studies have focused on photosensitized chemically amplified resist (PSCAR) technique in which the resist undergoes UV exposure is performed after EUV exposure, including EUV reactive photosensitizer precursor [7].

For these reasons, we hypothesized that the direct introduction of EUV high absorbance elements into PAG would improve sensitivity. We chose selenium, which is in the same group as sulfur, but has a much higher EUV absorption cross section than that of sulfur as shown in Fig. 1. Selenium is also used as a UV-PAG [8]; however, studies investigating its sensitivity to EUV light have only focused on MADMA-NORLAC resin [9]. This study attempts to address this gap.

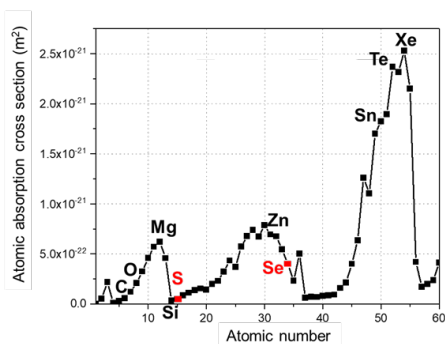


Fig. 1. Atomic absorption cross section at EUV ($\lambda = 13.5$ nm) of elements (atomic number Z from 1 to 60).

2. Experimental

2.1. Measurements

NMR (^1H and $^{19}\text{F}\{^1\text{H}\}$) spectra were recorded utilizing a JEOL JNM-ECZ400R (400 MHz for ^1H , 376 MHz for ^{19}F) spectrometer. Chemical shifts were reported in ppm based on the solvent resonance (^1H : DMSO- d_6 : 2.50 ppm) or electrical standard (^{19}F). The film thickness was measured utilizing a Nano-Spec (model 6100; Nanometrics, Inc.). The TG/DTA data was collected using TG/DTA6200 (EXSTAR6000; Seiko Instruments Inc.). Dose-to-clear experiments were carried out at the BL03 beamline of the NewSUBARU

Synchrotron light facility.

2.2.1. Materials

DMSO- d_6 , PGMEA (propylene glycol monomethylether acetate), potassium nonafluorobutanesulfonate, hexamethyldisilazane (HMDS), tetramethylammonium hydroxide in aqueous solution (TMAH $_{aq.}$), **PAG-2a** and **PAG-2b** were purchased from Wako and TCI, and used without further purification. **PAG-1a** was prepared according to the procedure in [10]. **PAG-3** and **PAG-4** were provided by San-Apro Ltd.

2.2.2. Preparation of **PAG-1b** [9]

PAG-1b was prepared using salt exchange process with **PAG-1a** and potassium nonafluorobutanesulfonate and obtained in 96% yield as solid. ^1H NMR: 7.79-7.65 ppm (15H, *m*); ^{19}F NMR: -80.3 ppm (3F, *m*), -114.8 ppm (2F, *m*), -121.3 ppm (2F, *m*), -125.6 ppm (2F, *m*).

2.3. Resist preparation for dose-to-clear experiments

PAG (equimolar to 10 wt% **PAG-2a** for ESCAP) was added to a mixture of PGMEA (5.46 g) and ESCAP resin (poly(hydroxystyrene-*co-tert*-butylacrylate)), 0.13 g) then stirred overnight. The resist solutions were filtered through a 0.22 μm PTFE syringe filter prior to spin-coating on 4-inch silicon wafers, which were treated via the adhesion process using HMDS (3000 rpm, then bake at 130 $^\circ\text{C}$ for 90 s). The resist solutions of PAGs in PGMEA were spin-coated on the silicon-wafers to prepare the corresponding films (1700~3000 rpm for 45 s, then pre-baked at 130 $^\circ\text{C}$ for 60 s). Subsequently, the initial film thicknesses were measured at 5 points on average and are shown in Table 1.

3. Results and discussion

3.1. Evaluation of PAGs in EUV lithography

Sensitivities of EUV resists were evaluated by obtaining dose-to-clear curves. Each wafer coated with the resist solution was exposed to EUV while changing exposure dose, followed by post-exposure bake (PEB) (110 $^\circ\text{C}$ for 90 s). The wafers were then developed using 2.38 wt% TMAH $_{aq.}$ for 60 s and rinsed with ultra-pure water; finally, they were blown dry by an N_2 gun. The thicknesses of the unexposed and exposed areas were measured. Thickness of the completely developed point of the exposed area which means the dose-to-clear point (E_0) is defined as the remaining thickness while its

ratio to that of the unexposed area is the normalizing remaining thickness (NRT (%)). Small E_0 implies good resist sensitivity because the required exposure dose to remove the resist is small. These results are listed in Table 1 and the dose-to-clear curves are shown in Fig. 2.

3.1.1. Sensitivity difference of selenium vs sulfur on onium center

First, we evaluated the effect of introducing selenium in the cation of onium center on the resist sensitivity. The results of the EUV exposure experiment for Samples 1 and 3 are shown in Table 1. It was observed that selenonium **PAG-1a** has a smaller E_0 than that of sulfonium **PAG-2a**, which indicates improved sensitivity.

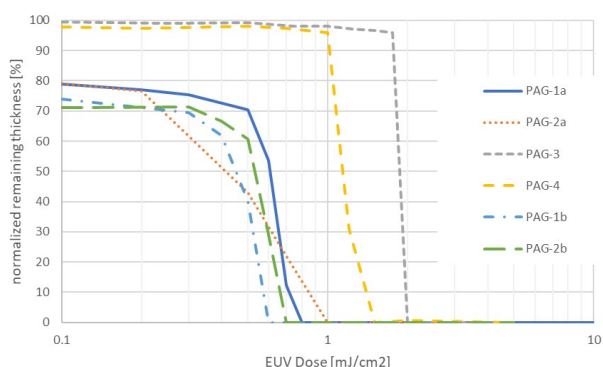


Fig. 2. Dose-to-clear curves of samples.

It has been reported that conventional PAGs have exhibit low EUV light absorption, and the secondary electrons generated in the polymer matrix plays an important role for EUV sensitivity [4].

3.1.2. Sensitivity difference between selenium and sulfur on functional group

Introduction of the high-EUV-absorption element on onium center yielded satisfactory results. Alternatively, it can be introduced as substituents on aromatic rings. It has been reported that introduction of substituents into sulfonium-based PAGs affects its resist sensitivity. For example, sulfonium PAGs containing tellurium substituent are suitable for EUV lithography [11]; however, there is no specific data of sulfonium containing selenium substituents. Therefore, we conducted experiments, and the results for samples 5 and 6 are listed in Table 1. Notably, sulfur substituted sulfonium **PAG-4** exhibits better sensitivity than selenium substituted **PAG-3**. Although the reason is unclear, the decomposition of PAGs were prevented by fast deactivation of EUV-absorbed selenium side chain, because selenium has many deactivate mode for high period element's nature [8(a)]. In other possibilities, since PhSe is a weaker electron-withdrawing group than PhS (2.40 vs 2.60) [12], it lowers the electron affinity of onium center.

3.1.3. Reliability improvement of sensitivity

We adopted Tf salts of PAG to evaluate resist sensitivity for availability; however, acid diffusion length and volatility of the generated acid generally affect EUV lithography [13]. Furthermore, PAGs with large anions have several advantages; therefore, we synthesized Nf salts of PAG and performed EUV

Table 1. Summary of samples and results (NRT: normalized remaining thickness).

Sample	Name	Structure		Rot. Speed (rpm)	Thickness (nm)	E_0 (mJ/cm ²)	NRT (%)
		Cation	Anion				
1	PAG-1a		CF ₃ SO ₃ ⁻ (Tf)	2500	43	0.8	84
2	PAG-1b		C ₄ F ₉ SO ₃ ⁻ (Nf)	1700	50	0.6	75
3	PAG-2a		CF ₃ SO ₃ ⁻ (Tf)	2500	46	1.0	79
4	PAG-2b		C ₄ F ₉ SO ₃ ⁻ (Nf)	2000	48	0.7	77
5	PAG-3		CF ₃ SO ₃ ⁻ (Tf)	3000	45	2.0	>99.5
6	PAG-4		CF ₃ SO ₃ ⁻ (Tf)	2500	47	1.5	98

However, this result suggests that the introduction of high-EUV-absorption selenium promotes direct photo decomposition of PAGs and improves the resist sensitivity.

exposure experiments. The results for sample 2 and 4 are listed in Table 1. Evidently, selenium Nf **PAG-1b** has the highest sensitivity. Bulky and low diffusional anions could decrease sensitivity; however, dose-to-clear experiments ignore the

effects of roughness and resolution. Therefore, in this case, the strength of the generated acid was dominant for sensitivity.

3.2. Thermal property of selenonium PAG

As is evident from Fig. 2, thickness reduction was observed in the unexposed film for several samples. In the actual production process, dissolution contrast between exposed and unexposed areas were utilized for pattern formation, as the reduction of unexposed film thickness is undesirable. Therefore, we conducted TG/DTA of selenonium **PAG-1b** to verify possibility of using PAG thermolysis to induce this reduction. Triphenylsulfonium salt **PAG-2a** is resistant to thermolysis until 300 °C [8]; moreover, no thermolysis peak was observed for selenonium **PAG-1b**. 5% weight loss temperature for each PAG is sufficiently higher than the heat processes temperature before development. This indicates that thermally induced acid generation and following thickness decrease of the unexposed area did not take place.

Because EUV resists contain high loadings of PAGs, when m.p. is below the prebake and PEB temperatures, melted PAG forms aggregates, which when extracted and washed off using the developer solution causes the thickness reduction. Comparing Tf salt type PAGs, only **PAG-2a** has higher m.p., however, there is no relationship between m.p. and NRT (%) (Table 2).

Furthermore, the dissolution rate of the resist was influenced by inhibition properties of PAG onium salts, and substituents on sulfonium had a significant effect [9, 14].

Table 2. Melting point (m.p.) and 5% weight loss temperature (Td5) of PAGs (unit: °C).

PAG-xx	1a	1b	2a	2b	4
Td5	>300*	368	>300*	394	420
m.p.	93	92	137	87	78

*TG/DTA above 300 °C of these compounds has not been acquired.

3.3. Outgasses analysis of selenonium **PAG-1a**

Because air absorbs EUV light, the exposure environment was maintained under high vacuum or dilute high purity gas atmosphere. Outgassing during exposure causes pollution of chamber and masks the contamination, which leads to reduced exposure power and pattern failure. The results of outgassing of the selenonium-**PAG-1a**-containing resist using the pressure rise procedure is shown in

Fig. 3.

Evidently, the partial pressure of outgassing is sufficiently small for all mass numbers. The observed peaks are derived from the matrix resin and atmosphere instead of selenonium PAGs. The chamber pressure before and after exposure were 4.83×10^{-5} Pa and 4.27×10^{-5} Pa, respectively. Pressure decreasing after exposure seems to be induced by exhaust of residual water on resist surface. Namely, the outgassing of resist during exposure is smaller than residual water. These results indicate that there is no inherent problem in using selenonium PAGs.

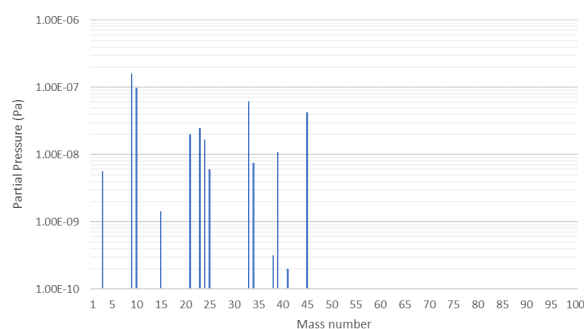


Fig. 3. Result of outgassing analysis of the resist using **PAG-1a**.

4. Conclusion

In this study, we evaluated the sensitivity of selenium-containing PAGs under EUV exposure and compared their fundamental characteristics with conventional sulfur PAGs. Resist sensitivities depend on the substituted position, and onium-center-substituted selenium exhibited improved sensitivity, particularly in **PAG-1b**. This indicates efficient PAG decomposition using high-EUV-absorbent selenium at onium-center. There is no problem observed in thermal property and outgassing. In case of Tf salts, it has minor issues related to process allowance due to its volatility. Introducing a substituent on the cationic part of the PAG significantly affected its sensitivity. The improvement in sensitivity resulting from the substitution of selenium backbone will be investigated in a future study.

Acknowledgement

T. K., S. Y., and T. S. express their gratitude to Hideki Kimura for support and discussion.

References

- H. Ito and C. G. Willson, *Polym. Eng. Sci.*, **23(18)** (1983) 1012.
- D. Van. Steenwinckel, J. H. Lammers, L. H. A.

- Leunissen, and J. A. J. M. Kwinten, *Proc. SPIE*, **269** (2005) 5753.
3. A. Kawai, "Advanced Technologies for Functional Resist Materials and Process Optimization", CMC Pub. Co., Tokyo (2017) p26 (in Japanese).
 4. T. Kozawa and S. Tagawa, *Jpn. J. Appl. Phys.*, **49** (2010) 030001.
 5. (a) S. Grzeskowiak, A. Narasimhan, E. Rebeyev, S. Joshi, R. L. Brainard, and G. Denbeaux, *J. Photopolym. Sci. Technol.*, **29(3)** (2016) 453. (b) H. Tsubaki, T. Tsuchihashi, K. Yamashita, and T. Tsuchimura, *Proc. SPIE*, **7273** (2009) 72733P.
 6. A. Sekiguchi, *IEEJ Trans. Fundam. Mater.*, **137(5)** (2017) 242.
 7. S. Tagawa, S. Enomoto, and A. Oshima, *J. Photopolym. Sci. Technol.*, **26(6)** (2013) 825.
 8. (a) J. V. Crivello and J. H. W. Lam, *J. Polym. Sci.: Polym. Chem. Ed.*, **17** (1979) 1047. (b) R. Taschner, R. Liska, and P. Knaack, *Polym. Int.*, **71(7)** (2022) 804.
 9. M. Glodde, D. L. Goldfarb, D. R. Medeiros, G. M. Wallraff, and G. P. Denbeaux, *J. Vac. Sci. Technol. B.*, **25(6)** (2007) 2496.
 10. (a) L. Racicot, T. Kasahara, and M. A. Ciufolini, *Org. Lett.*, **16** (2014) 6382. (b) L. Zhang, X. Li, Y. Sun, W. Zhao, F. Luo, X. Huang, L. Lin, Y. Yang, and B. Peng, *Org. Biomol. Chem.*, **15** (2017) 7181.
 11. (a) M. Naito, M. Hayakawa, and Y. Utsumi, Japan Patent WO2018/117167A1 (2018). (b) T. Kamakura and Y. Utsumi, Japan Patent WO2019/087626A1 (2019).
 12. N. Inamoto and S. Matsuda, *Chem. Lett.*, (1982) 1003.
 13. T. Kimura, K. Nishino, M. Shimizu, Y. Hirai, K. Maruyama, and T. Kai, *J. Photopolym. Sci. Technol.*, **23(5)** (2010) 643.
 14. (a) D. R. Medeiros, *J. Photopolym. Sci. Technol.*, **15(3)** (2002) 411. (b) H. Ito, D.-F. Alexander, and G. Breyta, *J. Photopolym. Sci. Technol.*, **10(3)** (1997) 397.

Grazing-Incidence Soft-X-ray Scattering for the Chemical Structure Size Distribution Analysis in EUV Resist

Atsunori Nakamoto¹, Shinji Yamakawa^{1*}, Tetsuo Harada¹, and Takeo Watanabe¹

¹ Center for EUV Lithography, Laboratory of Advanced Science and Technology for Industry, University of Hyogo, 1-1-2 NewSUBARU, Kouto, Kamigori, Ako-gun, Hyogo 678-1205, Japan *s.ymkw@lasti.u-hyogo.ac.jp

In extreme ultraviolet lithography (EUVL), it is required to develop EUV resist which has low line width roughness (LWR) for the further miniaturization of circuit pattern. In order to reduce LWR, it is necessary to analyze and control the chemical-components spatial distribution in the resist thin film. We have reported that the measurement of chemical-components spatial distribution in the resist thin film coated on the Si₃N₄ membrane using the method of the transmission-mode resonant soft X-ray scattering (RSoXS). In this study, in order to analyze the chemical-structure-size distribution in the resist thin film on a Si wafer under similar condition adapted to the resist-coating actual process, we examined the grazing-incidence RSoXS (GI-RSoXS). A chemically amplified resist (CAR) and a non-CAR were spin-coated on silicon wafers, which had varied film thickness of 20, 50, and 100 nm. The scattering profile of each sample was measured at the incident photon energy of 280 and 296 eV. As a result, it is suggested that the chemical-structure-size distribution in the resist thin films depends on the resist film thickness. It is confirmed that the GI-RSoXS method is very effective to evaluate the chemical-structure-size distribution of resist thin films.

Keywords: EUV resist, Grazing incident resonant soft X-ray scattering (GI-RSoXS), Chemical-structure-size distribution

1. Introduction

Since 2019, extreme ultraviolet lithography (EUVL) using the wavelength of 13.5 nm as exposure light has been used in high volume mass production of semiconductor logic devices. However, if the line width roughness (LWR) of resist pattern is large, it is difficult to improve of the electronic performances of devices such as the operating speed and power consumption etc. Thus, it is strongly required to develop low LWR resists. The acceptable LWR is less than 1/10 of the target line width. For example, 1 nm is acceptable for a line width of 10 nm. Therefore, it is required that the control and analysis of the spatial distribution of chemical components in the resist thin films.

Many measurement methods for the chemical-components-distribution analysis of the resist thin films such as TOF-SIMS [1-4], MC-SIMS [5], and contact angle measurement [6] have been reported. We reported the chemical-components-spatial-distribution evaluation by the resonant soft X-ray scattering (RSoXS) [7, 8]. The RSoXS combines

soft X-ray spectroscopy with X-ray scattering. In RSoXS, the scattering from sample was measured with several photon energy including absorption peaks of its chemical components. Since the scattering distribution depends on the absorption and refraction of the resist material, the chemical-components distribution can be evaluated. The scattering was measured with the transmission layout. The sample resist was coated on the thin Si₃N₄ membrane, which was very difficult to achieve uniform resist on the membrane. As a result, reproducibility of this transmission-mode in RSoXS method was low because of the non-uniform resist-coating. To achieve high reproducibility, the sample resist should be spin-coated on a Si wafer.

Recently, the grazing-incidence RSoXS (GI-RSoXS) which is a technique of the reflective-mode RSoXS has been reported [9-12]. Since this method has been used for the analysis of the morphology for polymer blend films [9, 10], and polymer bilayer systems [11, 12], it can be used to analyze the distribution of chemical components in the resist

Received	April 14, 2022
Accepted	June 10, 2022

thin films. The sample preparation for this method can be done by resist-spin-coating on a wafer. Therefore, we expected to obtain the results of the size distribution of chemical components in the resist thin film on a Si wafer under similar condition adapted to the resist-coating actual process. In this paper, it is reported that the GI-RSoXS for analyzing the chemical-structure-size distribution in the resist thin film coated on a Si wafer.

2. Experimental

2.1. Measurement method of GI-RSoXS

The GI-RSoXS measurements were performed at the vacuum chamber of the 2nd mask reflectometer of BL-10 beamline (BL-10) of the New SUBARU synchrotron light facility. This beamline provides monochromatized soft X-ray energy range from 60 to 1000 eV. Figure 1 shows the schematic drawing of GI-RSoXS. The incident X-ray beam was irradiated from the right side to the left side on the figure. There is $\phi 400 \mu\text{m}$ pinhole in the 1st mask reflectometer at the focusing point of BL-10 which was located 1.1 m upstream from the sample. The scattering component of the incident light was cut off by the $\phi 400 \mu\text{m}$ pinhole and 4 jaw slit (4WS). The 4WS was located just before the GI-RSoXS measurement chamber. The scattered light from the sample was detected by the CMOS camera [13]. The sensing area size of the CMOS camera was 22.5 mm (H) \times 22.5 mm (V). The camera has 2048 \times 2048 pixels and the pixel size is 11 μm in square.

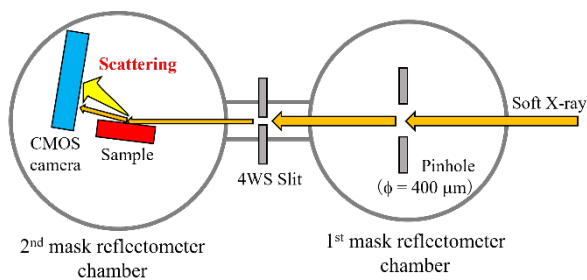


Fig. 1. Schematic drawing of the experimental setup of GI-RSoXS.

Figure 2 shows the GI-RSoXS scattering geometry. Each position on CMOS images can be translated to the scattering vectors. The intensities of the scattered light of the scattering vectors q_z in the horizontal direction and q_y in the horizontal direction to sample surface were recorded from the yellow dot area and the green dot area on CMOS images, respectively. The scattering vectors q_y and q_z can be obtained by the following equations (1) and (2), respectively, and where λ , α_i ($\alpha_i = 5^\circ$),

α_f , θ are the incident light wavelength, incidence angle between the incidence light and the surface of substrate, the scattering angle of vertically scattered light, and the scattering angle of the horizontally scattered light, respectively.

$$q_y = \frac{2\pi}{\lambda} \sin \theta \cos \alpha_f \quad (1)$$

$$q_z = \frac{2\pi}{\lambda} (\sin \alpha_f + \sin \alpha_i) \quad (2)$$

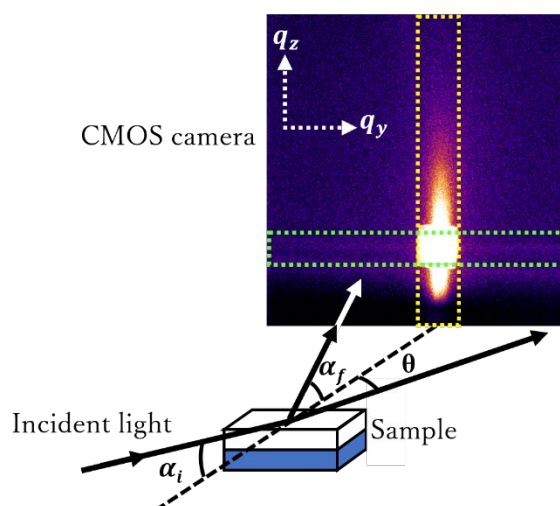


Fig. 2. Schematic drawing of the geometry of GI-RSoXS.

2.2 Sample preparation

Non-chemical-amplified EB resist ZEP520A (Nippon Zeon) (so called ZEP) (Fig. 3a), and chemically amplified resist (CAR) were employed for this study. These chemical structural formulas are shown in Fig. 3.

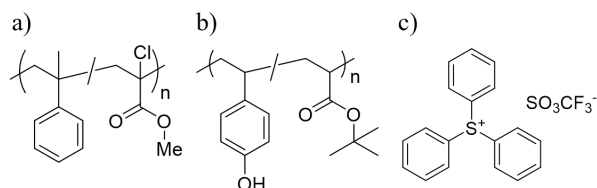


Fig. 3. Chemical structural formula employed in this study; (a) ZEP520 resist, and (b) base polymer and (c) photo acid generator of chemically amplified model resist.

The resist films with different film thickness of 20, 50, and 100 nm were prepared by using ZEP-A as a diluent for ZEP and dilution ratio such as ZEP : ZEP-A to 1 : 8, 1 : 3, and 1 : 1.3, respectively.

The resist films with different film thickness samples of 20, 50, and 100 nm were prepared by modifying the concentration of PHS-TBA such as 11, 25, and 42 g/L, respectively. The CAR used

poly(hydroxystyrene-*co-tert*-butylacrylate) (PHS-TBA) as base resin (Fig. 3b), triphenylsulfonium-triflate (TPS-TfO) as photoacid generator (PAG) at 10 wt% of the polymer (Fig. 3c), and propylene glycol monomethyl ether acetate (PGMEA) as solvent.

In the case of ZEP resist film preparation, the surface of the Si wafer was cleaned by the ozone ashing process before the resist spin-coating. After the ozone ashing process, 2.0 ml of the prepared ZEP solutions were dropped through a 0.22 μm PTFE syringe filter, and then the spin-coating was performed at 3000 rpm for 30 s. Then these spin-coating films were prebaked at a temperature of 180 $^{\circ}\text{C}$ for 180 s. In the case of CAR resist film preparation, the Si wafer was treated by the adhesion process with hexamethyldisilazane (HMDS). The spin-coating of the HMDS was performed at 3000 rpm for 30 s, and this wafer was prebaked at 130 $^{\circ}\text{C}$ for 90 s. The CAR solutions were filtered through a 0.22 μm PTFE syringe. Then, prepared CAR solutions were spin-coated on the silicon wafer at 2500 rpm for 45 s, and this wafer was prebaked at 110 $^{\circ}\text{C}$ for 60 s. The resist thickness was measured by the optical-interference-type film thickness measurement tool (NanoSpec6100, NANO metrics Inc.).

2.3. XAS measurement method

Since the absorption peaks on the soft X-ray absorption spectra (XAS) of the atoms which are consisted of the resist materials corresponds to the chemical bonds in the resist films, the incident photon energy selection was carried out from the absorption spectrum of the atoms which are consisted of the resist materials in the GI-RSoXS method in this study.

XAS spectra of ZEP and CAR were measured using total electron yield (TEY) method around carbon *K* absorption edge of 284 eV as shown in Fig. 4. The vertical axis shows the normalized TEY current intensity, which corresponded to the absorption amount of the resist. The horizontal axis shows the photon energy of the incident soft X-ray beam. The absorption peaks of 286, 289, and 296 eV were assigned to π^* (C=C), π^* (C=O), and σ^* (C-C) bondings, respectively [8]. There is no carbon absorption at the incident photon energy of 280 eV. If the sample has high absorption at measurement photon energy, GI-RSoXS is surface-sensitive [9] because incident light cannot penetrate into the sample films, and all the scattering signal is due to surface roughness. The absorptions at 280 eV and

296 eV were significantly different because of the polymer main chain of the resist consisted mainly of carbon atoms. Therefore, in this study, the photon energy of 280 eV was selected to measure the internal scattering of the resist thin films, and that of 296 eV was selected to measure surface roughness.

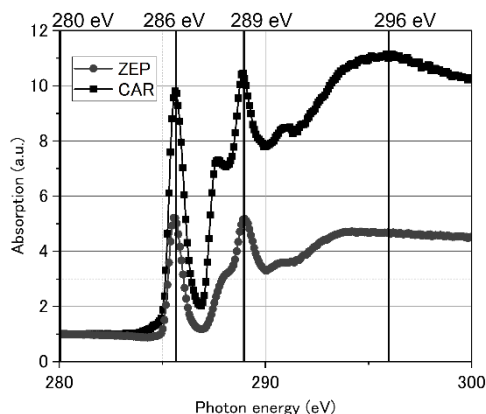


Fig. 4. XAS spectra of ZEP (gray circle), and CAR (black square).

3. Results and discussions

Figure 5 shows the CMOS image and scattering profiles obtained by the GI-RSoXS measurements for CAR for the different film thicknesses at the incident photon energy of 280 eV. The scattering

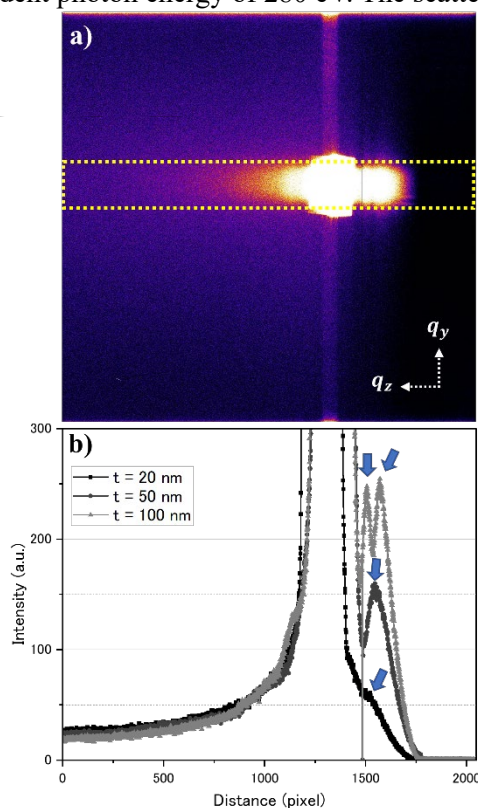


Fig. 5. The result of GI-RSoXS. (a) the scattering images on the CMOS camera of the CAR resist with the film thickness of 100 nm, and (b) scattering profiles of three different film thickness of the CAR resist.

profile of CAR was plotted with the q_z direction of the yellow dots on the scattering image on CMOS camera as shown in Fig. 5a. The vertical and horizontal axes indicate the scattering light intensity and the number of pixels of the image, respectively, as shown in Fig. 5b. As a result, interference fringes were observed at the marked region by blue arrows. We have reported that the resist thin film has three-chemical-layer structure by the soft X-ray resonant reflectometry [14]. These interference fringe indicates the three-chemical-layer structure, because the scattering profile of q_z vector is given scattering information in the depth direction in the resist thin films.

Next, the scattering profile of the q_y direction was evaluated that the corresponded to the in-plane information of resist thin film because the chemical components of the resist thin film were dispersed with in-plane direction uniformly. Figure 6 shows the scattering profiles of both ZEP and CAR with film thickness of 20, 50, and 100 nm. In the case of surface sensitive measurement with the incident

photon energy of 296 eV, the scattering intensity had almost no difference between each resist thickness, as shown in Figs. 6 (a) and (b). It indicates that the surface roughness does not depend on the film thickness, and it has good measurement reproducibility. On the other hand, for the incident photon energy of 280 eV, the scattering intensity is drastically increased when decreasing the film thickness as shown in Figs. 6 (c) and (d). And the scattering intensity of ZEP is smaller than that of CAR in the corresponding film thickness. These results mean that the chemical-structure-size distribution, on the other words, the chemical components aggregation of ZEP is smaller than that of CAR. Since the CAR has more complex chemical structures of the base polymer and PAG rather than that of ZEP containing only polymer, the PAG might aggregate in the CAR films. Thus, the spatial distribution of chemical components in CAR is considered to be less uniform than that of ZEP. Furthermore, it is known that the LWR of CAR is larger than that of ZEP.

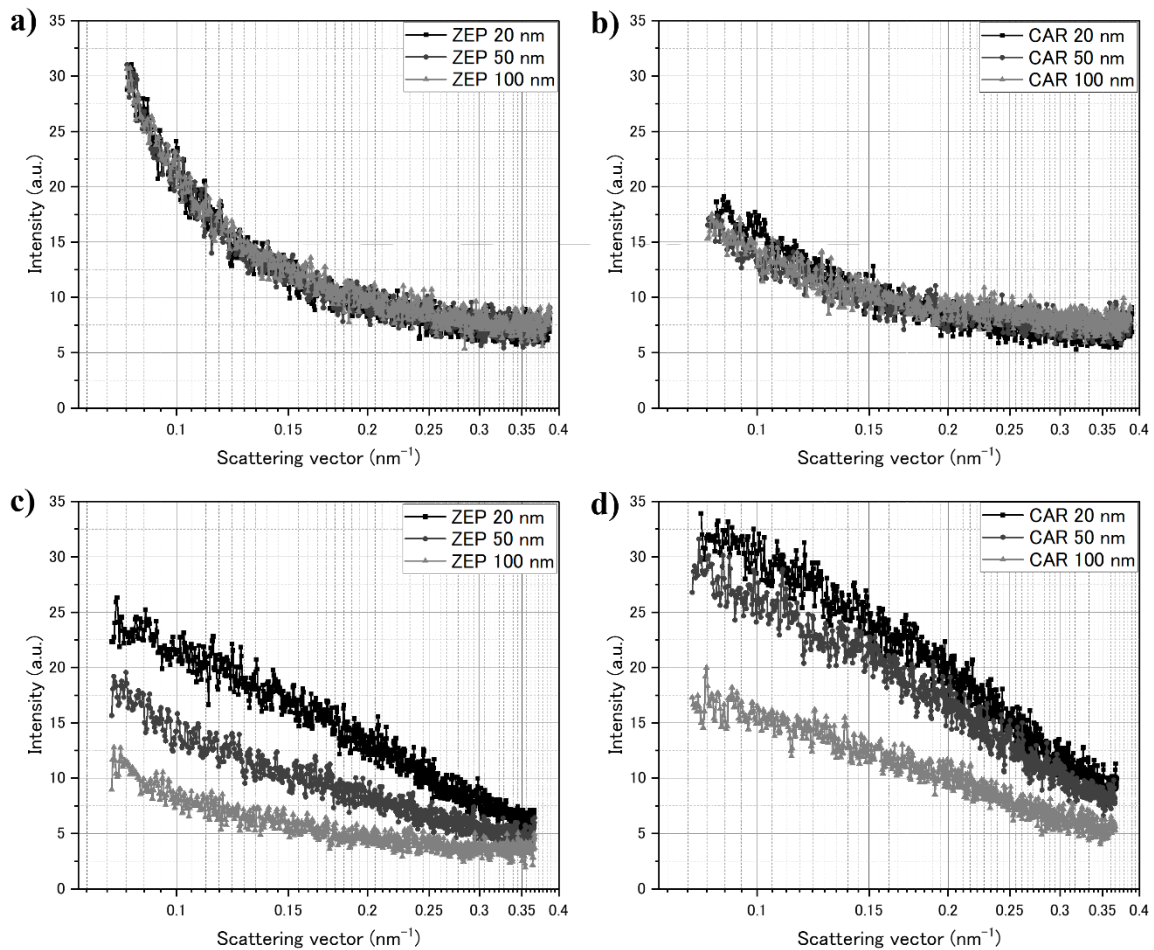


Fig. 6. The q_y scattering profiles of q_y vector direction using different film thickness (20, 50, 100 nm) of a) ZEP (296 eV), b) CAR (296 eV), c) ZEP (280 eV), and d) CAR (280 eV).

As results, it is confirmed the GI-RSoXS is an effective method to evaluate not only the aggregation and segregation but also the differences in the chemical structure size distribution in the resist thin films.

4. Conclusion

In this study, the GI-RSoXS tool was installed at the NewSUBARU BL-10 beamline, and the distribution of chemical structure size was evaluated with two kinds of resist samples such as CAR and non-CAR. The GI-RSoXS measurement method has good reproducibility than the transmission-mode RSoXS measurement. In the evaluation of the q_z vector scattering profile, the interference fringe was observed. This means that the scattering profile of q_z vector was included the scattering information of the three-layer structure in the resist thin film. On the other hand, the scattering profile of q_y vector gives the in-plane and surface information of resist thin films at the incident photon energies of 280 and 296 eV. It was confirmed that the surface roughness of resist thin films does not depend on the film thickness. However, the chemical-structure-size distribution in the resist thin films increased when the film thickness decreased. Furthermore, it was suggested that the CAR is easy to aggregate rather than ZEP. Since the resist sample which is spin-coated on a Si wafer can be evaluated using the GI-RSoXS method, this method is a more useful method for the chemical-structure-size distribution analysis in the resist thin films.

As results, it is confirmed the GI-RSoXS is an effective method to evaluate not only the aggregation and segregation but also the differences in the chemical-structure-size distribution in the resist thin films.

References

1. N. Man, H. Okumura, H. Oizumi, N. Nagai, H. Seki, and I. Nishiyama, *Appl. Surf. Sci.*, **231**, (2004), 353.
2. T. Hirayama, D. Shiono, S. Matsumaru, T. Ogata, H. Hada, J. Onodera, T. Arai, T. Sakamizu, A. Yamaguchi, H. Shiraishi, H. Fukuda, and M. Ueda, *Jpn. J. Appl. Phys.*, **44**, (2005), 5484.
3. T. Hirayama, D. Shiono, J. Onodera, A. Yamaguchi, and H. Fukuda, *Polym. Adv. Technol.*, **17**, (2006), 116.
4. T. Hagiwara, T. Ishibashi, M. Terai, T. Kumada, N. Shirota, O. Yokokoji, T. Matsunobe, N. Man, K. Yoshikawa, Y. Tanahashi and T. Hanawa, *J. Photopolym. Sci. Technol.*, **21**, (2008), 647.
5. X. Hou, M. Li, M. J. Eller, S. V. Verkhoturov, E. A. Schweikert and P. Trefonas, *J. Micro/Nanolith. MEMS MOEMS*, **18**, (2019), 033502.
6. S. Yamakawa, A. Yamamoto, S. Yasui, T. Watanabe, and T. Harada, *J. Photopolym. Sci. Technol.*, **34**, (2021), 111.
7. J. Tanaka, T. Ishiguro, T. Harada and T. Watanabe, *J. Photopolym. Sci. Technol.*, **32**, (2019), 327.
8. J. Tanaka, T. Ishiguro, T. Harada and T. Watanabe, *J. Photopolym. Sci. Technol.*, **33**, (2020), 491.
9. M. A. Ruderer, C. Wang, E. Schaible, A. Hexemer, T. Xu, and P. M-Buschbaum, *Macromolecules*, **46**, (2013), 4491.
10. J. Wernecke, H. Okuda, H. Ogawa, F. Siewert, and M. Krumrey, *Macromolecules*, **47**, (2014), 5719.
11. T. Pfadler, M. Coric, C. M. Palumbiny, A. C. Jakowetz, K.-P. Strunk, J. A. Dorman, P. Ehrenreich, C. Wang, A. Hexemer, R.-Q. Png, P. K. H. Ho, P. M.-Buschbaum, J. Weickert, and L. S.- Mende, *ACS Nano*, **8**, (2014), 12397.
12. E. Gann, A. Watson, J. R. Tumbleston, J. Cochran, H. Yan, C. Wang, J. Seok, M. Chabinye, and H. Ade, *Phys. Rev. B*, **90**, (2014), 245421.
13. T. Harada, N. Teranishi, T. Watanabe, Q. Zhou, J. Bogaerts, and X. wang, *Appl. Phys. Exp.*, **13** (2020), 103009.
14. T. Ishiguro, J. Tanaka, T. Harada, and T. Watanabe, *J. Photopolym. Sci. Technol.*, **32**, (2019), 333.

Effect of Alternative Developer Solutions on EUVL Patterning

Julius Joseph Santillan¹, Kyoko Shimizu², Ryuichi Otagawa², and Toshiro Itani¹

¹ *The Institute of Scientific and Industrial Research, Osaka University,
8-1 Mihogaoka, Ibaraki, Osaka 567-0047, Japan*

² *SACHEM JAPAN GK,
5-6-27 Mizuhai, Higashi Osaka 578-0921, Japan
Email: julius.santillan@sanken.osaka-u.ac.jp*

This work explores the application of alternative developer solutions (“developers”) with the aim of understanding their potential effectivity in the reduction of resist-based stochastic pattern defects (or “stochastic defects”) in extreme ultraviolet lithography (EUVL). Specifically, the application of a quaternary ammonium hydroxide type aqueous developer; ethyltrimethylammonium hydroxide (ETMAH) in comparison to the industry *de facto* standard aqueous alkali tetramethylammonium hydroxide (TMAH) developer was investigated. Focusing on EUV exposed contact hole (CH) patterns on a typical chemically amplified resist (CAR), the effect of these developers on stochastic defects were assessed. As a result, patterning investigations showed that the lithographic performance of the CAR developed in ETMAH is comparable to the those obtained with TMAH. *In situ* resist dissolution analysis using the high-speed atomic force microscope (HS-AFM) confirms this as it showed that the rate of CH formation during resist dissolution in both developers are relatively the same. Moreover, it was also understood that compared to the commonly used alkali developer concentration of 0.26N, a lower ETMAH developer concentration of 0.20N resulted in stochastic defect margin improvement, while maintaining lithographic performance. *In situ* resist dissolution analysis showed an obvious slowing down of CH pattern formation rate at 0.20N concentration, suggesting the possibility that of over-dissolution at the higher concentration condition, translating to an increase in merging CH defects. The results from this study show the advantages of further pursuing optimal developers for EUVL. This is especially significant as these findings indicate how optimal developers mitigate resist-based stochastic defects while maintaining lithographic performance.

Keywords: Developer Solution, TMAH, ETMAH, EUV Lithography, Stochastic Defects

1. Introduction

Extreme ultraviolet lithography (EUVL) has been pushing forward the development and patterning performance of resist materials¹⁻⁵. Even as first-generation EUVL (0.33 numerical aperture or NA) is now being utilized for high volume manufacturing^{1, 6}, the industry is already preparing for next-generation high-NA EUVL (0.55NA)⁷⁻¹⁰. However, given the very stringent target pattern sizes in these technologies (especially in high-NA EUVL), traditional resist materials such as chemically amplified resists (CAR) may already be reaching their physical limits²⁻⁵, making the control of pattern quality much more difficult. Aside from patterning resolution, the impact of resist-based randomly generated or stochastic pattern defects or

stochastic defects (e.g. line-to-line bridges, line breaks, missing and merging contact holes (CH), pattern collapse, residue in the spaces) is becoming a constant topic of discussion¹¹⁻¹⁴. Specifically, the occurrence of such defects is projected to affect process margins (e.g. exposure latitude) which may further limit the flexibility of present resist materials as target pattern sizes become smaller⁷.

Further enhancements in the resist process, such as the resist development (or resist dissolution) process are viewed as a possible solution to this issue¹⁵⁻¹⁸. The resist development step after all is the first instance where physical patterns are formed from the exposed resist film. Thus, controlling the efficiency of the resist development process is

Received	June 8, 2022
Accepted	June 24, 2022

regarded as an effective way of minimizing the generation of these stochastic defects. This work describes the application and effect of alternative developer solutions (referred to as “developers” from here on), specifically the aqueous alkali ethyltrimethylammonium hydroxide (ETMAH) in comparison to the industry *de facto* standard aqueous alkali tetramethylammonium hydroxide (TMAH) developer. Here, investigations were made on the reduction of resist-related stochastic pattern defects, specifically on CH patterning for EUVL.

2. Materials and processing

2.1 EUV lithography materials and processing

A CAR was utilized at a film thickness of 30 nm under optimal post application bake (PAB) and post exposure bake (PEB) conditions. The CAR (typically a hybrid of polyhydroxystyrene- and acryl-based polymers) was coated onto a 300-mm wafer coated with an organic underlayer at a thickness of 20 nm. The development process after PEB was performed at a development time of 30 s using two types of developer solutions as described below. The rinse process was performed using deionized water (DIW) with a rinse time of approximately 19 s.

For the developer solution; the industry *de facto* standard aqueous alkali TMAH ($M_w = 91.15$ g/mol) was utilized in comparison to an alternative aqueous alkali ETMAH developer ($M_w = 105.18$ g/mol). The ETMAH developer is (in M_w) the nearest available quaternary ammonium hydroxide to TMAH, but also exhibits roughly 5 times lower toxicity (ETMAH Dermal $LD_{50} = \sim 1000$ mg/kg vs TMAH Dermal $LD_{50} = \sim 150$ mg/kg)¹⁹⁻²⁰.

Resist processes were carried out using the SOKUDO DT-3000 coater/developer (SCREEN Semiconductor Solutions). Unless otherwise indicated, all EUV patterning exposures were done using the NXE:3400 (ASML) with a 0.33 numerical aperture and utilizing optimal illumination conditions. CD measurements were performed using CG5000 scanning electron microscope (SEM) by Hitachi High-Technologies.

2.2 *In situ* resist dissolution analysis using high speed atomic force microscope (HS-AFM)

To provide a visual appreciation of the resist dissolution process, the authors have in recent years proposed and reported on the use of an in-liquid HS-AFM²¹ which allows the *in situ* analysis of resist dissolution²²⁻²³. For these experiments, HS-AFM image scanning was performed over an area of 500

nm \times 500 nm (at 400 \times 400 pixels). This was done at an optimized scan rate of 0.5 frames/s. “Biolever fast” cantilevers (BL-AC10FS-A2 by Olympus) equipped with carbon nano-fiber tips (radius of curvature: ~ 7 nm)²⁴ were utilized.

For the experimental procedure²⁵ with the HS-AFM, the first step is to look for the target pattern, in-liquid (in this case; de-ionized water or DIW). After determining the exact position of the resist pattern, the developer solution is injected continuously into the analysis area while the DIW is being dispensed at the same rate (using an auto-inject-dispense module). This allows continuous and stable scanning of the pattern surface even as the DIW is replaced with the developer solution. However, during this process step, a temporary dilution of the standard developer solution occurs. This temporary dilution of the developer allows a slower, clearer observation of the initial stages of the pattern formation process but in effect, also extends the total resist dissolution process time, in comparison to typical values used in actual resist processes.

3. Results and discussions

3.1 Simple metric for analyzing the effect of developers on stochastic defects in CH

Figure 1 shows the SEM images obtained for the 18nm staggered CH (Pitch at x = 36 nm, Pitch at y = 62 nm) pattern at various doses and developed using the *de facto* industry-standard 0.26N TMAH developer. In this case, dose-to-size (also referred to as “Dose_{target}” in some sections) was found to be at 120 mJ/cm². Moreover, as also performed in succeeding experiments, a sampling of about 2800 holes (in a total observed area of around 4 μm^2) for each of the exposure dose conditions was made to determine the effect of developer on the occurrence of two main types of CH related defects; missing CH (mostly found on the underdose region) and merging CH (mostly found on the overdose region). These defects were determined by processing SEM image data with offline visual analysis. In the case of the 0.26N TMAH developer, missing CH were first observed the 103 mJ/cm² dose condition where CH diameter was 14.6 nm. The occurrence of missing CH further increased at dose conditions lower. Meanwhile, merging CH were detected at the 141 mJ/cm² dose condition where CH diameter was 23.6 nm. The occurrence of merging CH further increased at dose conditions higher.

Based on these results, two simple metrics for defect margins were adopted; “ EL_X ” which is an

	Dose (mJ/cm ²)								
	100	105	110	115	120	125	130	135	141
SEM Image									
CD (nm)	14.0	14.9	15.9	16.9	18.1	19.2	20.5	21.8	23.6
Defect Count (/μm ²)	4	0	0	0	0	0	0	0	4

Fig. 1 SEM images obtained for the 18nm staggered CH (Pitch at x = 36 nm, Pitch at y = 62 nm) pattern at various doses and developed using the de facto industry-standard 0.26N TMAH developer.

altered equation for exposure latitude (EL) which considers the occurrence of these defects (Eq (1)).

$$EL_X = \frac{Dose_{<merging} - Dose_{<missing}}{Dose_{target}} \quad (1)$$

Where $Dose_{<merging}$ means the highest dose before the occurrence of merging CH defects (typically at the overdose region) and $Dose_{<missing}$ means the lowest dose before the occurrence of missing CH defects (typically at the underdose region). $Dose_{target}$ indicates the dose at the target CH critical dimension i.e. CD_{target} (in this case, 18nm).

Moreover, with the same concept, an alternate equation for CD margin was also adopted in the form of " CDM_X " or CD margin before occurrence of defects (Eq (2)). $CD_{<merging}$ means the largest diameter achieved before merging CH defects occur (at the overdose region) and $CD_{<missing}$ means the smallest pattern size achieved before missing CH defects occurs (at the underdose region).

$$CDM_X = \frac{CD_{<merging} - CD_{<missing}}{CD_{target}} \quad (2)$$

Using the above-mentioned equations, the EL_X and CDM_X of the 18nm staggered CH developed in 0.26N TMAH developer were calculated to be 29.6% and 47.7%, respectively.

3.2 ETMAH as alternative developer

In earlier reports, the authors have focused on ETMAH as a potential alternative developer for EUV lithography. Utilizing lines-and-spaces (L/S) patterns, experiments using the ETMAH developer have shown that lithographic performance (resolution, line width roughness, sensitivity) of a typical EUV resist are comparable to those obtained with the TMAH developer¹⁶.

Developer type	TMAH 	ETMAH
18nm staggered CH (SEM image)		
Dose-to-size (mJ/cm ²)	120	122

Fig. 2 CH pattern lithographic performance of the EUV resist developed using 0.26N TMAH versus 0.26N ETMAH developers.

3.2.1 Lithographic evaluation

Figure 2 shows the CH pattern lithographic performance of the EUV resist developed using 0.26N TMAH versus 0.26N ETMAH developers. The CH resolution of the CAR was found to be the same at 18nm with a slight shift in dose-to-size of 122 mJ/cm² and 120 mJ/cm² when developed in ETMAH and TMAH, respectively.

Further investigations were carried out comparing the defect margin (EL_X and CDM_X) of the CAR utilized when processed using these developers. Figure 3 shows the defect margin analysis results of the EUV resist using 0.26N TMAH and 0.26N ETMAH developers; (a) EL_X and (b) CDM_X . Moreover, based on these results, table 1 summarizes the defect margin calculations for both 0.26N TMAH and 0.26N ETMAH.

Table 1 Defect margin calculations (EL_X and CDM_X) for 0.26N TMAH and 0.26N ETMAH developers.

Developer solution	EL_X (%)	CDM_X (%)
TMAH	29.6	47.7
ETMAH	30.1	47.4

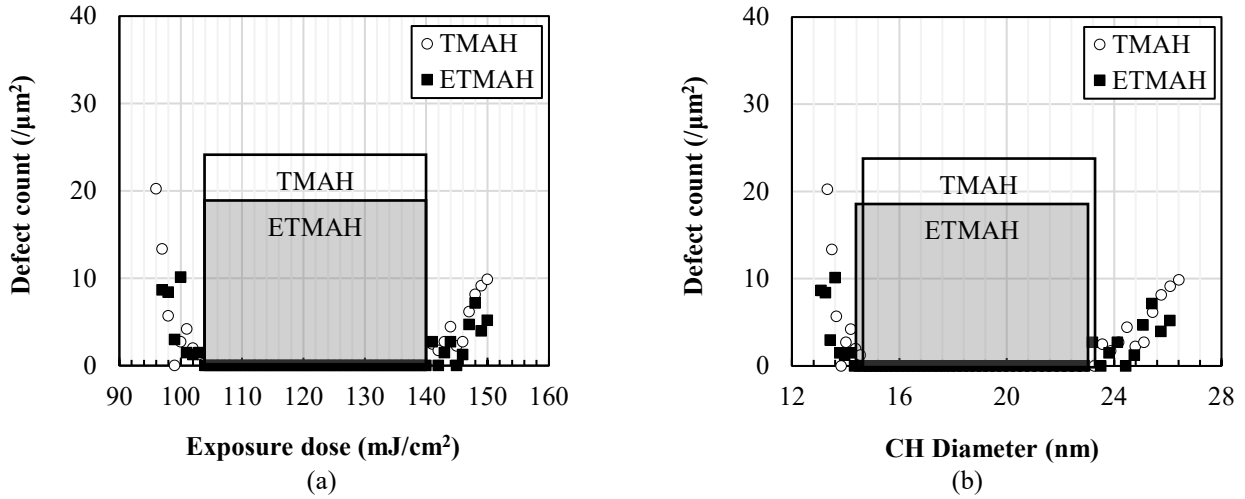


Fig. 3 Defect margin analysis results of the EUV resist using 0.26N TMAH and 0.26N ETMAH developers; (a) EL_X and (b) CDM_X .

These results show that in terms of the defect margin metrics indicated here, ETMAH has a comparable performance to that of TMAH.

3.2.2 *In situ* resist dissolution analysis

Figure 4 shows the *in situ* resist dissolution analysis results of the 23-nm staggered CH pattern during dissolution in 0.26N TMAH vs 0.26N ETMAH developer solutions, at various dissolution times. This larger CH pattern size was utilized for practical purpose as the 18nm pattern is too small for the commercially available cantilever utilized.

Based on these results, it can be observed that even before the formation of the CH pattern (in development time = 0s) exposed areas already exhibit some film thickness loss. This helps indicate the locations of each CH pattern even before dissolution starts. Resist dissolution was observed to start at around 34~54 s with the random occurrence of nano-swelling²⁶ on the exposed areas where these CH patterns are (indicated by white spots which suggest increase in height compared to original surface which is in brown). After these

nano-swollen areas start to dissolve at around 68~104s and further increase at around 124s, the formation of CH patterns can be observed (indicated by dark spots).

A comparative evaluation was made on the rate in which these CH patterns are formed during development with 0.26N TMAH and 0.26N ETMAH. Figure 5 shows a comparison of the total number of CH patterns formed during development in 0.26N TMAH versus 0.26N ETMAH in the 500nm × 500nm scanned area versus development time. A noticeable trend is observed where the rate to which the CH patterns are formed are slower in the initial stages (around development time = 30s to 100s) but after a specific time (development time = 100s), the CH patterns are formed at a consistently faster rate up until the total number of CH patterns in the area are fully formed (around development time = 140s).

The slower CH pattern formation rate in the initial stages is assumed to be largely affected by the existence of a two-step process wherein exposed resist first undergoes nano-swelling before the

Developer solution	Development time (s)								
	0	34	54	68	104	124	144	162	184
ETMAH									
TMAH									

Fig. 4 *In situ* resist dissolution analysis results of the 23-nm staggered CH pattern during dissolution in 0.26N TMAH vs 0.26N ETMAH developer solutions, at various dissolution times.

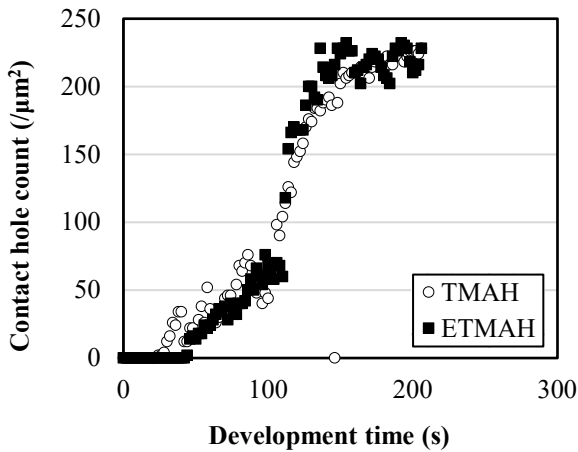


Fig. 5 Comparison of the total number of CH patterns formed during development in 0.26N TMAH versus 0.26N ETMAH in the 500nm × 500nm scanned area versus development time.

actual CH pattern is formed. Nevertheless, these results show a similar trend in which CH patterns are formed during development in both developers, confirming that the ETMAH is comparable to the TMAH in terms of performance as an EUV resist developer.

3.3 Effect of low developer concentration

Developer concentration has been a constant topic of discussion. Specifically, from the lithographic performance or stochastic defect margin point-of-view; there is a question on whether the present *de facto* standard developer concentration of 0.26N really is optimal for present-day EUV resists. In earlier reports utilizing L/S patterns, ETMAH when utilized at its optimal developer concentration (around 0.20N), improved stochastic defect margin while maintaining

lithographic performance¹⁶.

3.3.1 Lithographic evaluation

Figure 6 shows a comparison of the CAR's lithographic performance for CH patterning when utilizing ETMAH at a developer concentration of 0.26N versus 0.20N. CH resolution was found to be 18nm for both developer conditions with an obvious shift in dose-to-size of 127 mJ/cm² when the lower concentration developer 0.20N ETMAH was utilized (compared to 122 mJ/cm² when developed in 0.26N ETMAH). This suggests a diminished developer reactivity of the exposed CAR to the lower developer concentration.

Figure 7 shows the defect margin analysis results of the CAR using 0.26N and 0.20N ETMAH developers; (a) EL_X and (b) CDM_X . Moreover, based on these results, table 2 summarizes the defect margin calculations (EL_X and CDM_X) for both 0.26N and 0.20N ETMAH developers.

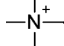
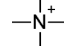
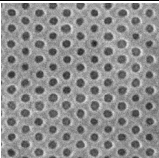
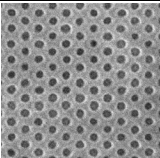
ETMAH developer concentration (N)	0.26	0.20
		
18nm staggered CH (SEM image)		
Dose-to-size (mJ/cm ²)	122	127

Fig. 6 Lithographic performance of the CAR developed using 0.26N versus 0.20N ETMAH developers.

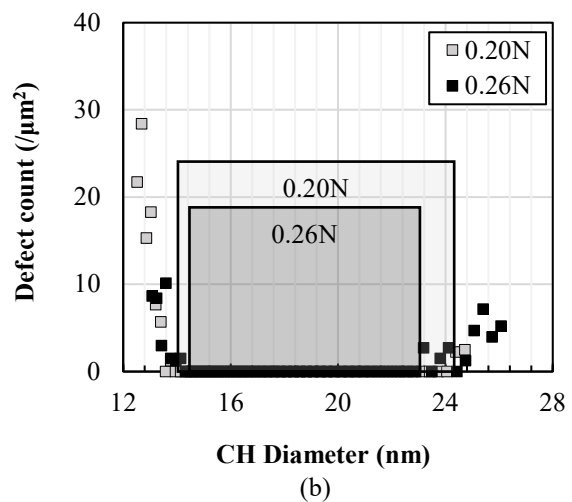
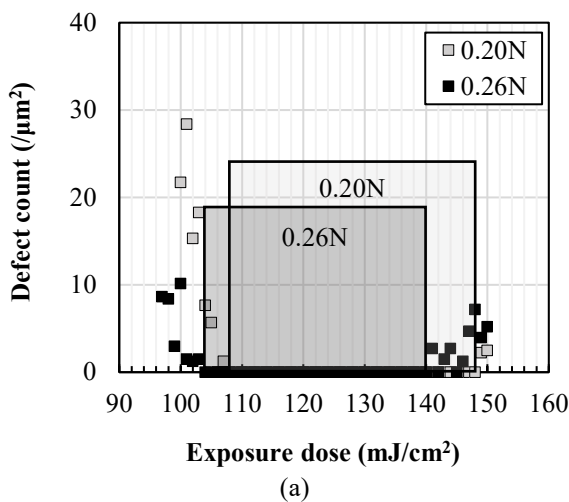


Fig. 7 Defect margin analysis results of the CAR using 0.26N and 0.20N ETMAH developers; (a) EL_X and (b) CDM_X .

Table 2 Defect margin calculations (EL_X and CDM_X) for 0.26N and 0.20N ETMAH developers.

ETMAH developer concentration (N)	EL_X (%)	CDM_X (%)
0.26	29.6	47.7
0.20	31.3	56.2

These results show a clear improvement in stochastic defect margins (while maintaining lithographic performance) when the lower developer concentration of 0.20N is utilized.

3.3.2 *In situ* resist dissolution analysis

Figure 8 shows the *in situ* resist dissolution analysis results of the 23-nm staggered CH pattern during dissolution in 0.26N vs 0.20N ETMAH developers solutions, at various dissolution times.

As discussed in chapter 3.2.2, for the 0.26N concentration ETMAH developer dissolution reaction started at around 34~54 s with the random occurrence of nano-swelling on the exposed areas where these CH patterns are (indicated by white spots which suggest increase in height compared to original surface which is in brown). Similarly, nano-swelling was also observed at around the same time for the 0.20N concentration condition. However, results clearly show the significant slowing down of CH pattern formation (dark spots) in the 0.20N concentration condition. Figure 9 shows a comparison of the total number of CH patterns formed during development in 0.26N versus 0.20N ETMAH developer concentrations in the 500nm × 500nm scanned area versus development time. This result confirms the effect of utilizing a lower developer concentration in slowing down the CH pattern formation characteristics of the CAR during the development process.

Developer conc. (N)	Development time (s)								
	0	34	54	104	124	162	200	260	300
0.20									
0.26								No image	No image

Fig. 8 *In situ* resist dissolution analysis results of the 23-nm staggered CH pattern during dissolution in 0.26N vs 0.20N ETMAH developer solutions, at various dissolution times.

3.4 Discussion on effect of low developer concentration on stochastic defects

The improvement in stochastic defect margins EL_X and CDM_X , which was mostly due to the suppression of merging CH defects in the overdose regions, is assumed to be largely due to two (2) contributing factors.

The first factor is that when using low developer concentrations, the slow occurrence of resist dissolution allows a smoother and stable pattern formation process. This minimizes the occurrence of defects that may have resulted from drastic physical reactions that have been reported to occur when higher developer concentrations are utilized²⁷.

The second factor is that using low concentration developer concentration slows down the pattern formation process delaying the formation of possible defects due to over-dissolution. The impact

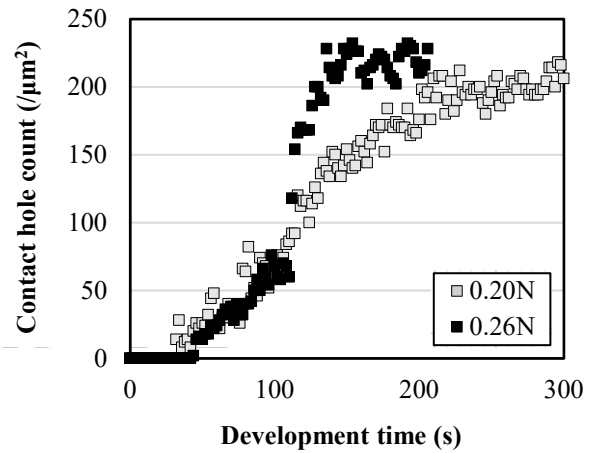


Fig. 9 Comparison of the total number of CH patterns formed during development in 0.26N versus 0.20N ETMAH in the 500nm × 500nm scanned area versus development time.

of such over-dissolution on defect generation is assumed to be more significant at the overdosed regions (where the effect of chemical blur and/or photon shot noise phenomena are assumed to be more pronounced). This explains the impact of the low developer concentration developer on the minimization of merging contact holes in the overdose regions.

Summary

The effect of an alternative aqueous alkali developer solution ETMAH on EUV CH patterning was investigated. ETMAH is (in M_w) the nearest available quaternary ammonium hydroxide to the current *de facto* aqueous alkali developer solution TMAH, but also exhibits roughly 5 times lower toxicity. EUV patterning investigations showed that the lithographic performance of a typical CAR material developed in ETMAH is comparable to the those obtained with TMAH (in terms of resolution, sensitivity and stochastic defect margins EL_X and CDM_X). This similarity in developer performance was further confirmed through *in situ* resist dissolution analysis using the HS-AFM which showed that the rate of CH formation during resist dissolution in both ETMAH and TMAH developers are relatively the same.

Moreover, it was also understood that compared to the commonly used alkali developer concentration of 0.26N, a lower ETMAH developer concentration of 0.20N results in the improvement in stochastic defect margins EL_X and CDM_X . This was achieved while maintaining lithographic performance. The positive impact of the low concentration ETMAH developer was observed on both missing and merging CH defects, but was especially manifested in the overdosed conditions of the CH pattern where merging CH defects are more frequently observed. *In situ* resist dissolution analysis comparing the effect of both developer concentrations showed an obvious slowing down of CH pattern formation rate at 0.20N developer concentration. These results suggest that at the higher developer concentration, there is a high possibility of over-dissolution (at the set develop time), which can translate to an increase in merging CH defects.

The results from this study show the advantages of further pursuing optimal developers for EUVL. This is especially significant as these findings indicate how optimal developers mitigate resist-based stochastic defects while maintaining lithographic performance.

Acknowledgments

We thank our colleagues at SCREEN Semiconductor Solutions Co., Ltd. for the collaborations, fruitful discussions and technical assistance in the EUV exposures.

A part of this work was conducted at the AIST Nano Characterization Facility (ANCF) supported by "Nanotechnology Platform Program" of the Ministry of Education, Culture, Sports, Science and Technology (MEXT), Japan.

References

1. E. Verhoeven, R. Schuurhuis, M. Mastenbroek, P. Jonkers, F. Bornebroek, A. Minnaert, H. Van Dijck, P. Yaghoobi, G. Fisser, P. Tayebati, K. Hummler, and R. Van Es, *Proc. SPIE* **11609** (2021) 1160908.
2. C. Anderson, A. Allezy, W. Chao, L. Conley, C. Cork, W. Cork, R. Delano, J. DePonte, M. Dickinson, G. Gaines, J. Gamsby, E. Gullikson, G. Jones, L. McQuade, R. Miyakawa, P. Naulleau, S. Rekawa, F. Salmassi, B. Vollmer, D. Zehm, and W. Zhu, *Proc. SPIE* **11323** (2020) 113230B.
3. T. Allenet, X. Wang, M. Vockenhuber, C.-K. Yeh, I. Mochi, J. G. Santaclara, L. Van Lent-Protasova, and Y. Ekinci, *Proc. SPIE* **11609** (2021) 116090J.
4. Z. Tasdemir, X. Wang, I. Mochi, L. van Lent-Protasova, M. Meeuwissen, R. Custers, G. Rispens, R. Hoefnagels, and Y. Ekinci, *Proc. SPIE* **10809** (2018), 108090L.
5. A. Lio, *Proc. SPIE* **9776** (2016) 97760V.
6. R-H. Kim, *Proc. SPIE* **10957** (2019) 1095706.
7. J. van Schoot, S. Lok, E. van Setten, R. Maas, K. Troost, R. Peeters, J. Finders, J. Stoeldraijer, J. Benschop, P. Graeupner, P. Kuerz, and W. Kaiser, *Proc. SPIE* **11517** (2020) 1151712.
8. L. de Winter, T. Tudorovskiy, J. van Schoot, K. Troost, E. Stinstra, S. Hsu, T. Gruner, J. Mueller, R. Mack, B. Bilski, J. Zimmermann, and P. Graeupner, *Proc. SPIE* **11517** (2020) 1151715.
9. L. Wischmeier, P. Graeupner, P. Kuerz, W. Kaiser, J. van Schoot, J. Mallmann, J. de Pee, and J. Stoeldraijer, *Proc. SPIE* **11323** (2020) 1132308.
10. E. van Setten, G. Bottiglieri, J. McNamara, J. van Schoot, K. Troost, J. Zekry, T. Fliervoet, S. Hsu, J. Zimmermann, M. Roesch, B. Bilski, and P. Graeupner, *Proc. SPIE* **10957** (2019) 1095709.
11. P. De Bisschop and E. Hendrickx, *Proc. SPIE* **11323** (2020) 113230J.
12. M. Sanchez, G. Wallraff, N. Megiddo, and W. D. Hinsberg, *Proc. SPIE* **11147** (2019) 1114717.
13. P. De Bisschop, *J. of Micro/Nanolithography, MEMS, and MOEMS* **17**(4) (2018) 041011.

14. T. Kozawa, J.J. Santillan, and T. Itani, *Jpn. J. Appl. Phys.* **53** (6) (2014) 066504.
15. J.J. Santillan, M. Harumoto, T. Motono, A. Figueiredo dos Santos, C. Mori, Y. Tanaka, H. Stokes, M. Asai, and T. Itani, *Proc. SPIE* **11609** (2021) 116090W.
16. J.J. Santillan, M. Harumoto, T. Motono, A. Figueiredo dos Santos, C. Mori, Y. Tanaka, H. Stokes, M. Asai and T. Itani, *Jpn. J. Appl. Phys.* **60** (2021) SCCC01.
17. J.J. Santillan, M. Harumoto, H. Stokes, C. Mori, Y. Tanaka, Y. Arisawa, T. Motono, M. Asai and T. Itani, *Proc. SPIE* **11323** (2020) 113231W.
18. M. Harumoto, J.J. Santillan, C. Nakayama, Y. Tanaka, T. Motono, M. Asai, and T. Itani, *J. Photopolym. Sci. Technol.* **32** (2019) 321.
19. Ethyltrimethylammonium hydroxide; SDS Code 3300; SACHEM Americas: Austin, TX, January 14, 2018.
20. Tetramethylammonium hydroxide; SDS Code 520; SACHEM Americas: Austin, TX, March 21, 2019.
21. T. Ando, T. Uchihashi, N. Kodera, D. Yamamoto, A. Miyagi, M. Taniguchi, and H. Yamashita, *Pflugers Arch.* **456** (2008) 211.
22. T. Itani and J.J. Santillan, *Appl. Phys. Express* **3** (2010) 061601.
23. T. Itani and J.J. Santillan, *Proc. SPIE* **7972** (2011) 79720H.
24. BL-AC10FS-A2 cantilever spec. sheet retrieved from <http://probe.olympus-global.com> (2014).
25. J.J. Santillan and T. Itani, *J. Photopolym. Sci. Technol.* **26** (2013) 611.
26. J.J. Santillan and T. Itani, *Proc. SPIE* **10146** (2017) 101460C.
27. J.J. Santillan and T. Itani, *Jpn. J. Appl. Phys.* **52** (2013) 06GC01.

Process and Sensitivity Optimisation of the Multi-Trigger Resist

C. Popescu¹, G. O’Callaghan¹, C. Storey¹, A. McClelland¹,
J. Roth², E. Jackson², A.P.G. Robinson^{1*}

(1) Irresistible Materials, Birmingham Research Park, Birmingham, UK

(2) Nano-C, 33 Southwest Park, Westwood, MA, USA.

*a.p.g.robinson@bham.ac.uk

Irresistible Materials (IM) is developing novel resist systems based on the multi-trigger concept, which incorporates a dose dependent quenching-like behaviour. In this study, we present the results that have been obtained using Multi Trigger Resists (MTR) by performing EUV exposures on the ASML NXE EUV scanner at IMEC. The MTR is a negative tone high opacity crosslinking resist incorporating. Pitch 28nm dense patterns can be patterned at a dose of 59mJ/cm², a line width of 12.5nm, and a biased LWR of 3.91nm. These resist formulations have also been used to pattern 20nm diameter pillars on a hexagonal 40nm pitch with a dose of 51 mJ/cm², and a CDU of 3.5nm; and also pillars at pitches of 34nm hexagonal with a dose of 80mJ/cm² to achieve 17.5nm diameter pillars. High photospeed approaches, which have patterned p28 lines and p34 hex pillars at sub-30 mJ/cm² doses are also introduced.

Keywords: EUV lithography, photoresist, molecular resist, multi-trigger resist, chemical amplification, crosslinking

1. Introduction

EUV lithography is starting to be established in high volume manufacturing but there are still many challenges with the tool and the materials. EUV photoresists with the appropriate capability to support future roadmap requirements such as high-NA remain a priority area of research. Currently traditional chemically amplified resists (CAR) [1] are being used, but several novel approaches are being investigated to support future patterning needs for high resolution and sensitivity, and low line width roughness and stochastic defects. [2–4]. It is, however, well-known that these resist metrics are fundamentally linked in a tradeoff relationship, and improvements to one often comes to the detriment of another. As an example, the resolution of a CAR can be improved by reducing the photoacid diffusion length with base additives or bulky acids, but with an unfavourable effect on the required dose and/or the line width roughness. Defectivity due to line collapse, bridging or line breaks is an increasingly common failure mode at pitches below 32 nm.

Irresistible Materials (IM) is developing novel resist systems based on the multi-trigger concept. In a multi-trigger resist multiple elements of the resist must be simultaneously activated to enable the catalytic reactions to proceed. In high dose areas the

resist therefore behaves like a traditional CAR, whilst in low dose areas, such as line edges, the reaction is second-order, increasing the chemical gradient. Effectively there is a dose dependent quenching-like behaviour built into the resist, enhancing chemical contrast and thus resolution and reducing roughness, whilst eliminating the materials stochastic impact of a separate quencher.

MTR utilises a catalytic ring opening propagation mechanism (CROP). The reaction front is a percolation, controlled by varying the relative reaction rates of initiation and propagation mechanisms. The incorporation of a proprietary dose dependant control molecule accelerates the reaction in high dose areas; in mid dose areas it quenches the photoacid and blocks (but does not quench) propagation; and in low dose areas it quenches all resist reactions. As the control molecule participates in the crosslinking mechanism it will not be leached out during development. The MTR mechanism also leads to film densification, which enhances etch durability.

In the MTR platform previously presented [5-11] it is possible to vary the relative importance (or ratio) of each aspect with a relatively high degree of flexibility, to achieve various performance changes. The baseline for the optimization is the previously

Received May 10, 2022

Accepted June 24, 2022

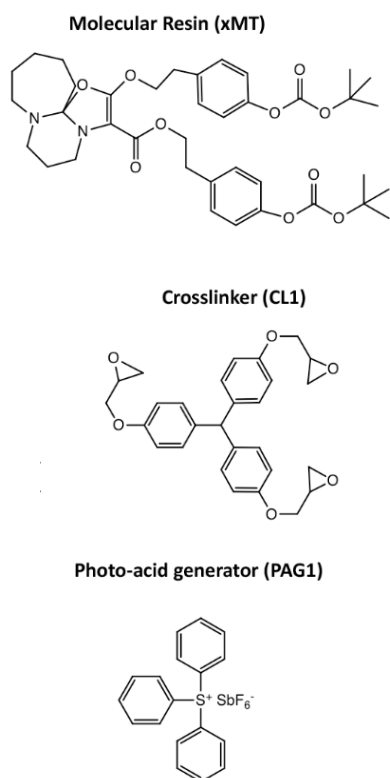


Figure 1: Resist components in the baseline xMT system.

introduced xMT resist system, (figure 1) from which the MTR1 series resist was developed. The molecular resin has been modified, to increase the glass transition temperature (T_g) (MTR2) and to modify the activation energy of the molecule (MTR4 and MTR8). A cross-linking molecule, XL-A, which incorporates non-metal high-Z elements compared to CL1, was introduced in the system for increased optical density. Triphenylsulfonium tosylate, which acts as a photo-decomposable quencher in epoxy-based systems, is also added. [12]. Whilst performance can be modulated through the formulation ratios, further enhancements are possible by optimizing the functional groups.

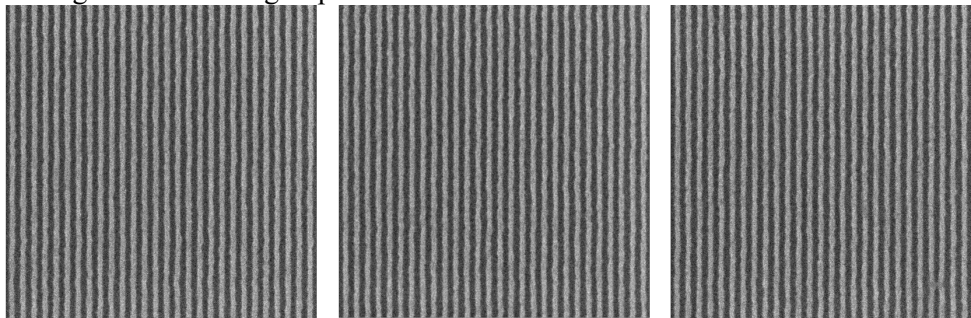


Figure 2: MTR resist with XL-A: Left: PEB 60 °C, Dose 58.75 mJ/cm², CD: 12.49 nm, LWR: 3.91 nm; Middle PEB 65 °C, Dose 56.5mJ/cm², CD 12.00nm, LWR 4.17nm; Right: PEB 70°C, Dose 55.75 mJ/cm², CD: 12.01 nm, LWR: 4.37 nm.

Research has been undertaken to improve this negative tone resist, in particular focusing on improving resist opacity and crosslinking density. Higher absorption is a potential route to overcome the photon shot noise limit in EUV lithography as well as potentially improving the sensitivity to enable high volume manufacturing at current source power output. EUV lithography suffers from the low volume of photons produced [13]. To address this, we have synthesised crosslinkers that have elements that have high EUV absorbance compared to carbon, hydrogen and oxygen [14]. The elements chosen have high EUV absorbances, are relatively straightforward to incorporate into a resist and are *non-metal*.

2. Experimental

The resist samples were prepared by dissolving the individual components in ethyl lactate or PGMEA. The solutions were then combined in various weight ratios and concentrations to give a range of formulations. The solutions undergo metal ion removal using 3M Zeta Plus filtration disks to reduce metals to levels appropriate for fab based processing.

The resist was spun onto a commercial organic underlayer, Brewer Scientific Optistack AL412.. After spin-coating of the resist using a track for film deposition, the samples received a post application bake (PAB) of 80°C for 1 minute, and were exposed using an ASML NXE3400 scanner at imec. After exposure the samples received a post exposure bake of between 60°C and 70°C, and were developed in n-butyl acetate for 30 seconds using a dynamic system with no subsequent rinse. The patterning was observed using Hitachi CD-SEM (CG-5000 or 6300 models) with 500eV and 8pA as beam conditions, and the LWR, LER, LCDU and CER values are biased values unless otherwise stated.

3. Results

Trials at pitch 28nm line space were carried out on formulations using XL-A and MTR 2, to assess the resolution of this crosslinker as a baseline. A narrow sweep of PEB temperatures from 60°C to 70°C was used to find the optimum temperature for minimum Z factor for XL-A at a film thickness of 20.5nm (figure 2). A negatively biased mask was used with a line width on the reticle designed at 12nm. It was found that for XL-A the optimum PEB temperature was between 60°C and 65°C, with both temperatures having a Z factor of 1.01×10^{-8} (where $Z\text{-factor} = (\text{Resolution})^3 \times (\text{LWR})^2 \times (\text{Sensitivity})$) for 12nm width lines. At 60°C the dose required to pattern 12nm lines was 57.6mJ/cm², and at 65°C it was 56.7mJ/cm². The average biased LWR was 4.20nm for 60°C and 4.23nm for 65°C.

3.2 Tunability of MTR resist

One of the most striking aspects of MTR resist is the ability to tune the resist formulation by changing the ratio of the solid components (indicated in figure 1) and modulate the lithographic response quite significantly, with the sensitivity of the resist being a readily apparent change. One aspect that was explored was to change the amount of quenching in the system and to investigate the impact on the and LCDU and CER of pillar patterning. A systematic experiment was designed where the amount of MTR molecule (MTR8) and the amount of photo-decomposable quencher, was varied within a narrow set of values. The results from 6 different formulations (all using the crosslinker XL-A) carried out using pillars arranged in an hexagonal pattern at pitch 40nm. The reticle used is designed with 23nm diameter pillars. As can be seen in table 1, a 33% reduction in dose to size can be achieved by using resist 3 rather than the baseline resist (resist 1). The increase in LCDU is 14%. By using, for example, resist 5, a 20% dose reduction can be achieved with less than a 7% increase in LCDU.

The graph in figure 3 shows that for all the resist formulations there is a general linear trend of

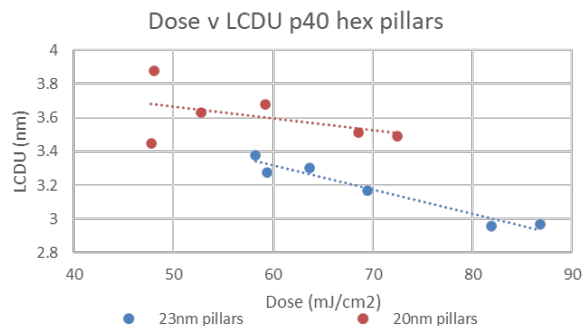


Figure 3: Impact of resist sensitivity on LCDU of p40 hexagonal pillars

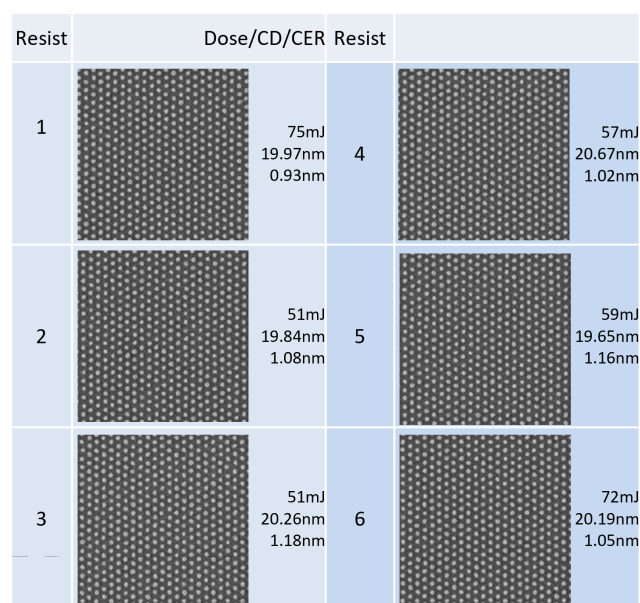


Figure 4: Images of pillar patterning using MTR resist with varying formulation ratios

decreasing LCDU with increasing dose for both 20nm and 23nm pillars. Figure 4 shows example CD SEM images of the pillars at 20nm diameter for the varying resist formulation ratios.

3.3 Generation 2 MTR resist – increasing sensitivity

The MTR resist using XL-A and PAG1 has been used to pattern pitch 28nm lines using a film thickness of 20nm as seen in figure 2. We also present here high resolution images using a 17nm

Resist	Dose to size (mJ/cm ²)	Percentage reduction in dose	LCDU/nm	Percentage increase in LCDU
baseline	86.76		2.97	
3	58.21	-32.9	3.38	13.8
2	59.42	-31.5	3.27	10.2
4	63.66	-26.6	3.30	11.1
5	69.46	-19.9	3.17	6.7
6	81.91	-5.6	2.96	-0.3

Table 1: Results of 6 resist formulations with resultant dose-to-size and LCDU changes

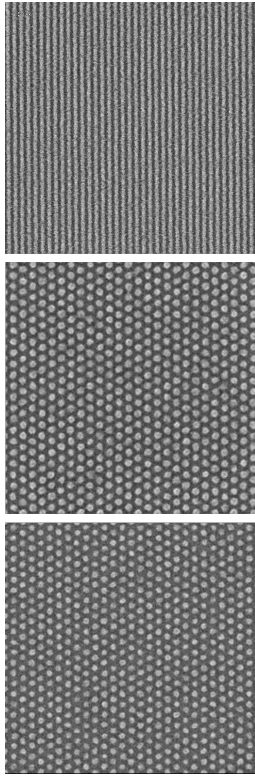


Figure 5 Patterning using MTR Pilot resist using XL-A. From Top to Bottom: p24 line/space (rectangular image), Dose 52.5mJ/cm², CD 11.3nm, p36 hex pillars, Dose 75.5mJ/cm², CD 21.0nm; p34 hex pillars, Dose 80mJ/cm², CD 17.5nm

film thickness. In figure 5, we present pitch 24nm lines with a CD of 11.3nm (as measured via the CD SEM program) and patterned at 52.5mJ/cm². We also present p36 and p34 hexagonal pillars with a dose of 75.5 - 80mJ/cm². However, there is always interest in decreasing the dose required for EUV resist to improve productivity, therefore research continues to try to maintain state of the art resolution of the resist whilst increasing the sensitivity for increased throughput capability. Initial results for MTR Gen 2 resist, see figure 6, show that by carefully controlling the rates of the various reactions in the CROP enables lines to be patterned with a sub 20mJ/cm² dose with an 18nm film thickness at pitch 28nm. Process optimization will continue to reduce the visible bridging defects. The tunability of the MTR resist, as explored in section 3.2, will allow for formulation changes to slightly increase the dose, potentially up to the 30mJ/cm² level, with a probable LWR reduction. There has also been research into changing the PAG cation compared to PAG1. As also shown in figure 6, using a 17nm film thickness, 18.7nm – 19.5nm diameter pillars at pitch 34nm, with a mask diameter of 19nm, with a dose of 27.75 – 28.75mJ/cm² can be patterned successfully.

	p28		p34
dose 18.0mJ/cm ² Line width 11.1nm		dose 27.75mJ/cm ² Diameter 18.7nm	
dose 19.0mJ/cm ² Line width 11.8nm		dose 28.25mJ/cm ² Diameter 19.0nm	
dose 20.0mJ/cm ² Line width 12.5nm		dose 28.75mJ/cm ² Diameter 19.5nm	

Figure 6: Patterning using MTR Gen 2 Resist using XL-A showing p28 patterning at 20mJ/cm² and less; and p34 pillar patterning at sub 30mJ/cm²

4. Conclusion

MTR Resist is a negative tone resist with an intrinsic dose dependent quenching mechanism, which can pattern high resolution patterns with EUV lithography. In this study we have shown pitch 28nm dense patterns can be patterned at a dose of 59mJ/cm², a line width of 12.5nm, and a biased LWR of 3.91nm. These resist formulations have also been used to pattern 20nm diameter pillars on a hexagonal 40nm pitch with a dose of 51mJ/cm², and a CDU of 3.5nm; and also pillars at pitches of 34nm hexagonal with a dose of 80mJ/cm² to achieve 17.5nm diameter pillars. The tunability of MTR resist by changing the ratio of the components has been demonstrated with a 33% reduction in dose to size achieved with a concurrent increase in LCDU is 14%. Research continues to try to maintain state of the art resolution of the resist whilst increasing the sensitivity for increased throughput capability we have introduced high photospeed approaches, where we have patterned p28 lines and p34 hex pillars at sub-30 mJ/cm² doses.

Acknowledgements

The authors would like to thank the Engineering and Physical Sciences Research Council (EPSRC) for support of this project. The authors thank Irresistible Materials Ltd, Merck, Brewer Science and Nano-C for support and provision of resist materials.

References

- [1] J. Severi, G.F. Lorusso, D. De Simone, A. Moussa, M. Saib, R. Duflou and S. De Gendta, "Chemically amplified resist CDSEM metrology exploration for high NA EUV lithography" *J. Micro/Nanopattern. Mater. Metrol.* 021207-13 2022
- [2] S. Nagahara, C. Que Dinh, K. Yoshida, G. Shiraishi, Y. Kondo, K. Yoshihara, K. Nafus, J.S. Petersen, D. De Simone, P. Foubert, G. Vandenberghe, H-J. Stock, B. Meliorisz, "EUV resist chemical gradient enhancement by UV flood exposure for improvement in EUV resist resolution, process control, roughness, sensitivity, and stochastic defectivity". *Proc. SPIE* **11326**, 113260A (2020).
- [3] A. Shirotori, M. Hoshino, D. De Simone, G. Vandenberghe, H. Matsumoto, "A novel main chain scission type photoresists for EUV lithography," *Proc SPIE* **11517**, 115170D (2020).
- [4] S.K. Sharma, R. Kumar, M. Chauhan, M.G. Moinuddin, J. Peter, S. Ghosh, C.P. Pradeep, K.E. Gonsalves, "All-new nickel-based Metal Core Organic Cluster (MCOC) resist for N7+ node patterning," *Proc SPIE* **11326**, 1132604 (2020).
- [5] Y. Vesters, A. McClelland, C. Popescu, G. Dawson, J. Roth, W. Theis, D. de Simone, G. Vandenberghe, A.P.G. Robinson, "Multi-trigger resist patterning with ASML NXE3300 EUV scanner," *Proc. SPIE* **10586**, (2018).
- [6] C. Popescu, D. Kazazis, A. McClelland, G. Dawson, J. Roth, W. Theis, Y. Ekinici, A.P.G. Robinson, "High-resolution EUV lithography using a multi-trigger resist," *Proc. SPIE* **10583**, 10583-54 (2018)
- [7] G. O'Callaghan, C. Popescu, A. McClelland, D. Kazazis, J. Roth, W. Theis, Y. Ekinici, A.P.G. Robinson, "Multi-trigger resist – Novel synthesis improvements for high resolution EUV lithography", *Proc. SPIE* **10960** (2019)
- [8] W. Montgomery, A. McClelland, D. Ure, J. Roth, A.P.G. Robinson, "Irresistible Materials multi-trigger resist: the journey towards high volume readiness," *SPIE* **10143**, 1014328 (2017).
- [9] C. Popescu, A. McClelland, D. Kazazis, G. Dawson, J. Roth, Y. Ekinici, W. Theis, A.P.G. Robinson, "Multi-trigger resist for electron beam and extreme ultraviolet lithography," *Proc. SPIE* **10775**, 10775-02 (2018).
- [10] C. Popescu, G. O'Callaghan, A. McClelland, J. Roth, T. Lada, A.P.G. Robinson, "Performance enhancements with high opacity multi-trigger resist" *Proc. SPIE* **11326**, 11326-11 (2020)
- [11] C. Popescu, G. O'Callaghan, A. McClelland, J. Roth, T. Lada, T. Kudo, R. Dammel, M. Moinspour, Y. Cao, A.P.G. Robinson, "Progress in the multi-trigger resist", *Proc. SPIE* **11612**, Advances in Patterning Materials and Processes XXXVIII, 116120K (2021)
- [12] R.A. Lawson, A. Frommhold, D.X. Yang, A.P.G. Robinson, "Negative-tone organic molecular resists," in Robinson A.P.G., Lawson R.A. editors. *Materials and Processes for Next Generation Lithography*. Oxford, Elsevier (2016).
- [13] Z-Y. Pan, C-K Chen, T-S Gau, B.J.L Taiwan., *Proc. SPIE*, 2008, **69241K**
- [14] R. Fallica, J. Haitjema, L. Wu, S. Castellanos, F. Brouwer, Y. Ekinici, *Proc. SPIE EUV Lithography VIII*, 2017, **101430°**

Chemical Mechanisms of Metal-Based Extreme Ultraviolet Resists

Albert M. Brouwer^{1,2*}

¹ *Advanced Research Center for Nanolithography, P.O. Box 93019, 1090 BA Amsterdam, The Netherlands*

² *University of Amsterdam, van 't Hoff Institute for Molecular Sciences, P.O. Box 94157, 1090 GD Amsterdam, The Netherlands*

**a.m.brouwer@uva.nl*

Hybrid organic/inorganic materials are considered as the Extreme Ultraviolet photoresists of the future. Compared to chemically amplified polymer-based photoresists they offer higher EUV absorption cross sections, and higher etch resistance. The chemical reactions that occur in these materials upon excitation with EUV or other high energy radiation have been investigated over the past 8 years. This paper summarizes the findings for two classes of metal-based resists: metal oxo clusters with acrylate ligands, and organotin oxo cages.

Keywords: Extreme Ultraviolet, Photoresist, metal oxoclusters, tin-oxo cages, reaction mechanism

1. Introduction

Extreme Ultraviolet Lithography (EUVL) has made its entrance into the large-scale production of high-end integrated circuits. The short wavelength of light used, 13.5 nm, allows smaller features to be written in a single process step than the well-established deep UV immersion lithography (193 nm). Many technological advances have made EUVL a reality [1]. For further improvement of the productivity, advances in hardware are in progress [2], but also the “software” of photolithography, the photoresist, needs to be updated. A breakthrough in UV lithography came with the introduction of chemically amplified photoresists (CAR), in which a photochemically generated acid acts a catalyst for the ester hydrolysis that switches the solubility of the photoresist [3]. This mechanism boosts the photon efficiency and through-put of the process. For high-resolution applications, however, the catalytic step has the disadvantage that it is accompanied by diffusion and thereby leads to a blurring of the image. For today’s lithographers it may be practically advantageous to adapt existing CAR materials for the use of the new wavelength of light, but for the future, other materials need to be considered. In particular, molecular hybrid

organic/inorganic materials are of interest [4–7]. The metal centers in such materials can help to increase the absorption of EUV photons, and strengthen the etch resistance, allowing to apply thinner resist layers with a smaller, more favorable aspect ratio. The molecular size should allow patterning down to the nanometer scale. In contrast to the chemically amplified resists, which have a history of 40 years of research and development, the organic/inorganic materials have been investigated only recently, and there is still much to learn about how their chemistry works, and which parameters can be tuned to optimize their patterning performance. This paper will address two classes of molecular materials, namely oxo clusters of metals such as Ti, Hf, Zr, and Zn, and organotin-oxo cage compounds. First, a general picture will be sketched of the processes that take place following EUV photon absorption. Next, the current knowledge of the reaction pathways in the two classes of material will be reviewed.

When an EUV photon, with an energy of 92 eV, is absorbed by a molecule, ejection of an electron will occur [8]. Depending on the energy level (molecular or atomic orbital) from which it originates, the ejected electron may have a kinetic

Received	April 30, 2022
Accepted	June 24, 2022

energy up to ~85 eV. The highest energy is determined by the binding energy of the Highest Occupied Molecular Orbital. When the electron comes from a metal core level, its kinetic energy will be smaller; it is likely that the core level vacancy is filled by an Auger process releasing a second electron. In any case, the primary photoelectrons have enough kinetic energy to ionize neighboring molecules, leading to a cascade of ionization processes generating multiple electrons of lower energy, and the associated holes (one-electron oxidized molecules). In addition, electron kinetic energy may be transferred to the molecules in the resist film in the form of vibrationally and electronically excited states. While there is no doubt that all these processes take place, in general little is known about their efficiencies and relative contributions to the energy dissipation and the chemical reactivity.

The electron energy loss processes mostly take place on a short timescale, of the order of picoseconds [9]. Very few chemical reactions occur on this time scale. After this, the sample contains “holes”, *radical cations* in the language of molecules, and electrons, mostly trapped in *radical anions*, and molecules in electronically excited states.

In the literature, emphasis has been placed on the electron yield [10], but the chemical reactions actually occur when bonds are broken or rearranged in the radical ions or excited molecules. The time scale for this may vary over many orders of magnitude. The radical ions can undergo reactions on the timescale of nanoseconds to milliseconds (or even longer) in competition with charge recombination. Electronically excited states (excitons) can have their specific reactions on timescales of nanoseconds to microseconds, in competition with luminescence and nonradiative decay processes. Time-resolved spectroscopies would be ideal to investigate transient species in these fast processes, but the technical requirements have precluded such experiments until now.

Our working hypothesis, based on the considerations of the previous paragraphs, is that the chemistry of molecular photoresists can -at least as a first approximation- be discussed in terms of the reactivity of the vibrationally relaxed radical ions and excited states, localized on single molecular units.

2. Metal oxoclusters

A wide variety of hybrid organic-inorganic metal

oxoclusters has been reported in the recent literature [11]. To date only a few of those have been explored for EUV lithography, in particular containing Ti [12], Zr [13,14], Hf [12,15], and Zn [16,17]. Two examples are shown in Figure 1. The characteristic feature of these structures is that they have an inorganic core consisting of a number of metal atoms bridged by oxygen or OH groups, surrounded by carboxylate ligands. The carboxylate anions can be exchanged with other carboxylates, giving access to a wide variety of materials [18] with the same metal oxo core.

For lithography, the ligands of choice are methacrylates, which are well known as monomers for radical polymerization. Ample spectroscopic evidence has been presented that the C=C double bonds disappear as a result of reactions upon EUV exposure, but most of the ligands are not lost and cross-linking is the likely reaction pathway that leads to an insoluble network.

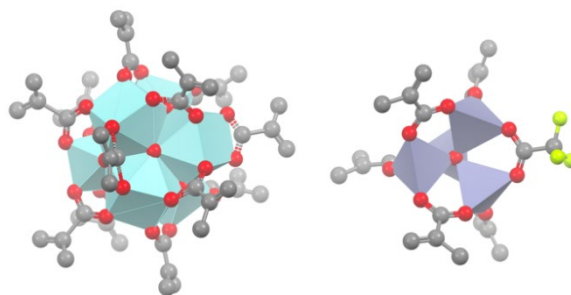
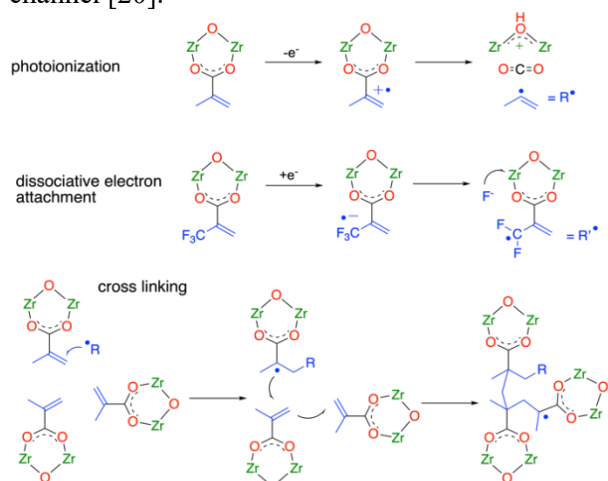


Fig. 1. Examples of oxoclusters with methacrylate ligands: $Zr_6(OH)_4O_4(OMc)_{12}$ [19] and $Zn_4O(TFA)(OMc)_5$ [17].

To form the radicals, decomposition of a fraction of the ligands is inferred (Scheme 1) as the initial step [14]. This will lead to a small loss of CO_2 which is consistent with the changes in the X-ray photoelectron spectra of the films after exposure. The loss of material via outgassing and some densification associated with the cross-linking of the ligands can be expected to lead to shrinkage of the material upon EUV-induced conversion, but this effect turns out to be small, in contrast to the case of the tin-oxo cages discussed below.

The absorption of EUV radiation by the metal oxo clusters can be enhanced by replacing hydrogen atoms in the ligands by fluorine atoms. The presence of carbon-fluorine bonds also opens a new reaction channel: a dissociative electron attachment in which a low energy electron ends up trapped in a stable fluoride anion, leaving a radical on the ligand which can initiate the cross-linking reaction. In the

case of $Zr_6O_4(OH)_4Mc_{12}$, replacement of one of the methacrylates by a trifluoromethyl acrylate led to an increased sensitivity, which may be attributable to the enhanced absorption and the additional reaction channel [20].



Scheme 1. Reactions occurring in (partly fluorinated) Zr MOC upon EUV excitation.

For a similar zinc-oxo cluster, however, the introduction of fluorinated methacrylates rendered the photoresist less sensitive than the parent one [21]. Here, the absorption enhancement is relatively smaller, because zinc has a higher EUV cross section than Zr, and it is counteracted by the smaller radical polymerization rate of trifluoromethylacrylate compared to methacrylate [22]. A practical challenge encountered with these highly fluorinated materials is in their physical properties, which affect the quality of film formation. Another noteworthy feature of this study is that the authors made an estimate of the quantum efficiency of the EUV induced conversion of the C=C double bonds to oligomers and polymers. This was found to be $\Phi \approx 10$, consistent with the formation of multiple reactive species per photon and/or a chain reaction.

Wu et al. introduced a carbazole unit in the ligand shell of the Zr_6 oxocluster [23]. This allowed to visualize the effect of EUV irradiation using fluorescence imaging. At the doses required for solubility switching, some bleaching of the organic chromophore occurred, but most of the carbazole absorption and fluorescence was retained. Interestingly, with (on average) 1 out of 12 methacrylate ligands exchanged by the carbazole ligand, the sensitivity of the material towards solubility switching was about $10\times$ smaller than that of the parent system. Since carbazole is a strong electron donor, a likely explanation for the reduced reactivity is that potentially reactive holes are filled by electron transfer from the carbazole. Once

trapped on this ligand the holes survive for a long time. This indicates that in the parent system the holes are responsible for a large part of the chemistry.

3. Organotin-oxo cages

The use of tin-oxo cages (figure 2) in EUV lithography was pioneered by the Brainard group, in the context of their MORE project [24]. In this ground-breaking work, several different organic groups connected to the Sn atoms were explored, as well as a number of different counter-ions. Negative tone EUV patterning was demonstrated, but the sensitivity appeared to be rather low. Most other researchers have restricted themselves to n-butyltin derivatives, probably because the n-butyltin precursors are commercially available. Instead of synthesizing and isolating pure tin-oxo cages, experiments have also been performed with the n-butylstannic acid [25], and dimeric [26] and hexameric tin-oxo compounds [27]. It has been suggested that the Sn_{12} tin-oxo cages are at the basis of the EUV resist materials developed by Inpria [28,29].

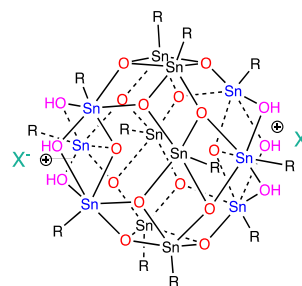
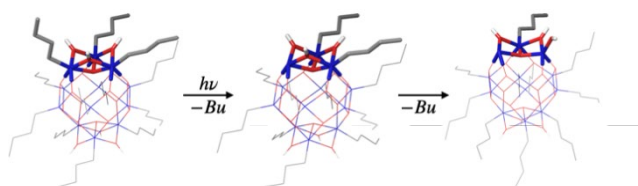


Fig. 2. General structure of Sn_{12} tin-oxo cages. R can be an aliphatic or aromatic substituent. X is a monovalent anion.

Regardless of the mode of activation, a common observation in the chemistry of organotin resists is the homolytic cleavage of the tin-carbon bond. In studies of thin resist films with methods such as infrared absorption [30], X-ray Photoelectron Spectroscopy (XPS) [25,31,32] or (near-edge) X-ray absorption spectroscopy ((NE)XAS) the loss of carbon is readily detected. It is difficult, however, to extract information on the structure of the material that remains in the exposed film. In simulation studies, it is assumed that after breaking of tin-carbon bonds, cross-linking between cages occurs, leading to the observed negative tone resist behavior [30,33,34]. The detailed chemical structures of the primary photoproducts, and the exact way they cross-link in the solid resist films, are still unknown.

In contrast to the metal oxo clusters discussed above, the sensitivity of the n-butyltin oxo cages is enhanced by post-exposure baking [35], indicating that metastable intermediates are formed after EUV irradiation that react (cross-link?) further upon heating under ambient conditions.

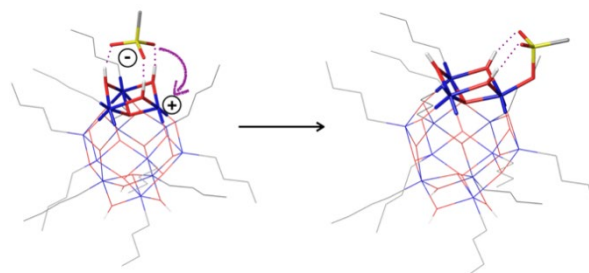
Some insight in the elementary steps of the photochemistry of n-butyltin oxo cages has emerged from gas phase studies of the isolated 2+ ions and their complexes with a counterion (net charge 1+) [36]. The ions were irradiated in an ion trap, with photon energies ranging from 4 eV to 35 eV, and the reaction products analyzed by means of mass spectrometry. At energies <12 eV for the bare dication and <10 eV for the complexes with one counterion, excitation can only take place to bound electronically excited states. This leads to the loss of one or two n-butyl groups. Computational quantum chemistry was used to predict the structures of the species formed. These strongly suggested that the first butyl group is lost as a radical from one of the “caps” of the rugby-ball shaped molecule. The tin-centered radical produced can easily lose a second butyl group, giving rise to a stable closed-shell product (Scheme 2).



Scheme 2. Reactions occurring upon UV excitation of the tin-oxo cage dication. Two butyl groups are lost, and one bridging OH group is localized on one Sn atom [36].

It seems likely that the same products can be formed in the solid state. Direct *experimental* evidence for the structures, however, is yet to be obtained. As one of the tin atoms is formally reduced to Sn(II), oxidation reactions may take place upon heating this product in ambient conditions, which would account for the enhanced resist sensitivity following post-exposure baking that is observed experimentally [35].

At higher photon energies, the bare 2+ tin-oxo cage (>12 eV) and the 1+ complex with the counterion (>10 eV) are ionized to 3+ and 2+ radical ions, respectively. These, however, are not detected because they lose a butyl radical. When a counterion is present, it can form a bond to the formally positively charged tin atom, as illustrated in Scheme 3.



Scheme 3 Photoionization of a tin-oxo cage dication complexed with a sulfonate anion, followed by rapid loss of Bu radical, and a rearrangement of the counterion [36].

In the chemistry of the photoresist this is not likely to be a stable product, because it is still positively charged, and can be neutralized by capturing an electron, or by transferring a proton to a neighboring molecule. There are many possibilities for follow-up reactions, which remain to be investigated. Ultimately, the reaction mechanisms must account for charge neutrality, and charge recombination and (in-cage) radical recombination processes should be considered.

The gas phase studies of tin-oxo cage ions have given us some insight into the role of the counterions in the chemistry, that corroborate our earlier observations that they have a small effect on the sensitivity of the negative tone photoresist response [35]. Recently, a more dramatic effect was encountered when tin-oxo cages with very non-nucleophilic tetrakis(pentafluorophenyl)borate anions were investigated [37]. In this case at low doses a positive tone behavior was found, which implies that reaction products at low conversion are more soluble in suitably chosen developers, suggesting that cross-linking is not important in the early stages of the exposure.

When the tin-oxo cage is ionized [38], an electron is released that can initiate a cascade of events in which more electrons and holes are generated. Some of the low energy electrons can be captured by pristine tin-oxo cages. Interestingly, as shown by computation [39,40] and experiments [41], the radical anions are unstable and like the radical cations and excited states undergo cleavage of a tin-carbon bond. A difference in this case is that the bonds in the central belt of the molecule are more reactive in the reduced form, rather than the ones in the caps. Which products are formed along this pathway remains to be investigated. It is certain, however, that low energy electrons can convert the tin-oxo cage films to a large extent. This means that the reaction products of the first step can be further degraded under further loss of carbon.

4. Conclusion

Although absorption of an EUV photon delivers a large amount of energy to a molecule, the mechanisms of the solubility switching reactions in metal oxoclusters with carboxylic acid ligands and in organotin-oxo cages have been discussed on the basis of the chemistry of radicals and radical ions that result from the photoionization, electron cascade and subsequent thermalization. For the metal oxoclusters, the main reaction that switches the solubility is the cross-linking of the acrylate ligands. When the ligands contain fluorine, dissociative electron attachment pathways are opened.

For the tin-oxo cages, the primary reaction following ionization, electron capture, or electronic excitation is the cleavage of one or two tin-carbon bonds. Structures of the primary products detected via mass spectrometry of the gas phase ions have been proposed based on quantum chemical studies. A clear molecular-level mechanistic picture for the solubility switching is still lacking.

Acknowledgement

This work was performed in part in the Advanced Research Center for NanoLithography (ARCNL), a public private partnership of the University of Amsterdam (UvA), the VU University Amsterdam (VU), the Dutch Research Council (NWO) and the semiconductor equipment manufacturer ASML. Many people have made essential contributions to the research behind this paper at ARCNL, UvA, and the synchrotron facilities BESSY 2, SOLEIL, PSI and Elettra. Their names can be found as coauthors on the publications from our laboratory, a.o. references [21,31,35–38,41].

References

1. J. P. Benschop, *Proc. SPIE* **11609** (2021) 1160903.
2. H. J. Levinson, *Jap. J. Appl. Phys.* **61** (2022) SD0803.
3. H. Ito, and C. G. Willson, *Polym. Eng. Sci.* **23** (1983) 1012.
4. A. Lio, *Synchrotron Rad. News* **32** (2019) 9.
5. Z. Wang, X. Yao, H. An, Y. Wang, J. Chen, S. Wang, X. Guo, T. Yu, Y. Zeng, G. Yang, and Y. Li, *J. Microelectron. Manuf.* **4** (2021) 21040101.
6. C. Luo, C. Xu, L. Lv, H. Li, X. Huang, and W. Liu, *RSC Advances* **10** (2020) 8385.
7. R. Kumar, M. Chauhan, M. G. Moinuddin, S. K. Sharma, and K. E. Gonsalves, *ACS Appl. Mater. Interfaces* **12** (2020) 19616.
8. T. Kozawa, and S. Tagawa, *Jap. J. Appl. Phys.* **49** (2010) 030001.
9. C. R. Arumainayagam, H.-L. Lee, R. B. Nelson, D. R. Haines, and R. P. Gunawardane, *Surf. Sci. Rep.* **65** (2010) 1.
10. J. Torok, R. D. Re, H. Herbol, S. Das, I. Bocharova, A. Paolucci, L. E. Ocola, C. Ventrice Jr, E. Lifshin, G. Denbeaux, and R. L. Brainard, *J. Photopolym. Sci. Technol.* **26** (2013) 625.
11. U. Schubert, *Chem. Soc. Rev.* **40** (2011) 575.
12. S. Castellanos, L. Wu, M. Baljovic, G. Portale, D. Kazazis, M. Vockenhuber, Y. Ekinci, and T. A. Jung, *Proc. SPIE* **10583** (2018) 10583A.
13. J. J. Santillan, and T. Itani, *J. Photopolym. Sci. Technol.* **31** (2018) 663.
14. L. Wu, M. Baljovic, G. Portale, D. Kazazis, M. Vockenhuber, T. Jung, Y. Ekinci, and S. Castellanos, *J. Micro/Nanolitho., MEMS, MOEMS* **18** (2019) 013504.
15. E. C. Mattson, Y. Cabrera, S. M. Rupich, Y. Wang, K. A. Oyekan, T. J. Mustard, M. D. Halls, H. A. Bechtel, M. C. Martin, and Y. J. Chabal, *Chem. Mater.* **30** (2018) 6192.
16. H. Xu, K. Sakai, K. Kasahara, V. Kosma, K. Yang, H. C. Herbol, J. Odent, P. Clancy, E. P. Giannelis, and C. K. Ober, *Chem. Mater.* **30** (2018) 4124.
17. N. Thakur, R. Bliem, I. Mochi, M. Vockenhuber, Y. Ekinci, and S. Castellanos, *J. Mater. Chem. C* **8** (2020) 14499.
18. L. Wu, J. Liu, M. Vockenhuber, Y. Ekinci, and S. Castellanos, *Eur. J. Inorg. Chem.* **2019** (2019) 4136.
19. G. Kickelbick, and U. Schubert, *Chem. Ber.* **130** (1997) 473.
20. L. Wu, I. Bepalov, K. Witte, O. Lugier, J. Haitjema, M. Vockenhuber, Y. Ekinci, B. Watts, A. M. Brouwer, and S. Castellanos, *J. Mater. Chem. C* **8** (2020) 14757.
21. N. Thakur, M. Vockenhuber, Y. Ekinci, B. Watts, A. Giglia, N. Mahne, S. Nannarone, S. Castellanos, and A. M. Brouwer, *ACS Materials Au* (2022) <http://dx.doi.org/10.1021/acsmaterialsau.1c00059>.
22. H. Ito, D. C. Miller, and C. G. Willson, *Macromolecules* **15** (1982) 915.

23. L. Wu, M. F. Hilbers, O. Lugier, N. Thakur, M. Vockenhuber, Y. Ekinici, A. M. Brouwer, and S. Castellanos, *ACS Appl. Mater. Interfaces* **13** (2021) 51790–51798.
24. B. Cardineau, R. Del Re, M. Marnell, H. Al-Mashat, M. Vockenhuber, Y. Ekinici, C. Sarma, D. A. Freedman, and R. L. Brainard, *Microelectron. Eng.* **127** (2014) 44.
25. R. T. Frederick, S. Saha, J. T. Diulus, F. Luo, J. M. Amador, M. Li, D.-H. Park, E. L. Garfunkel, D. A. Keszler, and G. S. Herman, *Microelectron. Eng.* **205** (2019) 26.
26. N. Kenane, M. A. Grove, C. K. Perkins, T. R. Reynolds, P. H. Cheong, and D. A. Keszler, *Inorg. Chem.* **59** (2020) 3934–3941.
27. M. C. Sharps, R. T. Frederick, M. L. Javitz, G. S. Herman, D. W. Johnson, and J. E. Hutchison, *Chem. Mater.* **31** (2019) 4840.
28. S. T. Meyers, D. A. Keszler, K. Jiang, J. Anderson, and A. Grenville, US9310684B2 (2016).
29. S. T. Meyers, J. T. Anderson, B. J. Cardineau, J. B. Edson, K. Jiang, D. A. Keszler, and A. J. Telecky, US2017010612A1 (2017).
30. C. D. Needham, A. Narasimhan, U. Welling, L. S. Melvin III, P. De Schepper, J. Wouters, J. Severi, D. De Simone, and S. Meyers, *Proc. SPIE* **11323** (2020) 113230G.
31. Y. Zhang, J. Haitjema, X. Liu, F. Johansson, A. Lindblad, S. Castellanos, N. Ottosson, and A. M. Brouwer, *J. Micro/Nanolitho., MEMS, MOEMS* **16** (2017) 023510.
32. R. T. Frederick, J. T. Diulus, D. C. Hutchison, M. Nyman, and G. S. Herman, *ACS Appl. Mater. Interfaces* **11** (2019) 4514.
33. W. D. Hinsberg, and S. Meyers, *Proc. SPIE* **10146** (2017) 1014604.
34. Z. Belete, P. De Bisschop, U. Welling, and A. Erdmann, *J. Micro/Nanopattern. Mater. Metrol.* **20** (2021) 014801.
35. J. Haitjema, Y. Zhang, M. Vockenhuber, D. Kazazis, Y. Ekinici, and A. M. Brouwer, *J. Micro/Nanolitho., MEMS, MOEMS* **16** (2017) 033510.
36. J. Haitjema, L. Wu, A. Giuliani, S. Castellanos, L. Nahon, and A. M. Brouwer, *Phys.Chem.Chem.Phys* **23** (2021) 20909.
37. Q. Evrard, N. Sadegh, Y. Ekinici, M. Vockenhuber, N. Mahne, A. Giglia, S. Nannarone, T. Goya, T. Sugioka, and A. M. Brouwer, *J. Photopolym. Sci. Technol.* in press (2022)
38. Y. Zhang, J. Haitjema, S. Castellanos, O. Lugier, N. Sadegh, R. Ovsyannikov, E. Giangrisostomi, F. O. L. Johansson, E. Berggren, A. Lindblad, and A. M. Brouwer, *Appl. Phys. Lett.* **118** (2021) 171903.
39. J. H. Ma, H. Wang, D. Prendergast, A. Neureuther, and P. Naulleau, *Proc. SPIE* **11323** (2020) 113231F.
40. J. H. Ma, C. Needham, H. Wang, A. Neureuther, D. Prendergast, and P. Naulleau, *ACS Appl. Mater. Interfaces* **14** (2022) 5514–5524.
41. I. Bepalov, Y. Zhang, J. Haitjema, R. M. Tromp, S. J. van der Molen, A. M. Brouwer, J. Jobst, and S. Castellanos, *ACS Appl. Mater. Interfaces* **12** (2020) 9881.

EUV Metal Oxide Resist Development Technology for Improved Sensitivity, Roughness and Pattern Collapse Margin for High Volume Manufacturing

Cong Que Dinh^{1*}, Seiji Nagahara², Yuhei Kuwahara¹, Arnaud Dauendorffer¹, Keisuke Yoshida¹, Soichiro Okada¹, Tomoya Onitsuka¹, Shinichiro Kawakami¹, Satoru Shimura¹, Makoto Muramatsu¹, Kosuke Yoshihara¹, John S. Petersen³, Danilo De Simone³, Philippe Foubert³, Geert Vandenberghe³, Lior Huli⁴, Steven Grzeskowiak⁴, Alexandra Krawicz⁴, Nayoung Bae⁴, Kanzo Kato⁴, Kathleen Nafus⁵, and Angélique Raley⁵

¹ Tokyo Electron Kyushu Ltd., 1-1, Fukuhara, Koshi-shi, Kumamoto 861-1116, Japan

² Tokyo Electron Ltd., 3-1 Akasaka 5-chome, Minato-ku, Tokyo 107-6325, Japan

³ imec, Kapeldreef 75, B-3001 Leuven, Belgium

⁴ TEL Technology Center, America, LLC., 255 Fuller Road, Suite 214, Albany, NY 12203, United States

⁵ Tokyo Electron America, Inc., 2400 Grove Blvd. Austin, Texas 78741, United States

*congque.dinh@tel.com

One of the critical challenges for delivering next nodes or high-NA extreme ultraviolet (EUV) lithography to high volume manufacturing (HVM) in the semiconductor industry is to have a high-performance EUV resist process. The high-performance resist process needs to simultaneously meet multiple requirements, such as high resolution, high sensitivity, low roughness, a low defect level, and good global CD uniformity (CDU). In this paper, we will introduce a new wet development (DEV) method to improve the performance of metal oxide resists (MOR), which is named ESPERT^{TM**} (Enhanced Sensitivity developER Technology). This newly invented method can meet multiple requirements together where it is not possible with the conventional development method. With 36 nm pitch pillar patterns, we have confirmed with after etch inspection (AEI) data that the new method produced 22% improvement in EUV dose and 7% improvement in LCDU, simultaneously. No pattern collapse was observed at least up to 15.4 nm pillar size. In the case of 30 nm pitch line/space (L/S) pattern, the improvements were 26% in EUV sensitivity and 12.3% in LWR also with AEI results. Furthermore, the new method could also shift the bridging cliff 0.5 nm to the larger line CD while its global CDU was improved 2.6 times. The new data achieved by the new wet development method make us believe that MOR are mostly ready for HVM and this new method is also aiming to be used in high NA EUV lithography in the near future.

***) ESPERTTM is trademarks of Tokyo Electron Limited.

Keywords: EUV resist, MOR, Roughness, Collapsing, Bridging, Global CDU

1. Introduction

Chemical amplified resists (CAR) have been used widely for many years in optical lithography. With the increasing requirements of scaling, CAR and the line width roughness (LWR) have also been constraints limiting the capabilities of extreme ultraviolet (EUV) lithography [1-7]. We have reported that we could improve the CAR

performance further in our previous literature [8-16]. However, currently metal oxide resist (MOR) is among the leading candidates for next nodes extreme ultraviolet (EUV) lithography thanks to its simplicity and small building blocks [17-20]. With the conventional (standard) development method, there are however still challenging problems for MOR, such as pattern collapse, reducing EUV

Received April 30, 2022

Accepted June 24, 2022

sensitivity with a reduced roughness.

The pillar pattern collapse is the main challenge using conventional development method for negative tone MOR. Figure 1 displays the pillar collapses in 36 nm pitch pillar pattern for two different post exposure bake (PEB) temperatures. Simply changing the PEB temperature did not solve the problem.

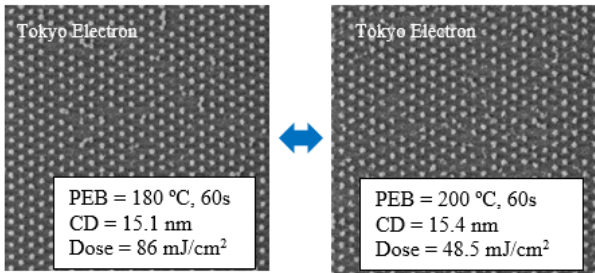
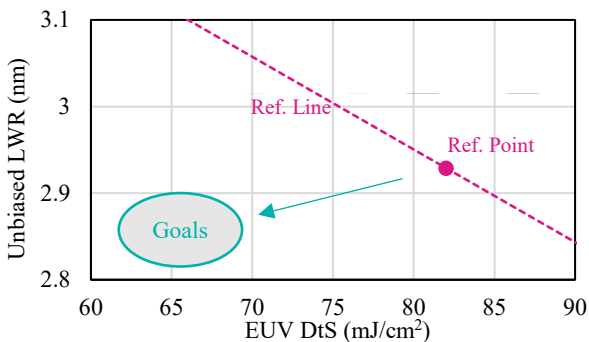
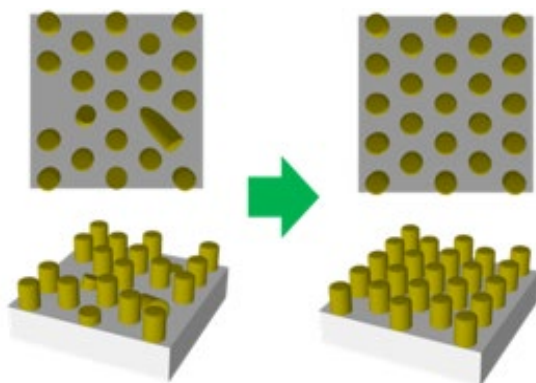


Fig. 1. Pattern collapses as one of the challenges in MOR.

In pillar patterns, if the PEB temperature is increased, the EUV dose to size (DtS) is reduced, but the local CDU uniformity (LCDU) is getting worse. In L/S patterns, likewise LWR is also getting worse when increasing PEB temperature. This is a well-known trade-off relationship in both CAR and MOR, and it has been extremely difficult to break.



(a) Dose/LWR points are below the reference line



(b) Mitigating collapsing defects

Fig. 2. Illustration of two main motivations of this work.

It is necessary to solve these problems for MOR to be applied in high volume manufacturing (HVM). Therefore, our main motivations of this work were mitigating pillar pattern collapses and shifting the DtS/LWR line to the left, as depicted in Fig. 2.

To achieve our goals, we have invented a novel wet development method. The new method has the capabilities of solving multiple problems simultaneously. The new method is introduced and EUV data of pillars and L/S patterns using both new and conventional methods are presented in this paper.

In conventional development method, after the PEB step, a developer solution is spun on top of the wafer to remove the EUV exposed area if it is a positive tone resist, or to remove the unexposed area if it is a negative tone. This is the standard development process which has been being used for many years for CAR without major problems. However, when moving to negative tone MOR for ultra-fine patterns, the exposed area profile normally has an inverted taper shape. Furthermore, during the standard developing step, the exposed area expands due to the swelling effect. These two main effects make the pattern easy to collapse, as depicted in Fig. 3.

The developer solution is also a homogenous solvent, making it difficult to modify the resist profile or to alter the developing thresholds of the process.

A new wet development method has been invented to solve all these difficulties in the conventional method. It has the capabilities to mitigate the swelling effect and to modify the resist profile to a slightly taper shape, for example as depicted in Fig. 3. A possible smaller swelling effect combined with a good resist profile prevent the pattern from collapsing.

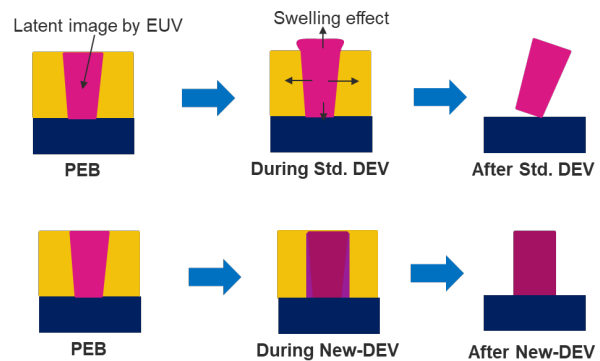


Fig. 3. Schematic illustration of standard DEV and the new wet DEV method.

In addition to the pattern collapse mitigation

capability, the new development method also has the possibility to dissolve the resist at different phases, resulting in breaking the sensitivity/roughness trade-off and an improved global CDU. This newly invented wet development method might be the new development standard for MOR in next nodes EUV lithography and possible in high-NA EUV lithography also.

2. Experimental

In this work, we have evaluated to compare the conventional and the new development methods using both pillars and line/space (L/S) patterns. For L/S patterns, the new wet development method was evaluated on both 32 nm and 30 nm pitches. The 32 nm pitch L/S pattern were exposed on EUVLINES mask using ASML NXE:3400B at imec. While 36 nm pitch pillars and 30 nm pitch L/S were exposed at the Albany Nanotech Complex in Albany, NY on different masks, separately.

Stacks for after etch inspection (AEI), which is illustrated in Fig. 4, were used for both pillar and L/S patterns. It was also used for inspecting the AEI cross-section of pillar patterns. Both top-view and cross-section data were measured at SOC layers.



Fig. 4. Stack for AEI in both pillar and L/S patterns.

For data analysis, unbiased roughness, local CDU, the fraction missing value and number of defects were all measured by MetroLER software (MetroLER version 3.0, Fractilia, LLC). The roughness values of L/S patterns were unbiased values calculated from 30 SEM images. 15 SEM images were used to measure the fraction missing and LCDU values in pillar patterns. All SEM images were obtained by Hitachi CD-SEM CG6300.

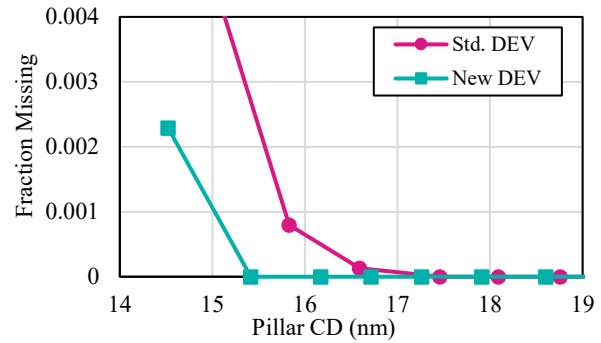
3. Results and discussion

3.1. Pillar patterns of 36 nm pitch

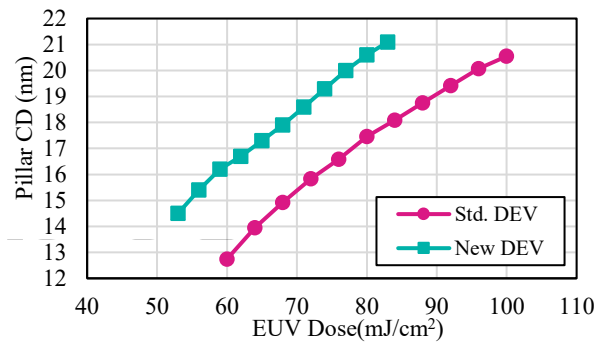
In this section, we compare the standard development and the new development method on 36 nm pitch MOR pillar patterns using both ADI (after development inspection) and AEI data.

With the conventional process, pattern collapse

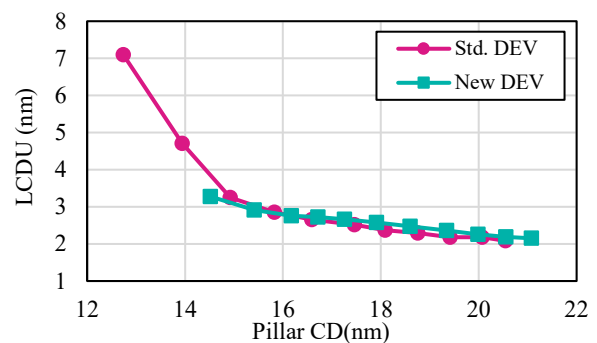
was observed around 17 nm pillar size as seen in Fig. 5 (a). However, with the new wet development method, there was no pattern collapse observed at least up to 15.4 nm. This resulted in an approximately 2 nm improvement in minimum CD without collapses. The improvement helps to widen the process window of this pitch pillars for HVM. In addition, this method could reduce approximately 20% in EUV dose with a similar LCDU (Figs. 5 (b) and 5 (c)).



(a) Fraction missing w.r.t CD



(b) LCDU w.r.t CD



(c) CD w.r.t EUV dose

Fig. 5. ADI data of 36 nm pitch pillar patterns with standard DEV and with the new DEV.

Table 1 shows the SEM images of samples with the conventional development method and with the new development method. The new method has reduced both the minimum CD by 2 nm

(approximately from 17 nm to 15 nm) and EUV dose by 20% (from 100 mJ/cm² to 80 mJ/cm²), simultaneously.

Table 1. SEM images of standard development (DEV) and new DEV.

	Std. DEV	New-DEV
CD	13.9 nm	14.5 nm
LCDU	4.7 nm	3.3 nm
Dose	64 mJ/cm ²	53 mJ/cm ²
	14.9 nm 3.2 nm 68 mJ/cm ²	15.4 nm 2.9 nm 56 mJ/cm ²
	20.5 nm 2.1 nm 100 mJ/cm ²	20.6 nm 2.2 nm 80 mJ/cm ²

Figure 6 displays AEI data (using the same etch condition) for the standard and the new development methods. Like ADI results, the new method also reduced approximately 22% EUV dose. There were similar LCDU values in ADI for both conventional and new methods. But in AEI results, the new development method produced 7% LCDU improvement (2.09 nm compared to 2.24 nm with the standard DEV). The possibility of having a better resist profile at ADI might be the reason of this improvement in AEI LCDU. The resist profile when using the new method will be discussed further in Sect. 4.2 for L/S patterns.

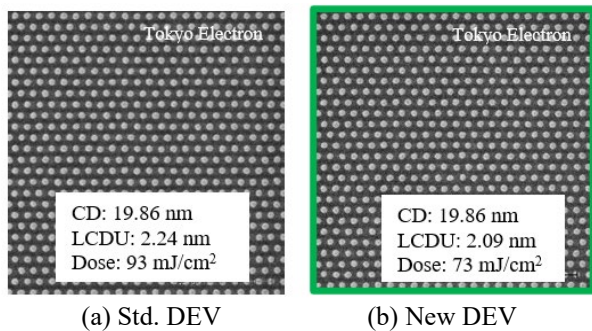


Fig. 6. AEI SEM images of 36 nm pitch pillar patterns.

When applying a new development method, it is always necessary to confirm if there is no residual left at the bottoms after etching. Figure 7 shows the AEI of a sample using the new wet development method. Both top view (Fig. 7(a)) and cross-section

view (Fig. 7(b)) confirm that the resist was completely etched to create a clear SOC profile.

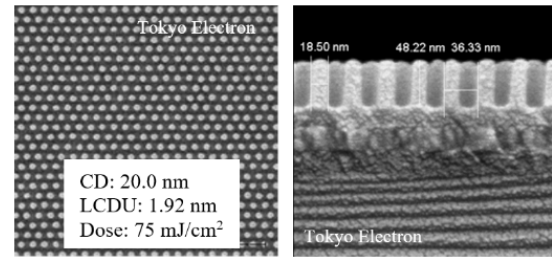


Fig. 7. AEI of sample using the new wet development method.

3.2. L/S patterns of 30 nm pitch

Like Sect. 3.1 about pillars, we used both ADI and AEI data to compare the standard development and the new development method on 30 nm pitch L/S patterns in this section. ADI results have confirmed that with the new method there was an improvement of 31% in EUV sensitivity while the roughness was unchanged. We have also confirmed that the resist profile has changed its profile as desired, from an inverted taper shape in the conventional method to a slightly taper shape in the new method, as displayed in Fig. 8. The pattern heights were similar for both development methods.

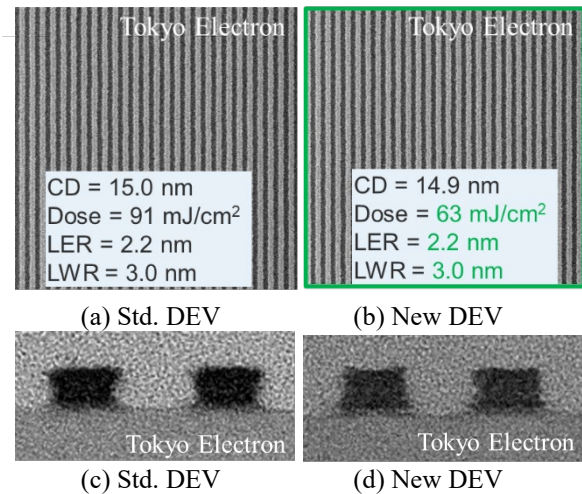


Fig. 8. Top-down ((a), (b)) and cross-section SEM ((c), (d)) images.

Figure 9 shows the AEI data, obtained by the same etch condition, for both development methods. The new development not only increased the EUV sensitivity (26%) but also improved the LWR (12.3%), compared to the conventional development. Like the case of pillars, the change in resist profile might help to reduce line roughness during etching. At ADI level, the LWR was the same,

but there was big improvement after etching (12.3% for LWR and 9.3% in LER).

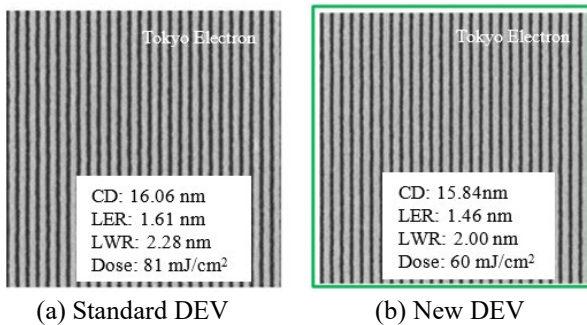


Fig. 9. AEI SEM images of 30 nm pitch L/S patterns.

3.3. Bridging of 32 nm pitch L/S patterns

The bridging defect is always a challenge in L/S patterns, especially at tight pitches. When using the conventional development method, simply changing the PEB temperature did not shift the bridging cliff. Figure 10 shows that the cliffs of both PEB = 180 °C and PEB = 160 °C were similar. However, when the new development method was used, the cliff was shifted to the right by approximately 0.5 nm if compared to the conventional method. This might be very beneficial in tighter pitches and in high-NA EUV lithography also.

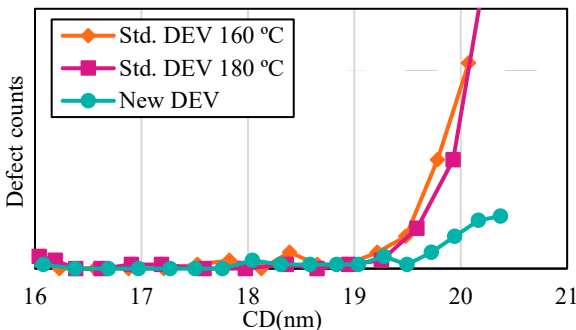
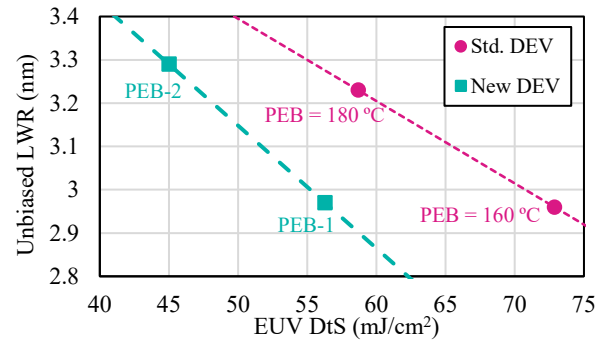


Fig. 10. Number of defects /cm² as a function of CD on 32 nm pitch L/S.

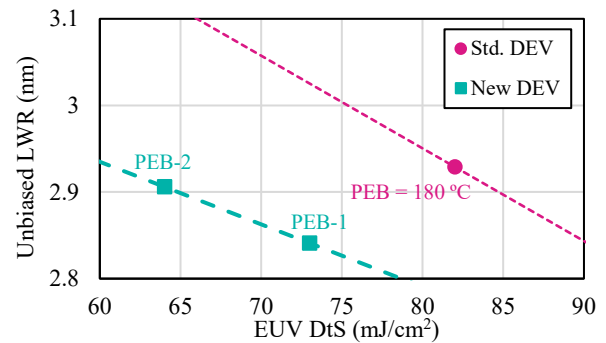
3.4. Breaking the trade-off relationship

Figure 11 displays DtS/LWR relationships of 32 nm pitch L/S patterns (Fig. 11 (a)) and 30 nm pitch L/S patterns (Fig. 11(b)) using both the conventional DEV (red lines) and the new DEV (green lines). In both pitches, the DtS/LWR lines of new DEV was on the left of the conventional DEV (reference line). It means that if compared to a point on the reference line, a better EUV sensitivity and a better roughness using the new DEV both can be obtained. Depending on the application, a higher EUV sensitivity improvement rate can be achieved without deteriorating the roughness or better

roughness improvement at a similar EUV DtS. For example, in the case of 32 nm pitch L/S patterns, the new DEV with PEB-1 condition had 23% better DtS than the reference at PEB = 160 °C with a similar roughness, while comparing to the reference at PEB = 180 °C, it had 4% better DtS and 8% better LWR.



(a) ADI data of 32 nm pitch L/S



(b) ADI data of 30 nm pitch L/S

Fig. 11. New DEV breaks the DtS/LWR trade-off relationship.

3.5. Global CD Uniformity

In tight pitches, especially in high NA EUV lithography, global CDU becomes a critical factor. With the new DEV, the global CDU was improved by 2.6 times, as shown in Fig. 12. This improvement was obtained possibly because we could dissolve the resist at different phases, where a more hydrophilic phase helped to develop the surface evenly.

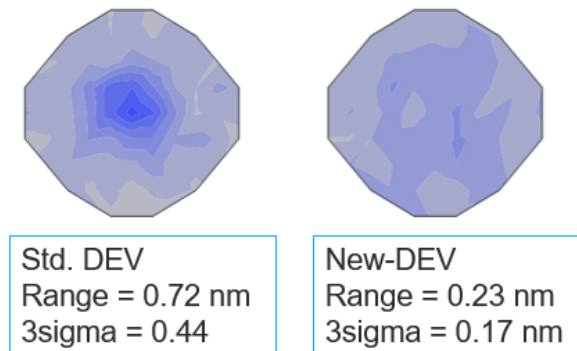


Fig. 12. Global CDU of wafers with standard DEV and with new DEV.

4. Conclusion

This paper has introduced a newly invented wet development method for MOR. The EUV data confirmed that with the new development method, multiple problems of MOR have been mitigated simultaneously. With 36 nm pitch pillar patterns, we have confirmed with AEI data that the new method produced 22% improvement in EUV dose and 7% improvement in LCDU, simultaneously. No pattern collapse was observed at least up to 15.4 nm pillar size. In the case of 30 nm pitch L/S pattern, the improvements were 26% in EUV sensitivity and 12.3% in LWR also with AEI results. Furthermore, the new method could also shift the bridging cliff 0.5 nm to the larger line CD while its global CDU was improved by 2.6 times. These improvements in both LCDU and global CDU might be very beneficial in high-NA EUV lithography when resist thickness is small and requirement for CDU is strict. The new wet development method has improved the performance of MOR generally, making it more feasible for next node EUV lithography and for high NA EUV lithography also.

Acknowledgements

We would like to acknowledge all the members of our collaboration partners, IBM Research, and material suppliers. We are also very grateful to Ms Reiko Tsuzuki and Mr Xiang Liu (Tokyo Electron Limited) for their support in simulation of the new wet development method. We would also like to thank Mr Shinji Kobayashi (Tokyo Electron Limited) for his support in preparing this paper.

References

1. R. Brainard, C. Higgins, E. Hassanein, R. Matyi, and A. Wüest, *J. Photopolym. Sci. Technol.*, **21** (2008) 457.
2. T. I. Wallow, R. Kim, B. LaFontaine, P. P. Naulleau, C. N. Anderson, and R. L. Sandberg, *Proc. SPIE*, **6533** (2007) 653317.
3. R. Gronheid, T. R. Younkin, M. J. Leeson, C. Fonseca, J. S. Hooge, K. Nafus, J. J. Biafore, and M. D. Smith, *J. Micro/Nanolithogr. MEMS MOEMS*, **10** (2011) 033004.
4. T. Kozawa, and S. Tagawa, *Jpn. J. Appl. Phys.*, **49** (2010) 030001.
5. C. A. Mack, *Proc. SPIE*, **7639** (2010) 763931.
6. H. J. Levinson, *J. Micro/Nanolithogr. MEMS MOEMS*, **8** (2009) 041501.
7. P. De Bisschop, *J. Micro/Nanolithogr. MEMS MOEMS*, **16** (2017) 041013.
8. H. J. Levinson, *Jpn. J. Appl. Phys.*, **61** (2022) SD0803.
9. S. Tagawa, A. Oshima, S. Enomoto, and C. Q. Dinh, *Proc. SPIE*, **9048** (2014) 90481S.
10. M. Carcasi, S. Nagahara, G. Shiraishi, T. Iseki, Y. Minekawa, K. Yoshihara, H. Nakagawa, T. Naruoka, T. Nagai, A. Oshima, and S. Tagawa, *Proc. SPIE*, **10143** (2017) 10143.
11. S. Nagahara, M. Carcasi, G. Shiraishi, H. Nakagawa, S. Dei, T. Shiozawa, K. Nafus, D. De Simone, G. Vandenberghe, H. J. Stock, B. Kuchler, M. Hori, T. Naruoka, T. Nagai, Y. Minekawa, T. Iseki, Y. Kondo, K. Yoshihara, Y. Kamei, M. Tomono, R. Shimada, S. Biesemans, H. Nakashima, P. Foubert, E. Buitrago, M. Vockenhuber, Y. Ekinci, A. Oshima, and S. Tagawa, *Proc. SPIE*, **10146** (2017) 101460G.
12. S. Nagahara, M. Carcasi, G. Shiraishi, Y. Kamei, K. Nafus, Y. Minekawa, H. Ide, Y. Kondo, T. Shiozawa, K. Yoshida, M. Enomoto, K. Yoshihara, H. Nakashima, S. Biesemans, R. Shimada, M. Tomono, K. Takeshita, T. Moriya, M. Hayakawa, R. Aizawa, Y. Konishi, M. Hori, K. Maruyama, H. Nakagawa, M. Miyake, T. Nagai, S. Dei, T. Naruoka, M. Shima, T. Kimura, G. Vandenberghe, J. S. Petersen, D. De Simone, P. Foubert, H. J. Stock, B. Meliorisz, A. Oshima, and S. Tagawa, *Proc. SPIE*, **10586** (2018) 1058606.
13. M. Carcasi, S. Nagahara, G. Shiraishi, Y. Minekawa, H. Ide, Y. Kondo, K. Yoshihara, M. Tomono, R. Shimada, K. Takeshita, T. Moriya, Y. Kamei, K. Nafus, S. Biesemans, H. Nakashima, M. Hori, K. Maruyama, H. Nakagawa, T. Nagai, S. Dei, M. Miyake, T. Naruoka, M. Shima, G. Vandenberghe, D. De Simone, P. Foubert, J. Petersen, A. Oshima, and S. Tagawa, *Proc. SPIE*, **10583** (2018) 105831M.
14. S. Nagahara, C. Q. Dinh, G. Shiraishi, Y. Kamei, K. Nafus, Y. Kondo, M. Carcasi, Y. Minekawa, H. Ide, Yoshida, Y., K. Yoshihara, R. Shimada, M. Tomono, K. Takeshita, S. Biesemans, H. Nakashima, D. D. Simone, J. S. Petersen, P. Foubert, P. D. Bisschop, G. Vandenberghe, H. J. Stock, and B. Meliorisz, *Proc. SPIE*, **10960** (2019) 109600A.
15. C. Q. Dinh, S. Nagahara, G. Shiraishi, Y. Minekawa, Y. Kamei, M. Carcasi, H. Ide, Y. Kondo, Y. Yoshida, K. Yoshihara, R. Shimada, M. Tomono, T. Moriya, K. Takeshita, K. Nafus, S. Biesemans, J. S. Petersen, D. D. Simone, P. Foubert, P. D. Bisschop, G. Vandenberghe, H. J. Stock, and B. Meliorisz, *Proc. SPIE*, **10957** (2019) 109571O.

16. S. Nagahara, C. Q. Dinh, K. Yoshida, G. Shiraishi, Y. Kondo, K. Yoshihara, K. Nafus, J. S. Petersen, D. D. Simone, P. Foubert, G. Vandenberghe, H. J. Stock, and B. Meliorisz, *Proc. SPIE*, **11326** (2020) 113260A.
17. C. Q. Dinh, S. Nagahara, K. Yoshida, Y. Kondo, M. Muramatsu, K. Yoshihara, R. Shimada, T. Moriya, K. Nafus, J. S. Petersen, D. D. Simone, P. Foubert, and G. Vandenberghe, *Proc. SPIE*, **11612** (2021) 116120L.
18. J. Stowers, J. Anderson, B. Cardineau, B. Clark, P. D. Schepper, J. Edson, M. Greer, K. Jiang, M. Kocsis, S. Meyers, A. Telecky, A. Grenville, D. D. Simone, W. Gillijns, and G. Vandenberghe, *Proc. SPIE*, **9779** (2016) 977904.
19. W. D. Hinsberg and S. Meyers, *Proc. SPIE*, **10146** (2017) 1014604.
20. A. V. Pret, M. Kocsis, D. De Simone, G. Vandenberghe, J. Stowers, A. Giglia, P. De Schepper, A. Mani, and J. J. Biafore, *Proc. SPIE*, **9779** (2016) 977906.

Influence of Counteranions on the Performance of Tin-based EUV Photoresists

Quentin Evrard^{1*}, Najmeh Sadegh¹, Yasin Ekinci², Michaela Vockenhuber²
Nicola Mahne³, Angelo Giglia³, Stefano Nannarone³, Tsuyoshi Goya⁴, Takuo
Sugioka⁴, and Albert M. Brouwer^{1,5}

¹ *Advanced Research Center for Nanolithography, Science Park 106, 1098 XG
Amsterdam, The Netherlands*

² *Paul Scherrer Institute, Forschungsstrasse 111, 5232 Villigen PSI, Switzerland*

³ *IOM-CNR, Strada Statale 14 km 163,5, 34149 Basovizza-Trieste, Italy*

⁴ *Nippon Shokubai Co., LTD.5-8 Nishi Otabi-cho, Suita, Osaka 564-0034, Japan*

⁵ *University of Amsterdam, van 't Hoff Institute for Molecular Sciences, PO Box 94157,
1090 GD Amsterdam, The Netherlands*

*q.evrard@arcnl.nl

A positive-tone extreme ultraviolet (EUV) photoresist was obtained via the exchange of the hydroxide ions of tin-oxo-hydroxo cages with tetrakis(pentafluorophenyl)-borate. Thin films were obtained after spin coating on silicon substrates and exposed to line patterns in interference lithography at 92 eV (13.5 nm). For low doses and development with ethylbenzene positive tone patterns were obtained. In contrast, the exchange of the hydroxide ions of tin-oxo-hydroxo cages with tetrakis(4-methylphenyl)-borate or tetrakis[3,5-bis(1,1,1,3,3,3-hexafluoro-2-methoxy-2-propyl)phenyl]-borate led to the negative-tone photoresist behaviour that has previously been observed for tin-oxo cages with all other counterions. In situ exposures at 92 eV and subsequent X-ray Photoelectron Spectroscopy were performed on a film of tin-oxo-hydroxo cages with tetrakis(pentafluorophenyl)-borate anions to probe the chemical changes induced by the EUV exposure. This shows that the C-F bonds of the anions are relatively stable.

Keywords: Positive-tone Resist, Tin-oxo-hydroxo Cage, Extreme Ultraviolet Lithography, Inorganic-organic Hybrid Photoresist

1. Introduction

Inorganic molecular materials are of prime interest in the Extreme UltraViolet (EUV) photoresist community [1-4] due to their increased EUV absorption cross section compared to conventional organic-based photoresists. Among these materials tin-oxo-hydroxo cages [5-6] are promising materials. The tin-oxo-hydroxo cages (molecular formula $\{(BuSn)_{12}(\mu_3-O)_{14}(\mu_2-OH)_6\}^{2+}$) are positively charged clusters of twelve tin atoms bridged by oxygens and have one butyl group attached to each tin atom forming a layer at the surface of the cluster enhancing its solubility. The bond between the tin atoms and their respective butyl groups is known to be labile when the cages are exposed to electrons [7], UV [8,9], or EUV [10]. A simulation model [11] of this type of photoresist

assumes that Sn-C bond breaking generates active sites on the tin atoms that lead to the cross-linking between neighbouring clusters, causing the exposed material to become insoluble.

In earlier work we have observed that the sensitivity and patterning behavior of tin-oxo cages with different small counterions differs somewhat, but not dramatically [6]. To gain more insight into the role of the counterions, in the present work we use large non-nucleophilic tetraphenylborate anions. Indeed, the anion exchange properties of tin-oxo-hydroxo clusters are well documented [12-14] and offer an opportunity to tailor the properties of the resist. One of the main challenges of the hybrid organic-inorganic resists is to further increase their EUV absorption cross-section to generate more active sites per volume of resist and thus potentially

Received March 31, 2022

Accepted June 24, 2022

increase the photoresist sensitivity. To that end, in the present work we introduce fluorinated borate counteranions on the tin-oxo-hydroxo cages. The EUV absorption cross-section of fluorine is 3.5 times higher than that of carbon and 1.3 times higher than that of oxygen. Three anions of interest are discussed in the present work, namely tetrakis(pentafluorophenyl)-borate ($B(PFP)_4^-$) (**1**), tetrakis(4-methylphenyl)-borate ($B(Tolyl)_4^-$) (**2**) and tetrakis[3,5-bis(1,1,1,3,3,3-hexafluoro-2-methoxy-2-propyl)phenyl]-borate ($B(HFOMePr)_4^-$) (**3**) (see figure 1).

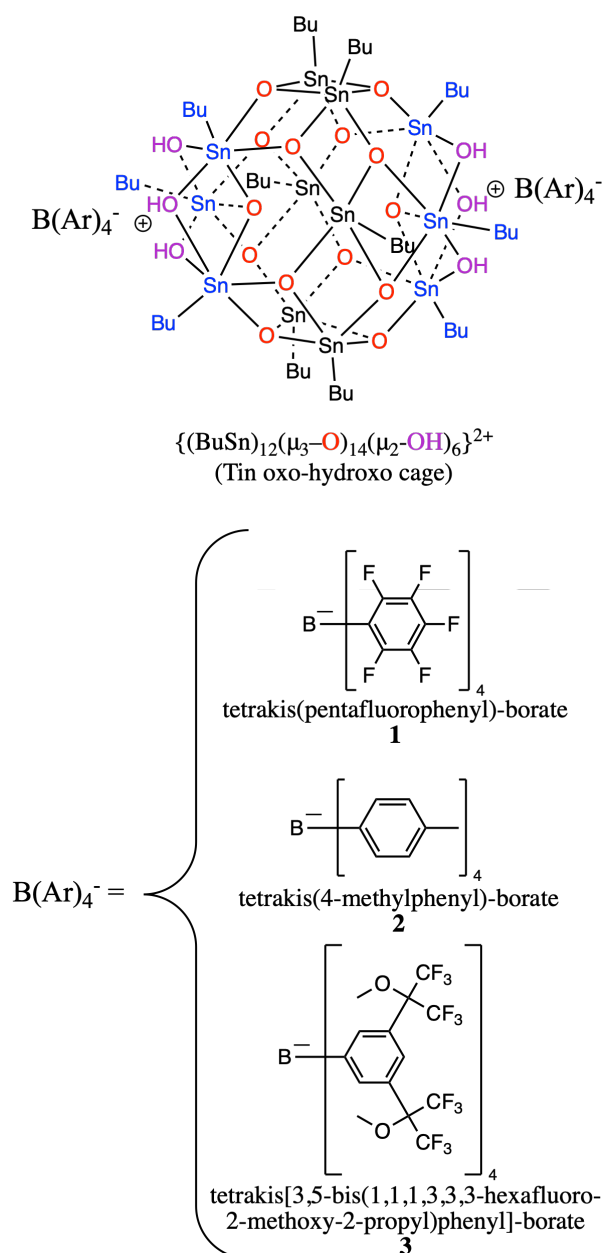


Fig. 1. Structure of the tin oxo-hydroxo cage and counteranions used in this work. TinOH is the same cage with two OH⁻ counterions.

It is expected that the fluorine content leads to an increase of the EUV absorption of the photoresist film. The lithographic properties of the three materials were studied, and in-situ EUV exposures coupled with X-ray photoelectron spectroscopy have been performed on the $B(PFP)_4$ system **1**.

2. Experimental

2.1. Chemical synthesis

The acid forms of $B(PFP)_4^-$ and $B(Tolyl)_4^-$ are obtained from their sodium salts via the reaction with a slight excess (1.07:1) of aqueous HCl (37%) in water heated at 40°C for 30 minutes. The obtained mixture is extracted with diethylether five times and the aqueous phase is discarded. The organic phase is then allowed to evaporate via heating at 35 °C. The obtained viscous liquid is dispersed in water and sonicated for a further two hours. The dispersion is then cooled down to room temperature, filtered and washed with water three times. The resulting white powder is used without further purification (yield 60 - 70%).

The synthesis of the tin-oxo-hydroxo cage with hydroxide anions (TinOH) is performed as in previous work [9] via the hydrolysis of butyltin-hydroxide-oxide in the presence of p-toluene-sulfonic acid followed by exchange of the toluene-sulfonate for hydroxide counterions using tetramethylammonium hydroxide aqueous (25%) solution. After recrystallization from isopropanol/water (6.5:1), TinOH (250 mg; 0.100 mmol) is dispersed in 4 mL of toluene and mixed with a 10 mL aqueous solution of tetrakis(pentafluorophenyl)-boric acid (136 mg; 0.200 mmol). After 2 hours of vigorous stirring and ultrasonication, the resulting two-phase system is allowed to cool down for two additional hours. The toluene layer is separated, filtered and washed with distilled water (5 mL) three times. The white powder resulting after evaporation of the solvent is used as photoresist material without further purification (yield of **1**: 80%) ¹H NMR (400 MHz, CDCl₃): For compound **1**: $\delta = 1.73$ (m, Sn₅-CH₂-CH₂-CH₂-CH₃), 1.44 (m, Sn₅-CH₂-CH₂-CH₂-CH₃), 1.28 (m, Sn₆-CH₂-CH₂-CH₂-CH₃, J = 7.2 Hz), 1.14 (m, Sn₆-CH₂-CH₂-CH₂-CH₃), 0.97 (t, Sn₅-/-CH₃ J = 7.3 Hz), 0.85 (t, Sn₆-/-CH₃ J = 7.3 Hz), 1.73 (m, Sn₅-CH₂-CH₂-CH₂-CH₃).

For compound **2**: $\delta = 6.91$ -7.04 (m, B-[**o**-HPh-CH₃]₄), 6.86 (d, B-[**m**-HPh-CH₃]₄ J = 7.4 Hz), 2.22 (s, B-[Ph-CH₃]₄), 1.71 (m, Sn₅-CH₂-CH₂-CH₂-CH₃, J = 7.3 Hz), 1.39-1.58 (m, Sn₆-CH₂-CH₂-CH₂-CH₃ and Sn₅-CH₂-CH₂-CH₂-CH₃), 1.32 (m, Sn₆-CH₂-

CH₂-CH₂-CH₃ J = 7.1 Hz), 1.03 (m, Sn₆-CH₂-CH₂-CH₂-CH₃) 0.96 (t, Sn₅-/-CH₃ J = 7.1 Hz), 0.89 (t, Sn₆-/-CH₃ J = 7 Hz).

For compound **3**: δ = 7.49 (s, B-[C₆H(o-H)₂ m-(C(CF₃)₂OCH₃)₄], 7.36 (s, B-[C₆H₂p-H m-(C(CF₃)₂OCH₃)₄], 3.25 (s, B-[C₆H₃ m-(C(CF₃)₂OCH₃)₄], 1.75 (m, Sn₅-CH₂-CH₂-CH₂-CH₃), 1.42-1.57 (m, Sn₆-CH₂-CH₂-CH₂-CH₃ and Sn₅-CH₂-CH₂-CH₂-CH₃), 1.35 (m, Sn₅-CH₂-CH₂-CH₂-CH₃), 1.25 (m, Sn₆-CH₂-CH₂-CH₂-CH₃), 0.97 (t, Sn₅-/-CH₃ J = 7.3 Hz), 0.89 (t, Sn₆-/-CH₃ J = 7.3 Hz). (Sn₅ refers to the 6 tin atoms that are 5-coordinated in the tin-oxo-hydroxo cage while Sn₆ refers to the 6 tin atoms that are 6-coordinated)

The anion exchange procedure is identical for the tetrakis(4-methylphenyl)-boric acid. The synthesis of **3** only differs by the use of the sodium salt of the borate instead of its acid form.

2.2. Thin film sample preparation

The photoresist solutions of interest (10 mg/mL) are all prepared using trifluorotoluene as solvent. Following the dissolution, they are sonicated for an additional 10 minutes. The solutions are filtered using a 0.20 μ m PTFE filter and directly spincoated.

All samples for EUV lithography were prepared on silicon wafers (Siegert Wafer, CZ growth, p-type B-doped, <100>, resistivity 5-10 Ohm-cm) used without further cleaning. The spin coating is done with a rotation speed of 2000 rpm, an acceleration of 750 rpm/s and no post-application or post-exposure baking are performed. The thickness of the obtained films using this procedure is 30-35 nm.

All the samples for in-situ EUV exposures with XPS spectroscopy were prepared on gold-coated Si substrates. The silicon wafer (Siegert Wafer, CZ growth, p-type B-doped, <100>, resistivity 5-10 Ohm-cm) is first diced in 25 \times 25 mm substrates. The substrates are cleaned with an 80°C base piranha solution for 15 minutes, rinsed with isopropanol and dried with nitrogen flow. They are then cleaned using an ozone plasma (Diener Electronic Pico QR-200-PCCE) with a two-minute oxygen plasma at 0.2 mbar working pressure. Next, the samples are coated with a gold layer using a sputter coater (Leica EM ACE600 double sputter coater) depositing a 5 nm layer of chromium as adhesion layer followed by 30 nm of gold. The gold-coated substrates are used for spin-coating of the resist solutions, with a rotation speed of 2500 rpm and an acceleration of 750 rpm/s. No pre- or post-exposure baking is performed.

Atomic Force Microscopy is performed on a Bruker Dimension Icon using tapping mode with Bruker TESP-SS tips (320 kHz, 42 N/m), fields of 3 \times 0.6 μ m were measured with 256 samples per line and a scanning frequency of 0.6 Hz. Raw data was corrected by truncated mean method and flattened by mean plane. No further corrections were made.

3. Results and discussion

3.1. Strategy

In TinOH, most of the EUV absorption originates from the tin atoms present in the tin oxo-hydroxo cage [15]. The replacement of the small OH⁻ with larger organic anions leads to a decrease of EUV absorption of the photoresist because the number of strongly absorbing tin atoms per unit volume is reduced, while the organic anions themselves have only small cross sections at 92 eV. When heavily fluorinated anions are used, the larger cross sections of fluorine will offset the loss of EUV absorption cross section due to dilution of tin. For a thin film of **1** we estimate that the absorption at 92 eV is in fact ~30% higher than that of TinOH.

The non-fluorinated samples prepared from tolylborate **2** are used as reference to investigate the system behaviour when the tin cages are diluted by large low absorption borate counteranions.

3.2. EUV Interference lithography

The EUV lithographic properties of all three photoresists have been studied at the Paul Scherrer Institute (Switzerland) on the XIL-II beamline and line/space patterns have been obtained as exemplified in figure 2.

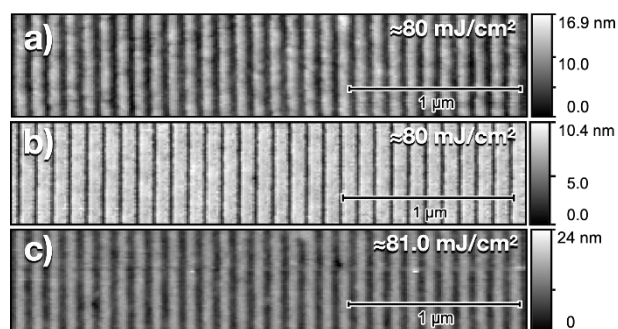


Fig. 2. Atomic force microscopy height images obtained for films of **1** (a), **2** (b) and **3** (c) exposed to EUV irradiation (Line-space patterns with 50 nm half-pitch) and developed with ethylbenzene ((a) and (b)) or n-hexane (c).

All the photoresist samples have been prepared from solutions in trifluorotoluene. A hexamethyldisilazane (HMDS) adhesion promoting layer was necessary to form good quality films with the non-fluorinated **2**. The developer chosen for **1**

and **2** is ethylbenzene. Chemical contrast for **3** could be obtained by using n-hexane. The EUV exposure doses required to see pattern formation are close to 30 mJ/cm^2 for **1** and **2** while higher doses of around 80 mJ/cm^2 are required for **3**. The lowest sensitivity is found for **3**, which has the largest anion. For tolylborate **2** the sample exposed to 80 mJ/cm^2 of EUV irradiation already exhibits signs of overexposure such as decrease of thickness in the middle of the exposed parts due to further material degradation.

While both **2** and **3** exhibit the commonly found negative tone photoresist behaviour of tin-oxo cages, **1** can be developed as a positive tone photoresist for doses ranging from 30 to around 100 mJ/cm^2 . The positive tone behaviour of **1** is identified by the widening of the grooves upon increasing the EUV dose. At higher doses the tone inverts to negative, resulting in a complete loss of pattern at intermediate doses. In comparison, the tolylborate **2** exhibits negative tone traits such as increase of line width at doses from 20 to 150 mJ/cm^2 combined with signs of overexposure appearing from 80 mJ/cm^2 and up with a decrease of the line height at its center due to further degradation of the resist on the highest intensity part of the exposed pattern.

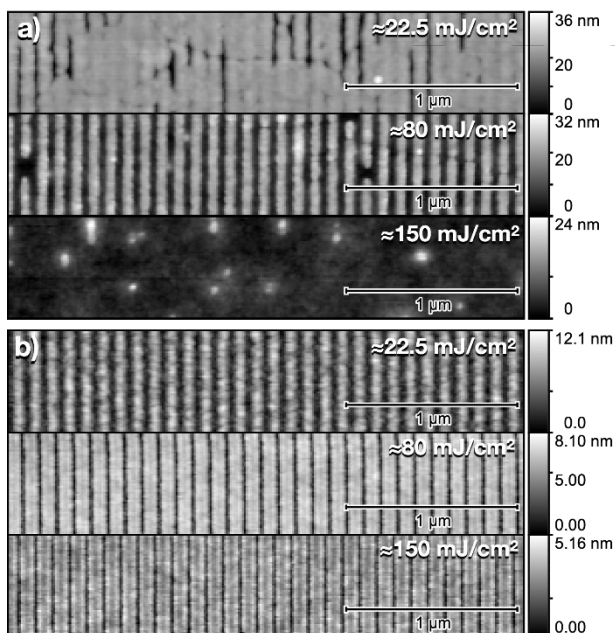


Fig. 3. Atomic force microscopy height images obtained for films of **1** (a) and **2** (b) exposed to EUV irradiation (Line-space patterns with 50-nm half-pitch) and developed with ethylbenzene.

3.3. In-situ EUV exposures with XPS.

To get more insight into the behavior of the highly fluorinated tin-oxo cage **1** we performed X-ray Photoelectron Spectroscopy (XPS) on films exposed to EUV irradiation in-situ. These experiments were carried out at the IOM-CNR BEAR beamline at the Elettra Synchrotron (Trieste, Italy). The samples of **1** were prepared as described in section 2.2 on gold substrates to mitigate charging effects. The sample is first exposed to a known dose of EUV irradiation and then C-edge XPS is performed. The photon energy of the probing beam hitting the grounded sample is 400 eV and experimental parameters are adapted to avoid sample degradation during the XPS measurements. To increase the signal/noise ratio, all measurements are done three times on different sample positions and averaged. Selected spectra are shown in figure 4.

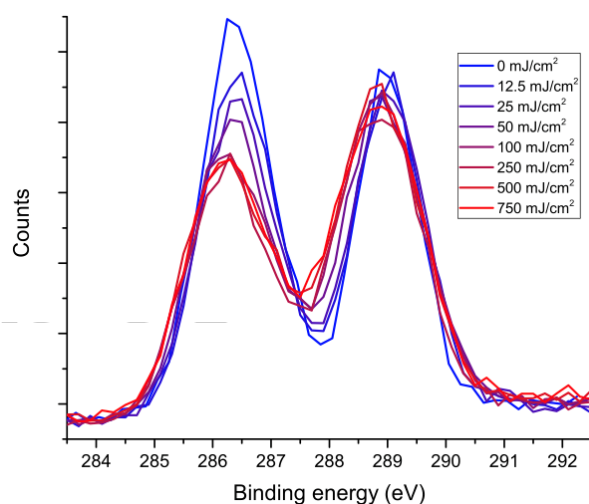


Fig. 4. Evolution of C-edge XPS spectra of bis(tetrakis(pentafluorophenyl)borate) tin-oxo cage **1** upon EUV exposure.

The peak at a binding energy of 289 eV corresponds to the C-F carbons present in the anion and appears to remain mostly unaffected by EUV radiation, while the area of the peak at 286.5 eV that corresponds to the carbons of the butyl chains of the tin-oxo-hydroxo cage is reduced by 30% upon EUV exposure of 250 mJ/cm^2 which is an indication that the butyl groups are outgassed in the high vacuum of the experimental chamber.

3.4. Discussion

The negative tone patterning of **2** and **3** is in line with the known behaviour of tin oxo-hydroxo cage systems. The tin-oxo cage **1**, with the fully fluorinated borate counterion, exhibits positive tone

behaviour over a wide range of doses. Positive tone behaviour has been observed for TinOH under e-beam exposure [16] but only at very small conversion, at which the patterns were too thin to be significant for application. The size of the anion on its own is ruled out as an explanation for this reactivity difference, because the anions in **1** and **2** have similar sizes so have the same effect on the distance between neighbouring tin clusters. The conversion leading to solubility switching of previously studied tin oxo-hydroxo clusters is initiated by the cleaving of Sn-C bonds upon EUV exposure. For the bare tin cage dication this leads to a structure rearrangement, but when a counterion is present, this can form a bond to a tin atom that has lost its organic group [9]. Subsequent cross-linking of neighbouring tin clusters, further enhanced by post-exposure baking [6], is likely to be responsible for the loss of solubility of the exposed material in the negative tone operation. In the present system, the direct cross-linking between neighbouring clusters is inhibited by the steric hindrance of the anions, but the anions are also non-nucleophilic, and less likely than hydroxide, or acetate, to form a bond to a tin atom of the cage.

The reactivity to irradiation of the anion itself can also play a role in the photoresist behavior. Studies of EUV reactivity of aryl-borate molecules have, to the best of our knowledge, not yet been reported although several examples of photolysis [17-18] or photo-induced single electron transfers [19] are present in the literature. Highly fluorinated tetraphenyl borates are much more difficult to oxidize, but at high positive potentials they are electrochemically unstable and can lead to the formation of biphenyl species upon oxidation [20].

The in-situ XPS analysis of **1** indicates that 30% of the butyl chains of the tin-oxo-hydroxo cage are lost upon EUV exposure of 250 mJ/cm². Interestingly, an analogous tin-oxo-hydroxo cage cluster with acetate anions exposed to the same EUV doses exhibit a loss of 40% of peak area, pointing towards a reduced reactivity of the tin cluster **1** with the fluorinated tetraphenylborate anion. This could be due to this borate anion acting as a relatively unreactive EUV absorber inhibiting the Sn-C bond cleavage of the tin cluster. Another hypothesis is that the polymerization of several clusters might also favour the cleaving of additional Sn-C bonds next to the bridging oxygen but there is no evidence to rule out either hypothesis. The XPS peak stemming from the carbons linked to fluorine of **1** is slightly broader with a FWHM increasing

from 1.28 eV to 1.82 eV during exposure which could indicate a modification of the chemical environment of the pentafluorophenyl groups or the formation of decomposition products with similar binding energies which remain inside the film. Further studies are being conducted on the fluorinated system **1** to gather more evidence on the reaction pathway leading to the solubility switch.

4. Conclusion

Three new photoresists derived from tin-oxo-hydroxo clusters have been synthesized, namely **1** (with B(PFP)₄ counterions), **2** (with B(Tolyl)₄) and **3** (with B(HFOMePr)₄). These photoresists all exhibit chemical contrast upon EUV exposure and development but while both **2** and **3** show the usual negative tone photoresist behaviour, **1** can be developed as a positive tone photoresist. In-situ XPS measurements have been performed on **1** and indicate the loss of butyl groups upon EUV exposure while the pentafluorophenyl groups of the anion mostly remain in the film.

Acknowledgement

Part of this work has been carried out within ARCNL, a public-private partnership between UvA, VU, NWO, and ASML. The project has received funding from the European Union's Horizon 2020 research and innovation programme under the Marie Skłodowska-Curie grant agreement No 722149. Synchrotron beam time was provided by the Paul Scherrer Institute where the interference lithography experiments were carried out (proposal 20200726) and the Sincrotrone Elettra (Trieste, Italy) where in-situ XPS experiments were performed (proposal 20205228) Part of this work was supported by Nippon Shokubai.

References

1. M. E. Krysak, J. M. Blackwell, S. E. Putna, M. J. Leeson, T. R. Younkin, S. Harlson, K. Frasure, F. Gstrein, *Proc. SPIE*, **9048** (2014) 904805.
2. Z. Wang, X. Yao, H. An, Y. Want, J. Chen, S. Wang, X. Guo, T. Yu, Y. Zeng, G. Yang, Y. Li, *J. Microelectron. Manuf.*, **4** (2021) 21040101.
3. S. Kataoka, K. Sue, *Eur. J. Inorg. Chem.*, **12** (2022) e202200050.
4. M. Murphy, N. S. Upadhyay, M. Ali, J. Passarelli, J. Grzeskowiak, M. Weires, R. L. Brainard *J. Photopolym. Sci. Technol.*, **34** (2021) 117.
5. B. Cardineau, R. Del Re, M. Marnell, H. Al-Mashat, M. Vockenhuber, Y. Ekinici, C. Sarma,

- D. A. Freedman, R. L. Brainard, *Microelectron. Eng.*, **127** (2014) 44.
6. J. Haitjema, Y. Zhang, M. Vockenhuber, D. Kazazis, Y. Ekinci, A. M. Brouwer, *J. Micro/Nanolith. MEMS MOEMS*, **16(3)** (2017) 033510.
 7. I. Bespalov, Y. Zhang, J. Haitjema, R. M. Tromp, S. J. van der Molen, A. M. Brouwer, J. Jobst, S. Castellanos. *ACS Appl. Mater. Interfaces*, **12(8)** (2020) 9881.
 8. Y. Zhang, J. Haitjema, X. Liu, F. Johansson, A. Lindblad, S. Castellanos, N. Ottosson, A. M. Brouwer, *J. Micro/Nanolith. MEMS MOEMS*, **16** (2017) 023510.
 9. J. Haitjema, L. Wu, A. Giuliani, L. Nahon, S. Castellanos, A. M. Brouwer, *Phys. Chem. Chem. Phys.*, **23(37)** (2021) 20909.
 10. J. Haitjema, L. Wu, A. Giuliani, L. Nahon, S. Castellanos, A. M. Brouwer, *J. Photopolym. Sci. Technol.*, **31** (2018) 243.
 11. W. D. Hinsberg and S. Meyers, *Proc. SPIE*, **10146** (2017) 1014604.
 12. C. Eychenne-Baron, F. Ribot and C. Sanchez, *J. Organomet Chem.*, **567** (1998) 137.
 13. F. Ribot, E. Banse, E. Diter, C. Sanchez, *New J. Chem.*, **19** (1995) 1145.
 14. F. Ribot, C. Sanchez, R. Willem, J.C. Martins, M. Biesemans, *Inorg. Chem.*, **37** (1998) 911.
 15. R. Fallica, J. Haitjema, L. Wu, S. Castellanos Ortega, A. M. Brouwer, Y. Ekinci, *J. Micro/Nanolith. MEMS MOEMS*, **17(2)** (2018), 023505.
 16. Y. Zhang, J. Haitjema, M. Baljovic, M. Vockenhuber, D. Kazazis, T. A. Jung, Y. Ekinci, A. M. Brouwer *J. Photopolym. Sci. Technol.*, **31** (2018), 249.
 17. J. L. R. Williams, J. C. Doty, P. J. Grisdale, R. Searle, T. H. Regan, G. P. Happ, D. P. Maier *J. Am. Chem. Soc.*, **90** (1968), 53.
 18. P. J. Grisdale, J. L. R. Williams, M. E. Glogowski, B. E. Babb *J. Org. Chem.*, **36** (1971), 544.
 19. S. T. Murphy, C. Zou, J. B. Miers, R. M. Ballew, D. D. Dlott, G. B. Schuster *J. Phys. Chem.*, **97** (1993), 13152.
 20. S. B. Beil, S. Mohle, P. Endersa, S. R. Waldvogel *Chem. Commun.*, **54** (2018), 6128.

Nanoimprint with CO₂ ambient

¹Toshiki ITO*, ²Yuto ITO, ²Isao KAWATA, ²Ken-ichi UEYAMA, ²Kouhei NAGANE
³Weijun LIU, ³Timothy STACHOWIAK, ³Wei ZHANG, ³Teresa ESTRADA

¹*Semiconductor Production Equipment Group, Canon Inc., 20-2, Kiyohara-Kogyodanchi, Utsunomiya-shi, Tochigi 321-3292 Japan*

²*R&D Headquarters, Canon Inc., 30-2, Shimomaruko 3-chome, Ohta-ku, Tokyo 146-8501, Japan*

³*Canon Nanotechnologies, Inc., 18707 West Braker Lane, Austin, TX USA*

In Jet and Flash Imprint Lithography (JFIL), ambient gas is trapped between the resist, the substrate and the mold. The volume of the trapped ambient gas is estimated about 9.7 ~ 21.5% of the resist volume. It takes time for the bubbles to disappear in the closed space. By using carbon dioxide as the atmospheric gas and applying an organic layer such as Spin on Carbon (SOC) to the top surface layer of the substrate, it is proposed by theoretical calculation that the gas disappearance time is shortened and the throughput is improved. When the thickness of the SOC layer on the substrate was 5 nm or more, it was indicated that the gas disappearance time was shorter in carbon dioxide ambient than in helium ambient.

Keywords: Nanoimprint lithography, Photoresist, Throughput, Helium, Carbon dioxide

1. Introduction

The JFIL imprint process [1] is depicted in Fig. 1.

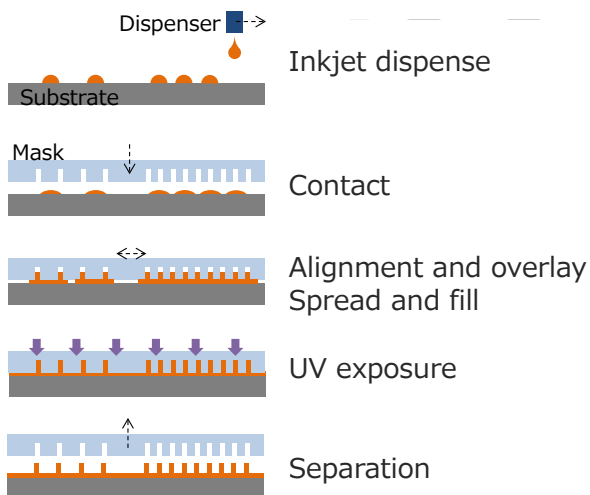


Fig. 1. J-FIL process

A resist liquid is discretely dispensed into the pattern forming region on the substrate. The drops of resist dispensed on the patterning region spread over the substrate. This phenomenon is called pre-spreading. Next, a mold having a pattern is contacted to the resist drops on the substrate. Thereby, the drops of the resist spreads to the whole

area of the gap between the substrate and the mold by the capillary force. This phenomenon is called spreading. The spreading process is classified into dynamic spreading (DS), which occurs after the mold surface contacts with the resist droplets until the droplets of the resist combine with each other, and static spreading (SS), which occurs after the bonding and the trapped gas disappears. The resist is also filled in the recesses forming the pattern of the mold by capillary force. This filling phenomenon is called filling. The time it takes to spread and fill is called the filling time. After the filling of the resist is completed, the resist is irradiated with UV light through the mold to cure the resist. Thereafter, the mold is pulled away from the cured resist. By performing these steps, the pattern of the mold is transferred to the resist on the substrate to form a pattern of the resist.

When JFIL is applied to semiconductor device manufacturing, high throughput is required to improve productivity. In JFIL, the volume of the atmospheric gas trapped between the resist, the substrate and the mold is 9.7% or more by the resist volume ratio when the arrangement of the resist droplets is a diamond-like array, and 21.5% or more when the arrangement is a square array. The time required for SS accounts for more than 50% of the

Received March 31, 2022
Accepted June 24, 2022

total process time of JFIL because it takes time to make the gas disappear in the closed space [2].

In JFIL using spin-on-carbon (SOC) as an intermediate transfer layer on a device substrate, it is known that the use of air as atmospheric gases results in shorter SS time than helium on a certain SOC [3]. The helium bubble is absorbed into the quartz of the mold by diffusion of helium atoms. The main mechanism of air bubbles is that oxygen and nitrogen molecules are dissolved and occluded in SOC.

The authors found that the thinner the SOC layer, the longer the SS time. The smaller the circuit pattern to be formed, the thinner the intermediate transfer layer must be. Therefore, the authors proposed carbon dioxide as an atmospheric gas that is expected to have a shorter SS time due to its high solubility to SOC than helium or air.

2. Calculation

2.1. Gas disappearance time

In order to theoretically calculate the time required for DS and SS, a simplified model of the JFIL process was developed as shown in Fig. 3.

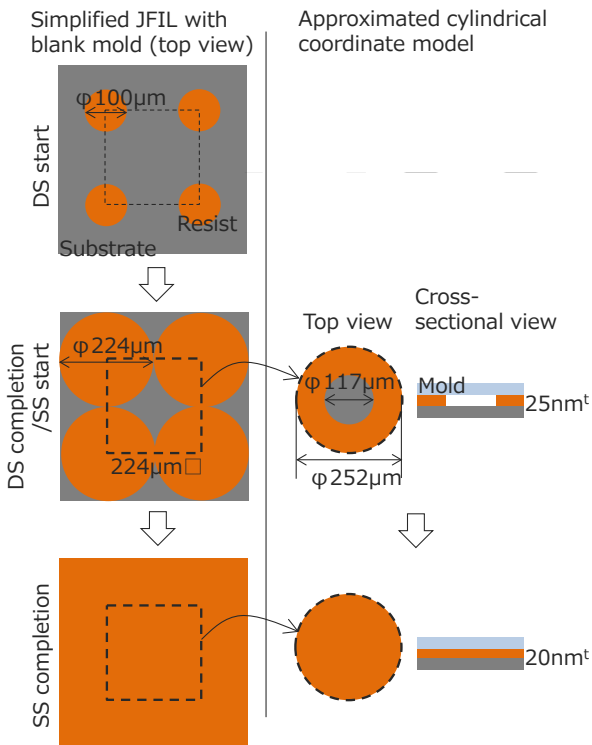


Fig. 3. Calculation model

The mold assumes a blank mold with no recess pattern formed. The drops of resist dispensed onto the substrate in a square arrangement are independent of each other before the mold is contacted. When the mold is contacted, the mold surface is brought into contact with the resist, and

dynamic spread (DS) is started. The drop of the resist is assumed to have a cylindrical shape and to spread while maintaining a cylindrical shape. It is defined that DS is completed and SS starts at the moment when the drops of the resist contact each other. In SS, the ambient gas is trapped by the resist, the mold and the substrate.

The unit cell of the square array in the SS process is approximated to a cylindrical coordinate system model as shown in Fig. 3. The same volume of gas and resist as the unit cell of the Cartesian coordinate system is sandwiched between the disk-shaped substrate and the mold in the cylindrical coordinate system. The outer boundary of the disk is a closed boundary. Atmospheric gas disappears by diffusion and dissolution with Laplace pressure as driving force. If the resist is assumed to be an incompressible fluid, the mold descends to compensate for the volume of the missing gas. When the volume of gas becomes zero, SS completion is defined. The various numerical values illustrated in Fig. 3 are calculated assuming a droplet volume of 1 pL, a drop diameter of 100 μm at the start of DS, and a resist liquid film thickness of 20 nm at the end of SS.

The DS time was calculated by coupling the lubrication equation for a cylindrical resist droplet with the mold equation of motion. The reason for adopting the lubrication equation is that the spacing of the applied droplets is about 100 μm and the height of the droplet distribution is on the order of several nm to several μm, and the pressure gradient in the height direction is negligible because of the high aspect. Since the Reynolds number can be considered sufficiently small, it was treated as an incompressible fluid. The above coupled equation has an analytical solution and the DS time T_{DS} is given below:

$$T_{DS} = \frac{\pi(R^4 - R_0^4)}{4V} \frac{3\mu\pi}{4\sigma(\cos\theta_u + \cos\theta_d)} \quad (\text{eq.1})$$

Here, V is the volume of one droplet, R is half the distance between the droplets, R_0 is the radius of the cylinder of the droplet of the resist, μ is the viscosity of the resist, σ is the surface tension, θ_u is the contact angle between the resist and the mold, and θ_d is the contact angle between the resist and the underlayer.

The calculation method of SS time in the cylindrical coordinate system model of Fig. 3 is described in detail below. The bubbles trapped by the collision of the resist drops are approximated by a cylinder of radius r_g having the same volume, and the calculation region is also approximated by a cylinder of radius r_c having the same volume. The equation of state of the ideal gas, the equation of

mass of the gas, the equation of diffusion of the gas into the mold, the equation of diffusion of the gas into the SOC, the equation of diffusion of the gas into the resist, the equation of mass conservation of the resist, the equation of lubrication of the resist region, and the equation of motion of the mold are coupled to obtain the equation of time evolution of the bubble volume, the pressure p_g , and the height h of the mold. The equation for the ideal gas is given below.

$$p_g = \rho_g RT \quad (\text{eq.2})$$

where p_g is the pressure of the gas, ρ_g is the density of the gas, R is the gas constant, and T is the temperature. The gas mass equation is given below.

$$\pi r_g^2 h \rho_g = M_g \quad (\text{eq.3})$$

where M_g is the mass of the gas.

The diffusion equation of the gas is given below, for example in the case of a mold.

$$\frac{dc_g}{dt} = D_g \nabla^2 c_g \quad (\text{eq.4})$$

Here, C_g is the gas concentration of the mold, and D_g is the diffusion coefficient of the gas into the mold. The boundary condition is that saturated dissolution according to Henry's law occurs only near the interface where the mold and the gas are in contact. The diffusion equation of the gas into the resist and the substrate was the same as the diffusion equation of the gas into the mold, and the same was applied to the boundary conditions.

The equation for the mass conservation of the resist is given below.

$$\rho_r \pi (r_c^2 - r_g^2) h = \rho_r V_d = M_r \quad (\text{eq.5})$$

where ρ_r is the density of the resist, V_d is the volume of the droplet of the resist, and M_r is the total mass of the resist.

The lubrication equation for the region of the resist is given by.

$$\frac{h^3}{12\mu} \frac{1}{r} \frac{\partial}{\partial r} r \frac{\partial p_r}{\partial r} = \frac{dh}{dt} \quad (\text{eq.6})$$

Here, μ is the viscosity of the resist as described above. The equation of motion of the mold is given below.

$$\pi r_c^2 \rho_m h_m \frac{d^2 h}{dt^2} = \pi r_g^2 p_g + \int_{\theta=0}^{2\pi} \int_{r=r_g}^{r_c} p_r(r) r dr d\theta \quad (\text{eq.7})$$

The target film thickness is defined as RLT (residual layer thickness), and the resist thickness is defined as h . The completion condition in the SS calculation was set as described below:

$$\frac{(h - RLT)}{RLT} < 10^{-5} \quad (\text{eq.8})$$

2.2. Molecular dynamics calculation

The diffusion coefficient of the gas in the resist was calculated by using molecular dynamics calculation for a molecular assembly containing 10 gas molecules per 500 molecules of isobornyl acrylate that can be used as a component of the JFIL resist. GROMACS -2016.4 (Copyright © 2001 - 2017, The GROMACS development team at Uppsala University, Stockholm University and the Royal Institute of Technology, Sweden.) was used for molecular dynamics calculations.

The sampling of the equilibrium state in the molecular dynamics calculation was obtained by placing the object molecule in the unit cell which imposed the periodic boundary condition, calculating the force acting between atoms included in each molecule for each time, and calculating the locus of all atoms for the time evolution.

The diffusion coefficients were calculated from the mean square displacements of gas molecules from the history of molecular motion obtained by Production Run.

3. Experimental

3.1. Measurement of gas disappearance time

FNIS-031A developed by FUJIFILM Corporation was used as the JFIL resist. ODL -301 provided by Shin-Etsu Chemical Industry Co., Ltd. was used as SOC.

Drops of 3.25 pL of resist in a square array of 140 μm per side were uniformly dropped in a range of 26×33 mm on a silicon substrate or on a silicon substrate coated with SOC having a thickness of 200 nm, and a quartz blank mold was brought into contact with the droplets.

The spreading behavior of the drops of the JFIL resist through the mold, that is, the shrinking and disappearance behavior of the gas bubble trapped in the three-phase interface of the mold, the substrate, and the resist were photographed by an optical microscope with magnification of 5 times. The time from the contact of the resist and the mold to the disappearance of the area occupied by the void down to 1% or less was measured as the gas disappearance time. An example of the measurement of gas disappearance time is shown in Fig. 4.

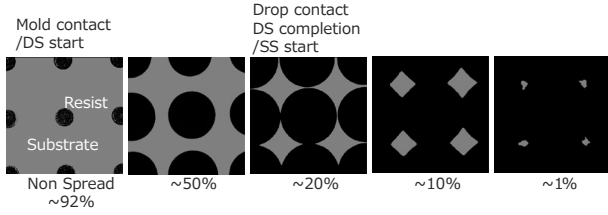


Fig.4. Measurement of gas disappearance time

3.2. Imprinting

The filling time in the imprint equipment NZ2 developed by Canon Inc. was measured by the following experiment. As the JFIL resist, FNIS-031A developed by FUJIFILM Corporation was used. ODL -301 provided by Shin-Etsu Chemical Industry Co., Ltd. was used as the SOC material. 0.6 pL drops of resist was dispensed into a 26×33 mm area on a silicon substrate coated with a 200 nm-thick ODL -301 at a uniform density so as to have an average liquid film thickness of 32 nm, carbon dioxide or helium was used as an atmospheric gas, and a quartz blank mold was brought into contact with the droplet. After a predetermined waiting time elapses after contact, ultraviolet light is irradiated through the mold to cure the resist, and the mold is separated to obtain a cured film of the resist. The number of non-fill defects originating from residual gas in the cured film was measured. The waiting time when the number of non-fill defects is less than $10/\text{cm}^2$ was defined as the filling time. Although the filling time does not always coincide with the gas disappearance time, it is expected that the shorter the gas disappearance time, the shorter the filling time.

4. Results and discussion

The gas disappearance time measured in a helium atmosphere was 2.7 seconds when the SOC layer was 0 nm, and 0.7 seconds when the SOC layer was 200 nm thick. In an air atmosphere, the gas did not disappear after 24 seconds when the SOC layer was 0 nm, and 0.6 seconds when the SOC layer was 200 nm thick. In a carbon dioxide atmosphere, when the SOC layer was 0 nm, the gas disappearance time was 2.67 times as long as that in a helium atmosphere. In the carbon dioxide atmosphere, the gas disappearance time was not measured when the SOC layer was 200 nm thick.

4.1. Coefficients of solubility and diffusion

The diffusion and solubility coefficients of the resist, SOC, and gas (Helium, nitrogen, oxygen, and carbon dioxide) in the mold necessary for the theoretical calculation of the SS time are summarized as shown in Table 1.

Table 1. Coefficient of solubility and diffusion

	He	N ₂	O ₂	CO ₂
<i>Ms</i>	0.0027	0	0	0
<i>Md</i>	1.2×10^{-12}	0	0	0
<i>Rs</i>	0.004	0.11	0.13	1.8
<i>Rd</i>	5×10^{-9}	2.5×10^{-10}	2.5×10^{-10}	5×10^{-11}
<i>Cs</i>	0.0018	0.18	0.21	2.8
<i>Cd</i>	1.4×10^{-9}	2.0×10^{-10}	1.75×10^{-10}	1.30×10^{-10}
<i>Ss</i>	0	0	0	0
<i>Sd</i>	0	0	0	0

Ms: Solubility coefficient to mold ($\text{kg}/\text{m}^3 \cdot \text{atm}$)

Md: Diffusion coefficient to mold (m^2/s)

Rs: Solubility coefficient to resist ($\text{kg}/\text{m}^3 \cdot \text{atm}$)

Rd: Diffusion coefficient to resist (m^2/s)

Cs: Solubility coefficient to SOC ($\text{kg}/\text{m}^3 \cdot \text{atm}$)

Cd: Diffusion coefficient to SOC (m^2/s)

Ss: Solubility coefficient to silicon ($\text{kg}/\text{m}^3 \cdot \text{atm}$)

Sd: Diffusion coefficient to silicon (m^2/s)

The method how to determine the coefficients described in Table 1 is explained below.

4.1.1. Si substrate

Solubility coefficients and diffusion coefficients of helium, nitrogen, oxygen, and carbon dioxide to the silicon substrate were all set to zero. This is based on the known fact that the lattice spacing of silicon crystals is smaller than the molecular diameters of these gases and cannot be permeated [4].

4.1.2. Quartz mold

The diffusion coefficient and solubility coefficient of helium for quartz, which is the material of the mold, are known values [5]. For carbon dioxide, nitrogen and oxygen, the solubility coefficient and diffusion coefficient for quartz were both zero. This is based on the fact that the lattice spacing of quartz is smaller than the molecular diameters of carbon dioxide, nitrogen, and oxygen and is impermeable [5].

4.1.3. Resist

The diffusion coefficients of helium, nitrogen, oxygen, and carbon dioxide to the JFIL resist were determined using the molecular dynamics calculation described above.

The permeability coefficient (P) is the product of the diffusion coefficient (D) and the solubility coefficient (S).

$$P = S \times D \quad (\text{eq.9})$$

The permeability coefficients to the mold and the silicon substrate are known in either gas. Therefore, the permeability coefficient which gives the same calculation result as the measured value of the gas

disappearance time at zero nm of the SOC layer can be calculated. A solubility coefficient in the resist was calculated based on eq. 9 from the obtained permeability coefficient.

4.1.4. SOC

The permeability coefficient of helium to the SOC was calculated by fitting to give the same calculated value as the measured gas disappearance time at the SOC of 200 nm. The solubility coefficient of helium for SOC was assumed to be equivalent to that for organic polymers such as natural rubber [6]. The diffusion coefficient of helium for SOC was calculated based on eq.9.

The permeability coefficients of nitrogen and oxygen to SOC were calculated by fitting to give the same calculated values as the measured values of the gas disappearance time when SOC was 200 nm. The diffusion coefficients of nitrogen and oxygen to SOC were calculated from the molecular weight ratio to helium, assuming that the diffusion coefficient of gas molecules was inversely proportional to the molecular weight of gas molecules. The solubility coefficients of nitrogen and oxygen for SOC were calculated based on eq.9.

The diffusion coefficient of carbon dioxide relative to SOC was calculated from the molecular weight ratio of helium and gas molecules assuming that the diffusion coefficient of gas molecules in SOC is inversely proportional to the molecular weight of gas molecules.

As for the solubility coefficient of carbon dioxide for SOC, the value obtained by assuming that the ratio of the solubility coefficient of carbon dioxide for SOC to the solubility coefficient of nitrogen for SOC coincides with the ratio of the solubility coefficient of carbon dioxide for resist to the solubility coefficient of nitrogen for resist was used.

4.2. Theoretical calculation of gas disappearance time

In the SOC thickness range of 0 ~ 200 nm, the gas disappearance time when the ambient gas (gas in the gap) is helium, nitrogen, or carbon dioxide was calculated by inputting various coefficients described in Table 1. The volume of the droplet of the resist was set to 3.5 pL, the film thickness after filling was set to 28 nm, and the diameter of the droplet at the start was set to 100 μm. The mold thickness was 1 mm. The calculation results are shown in Fig. 5.

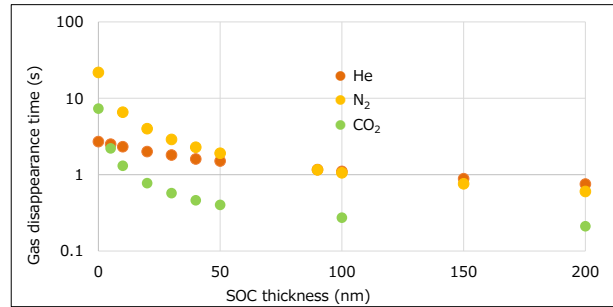


Fig.5. SOC thickness and gas disappearance time

In Fig. 5, when the SOC layer is zero nm, the value is based on the experimentally measured value, the helium atmosphere is the fastest. It is believed that helium diffused into the quartz mold. The thicker the SOC layer, the shorter the gas disappearance time for both gases. When the SOC layer is 5 nm or thicker, carbon dioxide is the fastest. This is considered due to the high solubility of carbon dioxide in SOC. Nitrogen is faster than helium when the SOC layer is larger than 100 nm.

Fig. 6 shows the measurement results of the waiting time dependence of the number of non-fill defects on the imprint device.

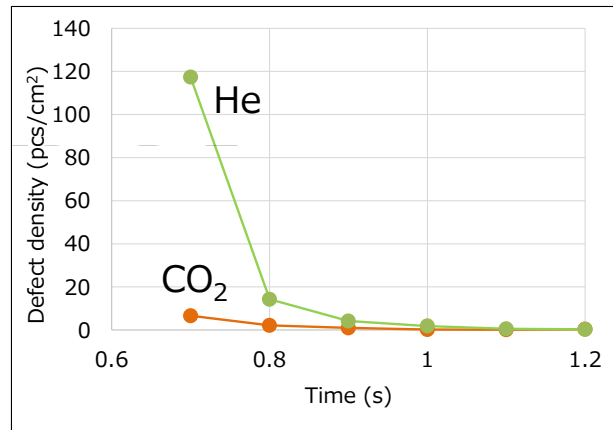


Fig.6. Waiting time and defect density

The longer the waiting time, the smaller the defect density was. In this defect inspection experiment, filling time is defined as a time required to get defect density less than 10 pcs/cm². The filling times were less than 0.7 seconds for carbon dioxide and 0.9 seconds for helium.

5. Conclusion

In imprint lithography on a substrate having SOC on the outermost surface layer, it is expected that the throughput of imprint lithography is improved by applying a carbon dioxide ambient.

References

1. M. Colburn, S. C. Johnson, M. D. Stewart, S. Damle, T. C. Bailey, B. Choi, M. Wedlake, T. B. Michaelson, S. V. Sreenivasan, J. G. Ekerdt, C. G. Willson, *Proc. SPIE*, **3676** (1999) 379.
2. Wei Zhang, Brian Fletcher, Ecron Thompson, Weijun Liu, Tim Stachowiak, Niyaz Khusnatdinov, J. W. Irving, Whitney Longsine, Matthew Traub, Van Truskett, Dwayne LaBrake, Zhengmao Ye, *Proc. SPIE*, **9777** (2016), 97770A
3. K. Okabe, T. Higuchi, M. Komori, T. Kono, *J. Micro/Nanopatterning, Materials, and Metrology*, **21**(2022)011006
4. P. Jung, *Nuclear Instruments and Methods in Physics Research Section B: Beam Interactions with Materials and Atoms*, **91**(1994) 362
5. J. F. Shackelford, *Procedia Materials Science*, **7**(2014)278
6. M. Khawaja, A. P. Sutton, A. A. Mostofi, *J. Phys. Chem. B*, **121**(2017) 287

A 3D-Simulation and Experimental Study of the Fluid Flow Around a Nano-Step Structure Formed by UV-NIL

Tadashi Ando^{1*}, Yusei Honda¹, Tomoki Yanagawa¹, Noriyuki Unno², Jun Taniguchi¹, and Shin-ichi Satake¹

¹Department of Applied Electronics, Faculty of Advanced Engineering, Tokyo University of Science, 6-3-1 Nijjuku, Katsushika-ku, Tokyo 125-8585, Japan

²Department of Mechanical Engineering, Faculty of Engineering, Sanyo-Onoda City University, 1-1-1 Daigakudori, Sanyo-Onoda Yamaguchi 756-0884, Japan

*tando@rs.tus.ac.jp

In this work, total internal reflection fluorescence microscopy (TIRFM) was combined with the refractive index matching method to measure the three-dimensional motion of a nanoparticle on a nanosized step structure in water. A step (height = 64 nm) based on an ultraviolet (UV)-curable resin was fabricated using UV nanoimprint lithography. The step has a refractive index similar to that of water to eliminate the optical distortion due to light refraction and reflection at the interface between the nano structure and water. TIRFM could clearly capture the motion of a fluorescent nanoparticle in the vicinity of the nanostep in water. Diffusion coefficients of the particle in the vicinity of the nanostep edge were obtained from its time-lapse images, indicating that the diffusion coefficient measured along the edge of the step was 1.2 times larger than that measured across the step. Molecular dynamics simulations were also conducted to calculate the diffusion coefficients of a rigid particle close to the top of the step. The simulation results were qualitatively consistent with the experimental observations. The experimental and simulation methods presented here would help understand the nanoparticle motions and solvent flow dynamics around more complicated nanostructures.

Keywords: Refractive index matching method, Total internal reflection fluorescence microscopy, UV-nanoimprint lithography, Molecular dynamics simulation

1. Introduction

Phase change (evaporation and boiling) at the fluid-solid interface are fundamental phenomena in heat and mass transport observed in energy equipment and heat exchangers when high heat fluxes are generated [1]. The enhancement of heat and mass transport at the interface during phase change (*i.e.*, heat transfer enhancement) is an important issue directly related to energy conservation technology. However, there are many unexplained phenomena of the heat transport coupled with phase changes near solid walls and general methods controlling them have not been established. On the other hand, with the recent development of nanotechnology and nano-

fabrication techniques, enhancement of heat transfer using the surfaces having vertically oriented nanometer-scale porous or columnar structures has been reported [2, 3]. Therefore, the microstructure fabrication at the fluid-solid interface would have a potential to control phase change phenomena and associated heat transfer phenomena.

Total internal reflection fluorescence microscopy (TIRFM) is one of the three-dimensional (3D) measurement methods used for nanoscale objects [4]. However, when microstructures based on polydimethylsiloxane (PDMS) and water (as the flow media) are used in this method, refraction and diffraction occur at the interfaces, which reduces the ability to measure the positions of the particles near

Received April 2, 2022

Accepted June 24, 2022

the wall [5]. In our previous study, we used a thermoplastic material called MEXFLON, which has a refractive index identical to that of water ($n = 1.33$), in TIRFM to avoid diffraction from the structure. In addition, we successfully measured the Brownian motion of the nanoparticles around the structure [6]. This water-based measurement method is versatile and suitable for several biological experiments. Recently, commercially available ultraviolet (UV) curable optical polymers (MY Polymers Ltd.) has been used to measure cellular forces [7]. The polymers have a potential for large-scale and high-throughput production because of their UV-curable properties and good moldability. Our group performed 3D calibration using nanoscaled steps fabricated by MY-133-V2000 (hereafter, referred to as V2000, MY Polymers Ltd) [8] and successfully measured the Brownian motions of particles in nanopores [9].

In this study, the diffusion coefficient of a fluorescent nanoparticle in the vicinity of a sub-micrometer structure fabricated by UV-nanoimprint lithography using V2000 was measured by the TIRFM method to understand the behavior of the fluid in the vicinity of a step. In addition, molecular dynamics (MD) simulations were performed on a system mimicking the experimental setup to calculate the diffusion coefficients and compare them to the experimental values.

2. Methods

2.1. Fabrication of a nanostep structure

Figure 1 shows the fabrication process of a nanostep resin structure with the same refractive index as that of water. First, a master mold with a stepwise cavity was fabricated using electron beam lithography. A replica mold was then fabricated by UV-nanoimprint lithography (UV-NIL). The UV-curable resin (PARQUIT OEX-028-X433-3, AUTEX Co., Ltd., Tokyo) was placed on the master mold. Next, the resin layer was covered using a polyester film (Cosmoshine A4300; Toyobo Co. Ltd., Osaka), pressed under 0.3 MPa, and cured using UV radiation. After curing, the polyester film was removed from the master mold and baked at 85°C for 30 min to induce the required antifouling effect [10]. A UV-curable resin (MY-133-V2000, MY Polymers Ltd., Nes-Ziona, Israel) was used to fabricate a nanostep structure on a cleaned glass slide (Micro cover glass No.1, Matsunami Glass Inc., Ltd.) by UV-NIL using the replica mold. The refractive index of V2000 matches that of water to prevent optical distensions such as those observed

with PDMS. The UV-NIL process was as follows. The transfer resin of V2000 was coated on a polyester film [Cosmoshine A4300, thickness = 0.5 μL , Fig. 1(a)]. The replica mold was then brought into contact with the liquid V2000 resin [Fig. 1(b)]. Next, the replica mold was separated from V2000 on the polyester-film surface. This is a liquid transfer process [Fig. 1(c)] [11] used to remove excess V2000 resin from the replica mold. The excess V2000 resin was captured on the polyester film. Thus, no residual layer pattern was formed. Next, a primer-coated glass slide was placed on the replica mold with a thin V2000 resin layer [Fig. 1(d)]. This primer acts as an adhesive promoter to allow the transfer of V2000 onto the glass slide. A contact pressure of 0.27 MPa was then applied for 10 min. The sample was exposed to a UV light (10 J/cm²) under the same pressure for 120 min to harden the V2000 resin [Fig. 1(e)]. Finally, the replica mold was removed from the glass slide [Fig. 1(f)], and the nanostep V2000 resin structure was obtained.

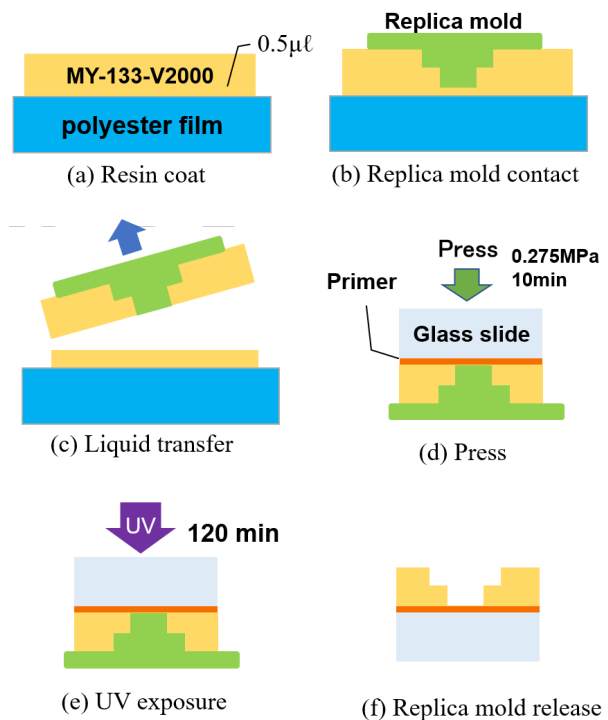


Fig. 1. The fabrication process of a nanostep resin structure.

2.2. TIRFM system

A green laser (85-YCA-025-040, CVI Melles Griot Co., continuous-wave) with a wavelength of 561 nm was used as a light source to generate an evanescent field. An Eclipse Ti-E (Nikon Co., Tokyo) was used as a TIRFM system with a 100 \times -objective lens (CFI Apo TIRF 100 \times , Nikon

Instruments Inc.) and a field of view of 30.72 μm . Fluorescent tracer nanoparticles (diameter = 200 nm, R200, Thermo Fisher Scientific Co.) were used in this study. The nanoparticles were diluted to a concentration of 0.02% using deionized water to prevent intensity saturation. The fluorescence image was captured using an electron multiplying charge-coupled device (EM-CCD, Andor, iXon3 860). The images (128×128 pixels) were captured at 512 Hz. A barrier filter was used to block the green laser light so that the EM-CCD only captures the fluorescence of the tracer particles. This experimental setup is similar to those reported in previous studies [12, 13]. The captured fluorescence images were analyzed using multilayer nanoparticle image velocimetry (MnPIV) [4] to track particles moving in water near the step structure.

2.3. Theoretical calculations of local diffusion coefficients

The fluctuation–dissipation theorem [14] is used to calculate the local diffusion coefficient from the autocorrelation function of the force exerted on a particle constrained at a point in an MD system [15] [Equation (1)].

$$D_\alpha(x_p, y_p, z_p) = \frac{(k_B T)^2}{\int_0^\infty \langle F_\alpha(t) F_\alpha(0) \rangle_{x_p, y_p, z_p} dt}, \quad (1)$$

where $F_\alpha(t)$ is the constrained force acting on the particle to fix its position at $x = x_p$, $y = y_p$, and $z = z_p$, $\alpha \in \{x, y, z\}$, t is the time, k_B is the Boltzmann constant, T is the temperature, and the subscript to the pointy brackets indicates an ensemble average, in which the particle is constrained at the position.

2.4. Molecular dynamics simulations

MD simulations of Lennard–Jones (LJ) fluid were performed using the LAMMPS simulation package [16] to study the near-step wall hindered diffusion of a colloidal particle. The basic idea and simulation methods are the same as those reported by Chio and Tse [17]. Figure 2 shows a snapshot of the simulation system, which consists of fluid particles (cyan spheres), a rigid colloidal particle formed with small particles (pink spheres), and a rigid step wall (purple spheres). In all MD simulations, periodic boundary conditions were imposed in all directions. Therefore, the fluid and colloidal particles are confined by two walls in the z -direction. The interaction potential between all particles, including the fluid and colloidal particles as well as the step wall, were described by the

Week–Chandler–Andersen (WCA) potential [18], which is a purely repulsive potential given by Equation (2).

$$U(r) = \begin{cases} 4\epsilon \left[\left(\frac{\sigma}{r}\right)^{12} - \left(\frac{\sigma}{r}\right)^6 \right] + \epsilon & \text{if } r < 2^{1/6}\sigma \\ 0 & \text{if } r \geq 2^{1/6}\sigma, \end{cases} \quad (2)$$

where r is the distance between particles, and ϵ and σ are the characteristic energy and distance parameters, respectively. The WCA potential is the LJ potential truncated at the minimum potential energy at a distance, $r = 2^{1/6}\sigma$, and shifted upward by an amount of ϵ so that the energy and force are zero at the cutoff distance and beyond it. Throughout this simulation, the LJ reduced units are employed, *i.e.*, the reduced density ($\rho^* = \rho\sigma^3$), reduced temperature ($T^* = k_B T / \epsilon$), and reduced time ($t^* = \sqrt{\epsilon/m\sigma^2}t$). All quantities quoted in this simulation are given in terms of these reduced quantities. Thus, the asterisk superscript and the prefix “reduced” will be omitted hereafter.

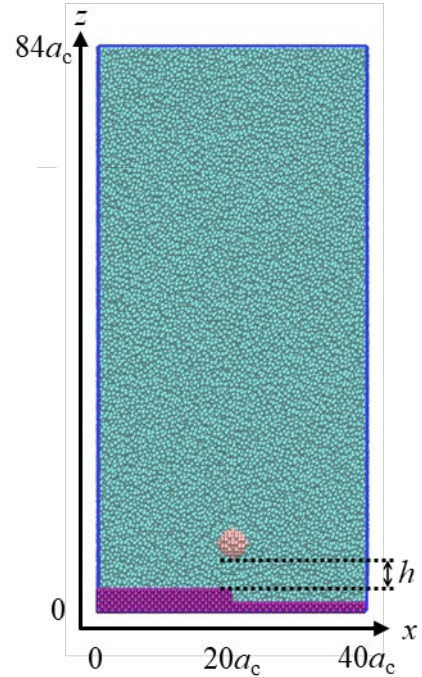


Fig. 2. A snapshot of the simulation system constructed using fluid particles (cyan), a rigid step wall (purple), and a colloidal particle (pink). The size of the box is given in terms of the face-centered cubic lattice constant, a_c . h is the surface distance between the colloidal particle and the upper step. The figure was generated by VMD [19].

The parameters used for all MD simulations are listed in Table 1. The simulation system was

modeled by first placing the fluid particles on a face-centered cubic (FCC) lattice with a lattice constant, a_c , ($a_c = 1.79$ and density = 0.7) in a simulation box. The step wall was modeled by fixing the fluid particles placed in $0 \leq x < 20a_c$ and $0 \leq z < 3a_c$ for the upper step and those in $20a_c \leq x < 40a_c$ and $0 \leq z < a_c$ for the lower step. The height of the step was $2a_c$ (3.6σ). The particles forming the step wall were excluded from the time integration in the MD simulations. The colloidal particle was constructed by placing the fluid particles inside a spherical volume (radius = 2.1σ) and was treated as a rigid body. The colloidal particle consisted of 141 particles.

Table 1. Basic parameters used for the MD simulations.

Parameter	Value
FCC cell constant, a_c	1.79
Size of the simulation box	$71.6 \times 71.6 \times 150.4$ ($40 \times 40 \times 84 a_c^3$)
Total number of particles	537,600
Density	0.7
Equilibration temperature	1.0
Time step	0.002
Steps for equilibration	10^5
Steps in a production run	5×10^6
Number of simulations at each fixed point	5
Particle mass	1.0
Number of particles forming the colloidal particle	141
Effective radius of the colloidal particle, R	3.4 ($\sim 1.9a_c$)
Height of the upper step ($0 \leq x < 20a_c$)	5.37 ($3a_c$)
Height of the lower step ($20a_c \leq x < 40a_c$)	1.79 ($1a_c$)

The system was first equilibrated through 10^5 simulation time steps in a canonical ensemble (NVT), in which the temperature was maintained at 1.0 using the stochastic velocity rescaling method [20]. Next, a production run was performed for 5×10^6 steps in a microcanonical ensemble (NVE). For each system, five independent runs were carried out using different random numbers for each coordinate of the center-of-mass of the colloidal particle.

In the analysis, the obtained diffusion coefficients of the colloidal particle were normalized based on the diffusion constant at the center of the simulation box, D^{center} , i.e., $x = 20a_c$, $y = 20a_c$, and $z = 42a_c$. The effective radius of the colloidal particle, which is defined as the largest distance without any fluid particles in the radial distribution function between the colloidal and fluid particles, was 3.4σ .

3. Results and discussion

3.1. Nanostep fabrication and particle motion observed in TIRFM near the edge of the step

Figure 3 shows an optical microscopy image of the nanostructured step fabricated with V2000. The height of the V2000-based step fabricated using UV-NIL was measured by profilometer, Alpha-Step IQ (KLA-Tencor Co., Ltd.), to be 64 nm.

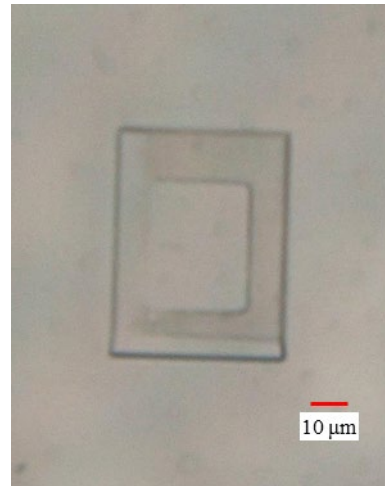


Fig. 3. Optical microscopy image of the V2000-based nanostructured step fabricated using UV-NIL.

Next, the motions of a fluorescent nanoparticle were measured in water in the vicinity of the fabricated nanostep using the TIRFM method. Figure 4 shows the x - y trajectory superimposed on an image of the step structure obtained using bright-field microscopy with a halogen lamp in the absence of water. The mean square displacement (MSD) of the x and y components were estimated based on 180 image frames (Fig. 5). Diffusion coefficients along the x axis (D_x) and y axis (D_y) obtained by a linear fitting of the MSD curve as a function of time were 2.9×10^{-12} and 3.4×10^{-12} m^2/s , respectively (Fig. 5). This indicates that, for the particle in the vicinity of the step edge, the diffusion coefficient measured along the edge of the step (D_y) was 1.2 times larger than that measured across the step (D_x).

3.2. Diffusion coefficients calculated by MD simulations

To validate the experimental results, MD simulations of a system mimicking the experimental setup (Fig. 2) was conducted to estimate the diffusion coefficient of the colloidal particle near the edge of the rigid step wall. The effective radius (3.4σ) was almost equal to the step height (3.58σ), which is roughly the same ratio obtained between the experimental values (step height = 64 nm;

particle radius = 100 nm). In the MD simulations, the center of the mass of the colloidal particles was fixed at $x = y = 20a_c$, and various z values and diffusion coefficients were estimated at each fixed point via the fluctuation–dissipation theorem as discussed in the Methods section. Figure 6 shows the diffusion coefficients of the colloidal particle along the x and y axes as a function of the surface distance between the particle and the upper step. These diffusion coefficients were normalized by those in the center of the simulation box, D^{center} , and the surface distance, h , is normalized by the effective radius of the colloidal particle, R . For $h/R < 3$, the diffusion coefficient along the y axis, D_y/D_y^{center} , was slightly larger than that along the x axis, D_x/D_x^{center} . This result is qualitatively consistent with the experimental result. For $h/R > 3$, the normalized diffusion coefficients for the x and y directions were close to 1.

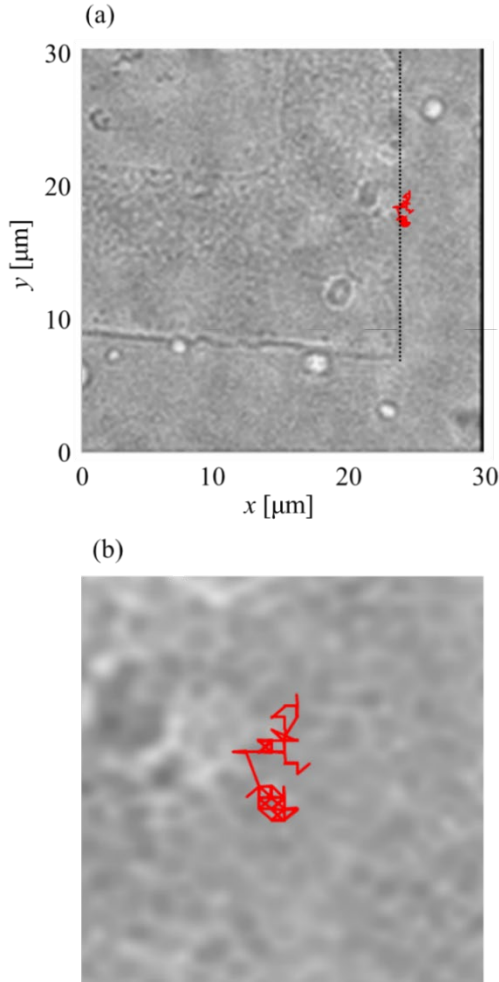


Fig. 4. Brownian trajectory of the nanoparticles (red line) in the vicinity of the nanostep edge superimposed on the image of the step structure obtained using bright-field microscopy in the absence of water. (a) the entire view and (b) a magnified view of the trajectory. In (a), the edge of the step along x ($\approx 24 \mu\text{m}$) is indicated by a dashed line.

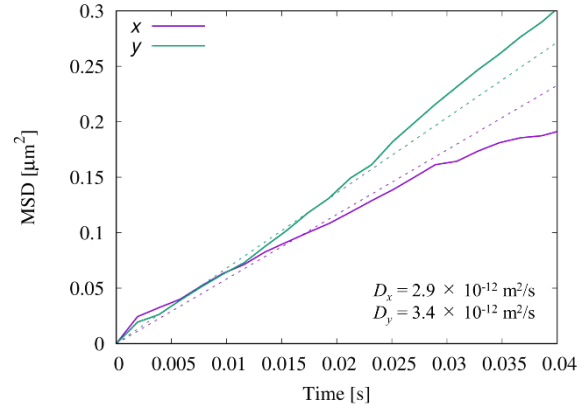


Fig. 5. MSD of the x and y components of the particle near the edge of the step measured using TIRFM. The diffusion coefficient of each component was obtained by fitting the MSD curve with $MSD(t) = 2Dt$ for $0 \leq t \leq 0.025$ s, where D is the diffusion coefficient and t is the time. The dashed lines in this figure represent the fitted lines. The diffusion coefficient of the x and y components obtained by the fitting are also shown in the figure.

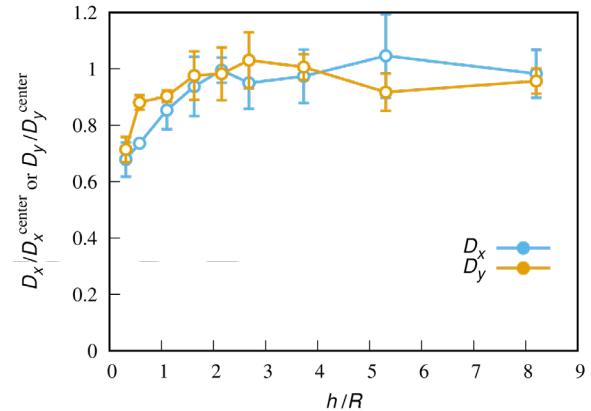


Fig. 6. Diffusion coefficients of the colloidal particle along the x and y axes as a function of the surface distance between the particle and the upper step. Diffusion coefficients are normalized using those in the center of the simulation box, D^{center} . The surface distance is normalized using the effective radius of the colloidal particle, R . The error bars of the data points indicate their standard deviation.

4. Conclusions

In this study, TIRFM was combined with the refractive index matching method to measure the 3D motion of nanoparticles on a nanosized step structure in water. The diffusion coefficient of the particle near the edge of the nanostep measured along the edge of the step was slightly larger than that measured across the step. This difference in the particle diffusion was also confirmed by MD simulations. The experimental and simulation methods presented in this work would be a powerful

tool for understanding the nanoparticle motions and solvent flow dynamics around more complicated nanostructures.

Acknowledgement

This work was supported by JSPS KAKENHI Grant Numbers JP19K04224.

References

1. D. Attinger, C. Frankiewicz, A. R. Betz, T. M. Schutzius, R. Ganguly, A. Das, C. J. Kim, and C. M. Megaridis, *MRS Energy and Sustainability*, **1** (2014) E4.
2. N. Unno, M. Asano, Y. Matsuda, S. Satake, and J. Taniguchi, *Heat Transf. Res.*, **49** (2018) 145.
3. N. Unno, K. Yuki, R. Inoue, Y. Kogo, J. Taniguchi, and S. Satake, *Journal of Thermal Science and Technology*, **15** (2020) JTST0007.
4. H. F. Li, R. Sadr, and M. Yoda, *Exp. Fluids*, **41** (2006) 185.
5. G. O. F. Parikesit, J. S. Guasto, S. Girardo, E. Mele, R. Stabile, D. Pisignano, R. Lindken, and J. Westerweel, *Biomechanics*, **3** (2009) 44111.
6. N. Unno, S. Nakata, S. Satake, and J. Taniguchi, *Exp. Fluids*, **57** (2016) 120.
7. A. Ravasio, S. Vaishnavi, B. Ladoux, and V. Viasnoff, *Acta Biomater.*, **14** (2015) 53.
8. N. Unno, H. Kigami, T. Fujinami, S. Nakata, S. Satake, and J. Taniguchi, *Microelectron. Eng.*, **180** (2017) 86.
9. T. Fujinami, H. Kigami, N. Unno, J. Taniguchi, and S. Satake, *Opt. Rev.*, **25** (2018) 437.
10. Y. Otsuka, S. Hiwasa, and J. Taniguchi, *Microelectron. Eng.*, **123** (2014) 192.
11. N. Koo, J. W. Kim, M. Otto, C. Moormann, and H. Kurz, *J. Vac. Sci. Technol. B*, **29** (2011) 06FC12.
12. N. Unno, A. Maeda, S. Satake, T. Tsuji, and J. Taniguchi, *Microelectron. Eng.*, **133** (2015) 98.
13. S. Nakata, N. Unno, S. Satake, and J. Taniguchi, *Microelectron. Eng.*, **160** (2016) 81.
14. R. Kubo, *Rep. Prog. Phys.*, **29** (1966) 255.
15. S. J. Marrink and H. J. C. Berendsen, *J. Phys. Chem.*, **98** (1994) 4155.
16. A. P. Thompson, H. M. Aktulga, R. Berger, D. S. Bolintineanu, W. M. Brown, P. S. Crozier, P. J. I. Veld, A. Kohlmeyer, S. G. Moore, T. D. Nguyen, R. Shan, M. J. Stevens, J. Tranchida, C. Trott, and S. J. Plimpton, *Comput. Phys. Commun.*, **271** (2022) 108171.
17. C. C. Chio and Y. L. S. Tse, *Langmuir*, **36** (2020) 9412.
18. J. D. Weeks, D. Chandler, and H. C. Andersen, *J. Chem. Phys.*, **55** (1971) 5422.
19. W. Humphrey, A. Dalke, and K. Schulten, *J. Mol. Graph. Model.*, **14** (1996) 33.
20. G. Bussi, D. Donadio, and M. Parrinello, *J. Chem. Phys.*, **126** (2007) 014101.

Fabrication of a Rose-Petal-Inspired Micro/Nanostructured Surface via the Ultraviolet Nanoimprint Lithography and Roll-Press Methods

Kazuki Fujiwara^{*1}, Hiroyuki Sugawara^{*2} and Jun Taniguchi^{*1}

^{*1}*Department of Applied Electronics, Tokyo University of Science, 6-3-1, Niiyuku, Katsushika-ku, Tokyo, 125-8585, Japan*

^{*2}*GEOMATEC Co., Ltd., Yokohama Landmark Tower, 9th Floor, 2-2-1 Minato Mirai, Nishi-ku Yokohama, Japan*

^{*1}*junt@te.noda.tus.ac.jp*

Rose petals exhibit functionalities, such as high contact angles (CAs) and high adhesion with water. Their surfaces comprise hierarchical micro/nanostructures. Nanopatterns can be fabricated on a microstructure via several conventional processes. However, the shortcoming of this approach is the challenge of fabricating a large hydrophobic surface. To address this issue, we employ a technology, which we had introduced to fabricate a large moth-eye film. First, we fabricate a nanostructure (moth-eye) as the hydrophobic surface, after which we fabricate the microstructure via a roll-press process on it to obtain the adhesion area. The fabricated surface exhibits high hydrophobicity and adhesion.

Keywords: Ultraviolet nanoimprint lithography, Moth-eye structure, Rose-petal effect, Roll-press process

1. Introduction

The surface of a rose petal is generally superhydrophobic and exhibits a high adhesion to water droplets [1]; this phenomenon is known as the “rose-petal effect” and can inspire the development of new biomimetic material [2-4]. This surface comprises hierarchical micro/nanostructures.

In the conventional fabrication of hierarchical micro/nanostructures, microstructures, such as pillar patterns, are first fabricated via photolithography, after which nanopatterns, including needle-like crystals or wrinkle patterns, are fabricated via etching [4], chemical vapor deposition (CVD) [5], the self-assembly method [6-10], etc. Therefore, the fabrication of a large-scale rose petal, as well as the control of its surface area exhibiting high adhesion, are challenging. Thus, this study proposes a solution to these challenges; the solution involves the fabrication of a nanostructure exhibiting a water-repellent (hydrophobic) surface via ultraviolet nanoimprint lithography (UV-NIL) [11-15], followed by the fabrication of a microstructure on that surface via

the roll-press method [16].

In our study, we focused on the moth-eye structure, which comprises a monolayer and an antireflection structure [17-28]. The needles in a moth-eye structure are lined up at a pitch that is lower than the visible-light wavelength (400–800 nm). We fabricated a moth-eye structure mold by irradiating an oxygen-ion beam onto a glassy carbon (GC) substrate employing an electron cyclotron resonance (ECR) instrument. The moth-eye structure can be transferred at low cost and with high throughput in our laboratory via the UV-NIL technology. Thus, we fabricated the rose-petal films with high throughput via our method.

In this study, a moth-eye structure mold was fabricated employing ECR equipment. Next, we transferred the fabricated superhydrophobic moth-eye films employing a UV-curable resin containing a fluorine compound [29,30]. Finally, the superhydrophobic moth-eye film and micropillar mold were pressed via the roll-press method to pattern the microholes on the moth-eye.

Received	March 28, 2022
Accepted	June 24, 2022

2. Experimental method

2.1 Fabrication of the moth-eye-structured mold

The moth-eye structure mold was fabricated by irradiating an oxygen-ion beam, which was generated from an ECR plasma source, onto a 2×2 cm² GC substrate (Tokai Carbon Co., Ltd.) employing the ECR equipment (ELIONIX Co., EIG-210ER) [18]. The etching conditions were, as follows: accelerating voltage = 600 V, machining time = 70 min, and oxygen mass flow = 4.00 sccm. The moth-eye structure was imparted with a sufficiently high aspect ratio to obtain a superhydrophobic film after the UV-NIL process.

2.2 Release treatment of the moth-eye mold

Fig. 1 depicts the release treatment of the moth-eye mold [26, 27]. First, a chromium layer (~30 nm) was deposited onto the mold by a vacuum deposition instrument (ULVAC KIKO, Inc., VPC-260F) (Fig. 1 (a)). Next, a silane coupling agent (Optool DSX; Daikin Industries, Ltd.) was diluted to 1 wt.%, after which the mold was dipped there in (Fig.1 (b)). Thereafter, the Optool solution was evaporated via heating at 60 °C, and the mold and Optool were sealed for 30 min (Fig.1 (c)). Next, the mold was heated at 120 °C (Fig.1 (d)) and rinsed with Novec 7300 (3M Company) and water (Fig.1 (e)).

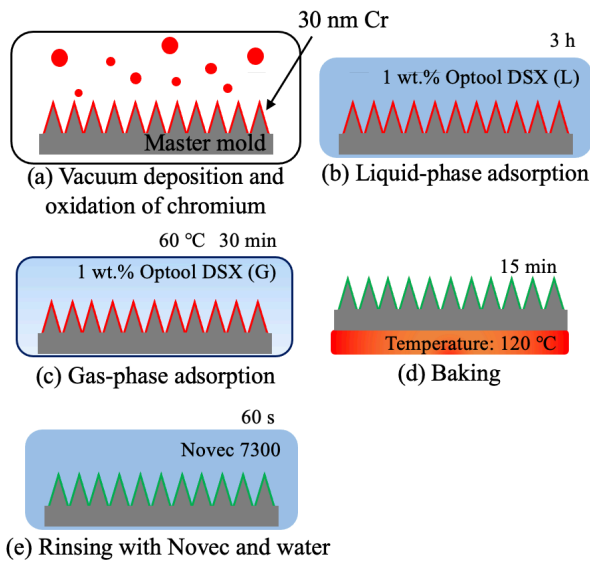


Fig. 1. Schematic of the release treatment of the moth-eye mold

2.3 Fabrication of the rose-petal film

Employing the fabricated mold, a UV-curable resin, which contained a fluorinate material that imparted it with hydrophobicity [29], was dropped on the GC moth-eye mold that had been heated at 80 °C (Fig. 2 (a)). Next, the resin was covered with a polyester film (Cosmoshine A 4300, Toyobo Co., Ltd.), and a

glass slide was placed on it to fill it (Fig. 2 (b)). Considering that the complete filling of the resin shortened the lifetime of the moth-eye needle, while the release force from the partial filling is lower than that from complete filling [31], partial filling was performed by applying an appropriate load employing the glass slide. Subsequently, to solidify the resin, it was exposed to UV radiation from a polyester film (Fig. 2 (c)). Next, the fabricated moth-eye film was released from the mold (Fig. 2 (d)) and baked to enhance its hydrophobicity (Fig. 2 (e)). Finally, the moth-eye film and micropillar mold (Fig. 3: square frustum array, height: 55 μm, tip width: 29 μm, pitch: 100 μm) were pressed via the roll-press method to pattern the microholes (Fig. 2 (f)). The obtained micropillar mold was fabricated to cross-cut tungsten carbide via a grinding process [16].

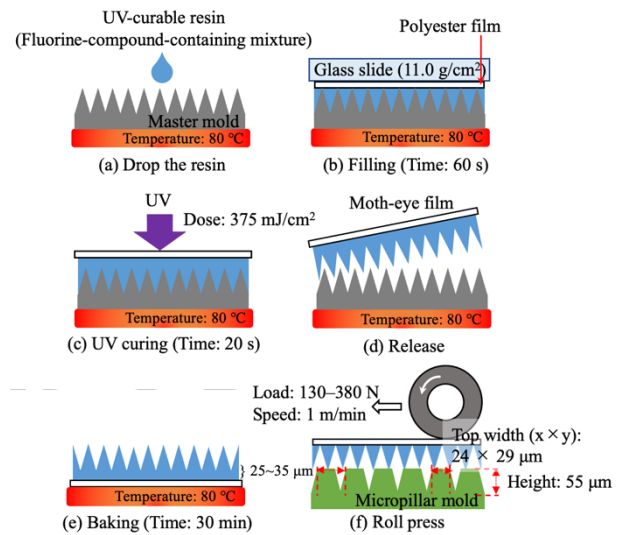


Fig. 2. Schematic of the fabrication of the rose-petal film

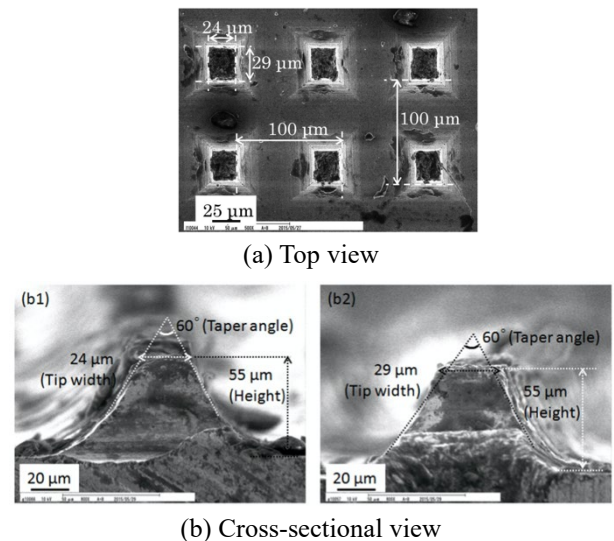


Fig. 3. Scanning electron microscopy (SEM) images of the micropillar mold

3. Results and discussion

3.1 Characterization of the fabricated moth-eye mold and film

Fig. 4 shows the SEM images of the moth-eye-structured mold and film. The height, pitch, and diameter of the GC moth-eye mold were 388.1, 48.4, and 39.3 nm, respectively, while the height, pitch, and diameter of the transferred moth-eye film were 223.3, 60.3, and 36.4 nm, respectively. The needles in the film did not bend; they improved its water-repellent activity.

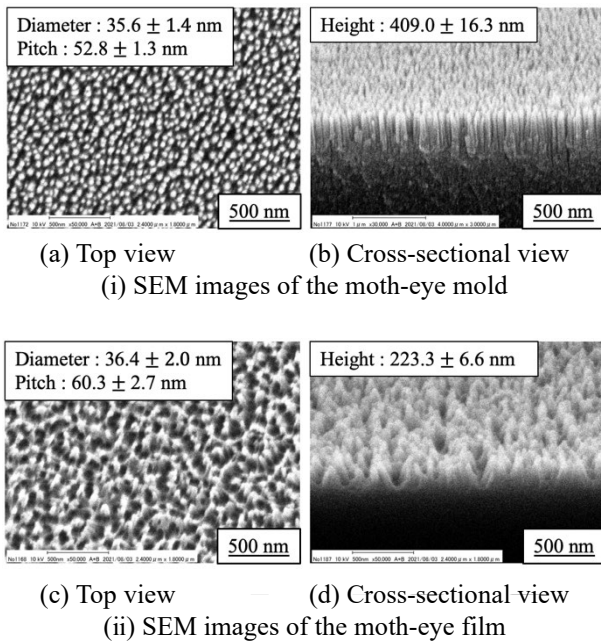
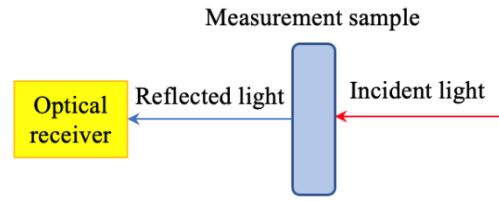


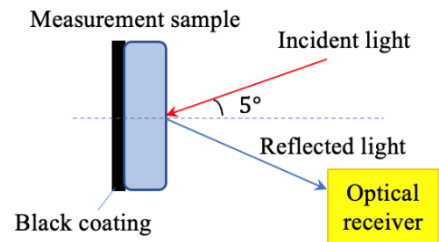
Fig. 4. SEM images of the moth-eye mold and film

Fig. 5 shows the setup of the sample, as well as the direction of light when measuring the reflectance and transmittance of the fabricated films. To measure the reflectance, the sample was coated with black employing vinyl tape to make it opaque.

Fig. 6 shows the transmittances and reflectances of the smooth UV-cured resin film, moth-eye mold, and moth-eye film. The reflection of the mold was ~0.2% at visible wavelengths. Conversely, the reflections of the moth-eye film in the short and long wavelength regions were approximately <0.8% and 1.4%, respectively, and its transmittance around a wavelength of 550 nm was ~91%. The transmittance and reflectance of the smooth UV-cured resin film were ~79.9% and 1.8%, respectively, at a wavelength of 550 nm, indicating that the moth-eye structure improved the anti-reflection of the material.



(a) Transmittance measurements



(b) Reflectance measurement

Fig. 5. Sample(films) setup when measuring their optical characteristics

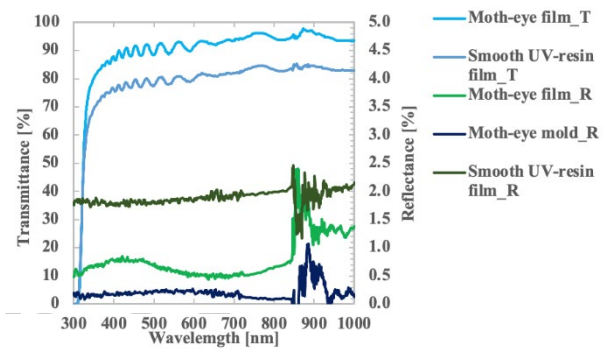


Fig. 6. Transmittances and reflectances of the moth-eye mold and film

The moth-eye film was patterned by a micropillar mold and roll-press instrument to fabricate the rose-petal film. Fig. 7 shows the SEM images of the rose-petal film (load: 230 N). The size of the microhole was, as follows: the sides of the rectangle (top-point) = $24.3 \mu\text{m} \times 29.3 \mu\text{m}$, with a depth of $16.9 \mu\text{m}$ (D). Fig. 7 (a) shows that the upper part around the hole was raised because of the load. The height, pitch, and diameter of the moth-eye structure between the holes were 218.3, 60.0, and 37.2 nm, respectively (Fig. 7 (d)), and its shape was maintained because the micropillar mold and film were not touched. The height of the moth-eye structure at the bottom of the microhole was 175.8 nm (Figs. 7(e-i) and (e-ii)). Moreover, the height of the moth-eye needle was reduced by the load.

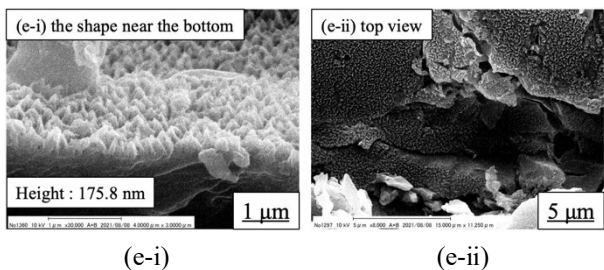
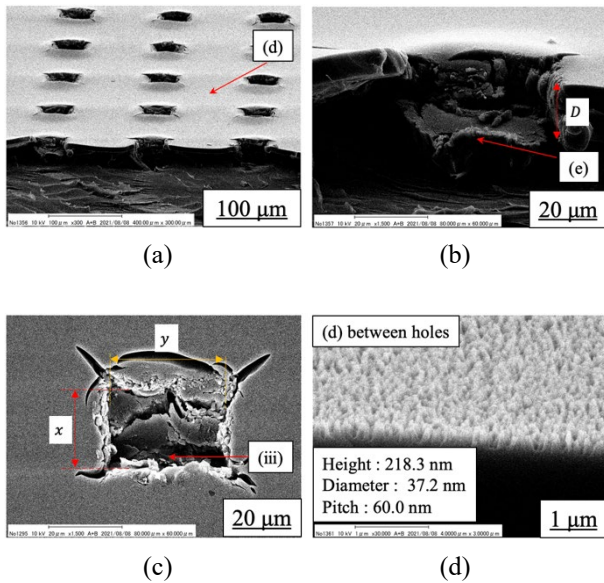


Fig. 7. SEM images of the rose-petal film (load: 230 N)

Figs. 8(a) and (b) show the transmittances and reflectances of the moth-eye and rose-petal films with loadings of 130, 230, and 330 N. These films exhibited reflection of $<0.8\%$ (higher loads would lower this reflection). However, the transmittance decreased in the pressed film as the load increased owing to the microconcave structures that resembled the antiglare structures. The depth of the microhole on the rose-petal film affected the transmittance and reflectance.

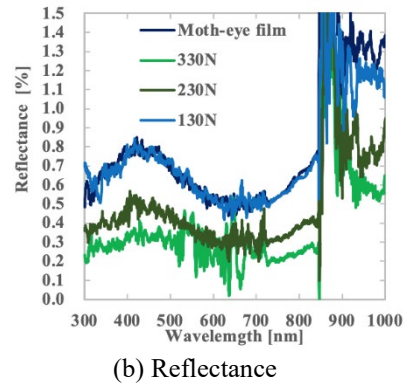
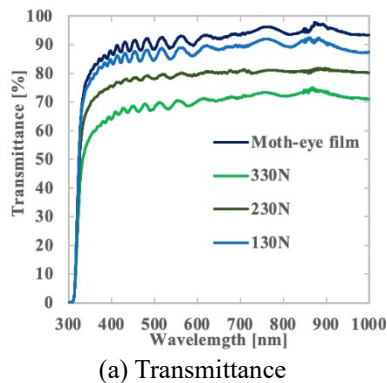
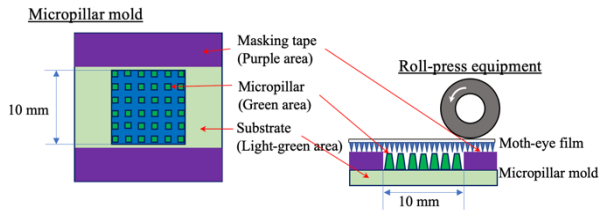


Fig. 8. Transmittances and reflectances of the moth-eye and rose-petal films (load: 130, 230, and 330 N)

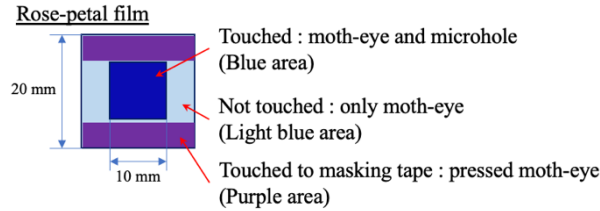
Fig. 9(a) shows the details of the micropillar mold. A masking tape was applied to the mold as a support for the partial roll pressing of the moth-eye film, and Fig. 9(b) shows the roll-pressed and unpressed areas. The surfaces of the “Touched” and “Not touched” areas comprised the moth-eye structure and microhole, as well as the moth-eye structure, respectively. These two areas were fabricated on the same film by controlling the area that was subjected to roll pressing. The water-repellent action and adhesiveness of these areas were also investigated.

Fig. 10 shows the models of the fabricated surface via UV-NIL. This sample was fabricated using same UV-curable resin.

Table 1 shows the contact angles (CA: $5\ \mu\text{L}$ water) and sliding angles (SA: $5\ \mu\text{L}$ water) of the smooth UV-cured resin, micropatterned (load: 260 N), moth-eye and rose-petal (load: 260 N) films. The micropatterned film without nanopattern was fabricated via roll pressing to generate microholes on the smooth UV-cured resin film. The CAs of the smooth and micropatterned films were 70.3° and 87.8° , respectively. The moth-eye film and “Not touched” area of the rose-petal film exhibited CAs and SAs of $>150^\circ$ and $\leq 30^\circ$, respectively. Hence, these areas exhibited superhydrophobicity and low adhesion. CA of the “Touched” area on the rose-petal film was 147.5° . It adhered to a water droplet when tilted at 180° . This area was characterized by its high CA and adhesion with water, indicating that the nanostructure had improved the water repellency and that the generation of the “rose-petal effect” via roll pressing enabled the control of the areas of low and high adhesions on the same film.



(a) Patterns of the micropillar mold and roll-pressed areas



(b) Areas of the moth-eye and rose-petal structures

Fig. 9. Control of the microhole patterning area via roll pressing

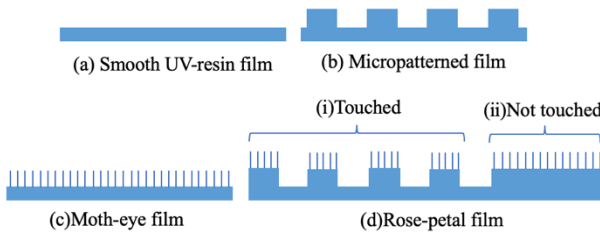


Fig. 10. Models of the fabricated surface

Table 1. Comparison of the wettabilities of the smooth UV-cured resin, micropatterned, moth-eye, and rose-petal films (load: 260 N)

Sample	CA [°]	SA [°] (Water: 5 μ L)
(a) Smooth UV-resin film	70.3 ± 2.3	TA : 180°
(b) Micropatterned film (Load : 260N)	87.8 ± 1.7	TA : 180°
(c) Moth-eye film	152.3 ± 1.1	SA : 29°
(d) Rose-petal film	(i) Touched	147.5 ± 1.9 TA : 180°
	(ii) Not touched	150.8 ± 2.0 SA : 30°

3.2 Characterization of the fabricated moth-eye film and the rose-petal film

Table 2 presents the relationship between the wettabilities of the fabricated moth-eye and rose-petal films. The maximum amount of adhering water is the maximum volume of adhering water,

which is measured from 5 μ L at intervals of 0.5 μ L if the water was adhered for a minimum of two out of three times. The surface free energy was measured with water, diiodomethane, and n-hexadecane and calculated by the Kitazaki–Hata and Kawlbel–Uy theories.

A further increase in the load generated deeper microholes, and since the layer of the UV-curable resin was thinner than that of the height of the micropillar mold, the depth of the microhole depended on the thickness of the resin layer when the load exceeded 300 N.

Fig. 11 shows the direction for measuring their CAs and SAs. As observed, the lengths of the microholes differed along the x and y directions. When the water droplets were placed on such a pattern, the CAs differed depending on the measurement direction since the water droplets spread differently [32]. CA, as observed from the y-axis, was smaller than that observed from the x-axis. We believe that it was very appropriate to measure the smaller CA when evaluating the wettability. Therefore, in this study, we measured CA while considering d_y .

In Table 2, the images of the water droplets on these films were captured from a vertical angle of y. The rose-petal film (load = 130 N) exhibited CA and SA of 150° and 45° , respectively. Conversely, the 160-N film exhibited a CA of 143.5° and adhered to a 5- μ L water droplet when inverted. Therefore, the threshold (marking the change from superhydrophobicity with low adhesion to hydrophobicity with high adhesion) was between the depths of 4.9–6.7 μ m. The CAs of the films subjected to loads of ≥ 160 N were 7° – 10° smaller than those of the moth-eye films because the microholes were filled with water. Further, we evaluated the adherence of the films to the maximum of adhering water, SA (11 μ L of water), and surface free energy. The deeper microholes corresponded to a larger maximum of adhering water, and its maximum value was 10.5 μ L. Fig. 12 shows the dependence of SA (11 μ L of water) and the maximum of adhering water.

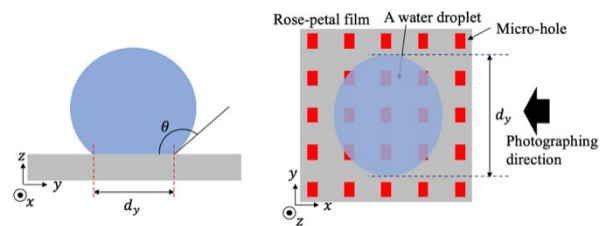
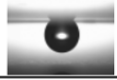
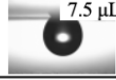
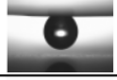
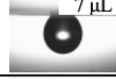
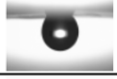
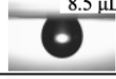
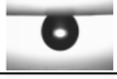
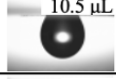
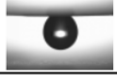
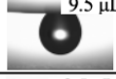
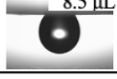


Fig. 11. Model of a water droplet on the rose-petal film

Table 2. Shape and wettability of the moth-eye and rose-petal films

Sample				Wettability					
Film	Load [N]	Size of micro-hole		CA [°] (5 μ L water)	SA [°] (11 μ L water)	Inverted (5 μ L water)	Maximum amount of adhering water	Surface free energy [mN/m]	
		$x \times y$ [μ m]	Depth D [μ m]					Kitazaki–Hata	Kawlbel–Uy
Moth-eye				152.3 \pm 1.1		SA: 29°		1.8	2.3
Rose-petal	130	23.8 \times 30.7	4.9 \pm 0.4	150.9 \pm 0.9	25	SA : 45°		1.8	2.3
	160	24.1 \times 26.8	6.7 \pm 0.5	143.5 \pm 1.8	44			2.3	2.4
	230	24.3 \times 29.3	16.9 \pm 0.6	146.4 \pm 0.6	45			2.0	2.3
	260	25.3 \times 32.4	18.7 \pm 0.8	147.5 \pm 1.9	50			2.3	2.7
	300	22.5 \times 28.6	23.6 \pm 0.6	142.5 \pm 1.0	79			2.6	2.8
	330	23.1 \times 30.0	34.3 \pm 1.6	145.3 \pm 1.8	76			2.2	2.5
	380	23.5 \times 28.5	23.2 \pm 0.6	141.7 \pm 1.0	61	Adhered		2.5	2.6

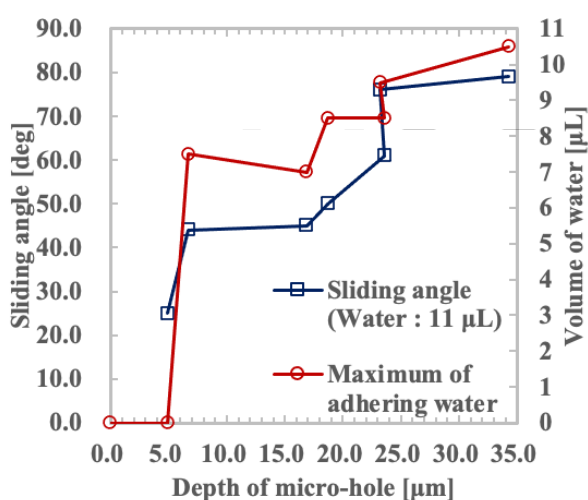


Fig. 12. Relationship between the depths of the microholes on the rose-petal films and adhesion

4. Conclusion

We proposed a technique for fabricating nanostructures before fabricating the desired microstructure. We fabricated a superhydrophobic moth-eye film via UV-NIL, followed by roll pressing the film and a micropillar mold to generate microholes on the nanostructure. This process enabled the control of the water adhesion area and ensured large-scale fabrication.

We fabricated the moth-eye structure mold by

irradiating an oxygen-ion beam onto a GC substrate employing an ECR instrument. Next, the moth-eye film was fabricated by UV-NIL employing the moth-eye mold. Finally, micropatterns were generated via the roll-press method to fabricate the desired rose-petal film.

The fabricated rose-petal films exhibited low reflectance and hydrophobicity with CA of $\geq 140^\circ$ and high adhesion to water droplets. Further, a surface with high CA and adhesion can be fabricated via roll pressing. Although the microholes, which availed high adhesion to water lowered the CA, the patterning method facilitated the simple and flexible control of the area that was subjected to the “rose-petal effect.” This result indicated that water adhered to the microholes. Our future study would include the influence of altering the structural parameters, such as the shape, size, and pitch, of the microholes to further increase CA.

References

1. L. Feng, Y. Zhang, J. Xi, Y. Zhu, N. Wang, F. Xia, and L. Jiang, *Langmuir*, **24** (2008) 4114–4119. <https://doi.org/10.1021/la703821h>
2. X. Hong, X. Gao, and L. Jiang, *J. Am. Chem. Soc.*, **129** (2007) 1478–1479. <https://doi.org/10.1021/ja065537c>

3. H. Zhu, Z. Guo, and W. Liu, *Chem. Commun.*, **50** (2014) 3900–3913. <https://doi.org/10.1039/C3CC47818A>
4. J. K. Park, Z. Yang, and S. Kim, *ACS Appl. Mater. Interfaces*, **9** (2017) 33333–33340. <https://doi.org/10.1021/acsami.7b11143>
5. E. D. Laird, R. K. Bose, H. Qi, K. K. S. Lau, and C. Y. Li, *ACS Appl. Mater. Interfaces*, **5** (2013), 12089–12098. <https://doi.org/10.1021/am403925f>
6. H. Endo, Y. Mochizuki, and M. Tamura, T. Kawai, *Colloids Surf. A Physicochem. Eng. Asp.*, **443** (2014) 576–582. <https://doi.org/10.1016/j.colsurfa.2013.10.050>
7. B. Bhushan, “*Biomimetics*, Springer,” 2012, pp.189–206.
8. D. Ishii, H. Yabu, and M. Shimomura, *Chem. Mater.*, **21** (2009) 1799–1801. <https://doi.org/10.1021/cm9006926>
9. E. Bormashenko, T. Stein, R. Pogreb, and D. Aurbach, *J. Phys. Chem. C.*, **113** (2009) 5568–5572. <https://doi.org/10.1021/jp900594k>
10. M. T. Z. Myint, G. L. Hornyak, and J. Dutta, *J. Colloid Interface Sci.*, **415** (2014) 32–38. <https://doi.org/10.1016/j.jcis.2013.10.015>
11. S. Y. Chou, P. R. Krauss, and P. J. Renstrom, *J. Vac. Sci. Technol.*, **14** (1996) 4129–4133. <https://doi.org/10.1116/1.588605>
12. J. H. Shin, H. J. Choi, K.S. Han, S. Ra, K. W. Choi, and H. Lee, *Curr. Appl. Phys.*, **13** (2013) S93–S97. <https://doi.org/10.1016/j.cap.2013.01.014>
13. J. Kawauchi, S. Hiwasa, and J. Taniguchi, *Photopolym. Sci. Technol.*, **32** (2019) 143–148. <https://doi.org/10.2494/photopolymer.32.143>
14. M. Vogler, S. Wiedenberger, M. Mu hlberger, I. Bergmair, T. Glinsner, H. Schmidt, E. B. Kley, and G. Gru tznern, *Microelectron. Eng.*, **84** (2007) 984–988. <https://doi.org/10.1016/j.mee.2007.01.184>
15. C. H. Chuang, D. M. Lu, P. H. Wang, W. Y. Lee, and M. O. Shaikh, *Microsyst. Technol.*, **24** (2018) 389–395. <https://doi.org/10.1007/s00542-017-3299-7>
ロールトウ
16. R. Fukuyama, J. Taniguchi, K. Yoshikawa, and H. Yagishita, *Microelectron. Eng.*, **150** (2016) 74–83. <https://doi.org/10.1016/j.mee.2015.11.009>
17. S. Wang, J. Dai, J. Hu, S. Zhang, L. Xu, H. Long, J. Chen, Q. Wan, H. C. Kuo, and C. Chen, *ACS Photonics*, **5** (2018) 3534–3540. <https://doi.org/10.1021/acsphotonics.8b00899>
18. J. Taniguchi, E. Yamauchi, and Y. Nemoto, *J. Phys. Conf. Ser.*, **106** (2008) 012011. <https://doi.org/10.1088/1742-6596/106/1/012011>
ECR 加工
19. T. Yanagishita, K. Nishio, and H. Masuda, *Appl. Phys. Exp.*, **1** (2008) 067004. <https://doi.org/10.1143/APEX.1.067004>
20. Y. Kanamori, M. Sasaki, and K. Hane, *Opt. Lett.*, **24** (1999) 1422–1424. <https://doi.org/10.1364/OL.24.001422>
21. S. H. Hong, E. J. Hong, B. J. Bae, and H. Lee, *Adv. Mat. Res.*, **47–50** (2008) 1241–1244. <https://doi.org/10.4028/www.scientific.net/AMR.47-50.1241>
22. D. G. Stavenga, S. Foletti, G. Palasantzas, and K. Arikawa, *Proc. Biol. Sci.*, **273** (2006) 661–667. <https://doi.org/10.1098/rspb.2005.3369>
23. K. Yajima, K. Adachi, Y. Tsukahara, and J. Taniguchi, *Microelectron. Eng.*, **110** (2013) 188–191. <https://doi.org/10.1016/j.mee.2013.03.104>
24. J. Taniguchi, Y. Kamiya, and N. Unno, *J. Photopolym. Sci. Technol.*, **24** (2011) 105–110. <https://doi.org/10.2494/photopolymer.24.105>
25. T. Okumoto, J. Taniguchi, and Y. Kamiya, *Microelectron. Eng.*, **88** (2011) 1832–1835. <https://doi.org/10.1016/j.mee.2011.02.062>
26. J. Taniguchi, Y. Kamiya, T. Ohsaki, N. Sakai, *Microelectron. Eng.*, **87** (2010) 859–863. <https://doi.org/10.1016/j.mee.2009.12.051>
27. J. Takahashi, J. Taniguchi, and Y. Kamiya, *J. Vac. Sci. Technol. B*, **28** (2010) C6M23. <https://doi.org/10.1116/1.3503896>
28. M. Moro and J. Taniguchi, *J. Vac. Sci. Technol. B*, **32** (2014) 06FG09. <https://doi.org/10.1116/1.4901877>
29. T. Nishino, M. Meguro, K. Nakamae, M. Matsushita and Y. Ueda, *Langmuir*, **15** (1999) 4321–4323. <https://doi.org/10.1021/la981727s>
30. N. B. A. Talip Yusof, T. Hayashi, J.

Taniguchi, and S. Hiwasa, *Microelectron. Eng.*, **141** (2015) 81–86.

<https://doi.org/10.1016/j.mee.2015.01.035>.

31. C. Semprebon, G. Mistura, E. Orlandini, G. Bissacco, A. Segato, and J. M. Yeomans,

Langmuir, **25** (2009) 5619–5625.

<https://pubs.acs.org/doi/abs/10.1021/la8041742>.

Using Machine Learning to Predict the Durability of a Mold for Producing Nanostructures in Ultraviolet Nanoimprint Lithography

Kazuki Okamoto¹, Tomohito Wakasa¹, Jun Taniguchi¹, and Shin-ichi Satake^{1*}

¹ *Department of Applied Electronics, Tokyo University of Science, 6-3-1 Niijuku, Katsushika-ku, Tokyo 125-8585 Japan*

**satake@te.noda.tus.ac.jp*

Performing the minimum number of ultraviolet nanoimprint lithography imprints is important for ensuring high throughput and low costs. The stamp lifetime can be estimated quickly from little information during imprint processing. We proposed two methods to predict the stamp lifetime from durability test data with a line-patterned mold. We characterized the contact angle, concentration of release resin, and the number of imprints from the data. Both of the proposed methods used machine learning. One method was binary classification, and the other was regression analysis. Under the binary classification method, the recall was 50% and the prediction showed that the recall becomes 0% when Gaussian random noise is added. Under the regression analysis, the prediction did not drastically change, with an approximately 100-fold increase in the mean absolute error. The results show that regression analysis is useful for predicting the lifetime of a line-patterned mold.

Keywords: UV-NIL, Machine learning, Release agent, Replica mold, Durability experiment

1. Introduction

A high throughput of nanoscale patterns can be achieved by ultraviolet nanoimprint lithography (UV-NIL) [1]. The durability of the release-coated imprint mold upon repeated transfer is important to allow an expensive mold to be used at low cost. However, repeated transfer eventually damages the master mold [2–5]. The use of a replica mold [6–8] is one method to avoid damaging the master mold. The ability to predict a master mold’s lifetime is important and requires a technology for quickly finding defects in the mold during repeated transfer.

Recently, Marumo developed a lifetime prediction method for a mold used in UV-NIL. The details are available elsewhere [9]; we here provide a brief explanation. In this method, a nanoscale line-and-space-patterned mold is used for repetitive UV-NIL transfer and mold surface repellency is evaluated on the basis of the water contact angle (CA). Capillary action occurs in the nanoscale line structure. The CA decreases with repeated transfers, and the water flows along the lines. Measuring the

CA in the x (along the lines) and y directions (across the lines) leads to different values. The water drop measured in the x direction is spread by capillary action; thus, the CA measured in the x direction is smaller than that measured in the y direction. This phenomenon is referred to as anisotropy of the CA. The lifetime can be estimated from the crossing point of the x direction (i.e., the saturated low-contact-angle value) curve and the corresponding y -direction curve.

Predicting physical phenomena based on the lifetime of a mold pattern is a problem suitable for a machine learning technique such as deep learning (DL) [10]. DL has been used in various physics and engineering fields, solid-state materials science [11], aided device simulation [12], multiphase flow detection [13], predicting two-phase flow patterns [14], predicting boiling heat transfer in helical coils [15], predicting boiling crisis [16], and the acoustic detection of boiling [17]. DL has also been used in nanoscience and technology research, nanoscience [18], defect classification in semiconductor

Received	March 20, 2022
Accepted	June 24, 2022

manufacturing [19], and computational nanotechnology [20].

In the present study, we assess the number of imprints with defects on the basis of anisotropic CAs in line patterns and the release agent concentration using a deep neural network (DNN).

2. Data acquisition of durability experiments of mold

The durability of a replica mold was evaluated by repeating the transfer using the machine (Mitsui Electric, Chiba, Japan) in Figure 1.

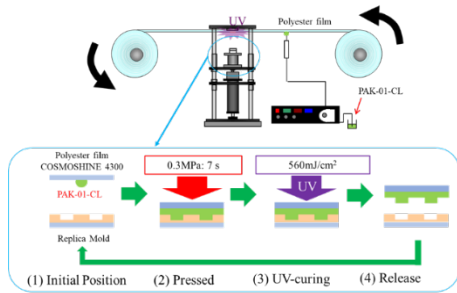


Fig. 1. Schematic of transfer endurance and the barge endurance device.

In the present work, replica molds were used for evaluation. The replica molds were fabricated as follows: A UV-curable resin, PAK-01-CL (Toyo Gosei, Tokyo, Japan), was dropped onto a Si master mold (Toppan, Tokyo, Japan) that had line-and-space (L&S) widths of 100 nm and a height of 200 nm. The PAK-01-CL was then filled on the Si master mold by pressing the film (Cosmoshine A4300; Toyobo, Osaka, Japan). The PAK-01-CL was then cured by UV irradiation at a dose of 120 mJ/cm². After the replica mold was fabricated, a mold release treatment was performed on its surface to improve mold release. Specifically, a 10 nm-thick Pt layer was deposited onto the mold surface and the mold was immersed in Optool DSX (Daikin, Osaka, Japan) for 24 h. In this experiment, Optool DSX concentrations of 0.02 wt% and 0.04 wt% were used. Later, heating was performed at 85°C for 30 min. The mold was then rinsed for 1 min with Optool HD-TH (Daikin, Osaka, Japan). The fabricated replica molds had L&S widths of 100 nm and a height of 200 nm.

Repeated transcription was performed using an automatic repetition machine (Fig. 1). PAK-01-CL was used as the resin during the durability test. PAK-01-CL was dispensed onto a web film (Fig. 1(1)), followed by pressurization at 0.3 MPa for 7 s to fill the mold with the resin (Fig. 1(2)). The pressure was maintained, and the mold was irradiated with UV light at a dose of 560 mJ/cm² (Fig. 1(3)). Finally, the mold was released (Fig.

1(4)), the transfer L&S patterns were fed forward, and new dispensed PAK-01-CL was placed over the mold (Fig. 1(1)). The machine could repeat this sequence automatically.

To measure the release performance of the replica mold, the water CA was measured (Drop Master 701, Kyowa Interface Science, Niiza City, Japan) after various imprint numbers. The water droplet volume used for the CA was measured was 2 μ L. In this experiment, the x -direction and y -direction CAs were measured by rotating the replica mold 90°.

3. Durability feature extraction

Figure 2 shows typical CAs measured in the x -direction and the y -direction when the Optool concentrations were 0.02 and 0.04 wt%. The data used for machine learning were four cases of an Optool concentration of 0.02 wt% and one case of an Optool concentration of 0.04 wt%. In both scenarios, the CA in the x direction decreased faster than that in the y direction. However, the cross point of the x, y direction could not be obtained because adhesion of the UV-curable resin occurred before the cross-point appeared. Thus, predicting the lifetime when a low concentration of the release agent is used is difficult. This difficulty is a limitation of this method. However, as shown in Fig. 2, the anisotropy of the CA was clearly measured and this trend provided deterioration data. To overcome the aforementioned limitation, we applied deep learning to the obtained data.

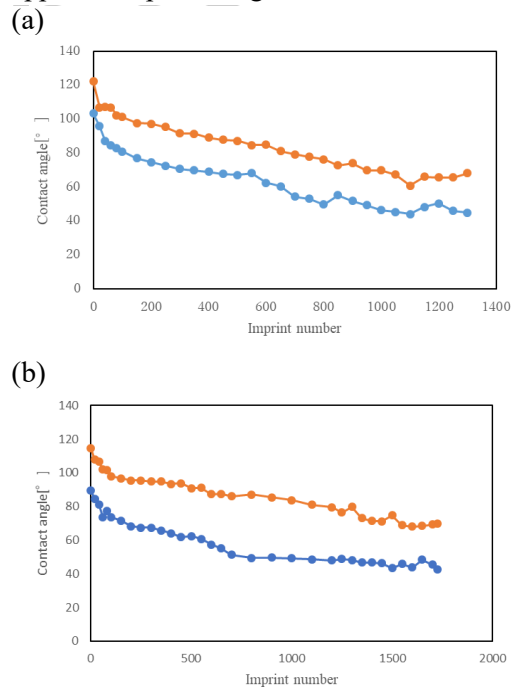


Fig. 2. Contact angles after imprints; the orange and blue lines are y - and x -direction data, respectively. (a) Release agent concentration = 0.02 wt%; (b) release agent concentration = 0.04 wt%.

4. Deep learning models

We propose a technique to construct a model by deep learning from the experimental data of a durability test and to predict the lifetime of a replica mold using unknown data. Model 1 is a method that predicts the lifetime on the basis of the presence of a defect with binary classification. Model 2 is a method that uses regression analysis to predict the lifetime using the number of imprints until a defect occurs. These models were implemented using Python (3.8.8), Keras library (2.6.0) with Tensorflow.

4.1. Method to predict the lifetime using the presence of a defect (Model 1).

A defect as a variable was established from durability experimental data. The defect state is represented as 1, and the non-defect state is represented as 0. The prediction model in which the presence of these states is classified was built. The Optool concentration, the imprint number, and the CAs in the x - and y -directions were used as the explanatory variables. A defect was used as the target variable. The constructed learning model is shown in Fig. 3. The batch size was 4, the output dimension was one, and the epoch number was 15. The Adam algorithm was used as the optimizer. Applying a sigmoid function to the output layer generated a defect probability output. A cross-entropy loss was solved using an estimated result and was labeled as training data; it was learned using a back-propagation method.

4.2. Method to predict the lifetime using the imprint number of times until the defect (Model 2).

A variable called R was set from the durability test experiments. R is defined as the number of imprint times T in the experiment following the use of the number of imprint times D produced by a defect:

$$R = D - T \quad (1)$$

This model was designed to predict the number of remaining possible imprints. The Optool concentration, imprint number, and the contact angles in the x -direction and the y -direction were used as explanatory variables. The remaining possible number of imprints was used as the target variable.

The constructed learning model is shown in Fig. 4. The batch size was 4, the output dimension was one, and the epoch number was 15. The RMSProp algorithm was used as an optimizer. Applying all the connection layers to the output layer gave the number of possible remaining imprints. The sum of

the squared error was solved using an estimated result and was labeled as training data; it was learned using a back-propagation method.

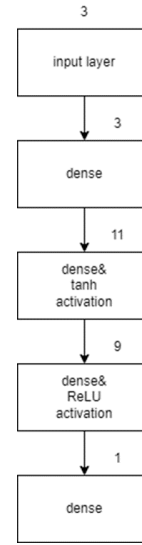


Fig. 3. Flow drawing of the network architecture of the DNN (Model 1).

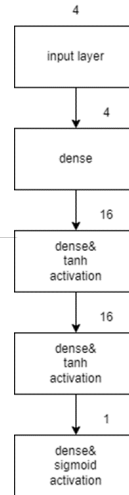


Fig. 4. Flow drawing of the network architecture of the DNN (Model 2).

5. Test data for machine learning

5.1. Procedure for Model 1.

This method estimates whether defects are introduced from unknown data. The number of experimental data points from the durability test was 226. The four variables—the Optool concentration, imprint number, CA in the x -direction, and the CA in the y -direction—were normalized. We divided the data so that test data became the learning data at a 7:3 ratio, where learning data were 158 cases and test data were 68 cases. In this case, the possibility that the precision of the machine learning model causes overlearning

should be considered because of the relatively small number of data. Therefore, we used stratified k -fold cross validation at $k = 3$. The number of data with no over-experimental data or defects was 218. The number of data with a defect was 8. Partiality caused overlearning; therefore, when learning, the weight of the class was made 1:3. Test data were predicted using the model that learned to calculate the precision of Model 1, an output value $p(1 | x)$, and then a threshold, $\theta_{th} = 0.5$. It was established and predicted that the value \hat{y} of a label can be decided as follows:

if $p(1|x) \geq 0.5$ then $\hat{y} = 1$ otherwise $\hat{y} = 0$.

(2)

5.2. Procedure for Model 2.

This method was designed to estimate the number of possible remaining imprints from unknown data. The number of experimental data from the durability test was 226. The four variables—the Optool concentration, imprint number, CA in the x -direction, and the CA in the y -direction—were normalized. We divided the data so that test data became the learning data at a 7:3 ratio, where learning data were 158 cases and test data were 68 cases. In this case, we considered the possibility that the precision of the machine learning model caused overlearning because of the limited number of data. Therefore, we used stratified k -fold cross validation at $k = 3$.

6. Results and discussion

6.1. Model 1.

The predicted values of the learning model and the values of the test data are shown in Table 1. The precision, recall, F-measured, and the accuracy are summarized in Table 2. In Table 2, the recall to express a ratio of the object that could predict it, which was 50%, is low among defects in the experimental values. Gaussian noise was added only to the test data, and the change in the correct answer rate was observed when the standard deviation changed. The change in accuracy with Gaussian noise is shown in Figure 5. The recall with Gaussian noise is shown in Figure 6. When the standard deviation of Gaussian noise was 0.1, the accuracy began to decrease, reaching ~94 % at 0.2. When the standard deviation was 0.2, the recall was 0%.

Table 1. Confusion matrix.

	Actual: With pattern defect	Actual: Without pattern defect
Predicted: With pattern defect	1	1
Predicted: Without pattern defect	1	65

Table 2. Precision, recall, F-measure, and accuracy.

	Value
Precision	0.5
Recall	0.5
F-measure	0.5
Accuracy	0.97

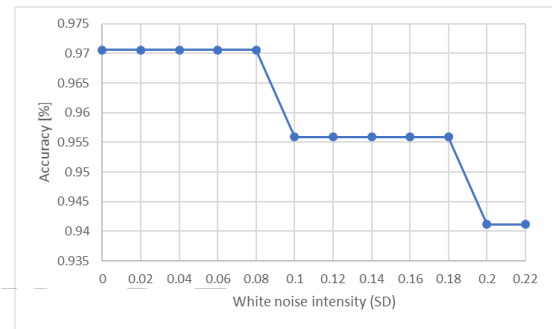


Fig. 5. Accuracy versus white noise intensity (SD).

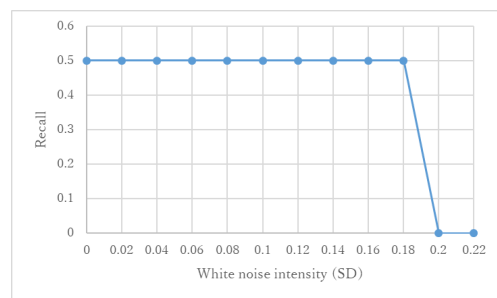


Fig. 6. Recall versus white noise intensity (SD).

6.2. Model 2.

Figure 7 shows a scatter plot for the true and predicted number of imprints. Note that the straight line represents predicted and original data with the same value. The calculation result does not greatly deviate from the prediction.

Figure 8 shows the averaged absolute error versus the white noise intensity (SD), and Figure 9 shows the coefficient of determination versus the white

noise intensity (SD). The calculated mean absolute error and coefficient of determination obtained using the prediction and experiment data are tabulated in Table 3. The coefficient of determination is 0.96, indicating that the prediction is in good agreement with the true data. With increasing Gaussian noise (SD), the mean absolute error increases and the decision coefficient becomes small.

Table 3. Mean absolute error and coefficient of determination.

	Value
Mean absolute error	121.3
Coefficient of determination	0.9556

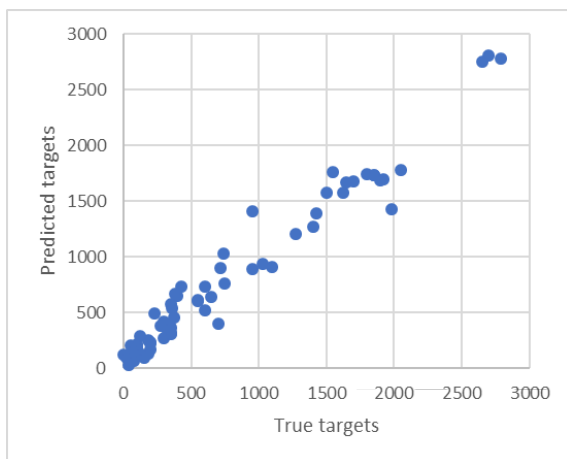


Fig. 7. Scatter plot for the true and predicted number of imprints.

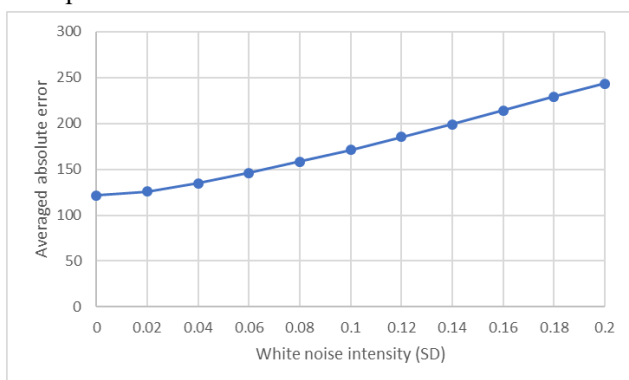


Fig. 8. Averaged absolute error versus white noise intensity (SD).

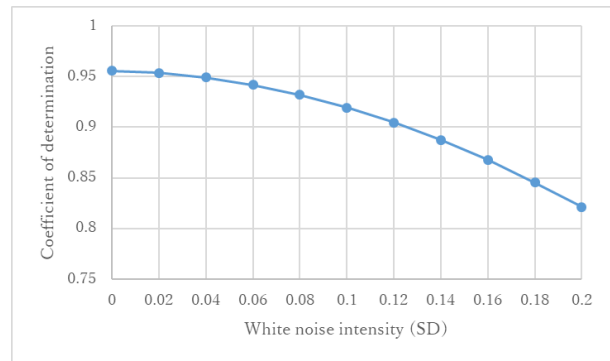


Fig. 9. Coefficient of determination versus white noise intensity (SD).

7. Conclusion

In this study, a deep learning model trained using durability test data was suggested as a technique to predict the lifespan of a replica mold.

The recall to express a ratio of the object able to predict it was low (50%) and was 0% in the case of 0.2 standard deviations at the time of the noise addition. Therefore, in the data with defects of Model 1, the model was revealed to be weak with respect to measurement error. In Model 2, the decision coefficient was very high and the behavior where the decision coefficient suddenly decreased to nearly 100 times the mean absolute errors was not observed even when the Gaussian noise increased. Given these results, we speculate that Model 2 is more useful than Model 1 for predicting the lifetime of a mold.

References

1. S.Y.C hou, P.R.Krauss, and P.J. Renstrom, *J. Vac. Sci. Technol. B*, **14** (1996) 4129.
2. D. Yamashita, J. Taniguchi, H. Suzuki, *Microelectron. Eng.*, **97** (2012) 109.
3. G.H. Jeong, J.K. Park, K.K. Lee, J.H. Jang, C.H. Lee, H.B. Kang, C.W. Yang, S.J. Suh, *Microelectron. Eng.*, **87** (2010) 51.
4. E.J. Jang, Y.B. Park, H.J. Lee, D.G. Choi, J.H. Jeong, E.-S. Lee, S. Hyun, *Int. J. Adhesion Adhesives.*, **29** (2009) 662.
5. H. Sun, J. Liu, P. Gu, D. Chen, *App. Surf. Sci.*, **254** (2008) 2955.
6. M. Muhlberger, I. Bergmair, A. Klukowska, A. Kolander, H. Leichtfrieda, E. Platzgummer, H. Loeschner, C. Ebm, G. Grutzner, R. Schoftner, *Microelectron. Eng.*, **86** (2009) 691.
7. N. Tucher, O. Hohn, H. Hauser, C. Muller, B. Blasi, *Microelectron. Eng.*, **180** (2017) 40.
8. A. Schleunitz, M. Vogler, I. Fernandez-Cuesta, H. Schiff, G. Gruetzner, *Photopolymer*, **26** (2013) 119.

9. M. Tetsuma, S. Hiwasa, and J. Taniguchi, *Nanomaterials*, **10**, (2020)1956.
10. Y. LeCun, Y. Bengio, and G. Hinton, *Nature* **521**, (2015) 436.
11. J. Schmidt, M. R. G. Marques, S. Botti, and M. A. L. Marques, *npj Comput Mater*, **5** (2019) 83.
12. C. Akbar, Y. Li, W. Li Sung, *IEEE Transactions on Electron Devices* **68**,(2021) 5490.
13. Feng, L., Natu, S., Som de Cerff Edmonds, V. et al. , *Nat Commun*, **13** (2022) 567.
14. H. B. Arteaga-Arteaga, A. Mora-Rubio, F. Florez, N. Murcia-Orjuela, C. E. Diaz-Ortega, S. Orozco-Arias, M. delaPava, M. A. Bravo-Ortiz, M. Robinson, P. Guillen-Rondon, and R. Tabares-Soto, *PeerJ Comput Sci.* (2021) 7:e798.
15. X. Liang, Y. Xie, R. Day, X. Meng, H. Wu, *Int. J. Heat Mass Transf.* **166** (2021)1207.
- 16.K. N. R. Sinha, V. Kumar, N.. Kumar, A. Thakur, and R. Raj, *Cell Reports Physical Science*, **2** (2021) 100382.
17. Y. Ueki, K. Ara, *Int. Commun. Heat Mass Transf.* **129**, (2021),105675.
18. K. A. Brown, S. Brittman, N. Maccaferri, D. Jariwala, and U. Celano, *Nano Letters* **20** (2020) 2.
19. K. Imoto, T. Nakai, T. Ike, K. Haruki and Y. Sato, 2018 International Symposium on Semiconductor Manufacturing (ISSM), (2018)1.
20. W. Liu, Y. Wu, Y. Hong, Z. Zhang, Y. Yue, and J. Zhang, *Nanotechnology* **33** (2022) 162501.

Fabrication of Freestanding Double-sided Through-hole Electrode Films using Imprint Technique

Atsuhiko Furuta¹, Jun Taniguchi^{1*}

¹ *Department of Applied Electronics, Tokyo University of Science,
6-3-1 Niijuku, Katsushika-ku, Tokyo 125-8585, Japan
junt@te.noda.tus.ac.jp

Recently, flexible electronic devices such as printed electronics have attracted attention. Interposers are required to flexibly connect circuit devices. However, most conventional interposers are not flexible because they are composed of silicon or glass substrates. To solve this problem, we developed a manufacturing process for flexible interposers. We used photolithography to fabricate columnar master molds with diameters of 10 μm and 20 μm . After applying a release agent to the master molds, hole patterns were produced using UV nanoimprint lithography. The holes were filled with silver ink. The flexible interposer was then completed.

Keywords: Flexible through electrode, Nanoimprint lithography (NIL), Through hole, Photolithography

1. Introduction

Flexible devices have attracted considerable attention in recent years [1]. Flexible devices are durable, lightweight devices that can be bent. The advantages of flexible device fabrication include high productivity because cooling and vacuum processes are not required, and a reduced initial capital investment because of the simplified processes [2–3]. In addition, as miniaturization continues to advance, devices with multiple functions over a small area are required. Although miniaturization has been progressing, there is a limit to what can be achieved by miniaturization alone. Thus, attention is being given to multilayer structures that provide multiple functions on a single substrate [4–6]. A through-hole is necessary to connect devices when fabricating a multilayer structure. However, a through-hole fabrication method for flexible substrates has not yet been established [7]. Nanoimprint and UV nanoimprint lithography are suitable techniques for fabricating through-holes on flexible substrates [8–12]. In this study, a master mold was fabricated using photolithography, and a concave replica mold was fabricated using UV nanoimprint lithography. A convex mold was then fabricated from the concave mold, and a through-hole was fabricated from the convex mold. Residual film formation has been an

issue in the past [13–16].

In this study, the through-holes were filled with silver ink to fabricate a through-hole electrode, and a flexible through-hole electrode was fabricated using a freestanding film [17–18]. The goal was to fabricate a film thickness that could be handled and to fabricate the film in two steps in order to achieve versatility by changing the diameter of the top and bottom surfaces. The fabricated through-hole electrode [19–20] was confirmed to be a through-hole by observing the silver ink from both the top and bottom surfaces.

2. Materials and methods

2.1 Master mold production

SU-8 3025 (Nippon Kayaku Co., Ltd.) was dropped onto a 2 cm Si square that had been washed with acetone (Gordo Co., Ltd.) and ethanol (Showa Chemical Co., Ltd.) at 500 rpm for 5 s at the first rotation and 10000 rpm at the main rotation. Spin coating was performed for 60 s (Fig. 1 (a)).

Pre-baking was performed at 95 °C for 10 min (Fig. 1 (b)). This was followed by incubation for 5 min at room temperature. Next, exposure was performed by irradiating with ultraviolet rays through a hole-type mask with a diameter of 20 μm and pitch of 40 μm at an exposure amount of 40

Received April 1, 2022
Accepted June 24, 2022

mJ/cm² (Fig. 1 (c)). After irradiation, PEB was performed at 95 °C for 10 min (Fig. 1 (d)). It was then immersed in an SU-8 Developer (Nippon Kayaku Co., Ltd.) for 5 min and developed. Thereafter, rinsing was performed using IPA (Kishida Chemical Co., Ltd.) and pure water (Fig. 1 (e)). Finally, hard baking was performed at 200 °C for 30 min (Fig. 1 (f)).

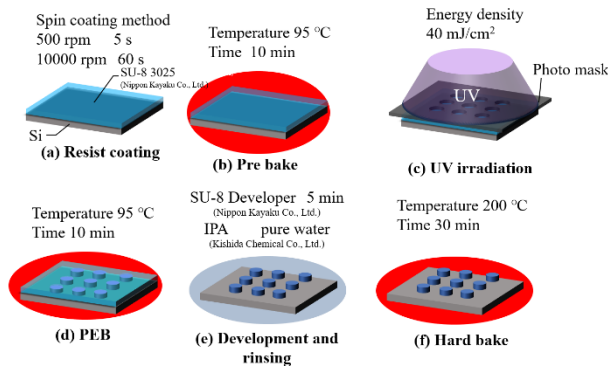


Fig. 1. Pattern of master molds.

2.2 Mold release processing

To form a thin film of platinum on the top surface of the prepared master mold, platinum was sputtered (Fig. 2(a)). It was then immersed in Optool DSX 1.0% (Daikin Industries, Ltd.) for 3 h to add a mold release agent (Fig. 2(b)). Next, baking was performed at 120 °C for 5 min to remove the moisture (Fig. 2(c)). Finally, it was immersed in Novec 7300 for 5 min and washed with water (Fig. 2(d)).

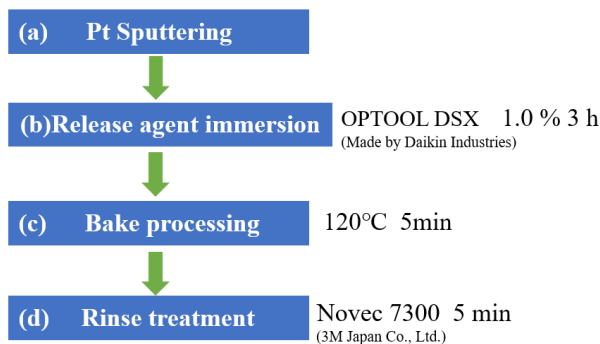


Fig. 2. Mold release processing.

2.3 Making replica molds

SU-8 3025 (Nippon Kayaku Co., Ltd.) was dropped onto the prepared master mold, and Cosmo Shine A4300 (Toyo Gosei Co., Ltd.) was held in place for 10 min while applying pressure at 0.5 MPa (Fig. 3 (a)). Thereafter, it was irradiated with ultraviolet rays at an exposure of 180 mJ/cm² (Fig. 3 (b)). The sample was then baked at 95 °C for 10 min (Fig. 3 (c)). The master mold was

peeled off to produce a hole-type replica mold (Fig. 3 (d)). This replica mold was also subjected to a release treatment in the same manner as the master mold.

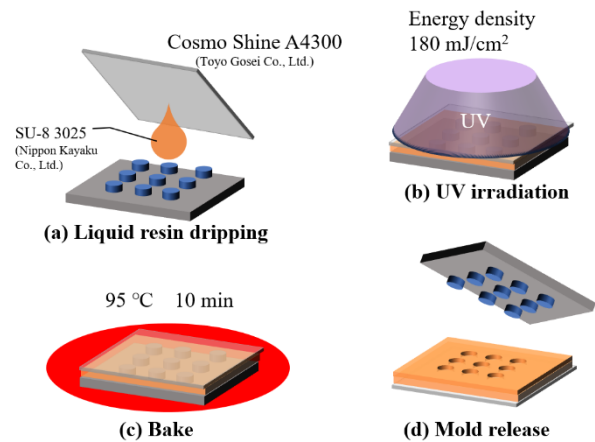


Fig. 3. Making replica molds.

2.4 Transcription by horizontal loading device

UV curable resin (PARQIT OEX-028-X433-3, Autex Co., Ltd.) was placed on the Cosmo Shine A4300 (Toyo Gosei Co., Ltd.) (Fig. 4 (a)), and a replica mold was installed (Fig. 4 (b)). The resin was filled at a pressure of 6 MPa for 10 min (Fig. 4 (c)). Thereafter, ultraviolet rays were applied for 5 min for curing (Fig. 4 (d)). Thus, a convex mold was produced (Fig. 4 (e)).

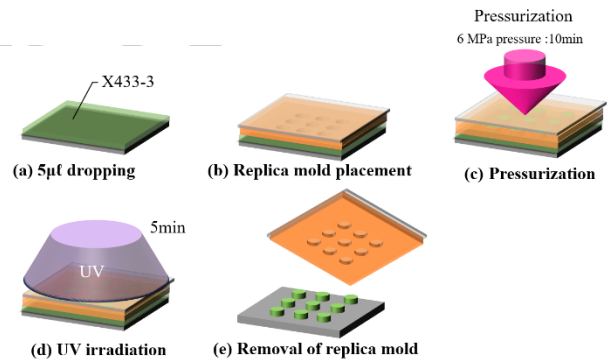


Fig. 4. Transcription by horizontal loading device.

2.5 Transfer by parallel plate

First, 0.5 µL of UV curable resin (PAK-01-CL; Toyo Gosei Co., Ltd.) was dropped on the Cosmo Shine A4300 (Toyo Gosei Co., Ltd.) (Fig. 5 (a)). Then, replica mold was placed on it (Fig. 5(b)). Subsequently, liquid transfer imprint lithography (LTIL) [14] was performed (Fig. 5(c)). This process can remove excess UV curable resin. It was placed on Si and charged at a pressure of 3 MPa for 10 min (Fig. 5 (d)). Thereafter, the resin was cured by irradiation with UV rays for 2 min (Fig. 5 (e)). Then, the replica mold was removed, and a concave mold was obtained (Fig. 5 (f)). The

concave mold was filled with silver ink (S-CS21303, Techno Alpha Co., Ltd.) (Fig.5 (g)), and the surface was rubbed with a Kim towel to remove the excess silver ink (Fig. 5 (h)). Thereafter, the samples were baked at 120 °C for 5 min (Fig. 5 (i)).

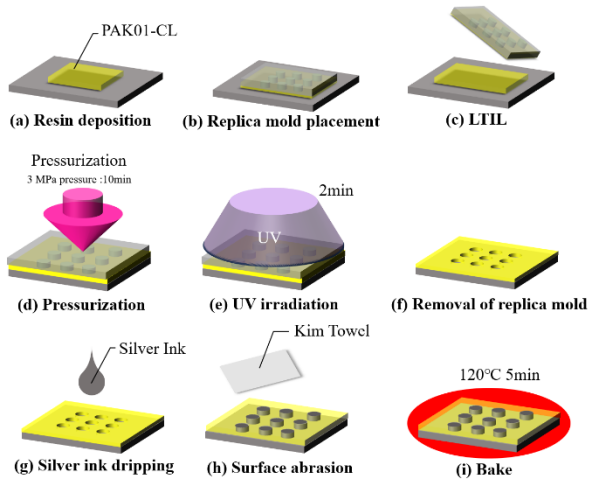


Fig. 5. Transfer by parallel plate.

2.6 Fabrication of first stage of two-stage through-hole electrode

The first two-stage through-hole electrode was fabricated. A drop of UV-curable resin (PARQIT OEX-073-X1, Autex Co., Ltd.) was dropped onto quartz glass (Fig. 6 (a)). A liquid separation operation was then performed using a film (Fig. 6 (b)), and the resin was cured at an exposure of 10 J/cm² (Fig. 6 (c)). The replica mold was released and through-holes were fabricated (Fig. 6 (d)).

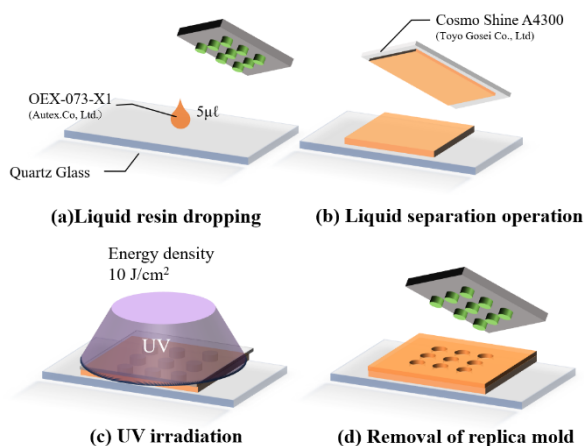


Fig. 6. Fabrication of first stage.

2.7 Fabrication of second stage of two-stage through-hole electrode

The second stage of the two-stage through-hole electrode was fabricated by first dropping 0.5 µL of UV-curable resin (PAK-01-CL; Toyo Gosei Co.,

Ltd.) onto the fabricated one-stage through-hole electrode (Fig. 7 (a)). A replica mold with a diameter of 20 µm was placed on top (Fig. 7 (b)). This was aligned using an optical microscope. The replica mold was then released after UV irradiation and curing of the resin (Figs. 7 (c) and (d), respectively). A concave mold was filled with silver ink (S-CS21303, Techno Alpha Co., Ltd.) (Fig. 7 (e)), and the surface was rubbed with a Kim towel and cellophane tape to remove the excess silver ink (Fig. 7 (f)). Thereafter, the samples were baked at 200 °C for 20 min (Fig. 7 (g)). Each was molded from quartz glass and made into a freestanding film (Fig. 7 (h)).

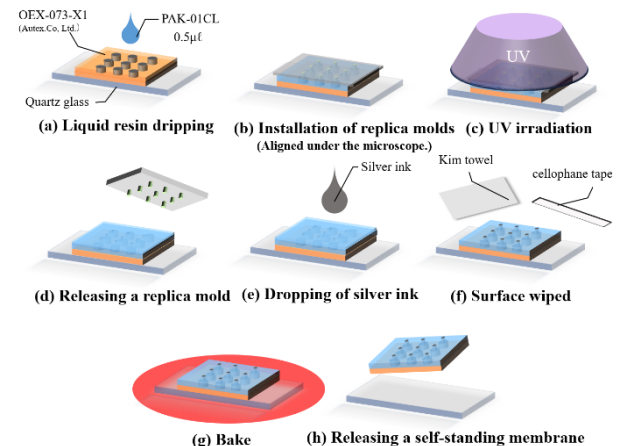


Fig. 7. Fabrication of second stage.

3. Result and discussion

3.1 Master mold production

Fig. 8 shows a scanning electron microscopy (SEM) image of the master mold obtained. This operation created a pillar pattern. The height of the pillars of the master mold was approximately 9.5 µm, and the pitch was 49.1 µm (Fig. 8 (a)). The depth of the hole in the replica mold was approximately 9.1 µm, and the pitch was 67.1 µm (Fig. 8 (b)). The height of the pillars of the replica mold was approximately 9.5 µm, and the pitch was 55.0 µm (Fig. 8 (c)).

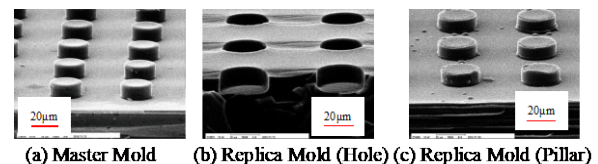


Fig. 8. SEM image of master mold.

3.2 Transcription by parallel plate device

Fig. 9 shows SEM images of the through-hole and through-electrode. The depth of the hole in the master mold was approximately 8.6 µm, and the pitch was 57.7 µm. Fig. 9 (b) shows an image of

the hole filled with silver ink.

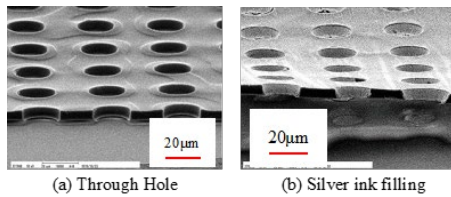


Fig. 9. SEM images of through-hole and through-electrode.

3.3 Fabrication of second stage of two-stage through-hole electrode

It was approximately 4 mm square and sufficiently transparent to see through the back (Fig. 10 (a)). Observation using an optical microscope confirmed that the alignment was correct (Fig. 10 (b)).

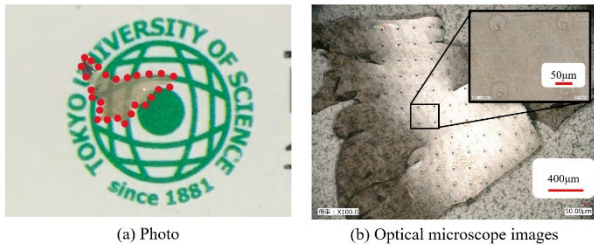


Fig. 10. Observation results for two-stage through-hole electrode freestanding film.

From the top surface, it was observed that the hole was filled with silver ink in a diameter of 20 μm (Fig. 11 (a)). The thickness of the upper section was approximately 8 μm . As observed from the cross section, the film thickness was approximately 28 μm (Fig. 11 (b)). From the bottom surface, it could be observed that the film was filled with silver ink in a diameter of 50 μm (Fig. 11 (c)). The thickness of the lower section was approximately 20 μm .

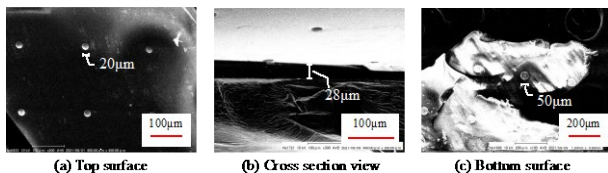


Fig. 11. SEM images of two-stage through-hole electrode freestanding film.

4. Conclusion

It was possible to observe a top surface area with a diameter of 20 μm and bottom surface area with a diameter of 50 μm . Because the film thickness (28 μm) was the same as the sum of the respective film thicknesses (8 μm , 20 μm), we were able to fabricate a freestanding film with a two-layer through-hole electrode structure.

References

1. T. Kamata, *J. Jpn. Inst. Electron. Packag.*, **14** (2011) 466.
2. N. B. T. Yusof and J. Taniguchi, *Microelectron. Eng.*, **110** (2013) 163.
3. V. Subramanian, P. C. Chang, D. Huang, J. B. Lee, S. E. Molesa, D. R. Redinger, and S. K. Volkman, *Proc. 19th Int. Conf. VLSI Des.*, (2006) 1.
4. G. van der Plas, et al., *IEEE J. Solid-State Circuits*, **46** (2011) 293.
5. I. Jeerapan and S. Poorahong, *J. Electrochem. Soc.*, **167** (2020) 037573.
6. Y. C. Tan, C. M. Tan, X. W. Zhang, T. C. Chai, and D. Q. Yu, *Microelectron. Reliab.*, **50** (2010) 1336.
7. X. Wang, M. Xiong, Z. Chen, B. Li, Y. Yan, and Y. Ding, *IEEE Electron Device Lett.*, **37** (2015) 216.
8. S. Y. Chou, P. R. Krauss, and P. J. Renstrom, *J. Vac. Sci. Technol. B*, **14** (1996) 4129.
9. J. Haisma, M. Verheijen, K. van den Heuvel, and J. van den Berg, *J. Vac. Sci. Technol. B*, **14** (1996) 4124.
10. J. Taniguchi, Y. Kamiya, T. Ohsaki, and N. Sakai, *J. Photopolym. Sci. Technol.*, **22** (2009) 175.
11. J. Taniguchi, Y. Kamiya, and N. Unno, *J. Photopolym. Sci. Technol.*, **24** (2011) 105.
12. N. Unno and J. Taniguchi, *J. Photopolym. Sci. Technol.*, **24** (2011) 57.
13. S. Gillesac, M. Meier, M. Prömpers, A. van der Hart, C. Kügeler, A. Offenhäusser, and D. Mayerac, *Microelectron. Eng.*, **86**, (2009) 661.
14. N. Koo, J. W. Kim, M. Otto, C. Moormann, and H. Kurz, *J. Vac. Sci. Technol. B*, **29** (2011) 06FC12.
15. J. Taniguchi and N. Unno, *J. Photopolym. Sci. Technol.*, **28** (2015) 547.
16. H. Ueda and J. Taniguchi, *J. Photopolym. Sci. Technol.*, **31** (2018) 283.
17. J. Taniguchi and T. Tsuji, *J. Photopolym. Sci. Technol.*, **29** (2016) 221.
18. A. Watanabe, G. Qin, and J. Cai, *J. Photopolym. Sci. Technol.*, **28** (2015) 99.
19. R. Ji, M. Hornug, M. A. Verschuuren, R. van de Laar, J. van Eekelen, U. Plachetka, M. Moeller, and C. Moormann, *Microelectron. Eng.*, **87** (2010) 963.
20. H. Wadayama, T. Okabe, and J. Taniguchi, *Microelectron. Eng.*, **193** (2018) 47.

Droplet-Dispensed Ultraviolet Nanoimprint Lithography in Mixed Condensable Gas of Trans-1,3,3,3-Tetrafluoropropene and Trans-1-Chloro-3,3,3-Trifluoropropene

Kenta Suzuki^{1*}, Tatsuya Okawa¹, and Sung-Won Youn¹

¹ *Device Technology Research Institute,
National Institute of Advanced Industrial Science and Technology (AIST),
Tsukuba, Ibaraki 305-8564, Japan,
ke.suzuki@aist.go.jp

Droplet-dispensed ultraviolet nanoimprint lithography (UV-NIL) in helium enables adaptive material deposition to match pattern variations in a mold. It is a potential lithographic technology for semiconductor devices, but process throughput is an issue. UV-NIL in trans-1,3,3,3-tetrafluoro-propene (TFP) and 1-chloro-3,3,3-trifluoropropene (CTFP) gases has enabled bubble-free and high-throughput processes for spin-coated films. This study investigated the applicability of a mixed condensable TFP/CTFP gas to droplet-dispensed UV-NIL. The filling time in a local area of the mold in a mixed condensable gas atmosphere was as low as 1/30th that in helium. Similarly, the filling in the entire mold was faster in a mixed condensable gas atmosphere than in helium, and micropatterns could be filled within 1.6 s. When the droplets were exposed to the mixed TFP/CTFP gas, the droplet diameter of 108 μm increased to 127 μm owing to gas absorption. The quality obtained for an L/S 90-nm pattern was the same as for the pattern of a spin-coated film, but the line width of patterns fabricated by UV-NIL in ambient TFP/CTFP was 6 nm narrower than that for UV-NIL in He.

Keywords: Nanoimprint lithography, Droplet, Condensable gas, Trans-1,3,3,3-Tetrafluoropropene, Trans-1-Chloro-3,3,3-Trifluoropropene

1. Introduction

Ultraviolet nanoimprint lithography (UV-NIL)[1–3] is a recently developed technology that facilitates low-cost nanofabrication. UV-NIL has strong potential for application in producing large-scale integrated circuits and wire grid polarizers[4–5]. Bubble-free filling is an important issue for achieving high-throughput mass production using UV-NIL. Although bubble-free filling can be accomplished by performing UV-NIL under vacuum, non-vacuum processes are desirable because of their lower equipment and operation costs.

Droplet-dispensed UV-NIL, known as J-FIL[5–8], is distinct from other imprint lithographic processes because it uses inkjet techniques to dispense picoliter volumes of low-viscosity UV curable resists. This enables adaptive material deposition to

match pattern variations in the mold. This, combined with low-viscosity resist formulations (<10 cP), leads to high-throughput processes. Helium gas flow is applied during the mold contact phase to avoid trapping of air bubbles between the mold and the resist [9-10].

UV-NIL in a condensable gas such as 1,1,1,3,3-pentafluoro-propane (PFP) is one of the most promising methods for bubble-free UV-NIL[11-12]. Not only can using a condensable atmosphere achieve quick and bubble-free cavity filling[13], but its use is also beneficial because it decreases the viscosity of the UV-curable resin [14], decreases the amount of resin that sticks to the mold during demolding, and lowers the demolding force to approximately one-third of that when using helium [15-16]. During UV-NIL, the trapped condensable gas in the mold recess is compressed by the

Received	April 14, 2022
Accepted	June 24, 2022

imprinting. The volume of the trapped gas is inversely proportional to the gas pressure; however, this relationship breaks down when the pressure reaches the saturated vapor pressure of the trapped gas. The pressure remains constant as the volume of the trapped gas decreases by condensation (liquefaction). The trapped gas then becomes completely liquefied.

We have recently studied mixed condensable gases with a low GWP of <6 that have virtually zero ozone depletion potential. One is trans-1-chloro-3,3,3-trifluoropropene (CTFP)[16], which has a saturated vapor pressure of 0.13 MPa, as shown in Table I. The other is trans-1,3,3,3-tetrafluoropropene (TFP)[17-18], which has a higher saturated vapor pressure of 0.5 MPa. Bubble-free filling of a thin spin-coated film via UV-NIL has been successfully demonstrated in a TFP/CTFP atmosphere [19]. Fine line patterns with a width of 16 nm were obtained by UV-NIL of a spin-coated UV-curable resin with a high TFP fraction (>66%) in a TFP/CTFP mixed-gas atmosphere[20].

In this work, condensable gas (TFP/CTFP) processes were further studied to investigate the applicability to droplet-dispensed UV-NIL. The cavity-filling behavior of an inkjet-dropped resin and the NIL pattern quality were also studied.

Table I. Characteristics of CTFP, and TFP.

	CTFP	TFP
Molecular formula	(E)CF ₃ -CH=CClH	trans-CF ₃ CH=CHF
Molecular weight	130	114
Boiling point (°C)	19.0	-19.0
Saturated vapor pressure at 25 °C (MPa)	0.129	0.499

2. Experimental methods

During the nanoimprinting experiments, process gas was introduced into the space between a wafer substrate and a mold through two gas inlet slits at a predetermined flow rate. We prepared a mold holder unit with an opening at a position 17.5 mm away from the center of the mold for insertion of the oxygen probe. The cross-sectional area of the

double-slit gas inlet was 20 × 1 mm². The gas percentage is the complement of the air percentage, and the percentage of introduced gas (ambient gas) can be easily calculated from the oxygen concentration. The oxygen concentration was measured using a high-sensitivity oxygen probe (Ocean Optics HIOXY-R) and an oxygen sensing system (Ocean Optics NeoFox) on the basis of the phase shift between excitation and emission fluorescence [21].

The introduced gas concentration during the approach of the mold to the substrate was varied when the initial gap between the mold and the substrate was 2000 μm. The gases introduced were condensable CTFP ((E)CF₃-CH=CClH, HFO-1233zd) and TFP (trans-CF₃CH=CHF, HFO-1234ze).

Two types of quartz molds were prepared with dimensions of 7 × 7 mm². One consisted of line patterns with a width of 2.5 μm and depth of 90 nm to examine the filling speed of the resin. The other consisted of nanopatterns with a width of 70–500 nm and depth of 200 nm (NTT AT NIM-PHL80). The molds were treated with an anti-adhesion reagent.

A UV-curable resin (TOYO GOUSEI PAK-02) with a viscosity of 9 cP was dispensed on 4-inch silicon wafers. An inkjet system (SIJ Technology) was used to deposit 1024 droplets with a drop volume of 3.1 pL on the 7 × 7 mm² area, which had a drop pitch of 250 μm.

PAK-02 was also spin-coated on another 4-inch silicon wafer. Both coating methods were adjusted so that the film thickness was 130 nm after UV-NIL.

UV-NIL was carried out using a UV-NIL stepper (Sanmei ImpFlex200as) equipped with a gas introduction system and a conformable contact mechanism, known as a sample-on-flexible-thruster stage. The conditions used for UV-NIL were an imprint pressure of 0.1 MPa, exposure dose of 100 mJ/cm², and exposure time of 1 s. The introduced condensable gas mixture of TFP/CTFP was controlled at 0.5/0.1 L/min using two mass flow controllers. The He gas flow rate was 1.2 L/min.

In UV-NIL, pattern cavity filling was recorded using two observation systems at a frame rate of 30 fps. One recorded at a full field of the 7 × 7 mm² mold with a dark-field illumination monitoring (DFIM) system [2] using a camera (Panasonic DC-

GH5) and a green light-emitting diode (LED) (Hayashi-Repic HDS50G). The other recorded at a local area ($1000 \times 750 \mu\text{m}^2$) in the center of the mold using a microscope system (Seiwa Optical MS-200-TWL).

Patterns fabricated by UV-NIL were inspected using a field-emission scanning electron microscope (FE-SEM; Hitachi, S-4800) at an accelerating voltage of 0.5 kV. To evaluate the line width, the SEM images were recorded without data compression in bitmap format with a resolution of 1280×960 pixels. The corresponding size of a pixel for the SEM images obtained at a magnification of 30,000 was 3.28 nm. Ten lines were selected at a given position in each nanoimprint die, and the average line widths were then calculated from the widths of the 800 scan lines analyzed with an edge detection program.

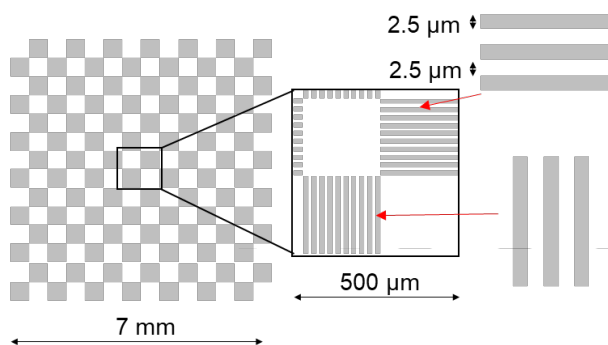


Fig. 1. Schematic design of the mold for evaluating cavity filling.

3. Results and discussion

Figure 2 shows the mixed condensable gas concentration calculated from the oxygen concentration measured when the gap between the mold and the wafer is changed. The flow rates of TFP and CTFP in the introduced condensable mixture were 0.5 and 0.1 L/min, respectively. The gas concentration was 55% for the widest gap of 2000 μm . When the gap was narrowed, the gas concentration increased. The TFP/CTFP gas concentration reached 99% for a gap of 800 μm , and when the gap was 700 μm or less, the gas concentration was 100%. The TFP/CTFP gas concentration during imprinting reached 100%. For a He gas flow rate of 1.2 L/min, the concentration was 100% for the 2000- μm gap. Because helium is light and diffuses easily, the flow rate was set higher

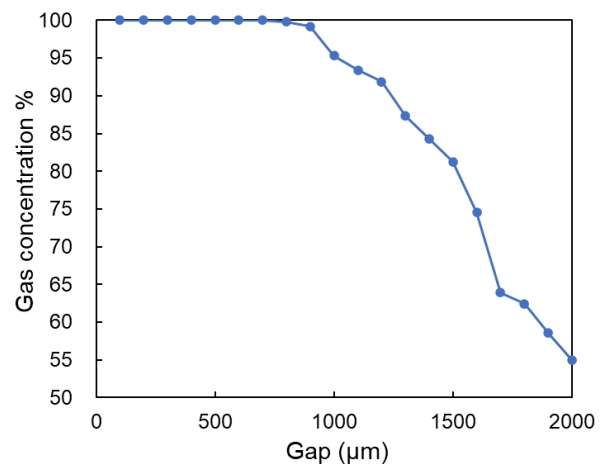


Fig. 2. Estimated TFP/CTFP gas concentration (at a flow rate of 0.5/0.1 L/min) for different gaps between the mold and wafer.

than that of the condensable gas.

Figure 3 shows microscope images of UV-curable resin droplets on the wafer after TFP/CTFP gas introduction. The droplet diameter increases while the droplet shape remains spherical.

Figure 4 shows a graph of the change in droplet diameter at 0–10 s (mold–wafer gap of 500–100 μm). The droplet diameter was initially 108 μm but increased as time passed and the gap decreased. For a gap of 100 μm , the droplet diameter was 127 μm , which was 19 μm larger than that at 0 s. We speculate that the cause of the increase in droplet diameter was absorption of the condensable gas into the UV-curable resin. However, in the helium atmosphere, the droplet diameter was constant at 105 μm . In helium, it seems that there is almost no gas absorption into the resin.

Figure 5 shows optical microscopy images of the resin surfaces nanoimprinted under the helium gas as a function of imprinting time. Droplets can be seen in contact with the mold and spreading. Bubble shrinkage was completed within 10 s because He can rapidly diffuse into the resin owing to its small molecular diameter (0.256 nm) [23].

As shown in Fig. 6, a capillary bridge [9] forms between the mold and the droplet before the mold and droplet come into contact with each other. The cavity filling in TFP/CTFP was much faster than in He, and the bubbles were completely eliminated within 0.3 s. Unlike the He case, the bubble shrinkage in TFP/CTFP is closely related to the

condensing mechanism of TFP/CTFP.

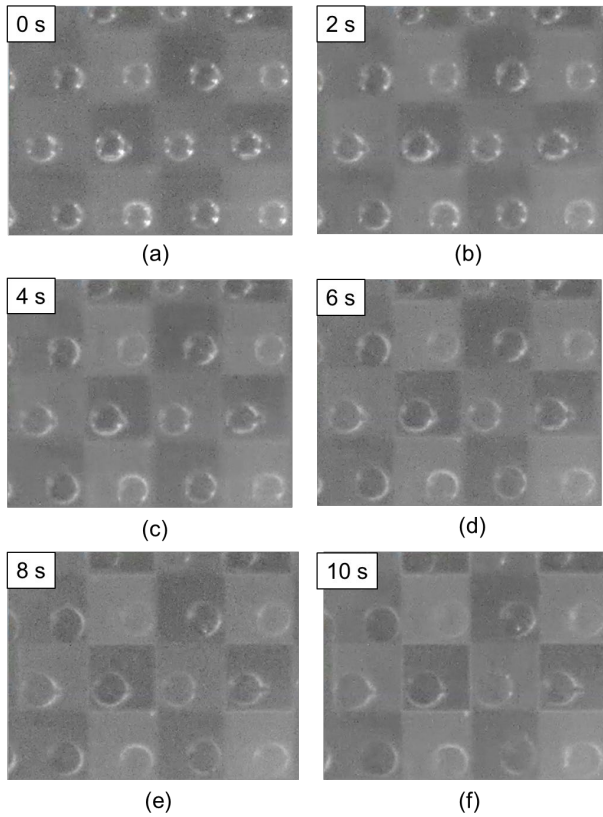


Fig. 3. Microscope image of UV-curable resin droplets on the wafer after TFP/CTFP gas introduction for an elapsed time/mold-wafer gap of (a) 0 s/500 μm , (b) 2 s/420 μm , (c) 4 s/340 μm , (d) 6 s/260 μm , (e) 8 s/180 μm , and (f) 10 s/100 μm .

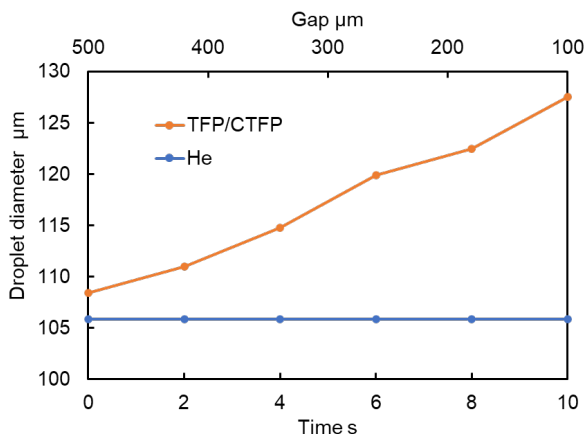


Fig. 4. Change in droplet diameter for a gap of 100–500 μm between the mold and wafer in TFP/CTFP and helium atmospheres.

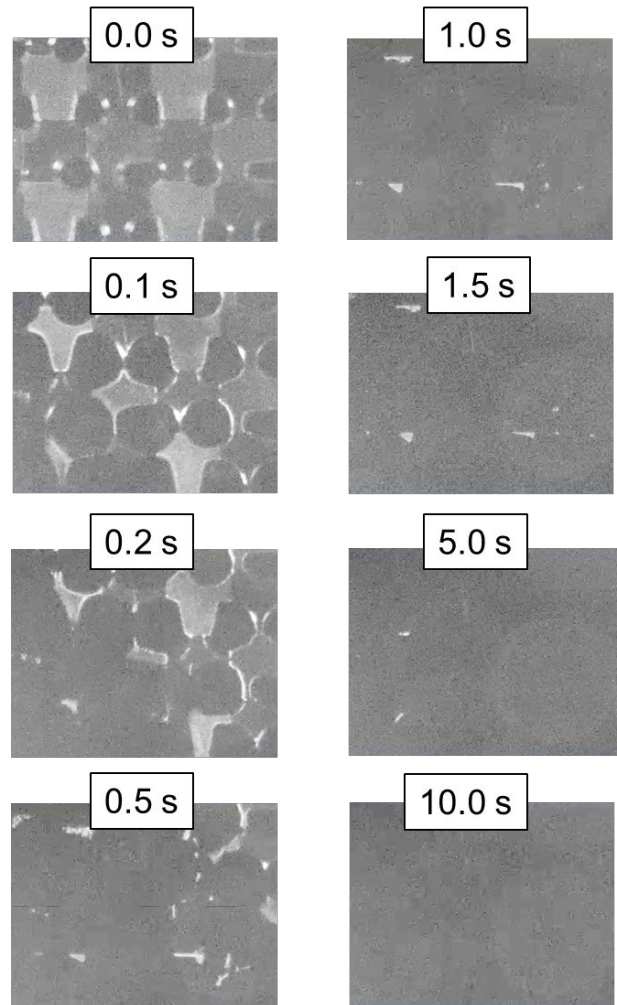


Fig. 5. Microscope images of bubble shrinkage in helium gas as a function of imprinting time.

Figure 7 shows consecutive dark-field illumination images of the entire mold filling process at 0–30 s in ambient helium gas. After the mold contact with the UV-curable resin slightly below the center of the mold, the contact area was spread at 1 second. However, helium gas bubbles remained in part of the cavity on the outer circumference of the mold, and disappeared after 30 seconds. Because the mold was in contact from its center, air bubbles tended to remain on the outer periphery.

Figure 8 shows consecutive dark-field illumination images of the entire mold filling process at 0–1.6 s in ambient TFP/CTFP gas. The droplet came into contact with a wide area of the mold in about 1.2 seconds, and filling was completed in the entire mold in 1.6 seconds. The filling speed was faster than in a helium atmosphere, demonstrating the

effectiveness of nanoimprinting under a mixed TFP/CTFP condensable gas even for fine inkjet-coated droplets.

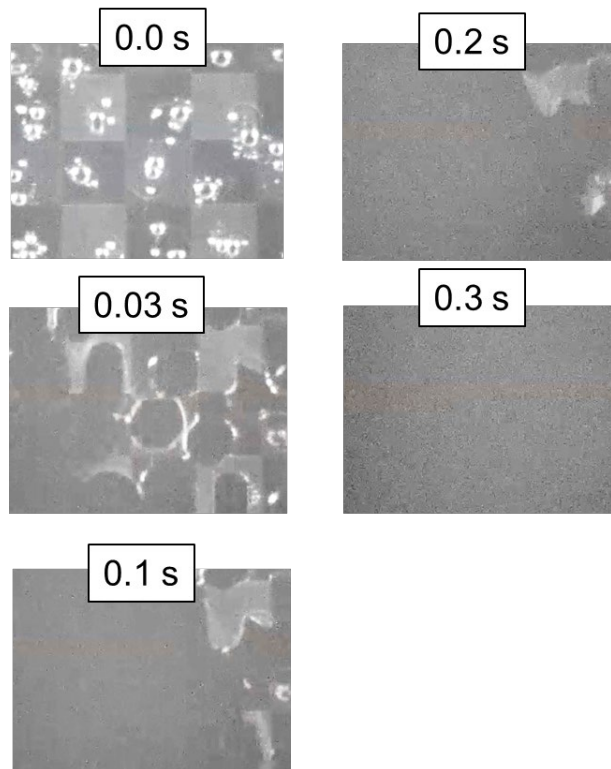


Fig. 6. Microscope images of bubble shrinkage in TFP/CTFP gas as a function of imprinting time.

Figure 9 shows SEM images of the UV-nanoimprinted PAK-02 with a nominal 90-nm 1:1 L/S pattern to compare spin-coated and droplet-dispensed UV-NIL in different gas conditions. All patterns were well fabricated under most conditions. The widths were 82.5, 82.2, 76.2, and 75.9 nm for nominal 90-nm L/S resin patterns for (a) droplet-dispensed UV-NIL in He, (b) spin-coated UV-NIL in He, (c) droplet-dispensed UV-NIL in TFP/CTFP, and (d) spin-coated UV-NIL in TFP/CTFP, respectively. There was no significant difference in line width between the patterns of droplet-dispensed

UV-NIL and spin-coated UV-NIL, but there was a difference of 6 nm in line width between the ambient He and ambient TFP/CTFP. The pattern of UV-NIL in TFP/CTFP was shrunk because PAK-02 with the UV-curable resin absorbs condensable gas.

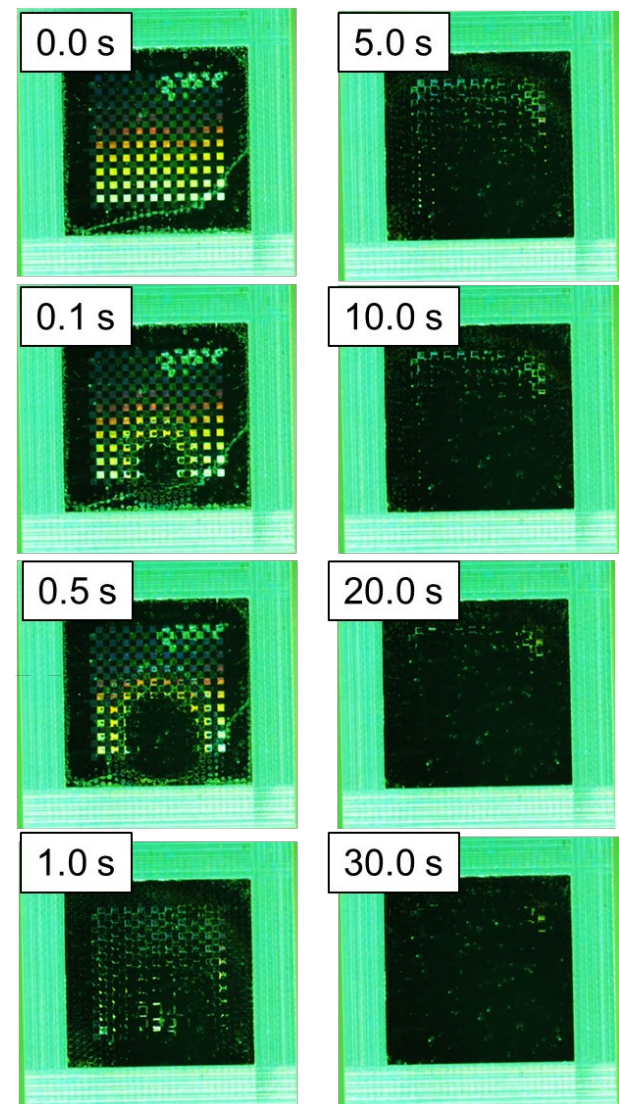


Fig. 7. Consecutive dark-field illumination images of the mold filling process at 0–30 s in ambient helium gas.

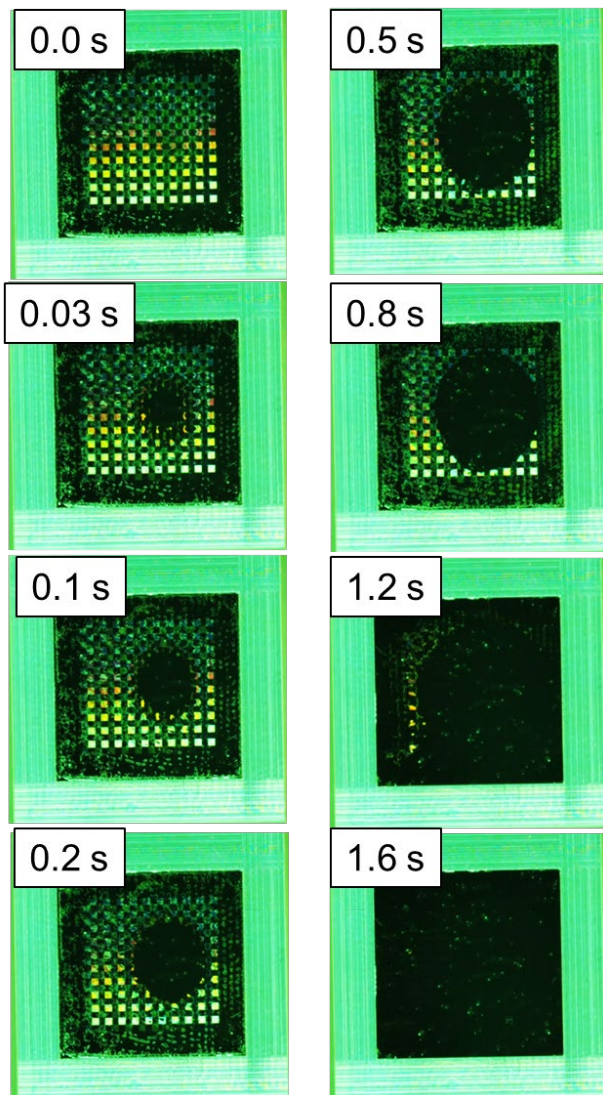


Fig. 8. Consecutive dark-field illumination images of the mold filling process at 0–1.6 s in ambient TFP/CTFP gas.

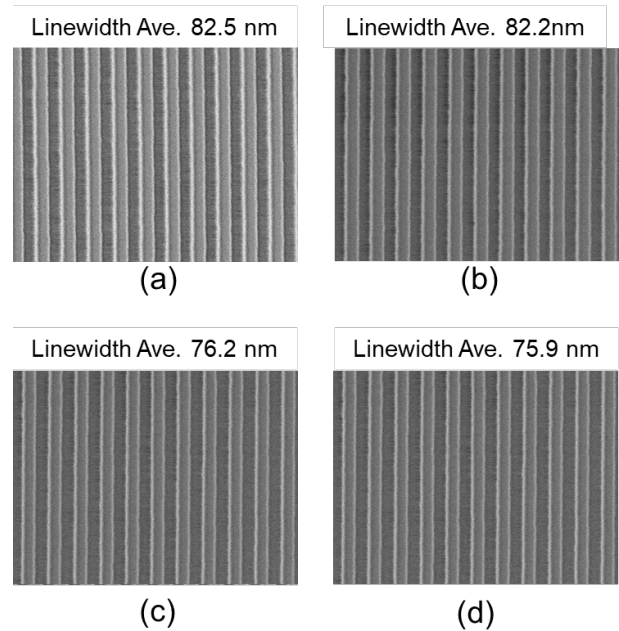


Fig. 9. SEM images of nominal 90-nm L/S resin patterns formed by (a) droplet-dispensed UV-NIL in He, (b) spin-coated UV-NIL in He, (c) droplet-dispensed UV-NIL in TFP/CTFP, and (d) spin-coated UV-NIL in TFP/CTFP.

4. Conclusion

In this paper, cavity filling was performed via droplet-dispensed UV-NIL in condensable CTFP/TFP gas and in ambient He, and the two cases were compared. The filling time was shorter in the TFP/CTFP atmosphere in both a local area and the entire mold. The difference in filling time is attributed to the difference between the gas permeation of helium and the liquefaction (condensation) of condensable gas due to mold pressing. A phenomenon was observed in which the droplet diameter changed owing to the introduction of condensable gas. The surface area of the resin droplets was larger than that for spin coating, so a difference in gas absorption was considered. There was no difference in nanopattern line width between inkjet and spin coating. However, the line width of patterns fabricated by UV-NIL in ambient TFP/CTFP was 6 nm narrower than for UV-NIL in He. Therefore, when a condensable gas is used, it is necessary to use a UV-curable resin with low gas absorption as in a spin-coated film.

Acknowledgement

This work was partly supported by the Japan Society for the Promotion of Science (JSPS) KAKENHI (Grant Number 19H02046).

References

1. J. Haisma, M. Verheijen, K. Heuvel, and J. Berg, *J. Vac. Sci. Technol. B*, **14** (1996) 4124.
2. M. Colburn, S. Johnson, M. Stewart, S. Damle, T. Bailey, B. Choi, M. Wedlake, T. Michaelson, S. V. Sreenivasan, J. Ekerdt, and C. G. Willson, *Proc. SPIE*, **3676** (1999) 379.
3. T. Higashiki, T. Nakasugi, and I. Yoneda, *J. Micro/Nanolith. MEMS MOEMS*, **10** (2011) 043008.
4. K. Takano, H. Yokoyama, A. Ichii, I. Morimoto, and M. Hangyo, *Opt. Lett.*, **36** (2011) 2665.
5. T. C. Bailey, D. J. Resnick, D. Mancini, K. J. Nordquist, W. J. Dauksher, E. Ainley, A. Talin, K. Gehoski, J. H. Baker, B. J. Choi, S. Johnson, M. Colburn, S. V. Sreenivasan, J. G. Ekerdt, and C. G. Willson, *Microelectron. Eng.* **61-62** (2002) 461-467.
6. K. Selenidis, J. Maltabes, I. McMackin, J. Perez, W. Martin, D. J. Resnick, S.V. Sreenivasan, *Proc. SPIE Vol. 6730, 67300F-1*, 2007.
7. T. Ito, K. Emoto, T. Takashima, K. Sakai, W. Liu, J. D. Young, Z. Ye and D. LaBrake, *J. Photopolym. Sci. Technol.*, **29** (2016) 159.
8. S.V. Sreenivasan, *Microsystems & Nanoengineering* **3**, (2017) 17075.
9. K. Usuki, *J. Photopolym. Sci. Technol.* **29** (2016) 45.
10. H. Kashiwagi, N. Sato, M. Hatano, W. Jung, T. Kono and T. Nakasugi, *Jpn. J. Appl. Phys.*, **57** (2018) 106507.
11. H. Hiroshima, M. Komuro, N. Kasahara, Y. Kurashima, J. Taniguchi, *Jpn. J. Appl. Phys.*, **42** (2003) 3849.
12. H. Hiroshima and M. Komuro, *Jpn. J. Appl. Phys.*, **46** (2007) 6391.
13. S.-W. Youn, Q. Wang, and H. Hiroshima, *Jpn. J. Appl. Phys.*, **49** (2010) 06GL06.
14. H. Hiroshima, H. Atobe, Q. Wang, *J. Photopolym. Sci. Technol.*, **23** (2010) 45.
15. H. Hiroshima, *J. Vac. Sci. Technol. B*, **27** (2009) 2862.
16. K. Suzuki, S. -W. Youn, and H. Hiroshima, *Jpn. J. Appl. Phys.*, **55** (2016) 076502.
17. Honeywell Technical Report, “Honeywell HFO-1234ze Blowing Agent”, October 2008.
18. K. Suzuki, S. -W. Youn, and H. Hiroshima, *Appl. Phys. Lett.*, **109** (2016) 143102.
19. K. Suzuki, S. -W. Youn, and H. Hiroshima, *J. Photopolym. Sci. Technol.*, **29** (2016) 181.
20. K. Suzuki, S. -W. Youn, and H. Hiroshima, *J. Photopolym. Sci. Technol.*, **32** (2019) 123.
21. Q. Wang, H. Hiroshima, K. Suzuki, and S. W. Youn, *Jpn. J. Appl. Phys.*, **51** (2012) 118002.
22. Q. Wang, H. Hiroshima, K. Suzuki, and S. W. Youn, *Microelectron. Eng.*, **136** (2015) 81.
23. T. Ohba, *Scientific Reports*, **6** (2016) 28992.

Flexible in-plane micro-supercapacitor prepared by laser annealing and ablation of a graphene/polyamide acid composite

Akira Watanabe¹, Ashiqur Rahman^{1,2}, Jinguang Cai³, and Md. Akhtaruzzaman⁴

¹*Institute of Multidisciplinary Research for Advanced Materials, Tohoku University, 2-1-1 Katahira, Aoba-ku, Sendai 980-8577, Japan*

²*Department of Electrical and Electronics Engineering, Faculty of Engineering, American International University Bangladesh, 408/1, Kuratoli Road, Kuril Dhaka-1229, Bangladesh*

³*Institute of Materials, China Academy of Engineering Physics, Jianguo 621908, Sichuan, P. R. China*

⁴*Solar Energy Research Institute (SERI), Universiti Kebangsaan Malaysia (UKM), 43600 Bangi, Selangor, Malaysia*

* *akira.watanabe.c6@tohoku.ac.jp*

An in-plane micro-supercapacitor (MSC) which has a unique interdigitated electrode structure with through-holes was developed by laser annealing and ablation of a carbon/polyamide acid composite coating on a polyimide film. The laser annealing of a composite film consisting of multi-layer graphene or activated carbon remarkably lowered the resistivity by laser carbonization of polyamide acid. The laser ablation was conducted to make an interdigitated electrode with a through-hole structure. The through-holes were effective to improve the capacitance of an in-plane MSC by enhancing the ion diffusion in carbon layer because the surface area of carbon layer can be increased using front and back sides of a polyimide film. An in-plane MSC consisting of an asymmetric interdigitated electrode which had an activated carbon composite layer on the front side and a multi-layer graphene composite on back side of a polyimide film showed the improvement of capacitance.

Keywords: Graphene, In-plane micro-supercapacitor, Laser direct writing, Laser annealing, Laser ablation, Flexible electronics.

1. Introduction

A supercapacitor has intermediate characteristics between secondary battery like a lithium ion battery (LIB) and capacitor. The supercapacitor is also called electric double-layer capacitor (EDLC) because the charge-discharge mechanism is based on the adsorption/desorption of the electrolyte ions through the electric double layer on the porous materials. The self-discharge of a supercapacitor caused by desorption of the electrolyte ions in micro- and nano-porous carbons is extremely lower than that of a capacitor by charge separation in parallel-plate electrodes. Although the energy density of a supercapacitor is usually lower than

LIB, it has advantages such as a short charging time and almost limitless product life, which are not found with LIB. Such features are suitable to an electronic device which harvests a low-level power from environmental energy source. A LIB is less compatible with fluctuated low-level power source because the charge-discharge mechanism is based on redox reactions of electrodes.

In-plane micro-supercapacitor (MSC) is a recent interest in energy storage devices towards flexible and wearable devices. The difference between conventional supercapacitor and in-plane MSC is the electrode structure. The structure of a conventional supercapacitor is sandwich-type

Received	March 29, 2022
Accepted	June 24, 2022

which consists of two metal electrodes and a separator. On the other hand, an in-plane MSC consisting of an in-plane interdigitated electrode needs no separator. In the early stage of in-plane MSC studies, in-plane interdigitated electrodes were fabricated by photolithography which needs multiple steps with a high process cost. A recent innovation for in-plane MSC is caused by laser processing for the interdigitated electrode formation [1-6]. The laser direct writing of a conductive carbon interdigitated electrode on a polymer film is one-step and low-cost method. In previous papers, we have reported flexible in-plane MSCs prepared by laser direct writing using a CW blue-violet semiconductor laser [4-6]. A micro-interdigitated electrode prepared by laser-carbonization of a polyimide (PI) film works both as a conductive electrode for current collector and a porous carbon electrode for the adsorption/desorption of electrolyte ions. The in-plane MSC is one of the candidates for wearable electronic devices due to the flexible and light-weight features.

The capacitance and energy density of an in plane MSC depend on characteristics of an interdigitated carbon electrode, where low resistivity, pore-size distribution, and specific surface area are important factors. Although laser carbonization of a polymer film gives an interdigitated electrode with excellent features, a challenging issue is the how to prepare a flexible and thick conductive carbon electrode because the thickness of the laser-carbonized layer on a PI film is limited. The combination of laser direct writing and additive manufacturing is an effective solution to improve the capacitance and energy density for in-plane MSCs. In this paper, we report a flexible in-plane MSC prepared by laser annealing and ablation of a film made from a carbon/polyamide acid composite. A thick conductive carbon electrode was prepared using multi-layer-graphene (ML-GR)/polyamide acid (PA) paste on a PI film. The laser ablation was applied to make an interdigitated electrode with a through-hole structure which enhances electrolyte ion diffusion between front and back sides of the carbon electrode.

2. Experimental

The ML-GR powders (Beijing Dingsheng Special Ceramics Manufacture Co.,Ltd, 6 -10 layers, specific surface area 100 – 300 m²/g) and PA solution (Sigma-Aldrich, poly(pyromellitic dianhydride-co-4,4-oxydianiline) 12.8 wt.% NMP solution) were mixed and coated on a PI film (60 x 30 mm², DuPont-Toray, Kapton 500H, 125 μm

thickness) to make an ML-GR/PA composite film (40 x 17 mm²). An activated carbon (AC, Sigma-Aldrich, Activated Charcoal 161511, 1776 m²/g)/PA composite film was also prepared by same procedures. The laser annealing of the carbon/PA composite film was conducted by a continuous-wave (CW) 445 nm blue semiconductor laser (2.14 W). The laser beam was scanned by a galvanoscanner through an f-θ lens with the focus length of 110 mm. A ns pulsed fiber laser (Raycus, 1064 nm, FWHM 125 ns, 30 kHz, 15 W) and a galvanoscanner system with a f-θ lens (focus length: 160 mm) were employed for the laser ablation of a carbon/PA composite film after laser annealing. The surface resistivity was measured by four-point probe method. A polyvinyl alcohol (PVA)- lithium bis(trifluoro methanesulfonyl)imide (LiTFSI) composite (1/8 w/w%) as a polymer electrolyte was coated on a carbon interdigitated electrode. The characteristics of in-plane MSCs were analyzed by an electrochemical workstation (Hokuto Denko Ltd, HZ-5000).

3. Results and discussion

The formation of an interdigitated electrode with a through-hole structure by laser annealing and laser ablation of a carbon/polyamide acid composite film is illustrated in Fig.1. A carbon/PA composite coating was prepared on a PI film by squeegee method using a PEN (polyethylene naphthalate) flame (thickness 250 μm) as illustrated in Fig.1a and b. The carbon/PA composite film was laser-

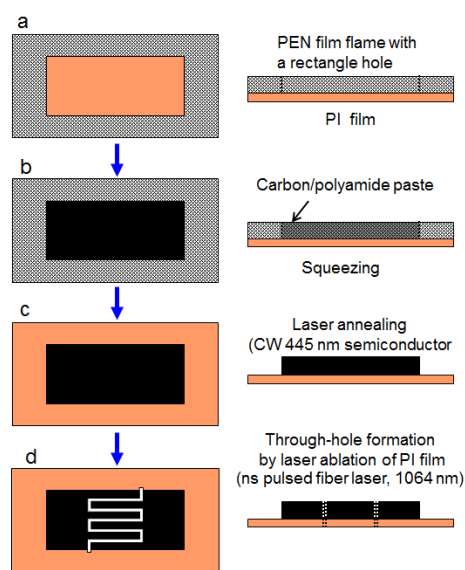


Fig.1. Formation of an interdigitated electrode with a through-hole structure by laser annealing and laser ablation of a carbon/PA composite film.

annealed by raster scanning of CW 445 nm laser beam. The film thickness was almost same before and after laser annealing. The laser ablation was applied to make an interdigitated electrode with a through-hole structure as shown in Fig.1d. The surface resistivities of carbon/PA composite films before and after laser annealing are summarized in Table 1. An insulating AC/PA composite film can be converted to a conductive film by laser annealing, which can be attributed to the laser carbonization of PA binder between carbon particles. The surface resistivity of a laser annealed ML-GR/PA composite film was as low as 18 Ω /sq.

Fig.2 shows interdigitated electrodes of laser-annealed ML-GR/PA composite film with through-holes. The laser annealed ML-GR/PA coating (40 x 17 mm²) on a PI film has holes of inter digitated shape (gap between fingers: 1 mm, finger length: 15mm, finger width: 2mm) and straight slit lines (length: 40 mm, width: 0.5 mm). The through-hole

Table 1. Surface resistivity of carbon/PA composite films.

Carbon of composite film	Abbreviation	Surface resistivity (Ω /□) before laser annealing	Surface resistivity (Ω /□) after laser annealing
Activated carbon	AC	insulator	316
Multi-layer graphene	ML-GR	36	18
AC/ML-GR composite 1/1 w/w%	AC/ML-GR	908	142

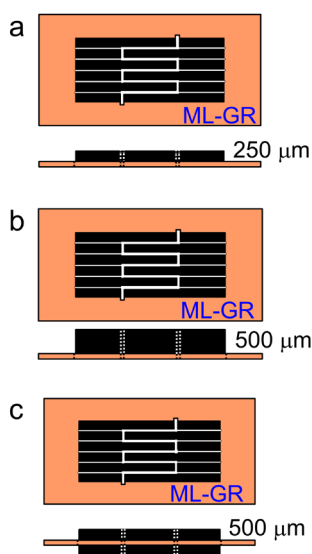


Fig.2. Interdigitated electrodes of laser-annealed ML-GR/PA composite film with through-holes. (a) Single layer, (b) double layers on front side, (c) double layers on front and back sides of a PI film.

structures were prepared to enhance the ion diffusion in carbon layer. The areal capacitances of the interdigitated electrodes are plotted against voltage sweep rate, where the capacitance was calculated by integrating the area of cyclic voltammogram (CV) curves. Although the capacitance was almost proportional to the carbon layer thickness at the slower sweep rate than 10 mV/s in comparing a single layer MSC (Fig. 3a) with a double layer MSC (Fig.3b), the capacitance became almost same with increasing in sweep rate. This result suggests that the ion diffusion at the surface of carbon layer is faster than that of the inner layer and the capacitance is mainly dominated by the ion diffusion around surface at the faster sweep rate in case of a rather thick film. An interdigitated electrode with through-holes is advantageous to enhance the ion diffusion in carbon layer because the surface area of carbon layer can be increased using front and back sides of a PI film as shown in Fig.2c. Although the total thickness of the interdigitated electrode of ML-GR layer on front and back sides (Fig.2c) was similar to that of interdigitated electrode of ML-GR layer only on front side (Fig.2b), the capacitance was higher than the latter in wide sweep rate range as shown in Fig.3.

The additional advantage of the interdigitated electrode with through-holes is the enhancement of the flexibility. Fig.4 shows the retention of resistance of carbon (ML-GR) electrode during bending for electrodes with and without through-hole slits. The carbon electrode with through-hole slits showed no change in resistance by bending up to the bending diameter of 30 mm, while that without through-hole slits showed cracking and peeling off of carbon layer f

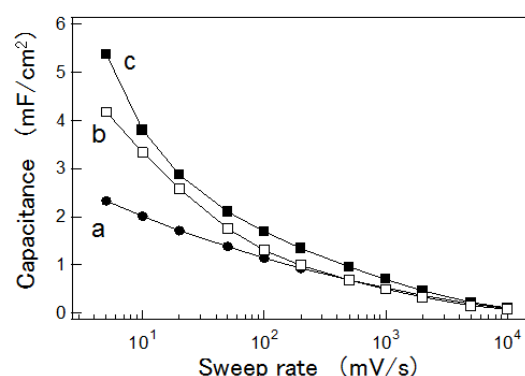


Fig.3. Influence of layered structure of interdigitated electrode consisting of laser-annealed ML-GR/PA film on capacitance. (a) single layer, (b) double layers on front side, (c) double layers on front and back sides of a PI film. Sweep voltage range: 0 – 1.0 V.

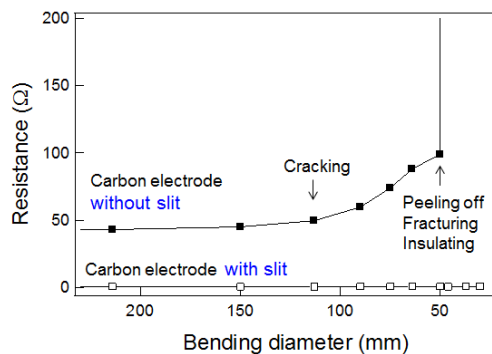


Fig.4. Retention of resistance of carbon (ML-GR) electrode during bending.

The interdigitated electrode with through-holes has further advantage by using the front and back sides of a film electrode. An asymmetric in-plane MSC consisting of different kinds of carbon materials at front and back sides was prepared as shown Fig.5b, where the interdigitated electrode has AC/PA composite layer at front side and ML-GR composite layer at back side. An MSC consisting of an activated carbon has a large capacitance due to a large specific area although the capacitance is seriously lowered with increasing in sweep rate because of a high resistivity of the interdigitated electrode. On the other hand, an ML-GR/PA interdigitated electrode has a low resistivity and the capacitance can be enhanced by the pseudocapacitive behavior by redox reactions of ML-GR in the higher voltage ranges as shown in Fig.6a. The asymmetric structure by combination of AC/PA and MLGR/PA composite films (Fig.5b) improved the capacitance at the lower sweep voltage ranges as shown in Fig.6b.

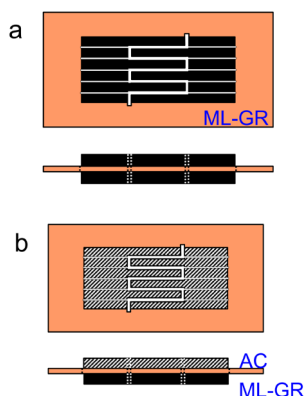


Fig.5. Interdigitated electrodes of laser-annealed carbon/PA composite film with through-holes. (a) ML-GR/PA symmetric structure, (b) AC/PA-MLGR/PA asymmetric structure.

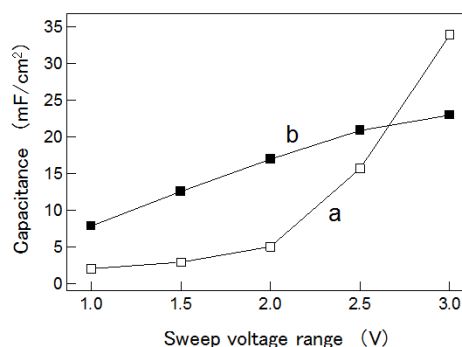


Fig.6. Areal capacitance of MSCs at various sweep voltage ranges. (a) ML-GR/PA symmetric structure, (b) AC/PA-ML-GR/PA asymmetric structure. Sweep rate: 50 mV/s.

4. Conclusion

A unique interdigitated electrode with through-holes was developed by laser annealing and laser ablation of carbon/polyamide acid composite coating on a polyimide film. The laser annealing of a carbon/ polyimide composite gave a conductive film with a low resistivity due to the laser-carbonization of the polyamide acid. The through-hole structure improved the flexibility of the electrode. The enhancement of ion diffusion by through-hole structure increased the capacitance of an MSC. An asymmetric interdigitated electrode has a possibility to improve the capacitance of in-plane MSC by combination of carbons with different features.

Acknowledgement

This work was partially supported by JSPS KAKENHI Grant Number JP19H05356 and JP21H00358.

References

1. J. Lin, Z. Peng, Y. Liu, F. Ruiz-Zepeda, R. Ye, E. L. G. Samuel, M. J. Yacaman, B. I. Yakobson and J. M. Tour, *Nat. Commun.*, **5** (2014) 5714.
2. J. B. In, B. Hsia, J.-H. Yoo, S. Hyun, C. Carraro, R. Maboudian and C. P. Grigoropoulos, *Carbon*, **83** (2015) 144
3. Z. Peng, R. Ye, J. A. Mann, D. Zakhidov, Y. Li, P. R. Smalley, J. Lin and J. M. Tour, *ACS Nano*, **9** (2015) 5868
4. J. Cai, C. Lv and A. Watanabe, *Nano Energy*, **30** (2016) 790.
5. J. Cai, C. Lv and A. Watanabe, *J. Mater. Chem. A*, **4** (2016) 1671.
6. J. Cai, C. Lv and A. Watanabe, *RSC Adv.*, **7** (2017) 415.

Micro Stirrer with Heater Mounted on SAW Actuator for High-speed Chemical Reaction

Masatoshi Takahashi^{1*}, Akinobu Yamaguchi^{1**}, Yuichi Utsumi^{1***}, Masahiro Takeo², Satoshi Amaya³, Hiroaki Sakamoto⁴, Tsunemasa Saiki^{5,6****}

¹ *Laboratory of Advanced Science and Technology for Industry, University of Hyogo, 3-1-2 Kouto, Kamigori, Ako, Hyogo 678-1205, Japan*

² *Department of Applied Chemistry, Graduate School of Engineering, University of Hyogo, 2167, Shosha, Himeji, Hyogo 671-2201, Japan*

³ *Department of Mechanical Engineering, Graduate School of Engineering, University of Tokyo, 7-3-1, Hongo, Bunkyo-ku, Tokyo 113-8656, Japan*

⁴ *Frontier Fiber Technology and Science, Graduate School of Engineering, University of Fukui, 3-9-1 Bunkyo, Fukui, Fukui 910-8507, Japan*

⁵ *Hyogo Prefectural Institute of Technology,*

3-1-12, Yukihiro-cho, Suma-ku, Kobe 654-0037, Japan

⁶ *Department of Electronics and Computer Science, Graduate School of Engineering, University of Hyogo, 2167, Shosha, Himeji, Hyogo 671-2201, Japan*

** masao7@lasti.u-hyogo.ac.jp, **yamaguti@lasti.u-hyogo.ac.jp,*

****utsumi@lasti.u-hyogo.ac.jp ****saiki@hyogo-kj.jp*

Mixing is difficult in microfluidic devices due to the low Reynolds' number. We proposed and demonstrated a surface-acoustic-wave (SAW)-based microfluidic system which can control the temperature by mounting a heater. This device has a hollow cylindrical reservoir made of resin on a piezoelectric substrate (LiNbO₃), and the solution can be rotated by injecting SAWs from both sides, which are shifted parallel to the central axis of the reservoir. 0.75 W of power was supplied to the IDT to generate SAWs, and the temperature rise of the liquid was measured with a thermographic camera when 0 to 0.55 W of power was supplied to the heater. As a result, by mounting the heater on the SAW actuator, it was possible to uniformly raise the temperature of a 40 μ L micro-liquid by 8 to 40 $^{\circ}$ C in about 80 seconds, demonstrating the usefulness of this heater-mounted SAW agitation device.

Keywords: surface acoustic wave, lithium niobate, stirrer, heater, actuator

1. Introduction

In recent years, micro total analysis systems (μ TAS) have been attracting attention in the medical and environmental measurement fields. In μ TAS, there are many advantages such as the ability to make measurements with small sample volumes, short reaction times, automation of measurements including pretreatment, smaller equipment, disposability of equipment, low cost, and reduced manpower. On the other hand, μ TAS requires the integration of multiple small devices (pumps, valves, agitators, sensors, etc.) on a chip. In addition, in microfluidic channels, there is a big problem to be solved. That is the problem associated with mixing

induced due to the low Reynolds' number in the micro-channel.

One of candidates for solving the problem is the creation of a mixer by surface acoustic waves (SAWs). The SAWs have been widely demonstrated for effectively driving both linear motion in microscale actuators and microfluidic rotation [1-16]. The SAWs have also been used for sensors [17-20]. Recently, an arbitrary axis rotor and solid-state rotational microscale motor have been developed [12]. Therefore, the SAWs enable to provide the micro-scale mixer in microfluidic systems.

In this study, aiming to further improve the efficiency of mixing, a SAWs-induced stirrer with a

Received March 31, 2022

Accepted June 24, 2022

heater mounted is fabricated because the solubility increases with the fluidic temperature increases. The stirring characteristics were evaluated by systematically measuring the dependence of temperature and rotation speed on input power.

2. Fabrication of heater mounted SAW stirring device

Figure 1 shows a typical photograph of SAW stirring device with a heater mounted. Here, a batch-type SAW device was fabricated to investigate its basic characteristics as a stirrer. As shown in Fig. 1, a liquid reservoir without lid is placed almost at the center of this device fabricated onto a piezoelectric substrate (LiNbO_3). The reservoir is consisting of a hollow cylinder with outer diameter of 9 mm, inner diameter of 5 mm, and depth of 2 mm and 40 μL of solution can be hold up in the reservoir. Pair interdigital transducers (IDTs) with pitch of 200 μm , aperture width of 2.5 mm, and pair number of 20 were placed to generate the SAWs. The propagation of SAWs are designed to be incident parallel and staggered with respect to the central axis of the liquid reservoir, allowing the solution to rotate. A heater consisting of gold wire with 100 μm in width and resistance of 55 Ω is installed at two locations on the bottom of the liquid reservoir, away from the IDTs. In this devices, the longitudinal wave radiation by SAWs from the surface is not disturbed, that is, the fluid can be efficiently driven by SAWs.

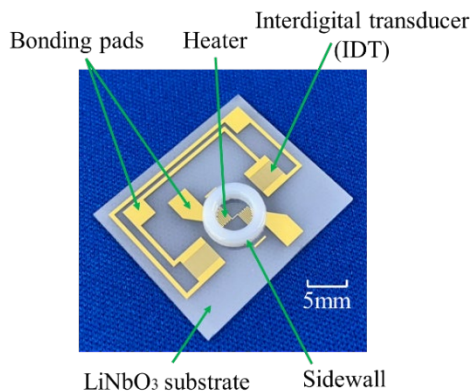


Fig. 1. A photograph of fabricated SAWs-induced stirring device with a pair heater mounted.

The stirring devices were fabricated onto a piezoelectric substrate, Y-cut 128-degree rotation Y-plate X-propagation LiNbO_3 substrate, by means of combination of lithography and etching process based on semiconductor processes. The schematic of device fabrication process is described as illustrated in Fig. 2. The thickness of the LiNbO_3 substrate was 500 μm and its surface roughness was less than 0.3 nm. To prepare the IDT electrodes, first,

Cr and Au were deposited by an RF sputter (CFS-4EP-LL, Shibaura Mechatronics co ltd.) as shown in Fig. 2. The thicknesses of Cr and Au were 10 nm and 100 nm, respectively. Next, UV exposure was performed using a positive-type resist (OFPR800LB-20cP, Tokyo Ohka Kogyo co. ltd.). At this time, both the IDT and heater patterns were simultaneously exposure by using a glass mask and UV aligner (MA6, SUSS Micro Tec. co. ltd.) After development, IDTs and heater were formed by etching Au and Cr and removing the resist. The device was then completed by attaching a liquid reservoir wall (photosensitive resin: Vero White, Stratasys co. ltd.) fabricated by a 3D molding process (Connex 500, Stratasys co. ltd.). The bonding the reservoir to this piezoelectric substrate was used an adhesive (Aron Alpha, Toagosei co. ltd.). The SAW injection part was not bonded.

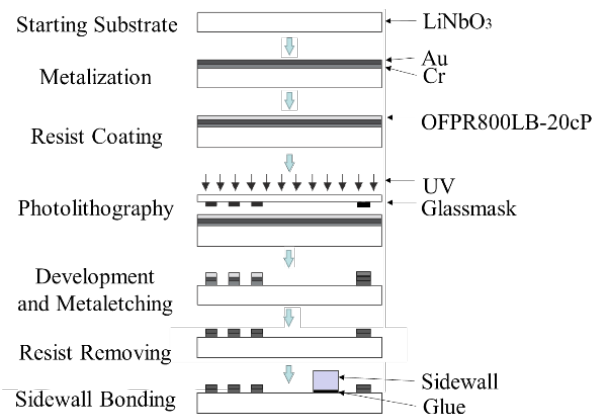


Fig. 2. Fabrication procedure for SAWs-induced stirring device with a heater mounted.

3. Experimental

A schematic of the experimental setup is shown in Fig. 3. A function generator (AFG3252, Tektronix co.) created 1 kHz burst waveforms consisting of 2000 cycles of 19.2 MHz sine waves. The input power was amplified by an RF amplifier (ALM00110-2840FM, R&K Co. Ltd.). The longitudinal wave radiation of the SAWs that reach the bottom of the liquid reservoir then rotates the liquid in the reservoir. Furthermore, a voltage is applied to the heater installed at the bottom of the liquid reservoir by a DC stabilized power supply (AD-8724D manufactured by A&D Co. Ltd.), and the liquid in the reservoir was heated by Joule heat. To keep the heat from escaping to the bottom side of the substrate, this SAW stirring device was placed on a paper sheet (Kimwipe S-200, Nippon Paper Crexia Co. Ltd.).

In the experiment, 40 μL of pure water at 20 $^{\circ}\text{C}$, the same as room temperature, was placed in the

reservoir. The thermal images near the reservoir were captured by an infrared thermography camera (G100, NEC Avio Infrared Technology) during the application of SAWs and heating. When the power supplied to the IDT was 1 W or more, the piezoelectric substrate cracked. When the power supplied to the heater was 0.6 W or more, disconnection often occurred. These supply powers were checked with an RF power meter (NRP-Z91, Rohde & Schwarz, and DC3001M1, AR) and two digital multimeters (TY530, Yokogawa Measurement Corporation and DM01 Custom), respectively. Therefore, the upper limits for the input power to the IDT and for the electric power to the heater were set below 1 W and 0.6 W, respectively. From the observation using the video camera with a tracer (Al powder), it was confirmed that 40 μL of pure water rotates at 96.5 rpm when the power supplied by the IDT is set to 0.75 W.

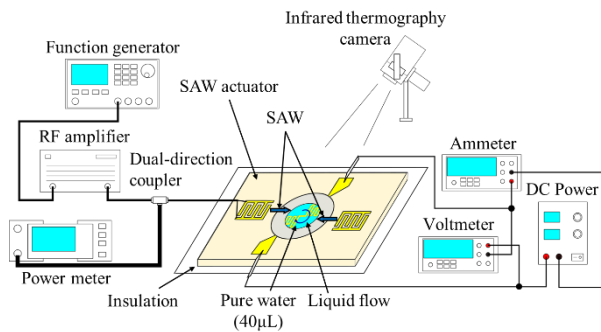


Fig. 3. Schematic of experimental setup

3. Results and discussion

Figure 4 shows time evolution of temperature distribution images of the liquid in the reservoir when the power of 0.75 W was only supplied to the IDT without heating by heater. Figure 4(a) shows that the temperature distribution of the entire device, including the liquid in the reservoir, was almost uniform before the start of power supply. Note that the temperature was almost the same as room temperature (20 $^{\circ}\text{C}$). As seen in Figs. 4(b) and 4(c), the temperature of the reservoir wall where the SAW first collides rose. After that, it can be seen that the temperature of the liquid in the reservoir sequentially rose as shown in Figs. 4(d)-4(g). Finally, the temperature distribution disappeared and reached about 28 $^{\circ}\text{C}$. These results suggest that our device can make the liquid temperature rise uniform in short time by rotation of a minute amount of pure water in the reservoir using the SAW generated by supplying less than 1 W of power to the IDT.

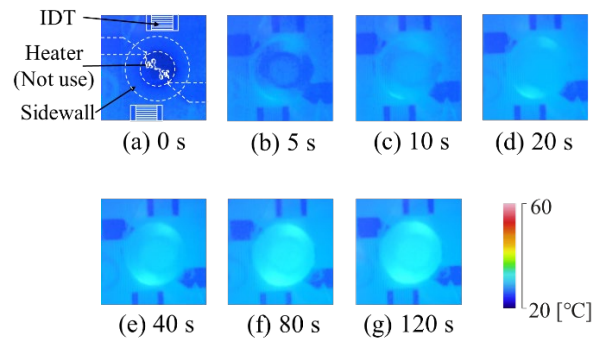


Fig. 4. Temperature distribution images obtained at (a) 0, (b) 5, (c) 10, (d) 20, (e) 40, (f) 80, and (g) 120 s when power (0.75 W) is supplied to the IDT without heating by the heater.

Next, we obtained thermal images of temperature distribution in the reservoir during the simultaneous applications of stirring by the SAW and heating. As shown in Fig. 5, the liquid temperature first rises at the two locations in the liquid reservoir where heaters are installed at the upper left and lower right regions of the reservoir in Fig. 5(a). It can be seen that the localized high-temperature region heated by the heater expands radially with time evolution. After 120 s, the temperature reaches 40 $^{\circ}\text{C}$ uniformly. Comparing the result of Fig. 4 with that of Fig. 5, it was found that the use of heater gave a much higher liquid temperature rise than that of the IDT. This result is a natural result in terms of energy conversion efficiency. In the case of the excitation by SAWs, electric power is directly converted into mechanical energy, and the mechanical energy is converted into thermal energy. On the other hand, if a heater is used, electric power can be directly generated as heat, so that the temperature of the liquid can be easily raised. Each temperature rise per unit input power is estimated to be 72.7 $^{\circ}\text{C}/\text{W}$ for the use of heater, while it is 10.7 $^{\circ}\text{C}/\text{W}$ for the use of SAW actuator. The value of heater use is much larger (about 7 times larger) than that of the SAW actuator.

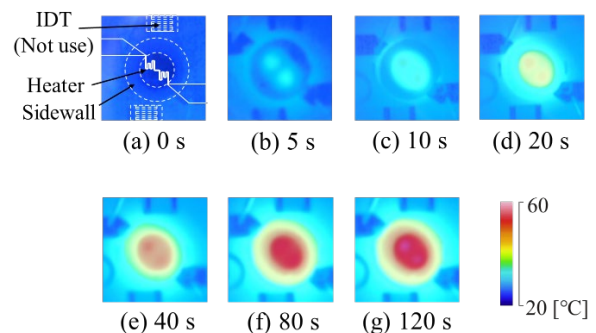


Fig. 5. Temperature distribution images obtained at (a) 0, (b) 5, (c) 10, (d) 20, (e) 40, (f) 80, and (g) 120 s when 0.55 W is supplied to the heater.

Finally, thermal distribution images were obtained when stirring by SAW excitation and heating with a heater were performed at the same time. Figures 6(a)-6(g) shows the time evolution of liquid temperature in the reservoir. Here, 0.75 and 0.55 W of electric power were applied to the IDT and heater, respectively. As shown in Fig. 6, the liquid in the reservoir rises almost uniformly as time elapsed. Although the temperature of the liquid in the vicinity of the reservoir wall is slightly lower, the temperature reaches 60 °C in almost the entire area of the reservoir at 120 s. By adding a heater to the SAW actuator, a small amount of liquid can be mixed, and the temperature of the liquid can be raised uniformly and significantly.

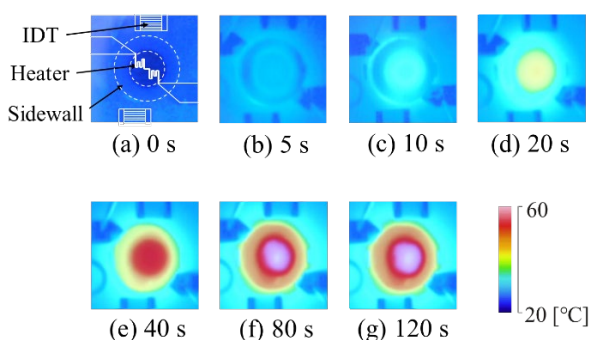


Fig. 6. Temperature distribution images obtained at (a) 0, (b) 5, (c) 10, (d) 20, (e) 40, (f) 80, and (g) 120 s when 0.75 W and 0.55 W were simultaneously applied to the IDT and heater, respectively.

The time variation of liquid temperature from the start of power supply to the IDT and heater is summarized in Fig. 7. This figure shows that the liquid temperature in the central position increases with increasing elapsed time and saturated then becomes almost constant at all power supplied to the heaters. The time constants were estimated to be 30, 25, 23, and 23 s for the power 0, 0.20, 0.40, and 0.55 W to the heater, respectively. As the power supplied to the heaters increases, the attained liquid temperature also increases. Furthermore, if it is desired to increase the attained liquid temperature, it is considered that the main cause of saturation of the liquid temperature increase is heat dissipation from the top of the liquid surface to the gas, and it is assumed that this can be achieved by adding an air layer above the liquid reservoir using a glass plate or the like to prevent heat dissipation. However, there are no devices other than heater-mounted SAW stirring devices that have the performance to uniformly raise the temperature of a 40 μL solution by 40 °C in about 80 seconds.

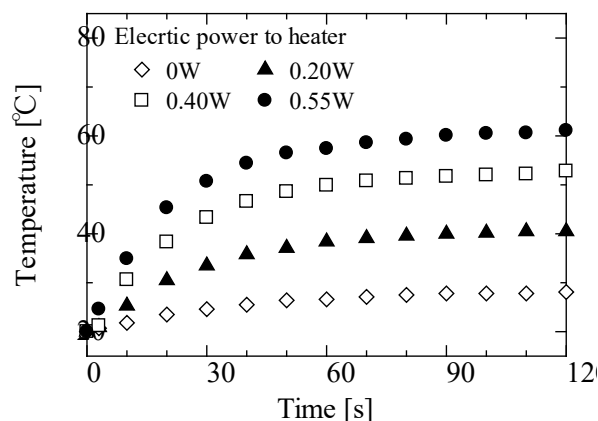


Fig. 7. Time variation of liquid temperature in the central position from the start of power supply to IDT and heater (IDT: 0.75 W constant)

From the above experimental results, mounting a heater on a SAW stirring device can raise the liquid temperature uniformly and efficiently. Therefore, from the Arrhenius equation (1), which shows the relationship between temperature and chemical reaction rate, the chemical reaction rate of this heater-mounted SAW stirring device is discussed using the hydrolysis of sucrose as an example.

$$\ln k = \ln A - \frac{E_a}{RT} \quad (1)$$

Here, we determine the respective reaction rate constants k with temperatures T as 301 K (28 °C) and 333 K (60 °C), since the attained liquid temperature increases from 28 °C to 60 °C by increasing the heater supply power of the heater mounted SAW stirring device from 0 to 0.55 W in the experiment. The gas constant R is 8.3145 [J K⁻¹ mol⁻¹] and the activation energy E_a is 107.9 [kJ mol⁻¹] [21] for the hydrolysis of sucrose. Here, the frequency factor A [dm³ mol⁻¹ s⁻¹] was assumed to be the same because the power supplied to the IDT is the same, so that there is almost no difference in the stirring of the solution by the SAW. Substituting these values into equation (1), the reaction rate constants k are $1.887 \cdot A \times 10^{-19}$ and $1.189 \cdot A \times 10^{-17}$ [dm³ mol⁻¹ s⁻¹] at attained temperatures of 28 and 60 °C, respectively. In other words, the reaction rate of sucrose hydrolysis is 63 times faster when a heater is implemented in the SAW stirring device, indicating the usefulness of this device.

6. Conclusion

In this study, we proposed a batch-type micro-scale stirring device in which a heater is mounted on a SAW actuator, because it is difficult to stir the material in a small area. The proposed micro-

stirring device has a hollow cylindrical liquid reservoir (5 mm in diameter and 2 mm in depth), and the solution is rotated by injecting SAWs from both sides, which are shifted parallel to the central axis of the reservoir. The pitch, pair number, and aperture width of these SAW-generating Interdigital transducers (IDTs) are 200 μm , 20, and 2.5 mm, respectively. Furthermore, two heaters (wire width 100 μm , resistance 55 Ω) are held in the liquid reservoir to heat the rotated solution. The proposed micro-stirred device was fabricated by first patterning the IDTs and heaters on a LiNbO_3 substrate using a Cr/Au exposure process, and then having a 3D-printed plastic sump wall placed on this substrate.

In the evaluation experiment of this device, 0.75 W of power was supplied to the IDT to generate SAW, and the liquid temperature rise when 0 to 0.55 W of power was supplied to the heater was measured with a thermographic camera. As a result, by mounting the heater on the SAW actuator, it was possible to uniformly raise the temperature of a 40 μL micro-liquid by 8 to 40 $^\circ\text{C}$ in about 80 seconds, demonstrating the usefulness of this heater-mounted SAW stirring device.

In the future, we plan to incorporate this heater-mounted SAW stirring device into the flow path in μTAS and investigate the chemical reaction characteristics in a continuous fluid.

Acknowledgments

We would like to thank Dr. Masaru Mori and Dr. Yohei Sutani of Hyogo Prefectural Institute of Technology for their advice in carrying out this research.

References

1. M. Takahashi and T. Higuchi, *IEEE Trans. Ultrason. Ferroelectr. Freq. Control*, **43** (1996) 901
2. A. Sano, Y. Matsui, and S. Shiokawa, *Jpn. J. Appl. Phys.*, **37** (1998) 2979
3. A. Wixforth, *Superlattices Microstruct.*, **33** (2003) 389
4. K. Chono, N. Shimizu, Y. Matsui, J. Kondoh, and S. Shiokawa, *Jpn. J. Appl. Phys.*, **43** (2004) 2987
5. A. Yamamoto, M. Nishimura, N. Tsukada, and T. Higuchi, *Proc. International Conference on Miniaturized Systems of Chemistry and Life Sciences ($\mu\text{TAS}2005$)*, No.9 (2005) 1072
6. A. Renaudin, K. Chuda, V. Zhang, X. Coqueret, J. C. Camart, P. Tabourier, and C. Druon, *Proc. International Conference on Miniaturized Systems of Chemistry and Life Sciences ($\mu\text{TAS}2005$)*, No.9 (2005) 599
7. E. Galopin, A. Renaudin, J. C. Camart, V. Thomy, C. Druon, and P. Tabourier, *Proc. International Conference on Miniaturized Systems of Chemistry and Life Sciences ($\mu\text{TAS}2006$)*, No.10 (2006) 651
8. K. Sritharan, C. J. Strobl, M. F. Schneider, and A. Wixforth, *Appl. Phys. Lett.*, **88** (2006) 054102
9. S. Ito, M. Sugimoto, Y. Matsui, and J. Kondoh, *Jpn. J. Appl. Phys.*, **46** (2007) 4718
10. N. Murochi, M. Sugimoto, Y. Matsui, and J. Kondoh, *Jpn. J. Appl. Phys.*, **46** (2007) 4754
11. Y. Utsumi, T. Saiki, and K. Okada, *Proc. International Conference on Miniaturized Systems of Chemistry and Life Sciences ($\mu\text{TAS}2008$)*, No.12 (2008) 715
12. T. Saiki, K. Okada, and Y. Utsumi, *Microsyst. Technol.*, **16** (2010) 1589
13. T. Saiki, K. Okada, and Y. Utsumi, *Electronics and Communications in Japan*, **94** (2011) 10
14. T. Saiki, and Y. Utsumi, *Electronics and Communications in Japan*, **97** (2014) 54
15. T. Saiki, Y. Takizawa, T. Kaneyoshi, K. Iimura, M. Suzuki, A. Yamaguchi, and Y. Utsumi, *Sensors and Materials*, **33** (2021) 4409
16. Y. Takizawa, Y. Fukuchi, K. Hamaguchi, S. Amaya, Y. Utsumi, M. Takeo, K. Iimura, M. Suzuki, and T. Saiki, *Sensors and Materials*, **33** (2021) 4427
17. J. C. Andle and J. F. Vetelino, *Sens. Actuators A*, **44** (1994) 167
18. J. Kondoh, T. Muramatsu, T. Nakanishi, Y. Matsui, and S. Shiokawa, *Sens. Actuators B*, **92** (2003) 191
19. S. Shiokawa, and J. Kondoh, *Jpn. J. Appl. Phys.*, **43** (2004) 2799
20. I. Sroyanov, M. Tewes, S. Glass, T. Gronewold, M. Koch, and M. Lohndorf, *Proc. International Conference on Miniaturized Systems of Chemistry and Life Sciences ($\mu\text{TAS}2005$)*, No.9 (2005) 1152
21. P. Atkins, and J. Paula, "Physical Chemistry, 8th Edition", Oxford University Press, (2006)

Novel Temporary Bonding/Debonding System Enabling Advanced Packaging Process

Tetsuya Enomoto^{1*}, Emi Miyazawa¹, Yuta Akasu¹, Shogo Sobue²,
Yuki Nakamura², and Takashi Kawamori¹,

¹ *Organic Materials Research Department, Advanced Technology Research & Development Center, Research & Innovation Promotion Headquarters, Showa Denko Materials Co., Ltd. 48, Wadai, Tsukuba-shi, Ibaraki 300-4247, Japan*

² *Packaging Materials Research & Development Department, Information & Communication Research & Development Center, Information & Communication Business Headquarters, Showa Denko Materials Co., Ltd. 14, Goi-minamikaigan, Ichihara-shi, Chiba 290-8567, Japan*

**enomoto.tetsuya.xikiz@showadenko.com*

Novel temporary bonding/debonding system including high heat resistant temporary bonding adhesive and debonding methods with conventional laser ablation or newly developed photonic release by Xe flash light irradiation will be introduced. Our new temporary bonding adhesive shows no delamination and no voiding after thermal treatment over 300 °C and can be easily removed by peeling off after debonding from the support carrier. In addition, by adopting the dual layer structure with adhesive layer and laser release layer, we can form the suitable structure for debonding with laser ablation. Furthermore, in the case that metal layer is applied instead of laser release layer, debonding by one-shot Xe flash light irradiation within 5 ms can be achieved, indicating the increased throughput at debonding process as compared to the other debonding methods. Process demonstration results of wafer thinning down to 50 μm, fan-out wafer level packaging (FOWLP) will also be shown in this paper.

Keywords: Temporary bonding/debonding, High heat resistance, Peel off, Laser ablation, Photonic release

1. Introduction

Temporary bonding/debonding system has been widely used for fragile thin wafer handling at back grinding process [1-7]. Generally in this process, wafer is supported on the rigid carrier through the temporary bonding adhesive and then thin wafer is debonded from the carrier after grinding. In order to prevent the wafer crack or chipping during processing and achieve the good thickness uniformity, higher co-planarity of adhesive surface and less stress at debonding are main requirements.

Recently, temporary bonding/debonding system is being extensively applied to advanced packaging process including fan-out wafer level packaging (FOWLP) and wafer-to-wafer (W2W) direct bonding [8-14]. For these applications, besides the requirements as mentioned above, in-process

reliability of temporary bonding adhesive is also required. No delamination, no voiding and no deformation are favorable during processing under severe treatment condition such as electro-plating, TSV (Through Silicon Via) formation, and thermal compression bonding *etc.* Especially, enhancing heat resistance is required because thermal treatment over 300 °C is applied for Cu anneal in W2W direct bonding process [15-21]. Needless to say, it is a mandatory to be able to debond at the final step of packaging process. In addition, shorter process time at debonding and easier removal of the residue after debonding are more preferable from the viewpoint of higher productivity and workability. Typical process flow of temporary bonding/debonding and requirements are shown in Fig. 1 and Table 1 respectively.

Received	April 1, 2022
Accepted	June 24, 2022

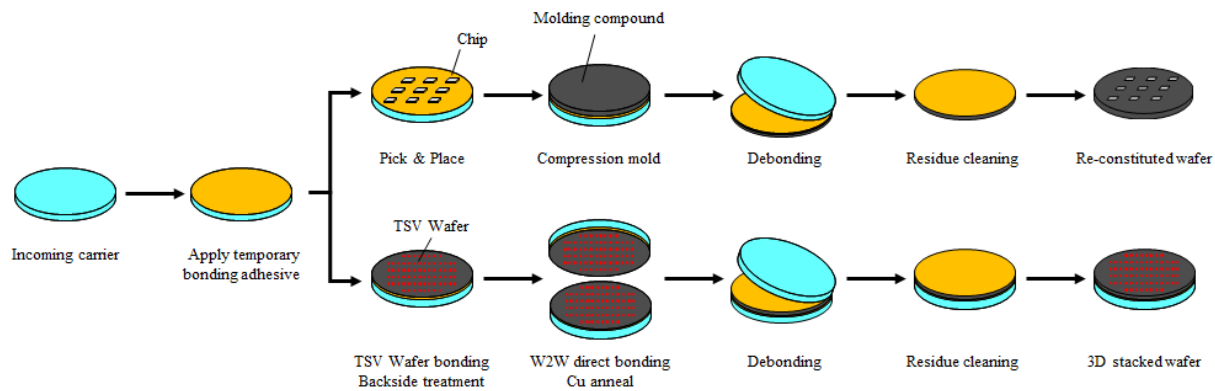


Fig. 1. Typical process flow of temporary bonding/debonding in FOWLP and W2W direct bonding

Table 1. Typical requirements for temporary bonding/debonding system

Classification	Item	Requirement
Temporary bonding adhesive	Co-planarity	Uniform thickness Smooth surface
	Bondability	Applicable to topographic surface (bumped wafer) Bondable at low pressure Enough adhesion strength to prevent displacement
	In-process reliability	No delamination during processing High heat resistance over 300 °C Good chemical resistance
	Residue cleaning	Easy removal after debonding
Debonding method	Debond stress	Less mechanical stress Less thermal damage
	Process time	Shorter debonding time
	Work size	Applicable to panel format (up to 600 mm x 600 mm)
	Carrier recycle	Possible

In order to meet the requirements on temporary bonding/debonding system, we are now developing the new temporary bonding adhesive and evaluating its in-process reliability and debonding capability with photonic release method using Xe flash light irradiation [22] as well as conventional laser ablation method. In this report, we will introduce the unique features of new temporary bonding adhesive and the process demonstration results.

2. Experimental

2.1 Adhesive property evaluation

Viscosity of adhesive was measured by a rheometer (ARES-G2, TA instruments Corp.). Weight loss was evaluated by a thermo-gravimetric analyzer (TG/DTA6300, Hitachi high-tech Corp.) in air or nitrogen atmosphere. Evaluation of chemical resistance were carried out by using the test vehicle of glass and silicon chip bonded with adhesive. Test vehicle after dipping in various chemicals such as

propyleneglycol monomethyl ether acetate (PGMEA), propyleneglycol monomethyl ether (PGME), 2-propanol (IPA), 2-methyl-pyrrolidone (NMP), dimethylsulfoxide (DMSO), 2.38 % aqueous tetramethylammonium hydroxide (TMAH), 5 % aqueous potassium hydroxide (KOH), and 30 % aqueous hydrogen peroxide (H₂O₂) at r.t. for 1 h was visually checked if appearance change happened such as delamination, swelling, and so on or not. In addition, weight change after chemical treatment was also evaluated. Regarding bondability, chip with Cu pillars (CC80, WALTSCORP. 7.3 mm x 7.3 mm, 150 μm thickness, Cu pillar 45 μm height) was bonded on the 80 μm thickness adhesive layer on glass carrier by using flip-chip bonder (LFB-2301, Shinkawa Corp.) with 50 N loading for 10 s at 130 °C following curing at 200 °C for 1 h and the cross-section of the bonded sample was visually checked after not only curing but also additional thermal compression bonding treatment with 25 N

loading for 6 s at 270 °C three times.

2.2 Debonding by laser method

Glass carrier coated with laser release layer material and silicon chip coated or laminated with temporary bonding adhesive were bonded by using vacuum laminator (V130, Nichigo-Morton Corp.) at 80 °C. After curing at 200 °C for 1 h, bonded samples were treated with 308 nm laser tool (IPEX-848, OPTEC Corp.) or 355 nm laser tool (PU-L3A, JCZ Technology Corp.).

2.3 Debonding by photonic release method

Glass carrier with sputtered metal layer and silicon chip coated or laminated with temporary bonding adhesive were bonded by using vacuum laminator (V130, Nichigo-Morton Corp.) at 80 °C. After curing at 200 °C for 1 h, bonded samples were treated with Xe flash light system (PulseForge[®] 1400, NovaCentrix Corp.).

2.4 Demonstration of wafer thinning

Temporary bonding adhesive film was laminated on glass carrier with sputtered metal layer and then 200 mm wafer was bonded on adhesive layer by using wafer bonder (LF12, SUSS MicroTec Corp.) at 140 °C. After curing at 200 °C, wafer thinning down to 50 μm was carried out with a wafer backgrinder (DAG810, DISCO Corp.). Debonding from glass carrier was carried out by photonic release method and the residual adhesive layer on thinned wafer was peeled off by manual.

2.5 Demonstration of FOWL P

Si chips (6 mm x 6 mm) were bonded on 80 μm thickness adhesive layer on 300 mm glass carrier with sputtered metal layer at 100 °C. After curing at 200 °C, molding was carried out with granule type epoxy molding compound (Showa Denko Materials Corp.) by using compression molding machine (CPM1080, TOWA Corp.) and then molding compound was cured at 175 °C. Bonding status was observed by scanning acoustic microscopy (SAM). Debonding the molded sample was conducted by photonic release method.

3. Results and discussion

3.1 New temporary bonding adhesive

3.1.1 Coating capability

Our new adhesive can be provided in both liquid and film type. Liquid type adhesive can form 5-20 μm thickness adhesive layer by spin-coating method as shown in Fig. 2.

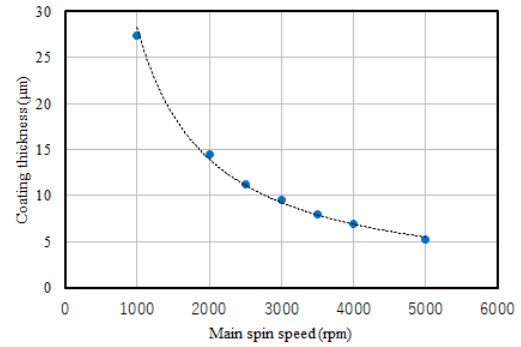


Fig. 2 Spin curve of liquid type adhesive
Pre-spin 1000 rpm/10 s + Main-spin 30 s
Soft bake 60 °C/10 min. + 100 °C/10 min.

Film type adhesive is suitable for thicker layer formation (30-100 μm) and advantageous for lamination to the topographic surface. Fig. 3 shows the smooth surface profile of adhesive film (40 μm thickness).

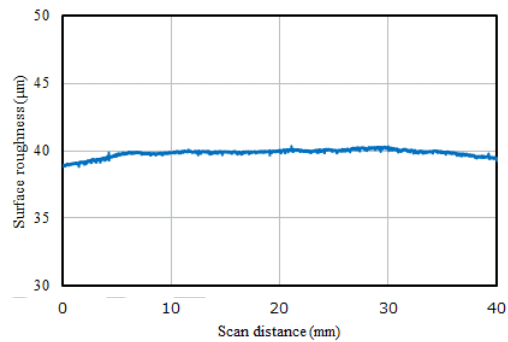


Fig. 3 Surface roughness of film type adhesive

3.1.2 Bondability

Temperature depended viscosity curve of new adhesive is shown in Fig. 4. Viscosity of this adhesive is lowered in the range between 70-130 °C and the good bondability in this temperature range can be achieved. Above 150 °C, thermosetting reaction proceeds and high heat resistance and good chemical resistance can also be achieved.

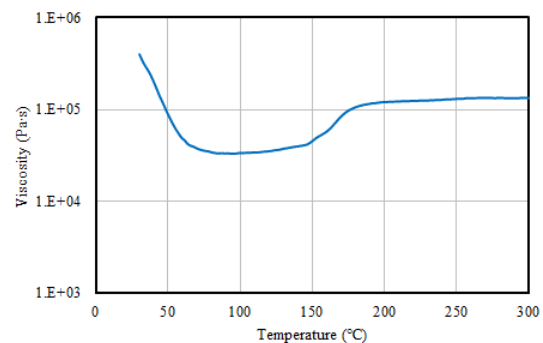


Fig. 4. Viscosity curve of new adhesive

Fig. 5 is the cross-section image after bonding the chip with bumps on adhesive layer at 130 °C. Cu pillar bumps with 50 μm height are fully embedded in 80 μm thickness adhesive layer.

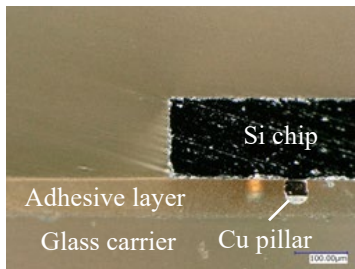


Fig. 5. Cross-section image after bonding the chip with bumps at 130 °C

In addition, once adhesive is cured at 200 °C after bonding the chip, the surface of adhesive layer is kept almost flat even if the following thermal compression treatment is applied to the chip as shown in Fig. 6.

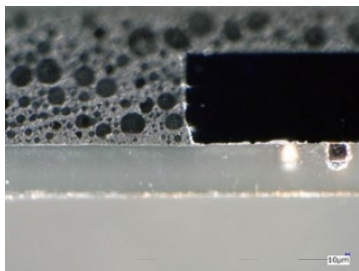


Fig. 6. Cross-section image after curing followed by thermal compression treatment (270 °C/0.5 MPa/3 times)

3.1.3 Heat resistance

Fig. 7 shows the measurement results of thermo-gravimetric analysis (TGA). Even in the air, 1 % weight loss temperature is over 300 °C, indicating high heat resistance of new adhesive.

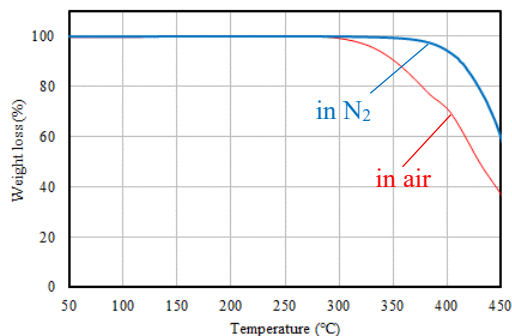


Fig. 7. Thermo-gravimetric analysis result of cured new adhesive

In addition, after thermal treatment at 300 °C for 1 h, glass carrier and 200 mm Si wafer bonded with new adhesive shows no void or no delamination as shown in Fig. 8.

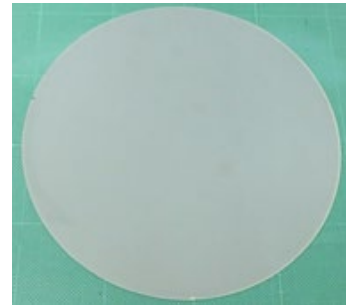


Fig. 8. Bonded sample after thermal treatment at 300 °C for 1 h

3.1.4 Chemical resistance

Table 2 summarizes the results of chemical resistance test. We haven't observed remarkable weight loss or appearance change after testing.

Table 2. Chemical resistance test results

Chemicals	Weight loss (wt%)	Appearance
PGMEA	0.0	No change
PGME	0.0	No change
IPA	0.0	No change
NMP	0.0	No change
DMSO	0.0	No change
2.38% TMAH	0.0	No change
5% KOH	0.0	No change
30% H ₂ O ₂	0.0	No change

Sample structure: Glass/adhesive/Si cured at 200 °C
Dipping the sample in each chemical at r.t. for 1 h

3.1.5 Removal by peeling off

Although new adhesive is thermosetting resin, the cured adhesive layer can be removed easily from Si wafer by peeling off as shown in Fig. 9. No obvious residue is detected by SEM (Scanning Electron Microscopy) observation and there is no significant difference in EDX (Energy Dispersive X-ray spectroscopy) elemental analysis result before and after peeling off as shown in Fig. 10.

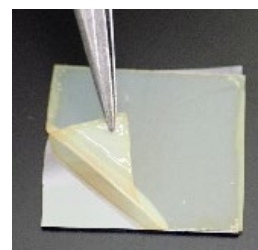
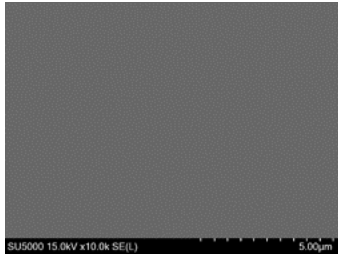


Fig. 9. Peeling-off capability of new adhesive



Element	Atomic %		
	C	O	Si
Initial	6.15	0.83	93.02
After peeling off	7.88	0.74	91.38

Fig. 10. SEM image and EDX analysis result of Si surface after peeling off

3.2 Debonding method

Fig. 11 shows a schematic image of the various debonding methods, including newly developed photonic release method, Table 3 shows a comparison of the various debonding methods.

Thermal method has been widely used especially for FOWLP process. However, its in-process temperature limit is around 200 °C due to the heat resistance of adhesive. On the other hand, higher

temperature condition is required in packaging process such as curing of dielectric material (230 °C), solder reflow (260 °C), Cu anneal (>300 °C) and so on. Therefore, laser method with high heat resistant adhesive has gradually been used. However, throughput of laser method is still not so high since it takes longer time to treat the whole debonding area by laser scanning. In contrast, photonic release method can complete debonding by one-shot Xe flash light irradiation within 5 ms for whole area and the area size doesn't affect its throughput. That's why higher productivity and scalability of photonic release method are expected.

Based on the current status and future perspective of debonding method, we evaluated the applicability of new temporary bonding adhesive to both laser method and photonic release method.

3.2.1 Applicability to laser method

Usually, dual layer structure of laser release layer and adhesive layer is adopted for laser debonding method. Our new temporary adhesive can be used together with laser release material having UV absorption property as shown in Fig. 12 and debonding is successful by using 308 or 355 nm laser. Debonded samples are shown in Fig. 13. After

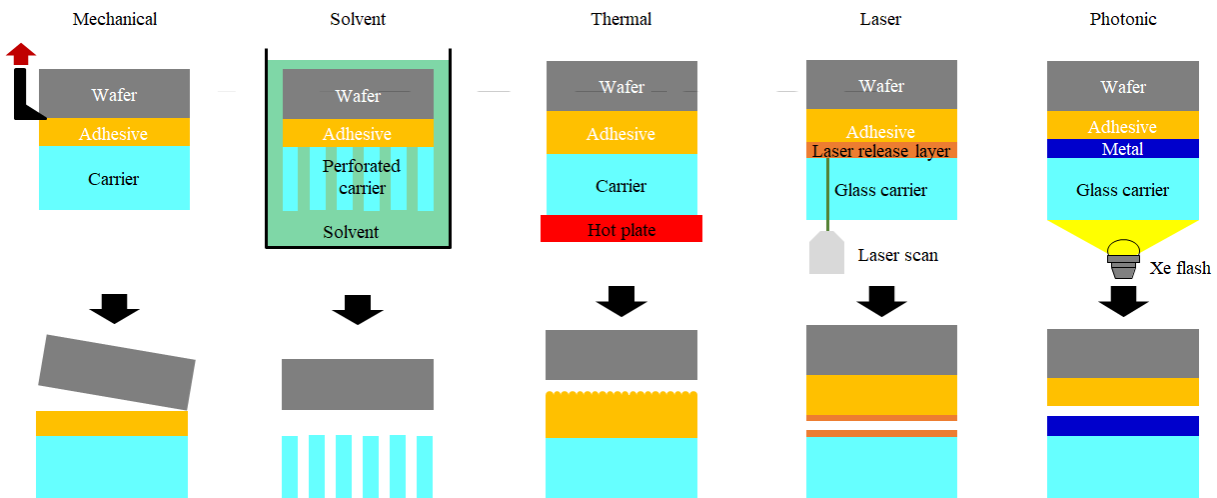


Fig. 11. Schematic image of various debonding methods

Table 3. Comparison of various debonding methods

Method	Mechanical	Solvent	Thermal	Laser	Photonic
Mechanism	Peel off	Dissolution	Topographic change	Ablation	Instant deformation
Debond stress	High	Low	Low	Low	Low
Debond temp.	r.t.	r.t.-80	150-200	r.t.	r.t.
Throughput (300 mm equiv.)	10-20 wph	10-20 wph	20-40 wph	20-40 wph	>60 wph
Release layer	No need	No need	No need	Laser active layer	Metal layer
Carrier	Si, Metal, Glass	Perforated glass	Si, Metal, Glass	Glass	Glass
In-process temp. limit	Depends on adhesive	Depends on adhesive	Up to 200 °C	Depends on adhesive	Depends on adhesive

debonding, slight residue on the surface of glass carrier can be wiped off easily and temporary bonding adhesive can be removed from the Si surface by peeling off as mentioned in section 2.5.

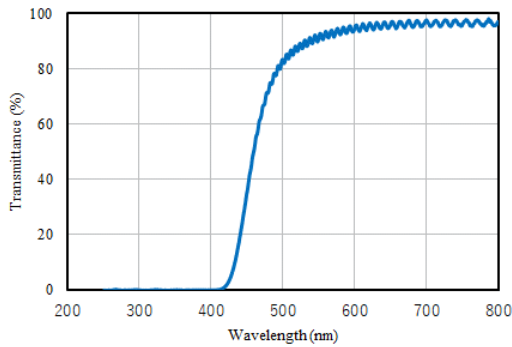


Fig. 12. UV-Vis spectrum of laser release layer

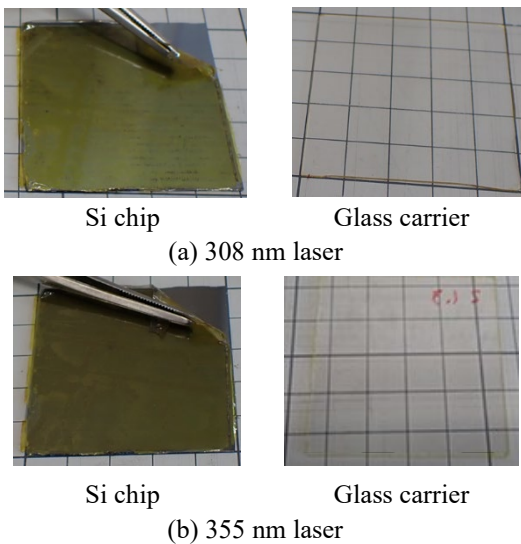


Fig. 13. Debonded sample by laser method

3.2.2 Applicability to photonic release method

Presumed mechanism of photonic release method is shown in Fig. 14.

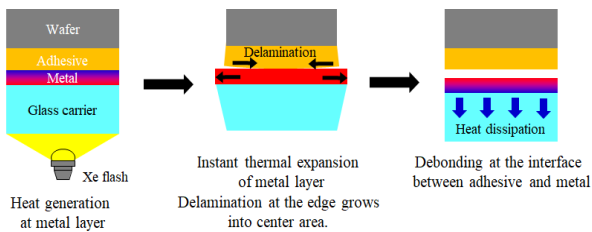
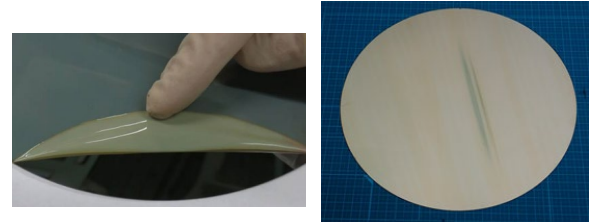


Fig. 14. Presumed mechanism of photonic release

Light energy is converted to the heat energy at metal layer on glass carrier, resulting in instant thermal expansion of metal layer. However, viscoelastic adhesive layer doesn't respond to this dimensional change simultaneously and the delamination at the edge grows to the center area.

Adhesive layer also works as heat insulating layer and the generated heat at metal layer doesn't propagate to temporary bonded wafer or package.

Debonding test result is shown in Fig. 15. Only by Xe flash light irradiation for 1 ms, 8 inch Si wafer can be debonded at the interface between adhesive and metal layer on glass carrier smoothly. Adhesive layer can be removed by peeling off after debonding as well.



Si wafer Glass carrier with metal layer
Fig. 15. Debonded sample by photonic release method.

3.3 Process demonstration

3.3.1 Wafer thinning

Fig. 16 summarizes the demonstration result of wafer thinning. No damage is observed during back grinding process down to 50 μm thickness and glass carrier can be debonded by photonic release method. The residual adhesive layer on thinned wafer can also be removed by peeling off.

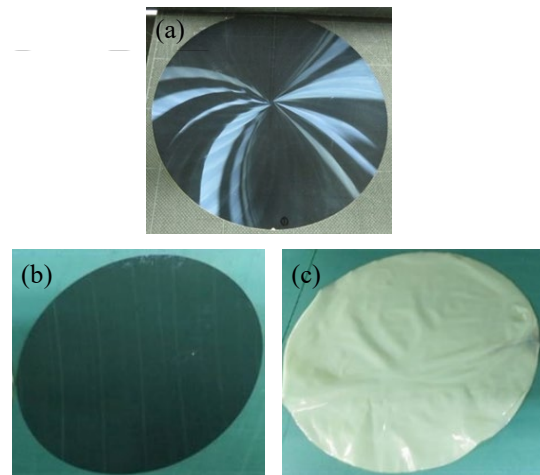


Fig. 16. Wafer thinning demonstration result (a) After back grinding, (b) Thinned wafer after peeling off, (c) Adhesive layer after peeling off

3.3.2 FOWLP

Fig. 17 summarizes the demonstration result of FOWLP process. Chips can be bonded on adhesive layer and no voids are observed by SAM (Scanning Acoustic Microscopy) inspection. No defects occur during molding and debonding by photonic release method and we can obtain re-constituted wafer.

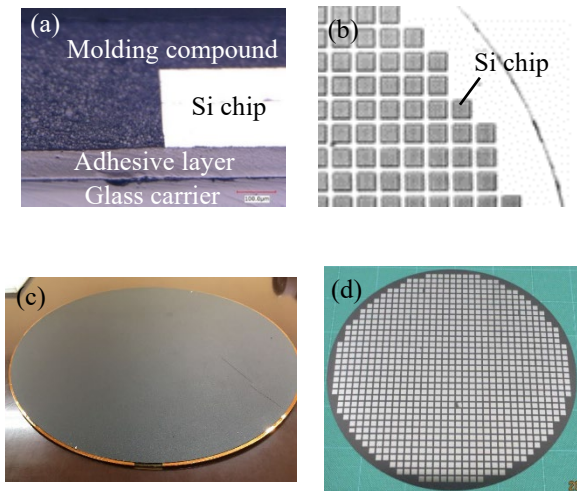


Fig. 17. FOWLP demonstration result (a) Cross-section of bonded chip, (b) SAM image of chip bonding area, (c) After molding, (d) Re-constituted 300 mm wafer

4. Conclusion

We introduced new temporary bonding adhesive and its applicability to both laser debonding method and newly developed photonic release method.

Our new adhesive having high heat resistance, good chemical resistance, good bondability, and peeling off capability is expected to be a promising candidate material for temporary bonding adhesive for advanced packaging process. In addition, our new adhesive is compatible with photonic release method enabling higher throughput as well as laser debonding method by combination with laser release material.

Based on these results, we continue to develop temporary bonding/debonding system for enhancing in-process reliability and productivity of advanced packaging process.

Acknowledgements

We would like to acknowledge the collaboration with Hitachi High-Tech Corporation and NovaCentrix for Xe flash lamp system.

References

1. Z. Dong, and Y. Lin, *Mater. Sci. Semicond. Process*, **105** (2020) 104681.
2. Y. Arimitsu, *J. Adhesion Soc. Jpn.*, **44** (2008) 26.
3. Y. Ohyama, *J. Rubber Soc. Jpn.*, **78** (2005) 441.
4. T. Inada, and M. Kume, *J. Rubber Soc. Jpn.*, **85** (2012) 26.
5. P. Montmeat, L. Bally, T. Enot, and F. Fournel, *Mater. Sci. Semicond. Process*, **123** (2021) 105550.

6. M. R. Marks, K. Y. Cheong, and Z. Hassan, *Crit. Rev. Solid State Mater. Sci.*, **40** (2015) 251.
7. S. Masuda, A. Yamaguchi, Y. Iwai, M. Sawano, K. Okabe, and Kazuto Shimada, *J. Photopolym. Sci. Technol.*, **32** (2019) 203.
8. K. Ohkita, H. Mizuno, H. Ishii, H. Kato, T. Mori, H. Ishikawa, Y. Maruyama, and K. Hasegawa, *JSR Technical Review*, **126** (2019) 18.
9. M. Woehrmann, T. Braun, M. Toepper, and K. D. Lang, *Proc. 68th Electron. Compon. Technol. Conf.* (2018) 675.
10. H. Zhang, X. Liu, S. Rickard, R. Puligadda, and T. Flaim, *Proc. 68th Electron. Compon. Technol. Conf.* (2018) 1925.
11. A. Phommahaxay, A. Podpod, J. Slabbekoom, E. Sleenckx, G. Beyer, E. Beyne, A. Guerrero, D. Bai, and K. Arnold, *Proc. 68th Electron. Compon. Technol. Conf.* (2018) 985.
12. J. Bertheau, F. Inoue, A. Phommahaxy, L. Peng, S. Iacovo, N. Rassoul, E. Sleenckx, K. Rebibs, A. Miller, G. Beyer, E. Beyne, and A. Nakamura, *Proc. 68th Electron. Compon. Technol. Conf.* (2018) 86.
13. Q. Wu, X. Liu, K. Hao, D. Bai, and T. Flaim, *Proc. 67th Electron. Compon. Technol. Conf.* (2017) 890.
14. J. H. Lau, *J. Electron. Packag.*, **141** (2019) 1.
15. K. Kennes and A. Guerrero, *Chip Scale Review*, **24** Nov./Dec. (2020) 19.
16. Y. S. Yang, K. U. Hwang, and R. Gorrell, *Proc. 69th Electron. Compon. Technol. Conf.* (2019) 330.
17. I. Daido, R. Watanabe, T. Takahashi, and M. Hatai, *Proc. 71st Electron. Compon. Technol. Conf.* (2021) 693.
18. C. H. Lee, B. Huang, J. See, X. Liu, Y. M. Lin, W. L. Chiu, C. J. Chen, O. H. Lee, H. E. Ding, R. S. Cheng, A. Y. Lin, S. T. Wu, T. C. Chang, H. H. Chang, and K. N. Chen, *Proc. 71st Electron Compon. Technol. Conf.* (2021) 736.
19. K. Hwang, K. S. Kim, R. Gorrell, K. W. Kim, Y. U. Yung, and W. Zou, *Proc. 71st Electron. Compon. Technol. Conf.* (2021) 754.
20. A. Guerrero, P. Bex, A. M. Jones, A. Southard, D. Dong, Alain Phommahaxay, and E. Beyne, *Proc. 54th Int. Symp. Microelectron.* (2021) 60.
21. V. Turkani, V. Akhavan, X. Liu, L. Prenger, and X. Martinez, *Proc. 54th Int. Symp. Microelectron.* (2021) 67.
22. Y. Akasu, E. Miyazawa, T. Enomoto, Y. Oyama, S. Sobue, R. Furutani, Y. Nakamura, and T. Kawamori, *Proc. 53rd Int Symp. Microelectron.* (2020) 302.

Negative Photo-Definable Polyimide Dry Films For Fine And High Aspect Ratio Patterning

Keigo Kato^{1*}, Yoshiko Tatsuta¹, Kazuyuki Matsumura¹,
and Akira Shimada¹

¹ Toray Industries, Inc.,
1-2, Sonoyama 3-chome, Otsu, Shiga 520-8420, Japan
*keigo.kato.x9@mail.toray

We newly developed a negative photo-definable polyimide dry films with higher photoreactivity than conventional ones. We succeeded in fine and high aspect ratio patterning with 90 μm thickness and 8 μm width by using new polyimide dry films. When compared after curing, the tensile breaking strength and share strength of new and conventional polyimide dry films were almost the same. However, when compared after PEB and exposure, the new ones showed clearly higher properties than conventional one. Using this polyimide dry film as an inter-layer dielectrics or a permanent resist was effective in improving the wiring density of electric devices.

Keywords: Photo-definable polyimide, Dry film, High aspect ratio, Permanent resist

1. Introduction

In order to support the 5G telecommunication system, smartphones and wearable terminals are required to have higher performance [1]. In addition, communication modules and sensors are being incorporated into everything such as home appliances and automobiles, and the demand for module parts is increasing explosively. Therefore, there is an increasing demand for higher functionality, higher frequency, and smaller size of electronic devices.

Polyimide is widely used as a surface protective layer, interlayer dielectrics of semi-conductor devices or electronic devices for its excellent heat stability, electrical and mechanical properties [2]. For those applications, polyimide was required to obtain suitable pattern. So we have developed photo-

definable polyimide dry films (PIDFs) which were able to obtain the polyimide pattern by using common photo lithographic technique for inter layer dielectrics applications in electronic devices [3].

– Recently, we have developed a negative photo-definable PIDF (PIDF-2) with higher light transmittance than conventional one (PIDF-1), and succeeded in patterning 15 μm via at 100 μm thickness [4]. We believe that PIDF-2 is effective materials for miniaturization of package of RF filters.

However, when patterning lines and spaces with a high aspect ratio using PIDF-2, the pattern was twisted or peeled off. We assumed that the cause of twist and peeling was insufficient photoreactivity of PIDF. In this work, we newly developed a negative photo-definable PIDF (PIDF-3) with improved

Table 1. The type of PIDFs prepared in this work.

	Type	Composition		
		Base polyimide	Cross linker	Photoinitiator
PIDF-1	Standard	P1	M1	I1
PIDF-2	Fine resolution	P2 (High light transmittance)	M2	I2
PIDF-3	High aspect ratio	P2 (High light transmittance)	M3 (High photoreactivity)	I2

Received April 1, 2022
Accepted June 20, 2022

photoreactivity, and compared the patterning properties, mechanical strength, and shear strength of PIDFs.

2. Experimental

In this work, we prepared negative photo-definable PIDFs in Table 1. These PIDFs were made to cast the solution of polyimide varnishes on the surface-treated PET film, and solvent was dried up in the oven. The thickness of dry films was 45 μm . These polyimide varnishes contained solvents, base-polyimides, cross linkers, photosensitizers, and so on.

PIDFs were laminated on the silicon substrates at 80 $^{\circ}\text{C}$ and PET films were peeled. The same films were laminated again to prepare 90 μm thick polyimide layers on the substrates. Exposure was performed through the photomask at 365 nm by using mercury lamp with band-path filter. Post exposure baking (PEB) was carried out at 90 $^{\circ}\text{C}$ for 10 min. The substrates with polyimide layers were dipped into 2.38 wt% tetramethylammonium hydroxide (TMAH) solution for 180s. After curing at 180 $^{\circ}\text{C}$ for 1 hour in N_2 atmosphere, we obtained patterned polyimides on the substrates. We observed these patterned polyimides by a scanning electron microscope (SEM).

The light transmittance of PIDFs were measured with an ultra violet-visible spectrophotometer at 365 nm.

The mechanical properties of PIDFs after development and after curing in the photolithography process described above was measured by using a universal tester (AG-Xplus). The load cell used was 50 N and the crosshead rates 50 mm/min.

The adhesion share strength of patterned polyimide on the silicon substrate after development and after curing in the above photolithography process was measured by using a Dage 4000 series. The pattern size was 120 μm \times 100 μm and the test speed was 200 $\mu\text{m}/\text{s}$.

3. Results and discussion

3.1. Patterning results

Fig. 1 shows cross-section SEM images of patterned polyimide after curing. In the case of PIDF-1, which is a conventional PIDF, polyimide was all dissolved because the bottom of PIDF was hardly reacted due to its low light transmittance. On the other hand, in the case of PIDF-2, we could obtain patterned polyimide at 90 μm thickness on the silicon substrate and the minimum size of patterned width which we could obtain was 15 μm (aspect ratio: 6). When the pattern width was 10 μm , the patterned polyimide was twist, and less than 10 μm ,

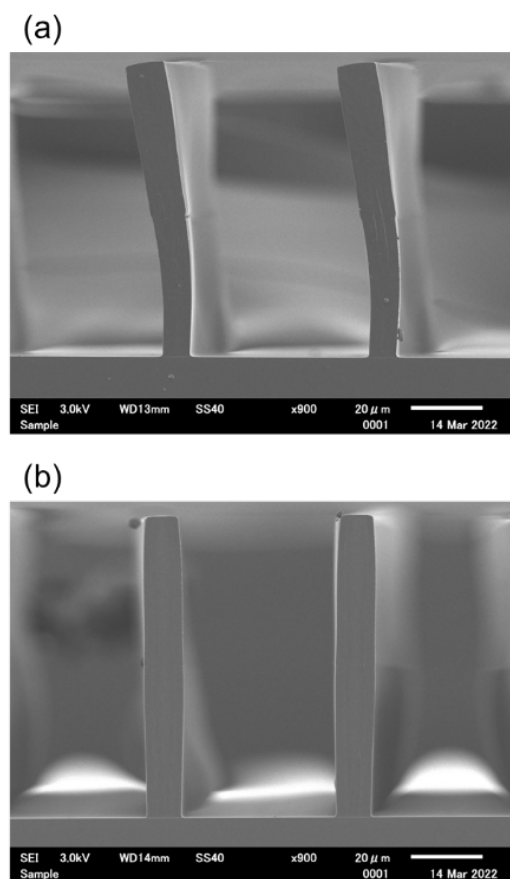


Fig. 1. Cross-section SEM images of patterned polyimide dry films at 90 μm thickness.

(a) PIDF-2 (L/S width: 10/50 ($\mu\text{m}/\mu\text{m}$), dose of exposure: 2000 mJ/cm^2)

(b) PIDF-3 (L/S width: 8/50 ($\mu\text{m}/\mu\text{m}$), dose of exposure: 1500 mJ/cm^2)

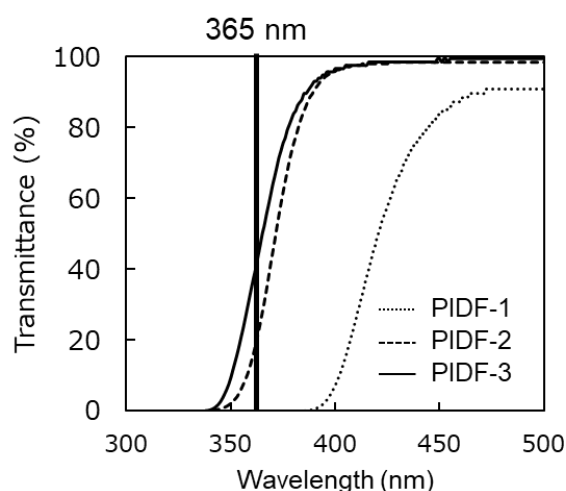


Fig. 2. The light transmittance of PIDF-1 (dot line), PIDF-2 (broken line) and PIDF-3 (solid line) at 90 μm thickness. Bold line shows the wavelength at exposure.

it was peeled off. We assumed that the photoreactivity of PIDF-2 was insufficient, so if the pattern width became smaller and aspect ratio became higher, patterned polyimide was more likely to be twisted or peeled off due to its weakness of mechanical strength and adhesive strength after development.

We newly developed PIDF-3 with improved photoreactivity by using highly reactive photo cross linkers (M3) so that finer and higher aspect ratio patterning can be performed. As expected, we could obtain the patterned polyimide with a pattern width of 8 μm (aspect ratio: 11.3) without twist by using PIDF-3. In addition, PIDF-3 could be patterned with lower exposure due to higher photoreactivity than PIDF-2.

Fig. 2 shows the light transmittance of PIDFs at 90 μm thickness. We designed monomer molecule of polyimide (P2) in order to increase the light transmittance below 400 nm by suppressing the intra-polymer chain interaction based on charge transfer complex of the polyimide. Therefore, the photoreaction of at the bottom of the pattern of PIDF-2 and PIDF-3 became easier to proceed. In addition, because photo cross linkers contained in PIDF-3 have higher photoreactivity, we could reduce the amount of photoinitiator in PIDF-3 and the light transmittance of PIDF-3 was higher than that of PIDF-2. As a result, the reverse taper shape of the cross section became improved by using PIDF-3.

3.2. Mechanical properties and Adhesive share strength

Fig. 3 shows the tensile strength after development and curing. When compared after curing, the tensile strengths of PIDF-2 and PIDF-3 were almost the same. However, when compared after development, PIDF-3 showed a clearly higher tensile strength than PIDF-2. From the results, in the case of PIDF-2, it was inferred that the cross-linking reaction by exposure and PEB was insufficient and the reaction proceeded to the extent that sufficient mechanical strength was exhibited by curing at 180 °C. On the other hand, in the case of PIDF-3, it was speculated that the cross-linking reaction by exposure and PEB was proceeded considerably due to its high photoreactivity, and the twist after development was improved.

Fig. 4 shows the adhesion share strengths after development and curing. Similar to the mechanical strength, the adhesion share strength after curing was almost the same between PIDF-2 and PIDF-3, while that after development was clearly higher in PIDF-3. This result supports the fact that PIDF-2 peeled off when photolithography with a finer pattern was

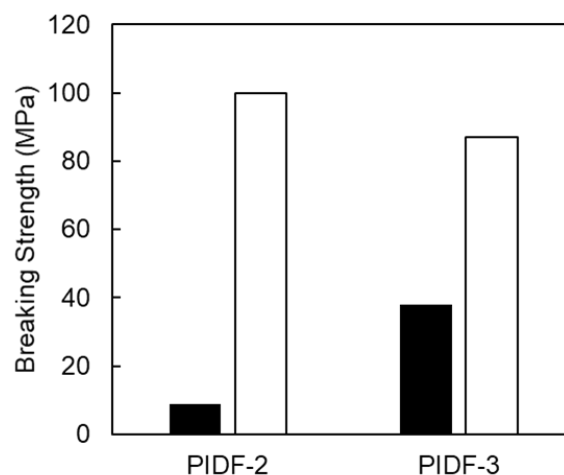


Fig. 3. The tensile strengths of PIDF-2 and PIDF-3 after development (black) and curing (white).

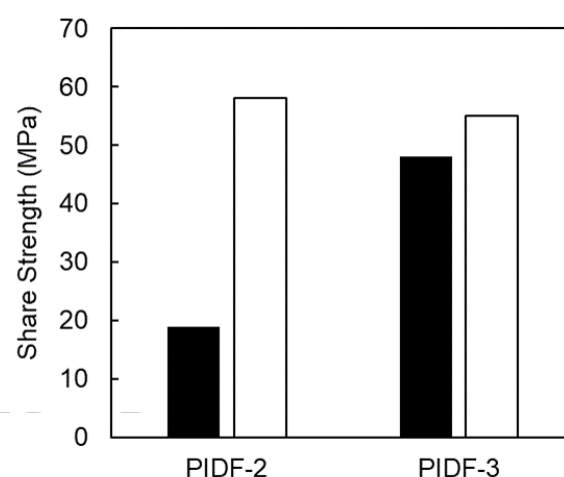


Fig. 4. The adhesion share strengths of PIDF-2 and PIDF-3 after development (black) and curing (white).

performed, whereas PIDF-3 succeeded in patterning. The difference in the adhesion share strengths after development between PIDF-2 and PIDF-3 was also explained by the difference in photoreactivity. From the above, it was found that when patterning with a high aspect ratio, it is important to increase the mechanical strength and the adhesion shear strength after exposure and PEB, not after curing.

4. Conclusion

We succeeded in fine and high aspect ratio patterning with 90 μm thickness and 6 μm width by using a newly developed photo-definable polyimide dry film, PIDF-3. The new polyimide dry film showed higher light transmittance and larger mechanical strength and adhesive strength after

exposure and PEB than the conventional polyimide films by designing monomer molecules of polyimide and using high photoreactive cross-linkers.

References

1. Y. Kishiyama, A. Benjebbour, S. Nagata, Y.Okumura, and T. Nakamura, *NTT Docomo Tech.J.*, **23** (2014) 6.
2. J. H. Kim, *J. Photopolym. Sci. & Technol.* **22**(2009) 403.
3. M. Tomikawa, R. Okuda, H. Ohnishi, *J. Photopolym. Sci. & Technol.* **28**(2015) 73.
4. An Organic Cavity Structure for FR-filter by Using High Elastic Modulus Photo-definable Dry film Polyimide, Wafer-Level Packaging Symposium 2022 Feb 15,2022

Visible-Light Sensitive Reworkable Resins for Dental Application: Improved Stability

Haruyuki Okamura^{1*}, Yuka Iwamoto², and Hitoshi Kawanabe³

¹ *Department of Applied Chemistry, Graduate School of Engineering,
Osaka Metropolitan University,*

1-1 Gakuen-cho, Naka-ku, Sakai, Osaka 599-8531, Japan

² *Department of Applied Chemistry, College of Engineering,
Osaka Prefecture University, 1-1 Gakuen-cho, Naka-ku, Sakai, Osaka 599-8531, Japan*

³ *Department of Oral Growth and Development, Ohu University, School of Dentistry,
Fukushima 963-8611, Japan*

**okamura@omu.ac.jp*

A reworkable resin, which is degradable after use, was developed for application as a dental resin with an enhanced stability. A dimethacrylate monomer containing a ketal linkage in the molecule was used as a reworkable monomer. The reworkable monomer was successfully cured by blue light irradiation (470-nm light) using the camphorquinone/amine photoinitiating system. The cured reworkable resins were degraded in the presence of a UV- and violet-light sensitive photoacid generator by subsequent irradiation of UV light (365-nm light) at room temperature. The degradation was due to the acid-catalyzed decomposition of the ketal linkages in the cured reworkable monomers. Selection of the evaluated photoacid generators is very important in order to improve the stability of the cured resin. The result suggested the possibility of application of the reworkable monomer as a dental resin.

Keywords: Reworkable resin, Dental material, Blue light, UV light, Degradation

1. Introduction

Reworkable resins, which are degradable after use, have attracted much attention for applications as functional materials [1-3]. On the other hand, visible light-sensitive photocuring materials have been widely applied for use in dental and biomaterials [4-8]. Recently, a preliminary result of a reworkable resin as a dental material was reported [9]. A dimethacrylate monomer containing a ketal linkage in the molecule [10-12] was used as a reworkable monomer. The reworkable monomer was successfully cured by blue light irradiation (470-nm light) using the camphorquinone (CQ)/amine photoinitiating system. The cured reworkable resins were degraded in the presence of a UV- and violet-light sensitive photoacid generator (PAG) [13] by prolonged irradiation at room temperature. The degradation was due to the acid-catalyzed

decomposition of the ketal linkages in the cured reworkable monomers. The preliminary result suggested the possible application of the reworkable monomer as a dental resin [9]. Unstability of the cured resins on irradiation at 470 nm was a serious problem for practical use. We extended the preliminary study to improve the stability of the photocured resins by evaluating various PAGs [13-20]. The photocuring and degradation properties of the reworkable resins were evaluated using UV-vis and in-situ FT-IR measurements. The effect of the PAGs on the stability of the cured reworkable resins are discussed.

2. Experimental

2.1. Materials

A reworkable monomer, 2,2-di(methacryloyloxy-1-ethoxy)propane (DMOEP) [10-12], was synthesized as already reported [9]. CQ and 2-

Received April 1, 2022

Accepted June 10, 2022

(dimethylamino)ethyl methacrylate (DMAEMA) were purchased from Nacalai Tesque (Japan) and used without further purification. *N*-trifluoromethanesulfonyloxy-1,8-naphthalimide (NITf, Midori Kagaku) [14], diphenyl[(4-phenylthio)phenyl]sulfonium hexafluorophosphate (DPTPSP, product name: CPI-100P, San Apro, Japan) [15], and a derivative of NITf (PAG1, product name: NP-SE10, San Apro, Japan) were used as received. 7-(1,1-Dimethylethyl)-1,3-dihydro-1,3-dioxo-2H[1,4]benzodithiino[2,3-*f*]isoindol-2-yl trifluoromethanesulfonate (tBuTHITf) [13] and benzanthrenylideneimino *p*-toluenesulfonate (BITS) [16] were prepared as previously reported. Structures of chemicals are shown in Fig. 1.

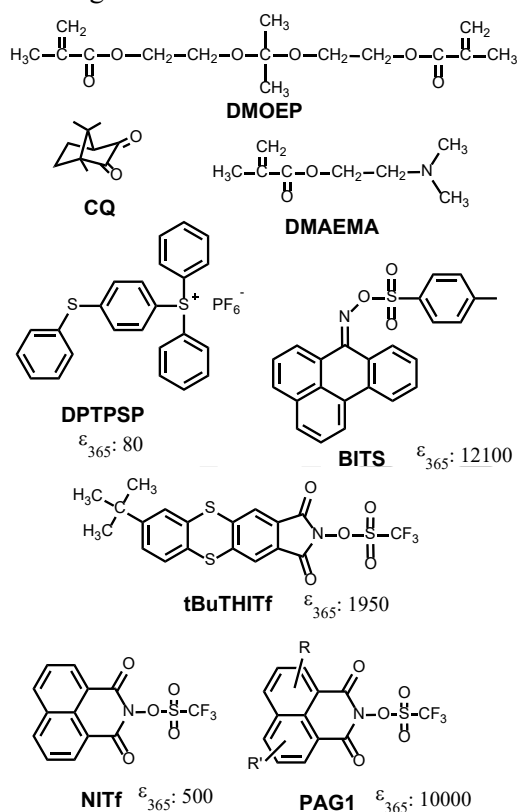


Fig. 1. Structures of chemicals used. The values of the molar absorption coefficients of the PAGs at 365 nm in acetonitrile (ϵ_{365}) are also shown.

2.2. Measurements

The UV-vis spectra were obtained using a Shimadzu UV-2450. The irradiations at 365 nm and at 470 nm were performed in air using a xenon lamp (Asahi spectra MAX-301, 300 W) in combination with a band path filter of 365 nm or 470 nm. The intensity of the light was measured by an Orc Light Measure UV-M02 or Ushio USR-45VA. The in-situ FT-IR measurements were

carried out using a Jasco FT/IR 4200 equipped with a horizontal stage (Jasco TH-4000M). Formulation of the liquid samples in this study was fixed at DMOEP/CQ/DMAEMA/PAG = 100/1/1/3 (wt/wt/wt/wt). The liquid sample was placed on a silicon wafer, covered with a CaF₂ plate (thickness of the liquid: ca. 10 μ m), and placed on the horizontal stage. Irradiation was performed at an angle of 45° to the sample. The curing and decomposition reactions of the sample were analyzed using the peak at 1637 cm⁻¹ ascribed to the C=C units of DMOEP, at 2990 cm⁻¹ ascribed to the ketal CH₃ units of DMOEP, and at 3470 cm⁻¹ ascribed to the OH groups that appeared after decomposition of the DMOEP. The thickness of the samples was determined by interferometry using a Nanometrics M3000.

3. Results and discussion

3.1. Formulation and characteristics of PAGs

In a previous study [9], we reported that the formulation DMOEP/CQ/DMAEMA/tBuTHITf = 100/1/1/3 (wt/wt/wt/wt) acted as a reworkable resin which was applicable as dental resins. In this formulation, DMOEP acts as a reworkable monomer, a dimethacrylate monomer containing a ketal linkage in the molecule. Compounds CQ and DMAEMA act as a photoinitiating system sensitive to blue light. tBuTHITf is a PAG which is sensitive to violet and UV light. Spontaneous degradation occurred after curing though an excess amount of tBuTHITf versus DMAEMA was added due to the quenching reaction of the produced acid by the amino groups of DMAEMA. We consider that the instability of the cured resin can be suppressed to optimize the PAGs used. In this study, five PAGs, which are sensitive to UV light (Fig. 1), were investigated. The values of the molar absorption coefficients of the PAGs at 365 nm in acetonitrile (ϵ_{365}) are also shown in Fig. 1. The effect of the PAGs on the curing and degradation properties are discussed in section 3.4.

3.2. UV-vis spectral changes

The penetration of light is very important for the determination of the formulation of the photosensitive materials. The UV-vis spectra of the sample liquids were observed using the samples sandwiched between quartz plates with spacers of several different thicknesses. Figure 2 shows the UV-vis spectrum of the sample containing PAG1 as a PAG (thickness: 10 μ m). The power spectra of the 470-nm light (broken line) and 365-nm light

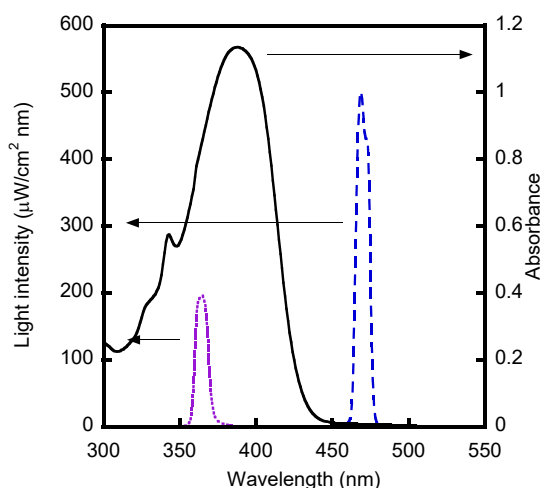


Fig. 2. Power spectra of 470-nm light (broken line) and 365-nm light (dashed line) and UV-vis spectrum of sample containing PAG1 as a PAG (solid line) (thickness: 10 μm). Light intensity: 5.5 mW/cm^2 (470 nm) and 2.2 mW/cm^2 (365 nm).

(dotted line) are also shown. Both the 470-nm light and the 365-nm light penetrated through the bottom of the samples.

The UV spectral changes upon irradiation were investigated. Figure 3 shows the samples which had thicknesses of 10 μm . Slight spectral changes were observed upon irradiation at 470 nm. The spectral changes may be due to the slight decomposition of both CQ and PAG1. After the irradiation, the sample liquid changed to a solid, which indicated that a curing reaction occurred during the irradiation. Significant changes were observed upon irradiation of 365-nm light instead of 470-nm light due to the decomposition of the PAG1.

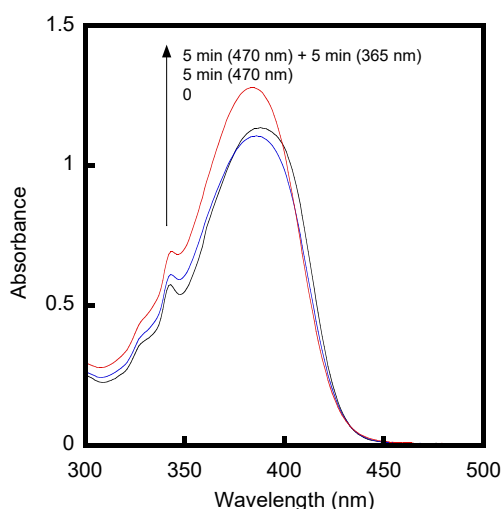


Fig. 3. UV-vis spectral changes of samples containing PAG1 as a PAG upon irradiation. Thickness: 10 μm . Light intensity: 1.63 mW/cm^2 (470 nm) and 0.65 mW/cm^2 (365 nm).

3.3. In-situ FT-IR measurements

3.3.1. Photocuring

In-situ FT-IR measurements of the sample were carried out. The thickness of the sample was adjusted to ca. 10 μm due to the limitation of the peak intensities of the samples. The sample was covered by a CaF_2 plate to avoid an oxygen inhibition. Figure 4 shows the FT-IR spectra of the samples containing PAG1 before and after the irradiation at 470 nm. The peak ascribed to the $\text{C}=\text{C}$ (1637 cm^{-1}) groups decreased during the

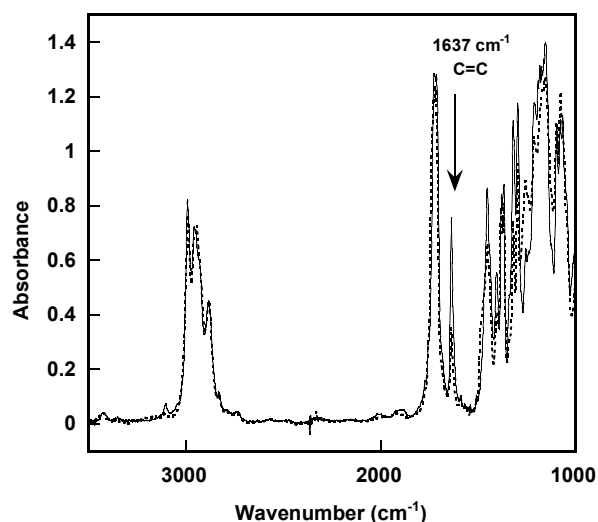


Fig. 4. FT-IR spectral changes of the sample containing PAG1 as a PAG upon irradiation. Solid line: before irradiation. Broken line: after irradiation at 470 nm for 5 min. Light intensity: 3.9 mW/cm^2 .

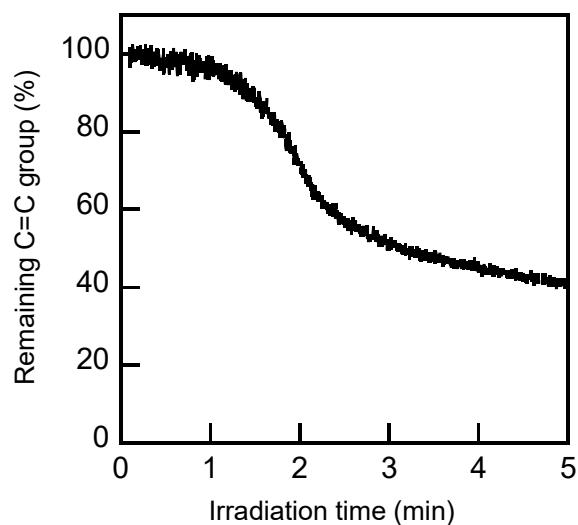


Fig. 5. Conversion of $\text{C}=\text{C}$ groups in the sample containing PAG1 measured by in-situ FT-IR.

irradiation, which indicated that photopolymerization of methacryl groups of DMOEP occurred. Figure 5 shows the conversion of the C=C groups calculated from the peak intensities at 1637 cm^{-1} measured by in-situ FT-IR. The conversion of the C=C group of DMOEP was 60% after irradiation for 5 min. The photopolymerization was observed using the samples containing all the PAGs used in this study. We reported that the sample containing tBuTHITf was degraded upon irradiation at 470 nm [9]. The peak at 3470 cm^{-1} ascribed to the OH group, which was generated after the decomposition of DMOEP, started to increase after irradiation for 1 min and gradually increased during the irradiation [9]. The irradiated samples containing PAGs except for tBuTHITf were stable even after removal of a CaF_2 plate. The choice of the PAG was very important in order to enhance the stability of the irradiated sample. The conversions of the samples after irradiation for 5 min ranged from 7 to 60%. The effect of the PAGs on the photopolymerization properties are discussed in Section 3.4.

3.3.2. Photodegradation

Photodegradation of the cured samples after irradiation was carried out upon irradiation at 365 nm . Figure 6 shows the FT-IR spectral changes of the cured sample containing PAG1 as a PAG upon irradiation at 365 nm . The peak at 3470 cm^{-1} ascribed to the OH group, which was generated after the decomposition of DMOEP, appeared and gradually increased during the irradiation. The increase in the peak at 3470 cm^{-1} accompanied with the decrease in the peak at 2990 cm^{-1} were ascribed to the ketal CH_3 units in DMOEP. Figure 7 shows the conversion of the ketal CH_3 groups calculated using the peak intensities at 2990 cm^{-1} in addition to the increased absorbance values of the -OH groups in the sample containing PAG1 measured by in-situ FT-IR. The result clearly suggests that the removal of the ketal CH_3 units in DMOEP and generation of OH groups simultaneously occurred. About an 80% degradation was observed after irradiation for 20 min. We concluded that the sample containing PAG1 as a PAG acted as a reworkable photocurable resin sensitive to 470 nm and is degradable upon irradiation at 365 nm after use. The plausible reaction mechanism using PAG1 as a PAG is shown in Scheme 1. The reworkable monomer, DMOEP, was polymerized upon irradiation by the 470-nm light in the presence of the CQ/DMAEMA photoradical initiating system. The crosslinked

DMOEP was formed. After irradiation at 365 nm , PAG1 decomposed to produce an acid. When the amount of the produced acid exceeded the amount of DMAEMA, a tertiary amine, the crosslinked DMOEP, decomposed to form poly(2-hydroxyethyl methacrylate) and acetone.

When DPTSP, BITS, and NITf were used as PAGs, degradation of the cured samples upon irradiation at 365 nm was not observed. The effect of the PAGs on the curing and degradation properties is discussed in the next section.

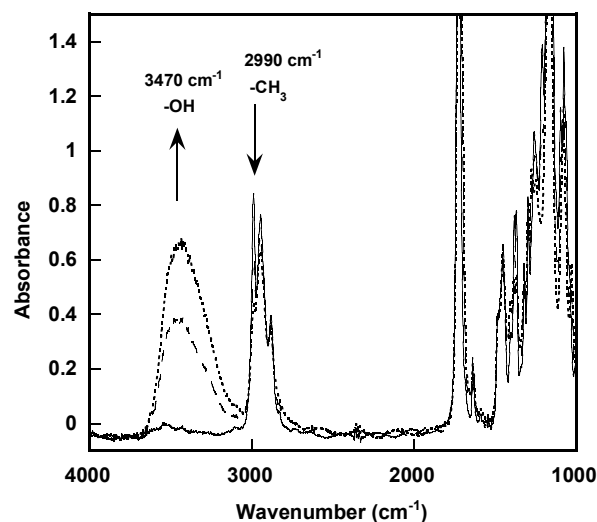


Fig. 6. FT-IR spectral changes of the cured sample containing PAG1 as a PAG upon irradiation. Solid line: before irradiation. Dashed line: after irradiation at 365 nm for 10 min. Broken line: after irradiation at 365 nm for 20 min. Light intensity: 3.9 mW/cm^2 . Curing condition: irradiated at 470 nm for 5 min.

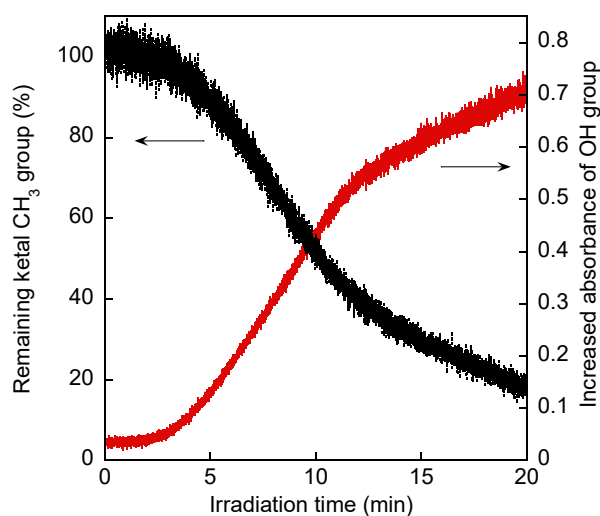
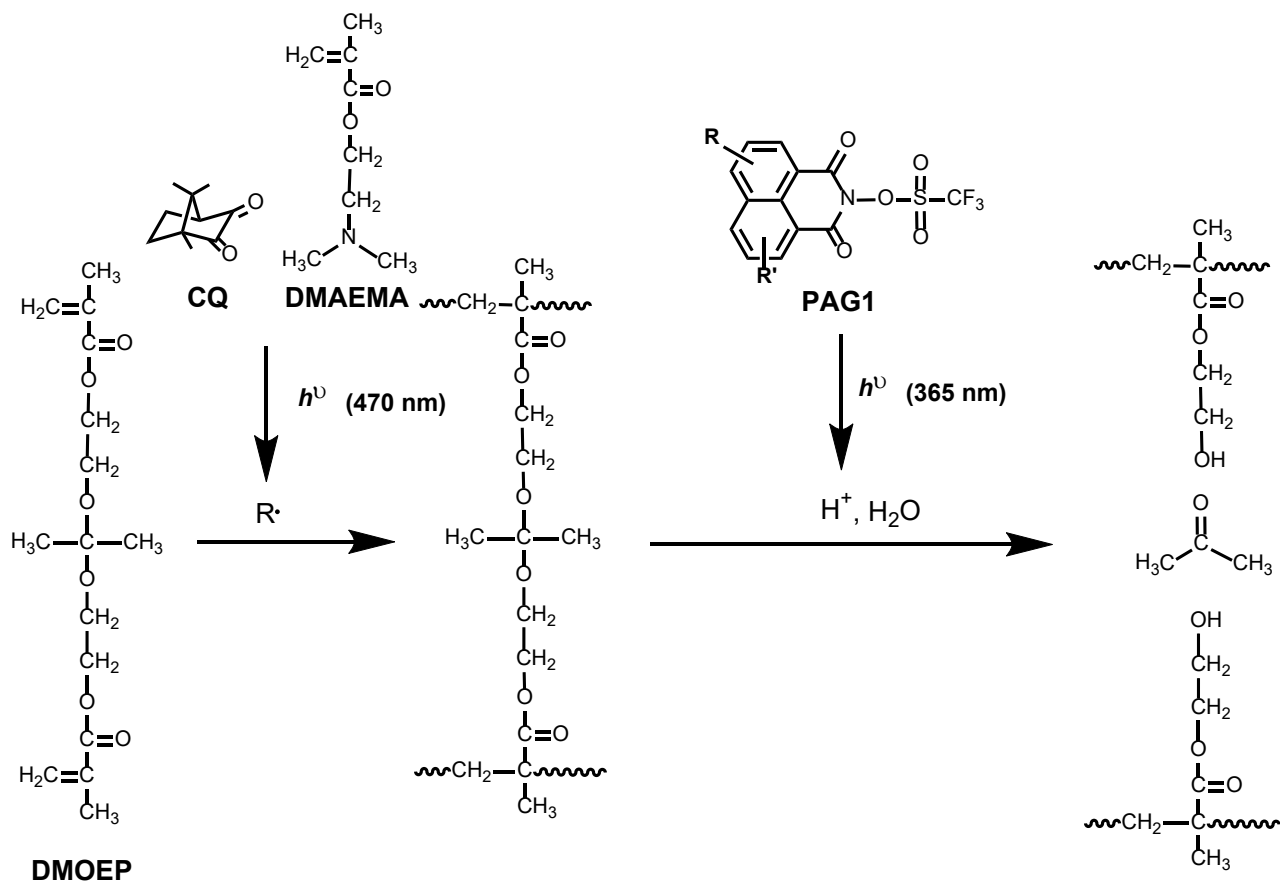


Fig. 7. Conversion of ketal CH_3 groups and increased values of absorbance of -OH groups in the sample containing PAG1 measured by in-situ FT-IR.



Scheme 1. Plausible reaction mechanism using PAG1 as a PAG.

3.4. Effect of the PAGs

Table 1 summarizes the effect of the PAGs on the curing and degradation properties. The values of ϵ_{365} ranged from 80 to 12100 which strongly affect the degradation property, but not the curing.

Table 1. Effect of PAGs on the curing and degradation properties.^a

PAG	ϵ_{365}^b	Conversion (%) ^c	Degradation
DPTPSP	80	50	Not observed
tBuTHITf	1950	7	Observed on irradiation at 470 nm
NITf	500	38	Not observed
BITS	12100	52	Not observed
PAG1	10000	60	Observed on irradiation at 365 nm

a) Formulation: DMOEP/CQ/DMAEMA/PAG = 100/1/1/3 (wt/wt/wt/wt). b) Molar absorption coefficient at 365 nm in acetonitrile. c) Conversion of C=C groups in DMOEP after irradiation at 470 nm for 5 min.

The curing reaction occurs upon irradiation at 470 nm. All the PAGs do not absorb the light except for tBuTHITf. We consider that the low conversion of the sample containing tBuTHITf (7% in Table 1) was because tBuTHITf worked as a quencher of the CQ/DMAEMA photoradical initiating system.

In terms of the degradation reaction, PAGs having high ϵ_{365} values are favorable due to their high acid yield. In addition, the acidity of the generated acid strongly affects the degradation reaction. PAG1 produces trifluoromethanesulfonic acid, which is stronger than *p*-toluenesulfonic acid generated from BITS [16]. Thus, we concluded that PAG1 was the best PAG investigated in this study. We believe that the optimization of the formulation, for example, the addition of bisphenol A diglycidyl methacrylate and tetraethylene glycol dimethacrylate, may be applicable for use as practical dental resins.

4. Conclusion

Reworkable resins, which are degradable after use, were used as dental resins. A reworkable

monomer, DMOEP, a dimethacrylate monomer containing ketal units in the molecule, was successfully cured by the irradiation of blue light (470-nm light) using a visible-light sensitive CQ/DMAEMA photoinitiating system. The effects of the PAGs on the curing and degradation properties were investigated. The cured reworkable resins were stable at room temperature except for the sample containing tBuTHITf as a PAG. The cured resins were degraded in the presence of PAG1 by irradiation at 365 nm. The degradation was due to the acid-catalyzed decomposition of the ketal linkages in the cured reworkable monomers which was revealed by in-situ FT-IR measurements. This result suggested the possible application of the reworkable monomer as dental resins.

Acknowledgements

This study was partly supported by a Grant-in-Aid by JSPS, KAKENHI Grant Number 16H02986 and by JST, CREST Grant Number JPMJCR21L3, Japan. We would like to thank the International Technology Exchange Society (ITE) for providing the English language editing service.

References

1. S. Ma and D. C. Webster, *Prog. Polym. Sci.*, **76** (2018) 65.
2. H. Okamura, *J. Network Polym. Jpn.*, **42** (2021) 223 (in Japanese).
3. H. Okamura, *J. Mater. Life Soc.*, **33** (2021) 45 (in Japanese).
4. T. Sakamoto, H. Kimura, K. Ohkawauchi, Y. Mizuta, and M. Hayashi, *J. Adhes. Soc. Jpn.*, **52** (2016) 153 (in Japanese).
5. I. Fujimori, T. Kaneko, H. Nishide, and E. Tsuchida, *Kobunshi Ronbunshu*, **50** (1993) 485 (in Japanese).
6. Z. Di and Y. Ito, *Sci. China Chem.*, **57** (2014) 510.
7. A. Aguirre-Soto, A. T. Hwang, D. Glugla, J. W. Wydra, R. R. McLeod, C. N. Bowman, and J. W. Stansbury, *Macromolecules*, **48** (2015) 6781.
8. S. Matsunaga, A. Tamura, M. Fushimi, H. Santa, Y. Arisaka, T. Nikaido, J. Tagami, and N. Yui, *ACS Appl. Polym. Mater.*, **2** (2020) 5756.
9. H. Okamura, Y. Iwamoto, and H. Kawanabe, *J. Photopolym. Sci. Technol.*, **34** (2021) 657.
10. J. A. Syrett, D. M. Haddleton, M. R. Whittaker, T. P. Davis, and C. Boyer, *Chem. Commun.*, **47** (2011) 1449.
11. P. Wang, Y. Yan, Y. Sun, R. Zhang, C. Huo, L. Li, K. Wang, Y. Dong, and J. Xing, *J. Mater. Chem. B*, **7** (2019) 6994.
12. E. J. Kepola and C. S. Patrickios, *Macromol. Chem. Phys.*, **219** (2018) 1700404.
13. H. Okamura, H. Naito, and M. Shirai, *J. Photopolym. Sci. Technol.*, **21** (2008) 285.
14. C. Iwashima, G. Imai, H. Okamura, M. Tsunooka, and M. Shirai, *J. Photopolym. Sci. Technol.*, **16** (2003) 91.
15. H. Okamura, S. Niizeki, T. Ochi, and A. Matsumoto, *J. Photopolym. Sci. Technol.*, **30** (2017) 405.
16. M. Shirai, T. Egusa, S. Morishita, and M. Tsunooka, *J. Photopolym. Sci. Technol.*, **12** (1999) 165.
17. H. Okamura and M. Shirai, *Trends Photochem. Photobiol.*, **15** (2013) 51.
18. T. Tsuchimura, *J. Photopolym. Sci. Technol.*, **33** (2020) 15.
19. S. Chen, X. Zhao, M. Jin, W. Huang, G. Ye, H. Pan, and D. Wan, *J. Polym. Sci.*, **51** (2021) 1899.
20. X. Lopez De Pariza, E. Cordero Jara, N. Zivic, F. Ruipérez, T. E. Long, and H. Sardon, *Polym. Chem.*, **12** (2021) 4035.

Photo-degradation of Di- and Trifunctional Oxime Ethers Bearing Polyphthalaldehyde Arms

Kanji Suyama^{1*}, Hirokazu Hayashi², and Hideki Tachi³

¹*Faculty of Liberal Arts and Sciences, Osaka Prefecture University,
1-1 Gakuencho, Nakaku, Sakai, Osaka 599-8531, Japan*

²*Research Division of Applied Material Chemistry,
Izumi Center, Osaka Research Institute of Industrial Science and Technology (ORIST),*

³*Research Division of Polymer Functional Materials,
Izumi Center, Osaka Research Institute of Industrial Science and Technology (ORIST),*

7-1 Ayumino-2, Izumi, Osaka 594-1157, Japan

**suyamakanji@omu.ac.jp*

Polyphthalaldehyde (PPA) is a representative degradable polymer that can be end-to-end depolymerized. Herein polymers bearing two and three PPA chains have been prepared, and their photochemical behaviors were investigated. The PPA chains were linked to fluorene and truxene cores via oxime ether units that are photoreactive moiety. Di- and trifunctional PPAs were obtained by anionic polymerization of phthalaldehyde monomer (*o*-PA) initiated by corresponding oximes and 1,8-diazabicyclo[5.4.0]undec-7-ene, even though the conversion of was low after purification. From the ¹H NMR spectral changes of CDCl₃ solutions of both PPA on irradiation with Hg-Xe lamp, it was found that PPAs decreased along with the formation of *o*-PA, and then the *o*-PA reduced along with the formation of phthalide. PPAs were also coated on CaF₂ substrates and irradiated with the lamp. UV spectral changes of the films showed the photochemical reaction of oxime ether moieties, and IR spectral changes indicated the formation of phthalide. These results clearly show that depolymerization and following photo-isomerization into phthalide proceeded both in solution and solid state. 2,7-Diacetylfluorene *O,O'*-dibenzylidioxime was newly prepared to discuss the photochemical reaction of oxime ether with fluorene chromophore.

Keywords: Polyphthalaldehyde, Anionic polymerization, Photo-degradation, Oxime ether, Depolymerization

1. Introduction

Controlled degradation of polymers is becoming more important technique from the viewpoint of fossil resource consume and polymer recycling and upcycling [1]. Polyphthalaldehydes (PPAs) have been known as a representative polymer that can be degradable even in solid state [2]. Since Aso and coworkers proposed PPAs as stable polyacetals with degradable nature [3], controlled degradation of PPAs has been accomplished by using stimuli such as acid [4-7], heat [8], fluoride ion [9], ultrasonic [10], deep UV [11], and EUV [12,13] irradiation in solutions and solid state.

On-demand degradation of the PPA has been utilized mainly as functional materials [2]. Especially, imaging is an important target for PPA degradation. Because the degradation with acids proceeds effectively even in solid state, micro-scale patterning by using photoacid generators has been demonstrated since 1980' [4]. Thermal scanning probe lithography (t-SPL) utilizes thermal degradation of layers only tapped area with hot needles, and the fabrication of sub-10 nm patterns is possible. PPAs are the most widely used materials for t-SPL because their depolymerization is endothermic which keeps the reaction localized, and resulting phthalaldehyde monomer (*o*-PA) do not

Received April 4, 2022

Accepted May 21, 2022

melt and flow, but rather directly sublimates [8]. In the use for EUV lithography, PPA-based photoresists gave moderate contrast curves with the assist of post-exposure bake [13]. Some of the above studies attempted end-to-end depolymerization (unzipping) by photoreaction of end-capping groups at PPA terminals [11,13].

We have synthesized PPAs with oxime ether terminals, and their photoreactions were investigated as a step of establishment of degradable networked polymers [14,15]. Oxime ether moieties proceed *E/Z* isomerization and homolytic N–O cleavage photochemically [16–18]. The thermal [19] and hydrolytic stability [20] of oxime ethers were also reported, which is advantageous in practical use. In our previous studies, PPAs had one naphthyl chromophore at their terminals. Utilizing the absorption of naphthyl groups, 313 nm irradiation was attempted both in solution and film state, and their depolymerization was confirmed in terms of spectral changes and nanoindentation technique.

In this study, we have prepared di- and trifunctional oxime ethers bearing PPA arms as shown in Fig. 1, and their photochemical behavior was investigated. Fluorene and truxene cores can be expected to enhance the sensitivity to near UV and visible region of light. To understand the depolymerization behavior, we have also prepared a model compound, 2,7-diacetylfluorene *O,O'*-dibenzylidioxime (FluBO) and discussed the mechanism.

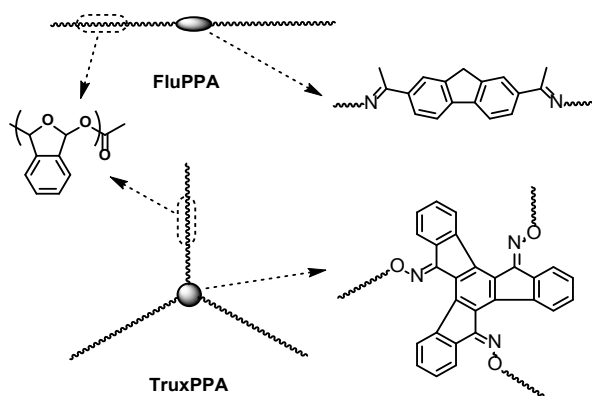


Fig. 1. Di- and trifunctional oxime ethers bearing PPA arms in this work.

2. Experimental

2.1. General

IR and UV spectra were recorded on Jasco FT-IR4200, and UV630 spectrometers, respectively. NMR spectra were measured by JEOL JNM-

ECX400 spectrometer. Melting point (mp) was measured with a Yanaco MPJ3 and uncorrected. Mass spectra were taken with a Thermo Scientific Q-Exactive by using electrospray ionization (ESI) in positive mode. Number (M_n) and weight (M_w) average molecular weights of polymers were obtained by size exclusion chromatography (SEC) by using a Shimadzu LC-20AD liquid chromatography system (Kyoto, Japan) composed of two Shodex KF-805L polystyrene mixed gel columns, and a Wyatt differential refractometer Optilab T-rEX detector with tetrahydrofuran (THF) eluent and polystyrene standards at 40 °C.

Chemicals were obtained from Nacalai Tesuque (Kyoto, Japan) as guaranteed reagent grade unless otherwise noted.

2.2. Oximes

Truxenone trioxime was obtained as described previously [21].

2,7-Diacetylfluorene dioxime was obtained as follows: 4.99 g (19.9 mmol) of 2,7-diacetylfluorene (Matrix Scientific, Colombia) and 5.59 g (80.45 mmol) of hydroxylamine hydrochloride were dissolved in 130 mL of pyridine and 30 mL of ethanol in a flask and heated at 70 °C for 3 h. The mixture was rotavapped, and the residue was washed with water. Obtained solid was recrystallized from acetone-methanol mixed solution to afford 4.57 g of colorless fine powder: Yield 81.8 %, mp 253.5–255 °C, ^1H NMR (DMSO- d_6): δ 11.20 (2H, s, OH), 7.70–7.91 (6H, m, aromatic), 3.98 (2H, s, CH₂), 2.21 (6H, s, CH₃). ^{13}C NMR (DMSO- d_6): δ 153.29, 143.80, 141.28, 135.95, 124.65, 122.48, 120.20, 36.67, 11.87. High Resolution MS (ESI) m/z : [$M+H^+$] calcd for C₁₇H₁₇N₂O₂ 281.1290; found 281.1275.

2.3. FluBO

In a flask, 1.60 g (10.0 mmol) of *O*-benzylhydroxylamine hydrochloride and 1.13 g (4.52 mmol) of 2,7-diacetylfluorene were dissolved in 25 mL of pyridine and heated at 60 °C for 2.5 h. After removing the solvents under reduced pressure, the residue was washed with water to obtain 2.02 g of ivory powder. After recrystallization from chloroform, 1.11 g (2.40 mmol) of colorless tissues was recovered: Yield 53.1 %, mp 195–196 °C ^1H NMR (CDCl₃): δ 7.84 (2H, s, fluorene 1H and 8H), 7.65–7.76 (4H, m, fluorene 3–6H), 7.25–7.45 (10H, m, phenyl), 5.27 (4H, s, CH₂), 3.92 (2H, s, fluorene 9H), 2.38 (6H, s, CH₃). ^{13}C NMR (CDCl₃): δ 155.28 143.85, 142.06, 138.08, 135.39, 128.38,

Table 1. Polymerization conditions and characteristics of resulting PPAs.

Entry (Abbrev.)	Oxime	Initiator solution ^a	P. T. ^b (min)	Conv. (%) ^c	M_n (kDa) ^d	M_w (kDa) ^d
1 (TruxPPA)	Truxenone trioxime	Pyridine 0.1 mL + CH ₂ Cl ₂ 1.1 mL	60	14.8	12.3	22.0
2	Truxenone trioxime	Pyridine 1 mL	20	8.7	20.2 ^e	26.1 ^e
3	Truxenone trioxime	Pyridine 1 mL	60	12.4	15.4	20.9
4 (FluPPA)	Diacetylfluorene dioxime	Pyridine 1 mL	20	15.9	24.0 ^e	32.0 ^e

a) Containing oxime and DBU and added to solution containing 960 mg of *o*-PA and 20 mL of CH₂Cl₂. OH group in oxime / DBU / *o*-PA = 1 / 1 / 80 (molar ratio).

b) Polymerization time at -80 °C.

c) Based on the weight of polymers after separation using a recycle SEC system.

d) From SEC with polystyrene standards, THF eluent, and RI detector.

e) Bimodal trace.

128.11, 127.76, 125.13, 122.67, 119.97, 36.91, 13.41. UV (CH₃CN): λ_{max} 323.2 nm (ϵ : 4.2×10^4 L·mol⁻¹·cm⁻¹). High Resolution MS (ESI) m/z : [$M+H^+$] calcd for C₃₁H₂₉N₂O₂ 461.2229; found 461.2273.

2.4. Polymerization

Typical polymerization was carried out as follows: In a flask, 960 mg (7.16 mmol) of *o*-PA (SP grade for fluorometry, recrystallized, Nacalai) was put, and the flask was purged with argon gas after equipment of a three-way cock with a septum and a balloon. Then 20 mL of CH₂Cl₂ (dehydrated grade, Nacalai, H₂O < 50 ppm) was added through a syringe to the flask and cooled to -80 °C in an aluminum block cryostat PSL-2500 A (EYELA, Tokyo, Japan). In another flask, the oxime, toluene, and 1,8-diazabicyclo[5.4.0]undec-7-ene (DBU) were dissolved and once rotavapped. The flask was equipped with a septum, purged with argon, and pyridine (dehydrated grade, Wako Chemical, Osaka, Japan) was added. Then, a part of the pyridine solution was taken out with a syringe, added to the flask dropwise over 15 s, and kept stirring at -80 °C for polymerization. After a given time, the polymerization was quenched by adding 1 mL of CH₂Cl₂ solution containing of acetic anhydride (2.3~3.5 eq. vs DBU) and kept stirring at -80 °C for 30 min. After the flask was taken out from the cryostat bath and stirred for 30 min at room temperature, 5 mL of methanol was added to the flask, stirred for a few minutes, and rotavapped. Resulting solid was thoroughly washed with water, dried, and reprecipitated from methanol. The obtained powder was further fractionated with recycle SEC system composed of a Japan Analytical Industry LaboACE LC-5060 recycling preparative HPLC, a Jaigel 2HR plus SEC column (exclusion limitation 5,000 Da vs. polystyrene), and a 400LA 4 channel UV detector (detected at 254, 313, 365, and

400 nm) using CHCl₃ eluent at ambient temperature.

2.5. Photo-irradiation of PPAs

Photo-irradiation was performed with a Hayashi Watch-Works LA410 Xe-Hg lamp (Tokyo, Japan). For NMR spectral changes, solutions were irradiated in commercially available Pyrex 5 mm^φ NMR tubes. The light intensity was 260 mW/cm² at 365 nm and 170 mW/cm² at 435 nm, which was measured by an Orc UV-M03 illuminometer (Tokyo, Japan).

Polymer films were obtained by spin coating on CaF₂ wafers from 5 wt% propylene glycol methyl ether acetate (Kishida Chemical, Osaka, Japan) solutions with a Kyowariken K-359SD-1 coater and prebaked at 80 °C for 2 min on a hotplate in air. The polymer films were irradiated with the above light source via PET film to cut the light shorter than 300 nm. The light intensity was 220 mW/cm² at 365 nm and 140 mW/cm² at 435 nm. FluBO was also irradiated in quartz cuvette or KBr pellet via PET film similarly.

3. Results and discussion

3.1. Preparation of PPA polymers

The anionic polymerization of *o*-PA was achieved by oximes and DBU in CH₂Cl₂ as observed in the previous studies [14,15]. DBU would abstract protons from oximes, and resulting oximate anions initiate the polymerization of *o*-PA in non-polar solvents. However, because truxenone trioxime showed lower solubility in CH₂Cl₂, herein we dissolved the oximes in pyridine prior to the addition. In addition, we had to separate PPAs having incomplete arms. Thus, we attempted to separate the obtained polymers with recycle SEC systems, although the column had a low exclusion limit.

Table 1 summarizes polymerization conditions and characteristics of obtained PPAs. Herein the

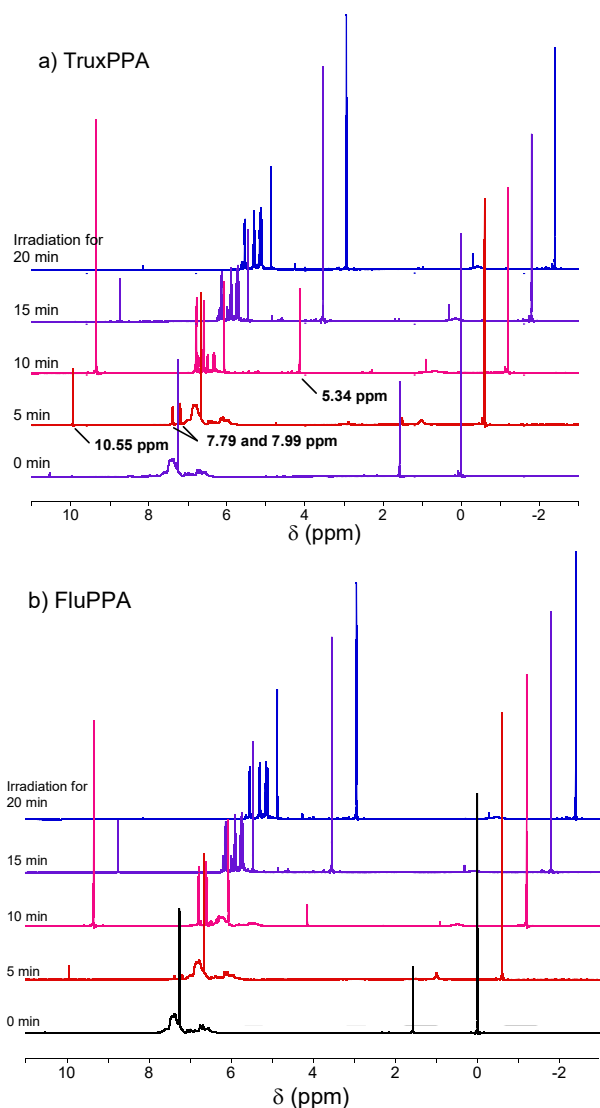


Fig. 2. ^1H NMR spectral changes of a) TruxPPA and b) FluPPA on irradiation. Numbers in the figures show total irradiation time. Concentration: 5 mg in 0.5 mL of CDCl_3 .

conversions are based on PPAs after separation. From the fractionation by using the recycle SEC system, we obtained three fractions in entry 1-3, and two fractions in entry 4. For example, we obtained 142 mg, 11 mg, and 3 mg of powders as first, second, and third fractions, respectively, in entry 1 polymerization. The first fraction indicated a monomodal peak at 18.0 min of retention time in analytical SEC traces, although the second had a weak peak at 18.6 min and a strong peak at 22.0 min. These results suggest that the separation of one, two, and three arms of PPAs in entry 1 would be attained. However, when we changed polymerization time and the amount of pyridine, first fractions often showed bimodal traces in analytical SEC

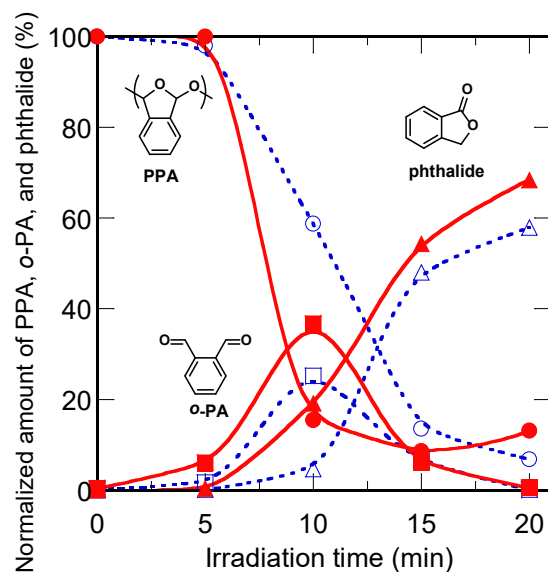


Fig. 3. Estimated amount of (■, □) *o*-PA, (▲, △) phthalide, and (●, ○) PPA on irradiation based on peak area at 10.55 ppm, 5.34 ppm, and aromatic region in Fig. 1, respectively. **Solid line and symbols: TruxPPA, dotted line and white symbols: FluPPA.** The peak areas are normalized to that with aromatic region of peaks, and the peaks at 10.55, 5.34 and those in aromatic region are assumed to have 2 H, 2 H, and 4 H, respectively. The signal of tetramethylsilane at 0 ppm is used as an internal standard.

measurement (entry 2 and 4). Also, all polymerization showed lower conversion compared to the previous studies (42~77 %). We used the PPAs of entries 1 (TruxPPA) and 4 (FluPPA) in the next section.

3.2. Photoreactions of PPAs

We firstly examined the photochemical change of PPAs in solutions. Figure 2 shows the ^1H NMR spectral changes of PPAs on irradiation in NMR tubes. On irradiation of TruxPPA (Fig. 2a), 5 min irradiation leads to new peaks at 10.55 ppm (CHO), 7.79 and 7.99 ppm (aromatic) due to *o*-PA. These peaks increased on 10 min irradiation along with a new singlet peak at 5.34 ppm and multiplet peaks at 7.27-8.00 that are assignable to phthalide. On further irradiation, the peaks due to *o*-PA decreased and those due to phthalide increased. These results clearly show the proceeding of depolymerization on irradiation as observed in PPAs with naphthyl oxime ether terminals [14,15].

The photo-isomerization of *o*-PA into phthalide is consistent with our previous study [14] and in literature [22].

FluPPA gave similar ^1H NMR spectral changes

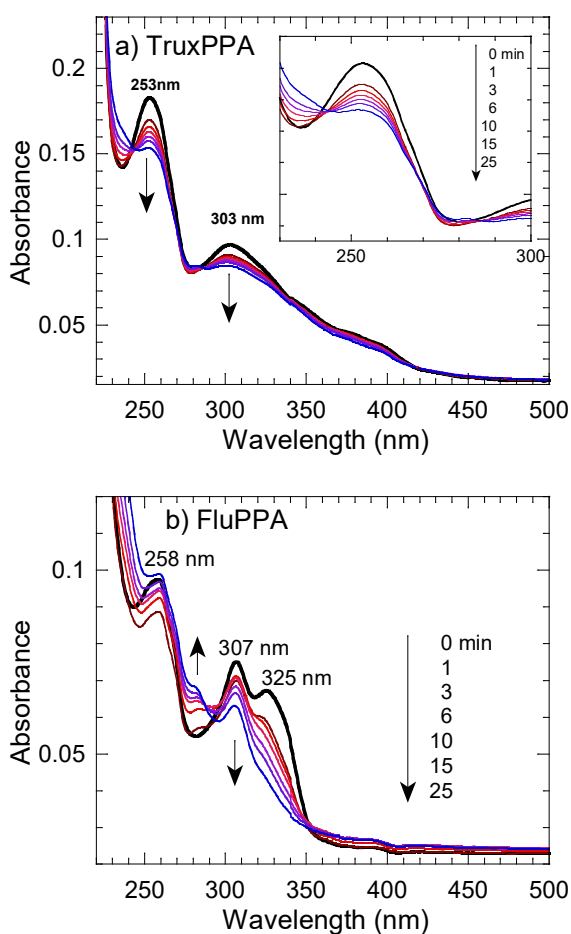


Fig. 4. UV-visible spectral changes of a) TruxPPA and b) FluPPA films on irradiation. Numbers in the figures show total irradiation time.

on irradiation, except that broad peaks due to polymers still remained after 10 min irradiation as shown in Fig. 2b. The difference against TruxPPA is shown more clearly in Fig. 3, where quantitative analysis based on peak area changes are summarized. The depolymerization of FluPPA was slower than TruxPPA. This difference might affect in the yields of *o*-PA and phthalide on further irradiation. However, it is clear that the depolymerization and photo-isomerization proceeded for FluPPA.

In the next step, we examined the changes of PPAs in solid state. We coated PPAs on CaF₂ substrates, and both UV-vis and IR spectral changes were measured.

As shown in Fig. 4a, TruxPPA had maximum peaks at 253 and 303 nm, and its absorption termination reached to 480 nm in UV spectrum before irradiation. This means that the film absorbed 365, 405 and 435 nm emission lights from the light source in addition to 313 nm-light. On

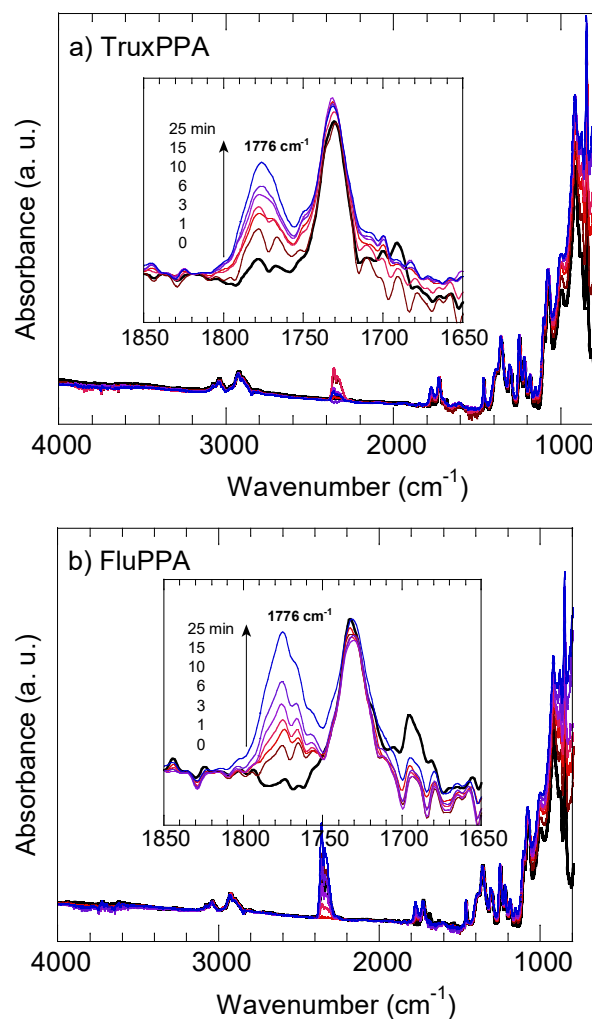


Fig. 5. IR spectral changes of a) TruxPPA, and b) FluPPA films on irradiation.

irradiation, the two peaks decreased, and isosbestic points were observed at 244 and 289 nm in spectra for 1~15 min irradiation. These results suggest that the simple photochemical reaction of truxenone-based oxime ether moiety proceeded in TruxPPA film.

In case of FluPPA (Fig. 4b), peaks at 258, 307, 325 nm were shown before irradiation. On irradiation, peaks at 258 and 325 nm decreased along with the appearance of a new peak around 280 nm. Although the behavior is complex, photochemical reaction of fluxene-based oxime ether units was observed.

IR spectral changes of the same films are shown in Fig. 5. On irradiation of TruxPPA films, new peaks appeared at 1767, 1778 cm⁻¹, and finally became one peak at 1776 cm⁻¹ due to phthalide C=O stretching band. FluPPA films showed similar trend. These IR spectral changes also show the

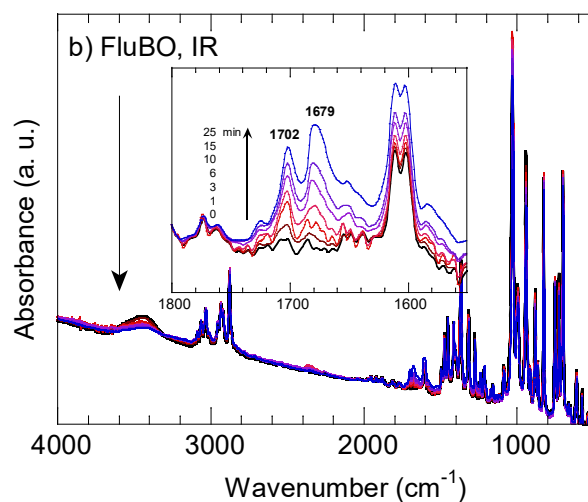
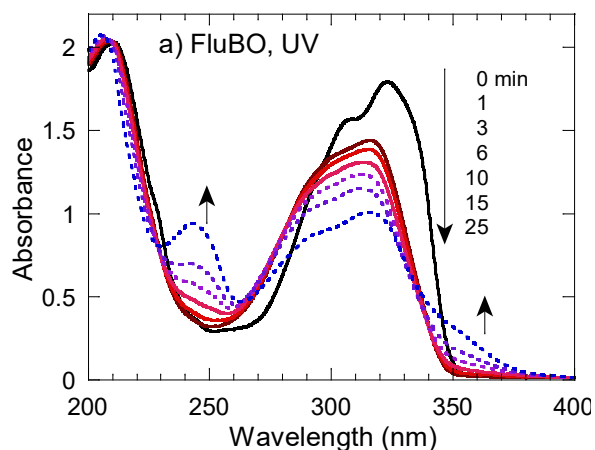


Fig. 6. Photochemical changes of FluBO. a) UV-visible spectra in 5.0×10^{-5} M acetonitrile solution, and b) IR spectra in KBr.

formation of phthalide in both TruxPPA and FluPPA films and are consistent with that observed in CDCl_3 solution in Fig. 2.

3.3. Photochemical reaction of molecular oxime ethers

In order to understand the photochemical changes in oxime ether moieties in PPAs, we have tried to prepare molecular oxime ethers bearing truxene and fluorene substituents. Similar to acetophenone *O*-benzyloximes [14], FluBO was successfully obtained from 2,7-diacetylfluorene and *O*-benzylhydroxylamine. However, truxenone-based molecular oxime ether was not obtained by the same procedure, and even after heating at 100 °C for 7 days or refluxing in pyridine for 1 day.

UV spectral changes of FluBO on irradiation in acetonitrile are shown in Fig. 6a. The first 1 min irradiation caused the decrease of the peak at 323

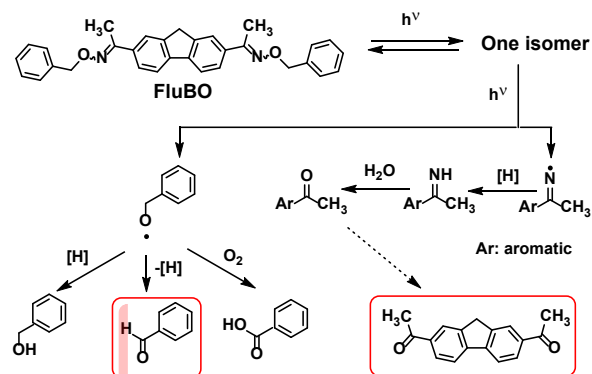


Fig. 7. Plausible photochemical reactions of FluBO.

nm with blue shift. Similar behavior has often been observed for PPAs containing oxime ethers [14], and also in oxime esters [23]. On irradiation for 1~6 min, isosbestic points were observed at 230, 282, and 340 nm. On further irradiation (10~25 min), new peak appeared around 245 nm with an increase in the region of 330-380 nm. In IR spectral changes, peaks appeared at 1679 and 1702 cm^{-1} on irradiation as shown in Fig. 6b.

These spectral changes can be explained by photoreactions that have already been proposed for oxime ethers by other researchers [17,18] and our previous works [14]. Plausible mechanisms are shown in Fig. 7. The C=N bonds in oxime ether units isomerize photochemically, and one isomer is preferentially photo-cleavable. The blue shift between 0~1 min irradiation will reflect photo-isomerization to the photo-cleavable isomer. In addition to the isomerization, N-O homolytic scission proceeds on irradiation for 1~10 min. Resulting O and N radicals oxidized or abstract hydrogen to form an aldehyde and an imine, and the latter is hydrolyzed to form ammonia and ketone. The new peaks can be attributed to benzaldehyde (lit. 249 nm [24] and 1703 cm^{-1} [25]) and 2,7-diacetylfluorene (authentic sample: 1687 cm^{-1}).

Unfortunately, it is still unclear that depolymerization proceeded with free-radical mode or not.

4. Conclusions

Polymers bearing two and three PPA chains were prepared, and their photochemical behaviors were investigated. In spite the low conversion and the need of fractionation, we could obtain two and three armed PPAs, TruxPPA and FluPPA. ^1H NMR spectral changes of PPA solutions revealed that the transformation of PPAs into *o*-PA, and further to phthalide, proceeded on irradiation for

both TruxPPA and FluPPA. In films, the photoreaction of oxime ether units and the formation of phthalide were observed in UV and IR spectral changes, respectively. These results show that the depolymerization and further photo-transformation proceeded both in solution and film state. The spectral analyses of model compound FluBO suggested photo-induced *E/Z* isomerization and homolytic cleavage. These results provide the fundamental information on photo-induced depolymerization of PPAs.

Acknowledgements

This work was supported by Ogasawara Foundation. The authors also thank to Prof. Haruyuki Okamura of Osaka Prefecture University for SEC measurement of PPAs and its interpretation.

References

1. Q. Hou, M. Zhen, H. Qian, Y. Nie, X. Bai, T. Xia, M. L. U. Rehman, Q. Li, and M. Ju, *Cell Reports Phys. Sci.*, **2**, 100514, (2021).
2. F. Wang and C. E. Diesendruck, *Macromol. Rapid Commun.*, **39** (2018) 1700519.
3. C. Aso and S. Tagami, *J. Polym. Sci. Polym. Lett.*, **5** (1968) 217.
4. H. Ito and C. G. Willson, *Polym. Eng. Sci.*, **23** (1983) 1012.
5. M. Tsuda, M. Hata, R. Nishida, and S. Oikawa, *J. Polym. Sci., Part A: Polym. Chem.*, **35** (1997) 77.
6. J. P. Lutz, O. Davydovich, M. D. Hannigan, J. S. Moore, P. M. Zimmerman, and A. J. McNeil, *J. Am. Chem. Soc.*, **141** (2019) 14544.
7. A. Engler, C. Tobin, C. K. Lo, and P. A. Kohl, *J. Mater. Res.*, **243** (2020) 2918.
8. S. T. Howell, A. Grushina, F. Holzner, and J. Brugger, *Macrosys. Nanoengineer.*, **6** (2020) 21.
9. A. M. Dilauro, H. Zhang, M. S. Baker, F. Wong, A. Sen, and S. T. Phillips, *Macromolecules*, **46** (2013) 7257.
10. G. I. Peterson and A. J. Boydston, *Macromol. Rapid Commun.*, **35** (2014) 1611.
11. A. M. DiLauro, J. S. Robbins, and S. T. Phillips, *Macromolecules*, **46** (2013) 2963.
12. J. Deng, F. Kaefer, S. Bailey, Y. Otsubo, Z. Meng, R. Segalman, and C. K. Ober, *J. Photopolym. Sci. Technol.*, **34** (2021) 71.
13. A. Rathore, I. Pollentier, S. S. Kumar, D. De Simone, and S. De Gendt, *J. Micro/Nanopattern. Mater. Metrology*, **20** (2021) 034602.
14. H. Hayashi, H. Tachi, and K. Suyama, *J. Photopolym. Sci. Technol.*, **33** (2020) 269.
15. H. Hayashi, H. Tachi, and K. Suyama, *J. Photopolym. Sci. Technol.*, **34** (2021) 219.
16. A. Padwa and F. Albrecht, *Tetrahedron Lett.*, **1974** (1974) 1083.
17. H. J. Peter de Lijser and C.-K. Tsai, *J. Org. Chem.*, **69** (2004) 3057.
18. M. Fréneau, P. S. Claire, N. Hoffmann, J.-P. Vors, J. Geist, M. Euvrard, and C. Richard, *RSC Adv.*, **6** (2016) 5512.
19. J. A. Blake, K. U. Ingold, S. Lin, P. Mulder, D. A. Pratt, B. Sheeller, and J. C. Walton, *Org. Biomol. Chem.*, **2** (2004) 415.
20. J. Kalia and R. T. Raines, *Angew. Chem. Int. Ed.*, **47** (2008) 7523.
21. K. Suyama and H. Tachi, *J. Photopolym. Sci. Technol.*, **30** (2017) 247.
22. S. Tshepelevitsh, A. Kütt, M. Lõkov, I. Kaljurand, and J. Saame, *Eur. J. Org. Chem.*, **2019** (2019) 6735.
23. K. Suyama and H. Tachi, *RSC Adv.*, **5** (2015) 31506.
24. I. G. Zenkevich, M. V. Kochetova, O. G. Larionov, and A. A. Revin, *J. Anal. Chem.*, **60** (2005) 655.
25. W. Qian, E. Jin, Weiliang Bao, and Y. Zhang, *Tetrahedron*, **62** (2006) 556.

Unimolecular Benzodioxole-based Photoinitiators for Free Radical and Cationic Photopolymerization Under LED Light Irradiation

Mengqi Li¹, Peng Hu¹, Junzhe Zhu¹, Ren Liu^{1*}, and Zhiquan Li^{2*}

¹*School of Chemical and Material Engineering, Jiangnan University, Wuxi, 214122, China*

²*School of Materials and Energy, Guangdong University of Technology, Guangzhou, 510006, China*
**lzq@gdut.edu.cn*

Compared to amines as coinitiators applied in photopolymerization, benzodioxole derivatives exhibit similar reactivity but less yellowing and lower toxicity. In this paper, a series of unimolecular type II photoinitiators, containing coumarins as chromophores and benzodioxoles as coinitiators, were synthesized. The substituents with different electron donating/withdrawing abilities were designed for systematical investigation of structure-property relationship. Under LED irradiation, the novel photoinitiators can induce not only free radical polymerization of acrylate monomers, but also cationic polymerization of epoxy monomers via radical promoted cationic polymerization mechanism.

Keywords: Coumarin, Benzodioxole, LED photopolymerization

1. Introduction

Free radical photopolymerization, featuring high efficiency, low energy consumption, wide adaptability, and full temporal and spatial resolutions [1,2], has rapidly developed and been applied in various fields, such as coatings, adhesive, 3D printings, and semiconductor industries [3-5]. Free radical photoinitiators (PIs) that absorb photons and subsequently generate active radicals, have great impact on photopolymerization rate and final functionality conversion, as well as the mechanical properties of the cured materials [6,7]. Generally, free radical PIs can be divided into two types, namely Norrish type I and Norrish type II PIs, following distinct mechanisms [8]. For Type I PIs, the active free radicals are formed via direct cleavage under irradiation [9,10], while Type II PIs commonly undergo hydrogen abstraction from suitable coinitiators that subsequently generate active initiating species [11,12]. Compared to type I PIs, the initiation system composing type II PIs and coinitiators are more practical and flexible because their photoinitiation performance can be facilely adjusted via simply altering the types and ratios of

the components [13].

Currently, tertiary amines are the most popularly used coinitiators due to their efficient electron/proton transfer process and anti-oxygen inhibition ability. However, amines suffer from several issues like yellowing, odor and toxicity [14]. The pioneer work by Nie et al. [15] demonstrated that benzodioxole (BDO) derivatives, derived from natural components sesame seeds, are promising alternative coinitiators with strong hydrogen donating ability. Compared to amines, BDO derivatives possess comparable reactivity, but less yellowing, lower toxicity and significant antibacterial properties [16]. The photoinitiating systems comprising typical type II PIs like camphorquinone (CQ), and BDO derivatives as coinitiators, have been used in self-etch dental adhesive formulations exhibiting improved dentin bond strength compared to the adhesive resin with tertiary amine ethyl 4-dimethylaminobenzoate (EDAB) as a coinitiator [17,18]. To suppress the back electron transfer generally occurred within multi-component systems with high viscosity, one-component sesamol-based PIs were prepared via chemically bonding the BDO moieties into the BP

Received	January 18, 2022
Accepted	April 16, 2022

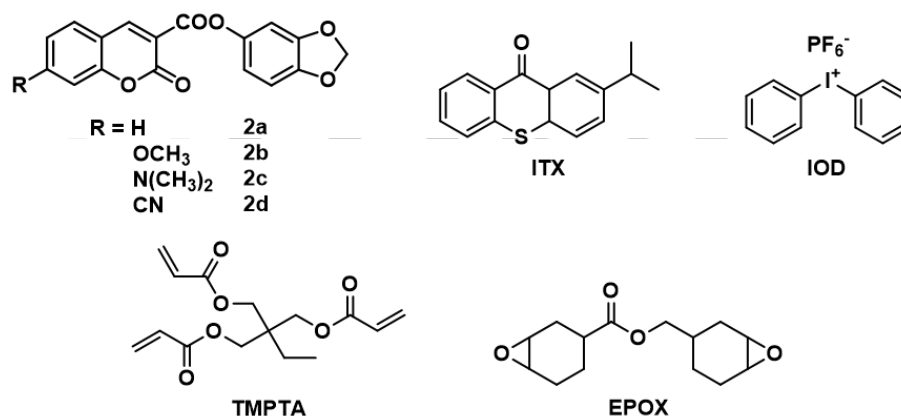
skeleton [19,20]. The unimolecular PIs, undergoing intramolecular hydrogen abstraction, are more efficient than the physically mixed initiating system BP/BDO under UV irradiation.

With the fast development of light emitting diodes (LEDs), featuring high energy utilization ratio, easy operation and no ozone generation [21], it is desired to develop efficient BDO-based PIs sensitive to LED light. However, the long emission wavelength of LED lamps combined with their narrow emission bands has imposed great challenges [22]. Currently only one example of unimolecular PI, containing a thioxanthone moiety as a chromophore and a benzodioxole as an initiation functionality, was reported by our group [23]. The PIs exhibited high initiation efficiency under UV-A and visible LED light irradiation. Therefore, the vast chemical and functional space of BDO-based PIs sensitive to LED light remains to be explored.

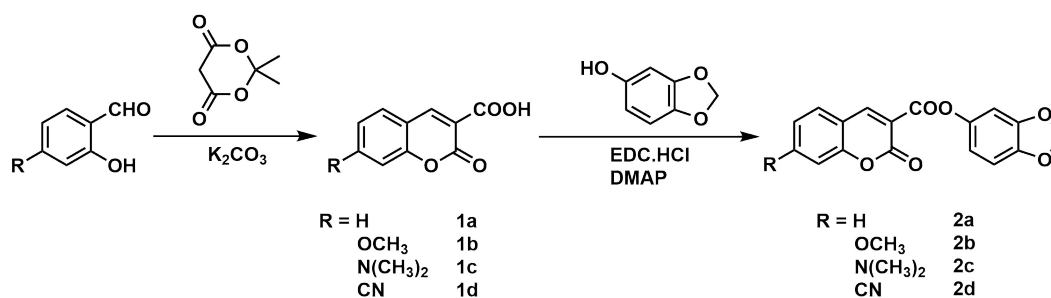
Coumarins as plant secondary metabolites not only exhibit strong antiviral and antimicrobial activities, but also possess interesting optical properties [24,25]. Their strong photo-luminescence properties enable coumarins becoming efficient fluorescent probes and laser dyes [26,27]. When

combined with suitable PIs, coumarins are also robust photosensitizers for photopolymerization due to their high electron transfer quantum yields, easily adjustable spectral ranges and good solubility [28,29]. With a proper molecular design to incorporate the oxime-ester into the functionalized coumarins, our group reported a series of efficient unimolecular PIs sensitive to visible light or even near infrared light [30-33]. Therefore, it is of great interest to explore BDO-based PIs containing coumarins as efficient chromophores sensitive to LED light.

In this paper, a series of novel unimolecular BDO-based PIs were synthesized via two steps. For systematical investigation of structure-property relationship, the substituents in the 7-position of coumarin were designed with different electron donating/withdrawing abilities. Interestingly, these novel PIs can effectively initiate not only free radical photopolymerization under LED irradiation, but also free radical-promoting cationic photopolymerization in the presence of iodonium salts. This new discovery would enrich the types of initiating species and therefore provide versatile tools for polymer synthesis.



Scheme 1. Chemical structures of the photoinitiators and the monomers used for photopolymerization.



Scheme 2. Synthetic routes of the novel photoinitiators.

2. Experimental

2-hydroxybenzaldehyde, 2,2-dimethyl-1,3-dioxane-4,6-dione, sesamol, 3-(3-dimethylaminopropyl)-1-ethylcarbodiimide hydrochloride (EDC·HCl), 2-isopropylthioxanthone (ITX), and 1,2-epoxycyclohexane (CHO) were obtained from Adamas Reagent Ltd. 2-Hydroxy-4-methoxybenzaldehyde and diphenyl iodonium hexafluorophosphate (IOD) were acquired from Energy Chemical Co. Ltd. 4-Dimethylaminopyridine (DMAP) and (3,4-epoxycyclohexane)-methyl-3,4-epoxycyclohexyl-carboxylate (EPOX) were purchased from Shanghai Macklin Biochemical Co. Ltd. K_2CO_3 and other reagents and solvents were supplied by Sinopharm Chemical Reagent Co. Ltd. 4-(Dimethylamino)-2-hydroxybenzaldehyde and 4-formyl-3-hydroxybenzotrile were purchased from Accela ChemBio Co. Ltd. Trimethylolpropane triacrylate (TMPTA) was obtained from Jiangsu Kailin Ruiyang Chemical Co. Ltd. All reagents were used as received without further purification.

Synthesis of 2-oxo-2H-chromene-3-carboxylic acid (1a): A mixture of 2-hydroxybenzaldehyde (1.50 g, 12.28 mmol), 2,2-dimethyl-1,3-dioxane-4,6-dione (2.66 g, 18.42 mmol), K_2CO_3 (0.93 g, 6.75 mmol) and water (50 mL) were stirred together for 24 h in a round-bottomed flask at room temperature [34,35]. The precipitation was collected and washed with water. A white solid was obtained after removing the solvent under vacuum (1.16 g, yield 57.5%). 1H NMR (400 MHz, DMSO- d_6) δ 13.25 (s, 1H), 8.75 (s, 1H), 7.91 (dd, $J = 7.7, 1.5$ Hz, 1H), 7.79 – 7.69 (m, 1H), 7.49 – 7.38 (m, 2H).

Synthesis of 7-methoxy-2-oxo-2H-chromene-3-carboxylic acid (1b): Compound 1b was obtained with a yield of 88.7% via a similar preparation procedure of 1a except replacing 2-hydroxybenzaldehyde with 2-hydroxy-4-methoxybenzaldehyde. 1H NMR (400 MHz, DMSO- d_6) δ 12.98 (s, 1H), 8.73 (s, 1H), 7.84 (d, $J = 8.6$ Hz, 1H), 7.08 – 6.92 (m, 2H), 3.90 (s, 3H).

Synthesis of 7-(dimethylamino)-2-oxo-2H-chromene-3-carboxylic acid (1c): Compound 1c was obtained with a yield of 34.6% via a similar preparation procedure of 1a except replacing 2-hydroxybenzaldehyde with 4-(dimethylamino)-2-hydroxybenzaldehyde. 1H NMR (400 MHz, DMSO- d_6) δ 12.54 (s, 1H), 8.61 (s, 1H), 7.66 (d, $J = 8.9$ Hz, 1H), 6.81 (d, $J = 8.0$ Hz, 1H), 6.59 (s, 1H), 3.10 (s,

6H).

Synthesis of 7-cyano-2-oxo-2H-chromene-3-carboxylic acid (1d): Compound 1d was obtained with a yield of 44% via a similar preparation procedure of 1a except replacing 2-hydroxybenzaldehyde with 4-formyl-3-hydroxybenzotrile. 1H NMR (400 MHz, DMSO- d_6) δ 13.54 (s, 1H), 8.76 (s, 1H), 8.08 (d, $J = 8.0$ Hz, 1H), 8.05 (s, 1H), 7.83 (dd, $J = 8.0, 1.3$ Hz, 1H).

Synthesis of benzo[d][1,3]dioxol-5-yl 2-oxo-2H-chromene-3-carboxylate (2a): Compound 1a (0.20 g, 1.05 mmol), sesamol (0.22 g, 1.58 mmol), EDC·HCl (0.30 g, 1.58 mmol), DMAP (0.06 g, 0.52 mmol) were added to 20 mL of dichloromethane (DCM). The mixture was heated to reflux and stirred for 4 h. The solvent was evaporated under reduced pressure and the obtained crude product was purified by column chromatography (DCM/ethyl acetate = 10:1) to yield 0.24 g light yellow solid (76.9%). 1H NMR (400 MHz, chloroform- d) δ 8.64 (s, 1H), 7.68 – 7.56 (m, 2H), 7.38 – 7.26 (m, 2H), 6.75 (d, $J = 8.4$ Hz, 1H), 6.69 (d, $J = 2.3$ Hz, 1H), 6.61 (dd, $J = 8.4, 2.4$ Hz, 1H), 5.94 (s, 2H). ^{13}C NMR (101 MHz, $CDCl_3$) δ 160.86, 155.36, 154.41, 148.90, 147.05, 144.66, 143.66, 133.87, 128.73, 123.99, 116.77, 116.37, 115.91, 112.98, 107.00, 102.69, 100.79. Q-Tof-MS (m/z): $C_{17}H_{10}O_6$ [$M+H$] $^+$ calcd, 311.0477, found, 311.0558.

Synthesis of benzo[d][1,3]dioxol-5-yl 7-methoxy-2-oxo-2H-chromene-3-carboxylate (2b): Compound 2b was prepared from 1b according to the procedure described for 2a. Purification by column chromatography (DCM/ethyl acetate = 10:1) yielded the product 2b as white crystals with a yield of 45%. 1H NMR (400 MHz, DMSO- d_6) δ 9.00 (s, 1H), 7.91 (d, $J = 8.7$ Hz, 1H), 7.08 (d, $J = 2.2$ Hz, 1H), 7.05 (dd, $J = 8.7, 2.4$ Hz, 1H), 6.96 (d, $J = 8.4$ Hz, 1H), 6.92 (d, $J = 2.3$ Hz, 1H), 6.70 (dd, $J = 8.4, 2.3$ Hz, 1H), 6.09 (s, 2H), 3.92 (s, 3H). ^{13}C NMR (101 MHz, DMSO) δ 165.76, 161.93, 157.80, 156.58, 151.19, 148.13, 145.55, 145.12, 132.46, 114.69, 114.03, 112.43, 111.94, 108.46, 104.40, 102.24, 100.84, 56.82. Q-Tof-MS (m/z): $C_{18}H_{12}O_7$ [$M+H$] $^+$ calcd, 341.0583, found, 341.0670.

Synthesis of benzo[d][1,3]dioxol-5-yl 7-(dimethylamino)-2-oxo-2H-chromene-3-carboxylate (2c): Compound 2c was prepared from 1c according to the procedure described for 2a. Purification by column chromatography (PE/ethyl

acetate = 1:1) yielded the product 2c as yellow crystals with a yield of 72.7%. ¹H NMR (400 MHz, DMSO-d₆) δ 8.87 (s, 1H), 7.77 (d, *J* = 9.0 Hz, 1H), 7.01 (d, *J* = 8.4 Hz, 1H), 6.95 (d, *J* = 2.3 Hz, 1H), 6.89 (dd, *J* = 9.0, 2.3 Hz, 1H), 6.72 (dd, *J* = 8.4, 2.3 Hz, 1H), 6.65 (d, *J* = 2.1 Hz, 1H), 6.13 (s, 2H), 3.18 (s, 6H). ¹³C NMR (101 MHz, DMSO) δ 162.42, 158.40, 157.35, 155.80, 151.04, 148.06, 145.36, 145.34, 132.26, 114.77, 110.75, 108.40, 107.83, 106.75, 104.56, 102.16, 96.85, 40.39. Q-ToF-MS (*m/z*): C₁₉H₁₅NO₆ [M+H]⁺ calcd, 354.0899, found, 354.1009.

Synthesis of benzo[d][1,3]dioxol-5-yl 7-cyano-2-oxo-2H-chromene-3-carboxylate (2d):

Compound 2d was prepared from 1d according to the procedure described for 2a. Purification by column chromatography (DCM/ethyl acetate = 10:1) yielded the product 2d as white crystals with a yield of 17.4%. ¹H NMR (400 MHz, DMSO-d₆) δ 9.15 (s, 1H), 8.22 (d, *J* = 8.0 Hz, 1H), 8.18 (d, *J* = 1.3 Hz, 1H), 7.94 (dd, *J* = 8.0, 1.5 Hz, 1H), 7.05 (d, *J* = 8.4 Hz, 1H), 7.01 (d, *J* = 2.3 Hz, 1H), 6.78 (dd, *J* = 8.4, 2.4 Hz, 1H), 6.16 (s, 2H). ¹³C NMR (101 MHz, DMSO) δ 161.27, 155.46, 154.56, 149.09, 148.20, 145.76, 144.85, 131.93, 128.44, 122.07, 120.86, 119.67, 118.06, 116.19, 114.59, 108.56, 104.23, 102.33. Q-ToF-MS (*m/z*): C₁₈H₉NO₆ [M+H]⁺ calcd, 336.0430, found, 338.3443.

Characterization of structure and photophysical properties: ¹H NMR and ¹³C NMR were measured using a Bruker instrument (AVANCE III HD 400 MHz). High-resolution mass spectrometer measurements were performed using a Q-ToF-MS from Bruker Daltonics. UV-Vis spectra were determined at a concentration of 5 × 10⁻⁵ mol L⁻¹ by a Shimadzu UV-1900i UV-vis spectrophotometer with acetonitrile as solvent. Molar extinction coefficients were calculated by measuring the absorbance of five concentration gradient solutions at the maximum absorption wavelength and fitting them to the slope of the obtained straight line. And steady state fluorescence spectra were recorded at a concentration of 10⁻⁶ mol L⁻¹ in acetonitrile on a CARY Eclipse fluorescence spectrophotometer.

Theoretical calculation method: The HOMO and the LUMO of PIs were calculated at the M06-2X / def2-TZVP level (iso-value = 0.03) [36,37]. The graph of molecular orbitals has been drawn by the GaussView.

Photolysis study: The photolysis study of the novel PIs was carried out in acetonitrile at room temperature. The compound 2a-2d (5 × 10⁻⁵ M

solvent) was dissolved in acetonitrile solvent in a cuvette and irradiated by broad-spectrum light source (320-500 nm). The absorbance of the exposed solvent was tested to obtain the UV-vis spectra with different irradiation time. The light intensity for the test was adjusted to 60 mW cm⁻².

ESR spin trapping (ESR-ST) experiments: ESR spin-trapping experiments were carried out using an EMXplus-10/12 X-band spectrometer at 100 kHz magnetic field modulation. The PIs (0.05 mol L⁻¹) and phenyl-N-tert-butyl nitron (PBN, 0.1 mol L⁻¹) were dissolved in dimethyl sulfoxide (DMSO) and degassed with nitrogen for 30 min before irradiation. The radicals generated when exposed to the 365 nm LED light (200 mW cm⁻²) were trapped by PBN. ESR spectra simulations were performed using the Bruker Xenon software.

Photopolymerization kinetics: Nicolet 6700 Fourier transform infrared (FT-IR) spectrometer was used to study the photopolymerization kinetics of PIs. An Omnicure Series 1000 UV spot curing system and a Runled UVP-60 monochromatic LED sources were used to irradiate the resins, with a UV-light radiometer (Beijing Normal University, China) to control the light intensity. The photocurable formulations were prepared by dissolving PIs in 0.3 mL DMSO, which were added to the monomer TMPTA. The formulations were mixed by ultrasonic vibration until a homogeneous resin was obtained. The investigated resin was dropped on a KBr tablet, covered by another KBr tablet. The photosensitive resins were irradiated for 900 s at room temperature. The spectrograms at different times were integrated and processed using OMNIC. The polymerization kinetics were measured by monitoring the disappearance of the double bonds. The double bond and the epoxy bond conversion was calculated using the formula 1.

$$Conversion(\%) = (1 - A_t/A_0) \times 100\% \quad (1)$$

Where *A_t* is the area of the double bond characteristic absorption peak (about 1600-1650 cm⁻¹) or the epoxy bond characteristic absorption peak (about 775-795 cm⁻¹) at time *t*, and *A₀* represents the initial area of the characteristic absorption peak.

The photocurable formulations of free radical-promoting cationic photopolymerization were prepared by dissolving PIs and IOD in 0.3 mL DCM, which were mixed with the monomer EPOX.

Thermal stability analysis: thermal gravimetric analysis (TGA) experiments were performed using Mettler Toledo TGA 1/1100SF apparatus with 4-5

mg samples under nitrogen atmosphere. Temperature was ramped from 50 to 600 °C, at a ramping rate of 10 °C min⁻¹.

3. Results and discussion

3.1. Synthesis

Compared with amines, BDO derivatives are good hydrogen donors with less yellowing and lower cytotoxicity, which make them become attractive alternatives to amines as co-initiators. In order to investigate the structure-property relationship, different substituents in the 7-position of the coumarin were designed. PIs 2b and 2c contain methoxy and dimethylamino groups with electron-donating ability, respectively, while 2d comprises cyano groups with electron-withdrawing ability. The PIs were prepared as described in Scheme 2.

In the presence of K₂CO₃, coumarin precursors with a carboxyl moiety were synthesized by a cyclization reaction between Meldrum's acid and hydroxybenzophenone. Subsequently, the esterification reaction of coumarin formic acid and sesamol was catalyzed by EDC·HCl / DMAP to obtain the PIs.

3.2. Photophysical properties

The UV-vis absorption spectra of the PIs in acetonitrile at room temperature is shown in Fig. 1(a). The synthesized PIs show broad absorption bands which extend even up to 450 nm. The maximum absorption wavelengths of 2a, 2b and 2d are located at 292 nm, 351 nm and 291 nm, respectively, while the maximum absorption wavelength of 2c is located at 417 nm.

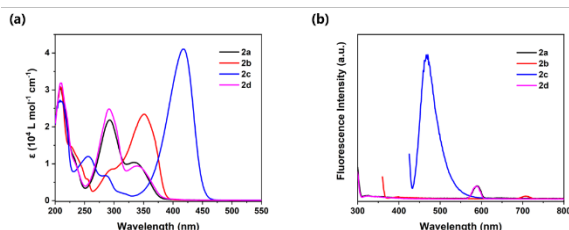


Fig. 1. (a) UV-vis absorption spectra and (b) emission spectra of the PIs in acetonitrile at room temperature.

The absorption behaviors of the PIs are significantly influenced by the introduced substituents in the 7-position of the coumarin. When increasing the electron-pushing ability of the substituent, obvious red-shift of the maximum absorption wavelength is observed. The introduced dimethylamino group with strong electron-donating ability, as in 2c, also enhance the molar extinction coefficient. The observation agrees with the molecular orbital calculations as shown in Fig. 2. The highest occupied molecular orbital (HOMO) and the lowest unoccupied molecular orbital (LUMO) are strongly delocalized over the whole skeleton of 2c. However, the introduction of dimethylamino group also enhances the fluorescence emission of 2c (Fig. 1(b)), which is a disadvantage to the generation of active species. On the other hand, when the substituent is an electron-withdrawing group, the absorption of the PI only shows a slight blue shift. The results demonstrate that the absorption ability of PIs can be facilely adjusted by changing the electron donor-acceptor capacity of the substituents of the chromophore, aiming to match the absorption of the PIs with the emission of different light sources for improved light harvesting efficiency.

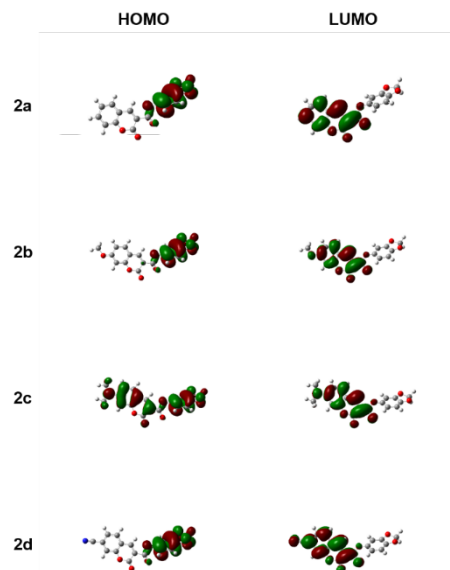


Fig. 2. The HOMO and LUMO calculations of the PIs.

Table 1. Photophysical properties of the PIs^a.

PIs	λ_{max} (nm)	ϵ_{365} (L mol ⁻¹ cm ⁻¹)	ϵ_{405} (L mol ⁻¹ cm ⁻¹)	ϵ_{max} (L mol ⁻¹ cm ⁻¹)	λ_{em} (nm)	λ_{ex} (nm)	T_d (°C)
2a	292	3483	59	21933	588	292	248.3
2b	351	19365	191	23926	706	351	241.3
2c	417	6355	36424	42505	470	417	202.5
2d	291	4183	134	24031	588	291	174.8

^a Where ϵ_{365} , ϵ_{405} , and ϵ_{max} (L mol⁻¹ cm⁻¹) stand for the molar extinction coefficient at 365 nm, 405 nm and λ_{max} , respectively, λ_{ex} and λ_{em} are the maximum fluorescence excitation and emission of photoinitiators in acetonitrile solution (10⁻⁶ M).

3.3. Photolysis study

The UV-vis spectra were recorded in acetonitrile at room temperature with different irradiation times to investigate the photolysis behaviors of the PIs. As shown in Fig. 3, the shape and intensity of the absorption peaks obviously change under irradiation. The absorption peaks of 2a at 292 nm and 334 nm decrease rapidly, while the absorption at 251 nm and 400 nm slightly increase. Similar photolysis behaviors of PI 2b-2d was observed.

In order to verify the generation of the radicals in the photoinitiation systems after photolysis, ESR experiments are carried out to capture the signals of adducts. Fig. 4 shows the ESR spectrum of 2b under the irradiation of 365 nm LED light source by using PBN as the spin trap. The values of the hyperfine splitting constant for a_N and a_H are presented in Table 2. The hyperfine splitting constant of the trapping products are similar to the previous study by Nie et al. [19,20], indicating the PI with the benzodiazazole would participate the photoinitiation as a hydrogen donor to generate cyclic acetal radicals after photolysis.

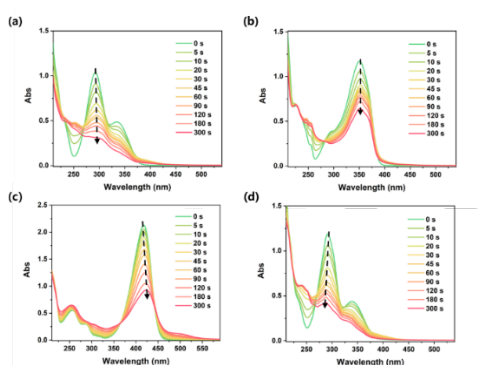


Fig. 3. Steady-state photolysis of (a) 2a, (b) 2b, (c) 2c and (d) 2d in acetonitrile (5.0×10^{-5} M) under the irradiation of broad-spectrum light source.

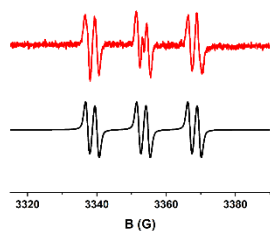


Fig. 4. ESR spectra of 2b with PBN in DMSO under 365 nm LED light: (up) experimental spectrum and (down) simulated spectrum.

Table 2. Hyperfine splitting constant of the radicals observed in the ESR-ST experiments.

PIs	2a	2b	2c	2d
a_N	14.85	14.75	15.01	14.86
a_H	2.78	2.68	3.01	2.81

3.4. Photopolymerization

Real-time FT-IR was employed to investigate the photopolymerization kinetics. The formulations for the tests contain trifunctional acrylate monomer TMPTA and the investigated PIs. Photopolymerization profiles are recorded during 900 s irradiation at room temperature using an Omnicure Series 1000 UV spot curing system by monitoring the disappearance of the double bond at $1600\text{-}1650\text{ cm}^{-1}$.

As shown in Fig. 5, all the novel PIs can efficiently induce the polymerization of TMPTA under irradiation. The unimolecular PIs, which undergo photoinduced intramolecular electron transfer, exhibit shorter induction period and higher final conversion than the bimolecular photoinitiation system containing the physical mixture of coumarin and 1,3-benzodioxole. Interestingly, the unsubstituted benchmark PI 2a exhibits the best photoinitiation performance among the investigated PIs when irradiated under a broad-spectrum light source (320-500 nm). The substituents with different electron donating/withdrawing abilities in 2b and 2d affect the initiation rate in varying degrees, but no significant differences of the final conversion were observed. Although the electron-pushing ability of dimethylamino is stronger than that of methoxy, the poor solubility of 2c in the photo-curing system and its strong fluorescence emission (Fig. 1(b)) lead to the decreased photoinitiation activity.

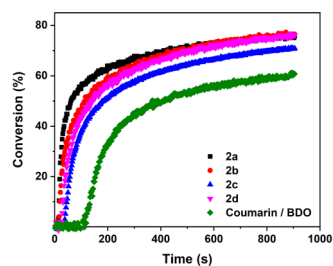


Fig. 5. Double-bond conversion of TMPTA with different PIs (1.6×10^{-5} mol g^{-1} resin), irradiated by a broad-spectrum light source (320-500 nm) with an intensity of 10 mW cm^{-2} .

LEDs, featuring high energy utilization ratio, easy operation and no ozone generation, have become popularly used irradiation sources in photocuring industry. Therefore, it is of great interest to study the photoinitiation performance of the new PIs under 365 and 405 nm LED light irradiation. PI 2a and 2b with suitable absorption and good solubility were chosen for the study. As shown in Fig. 6(a), both PIs can effectively initiate polymerization of TMPTA when irradiated by LED light with different

wavelengths and their photoinitiation performance under 365 nm LED is superior to that under 405 nm. The PI 2b exhibits faster polymerization rate and higher conversion than 2a due to its stronger absorption at both 365 and 405 nm, leading to improved light harvesting efficiency (Table 1). The results also indicate that although the main absorption of the investigated PIs are located in the UV region, the PIs can still initiate the photopolymerization effectively under the visible LED light even only with a weak tail absorption extended to the visible region.

Radical promoted cationic polymerization (RPCP) has become an efficient and flexible methodology to realize cationic photopolymerization [38,39]. In this process, photochemically formed radicals are oxidized by onium salts and the formed cations are used as initiating species for cationic polymerizations. Therefore, we continue to explore the photoinitiation performance of the BDO-based PIs in RPCP. As shown in Fig. 6(b), both PIs can effectively initiate cationic polymerization of EPOX in the presence of IOD, and the epoxy conversion reach to more than 50%. When adding PBN as a radical trap to the formulation, nearly no epoxy conversion was observed, confirming the cationic polymerization through RPCP rather than photosensitization mechanism.

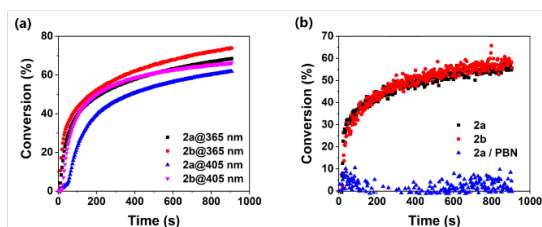


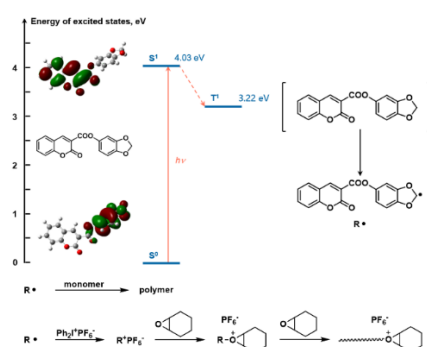
Fig. 6. (a) Double-bond conversion of TMPTA with 2a and 2b (3.2×10^{-5} mol g^{-1} resin), irradiated by different LED light sources (365 nm and 405 nm) with an intensity of 20 $mW\ cm^{-2}$; (b) epoxy conversion of EPOX with different PIs (6.4×10^{-5} mol g^{-1} resin), irradiated by a broad-spectrum light source (320-500 nm) with an intensity of 50 $mW\ cm^{-2}$.

Combining the previous investigations and the results of photolysis and polymerization, the proposed photopolymerization mechanism of the BDO-based PIs is shown in Scheme 3. After light absorption, the excited PI undergoes hydrogen abstraction through intra- or intermolecular reaction to produce cyclic acetal radicals. On the one hand, the formed active species can initiate free radical polymerization. On the other hand, the cyclic acetal radicals can also be oxidized by IOD to generate

carbon cation which can effectively initiate the cationic photopolymerization.

3.5. Thermal stability analysis

Thermal gravimetric analysis was employed to study the PIs' thermal stability, an important property significantly affects the pot life of the formulations. As shown in Table 1, the thermal decomposition temperatures of 2a, 2b, and 2c are higher than 200 $^{\circ}C$, while the corresponding temperature of PI is lower (174.8 $^{\circ}C$). The results indicate that the thermal stability of the PIs is sufficient for usual storage and can meet most application requirements.



Scheme 3. Proposed photopolymerization mechanism of 2a.

4. Conclusion

A series of unimolecular BDO-based PIs with different substituents were facily synthesized in two steps. The novel PIs show wide absorption bands with the main absorption peaks in the range of 260-450 nm. The introduced substituent with electron-pushing ability leads to red-shift of the maximum absorption wavelength, but also stronger fluorescence emission. The unsubstituted PI 2a exhibits the best free radical photoinitiation performance among the investigated PIs when irradiated under a high-pressure mercury lamp, but 2b with methoxy moiety is superior when irradiated with 365 and 405 nm LED lamps due to its better spectra overlap. In addition, the BDO-based PIs can effectively induce cationic polymerization of the epoxy monomers in the presence of iodonium salts via radical promoted cationic polymerization mechanism. The novel PIs would become versatile tools for polymer synthesis.

Acknowledgments

The authors acknowledge the financial support by the Natural Science Foundation of Jiangsu Province (BK20191336).

References

1. N. Corrigan, J. Yeow, P. Judzewitsch, J. Xu, and C. Boyer, *Angew. Chem. Int. Ed.*, **58** (2019) 5170.
2. Y. Yagci, S. Jockusch, and N. J. Turro, *Macromolecules*, **43** (2010) 6245.
3. T. Isik, M. M. Demir, C. Aydogan, M. Ciftci, and Y. Yagci, *J. Polym. Sci. Part Polym. Chem.*, **55** (2017) 1338.
4. Y. He, R. Yu, X. Li, M. Zhang, Y. Zhang, X. Yang, X. Zhao, and W. Huang, *ACS Appl. Mater. Interfaces*, **13** (2021) 36286.
5. F. Petko, M. Galek, E. Hola, R. Popielarz, and J. Ortyl, *Macromolecules*, **54** (2021) 7070.
6. S. Chatani, C. J. Kloxin, and C. N. Bowman, *Polym. Chem.*, **5** (2014) 2187.
7. K. Dietliker, R. Hüsler, J.-L. Birbaum, S. Ilg, S. Villeneuve, K. Studer, T. Jung, J. Benkhoff, H. Kura, A. Matsumoto, and H. Oka, *Prog. Org. Coat.*, **58** (2007) 146.
8. J. Zhou, X. Allonas, A. Ibrahim, and X. Liu, *Prog. Polym. Sci.*, **99** (2019) 101165.
9. R. Nazir, P. Danilevicius, D. Gray, M. Farsari, and D. T. Gryko, *Macromolecules*, **46** (2013) 7239.
10. A. Eibel, D. E. Fast, J. Sattelkow, M. Zalibera, J. Wang, A. Huber, G. Müller, D. Neshchadin, K. Dietliker, H. Plank, H. Grützmacher, and G. Gescheidt, *Angew. Chem. Int. Ed.*, **56**, (2017) 14306.
11. Y. Han, F. Wang, C. Y. Lim, H. Chi, D. Chen, F. Wang, and X. Jiao, *ACS Appl. Mater. Interfaces*, **9** (2017) 32418.
12. P. Xiao, and J. Lalevée, *Macromolecules*, **46** (2013) 7661.
13. G. Ding, C. Jing, X. Qin, Y. Gong, X. Zhang, S. Zhang, Z. Luo, H. Li, and F. Gao, *Dyes Pigments*, **137** (2017) 456.
14. J. Yang, S. Shi, and J. Nie, *New J. Chem.*, **39** (2015) 5453.
15. J. Yang, F. Xu, S. Shi, and J. Nie, *Photochem. Photobiol. Sci.*, **11** (2012) 1377.
16. R. Joshi, M. S. Kumar, K. Satyamoorthy, M. K. Unnikrisnan, and T. Mukherjee, *J. Agric. Food Chem.*, **53** (2005) 2696.
17. S. Shi, P. Xiao, K. Wang, Y. Gong, and J. Nie, *Acta Biomater.*, **6** (2010) 3067.
18. S. M. Almeida, C. T. W. Meereis, F. B. Leal, R. V. Carvalho, P. O. Boeira, L. A. Chisini, C. E. Cuevas-Suárez, G. S. Lima, and E. Piva, *Dent. Mater.*, **36** (2020) e29.
19. J. Yang, S. Shi, F. Xu, and J. Nie, *Photochem. Photobiol. Sci.*, **12** (2013) 323–329.
20. J. Wang, J. Yang, M. Atif, R. Bongiovanni, G. Li, Z. Xue, and X. Yang, *Polym. Adv. Technol.*, **29** (2018) 2264.
21. C. Dietlin, S. Schweizer, P. Xiao, J. Zhang, F. Morlet-Savary, B. Graff, J.-P. Fouassier, and J. Lalevée, *Polym. Chem.*, **6** (2015) 3895.
22. P. Xiao, J. Zhang, F. Dumur, M. A. Tehfe, F. Morlet-Savary, B. Graff, D. Gigmes, J. P. Fouassier, and J. Lalevée, *Prog. Polym. Sci.*, **41** (2015) 32.
23. X. Dong, W. Shen, P. Hu, Z. Li, R. Liu, and X. Liu, *J. Appl. Polym. Sci.*, **133** (2016) 43239.
24. I. A. Stringlis, R. de Jonge, and C. M. J. Pieterse, *Plant Cell Physiol.*, **60** (2019) 1405.
25. G. J. B. Gnonlonfin, A. Sanni, and L. Brimer, *Crit. Rev. Plant Sci.*, **31** (2012) 47.
26. Li. X, Huo. F, Yue. Y, Zhang. Y, and Yin. C, *Sens. Actuators B Chem.*, **253** (2017) 42.
27. Z.-S. Wang, Y. Cui, K. Hara, Y. Dan-oh, C. Kasada, and A. Shinpo, *Adv. Mater.*, **19** (2007) 1138.
28. R. Zhou, J.-P. Malval, M. Jin, A. Spangenberg, H. Pan, D. Wan, F. Morlet-Savary, and S. Knopf, *Chem. Commun.*, **55** (2019) 6233.
29. M. Abdallah, A. Hijazi, J.-T. Lin, B. Graff, F. Dumur, and J. Lalevée, *ACS Appl. Energy Mater.*, **2** (2020) 2890.
30. Z. Li, X. Zou, G. Zhu, X. Liu and R. Liu, *ACS Appl. Mater. Interfaces*, **10** (2018) 16113.
31. Z. Li, X. Zou, F. Shi, R. Liu, and Y. Yagci, *Nat. Commun.*, **10** (2019) 3560.
32. T. Wang, Y. Zhao, M. Shi, and F. Wu, *Dyes Pigments*, **75** (2007) 104.
33. W. Qiu, P. Hu, J. Zhu, R. Liu, Z. Li, Z. Hu, Q. Chen, K. Dietliker, and R. Liska, *ChemPhotoChem*, **3** (2019) 1090.
34. R. Maggi, F. Bigi, S. Carloni, A. Mazzacani, and G. Sartori, *Green Chem.*, **3** (2001) 173.
35. G. Brahmachari, *ACS Sustain. Chem. Eng.*, **3** (2015) 2350.
36. Y. Zhao, and D. G. Truhlar, *Theor. Chem. Acc.*, **120** (2008) 215.
37. B. P. Pritchard, D. Altarawy, B. Didier, T. D. Gibson, and T. L. Windus, *J. Chem. Inf. Model.*, **59** (2019) 4814.
38. Z. Li, J. Zhu, X. Guan, R. Liu, and Y. Yagci, *Macromol. Rapid Commun.*, **40** (2019) 1900047.
39. J. Zhu, Y. Zhu, Z. Li, Z. Yu, X. Guan, R. Liu, and Y. Yagci, *Macromol. Rapid Commun.*, **41** (2020) 2000004.

Synthesis, Properties, and Photovoltaic Characteristics of Fluoranthenedione-containing Nonfullerene Acceptors for Organic Solar Cells

Shreyam Chatterjee¹ and Yutaka Ie^{1,2*}

¹ *The Institute of Scientific and Industrial Research (SANKEN), Osaka University, 8-1 Mihogaoka, Ibaraki, Osaka 567-0047, Japan.*

² *Innovative Catalysis Science Division, Institute for Open and Transdisciplinary Research Initiatives (OTRI), Osaka University.
yutakaie@sanken.osaka-u.ac.jp

The progress of organic solar cells (OSCs) largely depends on the development of nonfullerene acceptors (NFAs) based on electron-accepting π -conjugated compounds. Therefore, the creation of its building unit is important to tune the properties and increase the OSC performance. In this contribution, a new electron-accepting building unit, fluoranthenedione (FDO), was designed by extending the π -conjugation of representative indene-1,3-dione (IDO) framework. The electron-accepting π -conjugated compound (FL-FDO) composed of thiophene-linked fluorene (FL) as a central unit and FDO as terminal units was designed and synthesized. Compared to the corresponding IDO-containing NFAs, the introduction of FDO led to the red-shifted absorption and increased frontier orbital energy levels. The OSCs based on FL-FDO and poly(3-hexylthiophene) (P3HT) as a donor showed improved power conversion efficiency, compared to the P3HT/FL-IDO-based devices. These results indicate that the FDO unit has the potential to act as a promising terminal unit of NFAs.

Keywords: Nonfullerene acceptors, Organic solar cells, Structure-property relationship, Semiconducting materials, Poly(3-hexylthiophene)

1. Introduction

Since the emergence of the nonfullerene acceptors (NFAs) [1-3] for the organic solar cells (OSCs) [4], the acceptor-donor-acceptor (A-D-A) molecular architecture has been proved to be the most effective design in the last few years [5,6]. For the construction of such molecular structures, aromatic fused rings with extended π -conjugation have been utilized as the D unit, and 1*H*-indene-1,3(2*H*)-dione (IDO) derivatives have been positioned as one of the most commonly used terminal A unit. However, in contrast to a variety of D units [7-10], the repertoires of effective A unit are still limited. Furthermore, the investigation of extended π -conjugation of the A unit on the A-D-A type NFAs is scarce in the literature [11,12].

Over the years, we have developed several NFAs compatible with poly(3-hexylthiophene) (P3HT) as a donor [13-19]. Recently, a novel electron-accepting π -conjugated system (FNTz-T_{ch}-FA)

consisting of new fluorinated naphthobisthiadiazole as a central unit and fluoranthene imide (FA) as terminal units showed good photovoltaic characteristics (Fig. 1) [14]. During this investigation, we hypothesized that the fluoranthene unit may be an appropriate framework to extend the π -conjugation of IDO, leading to the molecular design of 8*H*-cyclopenta[*k*]fluoranthene-8,10(9*H*)-dione (FDO) as a new A unit for NFAs. The resulting extension of the π -conjugation is expected to provide a red-shifted absorption while minimizing the adverse impact on the tuning of lowest unoccupied molecular orbital (LUMO) and the highest occupied molecular orbital (HOMO) levels [11]. Additionally, the introduction of a large π -conjugated moiety onto the end of small molecules would benefit the intermolecular end-to-end π - π interaction and thus the solid-state morphology, leading to the improvement of fill factor (FF) in OSCs.

Received April 9, 2022

Accepted June 24, 2022

In this contribution, we synthesized the new unit FDO and its-containing π -conjugated compound FL-FDO. A reference compound using IDO as the terminal units is also synthesized for comparison (Fig.1). The physical properties and the acceptor performance of these compounds was investigated.

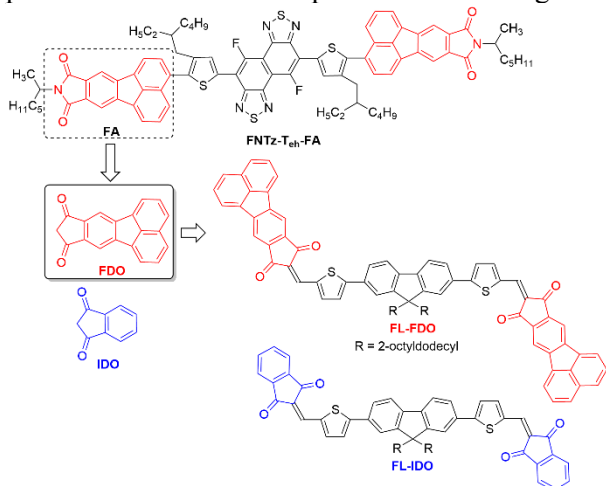


Fig. 1 Chemical structures of the terminal A units and NFAs.

2. Experimental

2.1 General Information Column chromatography was performed on silica gel, KANTO Chemical silica gel 60N (40–50 μm). Thermal gravimetric analysis (TGA) was performed under nitrogen with Shimadzu TGA-50. UV-vis absorption spectra were recorded on a Shimadzu UV-3600 spectrophotometer. The surface morphology of organic films was observed by atomic force microscopy (AFM) (Shimadzu, SPM9600). Photoelectron yield spectroscopy (PYS) was performed by Bunkoukeiki BIP-KV202GD.

2.2 Synthesis of FDO The solution of dimethyl fluoranthene-8,9-dicarboxylate (1) (300 mg, 0.94 mmol) in EtOAc (5 mL) was added to a 50% dispersion of NaH in mineral oil (140 mg, 2.8 mmol), and the mixture was refluxed at 100 $^{\circ}\text{C}$ for 4h. After removal of the solvent, the yellow solid was filtered and washed with EtOH-Et₂O (1:1). Treatment of this solid with a hot solution of 10% concentrated HCl in water over 10 min gave the new compound FDO as a buff solid with 47% yield (120 mg, 0.44 mmol). (Fig. 2, Scheme 1)

2.3 Device fabrication Organic solar cell devices were prepared with a structure of indium tin oxide (ITO)/poly (3,4-ethylenedioxythiophene):poly(styrenesulfonate) (PEDOT:PSS)/active layer/Ca/Al. ITO-coated glass substrates were first cleaned by ultrasonication in toluene, acetone, H₂O, and 2-propanol for 15 min,

respectively, followed by O₂ plasma treatment for 20 min. The ITO-coated glass substrates were then activated by ozone treatment for 2 h. The PEDOT:PSS layer was spin-coated on the ITO surface at 3000 rpm for 60 sec and dried at 135 $^{\circ}\text{C}$ for 10 min. Under this condition, the thickness of PEDOT:PSS is decided to be ca. 30 nm. The active layers were then prepared by spin-coating on the ITO/PEDOT:PSS electrodes at 1000 rpm for 2 min in a glove box. Then, the active layer was annealed at 135 $^{\circ}\text{C}$ for 15 min. Finally, Ca and Al electrodes were evaporated on the top of active layer through a shadow mask to define the active area of the devices (0.09 cm²) under a vacuum of 10⁻⁵ Pa to thicknesses of 20 and 80 nm, respectively, determined by a quartz crystal monitor. After sealing the device from the air, the photovoltaic characteristics were measured under simulated AM 1.5G solar irradiation (100 mW cm⁻²) (SAN-EI ELECTRIC, XES-301S). The current density–voltage (*J*–*V*) characteristics of OSC devices were measured by using a KEITHLEY 2400 source meter. The external quantum efficiency (EQE) spectra were measured by using Soma Optics Ltd. S-9240. The thickness of the active layer was determined by KLA Tencor Alpha-step IQ.

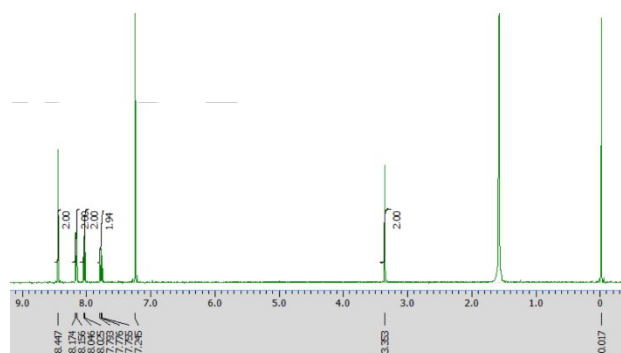


Fig. 2 ¹H NMR of FDO in CDCl₃ at 25 $^{\circ}\text{C}$.

3. Results and discussion

Computational analysis was carried out using density functional theory (DFT) at the B3LYP/6–31G(d,p) level. We first calculated the molecular orbitals of FL-FDO together with that of FL-IDO. All alkyl groups were replaced with methyl groups for the sake of reduced loads of the calculation. As shown in Fig. 3, the extended π -conjugation of the FDO unit contributed to increasing HOMO and LUMO energy levels of FL-FDO. Consequently, FL-FDO has a similar HOMO–LUMO energy gap with FL-IDO.

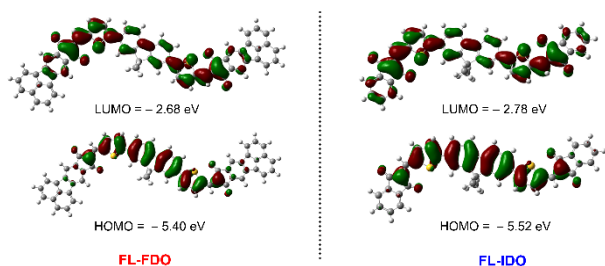
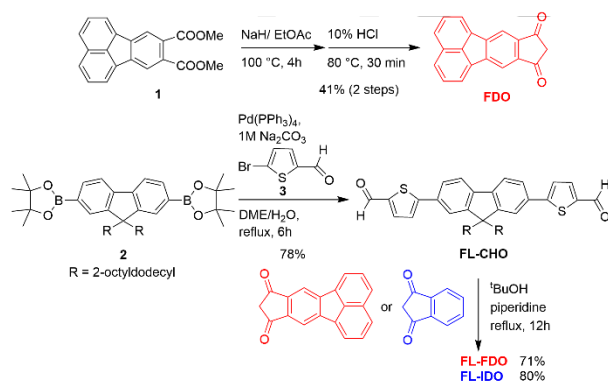


Fig. 3 Molecular orbitals of FL-FDO and FL-IDO calculated at B3LYP/6-31G(d,p) level.

The synthesis of FL-FDO is shown in Scheme 1. The Suzuki coupling of 2,2'-(9,9-dimethyl-9H-fluorene-2,7-diyl)bis(4,4,5,5-tetramethyl-1,3,2-dioxaborolane) (**2**) with 5-bromothiophene-2-carbaldehyde (**3**) afford FL-CHO, [20,21] which was subjected a condensation reaction with FDO to afford FL-FDO. A reference compound FL-IDO was also synthesized in the same procedure using the IDO as the terminal unit (Scheme 1). It should be mentioned that the presence of long alkyl chain (2-octyldodecyl group) in the fluorene unit ensured adequate solubility against common organic solvents such as chloroform, chlorobenzene (CB), and *o*-dichlorobenzene (*o*-DCB). Owing to the extension of π -conjugation, the solubility of FL-FDO is lower (7 mg mL⁻¹ in CB) than that of FL-IDO (22 mg mL⁻¹).



Scheme 1. Synthesis of FDO, FL-FDO and FL-IDO.

The TGA measurements indicate that FL-FDO and FL-IDO possess good thermal stability with 5%-weight-loss temperature of 365 and 351 °C,

respectively (Fig. 3a). These thermal properties are suitable for use in OSCs. The XRD measurements of the pristine films after thermal annealing are shown in Fig. 3b. The FL-FDO film showed small XRD signals at $2\theta = 10.3^\circ$, and the FL-IDO film did not show clear peaks. These results indicate that both compounds have almost amorphous nature in the solid state.

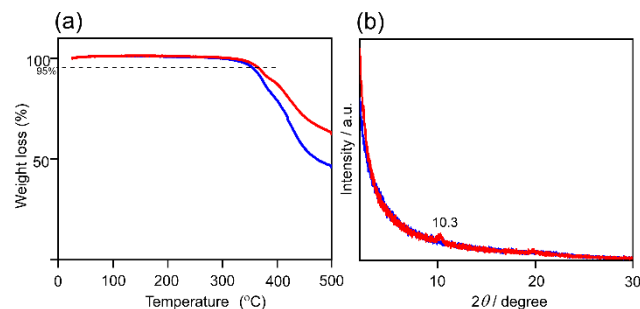


Fig. 4 (a) TGA curves and (b) XRDs of FL-FDO (red) and FL-IDO (blue).

The photophysical properties of FL-FDO and FL-IDO (Table 1) in chloroform solutions and thin films were measured by UV-vis absorption spectrometry (Fig. 5a). The main absorption bands of FL-FDO and FL-IDO appeared at about 534 and 523 nm, respectively. A small red-shift absorption of FL-FDO compared to that of FL-IDO is due to the extension of π -conjugation in the terminal part of FDO. It is to be noted that the molar extinction coefficient (ϵ) of FL-FDO is higher (2.14×10^5) than that of FL-IDO (8.60×10^4) in the chloroform solution. The absorption spectra of the films were red-shifted compared to those in solution for both compounds.

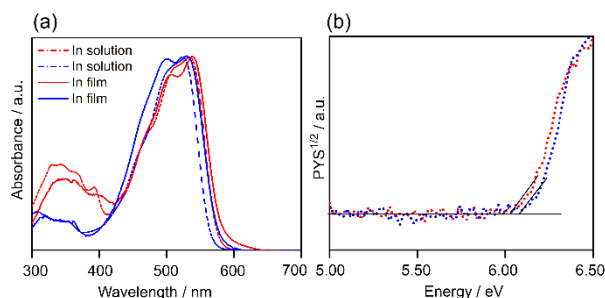


Fig. 5 (a) UV-vis absorption spectra in chloroform solutions (dashed line) and in films (solid line) and (b) PYS for FL-FDO (red) and FL-IDO (blue).

Table 1. Properties of compounds.

Compound	$T_d / ^\circ\text{C}$	$\lambda_{\text{abs}} / \text{nm}^a$	$\epsilon / \text{M}^{-1} \text{cm}^{-1}^a$	$\Delta E_{\text{opt}} / \text{eV}^b$	$\Delta E_{\text{opt}}(\text{film}) / \text{eV}^c$	IP / eV ^d	EA / eV ^e
FL-FDO	365	534	2.14×10^5	2.13	2.09	6.00	3.87
FL-IDO	351	523	8.60×10^4	2.16	2.12	6.07	3.95

^a In CHCl₃. ^b Estimated from the onset of UV-vis absorption spectra in CHCl₃. ^c Estimated from the onset of UV-vis absorption spectra in the film. ^d Determined by the PYS measurements in thin films. ^e Calculated from E_{HOMO} and ΔE_{opt} in film.

To estimate the frontier orbital energy levels of these compounds, the ionization potential (IP) and electron affinity (EA) were determined by a combination of PYS and UV-vis spectroscopy in thin films. The IPs based on the onset of the spectra were determined to be 6.00 eV for FL-FDO and 6.07 eV for FL-IDO (Fig. 5b). The optical energy gaps (ΔE_g^{opt}) of FL-FDO and FL-IDO extracted from the absorption onset were 2.09 and 2.12 eV, respectively. Based on these values, the EA was estimated to be 3.87 eV for FL-FDO and 3.95 eV for FL-IDO. This result indicated that the frontier orbital energy levels of FL-FDO are high-lying compared to those of FL-IDO.

OSCs were fabricated to investigate the influence of terminal A units on the photovoltaic characteristics. The active layers were composed of P3HT as donor and the newly synthesized molecules (FL-FDO or FL-IDO) as the acceptor. The fabrication conditions of the active layer were optimized as the blend composition of 1:1.2 ratio, a concentration of 10 mg mL⁻¹ in chlorobenzene for spin-coating, and thermal annealing at 135 °C for 15 min. The best-performance J - V characteristics and EQE spectra are shown in Fig. 6, and their key photovoltaic parameters are summarized in Table 2. As we expected, both compounds functioned as acceptors. These devices exhibited typical OPV J - V curves with higher open-circuit voltage (V_{oc}) in the P3HT/FL-FDO based devices, reflecting the high-lying LUMO energy level of FL-FDO relative to that of FL-IDO. Compared to the P3HT/FL-IDO-based device, the P3HT/FL-FDO-based device showed a superior power conversion efficiency (PCE) of 2.04%. This PCE improvement is attributed to the increased short-circuit current density (J_{sc}) and fill factor (FF). The EQE spectra of the P3HT/FL-FDO-based devices exhibited photoresponses between 300 and 680 nm with a maximum of 41%.

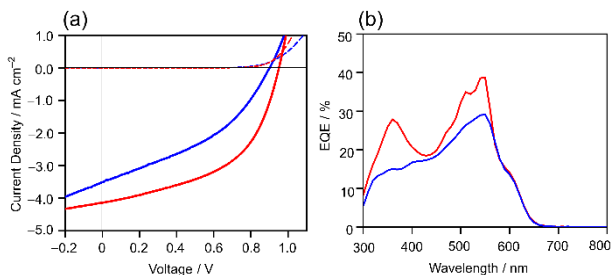


Fig. 6 J - V curves of the (a) P3HT/FL-FDO (red) and P3HT/FL-IDO (blue) under illumination (solid line) and in the dark condition (dashed line) and (b) EQE spectra of these devices.

Table 2. Photovoltaic parameters of OSC devices.

Blend	V_{oc} (V)	J_{sc} (mA/cm ²)	FF	PCE (%)
P3HT/FL-FDO	0.95	4.14	0.52	2.04
P3HT/FL-IDO	0.90	3.51	0.42	1.33

To understand why the end-group variation causes a difference in the device performance, we investigated the morphologies of the active layers using AFM measurements. As shown in Fig. 7, AFM images of the blend films showed significant different morphologies with the average roughness (R_a) of 2.36 nm for the P3HT/FL-FDO film and 1.63 nm for the P3HT/FL-IDO film. The relatively large R_a value of the P3HT/FL-FDO film may be decisive for the appropriate intermixing between the donor and acceptor with optimal domains length, causing good exciton dissociation leading to the higher J_{sc} [13]. On the other hand, because of the higher solubility of FL-IDO, high miscibility of P3HT and the FL-IDO compound might disturb the formation of phase-separated nanomorphology in the active layer of the devices, resulting in the decreased OSC performance. [17]

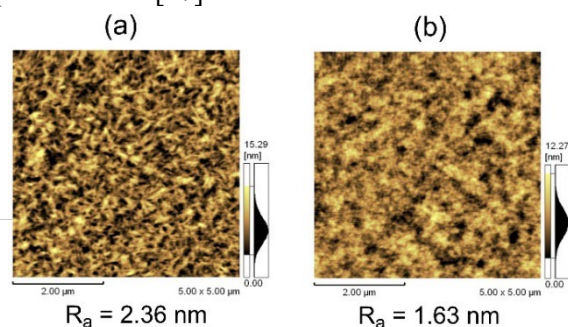


Fig. 7 AFM height images of (a) P3HT/FL-FDO and (b) P3HT/FL-IDO blend films.

4. Conclusion

In summary, to investigate the potential of FDO as a terminal unit of NFAs, we designed and synthesized FL-FDO. Photophysical measurements indicated that the replacement of FDO with IDO led to the slightly red-shifted absorption with higher molar extinction coefficient. The frontier orbital energy levels of FL-FDO are increased compared to those of FL-IDO. The OSCs based on FL-FDO and P3HT showed superior PCE of up to 2.04%, compared to the corresponding P3HT/FL-IDO-based devices. This result indicates that the FDO unit becomes a candidate for effective A unit. We are now currently investigating the potential of the terminal FDO unit by using different donor cores to achieve high-performance NFAs for OSCs.

Acknowledgement

This work was supported by MEXT (20H02814, 20K21224, 20H05841, and 20KK0123), CREST (J205101030), and NEDO (21500248-0), Japan, and "Dynamic Alliance for Open Innovation Bridging Human, Environmental and Materials" from The Ministry of Education, Culture, Sports, Science and Technology, Japan. We are thankful to Nanotechnology Open Facilities, Osaka University (JPMXP09S21OS0010) for PYS. The author, S.C gratefully acknowledge the "UCL-OU Partner Fund 2021" (Na20990020). Dr. S. Jinnai is also acknowledged for the help of the PYS measurements.

References

1. G. Zhang, J. Zhao, P. C. Y. Chow, K. Jiang, Z. Zhu, J. Zhang, F. Huang, and H. Yan., *Chem. Rev.*, **118** (2018) 3447.
2. W. Chen, and Q. Zhang., *J. Mater. Chem C*, **5** (2017) 1275.
3. S. Chatterjee, S. Jinnai, and Y. Ie., *J. Mater. Chem A*, **9** (2021) 18857.
4. N. S. Sariciftci, L. Smilowitz, A. J. Heeger, and F. Wuld, *Science*, **258** (1992) 1474.
5. Y. Lin, J. Wang, Z. G. Zhang, H. Bai, Y. Li, D. Zhu, X. Zhan, *Adv. Mater.*, **27** (2015) 1170.
6. D. Baran, R. S. Ashraf, D. A. Hanifi, M. Abdelsamie, N. Gasparini, J. A. Rohr, S. Holliday, A. Wardsworth, S. Lockett, M. Neophytou, C. J. M. Emmott, J. Nelson, C. J. Brabec, A. Amassian, A. Salleo, T. Kirchartz, J. R. Durrant and I. McCulloch, *Nat. Mater.*, **16** (2017) 363.
7. S. Dai, F. Zhao, Q. Zhang, T. K. Lau, T. Li, K. Liu, Q. Ling, C. Wang, X. Lu, W. You, and X. Zhan., *J. Am. Chem. Soc.*, **139** (2017), 1336.
8. F. Liu, Z. Zhou, C. Zhang, T. Vergote, H. Fan, F. Liu, and X. Zhu, *J. Am. Chem. Soc.*, **138** (2016), 15523.
9. W. Zhao, S. Li, H. Yao, S. Zhang, Y. Zhang, B. Yang, and J. Hou. *J. Am. Chem. Soc.*, **139** (2017), 7148.
10. W. Zhao, D. Qian, S. Zhang, S. Li, O. Inganas, F. Gao, and J. Hou., *Adv. Mater.*, **28** (2016), 4734.
11. H. Feng, N. Qiu, X. Wang, M. Zhang, A. Xia, Y. Wang, B. Kan, X. Wan, C. Li, F. Liu, H. Zhang, and Y. Chen., *Chem. Mater.*, **29** (2017), 7908.
12. Suman, and S. P. Singh, *J. Mater. Chem. A*, **7** (2019) 22701.
13. S. Chatterjee, Y. Ie, M. Karakawa, and Y. Aso, *Adv. Funct. Mater.*, **26** (2016) 1161.
14. S. Chatterjee, Y. Ie, T. Seo, T. Moriyama, G.-T. A. H. Wetzelaer, P. W. M. Blom, and Y. Aso, *NPG Asia Mater.*, **10** (2018), 1016.
15. S. Chatterjee, Y. Ie, and Y. Aso, *ACS Omega*, **3** (2018), 5814.
16. S. Chatterjee, Y. Ie, and Y. Aso, *J. Photopolym. Sci. Technol.*, **30** (2016) 557.
17. Y. Ie, S. Jinnai, M. Nitani, and Y. Aso., *J. Mater. Chem C*, **1** (2013) 5373.
18. S. Chatterjee, T. Ohto, H. Tada, S. Jinnai, and Y. Ie, *ACS Sustainable Chem. Eng.*, **8** (2020), 19013.
19. S. Jinnai, and Y. Ie., *J. Photopolym. Sci. Technol.*, **34** (2021) 385.
20. R. C. Mulherin, S. Jung, S. Huettner, K. Johnson, P. Kohn, M. Sommer, S. Allard, U. Scherf, N. C. Greenham, *Nano Lett.*, **11** (2011) 4846.
21. K. N. Winzenberg, P. Kemppinen, F. H. Scholes, G. E. Collis, Y. Shu, Th. B. Singh, A. Bilic, C. M. Forsyth, and S. E. Watkins, *Chem. Commun.*, **49** (2013) 6307.

Effect of UV-light irradiation on charge-accumulation states in PTzBT polymer solar cells

Dong Xue¹, Masahiko Saito², Itaru Osaka²,
and Kazuhiro Marumoto^{1,3*}

¹ *Division of Materials Science, University of Tsukuba, Tsukuba, Ibaraki 305-8573, Japan*

² *Graduate School of Advanced Science and Engineering, Hiroshima University, Higashihiroshima, Hiroshima, 739-8527, Japan*

³ *Tsukuba Research Center for Energy Materials Science (TREMS), University of Tsukuba, Tsukuba, Ibaraki, 305-8571, Japan*

**marumoto@ims.tsukuba.ac.jp*

Ternary polymer solar cells based on a polymer PTzBT have received a lot of attention because their power conversion efficiency (PCE) and thermal stability have been greatly improved by adding a small amount of an oligomer ITIC. However, the charge-accumulation states of the PTzBT ternary polymer solar cells have not yet been completely clarified. Here, we report electron spin resonance (ESR) spectroscopy of the PTzBT ternary polymer solar cells to investigate the charge-accumulation states from a microscopic viewpoint with examining the effect of UV-light irradiation. We observed a slight increase in the ESR intensity of the PTzBT cells and layered film samples under simulated solar irradiation with a UV-cut filter. Multiple signals were observed in the PTzBT cells under solar irradiation when the UV-cut filter was removed. Interestingly, no decrease was observed in the ESR signal of ZnO under solar irradiation with the UV-cut filter, although holes in ZnO in the PTzBT cells are known to decrease under solar irradiation. These findings will contribute to a deep understanding of the material properties of polymer solar cells.

Keywords: Charge accumulation, Electron spin resonance spectroscopy, Polymer solar cells

1. Introduction

Polymer solar cells have received a lot of attention because of their features including low manufacturing cost, enabling large-area, and flexibility [1–3]. The power conversion efficiency (PCE) of ternary polymer solar cells has been remarkably improved in recent years [4]. However, the internal deterioration mechanism has not yet been completely clarified. Ternary polymer solar cells with a wide-bandgap polymer based on thiophene and thiazolothiazole (PTzBT) (Fig. 1a) have received a lot of attention because the maximum PCE of the cells with PTzBT and [6,6]-phenyl C₆₁-butyric acid methyl ester (PC₆₁BM) have been improved from 7.4% to 10.3% by adding a small amount of ITIC (Fig. 1b). The PCE of these ternary cells has nearly not altered even after 1000 h of storage at 85°C under dark conditions under open-circuit conditions in a nitrogen-filled glove box. Thus, the PTzBT cells are expected to polymer

solar cells with high PCE and stability [5].

Extrinsic irreversible degradations from oxygen and moisture can be reduced by sealing solar cells [6–12]. However, there are still some internal deterioration factors such as charge accumulation that cannot be prevented by the sealings. Electron spin resonance (ESR) spectroscopy is a valuable approach for investigating the states of accumulated charges in polymer solar cells at a molecular level [13–25]. In previous studies, the holes in PTzBT, electrons on PC₆₁BM and holes in ZnO can be observed when the PTzBT cells are exposed to solar irradiation [24,25]. It is particularly fascinating to investigate the charge accumulation in the PTzBT ternary polymer solar cells under solar irradiation with a UV-cut filter to examine the effect of UV light on the charge accumulation.

In this study, we studied the PTzBT cells and layered film samples of the active layer and an electron transport layer (ETL) ZnO using ESR

Received	March 30, 2022
Accepted	June 20, 2022

spectroscopy under solar irradiation with a UV-cut filter or not. There is only a hole signal of PTzBT when the PTzBT cells or layered film samples are exposed to solar irradiation with the UV-cut filter. It is interesting to note that electrons on PC₆₁BM and holes in ZnO were observed when the UV-cut filter was removed. It has been reported that a decrease in holes in ZnO under simulated solar irradiation [25]. However, no decrease was observed in the ESR signal of ZnO under solar irradiation with the UV-cut filter. This finding for the effect of UV light on the charge-accumulation states is important for optimizing the device structures and for improving the PCE and stability of polymer solar cells.

2. Experimental

The ternary solar cells were fabricated with PTzBT, ITIC, and PC₆₁BM (Fig. 1c) (Solenne BV, purity > 99.5%). A quartz substrate (20 mm × 3 mm) was cleaned with acetone and 2-propanol in ultrasonic treatment. A ZnO layer was prepared by a spin-coating method (at 1500 rpm) from a diluted solution of ZnO nanoparticles. PTzBT, ITIC, and PC₆₁BM (1:0.2:2 w/w/w) dissolved in chlorobenzene (CB) solvent were mixed at 100 °C for 30 min with a vibrational method. Active layers (PTzBT:ITIC:PC₆₁BM) were fabricated by a spin-coating method (600 rpm, 20 s) on the quartz substrate in a nitrogen-filled glove box (O₂ < 0.2 ppm, H₂O < 0.5 ppm). The fabricated samples were measured under dark conditions or simulated solar irradiation with a solar simulator (AM1.5G, 100 mW cm⁻², OTENTOSUN-150LX). We measured the samples under simulated solar irradiation with a filter that cuts short wavelengths of ≤440 nm.

3. Results and discussion

3.1. ESR measurements

A continuous-wave ESR method was used in the experiments which performs a lock-in detection with an external magnetic field (*H*) modulation of 100 kHz. Thus, photogenerated charges with a lifetime (<10 μs) cannot be observed, and it is possible to observe only long-lived (or accumulated) photogenerated charges with an unpaired spin with a long lifetime (>10 μs) in thin films and solar cells [19,21–25].

The ESR signals of a fabricated sample and a same standard Mn²⁺ marker sample were simultaneously measured in a same ESR cavity in all ESR measurements to compare these *g*-factors directly [19,21–25]. Using ESR measurements makes it possible to investigate accumulated charge

states in the samples directly. [19,21–25]. In our study, the substrate plane was parallel to the *H* direction. All measured light-induced ESR spectra were averaged over 1 h irradiation [19,21–25].

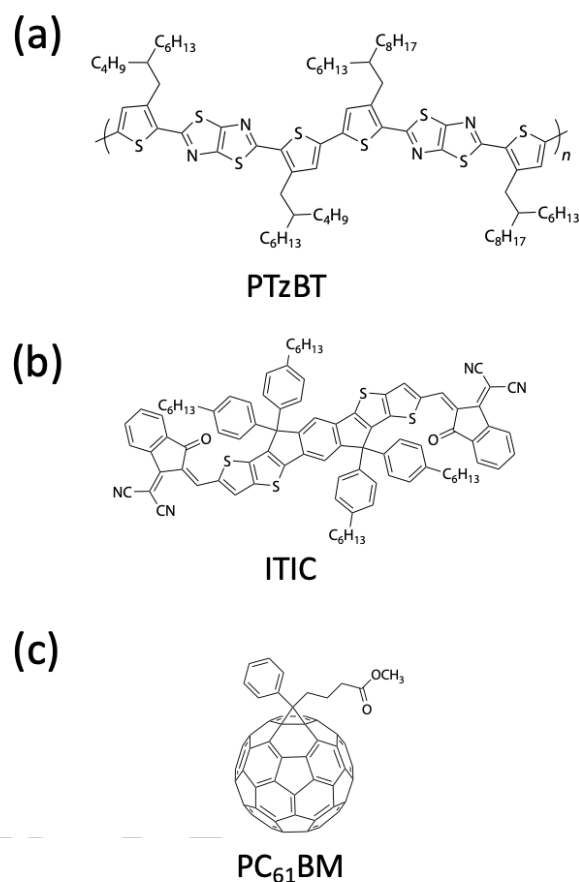


Fig. 1. Chemical structures of (a) PTzBT, (b) ITIC, and (c) PC₆₁BM.

3.2. ESR signals of layered film samples and PTzBT cells

The effect of UV-light irradiation on the PTzBT cells can be investigated by comparing the difference in the signals of the cells under solar irradiation with or without the UV-cut filter. For this purpose, PTzBT cells with a structure of ITO/ZnO/PTzBT:ITIC:PC₆₁BM/MoO_x/Ag and layered film samples of ITO/ZnO/PTzBT:ITIC:PC₆₁BM were fabricated and measured using ESR spectroscopy under solar irradiation with or without UV-cut filter. The observed ESR signals are shown in Fig. 2. In the signals of the cell (Fig. 2a), a signal with a *g*-factor $g = 2.0022 \pm 0.0002$ was observed under dark conditions. This signal is consistent with the hole signal of PTzBT which has been reported in previous studies [24,25]. After 1 h solar irradiation

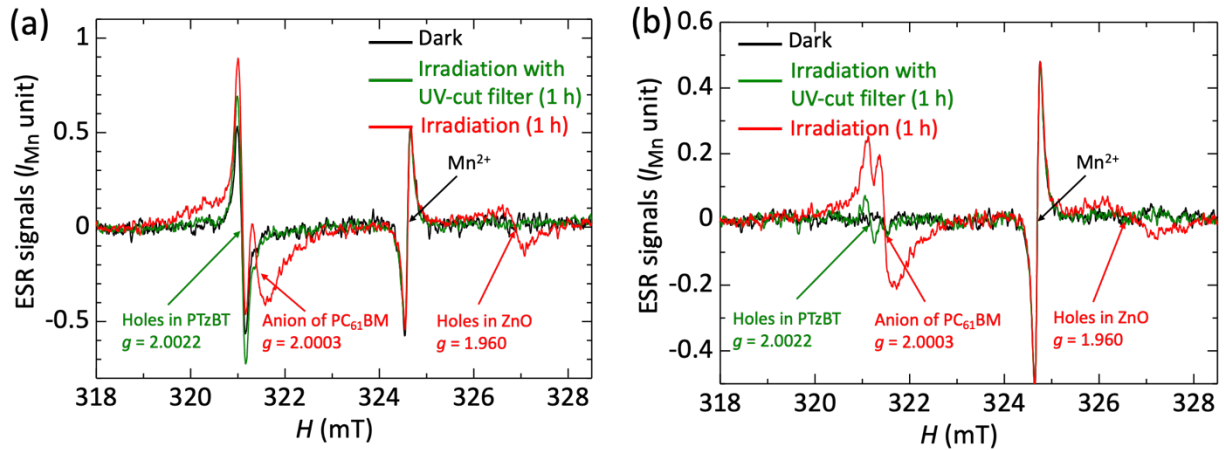


Fig. 2. ESR signals of (a) a PTzBT cell and (b) an ITO/ZnO/PTzBT:ITIC:PC₆₁BM layered film sample under dark (black lines), simulated solar irradiation with UV-cut filter for 1 h (green lines), and simulated solar irradiation without UV-cut filter for 1 h (red lines) conditions.

with the UV-cut filter, the PTzBT signal slightly increased. It is worth noting that we observed the signals with the g -factors $g = 2.0003 \pm 0.0002$ and $g = 1.960 \pm 0.005$ after 1 h solar irradiation without the UV-cut filter. These two signals are consistent with the electron signal of PC₆₁BM and the hole signal of singly charged zinc interstitials (Zn_i^+) in ZnO, respectively [25,26]. The results indicate that the charge accumulations of electrons on PC₆₁BM and holes in ZnO are correlated with UV-light irradiation. In the signal of ITO/ZnO/PTzBT:ITIC:PC₆₁BM sample, we also observed the electron signal of PC₆₁BM and the hole signal of ZnO under solar irradiation, which cannot be observed under solar irradiation with the UV-cut filter (Fig. 2b). Thus, UV-light irradiation plays a decisive role in the charge accumulations of electrons on PC₆₁BM and holes in ZnO. In previous studies, the Zn_i^+ signal, which cannot be observed under dark conditions, has been observed under solar irradiation [25]. The reason is that a lot of holes are trapped in zinc interstitials that are formed by solar irradiation with short wavelengths (Frenkel reaction) [25,27]. We think the same mechanism occurs after the removal of the UV-cut filter in the PTzBT cells where the variations of the ESR signals are similar to those in the previous studies [24,25]. No ESR observation for ITIC electrons in the PTzBT:ITIC:PC₆₁BM layer at room temperature has been confirmed in the previous study [25], which may be due to the efficient electron transfer from ITIC to PC₆₁BM.

3.3. Charge-accumulation mechanism in ZnO under solar irradiation with and without UV-cut filter

The charge-accumulation mechanism is very

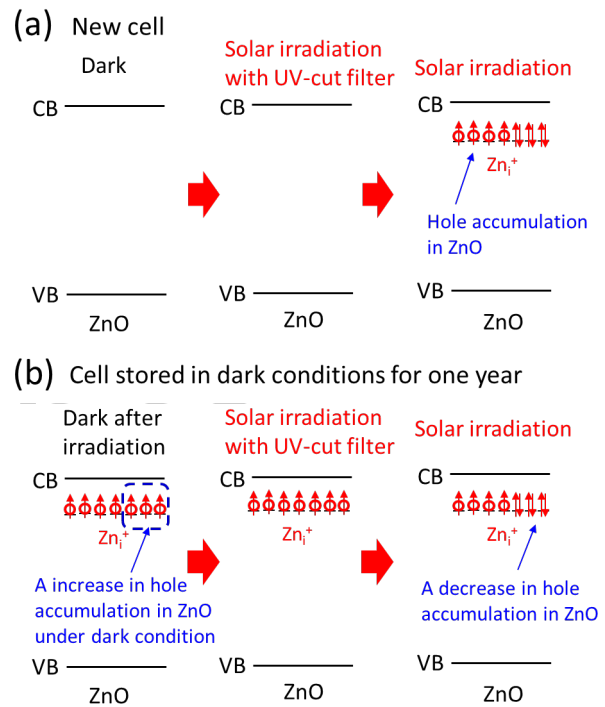


Fig. 3. Variation in the charge accumulation in ZnO under solar irradiation with and without UV-cut filter. (a) A new PTzBT cell. (b) A PTzBT cell stored in dark conditions for one year. This cell was irradiated by solar irradiation for 20 h and then stored in dark conditions for one year.

important for understanding and application of the materials. In this study, we did not observe the Zn_i^+ signal when we used the UV-cut filter (see the green lines in Fig. 2a,b). When the UV-cut filter was removed, the Zn_i^+ signal can be observed (see the red lines in Fig. 2a,b). Such different results under irradiation with and without the UV-cut filter are thought to be due to the absorption of UV light by

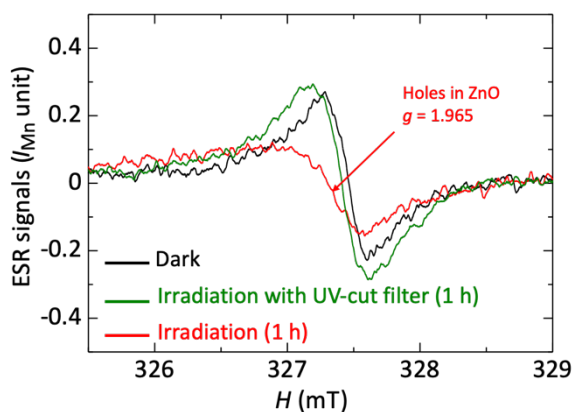


Fig. 4. ESR signals of an irradiated PTzBT cell under dark condition, and solar irradiation with and without the UV-cut filter conditions.

ZnO. Under the solar irradiation with the UV-cut filter, the zinc interstitials were not formed and thus there was no charge accumulation (Fig. 3a) [25,27]. After the removal of the UV-cut filter, the ZnO absorbed UV light and zinc interstitials were formed by Frenkel reaction, and thus the hole signal in ZnO can be observed (Fig. 3a) [25,27].

To study the effect of UV-light irradiation on ZnO in more detail, we measured the PTzBT cells after being exposed to solar irradiation for 20 h and then stored in dark conditions for one year. We have found that hole signal intensity increased in the ZnO layer after one year under dark conditions (Fig. 3b and 4). In our experiment, the g -factor of the cell after one-year storage ($g = 1.965$, Fig. 4) is slightly large than that of the new cell ($g = 1.960$, Fig. 2) under simulated solar irradiation. The difference of the g -factor may be caused by the slightly different charge-accumulation states and the arrangements of the ZnO defects in these two cells. According to the previous study on ZnO, the g -factor of bulk Zn_i^+ ($g = 1.960$) is slightly larger than that of surface Zn_i^+ ($g = 1.956$) [26]. Thus, we can infer that the hole accumulation states of the cell after one-year storage may be close to the bulk states in ZnO. Under solar irradiation with the UV-cut filter, we observed almost no decrease in the hole signal in ZnO, but after the removal of the UV-cut filter, a decrease in the hole signal in ZnO was observed (Fig. 3b and Fig. 4). The results suggest that UV-light irradiation is not only related to the generation of zinc interstitials but also has a direct relationship with the decrease of the hole accumulation in ZnO. The reason for this decrease in the hole signal in ZnO is thought to be the recombination between Zn_i^+ and electrons generated by UV-light irradiation [25]. The hole signal of PTzBT and the electron

signal of PC₆₁BM were not observed after one-year storage under dark conditions, which may be due to the recombination of the long-lived accumulated holes and electrons in the cells under dark conditions, indicating that the ternary bulk-heterojunction system is stable.

4. Conclusion

The PTzBT cells and layered film samples of ITO/ZnO/PTzBT:ITIC:PC₆₁BM have been investigated with ESR spectroscopy under simulated solar irradiation with and without the UV-cut filter. Only the hole signal of PTzBT has been observed under solar irradiation with the UV-cut filter. The electron signal of PC₆₁BM and the hole signal of ZnO have been observed under solar irradiation without the UV-cut filter. This is due to the absorption of UV light by ZnO, which creates zinc interstitial defects. The hole signal of ZnO has not been decreased under solar irradiation with the UV-cut filter but has been decreased when the UV-cut filter is removed. The reason is thought to be the recombination between Zn_i^+ and electrons generated by UV-light irradiation. This deep understanding of the charge-accumulation states in ZnO of ternary polymer solar cells will be useful for optimizing the device structures and for improving the PCE and stability.

Acknowledgements

This work was partially supported by JSPS KAKENHI Grant Number JP19K21955, by JST PRESTO, by The MIKIYA Science And Technology Foundation, by Iketani Science and Technology Foundation, by The Iwatani Naoji Foundation, by JST SPRING Grant Number JPMJSP2124, by JST ALCA Grant Number JPMJAL1603, and by JST MIRAI Grant Number JPMJMI20C5, Japan.

References

- [1] S. Günes, H. Neugebauer, N. S. Sariciftci, cells, *Chem. Rev.*, **107** (2007) 1324–1338.
- [2] T. M. Clarke, J. R. Durrant, *Chem. Rev.*, **110** (2010) 6736–6767.
- [3] R. Søndergaard, M. Hösel, D. Angmo, T. T. Larsen-Olsen, F. C. Krebs, *Mater. Today*, **15** (2012) 36–49.
- [4] Q. An *et al.*, *Sci. Bull.*, **65** (2020) 538–545.
- [5] M. Saito, Y. Tamai, H. Ichikawa, H. Yoshida, D. Yokoyama, H. Ohkita, I. Osaka, *Macromolecules*, **53** (2020) 10623–10635.
- [6] C. Y. Chang, C. T. Chou, Y. J. Lee, M. J. Chen, F. Y. Tsai, *Org. Electron.*, **10** (2009)

- 1300–1306.
- [7] S. Sarkar, J. H. Culp, J. T. Whyland, M. Garvan, V. Misra, *Org. Electron.*, **11** (2010) 1896–1900.
- [8] M. Hermenau, S. Schubert, H. Klumbies, J. Fahlteich, L. Müller-Meskamp, *Sol. Energy Mater. Sol. Cells*, **97** (2012) 102–108.
- [9] H. J. Lee, H. P. Kim, H. M. Kim, J. H. Youn, D. H. Nam, Y. G. Lee, J. G. Lee, A. R. Bin Mohd Yusoff, J. Jang, *Sol. Energy Mater. Sol. Cells*, **111** (2013) 97–101.
- [10] M. D. Clark, M. L. Jespersen, R. J. Patel, B. J. Leever, *Org. Electron.*, **15** (2014) 1–8.
- [11] T. M. Abdel-Fattah, E. M. Younes, G. Namkoong, E. M. El-Maghraby, A. H. Elsayed, A. H. Abo Elazm, *Synth. Met.*, **209** (2015) 348–354.
- [12] A. Singh, A. Dey, D. Das, P. K. Iyer, *ACS Appl. Mater. Interfaces*, **8** (2016) 10904–10910.
- [13] K. Marumoto, S. Kuroda, T. Takenobu, Y. Iwasa, *Phys. Rev. Lett.*, **97** (2006) 256603.
- [14] K. Marumoto, N. Arai, H. Goto, M. Kijima, K. Murakami, Y. Tominari, J. Takeya, Y. Shimoi, H. Tanaka, S. Kuroda, T. Kaji, T. Nishikawa, T. Takenobu, Y. Iwasa, *Phys. Rev. B*, **83** (2011) 075302.
- [15] T. Nagamori, K. Marumoto, *Adv. Mater.*, **25** (2013) 2362–2367.
- [16] T. Biskup, M. Sommer, S. Rein, D. L. Meyer, M. Kohlstädt, U. Würfel, S. Weber, *Angew. Chem. Int. Ed.*, **210** (2015) 148–155.
- [17] D. Son, T. Kuwabara, K. Takahashi, K. Marumoto, *Appl. Phys. Lett.*, **109** (2016) 4963285.
- [18] G. Sato, D. Son, T. Ito, F. Osawa, Y. Cho, K. Marumoto, *Phys. Status Solidi A*, **215** (2018) 1700731.
- [19] T. Kubodera, M. Yabusaki, V. A. S. A. Rachmat, Y. Cho, T. Yamanari, Y. Yoshida, N. Kobayashi, K. Marumoto, *ACS Appl. Mater. Interfaces*, **10** (2018) 26434–26442.
- [20] Y. Kobori, T. Ako, S. Oyama, T. Tachikawa, K. Marumoto, *J. Phys. Chem. C*, **123** (2019) 13472–13481.
- [21] V. A. S. A. Rachmat, T. Kubodera, D. Son, Y. Cho, K. Marumoto, *ACS Appl. Mater. Interfaces*, **11** (2019) 31129–31138.
- [22] D. Xue, S. Kamiya, M. Saito, I. Osaka, K. Marumoto, *ACS Appl. Energy Mater.*, **3** (2020) 2028–2036.
- [23] D. Xue, S. Kamiya, M. Saito, I. Osaka, K. Marumoto, *J. Photopolym. Sci. Technol.*, **33** (2020) 97–102.
- [24] D. Xue, M. Saito, I. Osaka, K. Marumoto, *J. Photopolym. Sci. Technol.*, **34** (2021) 351–356.
- [25] D. Xue, M. Saito, I. Osaka, K. Marumoto, *npj Flex. Electron.*, **6** (2022) 22.
- [26] M. Zhang, F. Averseng, F. Haque, P. Borghetti, J. Krafft, B. Baptiste, G. Costentin, S. Stankic, *Nanoscale*, **11** (2019) 5102–5115.
- [27] L. Schmidt-Mende, J. L. MacManus-Driscoll, *Mater. Today*, **10** (2007) 40–48.

Formation and Stability of Cs₂SnBr₆ Perovskite Nanocrystals from CsSn₂Br₅ Nanocubes

Maning Liu¹, Mohamed Abodya¹, Weisi Dai¹, Tokuhisa Kawawaki², Ryota Sato², Masaki Saruyama², Toshiharu Teranishi², and Yasuhiro Tachibana^{1,3}

¹ School of Engineering, RMIT University, Bundoora, VIC 3083, Australia

² Institute for Chemical Research, Kyoto University, Gokasho, Uji, Kyoto 611-0011, Japan

³ Forefront Research Center, Faculty of Science, Osaka University, 1-1 Machikaneyama, Toyonaka, Osaka 560-0043, Japan

*yasuhiro.tachibana@rmit.edu.au; tachibana-yasuhiro-c@alumni.osaka-u.ac.jp

Lead-free Sn(II) based, CsSn₂Br₅, perovskite nanocubes were synthesized using a modified hot-injection method by tuning the injection temperature and reaction conditions. The formation of Sn(IV) based, Cs₂SnBr₆, perovskite nanocrystals (PNCs) from CsSn₂Br₅ perovskite nanocubes was observed. X-ray diffraction measurements revealed that oxygen or water molecules in air gradually react with CsSn₂Br₅ perovskite nanocubes to form Cs₂SnBr₆ NCs. The stability of Cs₂SnBr₆ NCs was monitored by time-dependent absorption measurements. Both oxygen and water molecules react with the Cs₂SnBr₆ NCs to degrade, however water molecules appears largely to react with the NCs. The stability has been improved by dispersing the Cs₂SnBr₆ NCs in degassed anhydrous solvent.

Keywords: Perovskite nanocrystal, CsSn₂Br₅, Cs₂SnBr₆, Stability

1. Introduction

Metal halide perovskite nanocrystals (PNCs) have recently attracted considerable attention as one of promising materials to be applied for optoelectronic devices such as light-emitting diodes (LEDs) [1, 2], solar cells [3, 4] and lasers [5, 6], owing to their low cost preparation process, attractive optical properties including a band gap tunability, and choice of a variety of morphologies from 0D quantum dots to 2D nanoplatelets [7-12]. However, these applications have been investigated by employing toxic lead halide materials, since lead halide perovskites have so far shown the highest performance, and no alternative metal has not been identified to replace lead halide perovskite. Employing high toxic lead will therefore impede commercialization of lead halide perovskite devices.

Tin has been considered as one of the alternatives to replace lead with similar structural and electronic properties as those of lead based perovskites [13, 14]. However, the application of Sn based perovskites has been limited owing to their instability under ambient conditions. Sn²⁺ can be

rapidly oxidized to SnO₂ in air [15-17], indicating an extra degradation path compared to lead-based perovskite [18]. Moreover, the high density of intrinsic defect sites results in low photoluminescence quantum yield (<1%) of Sn-based PNCs [15]. Several strategies have been employed to limit the Sn(II)-to-Sn(IV) oxidation. Liu et al. synthesized Sn-based PNCs with the B site co-alloying with germanium (Ge), effectively improving the efficiency and stability of their solar cells compared to the CsSnI₃ NCs-based solar cells [14]. The inclusion of bulky organic cations in a precursor solution inhibits the Sn²⁺ oxidation by forming protective 2D perovskite layers.[19] Abate et al. reported that selection of appropriate solvent combinations stabilizes Sn(II)-based perovskites [20].

Employing tin as an alternative to lead is also attractive, as the toxicity of lead has still been the main concern to the environment [17, 21]. The nonbiodegradable nature of lead is the prime reason for its prolonged persistence in the environment, although lead has a wide variety of unique

Received May 9, 2022

Accepted June 24, 2022

properties [21]. Compared to lead, tin is less toxic, however tin is less stable compared to lead [17].

To synthesize PNCs, two methods have mainly been developed, (i) ligand-assisted reprecipitation method, and (ii) hot-injection method [22, 23]. Recently, several other synthetic methods were introduced to produce high quality PNC, e.g. emulsion-based [24] & solvothermal technique [25], ultrasonication [10, 26], microwave heating-assisted methods [10, 12] and synthesis of ink-based NCs [27]. Tin(II) based PNCs were synthesized using the injection methods, however their instability originates from Sn^{2+} oxidation to form SnO_2 [15, 16]. Even direct synthesis of Sn^{4+} halide PNCs shows poor stability and performance [28]. Although synthesis and instability of Sn based PNCs have been reported, their instability mechanism has rarely been studied.

In this paper, we demonstrate synthesis and stability of lead-free Sn(II) based, CsSn_2Br_5 , perovskite nanocubes. The synthesis was conducted using a modified hot-injection method by tuning the injection temperature and reaction conditions. The stability of the synthesized CsSn_2Br_5 PNCs was systematically investigated by measuring X-ray diffraction pattern and tunneling electron microscopy. The formation of Sn(IV) based, Cs_2SnBr_6 , spherical NCs from CsSn_2Br_5 perovskite nanocubes was observed. We demonstrate that the stability of the Cs_2SnBr_6 PNCs is closely related to the synthetic atmosphere, i.e., water-free (anhydrous) or oxygen-free.

2. Experimental

2.1. Chemicals

Tin(II) bromide (SnBr_2 , 99.9%), cesium carbonate (Cs_2CO_3 , 99.9%), oleic acid (OA, 90%), oleylamine (OLA, 90%), 1-octadecene (ODE, 90%) were purchased from Sigma-Aldrich Inc. *n*-Hexane (95%) was purchased from Univar Solutions Inc. *tert*-Butanol was purchased from ChemSupply Australia.

2.2 Synthesis of CsSn_2Br_5 NCs

Cs-Oleate was prepared by adding 0.814 g (2.4 mmol) of Cs_2CO_3 into 50 mL three-neck flask including 30 mL of ODE and 2.5 mL of OA, followed by de-gassing at <10 torr. and by purging with nitrogen gas at 120 °C. The degassing and purging cycles were repeated until Cs_2CO_3 reacted fully with OA.

To synthesize CsSn_2Br_5 NCs, 0.38 g (1.36 mmol) of SnBr_2 was added into 25 mL three-neck flask

including 10 mL of ODE, 1 mL of OA and 1 mL of OLA, followed by de-gassing at <10 torr. and by purging with nitrogen gas at 120°C until the solution becomes light yellow transparent. The temperature was then increased to 250°C under nitrogen atmosphere, and 1.7 mL of the as prepared Cs-Oleate solution was swiftly injected into SnBr_2 solution with vigorous stirring. After 10 s of the injection, the solution was cooled by transferring the flask into a cool water bath to quench the reaction.

2.3 Purification of synthesized NCs

The NC solution was centrifuged at 3,000 rpm for 5 mins. The supernatant was removed, and the precipitate was dispersed in *n*-hexane. This dispersed solution was drop-casted on slide glass and on a copper mesh grid coated by a carbon film, followed by drying them in air at room temperature for characterization. *tert*-Butanol was added into this dispersed solution to precipitate the NCs, and the solution was further centrifuged at 3,000 rpm for 2 mins. The supernatant was discarded, and the precipitate was dispersed in *n*-hexane. This process was repeated until the dispersed solution became fully transparent. The purified solution was used for characterization, drop-casted on slide glass to prepare NC films, or drop-casted on a carbon coated copper mesh grid, followed by drying them in air at room temperature for further characterisation.

2.4 Characterisation

Absorption spectra were measured using a JASCO V-670 UV-Vis-NIR spectrophotometer. The morphology of the NCs was observed by transmission electron microscopy (TEM) operated at 100 kV in Kyoto University (JEM-1011). X-ray diffraction (XRD) patterns were obtained by a PANalytical X'Pert PRO MPD diffractometer using a copper tube source ($\text{Cu K}\alpha$, $\lambda = 1.5406 \text{ \AA}$) operated at 45 kV and 40 mA. Data was collected in 20-80° 2θ angle range, with a 0.2° step size and 2 s dwell time per step.

3. Results and discussion

3.1 Synthesis and purification of CsSn_2Br_5 NCs

Compared to the widely reported hot injection methods [15, 29], we developed our own synthetic route to obtain CsSn_2Br_5 NCs with well-confined NC shape and size by increasing the injection temperature up to 250°C, while a lower injection temperature (<240 °C) was generally selected by previous methods. Immediately after the injection

of 3.4 mL Cs-Oleate solution into the SnBr₂ solution, the solution colour changed from light yellow to crimson, indicative of the formation of CsSn₂Br₅ NCs. While Wang et al [29]. quenched the reaction by directly injecting cool hexane into the reaction mixture, we simply put the flask in a cold water bath, in case hexane addition influences the NC size and shape.

For the purification process, we employed *tert*-butanol to precipitate the PNCs, and the precipitate was re-dispersed in *n*-hexane. During this process, we noticed that the NC solution colour changed from crimson to light brown. Note that the excess number of the purification processes further changed the solution colour to light yellowish white. These colour changes will be discussed in the following sections.

3.2 Morphological and optical properties of PNCs

To investigate the morphology of the as-synthesized Sn-based PNCs, we conducted TEM and electron diffraction measurements for both NC samples with and without the purification process. Figs. 1a and 1b show the TEM images of the unpurified and purified NCs. The unpurified NCs indicate nanocubes with an average edge length of 12 nm while the purified NCs indicate spherical nanoparticles. Figs. 1c and 1d show the electron diffraction patterns of the unpurified and purified NCs, assigned to CsSn₂Br₅ and Cs₂SnBr₆ crystal structure, respectively. This result is surprising, indicating that the purification process using *tert*-butanol induces the oxidation of Sn²⁺ to form Sn⁴⁺ based perovskite structure. Note that Sn⁴⁺ still prefers to form perovskite structure rather than SnO₂, even if Sn²⁺ is oxidized. We speculate that water content in *tert*-butanol induces this oxidation reaction. Fig. 1e shows the absorption spectrum of the purified Cs₂SnBr₆ NCs solution, exhibiting a unique shoulder between 550 to 650 nm. The absorption onset indicates an indirect allowed transition with the band gap of 1.6 eV.

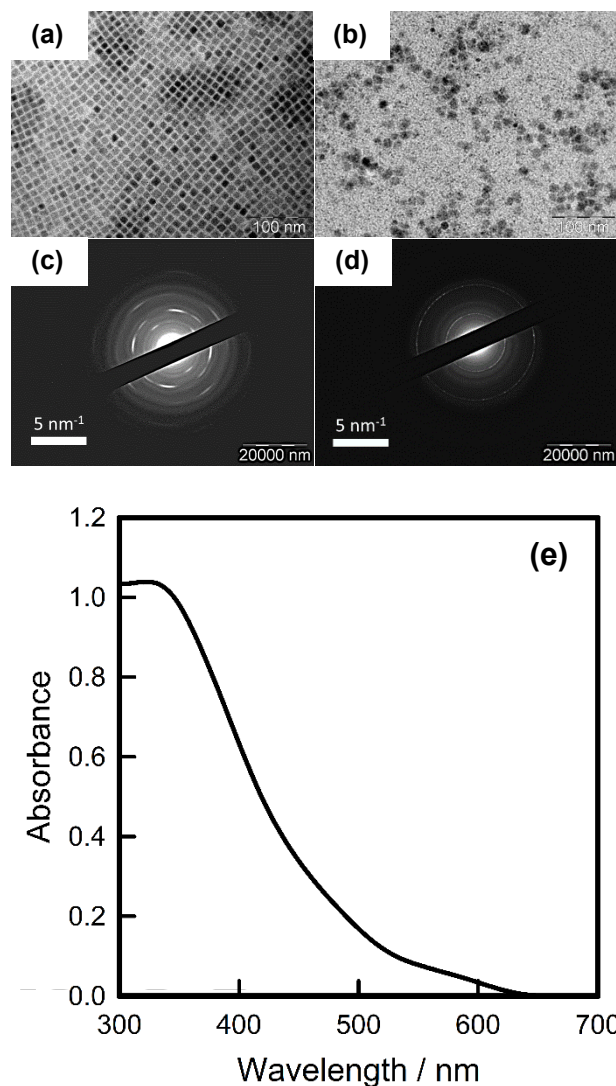


Fig. 1. TEM and electron diffraction images of the synthesized (a, c) and purified (b, d) PNCs. (e) Absorption spectrum of the purified NC solution.

3.3 Crystal structure change of CsSn₂Br₅ to Cs₂SnBr₆

We investigated transient crystal structure changes of the unpurified CsSn₂Br₅ NCs. The unpurified NC solution was drop-casted on a glass slide to form a NC film. As soon as the film is formed, XRD measurement was conducted. The film was left in an ambient atmosphere, and another XRD measurement was conducted. This process was repeated until the crystal structure was fully converted to Cs₂SnBr₆. Fig. 2 shows gradual change of XRD patterns as a function of time the film is left. The initial XRD pattern at 0 min indicates almost pure CsSn₂Br₅ phase with a strong characteristic peak at the 2θ angle of 30.8°. However, within 1 h exposure to air, the 30.8° peak intensity rapidly

reduced while two characteristic peaks at 28.7° and 33.2° were strongly increased, suggesting that the CsSn_2Br_5 NCs were gradually oxidized to form Cs_2SnBr_6 phase. We speculate that water or oxygen molecules in air induced Sn^{2+} oxidation, indicating this gradual crystal structure change. After 12 h exposure to ambient conditions, all the Sn^{2+} states were completely oxidised to Sn^{4+} states (XRD data is not shown).

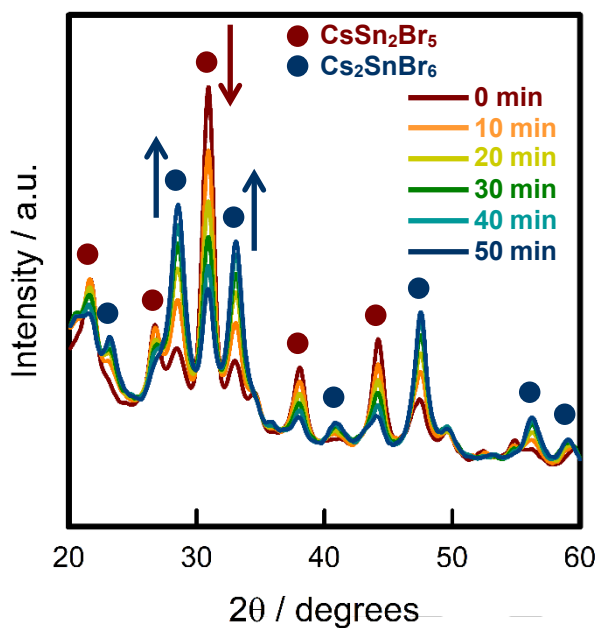


Fig. 2. Time dependent XRD pattern change of the NC film prepared by drop-casting the synthesized NC solution (without the purification) on a synthetic quartz glass substrate.

We next investigated the stability of Cs_2SnBr_6 structure. The purified Cs_2SnBr_6 NCs were dispersed in *n*-hexane treated by 3 different conditions, (i) untreated hexane, (ii) hexane purged by N_2 gas, and (iii) degassed anhydrous hexane. Figs. 3a and 3b shows time dependent absorption spectral change of NCs dispersed in untreated hexane and degassed anhydrous hexane (oxygen and water free), respectively. Within 45 min, the NCs dispersed in untreated hexane shows a huge absorbance decrease around 340 nm. In contrast, the NCs dispersed in degassed anhydrous hexane show slight absorbance decrease in 45 min. These results suggest that the NCs are degraded by reacting with impure materials contained in the untreated hexane, probably oxygen or water, as the solvent has been exposed to air prior to this experiment.

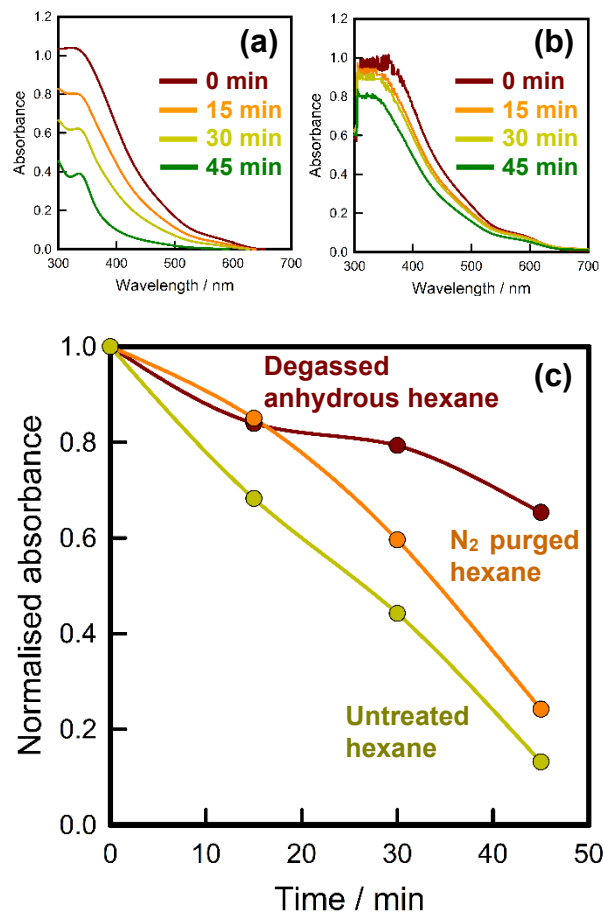
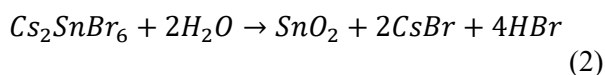
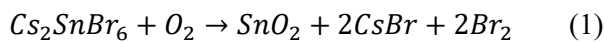


Fig. 3. Absorption spectral change of the purified Cs_2SnBr_6 NCs dispersed in untreated *n*-hexane (a) and in degassed anhydrous *n*-hexane (b). (c) Absorbance change of Cs_2SnBr_6 NCs dispersed in *n*-hexane treated by the specific condition at 450 nm.

To further investigate the influence of water or oxygen on degradation of the NCs, we monitored absorbance change at 450 nm as a function of monitoring time. Fig. 3 shows absorbance change of the purified NCs dispersed in hexane treated by 3 different conditions. As expected, the purified NCs dispersed in untreated hexane show the largest absorbance decrease, while the purified NCs dispersed in nitrogen purged hexane show slightly larger absorbance at any monitored time. These results suggest that both oxygen and water molecules react with the NCs to degrade, however water molecules appears largely to react with the NCs. The NCs dispersed in degassed anhydrous hexane show slight decrease in the absorbance, confirming that water and oxygen molecules as impure materials in hexane influence on the reactions with the NCs. We propose possible degradation routes for the purified Cs_2SnBr_6 NCs with the following reaction formula.



In either route, we speculate that oxygen or water molecule directly reacts with Sn^{4+} ions inside the crystal to form SnO_2 . Once SnO_2 is formed, it no longer forms halide perovskite structure. Therefore to maintain Cs_2SnBr_6 NCs in solution phase, it is important to use degassed anhydrous solvent, i.e. oxygen and water free environment.

4. Conclusion

We synthesized the lead-free CsSn_2Br_5 NCs using a modified hot-injection method by tuning the injection temperature and reaction conditions. The time-dependent XRD measurements revealed that the CsSn_2Br_5 NCs were gradually oxidized by water or oxygen molecules in air to form Cs_2SnBr_6 phase. The stability of Cs_2SnBr_6 NCs was monitored by time dependent absorption measurements. Both oxygen and water molecules react with the NCs to degrade, however water molecules appears largely to react with the NCs. In contrast, the NCs dispersed in degassed anhydrous hexane improves the stability. Therefore to maintain Cs_2SnBr_6 NCs in solution phase, it is important to use degassed anhydrous solvent, i.e. oxygen and water free environment.

Acknowledgement

This work was partly supported by JSPS KAKENHI Grant (19H02813) and (22H02182), and the Collaborative Research Program of Institute for Chemical Research, Kyoto University (grant number 2021-78 and 2022-99), Japan. We also acknowledge supports from ARC DP fund (DP180103815) and ARC LIEF fund (LE200100051), Australia, and Forefront Research Center, Faculty of Science at Osaka University.

References

- G. Li, F. W. R. Rivarola, N. J. L. K. Davis, S. Bai, T. C. Jellicoe, F. de la Peña, S. Hou, C. Ducati, F. Gao, R. H. Friend, N. C. Greenham, and Z.-K. Tan, *Adv. Mater.*, **28** (2016) 3528.
- Q. Zhao, A. Hazarika, L. T. Schelhas, J. Liu, E. A. Gaulding, G. Li, M. Zhang, M. F. Toney, P. C. Sercel, and J. M. Luther, *ACS Energy Lett.*, **5** (2020) 238.
- M. Hao, Y. Bai, S. Zeiske, L. Ren, J. Liu, Y. Yuan, N. Zarrabi, N. Cheng, M. Ghasemi, P. Chen, M. Lyu, D. He, J.-H. Yun, Y. Du, Y. Wang, S. Ding, A. Armin, P. Meredith, G. Liu, H.-M. Cheng, and L. Wang, *Nat. Energy*, **5** (2020) 79.
- D. Jia, J. Chen, M. Yu, J. Liu, E. M. J. Johansson, A. Hagfeldt, and X. Zhang, *Small*, **16** (2020) 2001772.
- Q. Zhang, Q. Shang, R. Su, T. T. H. Do, and Q. Xiong, *Nano Lett.*, **21** (2021) 1903.
- Y. Xu, Q. Chen, C. Zhang, R. Wang, H. Wu, X. Zhang, G. Xing, W. W. Yu, X. Wang, Y. Zhang, and M. Xiao, *J. Am. Chem. Soc.*, **138** (2016) 3761.
- G. Nedelcu, L. Protesescu, S. Yakunin, M. I. Bodnarchuk, M. J. Grotevent, and M. V. Kovalenko, *Nano Lett.*, **15** (2015) 5635.
- J. Shamsi, A. S. Urban, M. Imran, L. De Trizio, and L. Manna, *Chem. Rev.*, **119** (2019) 3296.
- H. Huang, A. S. Sussha, S. V. Kershaw, T. F. Hung, and A. L. Rogach, *Adv. Sci.*, **2** (2015) 1500194.
- Y. Tong, E. Bladt, M. F. Aygüler, A. Manzi, K. Z. Milowska, V. A. Hintermayr, P. Docampo, S. Bals, A. S. Urban, L. Polavarapu, and J. Feldmann, *Angew. Chem. Inter. Ed.*, **55** (2016) 13887.
- X. Zhang, C. Sun, Y. Zhang, H. Wu, C. Ji, Y. Chuai, P. Wang, S. Wen, C. Zhang, and W. W. Yu, *J. Phys. Chem. Lett.*, **7** (2016) 4602.
- Y. Li, H. Huang, Y. Xiong, S. V. Kershaw, and A. L. Rogach, *Angew. Chem. Inter. Ed.*, **57** (2018) 5833.
- W. Ke, C. C. Stoumpos, and M. G. Kanatzidis, *Adv. Mater.*, **31** (2019) 1803230.
- M. Liu, H. Pasanen, H. Ali-Löyty, A. Hiltunen, K. Lahtonen, S. Qudsiya, J.-H. Smått, M. Valden, N. V. Tkachenko, and P. Vivo, *Angew. Chem. Int. Ed.*, **59** (2020) 22117.
- T. C. Jellicoe, J. M. Richter, H. F. J. Glass, M. Tabachnyk, R. Brady, S. E. Dutton, A. Rao, R. H. Friend, D. Credgington, N. C. Greenham, and M. L. Böhm, *J. Am. Chem. Soc.*, **138** (2016) 2941.
- A. B. Wong, Y. Bekenstein, J. Kang, C. S. Kley, D. Kim, N. A. Gibson, D. Zhang, Y. Yu, S. R. Leone, L.-W. Wang, A. P. Alivisatos, and P. Yang, *Nano Lett.*, **18** (2018) 2060.
- A. Abate, *Joule*, **1** (2017) 659.
- F. De Angelis, *ACS Energy Lett.*, **6** (2021) 1586.
- S. Shao, J. Liu, G. Portale, H.-H. Fang, G. R. Blake, G. H. ten Brink, L. J. A. Koster, and M. A. Loi, *Adv. Energy Mater.*, **8** (2018) 1702019.
- D. Di Girolamo, J. Pascual, M. H. Aldamasy, Z. Iqbal, G. Li, E. Radicchi, M. Li, S.-H. Turren-Cruz, G. Nasti, A. Dallmann, F. De Angelis, and A. Abate, *ACS Energy Lett.*, **6** (2021) 959.
- G. Flora, D. Gupta, and A. Tiwari, *Inter. Toxicol.*,

- 5 (2012) 47.
- 22.L. Protesescu, S. Yakunin, M. I. Bodnarchuk, F. Krieg, R. Caputo, C. H. Hendon, R. X. Yang, A. Walsh, and M. V. Kovalenko, *Nano Lett.*, **15** (2015) 3692.
- 23.F. Zhang, H. Zhong, C. Chen, X.-G. Wu, X. Hu, H. Huang, J. Han, B. Zou, and Y. Dong, *ACS Nano*, **9** (2015) 4533.
- 24.H. Huang, F. Zhao, L. Liu, F. Zhang, X.-G. Wu, L. Shi, B. Zou, Q. Pei, and H. Zhong, *ACS Appl. Mater. Inter.*, **7** (2015) 28128.
- 25.M. Chen, Y. Zou, L. Wu, Q. Pan, D. Yang, H. Hu, Y. Tan, Q. Zhong, Y. Xu, H. Liu, B. Sun, and Q. Zhang, *Adv. Funct. Mater.*, **27** (2017) 1701121.
- 26.H. Huang, Q. Xue, B. Chen, Y. Xiong, J. Schneider, C. Zhi, H. Zhong, and A. L. Rogach, *Angew. Chem. Inter. Ed.*, **56** (2017) 9571.
- 27.Q. A. Akkerman, M. Gandini, F. Di Stasio, P. Rastogi, F. Palazon, G. Bertoni, J. M. Ball, M. Prato, A. Petrozza, and L. Manna, *Nat. Energy*, **2** (2017) 16194.
- 28.A. Wang, X. Yan, M. Zhang, S. Sun, M. Yang, W. Shen, X. Pan, P. Wang, and Z. Deng, *Chem. Mater.*, **28** (2016) 8132.
- 29.A. Wang, Y. Guo, F. Muhammad, and Z. Deng, *Chem. Mater.*, **29** (2017) 6493.

Synthesis and Characterization of a Non-Conjugated Backbone Polymer Bearing [1]Benzothieno[3,2-*b*][1]benzothiophene with a Herringbone Packing Motif

Kakaraparathi Kranthiraja¹, Mayuka Nomura¹, Fumitaka Ishiwari,^{1,2}
and Akinori Saeki^{1,2*}

¹ Department of Applied Chemistry, Graduate School of Engineering,
Osaka University, 2-1 Yamadaoka, Suita, Osaka 567-0871, Japan

² Innovative Catalysis Science Division, Institute for Open and Transdisciplinary
Research Initiatives (ICS-OTRI), Osaka University,
2-1 Yamadaoka, Suita, Osaka 565-0871, Japan., Japan

*saeki@chem.eng.osaka-u.ac.jp

Conjugated polymers encompassing delocalized π -electrons in their backbones exhibit high photoabsorption and efficient charge carrier transport through the intermolecular π - π stacking suitable for organic photovoltaics (OPV). By contrast, small molecules such as [1]benzothieno[3,2-*b*][1]benzothiophene (BTBT) derivatives, which demonstrates high field-effect transistor hole mobilities owing to their 2-dimensional herringbone packing, have not yet been applied to OPVs. Here we report a non-conjugated backbone polymer bearing phenyl- and decyl-substituted BTBT (Ph-BTBT-10) as the pendant conjugated unit, which was synthesized by ring opening polymerization of epoxy append. The polymer showed an X-ray diffraction pattern ascribed to the layered lamellar and less ordered herringbone packing. In addition, a model molecule of Ph-BTBT-10 showed charge separation upon photoexcitation when blended with a non-fullerene acceptor (ITIC) or fullerene (PCBM).

Keywords: [1]Benzothieno[3,2-*b*][1]benzothiophene (BTBT), Herringbone, Organic solar cell, Non-fullerene acceptor, Photoconductivity

1. Introduction

Light-weight, flexible, and potentially cost-effective organic photovoltaics (OPV) are expected as a wing of sustainable energy production based on the abundant photon energy flow from the sun.^{1,2} The photoactive layer of OPV cells utilizes the efficient charge separation at the interface of positive (p)-type and negative (n)-type organic semiconductors in their bulk heterojunction (BHJ), where a conjugated polymer and molecule (a soluble fullerene like [6,6]-phenyl-C₆₁-butyric acid methyl ester: PCBM and non-fullerene small molecular acceptor: NFA) are usually adopted for this purpose, respectively.^{3,4} Polymers bearing π -conjugation in their backbone and solubilizing alkyl (or alkoxy) side chains lead to the intramolecular hole transport in the main chain and intermolecular

one in the 1-dimensional π - π stacks of lamellar crystallites.^{5,6} The finely tuned energy levels of the highest occupied molecular orbital (HOMO), the lowest unoccupied molecular orbital (LUMO), and their bandgaps (E_g) are implemented by electron donor (D) and acceptor (A) coupling.⁷⁻⁹

In contrast to the D-A type polymers and molecules in OPV applications, organic semiconductors used in organic field-effect transistors (OFETs) have been developed in a different direction of molecular design. As evolved from the benchmark pentacene polycrystalline films prepared by thermal evaporation,¹⁰⁻¹² solution-processable [1]benzothieno[3,2-*b*][1]benzothiophene (BTBT) derivatives¹³⁻¹⁵ have shown a high hole mobility (14.7 cm² V⁻¹s⁻¹),^{16,17} owing to the 2-dimensional isotropic charge

Received March 14, 2022
Accepted June 24, 2022

transport in their herringbone (HB) packing.^{18,19} However, BTBT has never been directly used as a donor in OPV, because of its wide E_g (almost no photoabsorption in the visible region), deep HOMO level, and an coarse BHJ network due to the high crystalline nature of BTBT. Some limited examples of the use of BTBT in OPV are the lateral OPV with alternating multilayered junction composed of dioctyl BTBT (C8-BTBT) and perylene bisimide (PTCDI-C8) layers,²⁰ A-D-A type NFAs using the BTBT core as the D unit,^{21,22} component of a dye molecule for dye-sensitized solar cell (DSSC),²³ and thermally evaporated p-layer of p-n junction (biphenyl-BTBT: BPh-BTBT).²⁴ C8-BTBT reportedly shows a good performance as the hole transport material (HTM) in the lead halide perovskite solar cell (LH-PSC).²⁵

In this work, we designed, synthesized, and characterized a non-conjugated backbone polymer (NCBP) bearing 7-decyl-2-phenyl[1]benzothieno[3,2-*b*][1]benzothiophene (Ph-BTBT) as the pendant conjugated unit (Figure 1). This work

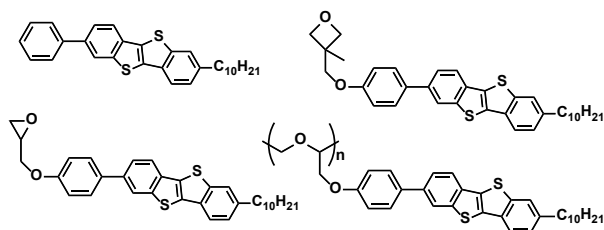


Fig. 1. Chemical structures of monomers and polymer.

is a concept study to examine the following questions: (1) Does ring opening polymerization (ROP) of epoxy- or 2-methyloxetane²⁶ work with the bulky Ph-BTBT pendant? (2) Is a HB structure formed among the pendant BTBT unit? (3) Is BHJ formed in the films blended with PCBM or NFA? Regarding (1), ROP of NCBP is completely different from the conventional metal-catalyzed Suzuki-Miyaura and Stille coupling reactions used in the synthesis of conjugated polymers, whereas a careful removal of remaining transitional metal catalyst (e.g. Pd and Ni) is unnecessary in ROP. Regarding (2), we performed 2-dimensional grazing-incidence X-ray diffraction (2D-GIXRD) for the pristine powder samples and compared them with the reference Ph-BTBT. Regarding (3), we should note that a high power conversion efficiency (PCE) is not expected even though a device is fabricated. A representative of NCBP with conjugated pendant units is poly(vinylcarbazole) (PCz),²⁷ which is widely known to show

photoconductivity upon exposure to the ultraviolet (UV) light, but is unsuitable for OPV applications, because of the high optical transparency and amorphous nature with a low hole mobility. Poly(triarylamine) (PTAA) is also a wide bandgap, amorphous semiconductor with a partly non-conjugated backbone, which shows excellent performance as the HTM of LH-PSC in the presence of LiTFSI dopants.²⁸⁻³⁰ A term of “non-conjugated polymer” has been used in IDIC (a narrow bandgap NFA)-incorporated thioalkyl polymer, which was applied in all-polymer OSC; however, this polymer has a large conjugated unit in the backbone.³¹

2. Experimental

Materials. Ph-BTBT, ITIC, and PCBM were purchased from Tokyo Chemical Industry Inc. (TCI), 1-Material Inc., and Frontier Carbon Inc., respectively. Lithium aluminum hydride, Aliquat 336, and tetrakis(triphenylphosphine)palladium(0) were purchased from Sigma-Aldrich Inc. Aluminum chloride, diethylether, potassium hydroxide, tetrabutylammonium bromide, *N,N*-dimethylformamide (DMF), sodium hydrosulfide n-hydrate, potassium carbonate, and ethyl acetate were purchased from Fujifilm-Wako Corp. Other solvents were purchased from Kanto Chemical Inc. Other chemicals were purchased from TCI. They were used as received without further purification.

[1]Benzothieno[3,2-*b*][1]benzothiophene (1, BTBT).³² 2-Chlorobenzaldehyde (80 mL, 0.71 mol) and 1-methyl-2-pyrrolidone (200 mL) were added to a 500 mL dried 1-neck flask at room temperature and heated to 80 °C. Then, sodium hydrosulfide n-hydrate (114 g, 2.0 mol) was added to the mixture and stirred for 1 h. The reaction mixture heated to 165 °C and stirred for 11 h. After cooling to room temperature, the reaction mixture was quenched by saturated aqueous ammonium chloride solution. The mixture was decanted, and water and acetone were added to get a solid. After filtration and recrystallization in toluene and chloroform, yellowish white powder was obtained (5.9 g, 0.02 mol, 7% yield). ¹H NMR (400 MHz, CDCl₃, 298 K), δ (ppm): 7.93 (dd, $J = 7.4$ Hz, 0.9 Hz, 2H), 7.90 (dd, $J = 7.8$ Hz, 0.9 Hz, 2H), 7.47 (ddd, $J = 7.4$ Hz, 7.4 Hz, 0.9 Hz, 2H), 7.41 (ddd, $J = 7.8$ Hz, 7.8 Hz, 0.9 Hz, 2H).

[1]Benzothieno[3,2-*b*][1]benzothiophene-2-decan-1-one (2).³³ [1]Benzothieno[3,2-*b*][1]benzothiophene (1) (2.4 g, 10 mmol) and dichloromethane (148 mL) were added to a dried 300 mL 3-necked flask under N₂ atmosphere and

cooled to 0 °C. Aluminum chloride (6.0 g, 45 mmol) was added to the mixture and stirred for 1 h at the same temperature. Then, the mixture was cooled to -78 °C and *n*-decanoyl chloride (2 mL, 10 mmol) was added dropwise to the flask with stirring. The reaction mixture was stirred for 2 h. After warming to the room temperature, the reaction mixture was quenched with cold water. The organic layer was extracted with dichloromethane and water. The solution was dried over anhydrous magnesium sulfate and subjected to evaporation. Then, the crude product was recrystallized from toluene to afford yellowish white crystals (3.0 g, 7.4 mmol, 74% yield). ¹H NMR (400 MHz, CDCl₃, 298 K) δ (ppm): 8.56 (d, *J* = 0.9 Hz, 1H), 8.07 (dd, *J* = 8.5 Hz, 1.4 Hz, 1H), 7.96-7.93 (m, 3H), 7.48 (dd, *J* = 7.5 Hz, 1.4 Hz, 2H), 3.07 (t, *J* = 7.3 Hz, 2H), 1.80 (q, *J* = 7.3 Hz, 2H), 1.45-1.28 (m, 12H), 0.88 (t, *J* = 6.9 Hz, 3H).

2-Decyl-[1]benzothieno[3,2-*b*][1]benzothiophene (3).³³ Aluminum chloride (3.3 g, 25 mmol) and diethylether (22 mL) were added to a dried 300 mL 3-necked flask under N₂ atmosphere. Then, the solution of lithium aluminum hydride (860 mg, 23 mmol) in diethyl ether (55 mL) was added dropwise with stirring. The solution of compound **2** (3.1 g, 9.0 mmol) in dichloromethane (176 mL) was added dropwise with stirring. The reaction mixture was stirred for 18 h at the room temperature. Then, the flask was cooled to 0 °C, and cold water (0.85 mL), sodium hydroxide aqueous solution (ca. 2 M, 0.85 mL) and cold water (2.4 mL) were added. The mixture was stirred again for 1 h. After quenching, the reaction solution was filtered by Celite. The organic layer was extracted with dichloromethane and water. The solution was dried over anhydrous magnesium sulfate, and the solvent was evaporated to afford yellowish white powder (2.9 g, 7.6 mmol, 84% yield). ¹H NMR (400 MHz, CDCl₃, 298K) δ (ppm): 7.91 (d, *J* = 7.8 Hz, 1H), 7.87 (d, *J* = 7.3 Hz, 1H), 7.79 (d, *J* = 8.2 Hz, 1H), 7.72 (d, *J* = 0.5 Hz, 1H), 7.45 (dd, *J* = 7.6 Hz, 0.9 Hz, 1H), 7.38 (dd, *J* = 7.5 Hz, 1.4 Hz, 1H), 7.28 (dd, *J* = 8.0 Hz, 1.6 Hz, 1H), 2.76 (t, *J* = 7.8 Hz, 2H), 1.70 (m, 2H), 1.40-1.26 (m, 14H), 0.88 (t, *J* = 6.9 Hz, 3H).

2-Bromo-7-decyl-[1]benzothieno[3,2-*b*][1]benzothiophene (4).³⁴ Compound **3** (2.2 g, 5.8 mmol) and chloroform (81 mL) were added to dried 2-necked 200 mL flask under Ar atmosphere and it was cooled to -10 °C. Then, the solution of bromine (0.30 mL) in chloroform (14 mL) was added dropwise with stirring. The reaction mixture was stirred for 18 h, during which it was slowly warmed

up to room temperature. The flask was quenched by a saturated sodium hydrogen sulfite aqueous solution, and the organic layer was extracted with chloroform and water. The solution was dried over anhydrous magnesium sulfate, and the solvent was evaporated. The crude product was recrystallized from hexane twice to afford yellowish white crystals (0.84 g, 1.8 mmol, 32% yield). ¹H NMR (400 MHz, CDCl₃, 298K) δ 8.05 (ppm): (d, *J* = 1.8 Hz, 1H), 7.78 (d, *J* = 8.2 Hz, 1H), 7.71 (s, 1H), 7.71 (d, *J* = 8.2 Hz, 1H), 7.55 (dd, *J* = 8.5 Hz, 1.6 Hz, 1H), 7.29 (dd, *J* = 8.0 Hz, 1.1 Hz, 1H), 2.76 (t, *J* = 7.6 Hz, 2H), 1.70 (dt, *J* = 7.3 Hz, 2H), 1.4-1.26 (m, 14H), 0.88 (t, *J* = 6.9 Hz, 3H).

4,4,5,5-Tetramethyl-2-[4-(2-oxiranylmethoxy)phenyl]-1,3,2-dioxaborolane (6). 4-(4,4,5,5-Tetramethyl-1,3,2-dioxaborolan-2-yl)phenol (2.4 g, 11 mmol), epichlorohydrin (108 mL, 1.3 mol), and potassium carbonate (5.3 g, 38 mmol) were added to a 2-necked 200 mL flask under N₂ atmosphere and stirred for 5.5 h at 100 °C. After the reaction, potassium carbonate was filtered, and the crude product was washed with acetone and chloroform. After dried in a vacuum oven at 70 °C, it was purified by column chromatography on silica gel with hexane : ethyl acetate (8:2 (v/v)) as an eluent. After the evaporation, the crude product was dissolved in chloroform and purified by recycling gel permeation high pressure liquid chromatography using chloroform as an eluent, and the solvent was evaporated to afford white solid (2.7 g, 9.6 mmol, 89% yield). ¹H NMR (400 MHz, CDCl₃, 298K), δ (ppm) 8.69 (d, *J* = 8.7 Hz, 2H), 6.91 (d, *J* = 8.7 Hz, 2H), 4.24 (dd, *J* = 11.0 Hz, 3.2 Hz, 1H), 3.99 (dd, *J* = 11.0 Hz, 6.0 Hz, 1H), 3.36 (m, 1H), 2.91 (dd, *J* = 5.0 Hz, 4.6 Hz, 1H), 2.76 (dd, 5.0 Hz, 2.7 Hz, 1H), 1.33 (s, 12H). ESI (*m/z*): calcd for [M+H]⁺: 299.14, found: 299.10.

4,4,5,5-Tetramethyl-2-(4-((3-methyloxetan-3-yl)methoxy)phenyl)-1,3,2-dioxaborolane (7). 4-(4,4,5,5-Tetramethyl-1,3,2-dioxaborolan-2-yl)phenol (1.1 g, 5.0 mmol), potassium carbonate (2.07 g, 15.0 mmol), and 3-(chloromethyl)-3-methyloxetane (1.80 g, 15 mmol) were dissolved in anhydrous DMF (20 mL), 18-crown-6-ether was added to the above mixture, and the reaction mixture was heated at 80 °C for 10 h. After completion of reaction, the reaction mixture was cooled to room temperature, and the DMF was removed. Crude product was extracted with diethyl ether, washed with water, brine solution, and dried over anhydrous sodium sulfate. The resulted crude was purified by column chromatography on silica

gel with hexane: ethyl acetate (8:2 v/v) as an eluent to furnish a white solid (0.91 g, 3.0 mmol, 60% yield). ^1H NMR (400 MHz, CDCl_3 , 298K), δ (ppm): 7.77 (d, $J = 8$ Hz, 2H), 6.94 (d, $J = 7.6$ Hz, 2H), 4.64 (d, $J = 6$ Hz, 2H), 4.45 (d, $J = 6$ Hz, 2H), 4.05 (s, 2H), 1.44 (s, 3H), 1.39 (s, 12H).

Epoxy-Ph-BTBT (8). Compound **4** (0.68 g, 1.5 mmol) and the solution of compound **6** (0.61 g, 2.2 mmol) in toluene (39 mL) were added to a dried 2-necked 200 mL flask under Ar atmosphere. Potassium carbonate aqueous solution (2 M, 14 mL) and 3 drops of Aliquat336 were added to the reaction mixture. After that, the mixture was bubbled by Ar for 20 min. Then, tetrakis(triphenylphosphine)palladium (21 mg, 0.018 mmol) was added. The reaction mixture was refluxed for 16 h. After the reaction mixture was cooled to room temperature, the organic layer was extracted with chloroform and water. The solution was dried over anhydrous magnesium sulfate. After the evaporation, the crude product was recrystallized from toluene to afford yellowish white crystals (86 mg, 0.16 mmol, 11% yield). ^1H NMR (400 MHz, CDCl_3 , 298K), δ (ppm): 8.06 (d, $J = 1.4$ Hz, 1H), 7.89 (d, $J = 8.2$ Hz, 1H), 7.79 (d, $J = 7.8$ Hz, 1H), 7.73 (s, 1H), 7.65 (d, $J = 1.4$ Hz, 1H), 7.62 (d, $J = 9.2$ Hz, 2H), 7.29 (dd, $J = 8.2$ Hz, 1.4 Hz, 1H), 7.04 (d, $J = 8.7$ Hz, 2H), 4.30 (dd, $J = 11$ Hz, 3.2 Hz, 1H), 4.04 (dd, $J = 11$ Hz, 6.0 Hz, 1H), 3.40 (m, 1H), 2.95 (t, $J = 4.6$ Hz, 1H), 2.80 (dd, $J = 4.8$ Hz, 2.5 Hz, 2H), 2.77 (t, $J = 7.8$ Hz, 1H), 1.70 (m, 2H), 1.41-1.27 (m, 14H), 0.88 (t, $J = 6.9$ Hz, 3H). FT-IR (KBr), ν (cm^{-1}): 3046, 2955, 2917, 2848, 1732, 1607, 1518, 1456, 1399, 1341, 1295, 1189, 1114, 1037, 916, 870, 809. MALDI-TOF (m/z): calcd for $[\text{M}+\text{H}]^+$: 528.77, found: 528.47. Glass transition temperature (T_g): 147.21 $^\circ\text{C}$.

Oxetane-Ph-BTBT (9). Compound **4** (0.17 g, 0.36 mmol) and **7** (0.12 g, 0.40 mmol) were dissolved in anhydrous toluene (5 mL) and 2 mL of aqueous potassium carbonate solution (2 M) was added to the mixture. Next, tetrakis(triphenylphosphine)palladium and Aliquat336 were added and refluxed the mixture for 14 h. Reaction mixture was cooled to room temperature, and the toluene was removed by evaporation. Crude product was extracted with chloroform and washed with water, brine solution and dried over anhydrous sodium sulfate. The resulted crude was purified by column chromatography on silica gel with hexane: ethyl acetate (9.5:0.5 v/v) as an eluent to furnish the compound **9** (pale greenish solid, 20 mg, 0.036

mmol, 10% yield). ^1H NMR (400 MHz, CDCl_3): δ (ppm) 8.08 (s, 1H), 7.90 (d, $J = 8.0$ Hz, 1H), 7.79 (d, $J = 8.0$ Hz, 1H), 7.73 (s, 1H), 7.63-7.67 (m, 3H), 7.30-7.28 (m, 1H), 7.06 (d, $J = 6.8$ Hz, 2H), 4.68 (d, $J = 6.0$ Hz, 2H). 4.51 (d, $J = 6.0$ Hz, 2H), 4.10 (s, 2H), 2.76 (t, $J = 8.0$ Hz, 2H), 1.73-1.66 (m, 2H), 1.48 (s, 3H), 1.34-1.26 (m, 14H), 0.88 (t, $J = 6.8$ Hz, 3H).

Poly-Ph-BTBT (10). Compound **8** (13 mg, 24 μmol), 18-crown-6-ether (0.21 mg, 0.8 μmol), and toluene (10 mL) were added to a 1-neck 50 mL flask under N_2 atmosphere and heated to 120 $^\circ\text{C}$. Then, a tetrahydrofuran (THF) solution of potassium *tert*-butoxide (2 μM , 50 μL) was added to the mixture and stirred for 8 h. After completion of reaction, the solvent was evaporated, and the crude product was washed with methanol, THF, and chloroform to give yellowish brown insoluble powder (2.0 mg, 3.8 μmol , 16% yield). FT-IR (KBr), ν (cm^{-1}): 3036, 2957, 2916, 2850, 1732, 1607, 1516, 1456, 1399, 1341, 1292, 1182, 1110, 1023, 868, 810.

Characterization. ^1H NMR, MALDI-TOF-MS, and ESI-MS measurements were performed on a JEOL JNM-ECZS400 spectrometer, Bruker AutoflexIII, and JEOL JMS-T100LP, respectively. UV-vis photoabsorption, photoemission, and Fourier transform infrared (FT-IR) spectroscopies were conducted using Jasco V-730 UV-vis, FP-8300, and FT/IR-4700AC spectrometers, respectively. Photoelectron yield spectroscopy (PYS) and differential Scanning Calorimetry (DSC) were performed on a Bunko Keiki BIP-KV202GD and Netzsch DSC 204F1, respectively. 2D-GIXRD on the BL46XU beamline at SPring-8 (Japan Synchrotron Radiation Research Institute, JASRI) was performed using 12.39 keV ($\lambda = 1$ \AA) X-rays at the grazing incidence angle of 0.12 $^\circ$. TRMC was performed for the films (or powder) prepared on a quartz substrate. The microwave frequency and its power were ~ 9 GHz and ~ 3 mW, respectively.^{35,36} A third harmonic generation (355 nm) of a Nd:YAG laser (Continuum Inc., Surelite II, 5–8 ns pulse duration, 10 Hz) was used for the excitation (incident photon density of 4.6×10^{15} photons cm^{-2}). The photoconductivity ($\Delta\sigma = A^{-1} \Delta P_r P_r^{-1}$ where A is the sensitivity factor, P_r is the reflected microwave power, and ΔP_r is the change in P_r upon exposure to light) was converted into the product of the quantum yield (ϕ) and sum of the charge carrier mobilities $\Sigma\mu$ by $\phi\Sigma\mu = \Delta\sigma(eI_0F_{\text{light}})^{-1}$, where e and F_{Light} are the electron charge and correction (or filling) factor, respectively. The experiments were performed at room temperature in the air.

3. Results and discussion

The monomers and polymer were synthesized according to the scheme in Figure 2. The synthetic route of compounds **1–4** was identical to the literatures,^{32–34} while those of compounds **5–10** were designed by following a typical procedure. The details and NMR data are described in Experimental. Due to the strong aggregation property, Poly-Ph-BTBT was insoluble powder unable to be characterized in solution and film (thus, its molecular weight was not determined). However, FT-IR spectrum of Poly-Ph-BTBT indicated the disappearance of 916 cm⁻¹ peak attributed to epoxy rings, which supported the polymerization reaction (Figure 3a). It should be noted that a norbornene random co-polymer that partially incorporates BTBT appendis is soluble in an organic solvent, and its optical properties have been characterized.³³ We also attempted polymerization of Oxetane-Ph-BTBT via anionic polymerization under the same condition of Epoxy-Ph-BTBT; however, it was

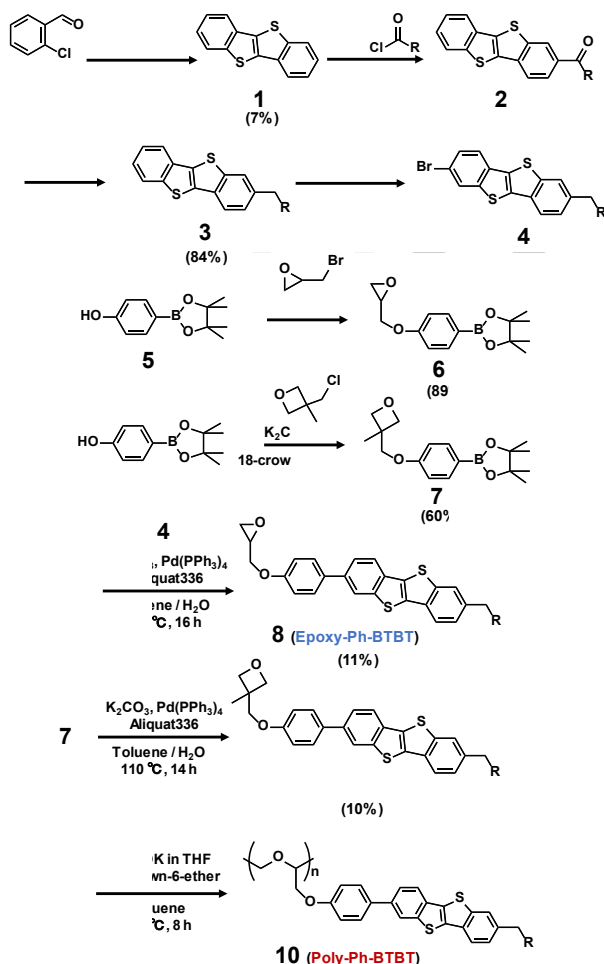


Fig. 2. Synthetic routes of Epoxy-Ph-BTBT, Oxetane-Ph-BTBT and Poly-Ph-BTBT.

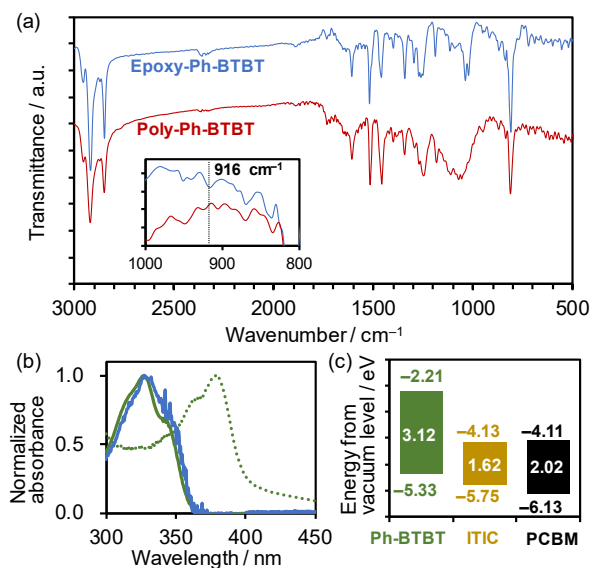


Fig. 3. (a) FT-IR spectra of Epoxy-Ph-BTBT (upper) and Poly-Ph-BTBT (lower). The inset is the magnification at 800–1000 cm⁻¹. (b) UV-vis photoabsorption spectra of Ph-BTBT (green solid line) and Epoxy-Ph-BTBT (blue solid line) in chloroform solution (< 20 μmol dm⁻³). The green dotted line is a Ph-BTBT film. (c) Energy diagram of Ph-BTBT, ITIC, and PCBM. The HOMO levels were measured by PYS in a film state, and E_g was calculated from the photoabsorption onset of a film.

unsuccessful without any changes in the reactant. A cationic polymerization scheme³⁷ (boron trifluoride diethyl etherate as the catalyst; CH₂Cl₂, CHCl₃, or toluene as the solvent; r.t. to 110 °C) was examined for an oxetane-naphthalene as a model compound (3-methyl-3-[(2-naphthalenyloxy)methyl]oxetane), which resulted in intramolecular cyclization with the neighboring phenyl via Friedel-Crafts reaction.

Figure 3b shows the ultraviolet (UV)-visible photoabsorption spectra of Ph-BTBT and Epoxy-Ph-BTBT in dilute chloroform solutions and a Ph-BTBT film. The spectra of Ph-BTBT and Epoxy-Ph-BTBT were identical, indicating no electronic effect of appended epoxy on the BTBT unit. The photoabsorption of Ph-BTBT film showed a redshift with the onset of 397 nm, which corresponded to the E_g of 3.12 eV. The HOMO level of Ph-BTBT, ITIC, and PCBM were measured by PYS in vacuum, and their resultant energy diagram is shown in Figure 3c. Despite the large E_g of Ph-BTBT unsuitable for high performance OPV application, it can act as a p-type material in combination with these n-type molecules (ITIC and PCBM).

The packing structure of powder samples were evaluated by 2D-GIXRD. Figure 4a shows the profiles obtained by integrating along the azimuthal

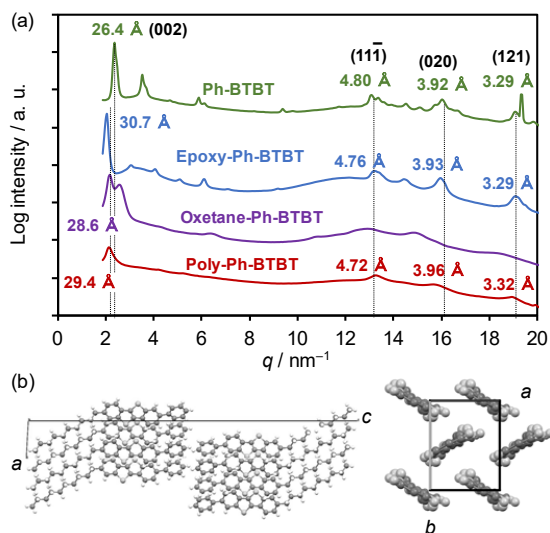


Fig. 4. (a) 2D-GIXRD profiles calculated by integrating in the azimuthal direction (0–90°) in a powder form. (b) Crystal structure of Ph-BTBT constructed from the reported single crystal data.³⁸

direction (0–90°, the 2D-GIXRD images are isotropic arches). Ph-BTBT exhibits the HB packing identical to the report,³⁸ the *d*-spacing and Miller indices of which are 26.4 Å (002) attributed to the *c*-axis, and 4.80 Å (11–1), 3.92 Å (020), and 3.29 Å (121) attributed to HB packing (Figure 4b). The peaks at the scattering vector *q* of 3–6 nm⁻¹ are the high-order diffractions along the *c*-axis: (003), (004), and (005). Epoxy-Ph-BTBT also showed the essentially identical HB packing, where the packing along the *c*-axis was widened to 30.7 Å owing to the epoxy unit. Oxetane-Ph-BTBT displayed a similar HB pattern, although the peaks were broadened, possibly due to the steric hindrance of bulky oxetane unit. Notably, Poly-Ph-BTBT was found to maintain the HB structure, while its crystallinity was reduced compared with its monomer as evident from the disappearance of high-order diffraction of (00*n*) (*n* ≥ 3).

To examine the photogeneration of charge carriers in BHJ films, we carried out TRMC measurements of Ph-BTBT:ITIC or PCBM blend films prepared by drop casting. As shown in Figure 5a, the TRMC transient maximum ($\phi\Sigma\mu_{\max}$: ϕ is the yield of photogenerated charge carrier and $\Sigma\mu$ is the sum of hole and electron mobilities: $\mu_h + \mu_e$) was increased by ca. 2-fold when Ph-BTBT was blended with ITIC or PCBM. The maxima of $\phi\Sigma\mu_{\max}$ were much larger than those of pristine ITIC and PCBM films, indicative of the charge separation in the BHJ films. The TRMC decays of the highest signals (Figure 5b; P:N = 1:1 for Ph-BTBT:PCBM and P:N

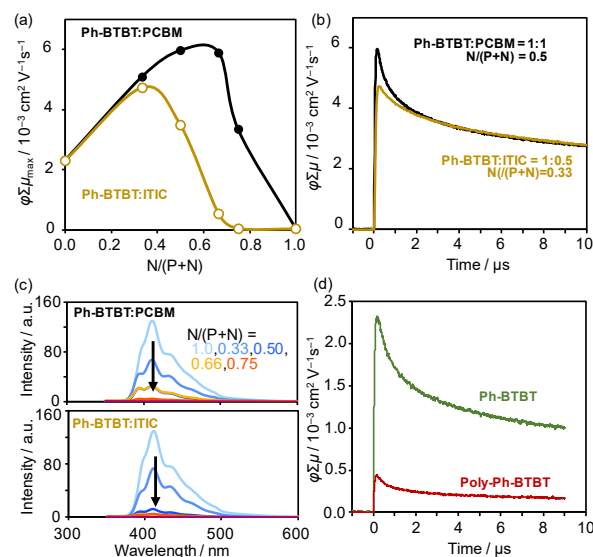


Fig. 5. (a) $\phi\Sigma\mu_{\max}$ of the TRMC transients observed in Ph-BTBT:PCBM (closed circle) and Ph-BTBT:ITIC (open circle). $N/(P+N)$ is the concentration (weight ratio) of n-type semiconductor (ITIC or PCBM). $\lambda_{\text{ex}} = 355$ nm. (b) TRMC decays of Ph-BTBT:PCBM=1:1 and Ph-BTBT:ITIC = 1:0.5. (c) PL quenching at the different blend ratio of the films. Upper: Ph-BTBT:PCBM; lower: Ph-BTBT:ITIC. $\lambda_{\text{ex}} = 320$ nm. (d) TRMC decays of pristine Ph-BTBT and Poly-Ph-BTBT.

= 1:0.5 for Ph-BTBT:ITIC) were long-lived, and the maximum values were relatively large ($4\text{--}6 \times 10^{-3} \text{ cm}^2\text{V}^{-1}\text{s}^{-1}$), suggesting the large hole mobility (μ_h) on the HB packing of BTBT units despite the low charge separation yield (ϕ). The electron transfer from Ph-BTBT to ITIC (or PCBM) was confirmed from the quenching of Ph-BTBT photoluminescence (PL) as shown in Figure 5c. The PL quenching is linked to the increase in the $\phi\Sigma\mu_{\max}$, while the ϕ cannot be resolved because the $\Sigma\mu$ is assumed to decrease upon blending Ph-BTBT with ITIC (or PCBM). The pristine Ph-BTBT film showed a high $\phi\Sigma\mu_{\max}$ value of $2.3 \times 10^{-3} \text{ cm}^2\text{V}^{-1}\text{s}^{-1}$, whereas the $\phi\Sigma\mu_{\max}$ of Poly-Ph-BTBT was decreased to $4.1 \times 10^{-4} \text{ cm}^2\text{V}^{-1}\text{s}^{-1}$. This 5–6 folds decrease is consistent with the 2D-GIXRD data that show the less ordered HB packing of Poly-Ph-BTBT. Nonetheless the decay rates are very similar for Ph-BTBT and Poly-Ph-BTBT.

4. Conclusion

We designed and synthesized a non-conjugated backbone polymer bearing a BTBT pendant. Although Poly-Ph-BTBT synthesized by ring opening reaction of epoxy was insoluble powder, the polymerization and HB packing of BTBT unit were confirmed by FT-IR and 2D-GIXRD

measurements, respectively. The photogeneration of charge carriers in Ph-BTBT monomer and ITIC or PCBM blend films was observed in TRMC and PL quenching experiments. Poly-Ph-BTBT exhibited a moderated photoconductivity signal, suggestive of the good charge transport on the pendant HB packing.

Acknowledgment

K. K. and M. N. equally contributed to this work. This work was supported by the Japan Society for the Promotion of Science (JSPS) with the KAKENHI (JP20H05836 and JP20H00398) and Iketani Science and Technology Foundation (0321013-A). The authors thank Dr. Tomoyuki Koganezawa at JASRI for his support during the 2D-GIXRD experiments at SPring8 (2020A1875).

References

1. S. Li, C.-Z. Li, M. Shi, and H. Chen, *ACS Energy Lett.*, **5** (2020) 1554.
2. C. J. Brabec, A. Distler, X. Du, H. -J. Egelhaaf, J. Hauch, T. Heumüller, and N. Li, *Adv. Energy Mater.*, **10** (2020) 2001864.
3. G. Zhang, J. Zhao, P. C. Y. Chow, K. Jiang, J. Zhang, Z. Zhu, J. Zhang, F. Huang, and H. Yan, *Chem. Rev.*, **118** (2018) 3447.
4. H. Fu, Z. Wang, and Y. Sun, *Angew. Chem. Int. Ed.*, **58** (2019) 4442.
5. P. Meredith, W. Li, and A. Armin, *Adv. Energy Mater.*, **10** (2020) 2001788.
6. Y. Miyake and A. Saeki, *J. Phys. Chem. Lett.*, **12** (2021) 12391.
7. L. Zhan, S. Li, X. Xia, Y. Li, X. Lu, L. Zuo, M. Shi, and H. Chen, *Adv. Mater.*, **33** (2021) 2007231.
8. T. Fukuhara, Y. Tamai, and H. Ohkita, *Sustainable Energy Fuels*, **4** (2020) 4321.
9. I. Osaka and K. Takimiya, *Adv. Mater.*, **30** (2017) 1605218.
10. T. Minari, T. Nemoto, and S. Isoda, *J. Appl. Phys.*, **99** (2006) 034506.
11. O. D. Jurchescu, J. Baas, and T. T. M. Palstra, *Appl. Phys. Lett.*, **84** (2004) 3061.
12. T. Yasuda, T. Goto, K. Fujita, and T. Tsutsui, *Appl. Phys. Lett.*, **85** (2004) 2098.
13. K. Takimiya, S. Shinamura, I. Osaka, E. Miyazaki, *Adv. Mater.*, **23** (2011) 4347.
14. K. Takimiya, H. Ebata, K. Sakamoto, T. Izawa, T. Otsubo, Y. Kunugi, *J. Am. Chem. Soc.*, **128** (2006) 12604.
15. H. Ebata, T. Izawa, E. Miyazaki, K. Takimiya, M. Ikeda, H. Kuwabara, T. Yui, *J. Am. Chem. Soc.*, **129** (2007) 15732.
16. H. Iino, T. Usui, J. Hanna, *Nat. Commun.*, **6** (2015) 6828.
17. H. Minemawari, T. Yamada, H. Matsui, J. Tsutsumi, S. Haas, R. Chiba, R. Kumai, and T. Hasegawa, *Nature*, **475** (2011) 364.
18. G. R. Hutchison, M. A. Ratner, and T. J. Marks, *J. Am. Chem. Soc.*, **127** (2005) 2339.
19. D. A. Filho, E. G. Kim, and J. L. Brédas, *Adv. Mater.*, **17** (2005) 1072.
20. M. Kikuchi, M. Hirota, T. Kunawong, Y. Shinmura, M. Abe, Y. Sadamitsu, A. M. Moh, S. Izawa, M. Izaki, H. Naito, and M. Hiramoto, *ACS Appl. Energy Mater.*, **2** (2019) 2087.
21. Z. Zhou, J. Duan, L. Ye, G. Wang, B. Zhao, S. Tan, P. Shen, H. S. Ryu, H. Y. Woo, and Y. Sun, *J. Mater. Chem. A*, **8** (2020) 9684.
22. Y. Wang, M. Chang, X. Ke, X. Wan, and G. Yang, *Polymer*, **185** (2019) 121976.
23. A. L. Capodilupo, E. Fabiano, L. De Marco, G. Ciccarella, G. Gigli, C. Martinelli, and A. Cardone, *J. Org. Chem.*, **81** (2016) 3235.
24. M.-C. Jung, H. Kojima, I. Matsumura, H. Benten, and M. Nakamura, *Org. Electronics*, **52** (2018) 17.
25. X. Lian, J. Chen, Y. Zhang, G. Wu, and H. Chen, *Chin. J. Chem.*, **37** (2019) 1239.
26. J. Herzberger, K. Niederer, H. Pohlitz, J. Seiwert, M. Worm, F. R. Wurm, and H. Frey, *Chem. Rev.*, **116** (2016) 2170.
27. H. Hoegl, *J. Phys. Chem.*, **69** (1965) 755.
28. J. H. Heo, S. H. Im; J. H. Noh, T. N. Mandal, C. S. Lim, A. A. Chang, Y. H. Lee, H.-j. Kim, A. Sarkar, M. K. Nazeeruddin, M. Grätzel, S. I. Seok, *Nat. Photonics*, **7** (2013) 486.
29. N. J. Jeon, J. H. Noh, Y. C. Kim, W. S. Yang, S. Ryu, S. I. Seok, *Nat. Mater.*, **13** (2014) 897.
30. N. Ishida, A. Wakamiya, and A. Saeki, *ACS Photonics*, **3** (2016) 1678.
31. Q. Fan, W. Su, S. Chen, T. Liu, W. Zhuang, R. Ma, X. Wen, Z. Yin, Z. Luo, X. Guo, L. Hou, K. Moth-Poulsen, Y. Li, Z. Zhang, C. Yang, D. Yu, H. Yan, M. Zhang, and E. Wang, *Angew. Chem. Int. Ed.*, **59** (2020) 19835.
32. M. Saito, I. Osaka, E. Miyazaki, K. Takimiya, H. Kuwabara, M. Ikeda, *Tetrahedron Lett.*, **52** (2011) 285.
33. C. Combe, B. Schroeder, and I. McCulloch, *J. Mater. Chem. C*, **2** (2014) 538.
34. C. Niebel, Y. Kim, C. Ruzie, J. Karpinska, B. Chattopadhyay, G. Schweicher, A. Richard, V. Lemaur, Y. Olivier, J. Cornil, A. R. Kennedy, Y. Diao, W. Lee, S. Mannsfeld, Z. Baoc, Y. H. Geerts, *J. Mater. Chem. C*, **3** (2015) 674.
35. A. Saeki, *Polym. J.*, **52** (2020) 1307.
36. R. Shimono, R. Nishikubo, F. Ishiwari, and A. Saeki, *J. Photopolym. Sci. Technol.*, **34** (2021) 263.
37. P. Knauer, T. Hahn, A. Köhler, and P. Strohmriegel, *J. Mater. Chem. C*, **4** (2016) 10347.
38. H. Minemawari, J. Tsutsumi, S. Inoue, T. Yamada, R. Kumai, and T. Hasegawa, *Appl. Phys. Express*, **7** (2014) 091601.

Polymeric Antibacterial Surfaces with Nano-pillar Arrays Mimicking Cicada Wings

Natsuki Ogawa¹, Kodai Sato¹, Kayano Sunada², Hisashi Ishiguro²,
Hiroaki Kojima³, and Takeshi Ito^{1*}

¹ *Department of Engineering Science, Kansai University, 3-3-35 Yamate-cho, Suita, Osaka 564-8680, Japan*

² *Kanagawa Institute of Industrial Science and Technology, 3-25-13 Tonomachi, Kawasaki-ku, Kawasaki, Kanagawa 210-0821, Japan*

³ *National Institute of Information and Communications Technology, 588-2 Iwaoka, Iwaoka-cho, Nishi-ku, Kobe, Hyogo 651-2492, Japan*

*t.ito@kansai-u.ac.jp

Cicada wings consist of nanopillar arrays with a pitch, diameter, and height of a few hundred nanometers. These arrays show strong antibacterial performance owing to cell membrane damage caused by the physical interaction with the nanopillars. Polymer-based nanopillars are essential for various industrial applications. Herein, we present the fabrication process of polymer-based nanopillars using a facile thermal nanoimprint technique. Moreover, the conformational information of the nanopillars has been provided.

Keywords: Nano structure, Bactericidal performance, Thermal nanoimprint

1. Introduction

Pandemics pose significant threats to humanity, as worldwide deaths due to COVID-19 (CORonaVirus Infectious Disease, emerged in 2019) are expected to exceed 5,000,000 [1]. These infections are caused by various bacteria and viruses. Moreover, the increase in the number of antimicrobial-resistant (AMR) bacteria has emerged as a global issue [2, 3]. The number of deaths due to AMR bacterial infections is increasing and is over 1.2 million according to a recent report [3]; it is expected to reach 10 million by 2050 [2]. To combat AMR bacteria, the use of newly developed antibacterial surfaces inspired by nano and microstructures of natural origin are gaining attention. These nano and microstructures have been observed in insect wings (cicada and dragonflies), gecko fingers, shark skin, and leaf surfaces [4–8]. The nano/microstructure-based antibacterial materials are advantageous because they are not toxic to animal cells, and if their structural integrity is maintained, their antibacterial effects are permanent. Furthermore, these effects occur physically, without the use of chemicals, such

as antimicrobials.

Cicada wings have an ordered nanopillar array with an approximate diameter of 100 nm, height of 200 nm, and pitch of 200 nm [9]. A recent study demonstrated that nanopillars did not penetrate the bacteria cell membrane; however, they deformed it significantly. This deformation causes cell stress [10], and might lead to autolysis [11].

We have prepared a periodic nanopillar array composed of Si and reported that the bactericidal performance of Si-based nanopillars is significant [9, 12, 13]. However, their fabrication cost remains high. There are also several reports on inorganic nanostructures such as CuO, ZnO and TiO₂, and their antibacterial performance [14–16]. However, there is concern about the effects on human body. Therefore, polymer-based nanopillars are essential for various industrial applications. The bactericidal performance of polymer-based nanopillars obtained via the ultraviolet (UV) nanoimprint technique has been reported [17, 18]. However, to the best of our knowledge, there have been few reports on the fabrication of polymer-based nanopillars using the thermal nanoimprint technique. Therefore, in this

Received March 25, 2022

Accepted June 20, 2022

study, we demonstrate the fabrication of polymer-based nanopillars using the thermal nanoimprint technique and compare their shapes and their bactericidal performance.

2. Experimental

2.1 Chemicals

Oxalic acid, phosphoric acid, chrome oxide (VI), perchloric acid, propidium iodide (PI), and ethanol were purchased from Fujifilm Wako Chemicals (Tokyo, Japan). SYTO 9 was obtained from Thermo Fisher Scientific (Waltham, MA). Al plate (99.999%, 50 × 50 × 0.5 mm) was obtained from Nilaco Corporation (Tokyo, Japan). The mold release agent was supplied by AGC Seimi Chemical Co., Ltd. (Chigasaki, Japan). The cyclo-olefin polymer (COP) film (ZeonorFilm, 100 μm) was obtained from Zeon Corporation (Tokyo, Japan).

2.2 Fabrication of the anodic aluminum oxide (AAO) mold

AAO has periodic nanoholes with a high aspect ratio. The holes are self-arranged on a pure Al plate by applying a constant voltage in an acidic electrolyte [19]. Al and Pt was used as the anode and cathode, respectively. The dimensions of the nanoholes can be easily controlled by changing the acid solution, applied voltage, and treatment time. We applied a two-step anodization process [20] to form periodic nanoholes, as shown in Fig. 1. Before the two-step anodization, the Al plate was flattened on its top surface, and surface irregularities were removed via electropolishing in a solution of ethanol and perchloric acid (step 1). The first step of anodization was then performed in an oxalic acid solution (step 2). Regularly arranged nanoholes were obtained for use as indentations during the second anodization. After the first anodization, the anodic layer was etched by dipping in a mixed solution of phosphoric acid (6 wt.%) and chrome oxide VI (1.8 wt.%) (step 3). Next, the second anodization was performed as described above, starting from the indentations (step 4). Vertical nanoholes with high aspect ratios were obtained. The AAO nanoholes were then etched by dipping the sample into a phosphoric acid solution (5 wt.%) to increase the diameter of the nanoholes (step 5). To fabricate the taper-type mold, the second anodization (step 4) and pore widening process (step 5) were repeated over a short time. After the mold was dipped in a mold release agent for 10 min, it was rinsed with pure water and then dehydrated.

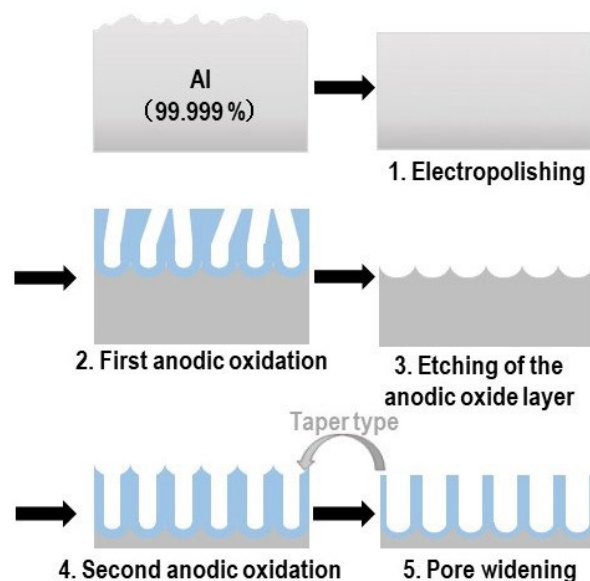


Fig. 1. Schematic illustration of the fabrication of the AAO mold.

2.3 Thermal nanoimprint of nanopatterns

The thermal nanoimprinting technique is a facile low-cost process for thermoplastic resins. The pressure plates were heated to the glass transition temperature ($T_g = 163\text{ }^\circ\text{C}$) of the resin, and afterward, the AAO mold and the resin sample were inserted into the pressure plates. The temperature was controlled near T_g at a certain pressure. In this study, we used $180\text{ }^\circ\text{C}$ and 4 MPa and maintained these conditions for 10 min. Thereafter, the pressure plates were cooled below T_g at the same pressure. The pressure was finally released, and the sample and mold were removed. An electric hot-press machine (G12-RS2000, Orihara Industrial Co., Ltd., Tokyo, Japan) was used to press and maintain the temperature.

2.4 Bactericidal performance test

Escherichia coli (*E. coli*) cells (RP437, WT) were grown in tryptone broth (TB) (1% BactoTryptone, 0.5% NaCl) at $37\text{ }^\circ\text{C}$ with shaking at 170 rpm for 3 h. Cultured cells were suspended twice in a motility buffer (10 mM potassium phosphate buffer, PBS, at a pH of 7.0). The cell suspension was diluted with the motility buffer to an OD_{600} of 0.1. The cells were stained with SYTO 9 and PI. One milliliter of the diluted cell suspension was mixed with 3.3 mM SYTO 9 and 10 mM PI. After mixing, the cell suspension was allowed to stand for 15 min. The cell envelope was stretched by the nanostructured surface, which caused cell breakage. The cell envelope damage was assessed using DNA staining chemicals; PI (red) and SYTO 9 (green). PI cannot

penetrate the cell when the cell membrane is not damaged; however, SYTO 9 can penetrate the cell without any membrane damage. Therefore, we analyzed the time course of bacterial activity, meaning the active cell rate, which was calculated by multiplying the ratio of the number of SYTO 9-stained cells (green-stained cells) and attached cells (green- and red-stained cells) by 100.

3. Results and discussion

3.1. Morphology of fabricated resin nanopillars

We prepared two major types of AAO molds: those with cylindrical and tapered holes. Two hole depths of 100 and 300 nm were created. The surface and cross-sectional profiles were observed using scanning electron microscopy (SEM), as shown in Fig. 2. The analysis of the surface profiles revealed that ordered holes with a pitch of 200 nm and a diameter of 100 nm were obtained for both the cylindrical and tapered types. The tapered holes are relatively three-dimensional in shape.

The SEM image of the cross-sectional shape of the tapered types showed that the diameter decreased toward the bottom, while at the top it was ca. 100 nm. The depth was 310 nm. On the contrary, the cross-sectional view of cylindrical holes shows a rectangular hole array, with a diameter of approximately 100 nm and a depth of 324 nm.

Fig. 3 show the SEM images of imprinted COP films with the same pitch (200 nm) and different pillar shapes: (sample A) cylinders with pillar diameter and height of 100 and 300 nm, respectively; (sample B) cylinders with pillar diameters and heights of 100 and 100 nm, respectively; (sample C) cylinders with a pillar diameter and height of 70 and 300 nm, respectively; (sample D) tapered type with a pillar bottom diameter and height of 100 and 300 nm, respectively. Among all four samples, the morphology of D is the most similar to the nanostructure shape of the cicada wing surface. All pillars were well transcribed in the mold structure with freestanding and ordered structures. Next, we evaluated the bactericidal performance based on the pillar shape.

3.2. Bactericidal performance as a function of the nanopatterns

The bactericidal testing of the fabricated polymeric nanopatterns was performed using a live/dead assay. After the cell suspension (10 μ l) was dropped onto the fabricated polymeric nanopillar film, a coverslip (18 \times 18 \times 0.15 mm) was placed over it and fixed using a double-sided tape

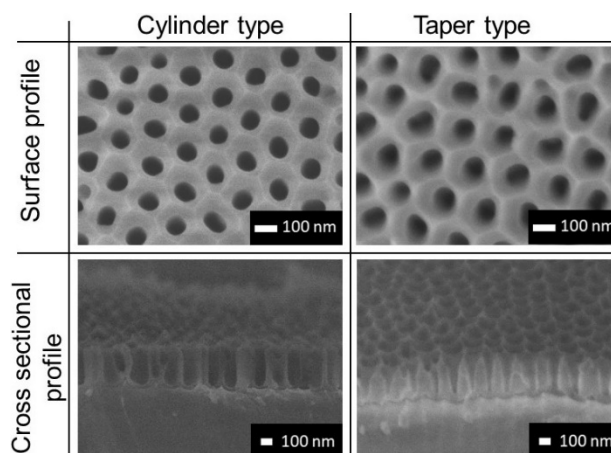


Fig. 2. Surface (top) and cross-sectional (bottom) SEM images of the cylinder (left) and taper tape (right) mold patterned by AAO.

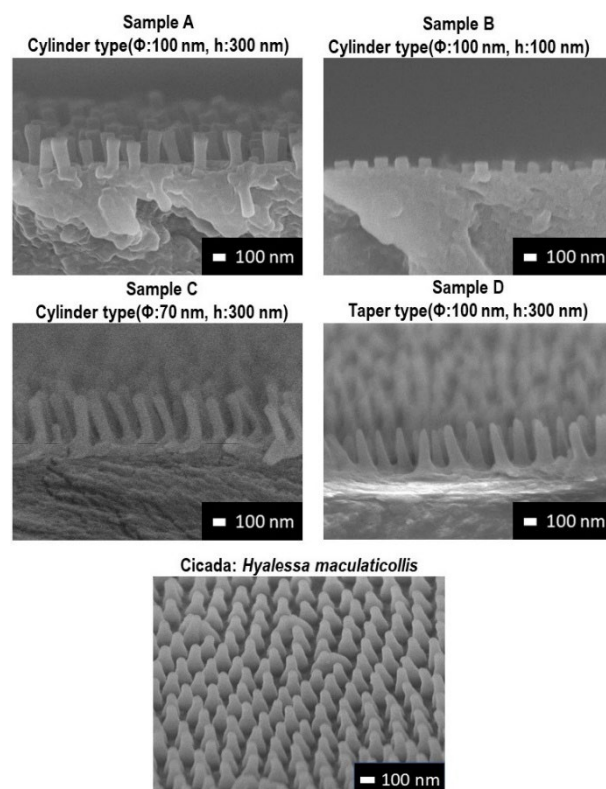


Fig. 3. SEM images of the imprinted nanopatterns obtained on the COP film and cicada wings. Shape dimensions of samples are provided.

(0.1 mm thick). The dropped suspension was pushed out by the coverslip to ensure that the cell suspension covered the entire area of the nanostructured surfaces. After the sample was held undisturbed for 10 min to allow cell adherence to the nanostructures surfaces, it was placed on a fluorescence microscope stage (Eclipse Ti-E, Nikon, Tokyo, Japan). Microscope images were obtained every 5 min for up to 60 min by changing the filter set for the red and green fluorescent images. The

obtained images were analyzed using the ImageJ software.

Fig. 4 shows representative fluorescent images on sample B after 0 (a) and 60 min (b). While there are few red fluorescent bacteria at 0 min, the number of green fluorescent cell decreased and that of red fluorescent cell increased after 60 min. The active cell rate of B was calculated as 60.7 %. The results for all samples are summarized in Fig. 5. For the cylindrical shapes (samples A, B, and C), the pillar (B) with the lowest height possessed the lowest viability, and pillar (C) with the highest aspect ratio did not show high sterilizability. These results do not match with those of Si nanopillar arrays that we previously reported [13] and showed that bactericidal performance increased with aspect ratio. These differences are considered to be caused by the difference in Young's moduli of the materials. Young's moduli of Si and COP are 131 and 2 GPa, respectively. Therefore, the polymeric nano-pillar with high aspect ratio would bend easily when the bacterial cells adhere to its surface. Considering the shape dependence of the activity of samples with same aspect ratios (samples A and D), the active cell rate on D was lower than that on A. These data indicate that an acute shape is better to damage the cell membranes. Overall, these preliminary data provide a guideline for the choice of structures for antibacterial polymeric films.

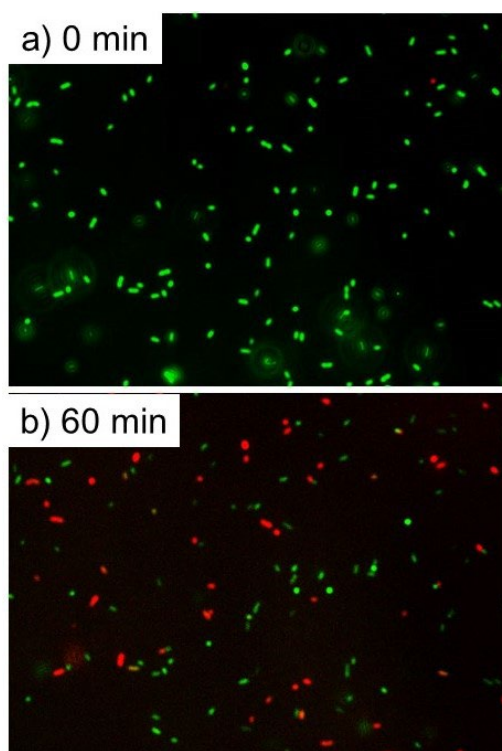


Fig. 4. Fluorescent images of the bactericidal performance test on the sample B after 0 and 60 min.

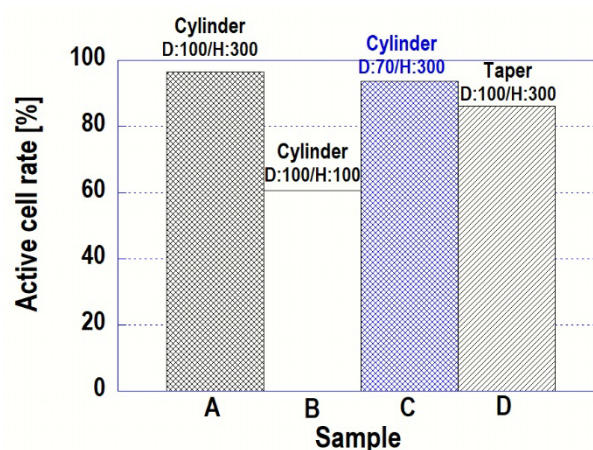


Fig. 5. Bacterial activity (obtained via bactericidal property test) for four fabricated samples. Sample conditions are displayed on top of the bars.

4. Conclusion

Artificial nanopillar arrays have attracted attention for application in combating infectious diseases. In this study, we demonstrated polymeric nanopillar arrays using a thermal nanoimprint technique. A mold with a fine nanohole array was fabricated using AAO. The nanopillars were arranged in cylindrical and tapered shapes. Bactericidal performance tests revealed that nanopillars with lower aspect ratios exhibits stronger bactericidal performances. In addition, the bactericidal performance of the tapered type is superior to that of the cylinder structures with the same height. These findings provide a guideline for the fabrication of antibacterial surfaces for polymeric substrates.

Acknowledgements

This study was partially supported by the A-STEP program JPMJTR20U8 of Japan Science and Technology Agency.

References

1. WHO Coronavirus (COVID-19) Dashboard: <https://covid19.who.int>
2. L. M. Weiner-Lastinger, S. Abner, J. R. Edwards, A. J. Kallen, M. Karlsson, S. S. Magill, D. Pollock, I. See, M. M. Soe, M. S. Walters, and M. A. Dudeck, *Infection control and hospital epidemiology*, **41** (2020) 1.
3. Antimicrobial Resistance Collaborators, *Lancet*, **399** (2022) 629.
4. E. P. Ivanova, J. Hassan, H. K. Webb, V. K. Truong, G. S. Watson, J. A. Watson, V. A. Baulin, S. Pogodin, J. Y. Wang, M.

- J. Tobin, C. Löbbe, and R. J. Crawford, *Small*, **8** (2012) 2489.
5. E. P. Ivanova, J. Hassan, H. K. Webb, G. Gervinskas, S. Juodkazis, V. K. Truong, A. H.F. Wu, R. N. Lamb, V. A. Baulin, G. S. Watson, J. A. Watson, D. E. Mainwaring, and R. J. Crawford, *Nature Communications*, **4** (2013) 2838.
 6. G. S. Watson, D. W. Green, L. Schwarzkopf, X. Li, B. W. Cribb, S. Myhra, and J. A. Watson, *Acta Biomaterialia*, **21** (2015) 109.
 7. E. E. Mann, D. Manna, M. R. Mettetal, R. M. May, E. M. Dannemiller, K. K. Chung, A. B. Brennan, and S. T. Reddy, *Antimicrobial Resistance and Infection Control*, **28** (2014) 3:28.
 8. R. Jiang, L. Hao, L. Song, L. Tian, Y. Fan, J. Zhao, C. Liu, W. Ming, and L. Ren, *Chemical Engineering Journal*, **198** (2020) 125609.
 9. K. Nakade, K. Jindai, T. Sagawa, H. Kojima, T. Shimizu, S. Shingubara, and T. Ito, *ACS Applied Nano Materials*, **1** (2018) 5736.
 10. J. Jenkins, J. Mantell, C. Neal, A. Gholinia, P. Verkade, A. H. Nobbs, and B. Su, *Nature Communications*, **11** (2020) 1626.
 11. S. Mimura, T. Shimizu, S. Shingubara, H. Iwaki, and T. Ito, *RSC Advances*, **12** (2022) 1645.
 12. K. Jindai, K. Nakade, K. Masuda, T. Sagawa, H. Kojima, T. Shimizu, S. Shingubara, and T. Ito, *RSC Advances*, **10** (2020) 5673.
 13. T. Ito, K. Nakade, N. Asai, T. Shimizu, and S. Shingubara, *Proc. IEEE Nano*, (2016) 82.
 14. F. Nishino, M. Jeem, L. Zhang, K. Okamoto, S. Okabe, and S. Watanabe, *Scientific Reports*, **7** (2017) 1063.
 15. K.S. Lee, C.H. Kim, S.W. Jeong, Y. Song, N.H. Bae, S.J. Lee, and K.G. Lee, *Colloids Surf. B Biointerfaces*, **170** (2018) 172.
 16. X. Zhang, G. Zhang, M. Chai, X. Yao, W. Chen, and P. K. Chu, *Bioactive Materials*, **6** (2021) 17.
 17. M. N. Dickson and E. I. Liang, *Biointerfaces*, **10** (2015) 021010.
 18. S. C. Lohmann, A. Tripathy, A. Millionis, A. Keller, and D. Poulidakos, *ACS Applied Bio Materials*, **5** (2022) 1564.
 19. N. Asai, T. Shimizu, S. Shingubara, and T. Ito, *Sensors and Actuators B*, **276** (2018) 534.
 20. H. Masuda and K. Fukuda, *Science*, **268** (1995) 1466.

Fabrication of Glass Microchannels Using Plant Roots and Nematodes

Tetsuro Koga¹ and Fujio Tsumori^{2*}

¹ *Department of Aeronautics and Astronautics, Faculty of Engineering, Kyushu University, 744 Motoooka, Nishi-ku, Fukuoka 819-0395, Japan*

² *Department of Aeronautics and Astronautics, Graduate School of Engineering, Kyushu University, 744 Motoooka, Nishi-ku, Fukuoka 819-0395, Japan*

**tsumori@aero.kyushu-u.ac.jp*

Microchannels have been studied actively in recent years. Various types of materials are used for fabricating microchannels in different types of applications including polymers, and ceramics. Since glass materials have appealing properties such as hardness, transparency, thermal resistance, and chemical resistance, they are used in biomedical devices and microfluidic application. Glass microchannel fabrication methods include chemical etching, imprinting, and 3D printing. This paper proposes unprecedented methods to fabricate glass microchannels using plant roots growth and nematodes migration. The microchannels fabricated by these methods have a complex three-dimensional structure, and the smallest channels have a diameter of several tens of micrometers in the glass. Although glass is attractive material, it is challenging to sinter the green body to fully dense and transparent solid structure. Hence, experiments were also conducted to establish a fabrication technique for transparent silica glass.

Keywords: Microchannel, Silica, Sintering, Transparent glass chip

1. Introduction

Recently, research on micro and nano sized devices has been studied as industry miniaturizes its products [1-4]. Particularly, microfluidics technology enables liquids to flow in channels tens to hundreds of micrometers wide on substrates such as glass, silicon, and resin, enabling efficient chemical reactions, mixing, and analysis in a small area.

The first research of microfluidic channels was conducted by Tuckerman and Pease in 1981 for cooling VLSI (Very Large-Scale Integration) devices. This research designed and implemented a compact water-cooled heat sink for integrated circuits. Experimental results show that the heat sink greatly improves the feasibility of ultra-fast VLSI circuits at high power density [5]. Today, microchannel technology is indispensable in industry and applied cooling microelectronics [6], automotive heat exchangers [7], fuel cells [8], gas turbine blade cooling [9], and renewable energy [10,

11], and so on.

Materials for microfluidic devices are requested excellent optical, mechanical, chemical, electrical, and thermal properties depending on the application. Currently, a variety of microfluidic materials are used, including polymeric materials such as PDMS and PMMA [12, 13], glass [14], and ceramics [15]. Polymer materials have excellent workability and elasticity, but not excellent chemical resistance. Although ceramics have excellent chemical resistance, they are not used for optical evaluation due to their lack of light transmittance. Glass is an ideal material for microchannels because of its excellent processing accuracy, light transmittance, and chemical resistance [16]. Research on the fabrication of transparent silica glass has been conducted from various perspective. Various methods have been used for glass fabrication such as melting, sol-gel [17, 18], and sintering [19]. Melting point of glass is high, and high temperatures of around 2073-2273 K are required to

Received April 4, 2022

Accepted June 24, 2022

obtain transparent silica glass by melting. The sol-gel method is difficult to produce transparent silica glass because of the crushing and foaming of the gel during the drying and sintering processes. In the fabrication of microfluidic channels using silica glass, it is desirable that they should be transparent and no bubbles and impurities. In a previous study, it was reported that devitrification due to crystallization of cristobalite and β -quartz occur in atmospheres above 1673 K [20]. In addition to the sintering temperature and atmosphere, the particle size of silica powder and holding time also affect the densification of glass, making it necessary to sinter under optimal conditions.

Microchannels are typically two-dimensional structures and are fabricated by photolithography and imprinting and so on [21-31]. Three-dimensional microchannels are fabricated by various methods, such as stacking layers fabricated by photolithography [32, 33], deforming by imprinting [34], and using sacrificial layers fabricated by a 3D printer [35-37].

In this study, we fabricated three-dimensional glass microchannels using plant roots and nematodes. We also aim to establish a technique for fabricating transparent silica glass by sintering. Although studies have already been conducted to create microchannels in ceramics using plants and in glass using mycelia, the technology to create microchannels in transparent glass using plants and nematodes has not been established yet [38-40]. In this proposal, we used root-knot nematodes that move through the soil and invades from tip of the roots. The diameter of root hairs which are the most minute parts of plant root tips is about 10 μm , and the diameter of root-knot nematodes is about 20 μm .

The root network structure of plants can lead to the fabrication of minute and complex three-dimensional network, because of it is characterized by complex branching and increasing miniaturization toward the tip. Future applications of this processing technique could include the fabrication of organ-on-a-chip with a vascular network. The vascular network resembles the root structure of plants in that the diameter tapers toward the tip while branching in three dimensions, and the diameters of the most minute parts are same order. We also thought possibility of other applications like filters and composite materials with improved functionality by inserting other materials into the formed cavities.

2. Materials

We used silica powder (SC2500-SQ, Admatechs)

with a particle size of 0.4-0.6 μm , HPMC (Metolose, Shin-Etsu Chemical) solution as a binder, and water. This binder is selected to have no effect on plant growth. The objective of this study is to create a channel by plants and nematodes. We chose *Trifolium repens* and root-knot nematodes which are plant-parasitic nematodes from the genus *Meloidogyne*.

3. Fabrication of microchannels by plant roots

3.1. Fabrication of transparent silica glass

We first needed a technique of transparent silica glass for fabricating glass microchannels using plant roots and nematodes. The following experiments conducted to remove agglomerates and bubbles, which are problems in the fabrication of transparent silica glass.

3.1.1. De-agglomeration

We crushed the agglomerates by the method of mixing nanosilica powder and HPMC solution. The following three mixing methods were tried in this experiment; mixing with planetary centrifugal mixer (SK-350T, Photo Chemical Co., Ltd.) at (a) the preset speed for standard mixing, (b) the maximum speed setting, and (c) with planetary a ball mill (P-6, FRITSCH) at 300 rpm for 1.8 ks.

Figure 1 shows the experimental results. Agglomerates were not crushed in method (a), while crushed in methods (b) and (c). We considered to have crushed the agglomerates due to stronger shear force generated inside the slurry in method (b) and collision of the milling ball and friction with the container in method (c). The agglomerates were crushed equally in both methods, but sample (c) became clouded probably due to contamination caused by wear of the milling balls and containers. Consequently, we determined method (b) mixing with planetary centrifugal mixer at the maximum speed setting as a crushing agglomerates method.

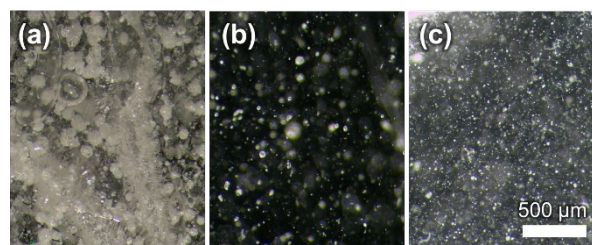


Figure 1 Microscope images of sintered silica body mixing with planetary centrifugal mixer at (a) preset speed for standard mixing, (b) the maximum speed setting and (c) with a ball mill at 300 rpm for 1.8 ks.

3.1.2. Removing of air bubbles

Bubbles generated during the mixing process can remain as defects in the final glass structure. In this experiment, compounds were placed in air for 0, 86.4, 172, and 259 ks (0, 1, 2, 3 days) before sintering and the amount of air bubbles was observed.

Figure 2 shows a microscope images of the sintered body. Relatively large bubbles larger than $80\ \mu\text{m}$ disappeared within one day. This is because large bubbles rose to the surface due to buoyancy, since the power of resistance during bubble movement is proportional to the square of the diameter and the buoyancy force is proportional to the cube of the diameter. In addition, the gas dissolved into the compound during the leaving process which may have been the reason for the removal of bubbles.

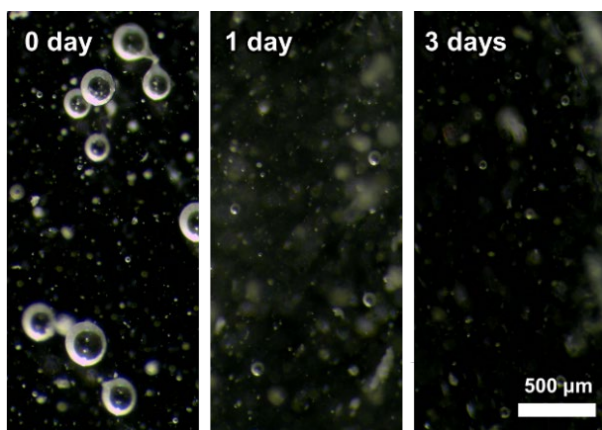


Figure 2 Microscope images of sintered silica bodies left for 0, 1, and 3 days. Less bubbles were found after 3 days.

3.2. Fabrication of microchannel by plant roots

We fabricated transparent silica glass using methods that showed good results in the preliminary experiments. Materials were mixed using the maximum speed setting of planetary centrifugal mixer and the compound was placed in the air for 259 ks (5 days) to incubate plant and defoam. In addition, we placed the compound with plants in a container made of agar to keep the moisture content.

3.2.1. Methods

We chose *Trifolium repens* for plants since it has good germination rate and quick growth speed. Total compound weight was decided 20.0 g, and it consists of silica powder and 0.5 mass% HPMC solution in volume ratio of 50:50.

First, 13.82 g of silica powder was added to 4.64 g of pure water and were mixed twice at maximum speed setting using a planetary centrifugal mixer.

The compound was defoamed for 0.6 ks (10 min) using vacuum pump after mixing. Next, we added 1.55 g of 2 mass% HPMC solution and mixed twice using a same mixer. Then, the compound was poured into the prepared agar container and defoamed for 0.6 ks (10 min). Finally, we incubated for 432 ks (5 days) after seeded *Trifolium repens* in the compound.

After cultivation, it was placed in an oven set at $80\ ^\circ\text{C}$ for 1.8 ks (30 min) to dry the compound. Figure 3 shows a sintering program. Sintering was conducted by raising the temperature at $0.083\ ^\circ\text{C/s}$ ($300\ ^\circ\text{C/h}$), holding at $1400\ ^\circ\text{C}$ for 3.6 ks (1 h), and then lowering the temperature at $0.042\ ^\circ\text{C/s}$ ($150\ ^\circ\text{C/h}$) using the electric furnace (BF-1700-II-T, Crystal Systems Corporation).

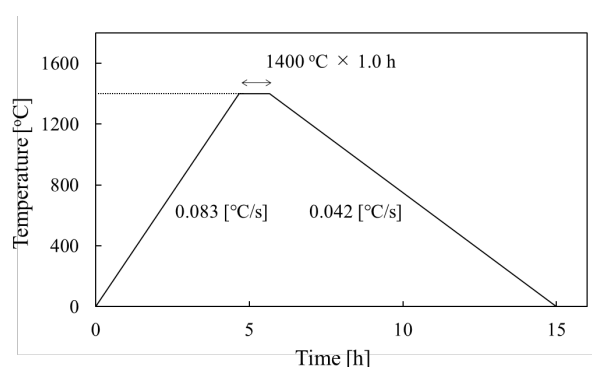


Figure 3 Heating program for sintering.

3.2.2. Results and discussion

Figure 4 shows sintered silica glass with microchannels made by plant roots. Plant roots cavities were fixed within the glass, resulting in a transparent silica glass with multiple channels. We clearly observed fine channels fabricated by main root about $150\ \mu\text{m}$ and root hairs less than $10\ \mu\text{m}$ in diameter. Moreover, the agglomerates within this

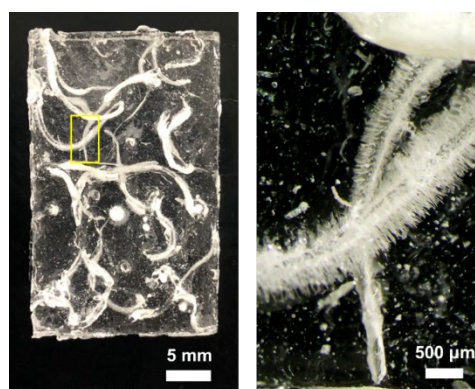


Figure 4 Sintered silica sample with microchannels (left) and, Optical micro photo of the sample. Fine and clear structures fabricated by plants are observed (right). Yellow frame in left photo shows the observation area of the right image.

sintered body were removed and no air bubbles remained. If the direction of plant root growth can be controlled by using gravitropism, the shape of the compound container, and controlling the hydrostatic stress of the culture medium, it will be possible to fabricate silica glass with arbitrarily shaped three-dimensional structural channels.

4. Fabrication of microchannel by nematodes

We used Root-knot nematodes which moves in the soil and parasitizes plant roots. Microchannels which have different types of structures can be expected to be realized by integrating channels created by plant roots and nematodes. First, plants were planted and grew in the compound. Then, water containing nematodes was dropped, and the pathway created when the nematodes move toward the plant in the compound was used as microchannels. The compound turned into gel to remain the channels created by nematodes in this experiment.

4.1. Methods

The compound consisted of silica powder and 1.0 mass% agar solution in volume ratio of 60:40 and total weight was decided 20.0 g.

First, 11.90 g of silica powder was added to 8.02 g of water and were mixed twice at maximum speed setting using a planetary centrifugal mixer. The compound was defoamed for 0.6 ks (10 min) using vacuum pump after mixing. Next, we added 0.08 g of agar powder and dissolved by heating in a microwave oven. Then, the compound was poured into the prepared agar container and defoamed for 0.6 ks (10 min). Finally, we incubated for 432 ks (3 days) after seeded *Trifolium repens* in the compound.

After 3 days, 0.5 mL of water containing 0.65 nematode per 1 μL was dropped onto the compound. The compound was incubated for approximately 604.8 ks (7 days) as the period which the nematodes moved to the plants. Lastly, the compound was placed in an oven set at 80 $^{\circ}\text{C}$ for 2.4 ks (40 min) to be dried, and it sintered in the same program as fabricating microchannels using plant roots.

4.2. Results and discussion

Figure 5 shows sintered silica glass with microchannels of about 15 μm width created by nematodes. Figure 6 illustrates the obtained cavity of the nematodes. Optical microscopy revealed that the channels obtained were located on the surface of the silica glass and were semi-circular channels. These results suggest that the nematodes moved at the interface between the agar container and the silica compound. It would be possible to create

complex three-dimensional channels that are integrated with plant channels by controlling movement of the nematodes.

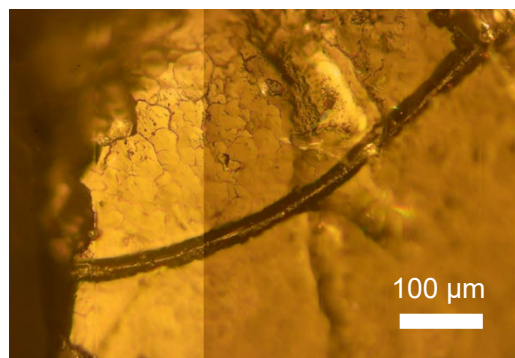


Figure 5 Microchannel fabricated by nematodes on silica glass surface.

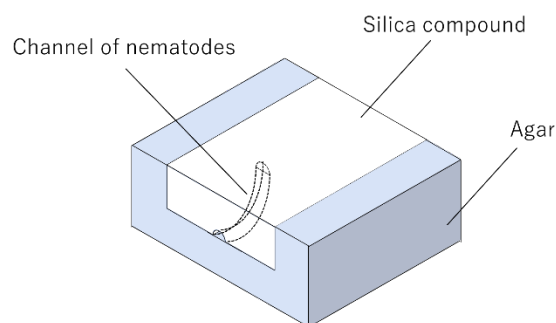


Figure 6 Illustration of a microchannel fabricated by nematodes.

5. Conclusion

Glass microfluidic channels were fabricated using plants based on the results obtained in the fabrication of transparent silica glass. We solved the problems of agglomerates and air bubbles. Root hair cavities of less than 10 μm in diameter were also fixed in the glass. At the present stage, the plants are allowed to grow freely, but if the direction of growth can be controlled by gravitropic or hydrostatic stress loading, silica glass with desired channel structures can be fabricated.

Compounds were designed to remain nematodes migration holes by mixing silica powder and agar solution. The silica glass had an approximately 15 μm width channel that were created when a nematode moved. In the future, it is expected to control plant growth and nematodes movement, and to fabricate complex channels with integrated channels.

Acknowledgements

This work was supported by KAKENHI Grant Number JP21H00371.

References

1. X. Mu, W.F. Zheng, J.S. Sun, W. Zhang, and X.Y. Jiang, *Small*, **9** (2013) 9.
2. L.F. Zhu, B. Wang, S. Handschuh-Wang, and X.C. Zhou, *Small*, **16** (2020) 1903841.
3. W.B. Zimmerman, *Chem. Eng. Sci.* **66** (2011) 1412.
4. C. Revet, H. Lee, A. Hirsch, S. Hamilton, and H. Lu, *Chem. Eng. Sci.* **66** (2011) 1490.
5. D. B. Tuckerman, and R. F. W. Pease, *IEEE Electron Device Lett*, **2** (1981) 126.
6. X. Wei, Y. Joshi, and M. K. Patterson, *J. Heat Transf.*, **129** (2007) 1432.
7. J. Shi, X. Qu, Z. Qi, and J. Chen, *Int. J. Refrig.*, **34** (2011) 292.
8. R.S. Wegeng, L.R. Pederson, W.E. TeGrotenhuis, and G.A. Whyatt, *Fuel Cells Bull.*, **3** (2001) 8.
9. T. Stevens, and M. Baelmans, *Appl. Therm. Eng.*, **28** (2008) 2353.
10. R.W. Moss, G.S.F. Shire, P. Henshall, P.C. Eames, F. Arya, and T. Hyde, *Sol. Energy*, **153** (2017) 718.
11. M.A. Oyinlola, G.S.F. Shire, and R.W. Moss, *Exp. Thermal Fluid Sci.*, **67** (2015) 102.
12. A. Muck, J. Wang, M. Jacobs, G. Chen, M.P. Chatrathi, V. Jurka, Z. Vyborny, S.D. Spillman, G. Sridharan, and M.J. Schoning, *Anal. Chem.*, **76** (2004) 2290.
13. N. Bao, Q. Zhang, J.J. Xu, and H.Y. Chen, *J. Chromatogr. A*, **1089** (2005) 270.
14. M. Castano-Alvarez, D.F.P. Ayuso, M.G. Granda, M.T. Fernandez-Abedul, J.R. Garcia, A. Costa-Garcia, *Sens. Actuators B Chem.*, **130** (2007) 436.
15. J.M. Fernandez-Pradas, D. Serrano, P. Serra, and J.L. Morenza, *Appl. Surf. Sci.*, **255** (2009) 5499.
16. T. Tang, Y.P. Yuan, Y. Yalikul, Y. Hosokawa, M. Li, and Y. Tanaka, *Sens. Actuators B Chem.*, **339** (2021) 129859.
17. D. Kundo, G. De, B. Karmakar, A. Patra, and D. Ganguli, *J. Mater. Sci.*, **15** (1992) 453.
18. O. Yong-Taeg, S. Fujino, and K. Morinaga, *Sci. Technol. Adv. Mater.*, **3** (2002) 297.
19. E. M. Rabinovich, *J. Mater. Sci.*, **20** (1985) 4259.
20. O. Yong-Taeg, H. Takebe, and, K. Morinaga, *J. Ceram. Soc. Japan*, **105** (1997) 171.
21. P. Gravesen, J. Branebjerg, O. Ssnderg, D. Ns, and D. K. Nordborg, *J. Micromech. Microeng.*, **3** (1993) 168.
22. K. Tokumaru, S. Hunt, and F. Tsumori, *Proc. MicroTAS*, (2018), 522.
23. F. Tsumori, S. Hunt, K. Kudo, T. Osada, and H. Miura, *J. Jpn. Soc. Powder Powder Metallurgy*, **63** (2016) 511.
24. F. Tsumori, S. Hunt, T. Osada, and H. Miura, *Jpn. J. Appl. Phys.*, **54** (2015) 06FM03.
25. T. Miyata, K. Tokumaru, and F. Tsumori, *J. Photopolym. Sci. Technol.*, **33** (2020) 199.
26. T. Miyata, K. Tokumaru, and F. Tsumori, *Jpn. J. Appl. Phys.*, **59** (2020) S11J07.
27. K. Tokumaru, K. Yonekura, and F. Tsumori, *J. Photopolym. Sci. Technol.*, **32** (2019) 315.
28. K. Yonekura, K. Tokumaru, and F. Tsumori, *Jpn. J. Appl. Phys.*, **57** (2018) 06HG05.
29. K. Tokumaru, F. Tsumori, K. Kudo, T. Osada, and K. Shinagawa, *Jpn. J. Appl. Phys.*, **56** (2017) 06GL04.
30. F. Tsumori, K. Tokumaru, K. Kudo, T. Osada, and H. Miura, *J. Jpn. Soc. Powder Powder Metallurgy*, **63** (2016) 519.
31. F. Tsumori, Y. Tanaka, Y. Xu, T. Osada, and H. Miura, *Jpn. J. Appl. Phys.*, **53** (2014) 06JK02.
32. J. R. Anderson, D. T. Chiu, R. J. Jackman, O. Cherniavskaya, J. C. McDonald, H. K. Wu, S. H. Whitesides, and G. M. Whitesides, *Anal. Chem.*, **72** (2000) 3158.
33. D. T. Chiu, N. L. Jeon, S. Huang, R. S. Kane, C. J. Wargo, I. S. Choi, D. E. Ingber, and G. M. Whitesides, *Proc. Natl. Acad. Sci. U. S. A.*, **97** (2000) 2408.
34. H. Wu, T. W. Odom, D. T. Chiu, and G. M. Whitesides, *J. Am. Chem. Soc.*, **125**-2 (2003) 554.
35. W. Wu, A. Deconinck, and J. A. Lewis, *Adv. Mater.*, **23** (2011) 1.
36. F. Kotz, K. Arnold, W. Bauer, D. Schild, N. Keller, K. Sachsenheimer, T. M. Nargang, C. Richter, D. Helmer, and B. E. Rapp, *Nature*, **544** (2017) 337.
37. F. Kotz, P. Risch, K. Arnold, S. Sevim, J. Puigmarti-Luis, A. Quick, M. Thiel, A. Hrynevich, P. D. Dalton, and D. Helmer, *Nat. Commun.*, **10** (2019) 1.
38. S. Nakashima, K. Tokumaru, and F. Tsumori, *Jpn. J. Appl. Phys.*, **57**-6S1 (2018) 06HJ07.
39. S. Nakashima, K. Tokumaru, and F. Tsumori, *Proc. MicroTAS*, (2018) 535.
40. D. Sato, F. Tsumori, *J. Photopolym. Sci. Technol.*, **34** (2021) 381.

Biomimetic Wave Propagation in Magnetic Soft Actuator

Fujio Tsumori^{1*} and Hayato Shinoda²

¹ *Department of Aeronautics and Astronautics, Faculty of Engineering, Kyushu University, 744 Motoooka, Nishi-ku, Fukuoka 819-0395, Japan*

² *Department of Mechanical Engineering, Graduate School of Engineering, Kyushu University, 744 Motoooka, Nishi-ku, Fukuoka 819-0395, Japan*

**tsumori@aero.kyushu-u.ac.jp*

In this paper, a simple but effective method is proposed to generate a bio-mimic wave propagating motion in a magnetic soft actuator. Two examples, a metachronal wave in artificial cilia and a crawling motion of an artificial caterpillar, are shown as demonstrations. These are kinds of wave propagating motions which are popular in natural systems and are also primitive systems of natural creatures. In the proposed system, an elastic material and a magnetic powder were used to fabricate a flexible magnetic structure. There are 2 essential features in the system; one is periodic arrangement of magnetic anisotropy, and the other is application of a rotating magnetic field. Using this method of wave generation, we realized drastic change in flow making behavior of artificial cilia and a crawling motion very similar to living caterpillars. The proposed system would be useful to enhance the field of the bio-mimic soft robotics.

Keywords: Magnetic particles, Soft material, Silicone, Magnetic anisotropy

1. Introduction

Recently, soft motion of natural creatures has been focused on to realize biomimetic robots [1-4]. For example, worms, caterpillars, snakes and centipedes are attractive targets. These creatures locomote by repeating the propagation of muscle contraction and extension. Some living organs perform similar behavior. Digestive tracts show peristaltic movement to transport digestives. Cilia is also a good example. Each cilium makes simple beating patterns, while they exhibit cooperative manner as they aligned [5]. They generate a metachronal wave, which is like a “Mexican wave” in a football stadium. Every cilium beats the same pattern but the phase of the motion shifts as its position shifts. As mentioned here, the wave propagation is popular in natural systems and is a primitive motion system of natural creatures.

There are 2 possible approaches to mimic the wave propagating motions of these creatures or organs. One is to employ mechanical structures with joints. Snake-like robot is an example, which has been developed by many research groups [6-8].

These snake robots consist of links and joints, so the system is similar to the conventional robotic system. Of course, there are difficulties in controlling many degrees of freedom and implement of lots of mechanical parts. If we could prepare enough number of joints, they could propagate wavy motion in their bodies. The other approach is to employ soft actuators. Many kinds of polymer actuators could be used for this purpose. Pneumatic soft actuators are most popular for soft robotics [2, 9, 10]. There are examples of stimuli-responsive gel materials such as ionic liquid-based gel system [11, 12] and electrohydraulic transducers [13]. These soft materials could make wave propagations like live creatures by driving each element in turn. There is another special example, a gel actuator with Belousov-Zhabotinsky (BZ) reaction. It can make autonomously oscillating motion [14, 15].

We focused on magnetic elastomer [16-21], which consists of elastic matrix and magnetic powder, for this purpose. Rubber or gel material can be used for the matrix, and magnetite powder was mixed into it. There are some advantages to this

Received	March 28, 2022
Accepted	June 24, 2022

material. As the actuator can be driven by an applied magnetic field, no electronic wiring is necessary, and the simple process is enough for fabrication. As described later, it is easy to generate wave propagation of the motion by periodic change of the applied magnetic field. In this work, a rotating magnetic field was used for the wavy motion. Variation of the motion could be designed by setting anisotropic magnetic property in each portion of the structure. In this paper, we will show 2 examples as shown in Fig. 1.

The first example is artificial cilia as schematically shown in Figs. 1(a, b). Simple pillar structures of magnetic elastomer could work as cilia [22-28]. Each pillar structure shows reciprocating beating pattern under a rotating magnetic field (Fig. 1(a)). A key point of this work is setting magnetic anisotropy. Different orientation of magnetic property was set to each pillar so that we could change phase shift of the beating pattern in each pillar. We can generate a metachronal wave, or “Mexican wave”, by setting each pillar in turn while shifting orientation angle (Fig. 1(b)) [26-31]. The other example is an artificial crawler. Unlike the previous case, a magnetic element, which is not deformable, is set on a flexible sheet so that the sheet will deform as shown in Fig. 1(c). A rotating magnetic field causes moment to the magnetic element and resulted deformation in the base sheet. Wave deformation could be generated by putting several magnetic elements in order with changing the orientation of magnetic moment, and the wave proceeds with rotation of the magnetic field (Fig. 1(d)).

It is important to set anisotropic magnetic properties to the material for implementation of these artificial structures. We used a magnetic field in order to set magnetic orientation. For the soft-magnetic powder, we applied a magnetic field to the mixed material before curing. The soft-magnetic particles generated chain-like clusters parallel to the applied magnetic field, and the cluster structures were fixed in the matrix after curing. On the other hand, for the hard-magnetic material was magnetized and became a permanent magnet with N- and S-poles.

If these magnetic elements were set under an applied magnetic field, rotational moment, M , would be exerted as following equation:

$$M = mH \sin(\theta_m - \theta_H) \quad (1)$$

where, m is magnetic moment, H is a magnetic external magnetic field, and θ_m and θ_H are angle of the magnetic moment and the applied magnetic field,

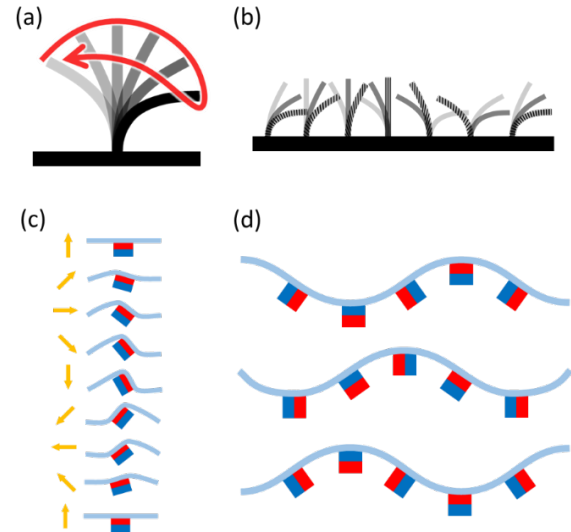


Fig. 1. Schematic illustration of the present artificial cilia and crawler. (a) Beating pattern of a cilium in 1 cycle. (b) Metachronal wave by a group of cilia. Each cilium has different magnetic orientation for the phase shift of the motion in collaborative work. (c) A deformation pattern of a flexible base sheet with a single magnetic element. (d) Wavy motion by multiple magnetic elements. A wave will propagate to one direction by rotating a magnetic field.

respectively. In the case of soft-magnetic material, the magnetic moment, m , is defined as a function of H , and the direction of the magnetic moment would be parallel to the direction of the generated chain-like clusters during the fabrication process. While in the case of hard-magnetic material, m would be a constant as a residual magnetic moment [30].

If a rotating magnetic field was applied to these magnetic materials, the exerted rotational moment would periodically change in time. We showed schematic images of 2 examples in Fig. 1. The first example is pillar structures which could work as artificial cilia. In this case, each pillar repeats beating motion due to the rotational moment and the elastic recovery force. It is noted that we can control the phase of the motion by setting the orientation of the magnetic moment to each pillar, so that we can design the metachronal wave. The similar approach could be taken for the other example, an artificial crawler, to generate wavy motion. Assuming that a base silicone rubber was linear elastic, the deformation would be predicted by a simple computational calculation [28, 29]. Finite element analysis would be also a powerful designing tool for this system.

2. Materials and methods

The flexible magnetic structures in this work

were fabricated using conventional materials. We employed silicone rubber (Ecoflex 00-30, Smooth-on) and magnetic powders. Two kinds of magnetic materials, soft- and hard-magnetic particles, were prepared. The first one was a carbonyl iron powder of 4.4 μm mean particle diameter (Grade-OM, BASF). The other was a strontium ferrite powder of 1.4 μm mean particle diameter (SF-500, Dowa Electronics Materials) generally used for fabrication of rubber magnets. Silicone and magnetic powder were mixed by a planetary milling machine (Kakuhunter, Shashin Kagaku). In order to apply a magnetic field, 2 neodymium permanent magnets were used for soft-magnetic material, and electric coils of vibrating sample magnetometer (VSM) were used for hard-magnetic material. This magnetic elastomer could be formed by conventional molding or cutting & gluing methods.

The obtained structures were actuated by applying a rotating magnetic field. We used a permanent magnet for this purpose. A neodymium magnet was connected to a motor shaft and was rotated below the stage. We prepared 2 permanent magnets in this work, the one was a cylindrical shape of 40 mm diameter and 20 mm thickness, and the other was a rectangular shape of 20 mm \times 30 mm \times 60 mm. The former one was used to actuate artificial cilia, and the latter one for the caterpillar.

3. Results and discussion

In this section, we show 2 examples of wave propagating motions. One is metachronal wave of artificial cilia and the other is wavy motion of an artificial caterpillar. Both results are described in the following sections.

3.1. Metachronal wave of artificial cilia

Cilia are hair-like organelles generally found on natural organs; for examples, surfaces of tiny creatures such as Paramecium, and respiratory epithelium in the mammalian lungs [32]. Paramecium can swim by beating of cilia, and we, mammals, can sweep out mucus and dirt out of the tracheas. Cilia perform these works more effectively by making coordinated motion. This motion is called metachronal wave, in which the beating pattern of individual cilium is similar, but the beating phase of neighboring cilia is different. It has been reported that metachronal wave can increase 3 times in flow rate and 10 times in flow efficiency [5]. There have been some reports of magnetic-driven artificial cilia, but only little with an artificial metachronal wave [26, 28, 29, 33]. As

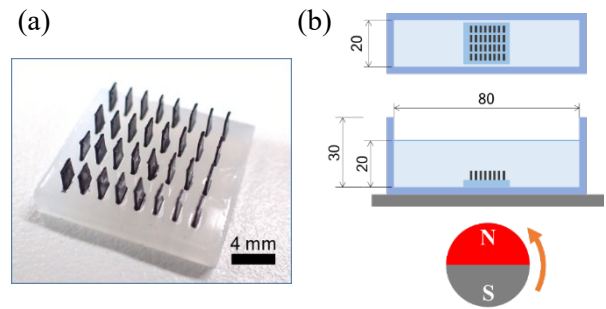


Fig. 2. (a) Overview of fabricated artificial cilia, and (b) experimental setup for flow test.

described in the previous section, we tried to emerge a metachronal wave using magnetic elastomer.

We fabricated artificial cilia as shown in Fig. 2. A total of 32 plate-like pillars of 3.0 mm in height, 2.0 mm in width, and 300 μm in thickness were arranged at 2.0 mm intervals in the horizontal direction and 4.0 mm intervals in the depth direction on a silicone substrate. The cilia had different magnetic anisotropy in each row, and the orientation was shifted 45 degrees by each neighbor. In this structure, mixture of 20 mass% carbonyl iron powder in a silicone rubber was used.

The sample was actuated in 75 % glycerin aqueous solution of about 35 mPa·s. We also prepared another cilia sample in which all cilia worked in synchronization. These two artificial cilia were driven in a pool filled with aqueous glycerin. The size of the pool was 80 mm \times 20 mm \times 20 mm, and each cilia array was set on the bottom of the pool as shown in Fig. 2(b). They were actuated by a rotating magnetic field of 50 mT, and the rotational speed of the applied magnetic field was set to 100 rpm.

Figure 3 shows the flow velocity maps of both samples by particle imaging velocimetry (PIV). The first frames of consecutive 2 periodic motions were used for PIV so that averaged flow maps could be obtained. When the cilia beat in synchronization, the fluid near the cilia reciprocated, and a little convection with pulsating occurred in the same direction as the effective stroke. The convection direction was anticlockwise and the flow velocity was around 0.2 mm/s. On the other hand, the flow map was completely different as the cilia generated a metachronal wave. The fluid was convecting without pulsating, and the flow direction was clockwise that was opposite to the phase propagation direction of the metachronal wave. The flow velocity was about 0.4 mm/s.

Generally, a beating pattern of a natural cilium consists of effective and recovery strokes. This

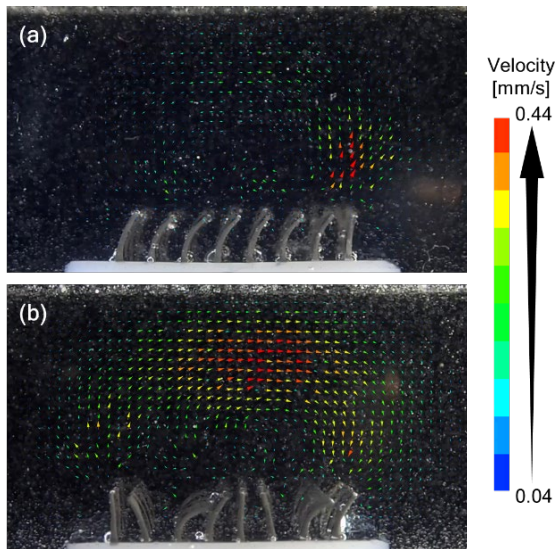


Fig. 3. Flow vector maps by PIV. (a) Cilia with synchronization motion, and (b) cilia with metachronal wave.

asymmetric beating pattern enables to make an effective flow at low Reynolds number range. It has been reported that magnetic pillar structures emerge these 2 strokes under a rotating magnetic field [22, 23]. In this work, asymmetric beating of cilia caused anticlockwise convection as shown in Fig. 3(a). A metachronal wave could change flow behavior drastically. Metachronal motion made flow pattern with many local vortices. As a result, metachronal wave contributed more to the averaging flow rate.

3.2. Locomotion of artificial caterpillar

The next example is an artificial caterpillar. In the previous chapter, flexible magnetic pillars were arranged on a fixed base as artificial cilia. In this chapter, the harder magnetic elements were fixed on a flexible sheet so that the sheet was deformed by moment exerted by the elements.

The base material for elastic matrix was the same silicone as used for the artificial cilia. Based on our previous report [34], hard-magnetic powder, Strontium ferrite, was employed to be mixed with the silicone matrix. The fabrication process is shown in Fig. 4. A rubber magnet sheet of 2 mm thickness was prepared using mixture of the silicone and the Sr-ferrite powder at a ratio of 30 mass%. The sheet was magnetized under a magnetic field of 15 kOe (Fig. 4(a, b)), and was cut into square columns (Fig. 4(c)). Cut columns were glued onto a flexible silicone sheet of 0.6 mm thickness. The magnetized angle of each column was changed by 90 degree from the neighbors. The obtained “artificial caterpillar” was set on a substrate and actuated by applying a rotating magnetic field. The

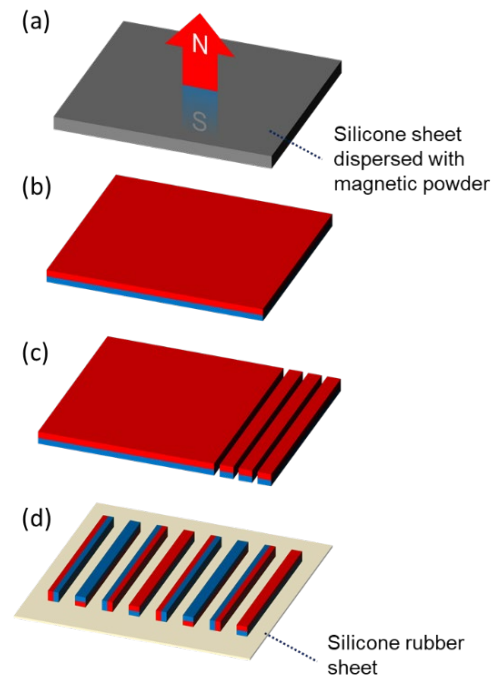


Fig. 4. Flow of the fabrication process of artificial caterpillar.

magnetic field was applied by a rectangular neodymium magnet set below the substrate. The distance from the center of the permanent magnet to the substrate surface was 46 mm.

Snapshots of the actuated caterpillar under a rotating magnetic field at 60, 720 and 1200 rpm are shown in Fig. 5. As rotational moment was exerted in each magnetic column, the main flexible sheet structure deformed into a wavy shape. The wavy pattern consisted of 2 periodic units since the same arrangement of the 4 magnetic columns was repeated twice on the sheet. The deformation patterns at 60 and 720 rpm shown in Fig. 5 were similar to each other, however, the behavior changed over 1000 rpm since the both ends of the structure vibrate largely due to resonance. The structure bounced like a rampage horse by beating the substrate.

Figure 6 shows relationship between the maximum velocity and the rotating speed of the magnetic field. The velocity increased almost linearly at the lower rotating speeds. The caterpillar tended to bounce over 1000 rpm that resulted less contact time to the substrate so that the increase of the velocity settled. At 1200 rpm, the unstable motion resulted the highest velocity in this experiment, however, it would be difficult to control this state.

Next, the behavior of the fabricated caterpillar was compared with that of a live caterpillar. A larva (*Lemyra imparilis*) of 16 mm in length was caught in Ito campus of Kyushu University. It had 3 pairs

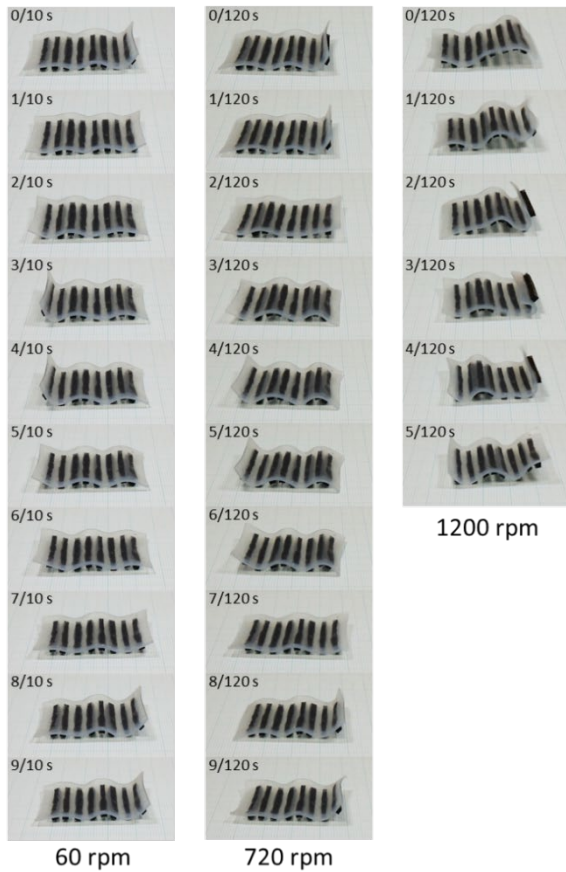


Fig. 5. Snapshots of actuated caterpillar at 60, 720 and 1200 rpm.

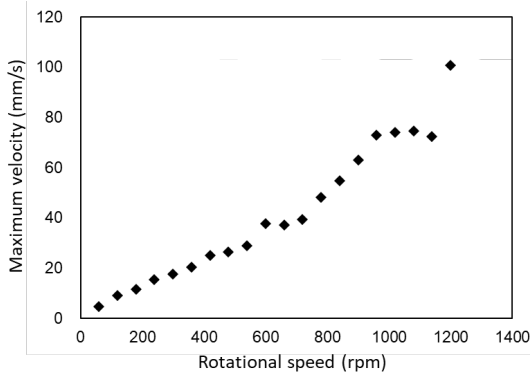


Fig. 6. Relationship between maximum velocity of the artificial caterpillar and rotating speed of the magnetic field.

of legs, 4 pairs of prolegs, and 1 pair of anal prolegs, and used these 8 pairs of legs repeatedly with bending the body. Figure 7 shows snapshots during 1 periodic motion. Red lines were added to show the direction of the legs clearly. An observed wave number of deformations in full length of the larva was 1.5 cycles, which corresponded to 3 quarters of the artificial caterpillar. Corresponding 6 legs of the artificial structure are picked up in Fig. 7. Similar wave motions were generated in the live and artificial caterpillars. Figure 8 shows change of angle of each leg in one motion period. The change

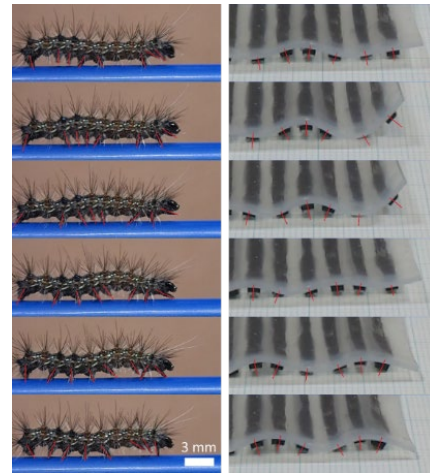


Fig. 7. Crawling of live caterpillar (left) and artificial one (right).

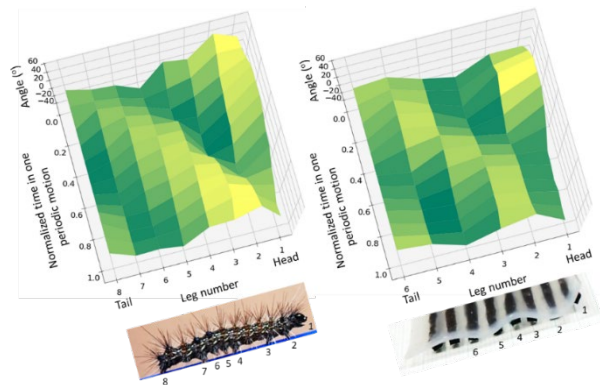


Fig. 8. Change of angle of each leg in one motion period; (left) for a live caterpillar, and (right) an artificial caterpillar.

of the angles corresponds to the wave propagation, and it is shown that the artificial caterpillar well mimicked the motion of a live larva.

As the final demonstration, Fig. 9 shows the magnetic caterpillar crawling across hands. One of the most important merit of the present actuation system is that the magnetic actuators could work without air pressure supply or electric wiring. In this case, a magnetic field could transmit through live hands. It is also noted that this caterpillar could crawl on the not-flat rough surface of the fingers.

4. Conclusion

In this paper, we proposed a simple but effective method to generate bio-mimic wavy motions using elastic matrix dispersed with magnetic powders. Wave propagation is generally observed in natural world and plays an important role for locomotion and transportation system inside the living organs. Among many kinds of natural motion, 2 examples, cilia with metachronal wave and caterpillar motion, were demonstrated in this work. Even though the

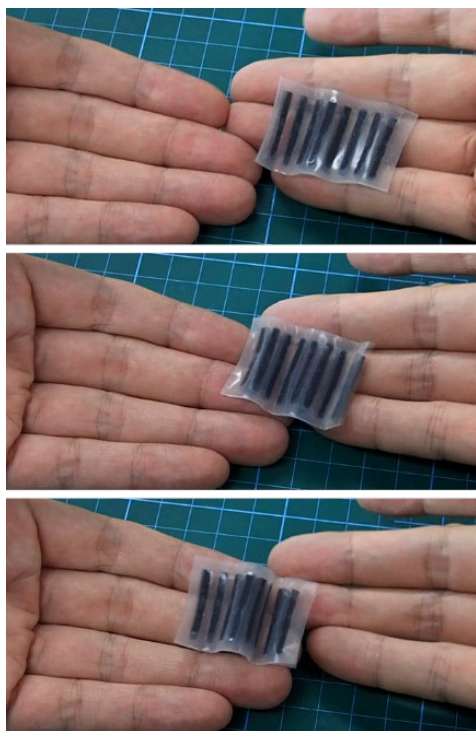


Fig. 9. Artificial caterpillar crawling across hands.

system was simple, we could show quite similar behaviors observed in natural creatures in these cases.

Essential features of this study are summarized in the following two points; the periodic arrangement of magnetic anisotropy, and the application of a rotating magnetic field. Also, it is important not only to develop a designing system but also to develop fabrication processes. Some research groups have been developing new 3D printing systems for elastic materials dispersed with magnetic powder [28, 29, 35-38]. In these processes, magnetic orientation is set by applying a magnetic field at a building point. These new 3D printing techniques would be helpful for the soft robotics field to realize many kinds of natural wave propagation, such as worms, snails, nematodes and so on. It is also important to tougher materials and DN-gel would be one of the candidates [39, 40].

Acknowledgement

This work was supported by JSPS KAKENHI Grant Numbers JP17K18830 and JP21K18702.

References

1. D. Rus, and M.T. Tolley, Design, *Nature*, **521** (2015) 467.
2. R.F. Shepherd, F. Ilievski, W. Choi, S.A. Morin, A.A. Stokes, A.D. Mazzeo, X. Chen, M.Wang, and G.M. Whitesides, *PNAS*, **108** (2011) 20400.

3. H. Lin, G.G. Leisk, and B. Trimmer, *Bioinsp. Biomim.*, **6** (2011) 026007.
4. S. Seok, C.D. Onal, R. Wood, D. Rus, and S. Kim, *IEEE Int. Conf. Robot. Autom.* (2010) 1228.
5. J. Elgeti and G. Gompper, *PNAS*, **110** (2013) 4470.
6. P. Liljebäck, K.Y. Pettersen, Ø. Stavadahl, and J.T. Gravdahl, *Robot. Autonomous Sys.*, **60** (2012) 29.
7. A. Crespi, A. Badertscher, A. Guignard, and A.J. Ijspeert, *Robot. Autonomous Sys.*, **50** (2005) 163.
8. Z. Lu, D. Feng, Y. Xie, H. Xu, L. Mao, C. Shan, B. Li, P. Bilik, J. Zidek, R. Martinek, and Z. Rykala, *Perspect. Sci.*, **7** (2016) 101.
9. B. Mosadegh, B. Polygerinos, C. Keplinger, S. Wennstedt, R.F. Shepherd, U. Gupta, J. Shim, K. Bertoldi, C.J. Walsh, and G.M. Whitesides, *Adv. Func. Mater.*, **24** (2014) 2163.
10. F. Connolly, P. Polygerinos, C.J. Walsh, and K. Bertoldi, *Soft Robot.*, **2** (2015) 26.
11. G.H. Kwon, J.Y. Park, J.Y. Kim, M.L. Frisk, D.J. Beebe, and S.H. Lee, *Small*, **4** (2008) 2148.
12. T. Fukushima, K. Asaka, A. Kosaka, and T. Aida, *Angew. Chem.*, **44** (2005) 2410.
13. N. Kellaris, V.G. Venkata, G.M. Smith, S.K. Mitchell, and C. Keplinger, *Sci. Robot.*, **3** (2018) eaar3276.
14. R. Yoshida, T. Takahashi, T. Yamaguchi, and H. Ichijo, *J. Amer. Chem. Soc.*, **118** (1996) 5134.
15. S. Maeda, Y. Hara, R. Yoshida, and S. Hashimoto, *Angew. Chem.*, **47** (2008) 6690.
16. T. Mitsumata and S. Ohori, *Polym. Chem.*, **2** (2011) 1063.
17. Y.L. Raikher, O.V. Stolbov, and G.V. Stepanov, *J. Phys. D*, **41** (2008) 152002.
18. F. Tsumori, N. Miyano, and H. Kotera, *J. Jpn. Soc. Powder Powder Met.*, **56** (2009) 127.
19. F. Tsumori, N. Miyano, and H. Kotera, *J. Jpn. Soc. Powder Powder Met.*, **56** (2009) 133.
20. F. Tsumori and J. Brunne, *Proc. IEEE MEMS* (2011) 1245.
21. K. Hatama, F. Tsumori, Y. Xu, H. Kang, T. Osada, and H. Miura, *Jpn. J. Appl. Phys.*, **51** (2012) 06FL14.
22. M.T. Downton, and H. Stark, *Europhysics Letters*, **85** (2009) 44002.
23. E.M. Gauger, M.T. Downton, and H. Stark, *Euro. Phys. J. E*, **28** (2009) 231.
24. A.R. Shields, B.L. Fiser, B.A. Evans, M.R. Falvo, S. Washburn and R. Superfine, *PNAS* **107** (2010) 15670.
25. F. Tsumori, A. Saijou, T. Osada, and H. Miura,

- Jpn. J. Appl. Phys.*, **54** (2015) 06FP12.
26. F. Tsumori, R. Marume, A. Saijou, K. Kudo, T. Osada, and H. Miura, *Jpn. J. Appl. Phys.*, **55** (2016) 06GP19.
 27. R. Marume, F. Tsumori, K. Kudo, T. Osada, and K. Shinagawa, *Jpn. J. Appl. Phys.*, **56** (2017) 06GN15.
 28. H. Shinoda, S. Azukizawa, K. Maeda, and F. Tsumori, *J. Electrochem. Soc.*, **166** (2019) B3235.
 29. S. Azukizawa, H. Shinoda, and F. Tsumori, *Proc. IEEE MEMS*, (2019) 248.
 30. M. Furusawa, K. Maeda, S. Azukizawa, H. Shinoda, and F. Tsumori, *J. Photopolym. Sci. Tech.*, **32** (2019) 309.
 31. S. Gaysornkaew and F. Tsumori, *Jpn. J. Appl. Phys.*, **60** (2021) SCCL02.
 32. M.A. Sleigh, *The Biology of Cilia and Flagella* (Pergamon, Oxford, 1962).
 33. S. Hanasoge, P.J. Hesketh, and A. Alexeev, *Soft Matter*, **14** (2018) 3689.
 34. K. Maeda, H. Shinoda, and F. Tsumori, *Jpn. J. Appl. Phys.*, **59** (2020) SIIL04.
 35. S. Azukizawa, H. Shinoda, K. Tokumaru, and F. Tsumori, *J. Photopolym. Sci. Tech.*, **31** (2018) 139.
 36. Y. Kim, H. Yuk, R. Zhao, S.A. Chester, and X. Zhao, *Nature*, **558** (2018) 274.
 37. H. Shinoda and F. Tsumori, *Proc. IEEE MEMS*, (2020), 497.
 38. K. Ninomiya, S. Gaysornkaew, and F. Tsumori, *Proc. IEEE MEMS*, (2022) 235.
 39. S. Shigetomi and F. Tsumori, *J. Photopolym. Sci. Tech.*, **34** (2021) 369.
 40. S. Shigetomi, H. Takahashi, and F. Tsumori, *J. Photopolym. Sci. Tech.*, **33** (2020) 193.

Development of Bile Duct Stent with Antifouling Property Using Atmospheric Pressure and Low Temperature Plasma

Masashi Yamamoto^{1*}, Tomoyuki Hamasaki¹, Atsushi Sekiguchi^{2,3}, Hiroko Minami³, Masayasu Aikawa⁴ and Hideo Horibe⁵

¹ National Institute of Technology, Kagawa College, Department of Electrical and Computer Engineering, 335 Chokushi-cho, Takamatsu, Kagawa 761-8058, Japan

² Osaka Prefecture University, Department of Physics and Electronics, 1-1 Gakuen-cho, Naka-ku, Sakai, Osaka 599-8531, Japan

³ Litho Tech Japan Corporation, 2-6-6 Namiki, Kawaguchi, Saitama, 332-0034, Japan

⁴ Saitama Medical University, International Medical Center, 1397-1, Yamane, Hidaka, Saitama, 350-1298, Japan

⁵ Osaka City University, Department of Physics and Electronics, 3-3-138 Sugimoto-cho, Sumiyoshi-ku, Osaka 558-8585, Japan

*m-yamamoto@t.kagawa-nct.ac.jp

Bile duct stent placement surgery is often performed to improve bile flow that has been impaired by biliary stricture. Conventional stents made of polyethylene cause blockage easily. We were inspired by the antifouling function of snail shells as a method for preventing blockages. For this study, we fabricated microstructures directly on the interior wall of the stent using an atmospheric pressure low-temperature plasma and verified its antifouling function. Plasma treatment fabricated microstructures, thereby improving the surface area by 2.1 times and roughness by 1.4 times. Results of animal experiments revealed that the substance adhering on the interior wall of the plasma-treated stent was about 40% less than those of the untreated stent. The plasma-treated stent can contribute considerably to reducing the burdens of surgery on patients by decreasing the frequency of replacement surgery.

Keywords: Atmospheric pressure low-temperature plasma, Bile duct stent, Biomimetics, Microstructure, Snail shell

1. Introduction

Bile, a fluid secreted by the liver, activates lipase, a digestive enzyme that facilitates the dissolution of oils in water and which assists in the digestion and absorption of lipids. Before being excreted to the duodenum, bile is stored temporarily in the gall bladder. Biliary stricture caused by bile duct cancer or biliary atresia inhibits the flow of bile from the gall bladder to the duodenum. Then, bile might flow back into the liver, resulting in jaundice. If left untreated, it causes liver failure, and in the worst case, death. Bile duct stent placement surgery is often performed to improve bile flow [1].

Bile duct stents can be classified broadly as plastic and metallic stents. Plastic stents, made of

polyethylene (PE), are often used because of the necessary labor and costs of surgery. Bile is a viscous liquid containing fats such as cholesterol [2]. Unfortunately, PE stents cause blockage in them easily because of their high affinity with fat-containing bile. Even now, the examination of effective countermeasures for this pernicious difficulty remains insufficient. If the stent becomes clogged, then only symptomatic treatment remains: replacement of the bile duct stent by reoperation. Usually, bile duct stents are replaced using an endoscope. If such replacement is difficult, then a percutaneous approach or open surgery is performed. In general, patients requiring stent placement surgery are older adults, for whom

Received April 4, 2022

Accepted June 19, 2022

replacement surgery is a heavy burden. By providing an antifouling function to the interior wall of the stent, the burdens of surgery on the patients can be reduced by decreasing the frequency of replacement surgery.

As a method for providing an antifouling function to bile duct stents, we were inspired by the antifouling function of snail shells. Snail shell surfaces have convexo-concave microstructures. When the surface is covered with water, a thin water film is formed on the surface. This water film can repel smears and provide superior antifouling functionality. This structure, designated as a super nanohydrophilic structure, has antifouling functions for repelling oil-containing proteins. This super nanohydrophilic effect can be achieved by fabricating convexo-concave microstructures at 200–400 nm pitch, thereby mimicking the snail's shell, on the interior wall surface of the stent [3–5]. This technique, called *biomimetics*, artificially mimics widely diverse functions shown by living organisms in the natural world [6, 7]. *Biomimetics* was applied for this study to develop a technique for providing an antifouling function in a bile duct stent.

The most common method of fabricating microstructures is lithographic technology. However, because the stent inner diameter is only a few millimeters, applying lithography technology is difficult. Therefore, we investigated a method of fabricating microstructures directly on the stent interior wall using glow discharge plasma, an atmospheric pressure low-temperature plasma, in a tube [8, 9]. Plasma was generated inside the stent. Microstructures were fabricated directly on its interior wall. After examining the surface morphology of the interior wall of the plasma-treated stent, we verified its antifouling function.

2. Experimental

2.1 Stent sample and plasma treatment instrument

Figure 1 portrays a photograph of the bile duct stent sample used for this study, with 2.40 mm outer diameter, 1.35 mm inner diameter, and 70 mm total length. It is made of PE, with barbs at both ends to grapple in the bile duct. The straight area is 50 mm. Figure 2 shows a plasma treatment equipment diagram. A stent was set so that plasma could be formed in this straight area.

2.2 Plasma treatment and surface observation

Table 1 presents the plasma treatment conditions for bile duct stent samples. An RF power supply (Pearl Kogyo Co., Ltd.) was used to generate an atmospheric pressure, low-temperature plasma. The RF power was controlled to 25–50 W. Its frequency

was 13.56 MHz. The helium gas ($\geq 99.99\%$; Takamatsu Teisan) flow rate was fixed at 1.40 slm using two mass flow controllers (SEC-400MK2; STEC Inc.). The oxygen gas ($\geq 99.5\%$; Iwatani Sangyo Corp.) flow rate was controlled at 0–4.0 sccm using another mass flow controller (SEC-400MK3; STEC Inc.). The He/O₂ mixture was introduced into the stent sample. When no oxygen gas was added, the minimum power necessary to turn on the plasma was 25 W. When 4.0 sccm of oxygen gas was added, the minimum power was 37 W. The distance between the facing electrodes was 12.5 mm. The electrodes were separated from the stage by 7.0 mm. The plasma treatment time per irradiation was 10 s. Also, the cooling time before the next irradiation was 30 s. The treatment and cooling were one set; it was repeated several times. The area near the center of the stent was punched out. Its surface morphology of the interior wall of the stent was examined using a digital microscope (VHX-7000; Keyence Co.). The relation between the microstructures and the plasma treatment conditions was evaluated.

The microstructure shape was analyzed using two parameters in accordance with ISO 25178, which is used for the non-contact measurement



Fig. 1. Photograph of bile duct stent sample.

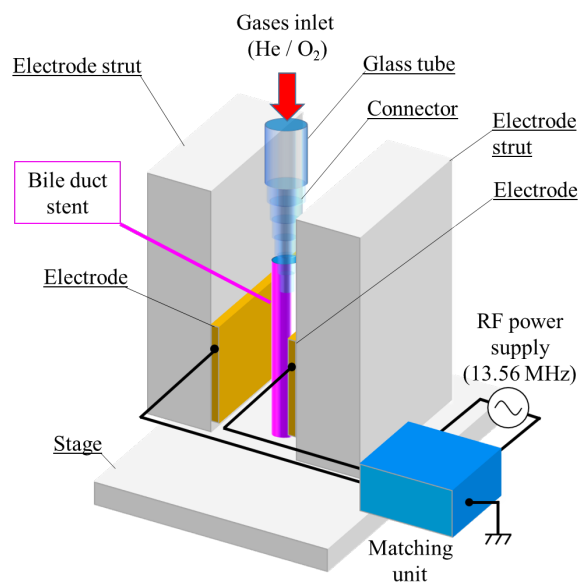


Fig. 2. Diagram of plasma treatment equipment.

Table 1. Conditions of plasma treatment for bile duct stent samples. Helium gas flow rate is fixed at 1.4 slm.

No.	RF power [W]	Exposure time [s]	O ₂ gas flow rate [sccm]	Electric energy [J]
1	–	–	–	–
2	25	10 × 3	0	750
3	25	10 × 6	0	1500
4	35	10 × 3	4.0	1050
5	35	10 × 6	4.0	2100
6	50	10 × 4	4.0	2000

method. The first is the surface area. This is one important parameter used to evaluate the surface morphology because it increases or decreases according to convexo-concave microstructures. The second is the root mean square height (rms). This is also called surface roughness. This is a parameter corresponding to the standard deviation of the height of the microstructures. The surface roughness can be large even if the surface has large convexo-concave structures. However, in this case, the surface area cannot be so large. The surface morphology was evaluated based on surface area and surface roughness.

2.3 Animal experimentation

A pair of plasma-treated and untreated stents was put in the bile ducts of two pigs for 14 days. Then we examined degree of material adherence on the interior wall of the retrieved bile duct stent. The animal experiment procedures are shown below. The pigs were acclimatized with a normal diet. After the pigs were fixed in a supine position under general anesthesia, their upper abdomen was incised in the median line. After their common bile duct and duodenum were exposed, the anterior wall of the duodenum was opened by incision. A pair of bile duct stents with and without plasma treatment was inserted through the duodenal papilla. The stent was sewn to the duodenal wall using 0.15 mm synthetic monofilament absorbent thread (4-0 PDS). The opened duodenal wall was also closed using 4-0 PDS. From the day after surgery, they started a liquid diet. On the third day after surgery, after confirming that their condition showed no trouble, their diet was changed to a normal diet. On day 14, they were euthanized. Then the indwelling stents were removed from them. Intravenous ketamine hydrochloride (20 mg/kg) was used for their euthanasia.

3. Results and Discussion

3.1. Relation between plasma condition and surface morphology

Figure 3 presents the surface morphology of the interior wall of the stents at various plasma treatment conditions. Table 2 presents analysis results of those surfaces.

First, the untreated stent sample (No. 1) and the sample treated with 50 W (No. 6) are compared. Plasma treatment increased both the surface area and surface roughness. The surface area was improved by 2.1 times; roughness was improved by 1.4 times.

Next, No. 2 and No. 3 are described. Both are samples treated in the absence of oxygen gas. Even under these conditions, plasma treatment increased the surface area. However, the production of active species such as oxygen radicals cannot be expected. In this case, the fabrication of microstructures might be ascribed only to increasing input electrical energy. However, the surface area and surface roughness of No. 3 were similar to those of the untreated sample (No. 1). For No. 2, they were rather smaller than those of the untreated sample (No. 1). Under the conditions of No. 2, the fabrication of microstructures is impossible because of the small amount of electrical energy.

Table 2. Results of surface analysis on interior wall of the stent at various plasma treatment conditions

No.	Surface area × 10 ³ [μm ²]	Surface roughness [rms μm]
1	22.0 ± 4.1	0.74 ± 0.20
2	15.8 ± 0.9	0.47 ± 0.03
3	24.8 ± 4.5	0.77 ± 0.12
4	35.5 ± 3.3	0.75 ± 0.03
5	25.8 ± 7.0	0.57 ± 0.09
6	46.6 ± 8.8	1.05 ± 0.26

Finally, No. 4 and No. 5 are described. Both samples were treated by adding oxygen gas at 4.0 sccm. The surface area and surface roughness of the No. 4 sample were larger than those of No. 5. The surface roughness was equivalent to that of the untreated sample (No. 1). This similarity implies similar shapes of the average microstructures of both. The No. 4 sample surface area was larger than that of No. 1. This finding might be explained by the large number of microstructures. The surface area and surface roughness of the No. 5 sample were reduced respectively to 72.6% and 75% of those of the No. 4 sample. The ratio of these declines was almost identical. The decrease in surface area might be ascribed to the larger pitch size of the average microstructure. Active species such as oxygen radicals are producible under these treatment conditions [10, 11]. Degradation of microstructures by active species must be promoted further by plasma treatment [12, 13].

Next we present supplementary information related to the unprocessed sample (No. 1). The surface area and surface roughness of the untreated sample (No. 1) showed fluctuations of 19% and

27%, respectively. These fluctuations were greater than for the sample treated with plasma. The untreated sample might have had some protrusions on its interior wall when it was manufactured. These protrusions, which might be removed by plasma treatment, might be a kind of dust or dirt. The fluctuations were small in the absence of oxygen gas. Although the protrusions might be removed, the microstructures cannot be fabricated much. However, when oxygen gas was added, the fluctuations increased to about 20%. Appropriate amounts of active species must promote the fabrication of microstructures.

According to the results presented in Table 2, we discuss the plasma treatment conditions for superior antifouling functionality. The addition of oxygen, with moderately high power, and short plasma exposure might be desirable for the formation of microstructures that exhibit an antifouling function. From an earlier study, we reported the addition of an antifouling function to the interior walls of PE tubes with different inner diameters using atmospheric-pressure, low-temperature plasma treatment [14]. Tubes with 2.0 mm and 3.0 mm inner diameters

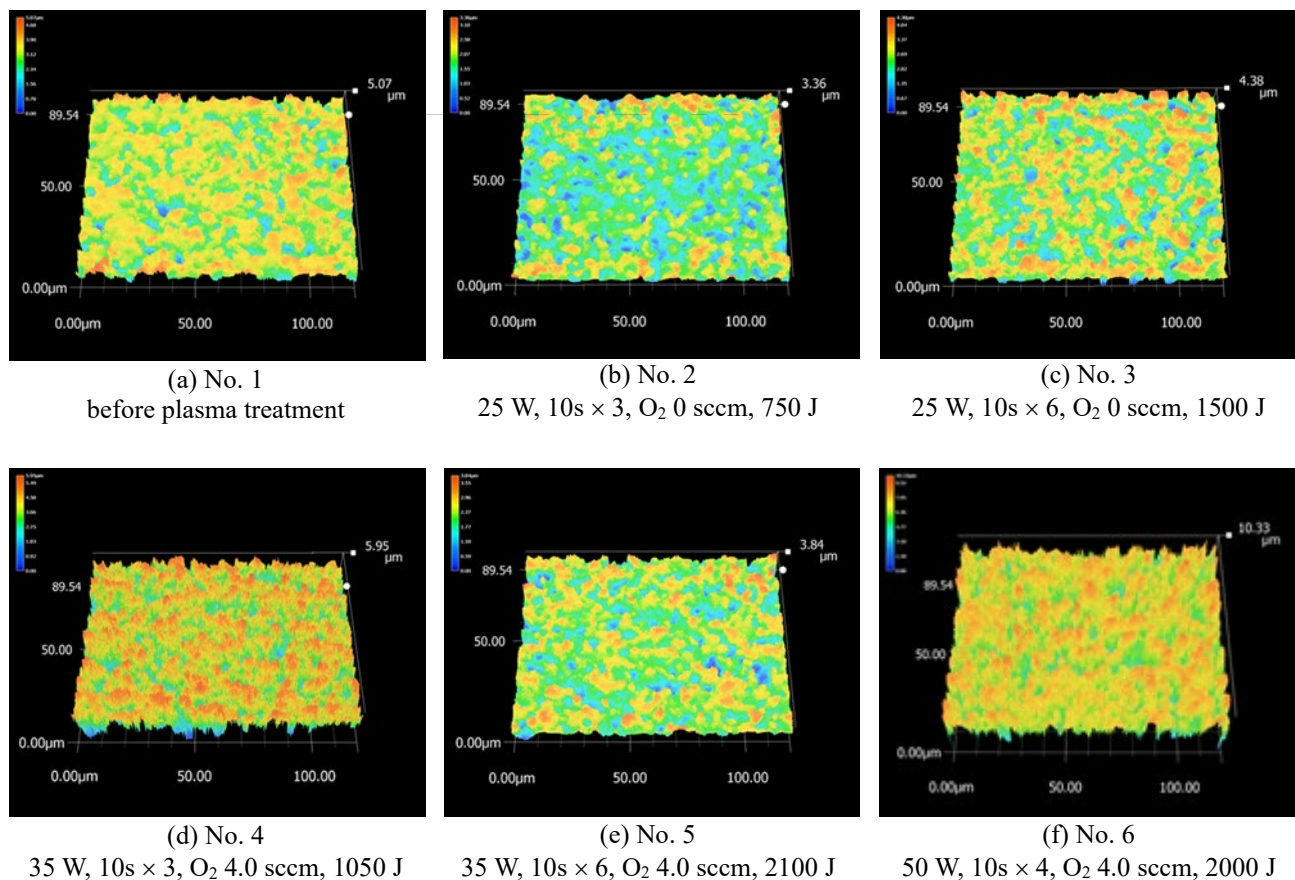


Fig. 3. Surface morphology of interior wall of stents under various plasma treatment conditions.

were treated respectively using electric energy of 2000 J with oxygen gas at 4.0 sccm. Results show that both tubes exerted an excellent antifouling function in liquid flow tests using pseudo-bile. Both tubes have a larger inner diameter than that of the bile duct stent. Even for the case of a bile duct stent, it can be readily inferred that the input electric energy of around 2000 J would be appropriate. Therefore, we chose to treat the samples used for animal experiments at 2000 J (50 W, 10 s, four times) with oxygen at 4.0 sccm.

3.2. Validating antifouling properties of bile duct stents by indwelling in pig

Figure 4 shows a photograph of a pair of bile duct stent samples resected from one pig. Because the outside of the stent is not treated by plasma, it is difficult to distinguish the presence or absence of plasma treatment based on its appearance. Therefore, we cut the stent open and observed the interior wall. Figure 5 portrays the interior wall of each stent sample. Both interior walls of the non-plasma-treated samples were covered with an adherent substance. The main constituents of the substance are probably bilirubin (an end product of red-blood cell breakdown), cholesterol, and bile acid [2]. The plasma-treated samples clearly had less substance. Individual differences in pigs were confirmed. They are described below. In the plasma-treated samples, pink color, the color of the interior wall of the unused stent, was confirmed.

Table 3 presents the stent weight and the thickness of the substance adhering on their surfaces. The weight of the stent for pig 1 cannot be described because part of the stent was missing: it was difficult to make a fair weight comparison. The non-treated stent weight was greater by 11.2 mg than that of the unused stent. However, for plasma-treated stents, the increase was only 6.1 ± 0.8 mg.

Figure 6 shows cross-sectional images of the stent samples. The adhesive thickness shown in Table 3 was evaluated from these observation



Fig. 4. Photograph of a set of stent samples after indwelling in pig for 14 days.



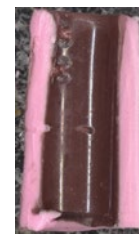
(a) Before indwelling



(b) Non-treated stent after indwelling in pig 1



(c) Plasma-treated stent after indwelling in pig 1



(d) Non-treated stent after indwelling in pig 2



(e) Plasma-treated stent after indwelling in pig 2

Fig. 5. Photographs of inside of the stent samples before and after indwelling in pigs.

Table 3. Weights of stents and thicknesses of adhering substance on their surfaces before and after indwelling in pigs

Stent sample	Pig No.	Weight [mg]	Thickness of adhering substance	
			Interior wall surface [μm]	Exterior wall surface [μm]
Fig. 5(a) Before indwelling	–	235.4	–	–
Fig. 5(b) Non-treated stent	Pig 1	–	17.5 ± 3.8	11.4 ± 7.5
Fig. 5(c) Plasma-treated stent	Pig 1	240.7	9.4 ± 0.5	13.4 ± 3.0
Fig. 5(d) Non-treated stent	Pig 2	246.6	27.6 ± 4.5	18.4 ± 5.6
Fig. 5(e) Plasma-treated stent	Pig 2	242.3	10.7 ± 2.9	10.0 ± 1.9

images. Individual differences in pigs can be distinguished clearly by comparing the substance thicknesses in untreated stents. The pig 1 thickness is less than that of pig 2. Consequently, the bile of pig 1 must be less clogged than that of pig 2. The average total adhesive thickness on the interior and exterior walls of the untreated stent was 37.5 μm . For plasma-treated stents, the average total thickness was 21.7 μm . Although results for only these two samples were obtained, plasma treatment reduced the weight of the adhering substance by 46%. In addition, the adhesive thickness was reduced by 42%. We demonstrated that plasma treatment provided an antifouling function to the bile duct stents. Plasma treatment conditions shown as results in Table 2 were suitable. Although we calculate them simply by assuming that the deposition rate of adhering substance is constant, the time necessary for the plasma-treated stent to

become clogged was 2.2 times longer than that of the conventional stent. We infer that, if using the plasma-treated stent, then the frequency of stent replacement surgery can be reduced to about half of that using conventional stents.

4. Conclusion

For this study, we fabricated microstructures directly on interior walls of a stent using an atmospheric pressure, low-temperature plasma. We then verified the antifouling function of the microstructures.

Plasma treatment increased both the surface area and surface roughness. We demonstrated that the microstructures can be fabricated directly on the stents' interior walls. The addition of oxygen, moderately high power, and short plasma exposure might be desirable to form suitable microstructures.

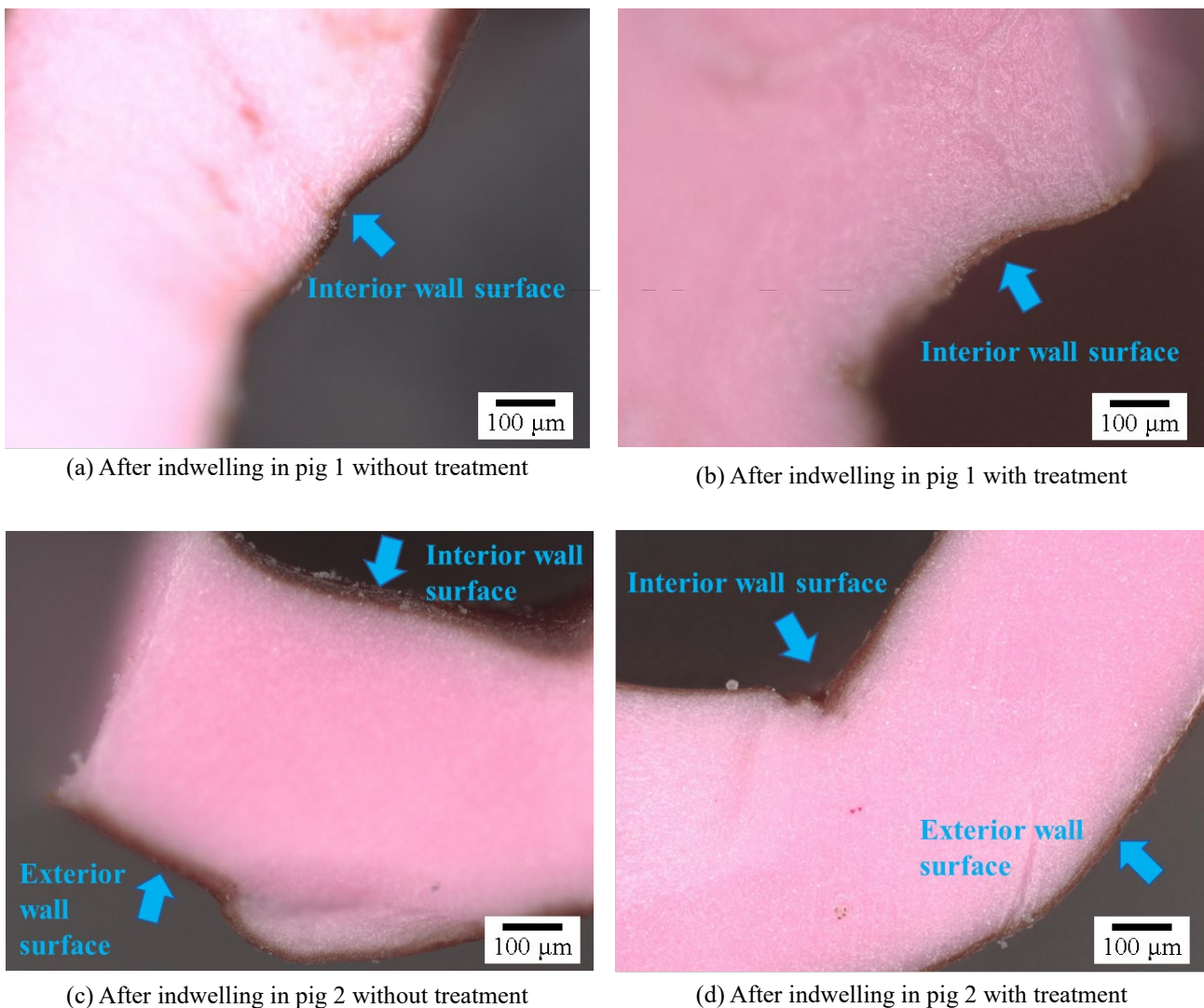


Fig. 6. Cross-sectional images of the stent samples before and after indwelling in pigs.

Effects of the antifouling function by plasma treatment were verified through animal experiments using pigs. The weight of the adhering substance was reduced by 46% by plasma treatment, with 42% thickness reduction. Plasma-treated stents can play an important role in reducing the burdens of surgery on patients by decreasing the frequency of replacement surgery.

Acknowledgments

We thank Mr. Hirano at Hanaco Medical Corporation for supplying the PE bile duct stents.

References

1. A. C. Smith, J. F. Dowsett, R. C. Russell, A. R. Hartfield, and P. B. Cotton, *Lancet*, **344** (1994) 1655.
2. G. Masselli, R. Manfredi, A. Vecchioli, and G. Gualdi, *Eur. Radiol.*, **18** (2008) 2213.
3. T. Nishino, H. Tanigawa, and A. Sekiguchi, *J. Photopolym. Sci. Technol.*, **32** (2019) 661.
4. A. Sekiguchi, Y. Matsumoto, H. Minami, T. Nishino, H. Tanigawa, K. Tokumaru, and F. Tsumori, *J. Photopolym. Sci. Technol.*, **31** (2018) 121.
5. T. Nishino, H. Tanigawa, A. Sekiguchi, and H. Mayama, *J. Photopolym. Sci. Technol.*, **32** (2019) 383.
6. S. Shuheia and M. Shimomura, "Academia that utilizes the shapes and abilities of living things "Biomimetics" Chapter 1 Definition and history of biomimetics, future prospects, National Science Museum 16", *Tokai University Press*, 2-11 (2016). [in Japanese]
7. J. Knippers, K. G. Nickel, and T. Speck, "Biomimetic Research for architecture and Building Construction, Biological Design and Integrative Structures, Biologically Inspired Systems Vol. 8", *Springer*, 69 (2016).
8. C. Tendero, C. Tixier, P. Tristant, J. Desmaison, and P. Leprince, *Spectrochimica Acta Part B: Atomic Spectroscopy*, **61** (2006) 2.
9. C. Jen-shin, *J. Plasma Fusion Res.*, **82** (2006) 6288.
10. M. Kogoma, *J. Surf. Finish. Soc. Jpn. (Hyomen Gijutsu)*, **58** (2007) 779 (in Japanese).
11. T. Murakami, *J. Plasma Fusion Res.*, **92** (2016) 688 (in Japanese).
12. K. Shinagawa, H. Shindo, K. Kusaba, T. Koromogawa, J. Yamamoto, and M. Furukawa, *Jpn. J. Appl. Phys.*, **40** (2001) 5856.
13. E. P. G. T. van der Ven and H. Kalter, *Electrochem. Soc. Ext. Abst.*, **76-1** (1976) 332.
14. A. Sekiguchi, M. Yamamoto, T. Kumagai, Y. Mori, H. Minami, M. Aikawa and H. Horibe, *J. Photopolym. Sci. Technol.*, **34** (2021) 401.

Developing an endoscope lens with anti-fogging and anti-fouling properties using nanoparticle materials

Atsushi Sekiguchi^{1*,2}, Hiroko Minami²

¹ Osaka Prefecture University, Department of Physics and Electronics
1-1 Gakuen-cho, Naka-ku, Sakai, Osaka 599-8531, Japan

² Litho Tech Japan corporation
2-6-6 Namiki, Kawaguchi, Saitama 332-0034, Japan

*tas35035@osakafu-u.ac.jp

Endoscopes are widely used in clinical settings. Gastric endoscopes in particular are useful for detecting early-stage gastric cancers and polyp removal. During polyp removal or other simple surgical procedures, however, the spatter of blood and bodily fluids resulting from excision of the affected areas can fog the endoscope lens. Condensation caused by temperature differences between the instrument interior and exterior can also affect image clarity. Any obstruction of the field of view during the surgical procedure must be addressed by removing the endoscope and cleaning the lens; however, doing so prolongs the time required for the procedure, makes it more invasive, and increases patient burdens. Drawing on biomimicry principles, we developed an endoscope lens with anti-fogging and anti-fouling features. This paper reports our results.

Keywords: Endoscope, Less invasive, Biomimetics, Nano-particle resists, ZrO₂ nanoparticles, Baking method

1. Introduction

Our study applied biomimetics to the development of a technology to improve the anti-fouling properties of surfaces, regardless of substrate shape. The field of technologies based on the imitation of properties and structures observed in living organisms is known as biomimetics [1-3]. As the observation There are no dirty snails suggests, snail shells have long been known to have superior anti-fouling properties. Snail shells have both convex and concave nanoscale structures on their surfaces (Fig. 1).

A thin film of water formed when water collects on the surface of the shell repels staining by oils and other substances. The structure is referred to as a ultrahydrophilic nanoscale structure, whose properties repel oils containing proteins and confer antifouling properties (Fig. 2).

Endoscopes are widely used in clinical settings. Gastric endoscopes in particular are useful for detecting early-stage gastric cancers [4] and polyp removal. During polyp removal or other simple surgical procedures, however, the spatter of blood

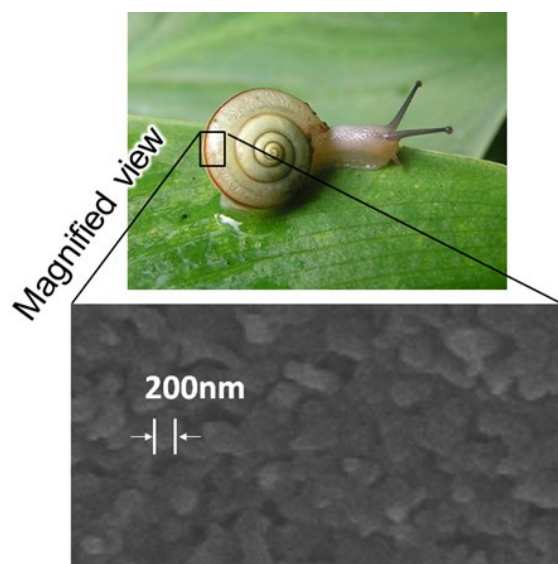


Fig. 1. Structure of a snail shell.

Received March 31, 2022
Accepted June 24, 2022

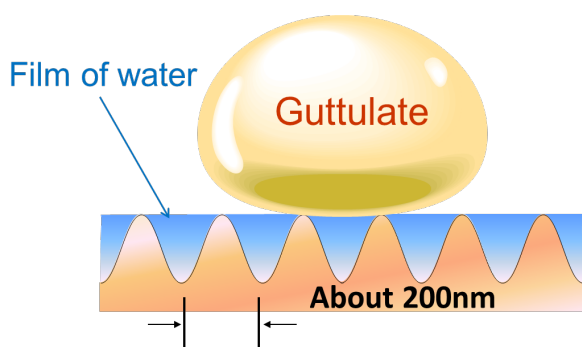


Fig. 2. Mechanism underlying ultrahydrophilic nanoscale structure.

and bodily fluids resulting from excision of the affected areas can fog the endoscope lens. Condensation due to temperature differences between the internal and external areas of the instrument can also affect image clarity. Any obstruction of the field of view during the surgical procedure must be addressed by removing the endoscope and cleaning the lens; however, doing so prolongs the time required for the procedure, makes it more invasive, and increases patient burdens [5,6]. Drawing on biomimetic principles, we developed an endoscope lens with anti-fogging and anti-fouling properties. By forming a convex-concave nanoscale structure mimicking a snail shell on the surface of the endoscope lens, we hoped to impart nanoscale ultrahydrophilic properties. As reported in an earlier paper, to examine the feasibility of a biliary stent offering anti-fouling properties, we formed minute convex-concave structures on the interior surface of a polyethylene stent by the atmospheric pressure plasma method to impart anti-fouling properties [7–11]. Our current paper discusses ultrahydrophilic nanoscale

structures formed on quartz glass by baking nanoparticle materials onto the surface and potential applications to endoscope lenses.

2. Ultra nanoparticle materials

Extreme ultraviolet (EUV) lithography is currently emerging as one the most advanced lithographic technologies [12–14]. In EUV lithography, light with a wavelength of 13.5 nm is employed to form electric circuits (resist patterns) at sub-10-nm scales. Such fine patterning processes requires photosensitive materials of extremely fine molecular structures [15]. In a study of metal oxide nanoparticles undertaken by a team at Cornell University [16] as part of research on high refractive index resists [17] and immersion liquids for ArF immersion lithography, researchers formed metal oxide nanoparticles by the sol-gel process [18], which involves forming sol (colloidal) solutions from solutions of metal alkoxides through hydrolysis and condensation polymerization, then promoting the reaction to form a solid gel [19]. This method was successfully applied to EUV lithography to form patterns at sub-10-nm scales [20].

Figure 3 illustrates the basic structure of a metal oxide nanoparticle.

The core consists of an amorphous metal oxyacid. The ligand of the shell molecule corresponding to its counterion is in an anionic state—for example, carboxylate (RCOO^-). Examples of ligands include methacrylic acid (MAA), 2,3-dimethylacrylic acid (DMA), benzoic acid (BA), isobutyric acid (IBA), and 3-(trimethoxysilyl)propyl-methacrylate (TSM) [21].

Our study used ZrO_2 as the core and MAA as the ligand.

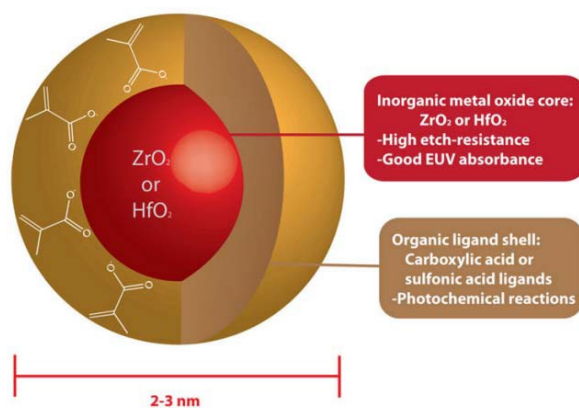
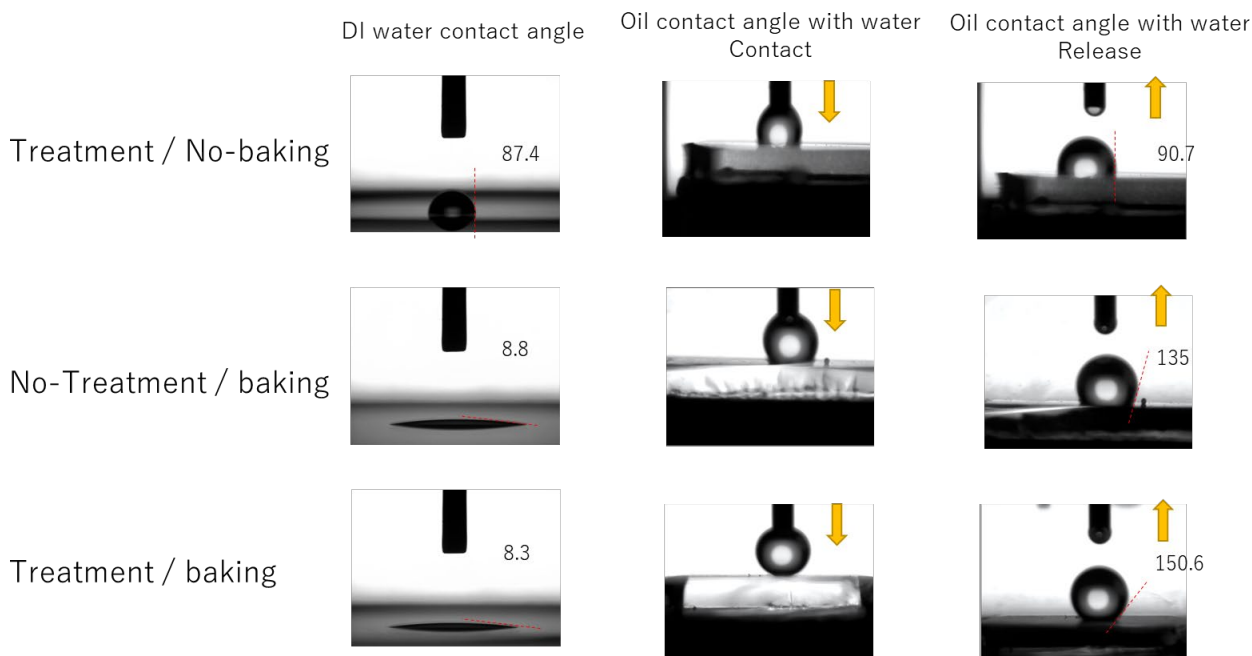


Fig. 3. Structure of metal oxide nanoparticle.

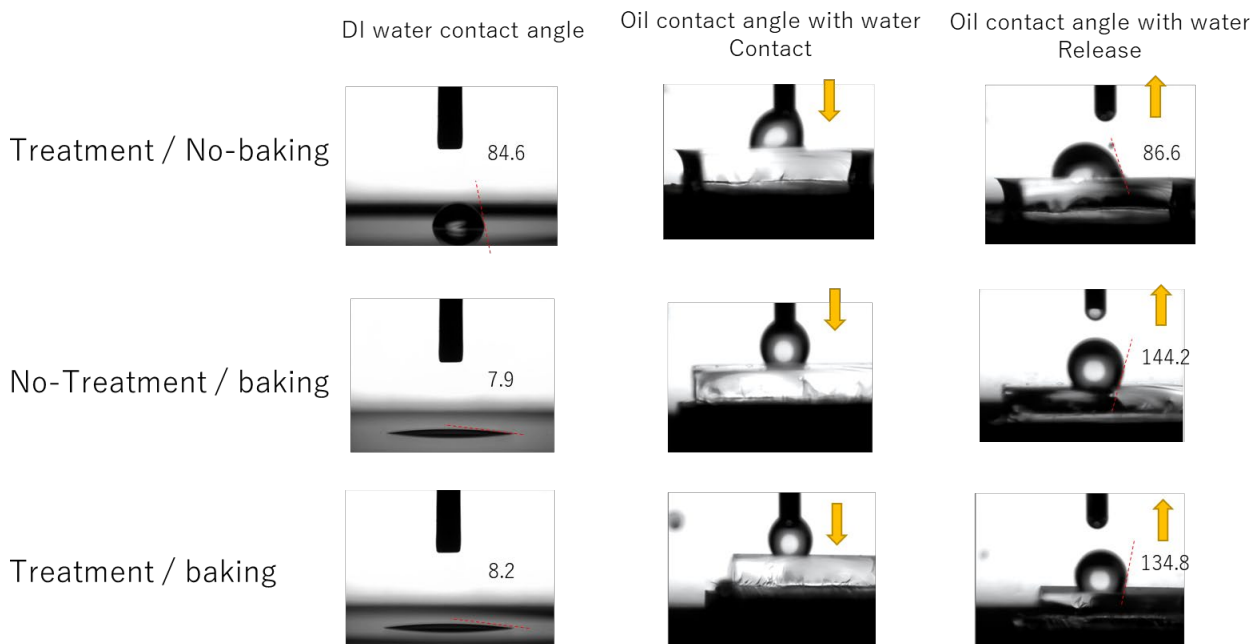
3. Fabricating ultrahydrophilic nanoscale structures

We dispersed ultra nanoparticle materials in a butyl acetate solution and spin-coated this solution onto a quartz substrate, then baked the substrate at 80 °C for 60 seconds. The film thickness at this

point was 24 nm. We chemically treated the film to remove most of the nanoparticle materials and form a single-molecule film on the substrate; we then baked the substrate in an electric furnace at 800 °C for 30 minutes in a nitrogen atmosphere to fabricate a concave-convex structure on the scale of



(a) 2 nm of core particle diameters

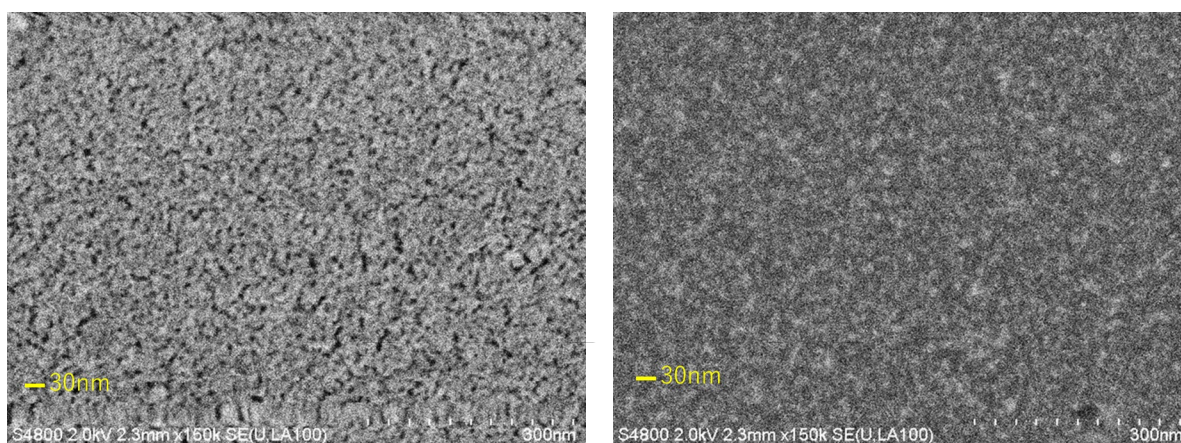


(b) 5 nm of core particle diameters

Fig. 4. Evaluating hydrophilic properties and oil repellency in water for substrates baked and not baked.

Table 1. Contact angle for each fabrication state.

Core size	Baking (800 °C)	Di water CA	Oil CA with water
2	without	87.4	90.7
2	with	8.8	135.0
2	with	8.3	150.6
5	without	84.6	86.6
5	with	7.9	144.2
5	with	8.2	134.8



(a) Without treatment

(b) With treatment

Fig. 5. Images from SEM observations of substrate fabricated using nanoparticle materials with core diameter of 2 nm (baking temperature 800 °C).

several nanometers on the substrate surface.

Figure 4 shows the hydrophilic properties and oil repellency in water of substrates having an ultra nanoporous structure formed using ultra nanoparticle materials with core diameters of 2 nm and 5 nm.

If the substrate is not baked, the results show that neither substrate, whether having a core diameter of 2 nm nor 5 nm, is hydrophilic; additionally, their oil repellency in water (anti-fouling property) is poor. In contrast, baked substrates exhibit ultrahydrophilic properties ($CA < 8^\circ$) whether or not

they have undergone chemical treatment. With regard to oil repellency, contact angles were 150.6° and 134.8° , respectively, for treated substrates with a core diameter of 2 nm and 5 nm. Both exhibited high oil repellency.

Figure 5 shows the results of SEM observations of substrates fabricated using nanoparticle materials with a core diameter of 2 nm.

Ultra nanoporous structures are visible on untreated substrates. Treated substrates exhibit a single-molecule convex-concave structure.

4. Transparency

Figure 6 presents spectral transmittance data for substrates fabricated using nanoparticles of core diameters of 2 nm and 5 nm.

We confirmed absorption in the DUV region (190–250 nm) for substrates with a core diameter of 5 nm. In contrast, the substrate with a core diameter of 2 nm exhibited high transparency, even in the DUV region. Given the obvious preference for materials of higher transparency as lens materials, we found the substrate made with 2 nm nanoparticles more suitable for our purposes.

5. Mounting evaluation test

We evaluated the anti-fogging properties of

substrates fabricated using nanoparticles with core diameters of 2 nm and 5 nm. To evaluate anti-fogging performance, we heated a water-filled beaker to 65 °C, then set each substrate above the beaker at a height of 10 mm from the surface of the water (Fig. 7).

All tested substrates were treated and baked at 800 °C. A quartz substrate without treatment was used as the blank. With the blank substrate, we observed fogging after 1 minute and observed water droplets beginning to form after 3 minutes. On the surface of the substrate with a core diameter of 2 nm, we observed only minor fogging. The substrate with the 5 nm core diameter remained clear even after 1 minute, but water droplets began to form on

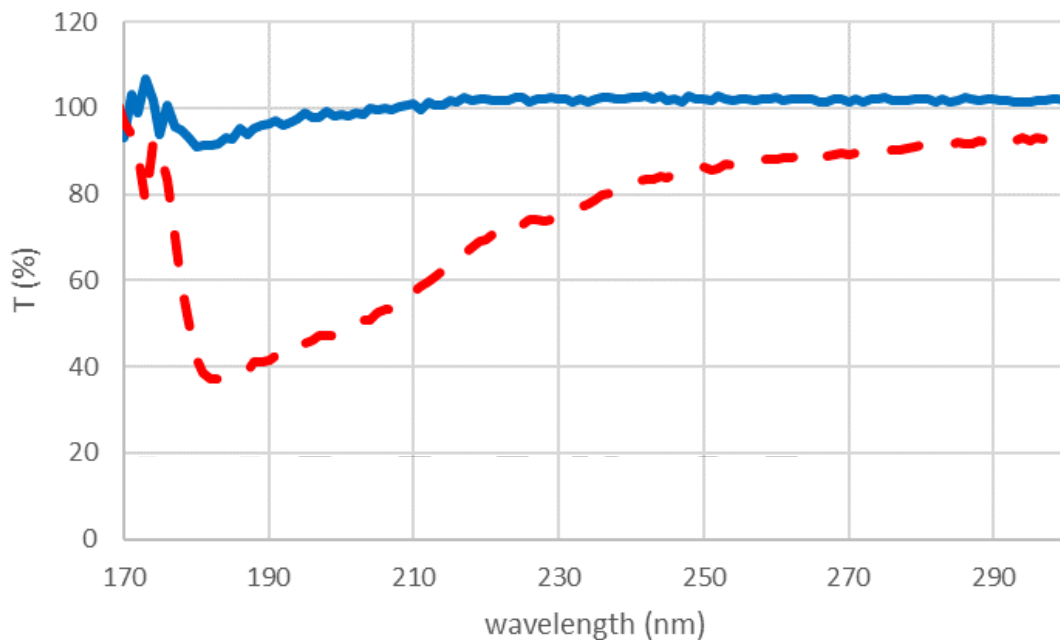


Fig. 6. Spectral transmittance of substrates formed using nanoparticles of core diameters of 2 nm and 5 nm.

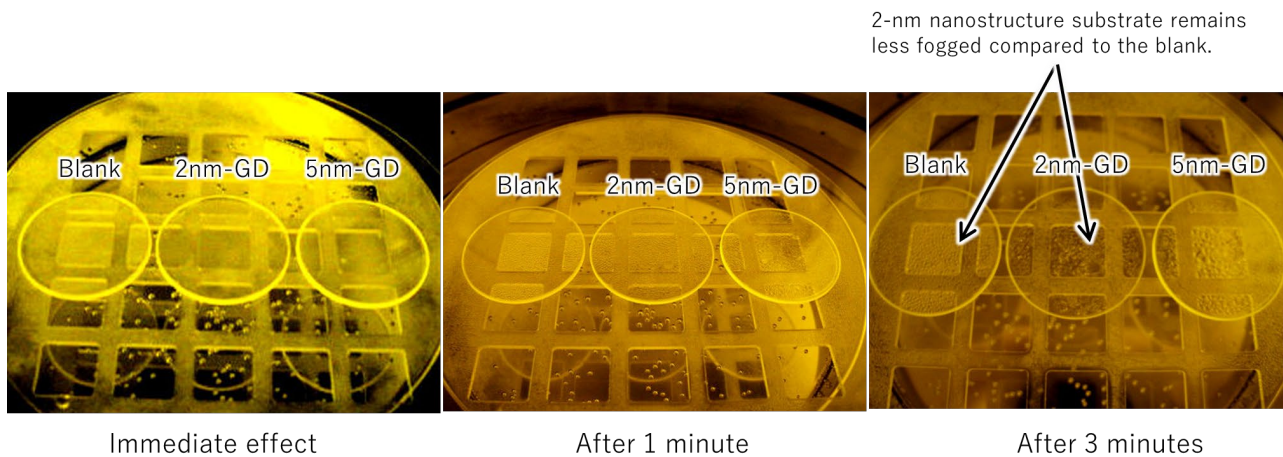
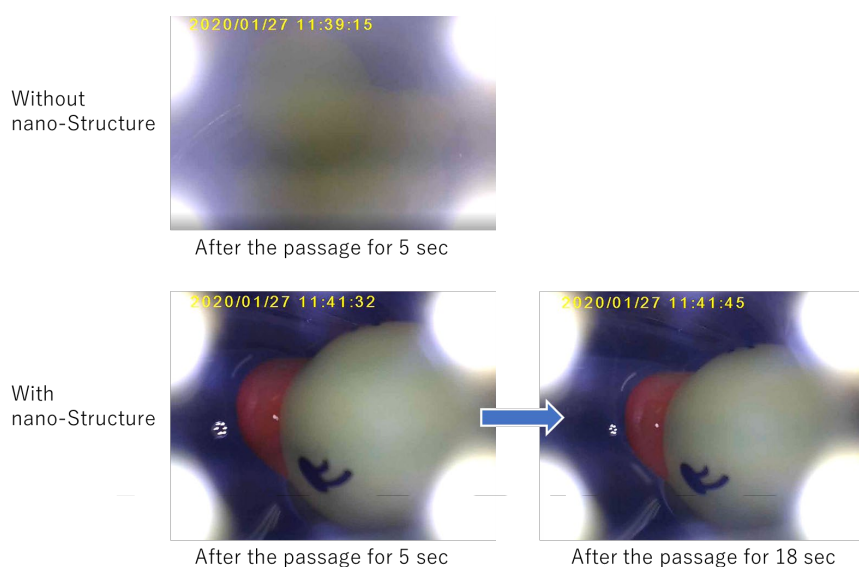


Fig. 7. Comparison of anti-fogging effect.



(a) Mounted on endoscope



(b) Comparison of anti-fogging effect

Fig. 8. Endoscope mounting test.

the surface after 3 minutes. These results indicate superior anti-fogging performance for the substrate with a core diameter of 2 nm.

Next, we produced a prototype endoscope lens using nanoparticle materials with a core diameter of 2 nm and mounted it onto an endoscope to confirm anti-fogging properties. The prototype lenses were made of quartz glass substrates fabricated with and without treatment at a baking temperature of 800 °C (Fig. 8 (a)).

To evaluate fogging, we heated a water-filled beaker to 40 °C and inserted the endoscope into the beaker so that the tip of the endoscope stood 20 mm from the surface of the water. Figure 8 (b) shows the results. The untreated lens began to fog immediately after the endoscope was inserted into the beaker. In contrast, the lens with the surface

fabricated with the nanoporous structure remained fog-free even after 18 seconds and provided a clear field of view.

6. Assessment of self-cleaning effect

We assessed the self-cleaning effect. We wetted an untreated substrate and a treated substrate with nanoporous structure with 1 ml of water. We placed an oil droplet on each surface with a Pasteur pipette, then attempted to rinse off the oil with water. We found that the oil remained on the surface of the substrate without treatment even after several washes; in contrast, oil on the substrate with the nanoporous structure was easily rinsed off. Since endoscopes incorporate a mechanism for releasing water from the tip, a lens with a nanoporous coating would allow rapid self-cleaning when needed.

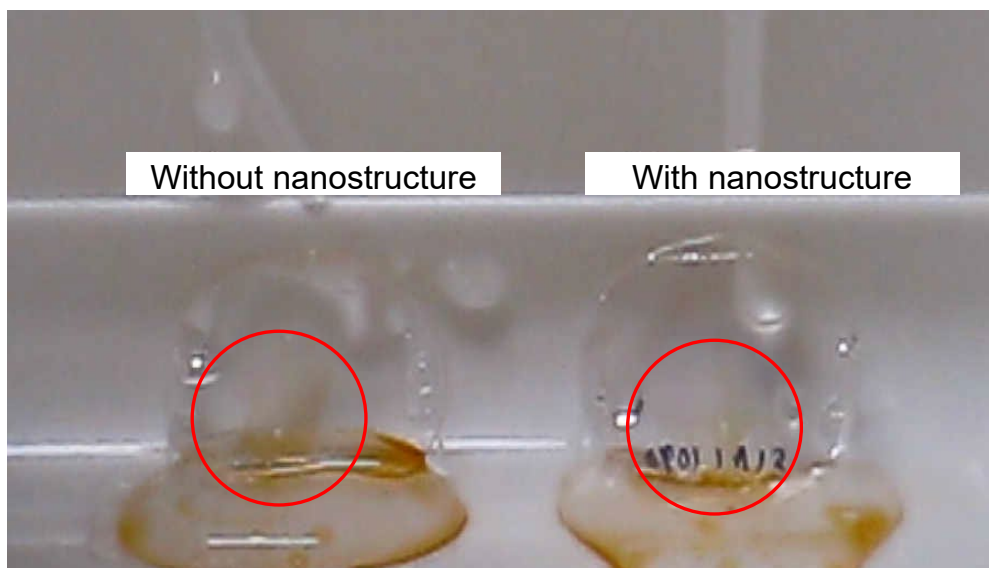


Fig. 9. Comparison of self-cleaning effect.

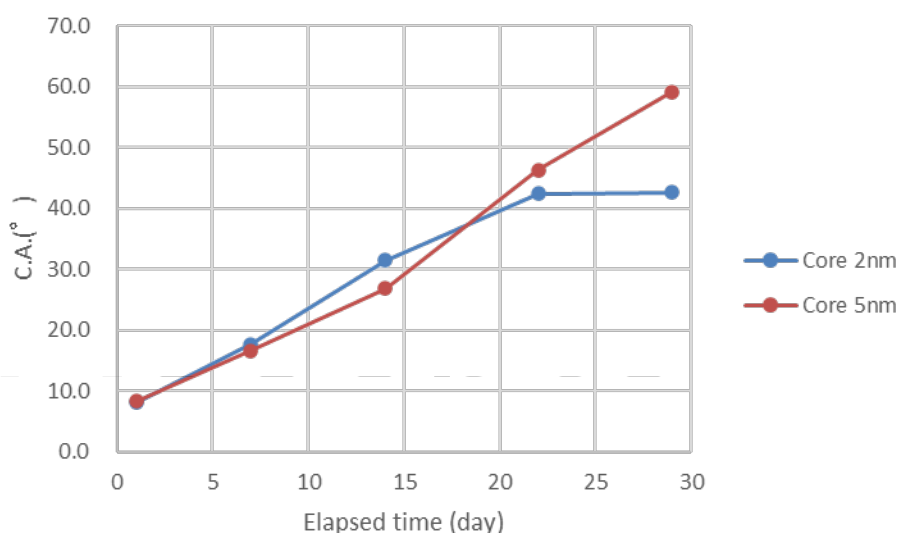


Fig. 10. Relationship between elapsed time and contact angle.

7. Themes for future studies

Figure 10 shows the change in contact angle with elapsed time of the baked substrate. We see that the contact angle increases with elapsed time. This increase in contact angle is believed to be caused by the adhesion of organic matter to the porous surface. Both anti-fogging and anti-fouling properties degrade with increasing contact angles.

8. Summary

Employing metal nanoparticle resists used in EUV lithography, we fabricated nanoscale ultrahydrophilic substrates with nanoporous structures formed on the substrate surface. We then applied this technology to an endoscope lens and assessed the resulting anti-fogging and anti-

fouling effects. Our results demonstrated that this procedure confers both high anti-fogging and anti-fouling properties. However, we also discovered that these effects degrade over time when the lens is left under ordinary conditions due to contamination by organic matter. Further study is required to identify methods for maintaining these properties and to develop surface rejuvenation technologies.

Acknowledgements

We wish to express our gratitude to Mr. Fujiwara of Mitsubishi Chemical Corporation for the nanoparticle materials used in the present study.

References

1. M. Shimomura, "Biomimetics, National Science Museum16", Tokai University Press, 2

- (2016).
2. R. N. Wenzel, *Ind. Eng. Chem.*, **28** (1936) 988.
 3. Y. C. Jung and B. Bhushan, *J. Microsc.*, **229** (2008) 127.
 4. D. Hirata, A. Teramoto, M. Iwatate, S. Hattori, and W. Sano, *Colon cancer perspective 2019 4 (3)* (2019) 27 (in Japanese).
 5. T. Utsumi, Y. Sano, M. Iwatate, H. Snakawa, A. Teramoto, D. Hirata, S. Hattori, W. Sano, N. Hasuike, K. Ichikawa, and T. Fujimori, *World J Gastrointest Oncol*, **10(4)** (2018) 96.
 6. Y. Sano, H. Chiu, X. Li, S. Khomvilai, P. Pisespongsa, J. Co, T. Kawamura, N. Kobayashi, S. Tanaka, D. Hewett, Y. Takeuchi, K. Imai, T. Utsumi, A. Teramoto, D. Hirata, M. Iwatate, R. Singh, S. Ng, S. Ho, P. Chiu, and H. Tajiri, *Digestive Endoscopy*, **31** (219) 227.
 7. A. Sekiguchi, T. Nishino, M. Aikawa, Y. Matsumoto, H. Minami, K. Tokumaru, F. Tsumori, and H. Tanigawa, *J. Pohotopolym. Sci. Technol.*, **32** (2019) 373.
 8. A. Sekiguchi, T. Nishino, H. Tanigawa, H. Minami, Y. Matsumoto, and H. Mayama, *J. Pohotopolym. Sci. Technol.*, **33** (2020) 205.
 9. A. Sekiguchi, M. Yamamoto, T. Kumagai, Y. Mori, H. Minami, M. Aikawa, and H. Horibe, *J. Pohotopolym. Sci. Technol.*, **34** (2021) 401.
 10. M. Yamamoto, Y. Mori, T. Kumagai, A. Sekiguchi, H. Minami, and H. Horibe, *J. Pohotopolym. Sci. Technol.*, **34** (2021) 385.
 11. A. Sekiguchi, *C & I commun Vol46, No.4* (2021) 1.
 12. H. Kinoshita, T. Kaneko, H. Takei, N. Takeuchi, and S. Ishihara, *47th Autumn Meeting of the Japan Society of Applied Physics*, **28-ZF-15** (1986) 332 (in Japanese).
 13. H. Kinoshita, K. Kurihara, T. Mizota, T. Haga, H. Takenaka, and Y. Torii, *Appl. Opt.*, **32** (1993) 7079.
 14. T. Haga, M. Tinone, H. Takenaka, and H. Kinoshita, *Microelectron Eng.*, **30** (1996) 179.
 15. Y. Ekinci, M. Vockenhuber, M. Hojeij, L. Wang, and N. Mojarad, *Proc. SPIE*, **8679** (2013) 867910.
 16. W. J. Bae, M. Trikeriotis, R. Rodriguez, M. F. Zettel, E. Piscani, C. K. Ober, E. P. Giannelis, and P. Zimmerman, *Proc. SPIE*, **7273** (2009) 727326.
 17. M. E. Krysak, J. M. Blackwell, S. E. Putna, M. J. Leeson, T. R. Younkin, S. Harlson, K. Frasure, and F. Gstrein, *Proc. SPIE*, **9048** (2014) 904805.
 18. C. J. Brinker and G. W. Scherer, "Sol-Gel Science", Academic Press (1990).
 19. S. Chakrabarty, C. Sarma, L. Li, E. P. Giannelis, C. K. Ober, *Proc. SPIE*, **9048** (2014) 90481C.
 20. M. Trikeriotis, M. Krysak, Y. S. Chung, C. Ouyang, B. Cardineau, R. Brainard, C. K. Ober, E. P. Giannelis, K. Cho, *Proc. SPIE*, **8322** (2012) 83220U.
 21. C. Y. Ouyang, Y. S. Chung, L. Li, M. Neisser, K. Cho, E. P. Giannelis, C. K. Ober, *Proc. SPIE*, **8682** (2013) 86820R.

Evaluation of Surface-Enhanced Raman Scattering Substrate Consisting of Gold Nanoparticles Grown on Nanoarrays of Boehmite Fabricated using Magnetron Sputtering Process

Taku Tanaka*, Syunya Saegusa, Masayuki Naya, Takao Fukuoka, Sho Amano, Yuichi Utsumi, Akinobu Yamaguchi

Laboratory of Advanced Science and Technology for Industry, University of Hyogo, 3-1-2 Kouto, Kamigori, Ako, Hyogo 678-1205, Japan
*tt1413@lasti.u-hyogo.ac.jp

A surface-enhanced Raman scattering (SERS) active structure allows the highly sensitive imaging of label-free molecular trace. A gold nanostructure with boehmite as a skeleton was fabricated by the inclined magnetron sputtering method. The characteristics of the prepared SERS imaging plate consisting of gold nanostructure on boehmite were evaluated as the follows. The distance dependence of the SERS intensity of 4,4'-bipyridine from the edge of the substrate indicated that the larger the SERS intensity becomes as the closer the distance approaches the substrate edged where the gold nanolayer was thicker. The trend of SERS dependence on distance was more pronounced at higher concentration of molecule and less pronounced at lower concentration. Using the SERS imaging plate will enable the further demonstration of ultrasensitive detection of chemical and biological molecules as environmental contaminants within a broad range of common fluids for potential applications related to analytical chemistry and environmental monitoring.

KEYWORDS: Surface-enhanced Raman scattering, Boehmite, Nanoscale gaps

1. Introduction

In general, plastics are widely used in modern society because they are light, easy to form various shapes, and inexpensive. Furthermore, they have long-term stability and keep their own material characteristics. However, this long-term stability has become a detriment, as they do not decompose even after a long period of time, resulting in causing serious environmental problems [1, 2]. A variety of discarded plastic products are leaking into the ocean, threatening the marine ecosystem. One of the major environmental problems is how to manage and dispose of the increasing amount of plastics that are discharged. Recently, to solve this problem, biodegradable plastics, which degrade in the natural environment, are attracting attention and have been developed by several research groups and companies [3 - 5].

Generally, biodegradable plastics are degraded to water and carbon dioxide by microbial enzymes or hydrolysis to lower molecular weight. Then, they can be metabolized by microorganisms. However, the mechanism of microbial degradation of plastics in the marine environment has not been elucidated

yet. It is very important to clarify the structure of plastics suitable for degradation and the degradation ability of enzymes.

The precise evaluation for the degradation of biodegradable plastics is difficult because the plastics left in the lump changes little in a short time and the degraded molecules taken up by the cells through the endocytosis are undetectable.

Surface enhanced Raman Scattering (SERS) is a spectroscopic technique that can obtain Raman scattering intensities up to 10^{14} times higher than those of conventional Raman spectroscopy due to the electric field enhancement effect in the noble metal nanostructured gaps. The SERS enables us to detect a single molecule [6-16]. Raman spectroscopy has attracted much attention as a powerful analytical technique to understand the spatio-temporal dynamics of biomolecules in cells for in vivo or in vitro monitoring of biomolecules. However, in conventional Raman spectroscopy, the weak Raman light makes it difficult to perform rapid molecular sensing at small concentrations. The SERS enables label-free, non-destructive, real-time quantitative chemical composition analysis

Received	March 31, 2022
Accepted	June 20, 2022

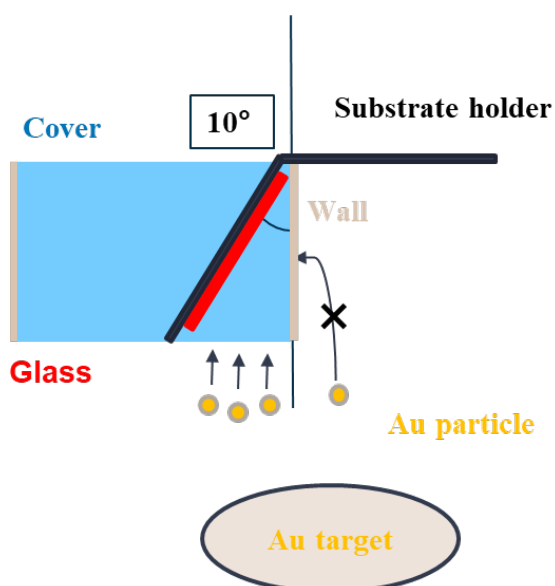


Fig. 1 Schematic diagram of incline magnetron sputtering and designed jig.

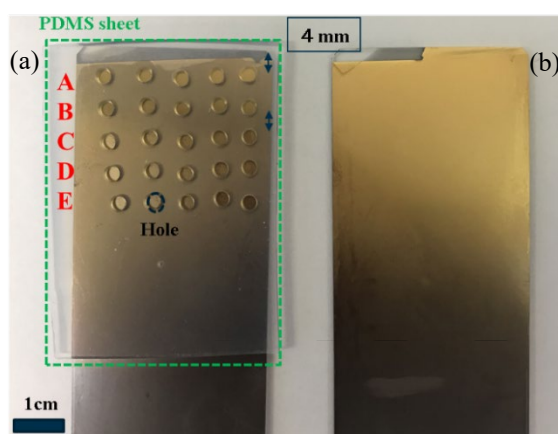


Fig. 2 Photographs of prepared SERS-active substrate (a) with and (b) without PDMS sheet with 25 punched holes (wells).

without selecting molecules. However, there is some issues for improvement in the observation range and sensitivity. Until now, it is insufficient for real-time imaging. The use of the SERS-active structure, gold nanofève (GNF) substrate, which utilizes the boehmite structure, enables observation with a wide range, high sensitivity, and high resolution [17-18]. The GNF substrate was fabricated by an incline electron beam deposition [19 - 22]. This manufacturing method is a very simple and useful. However, it has a problem that the structure has poor adhesion to the substrate and fragile. Therefore, it is also difficult to mount the GNF structure on a microchemical system. The further research and development are required for improving the manufacturing process to conduct the stronger adhesion because the SERS-active substrate can be

mounted in the microchemical system for studying the evaluation of decomposition process of plastics in vivo monitoring.

In general, the adhesion of film deposited by the magnetron sputtering technique is stronger than that of film made by the vapor electron beam deposition technique because the sputtered atoms have higher energy and go deeper into the layered to be joined. In this study, to integrate the microfluidic channel on this SERS-active substrate, we study for the replacement of the electron beam deposition process with the magnetron sputtering process in the SERS-active layer formation process. Next, we evaluated the characteristics of the GNF substrate fabricated by the magnetron sputtering process. We investigated the distance dependence of the SERS intensity of 4, 4'-bipyridine (4bpy) as the observables.

2. Experimental

2. 1. SERS imaging plate preparation

The GNF based SERS imaging plate was fabricated by the magnetron sputtering. Gold layer was deposited onto a boehmite, that is a type of alumina oxide, on a glass slide. The gold layer was deposited obliquely by the sputtering. The preparation procedure was described as follows. First, glass slides were cleaned to remove dirt from the surface. The glass slides (purchased by Matsunami co. ltd.) were washed with acetone for 10 min, isopropanol (IPA) for 10 min, and pure water for 10 min. Next, the cleaned glass slides were set in the magnetron sputtering apparatus. Then, after 10 min of back sputtering, films with a thickness of 7 nm for Cr and 84 nm for Al were sequentially deposited. The sputtered substrates were immersed in boiling water for 10 min, and then the water was blown by nitrogen air. This procedure enabled the formation of a boehmite substrate.

Next, in order to create SERS-active structures, it is important to fabricate anisotropic nanopores (nanoscale gaps) in the longitudinal direction. In some previous studies, the oblique deposition method using an electron beam was used [19-22]. The electron beam evaporation can provide the easy fabrication of the desired structure because the atomic and molecular beams have a straightness and good controllability of thin film formation. On the other hand, in magnetron sputtering, the sputtered atoms and molecules are plasmaized in the vacuum chamber and do not travel in a straight line as in electron beam deposition.

To prevent the sputtered atoms from wrapping

around and adhere to the undesired area, the film formation path was limited. A special jig was installed into the magnetron sputtering chamber. Figure 1 shows a schematic diagram of the positional relationship between the cover, glass and gold (Au) target in the magnetron sputtering chamber. The glass was set on a substrate holder tilted at 10° and covered with a cover. The wall of the cover prevented the penetration of the sputtering particles from going around, and the film was deposited only with particles from almost directly below. After the preparation of the boehmite substrate, Cr sputtering of 7 nm and Au sputtering of 230 nm were carried out. Consequently, GNF structure was fabricated along the longitudinal direction of glass substrate.

2. 2. Evaluation of SERS substrates

Figure 2 shows the fabricated GNF substrate consisting of gold nanostructure deposited on boehmite substrate. As shown in Fig. 2, at a glance, it is clear that the color shade is distinct. This indicates that a gradient in the thickness of the gold film is formed by oblique sputtering. The upper surface of the glass substrate in Fig. 2 is closer to the sputtering target. To evaluate the SERS activity, we prepared a structure with holes of 2 mm in diameter drilled at intervals of 4 mm in distance from the top edge of the glass as shown in Fig. 2. The well structure was fabricated by Poly (dimethylsiloxane) (PDMS). Five different concentrations of 4bpy dispersed in pure water were prepared to investigate the characteristics of SERS intensity. The prepared concentrations were 10 μM , 2 μM , 500 nM, 200 nM, and 100 nM, respectively. The water reservoir structure was arranged as shown in Fig. 2 to investigate the molecular concentration and position dependence of SERS activity on the GNF substrate. In Fig. 2(a), the indexes A, B, C, D, and E denote the positions for every 4 mm in order from the one closest to the top of the glass. Below, we described the distance dependence of SERS intensity.

To evaluate the dependence of the gold film thickness on the distance from the edge of the glass substrate, 4bpy was dropped into the wells at positions A, B, C, D, and E from the edge of the substrate, as shown in Fig. 2. In order to investigate the concentration dependence simultaneously, different concentrations of the solution were dropped at positions A, B, C, D, and E. The SERS measurements were totally performed at $5 \times 5 = 25$ positions. After drying, Raman spectra were

measured at each position. In addition, five SERS-active substrates were fabricated under the same conditions in order to acquire the statistical accuracy and the process variation of the substrate fabrication.

3. Results and discussion

Figure 3 shows the characteristic Raman spectrum of 4bpy measured by the prepared SERS-active substrate. There are two vibration modes of 4bpy. One is the in-plane vibration mode when pyridine rings are oscillating only in plane. The other is the out-of-plane vibration mode including vibration components normal to the pyridine ring plane. Here, 1020 cm^{-1} is ring stretching vibration mode ν_{ring} ; peaks around 1080, 1230, and 1300 cm^{-1} correspond to $\nu_{\text{ring}} + \gamma_{\text{CH}}$, γ_{CH} , and $\gamma_{\text{CC}} + \gamma_{\text{CH}}$, respectively. A highest peak near 1580 cm^{-1} corresponds to molecular stretching vibration mode of 4bpy [23 - 24]. Below, we will investigate the change in the peak intensity at 1580 cm^{-1} depending on the distance from the top edge of the glass and the concentration of 4bpy.

Figure 4 shows the summary of relationship between the distance from the top edge of the glass and the Raman peak intensity at 1580 cm^{-1} . The Raman peak intensity is defined as peak height as shown in Fig. 3. We plotted the mean value and standard deviation of the measured peak intensity values for the five substrates. It can be seen that the Raman intensity decreases as the distance from the glass edge near the gold sputtering target increases. This distance dependence is more pronounced for higher concentrations of 4bpy and less pronounced for lower concentrations.

Next, the SERS intensities are plotted as a function of the 4bpy concentration in Fig. 5. The SERS peak intensity increases with increasing the 4bpy concentration regardless of the distance from the top of the glass. When the concentration of 4bpy was increased by a factor of 4 from 500 nM to 2 μM , the Raman peak intensities doubled at all distances. However, when the concentration of 4bpy was increased by a factor of 5 from 2 μM to 10 μM , the Raman peak intensity increased only by a factor of 1.2 to 1.3. That is, it was found that the SERS intensity did not increase linearly with respect to the concentration, but tended to saturate.

In order to examine these features mathematically, fitting was performed. At distances A, B, C, D, and E, respectively, $y = 585.26x^{0.3473}$, $y = 397.24x^{0.3574}$, $y = 427.25x^{0.3354}$, $y = 452.56x^{0.3168}$, and $y = 519.78x^{0.2691}$, respectively. Here, y and x denote the

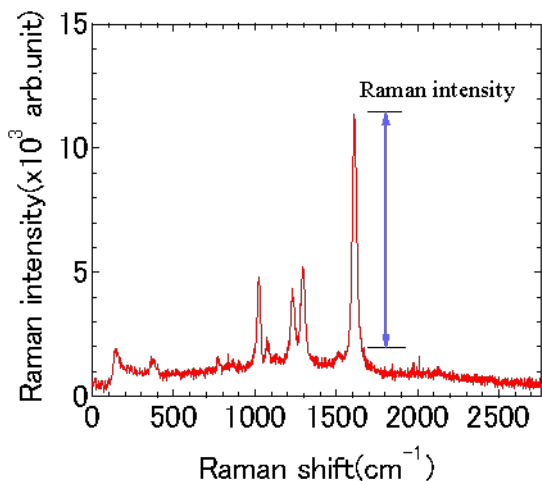


Fig. 3. Typical SERS spectrum of 4bpy measured by using the SERS-active substrate.

SERS intensity and concentration of 4bpy, respectively. It was found that the relationship between the concentration and the Raman intensity is a power function. This result shows a value similar to that of previous study [25].

In the present SERS-active structure, the nanoscale gaps derived from the boehmite are almost uniformly distributed on the glass substrate, and the gold thickness has a slope in the longitudinal direction of the substrate due to the oblique sputtering process. As described the above, the SERS intensity strongly depends on positions, indicating that the spatial gold nanostructure distribution affects the SERS activity. The measured dependence of Raman intensity on concentration and spatial distribution could be derived from the following two factors. One is that the concentration of gold nanopores (nanoscale gaps between GNFs)

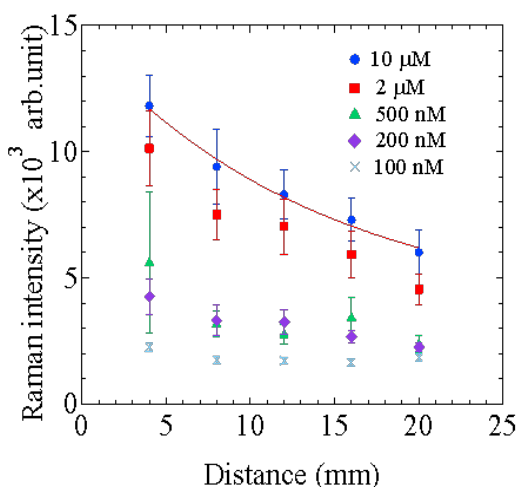


Fig. 4. Relationship between distance and Raman intensity.

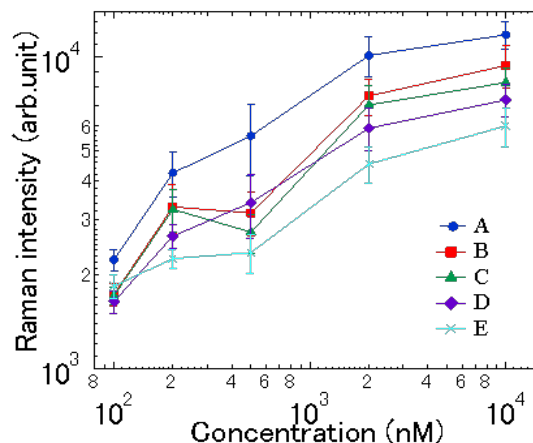


Fig. 5. Relationship between concentration and Raman intensity. Legends A, B, C, D, and E correspond to the relative positions in Figure 2.

for generating the electric field enhancement effect depends on the nanoscale gap distance which depends on the distance from the top edge of the substrate due to the incline sputtering deposition. As a result, in our SERS substrate, the thicker the gold thin film is, the higher the SERS activity is, so that more sensitive SERS detection is possible. Regarding the concentration dependence, the higher the concentration, the higher the concentration of hotspot formation, which enables stronger SERS signal detection. Therefore, the higher the concentration and the thicker the gold thin film, the stronger the SERS signal. However, when the gold thin film becomes thick enough to prevent the formation of nanoscale gaps, the SERS activity is lost. At this film thickness, the thickness was not sufficient to prevent the formation of nanoscale gaps which have the SERS activity, so the above results were obtained. We have succeeded in producing a molecular imaging plate having a size of about 2 mm × 2 mm and having sufficient SERS activity for the analysis of plastic decomposition process in microchemical systems.

5. Conclusion

We fabricated the SERS-active imaging plates with GNF structures by using the incline magnetron sputtering process. The spatial distribution and molecular concentration dependence of SERS activity were evaluated. As a result, it was found that the thicker the gold thin film, the higher the SERS activity. In addition, the concentration dependence of SERS intensity became a function of power, and the results were consistent with the results reported previously. We succeeded in obtaining sufficiently excellent SERS activity in the

region of 2 mm × 2 mm. From this result, it can be said that we have succeeded in creating a SERS analysis substrate that can be used for plastic decomposition processes and other environmental analysis. By introducing it into a microchemical system, we will be able to expect molecular tracking in a system that simulates the biological environment.

6. References

1. R. Bouhroum, A. Boulkamh, L. Asia, S. Lebarillier, A. Ter Halle, A. D. Syakti, P. Doumenq, L. Malleret, and P. Wong-Wah-chung, *Regional Studies in Marine Science*, **29** (2019) 100611.
2. R. Bouhroum, A. Boulkamh, L. Asia, S. Lebarillier A. Ter Halle, A. Dhamar Syakti, P. Doumenq, and P. Wong-Wah-Chung, 15th *International Conference on Environmental Science and Technology (CEST2017) 00855* (2017).
3. Maja Rujnić-Sokele and Ana Pilipović, *Waste Management & Research*, **35** (2017) 132.
4. T. M. Aminabhavi, R. H. Balundgi, and P. E. Cassidy, *Talor Francis*, **29** (1990) 235.
5. Roohi, Bano Kulsoom, Kuddus Mohammed, R. Zaheer, Zia Qamar, F. Khan, Md. Ashraf, Gupta Anamika, and Aliev Gjumrakch, *Current Pharmaceutical Biotechnology*, **18** (2017) 429.
6. Megumi Shiota, Masayuki Naya, Takehiro Yamamoto, Takako Hishiki, Takeharu Tani, Hiroyuki Takahashi, Akiko Kubo, Daisuke Koike, Mai Itoh, Mitsuyo Ohmura, Yasuaki Kabe, Yuki Sugiura, Nobuyoshi Hiraoka, Takayuki Morikawa, Keiyo Takubo, Kentaro Suina, Hideaki Nagashima, Oltea Sampetreat, Osamu Nagano, Hideyuki Saya, Shogo Yamazoe, Hiroyuki Watanabe, and Makoto Suematsu, *nature communications*, **9** (2018) 1561.
7. Shogo Yamazoe, Masayuki Naya, Megumi Shiota, Takayuki Morikawa, Akiko Kubo, Takeharu Tani, Takako Hishiki, Tadashi Horiuchi, Makoto Suematsu, and Mayumi Kajimura, *ACS Nano*, **8** **6** (2014) 5622.
8. A. Rebecca, and J. Peter, *Sci. Technol*, **44** **20** (2010) 7749.
9. Katrin Kneipp, Yang Wang, Harald Kneipp, T. Lev, Irving Itzkan, R. Ramachandra, and S. Michael, *Phys. Rev. Lett.*, **78** (1997) 1667.
10. L. Paul, A. Jon, C. Nilam, and P. Richard, *Annual Review of Analytical Chemistry*, **1** (2008) 601.
11. Masahiko Kashin, Yasumasa Kakei, Shun Teraoka, Takumi Hasegawa, Akinobu Yamaguchi, Takao Fukuoka, Ryohei Sasaki, and Masaya Akashi, *Jane Hanrahan*, **2020** (2020) 1281645.
12. Shikuan Yang, Xianming Dai, Birgitt Boschitsch Stogin, and Tak-Sing Wong, *NAS*, **113** (2015) 268.
13. G. Gitchka, D. Neno, C. Stoyan, V. Miroslav, G. Victor, and V. Alexey, *Nanomaterials*, **11** (2021) 3184.
14. K. Kneipp, *Phys. Today*, **11** (2007) 40.
15. Christian Steuwe, F. Clemens, J. Jeremy, and Sumeet Mahajan, *Nano Lett.*, **11** **12** (2011) 5339.
16. J. Jeremy, A. Timothy, Yoshihiro Sugawara, Suzanne Cintra, E. Mamdouh, N. Phillip, and E. Andrea, *Nano Lett.*, **5** **11** (2005) 2262.
17. József Karger-Kocsis and László Lendvai, *Applied Polymer Science*, **135**(2017) 45573.
18. Rodney Tettenhorst and A. Douglas, *Clays and Clay Minerals*, **28** (1980) 373.
19. J. J. Merkel, T. Sontheimer, B. Rech, and C. Becker, *Journal of Crystal Growth*, **367** (2013) 126.
20. Angel Barranco, Ana Borrás, and Alberto Palmero, *Progress in Materials Science*, **76** (2016) 59.
21. R. Alvarez, J. M. Garcia-Martín, M. Macías-Montero, L. Gonzalez-Garcia, J. C. González, V. Rico, J. Perlich, J. Cotrino, A. R. González-Elipé, and A. Palmero, *Nanotechnology*, **24** (2013) 045604.
22. Katja Höflich, Ren Bin Yang, Andreas Berger, Gerd Leuchs, and Silke Christiansen, *Advanced Materials*, **23** (2011) 2657.
23. S. -W. Joo, *Vib. Spec*, **34** (2003) 269.
24. J. A. Creighton, C. G. Blatchford, and M. G. Albrecht, *J. Chem. Soc. Faraday Trans*, **2** (1979) 790.
25. M. Sackmann, and A. Materny, *JOURNAL OF RAMAN SPECTROSCOPY*, **114** (2006) 305.

Determination of Radiation Dose Leading to Molecular Chain Destruction of Amino Acids

Shunya Saegusa^{1,2*}, Ryo Nakamura^{1,2}, Naoya Akamatsu^{1,2}, Yuichi Utsumi¹,
Tomoko Ishihara^{2,3}, Masaki Oura², Akinobu Yamaguchi^{1,2**}

¹ *Laboratory of Advanced Science and Technology for Industry, University of Hyogo,
3-1-2 Kouto, Kamigori, Hyogo 678-1205, Japan*

² *RIKEN SPring-8 Center, 1-1-1 Kouto, Sayo, Hyogo, 679-5148, Japan*

**saesae54@lasti.u-hyogo.ac.jp, **yamaguti@lasti.u-hyogo.ac.jp*

³ *Present address: Japan Synchrotron Radiation Research Institute (JASRI),
1-1-1 Kouto, Sayo, Hyogo 679-5148, Japan*

The soft X-ray absorption spectroscopy (XAS) spectra of Alanine, L- and D-phenylalanine, and L- and D-tyrosine dissolved in a solid state were measured at BL17SU of SPring-8. The spectra exhibited characteristic features dependent on the molecular structure. It was found that almost the same spectra were obtained for Alanine and Phenylalanine, while for Tyrosine, the spectral shape indicated a drastic change owing to the existence of the oxygen $1s \rightarrow \pi^*$ transitions of COO^- . It is found that the X-ray irradiation promotes the destruction reaction of amino acids and changes the spectral shape during the spectroscopic measurement. The molecular destruction rate by X-ray was estimated from the change of spectral intensity as a function of irradiation time. Our results indicate that the ratio of the destruction rate depends on the molecular structure and is facilitated by the oxygen $1s \rightarrow \pi^*$ transitions.

Keywords: Synchrotron radiation, X-ray, Microfabrication, amino acid

1. Introduction

In recent years, attempts have been made all over the world to replace conventional plastic materials made from petroleum with biodegradable plastics, which are decomposed in nature, to solve environmental problems and health hazards caused by the adhesion of persistent organic pollutants (POPs) [1]. Biodegradable plastics are often made from bio-derived materials that are expected to be degraded by microorganisms. For example, polylactic acid (PLA) [2], which is used in three-dimensional (3D) printer filaments, is derived from corn or potato starch. Poly(3-hydroxybutyrate-co-3-hydroxyhexanoate) (PHBH) [3], which is used in straws and plastic bags, is made from vegetable oil. The development of biodegradable plastics is required for saving and forming the sustainable society.

On the other hand, basic research has been performed from the viewpoint of biochemistry and medicine on the process of decomposition of biodegradable plastics in vivo. Simultaneously, they are attracting attention in the development of

devices that work in vivo [4-7]. Currently, stents made of titanium are used in the treatment of myocardial infarction. If these treatment devices dissolve in the body and become a part of the body, it is expected that the burden on the patient will be reduced. In addition, both the risks of infection after treatment and excessive immune reaction due to contamination with foreign substances can be reduced.

Like the decomposition of organic molecules in vivo, the decomposition of organic materials by irradiation with sunlight, X-rays, and γ -rays has attracted much attention in recent years. There are many studies with respect to the molecular mechanisms of irradiation-induced degradation of biological molecules. In particular, the decomposition of some amino acids in solid state, induced by irradiation with soft X-rays, was investigated under ultrahigh vacuum (UHV) conditions by some spectroscopic measurements such as X-ray photoemission spectroscopy (XPS), near-edge X-ray absorption fine structure (NEXAFS) spectroscopy, and mass spectroscopy,

Received April 1, 2022

Accepted June 20, 2022

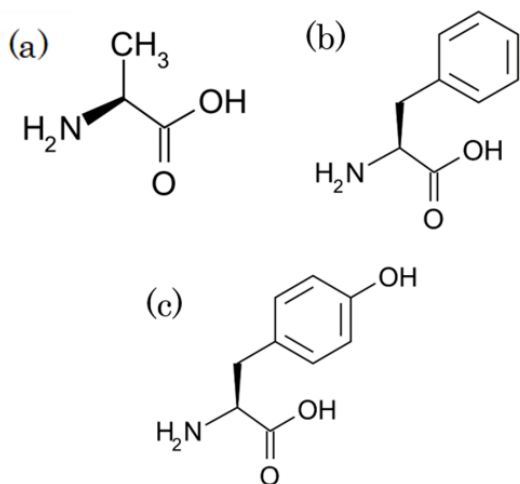


Fig.1 Molecular structures of (a) Alanine, (b) Phenylalanine, and (c) Tyrosine.

etc[8-22]. For example, Zubavichus *et al.* showed comparison of characteristics for the decomposition induced by the X-ray irradiation of phenylalanine (Phe) and tyrosine (Tyr) [20]. They concluded that the Tyr has higher stability of the molecule against radiation since the formation of molecular tyrosyl radicals apparently suppresses alternative decomposition routes. Tyr merely differs from Phe by an OH substituent in the para position of the phenyl ring.

In this study, we focus on the different radiation-induced decomposition paths of five amino acids, alanine (Ala), L- and D-Phe, L- and D-Tyr, which are described by similar molecular formulas as shown in Fig. 1. We investigated the decomposition process of isomers. Also, we focused on the decomposition process by irradiating under the relatively lower vacuum. Our study paves the way for elucidating the nature of decomposition process of bioplastics, proteins, amino acids, etc. under the influence of sunlight in the environment closer to the actual decomposition process in the ocean or the atmosphere.

2. Experimental methods and procedures

Amino acids ($\geq 99.9\%$ purity) used in this study were purchased from PEPTIDE INSTITUTE, INC as powders. Samples were prepared by pelleting L- and D-Phe, Tyr, and Ala as the follows. These amino acid powders were solidified by a pressure molding machine and molded into a tablet shape having a diameter of 15 mm. We investigated the influence of decomposition during the X-ray Absorption Spectroscopy (XAS) measurement. Oxygen *K*-edge XAS measurements were performed by using

circularly polarized light emitted from the multi-polarization-mode undulator [24,25] of at the beamline BL17SU of SPring-8[24-27]. The schematic experimental setup is illustrated in Fig.2. The samples were mounted on a holder in vacuum as schematically illustrated in Fig. 2. The vacuum pressure was set at about 4×10^{-4} Pa, which was far lower than that of the previous studies [18-22]. The Oxygen *K*-edge XAS spectra were recorded as total fluorescence yield (TFY) spectra using a standard 100 mm² Si photodiode (IRD AXUV-100G, Opto Diode Corp., USA). The photon flux was over 10^{11} photon/s, and the energy resolution was $\Delta E/E > 10^{-4}$. To investigate the effect of amino acid decomposition, the exposure was performed at a fixed point for 5 hours in a vacuum of 10^{-4} Pa. The beam size was 100 $\mu\text{m} \times 10 \mu\text{m}$ in this experiment.

The XAS analyses of the π^* orbital of the carboxyl group, which is considered to progress the decomposition, were performed. It is possible to compare the difference in the decomposition rate for each type of amino acid by following the change in the spectral intensity of XAS.

3. Results and discussion

Figure 3 shows TFY-XAS spectra of Ala, Phe, and Tyr, respectively. First, to conclude only, the difference between L- and D-Phe and L- and D-Tyr was not so remarkable in the XAS spectral measurements. Therefore, in the following, we will proceed exclusively with the discussion of the L-form. In the comparison of the spectra for Ala, Phe, and Tyr, the peak positioned at 532.5 eV, derived from the oxygen $1s \rightarrow \pi^*$ transitions of COO^- , is commonly observed in all. The XAS spectra of Ala and Phe do resemble each other because the X-ray absorption is originated from the oxygen $1s \rightarrow \pi^*$ transitions of COO^- . This trend of XAS spectra for Ala and Phe is in good agreement with the previous studies [18-22]. In contrast, as immediately noticed, a satellite peak appears only in Tyr at 531 eV. This feature is attributed to be $1s \rightarrow \pi^*$ ($\text{C}=\text{O}$) transitions associated with ketone- or aldehyde-like

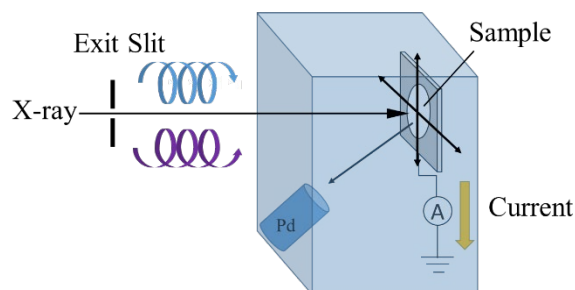


Fig. 2 Schematic of XAS measurements achieved by TFY and TEY spectroscopies.

species [20,23]. This XAS spectral shape is different from the results reported by Zubavichus *et al.* [18], and Frati *et al* [22]. The measurement of the oxygen *K*-edge XAS in amino acids has been reported and summarized in Refs. [18~22]. The oxygen electronic state depends on bonding environments, and the different chemical shifts are observed for each oxygen in amino acids. Zubavichus *et al* [18], summarized the measured oxygen *K*-edge spectra of the 22 amino acids. They assigned the energy positions: (1) 532.3 – 532.5 eV : π^* (COO)/(COOH) in all amino acids, (2) 538 - 539.4 eV : σ^* (C-OH) in Tyrosine (Tyr),, and (3) 542 - 549 eV : σ^* (COO)/(COOH) in all amino acids. By comparing our measurement results with those of previous studies [18-22], the XAS spectrum of Phe is in good agreement with that reported by Zubavichus *et al* [18]. On the other hand, the relative intensity of the σ^* (C-OH) is significantly higher for Tyr than Ala or Phe. This is because the OH groups attached to the benzene ring of the tyrosine molecule form mainly σ^* bonds. The peak at 531 eV, which was not observed in previous studies, is appeared as described the above. This peak at 531 eV might be caused by the

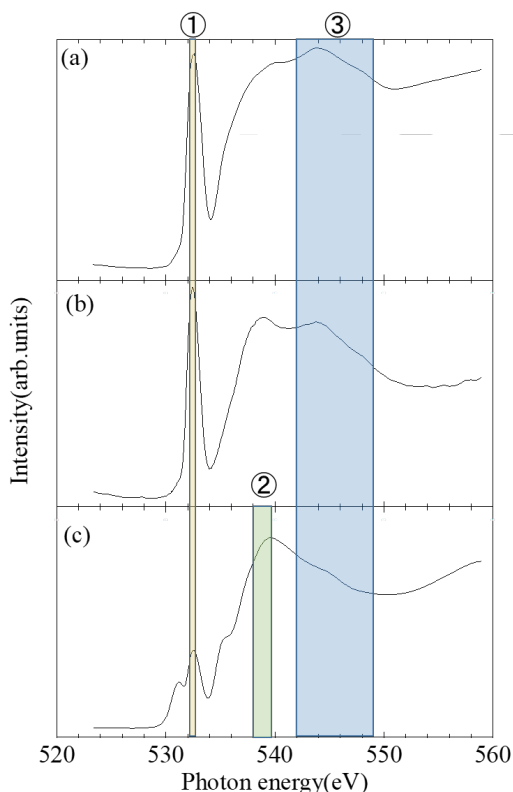


Fig.3 Averaged TFY-XAS spectra of (a) Alanine (Ala), (b) Phenylalanine (Phe) and (c) Tyrosine (Tyr), respectively. The numbered indexes ① - ③ denote following transitions: ① π^* (COO)/(COOH), ② σ^* (C-OH), and ③ σ^* (COO)/(COOH), respectively.

transformation of carboxyl groups to ketone.

In fact, in previous irradiation experiments of Tyr [20], the peak at 532.5 eV decreases as the irradiation time increases, and a shoulder appears around 531 - 532 eV. The reason why this peak appeared clearly in this experiment is originated from the difference of vacuum and flux density. The vacuum in the previous experiment was 5.0×10^{-8} Pa²⁰, while the vacuum in this experiment is lower than previous studies [18-22]. The lower vacuum may prevent the evaporating and scattering Tyr, and many Tyr molecules stayed around the surface for enough time to proceed the recombination reaction. The photon flux density was 3.3×10^{14} photon/s/mm² for BL17SU and 3.3×10^{13} photon/s/mm² for ALS in the previous experiment, suggesting that the higher incident energy in this experiment, resulting in acceleration of the heating and evaporation of fragments. On the other hand, due to the low degree of vacuum, the low molecular weight fragment may remain near the sample. Since Tyr forms a stable radicals state, it is possible that the Tyr in the tablet reacts with the radicalized Tyr to form a ketone because a dehydrogenation of the OH group in Tyr leads to the formation of a very stable radical with an unpaired electron delocalized over the oxygen atom and the six carbon atoms of the benzene ring [28]. We considered it from the process of decomposition of Tyr, but conversely, we consider it from the process of decomposition of Ala and Phe. Both Ala and Phe have the lower boiling point (decomposition temperature) and evaporate more easily than Tyr [29-31]. As a result, the measured facts suggest that they do not participate in recombination due to the shorter lifetime for the stable radical.

As mentioned above, the most notable issue in the present XAS results for Ala, Phe, and Tyr is the difference in the fine structure of respective spectra.

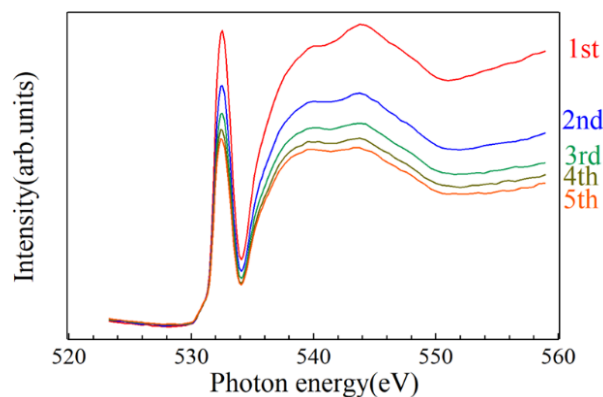


Fig. 4 Changes in the spectra of L-Ala with the number of exposures.

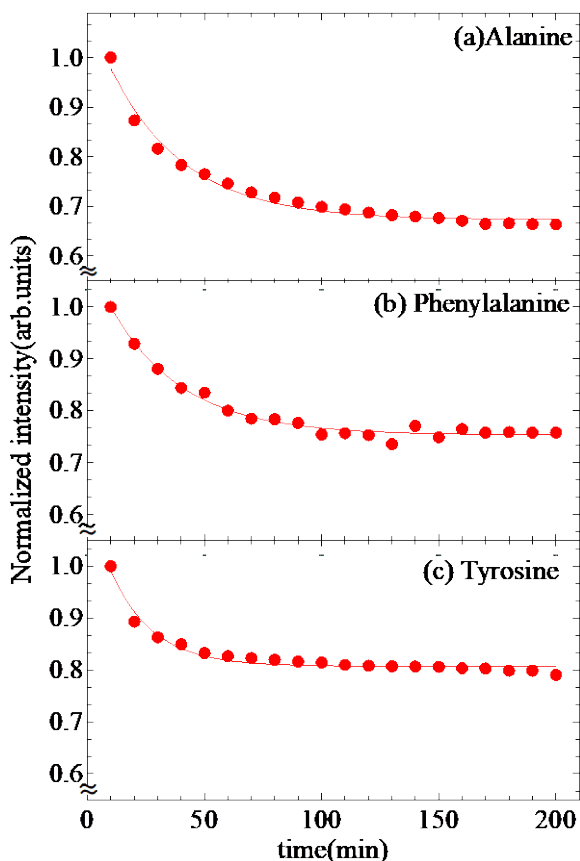


Fig. 5 TFY-XAS intensity as a function of time with respect to the amino acids of (a) Alanine, (b) Phenylalanine, and (c) Tyrosine.

It is originated from the σ^* associated with (C-OH) bonding of Tyr. The C-OH bonding is expected to affect relaxation constant for the scission of molecular chain. To evaluate the difference in the decomposition of the molecular chains of amino acids, a long-time XAS measurement at a fixed point was performed. Figure 4 shows a typical example of the results of the long-time exposure of the O1s absorption edge of L-Ala. A clear peak was shown at about 532.5 eV, which indicates the π^* orbit of the carboxyl group. As shown in Fig. 4, the XAS intensity decreases with increasing number of measurements, whereas no peak shifting was observed. The tablet has a thickness of a few millimeters, and the irradiation position was monitored by a charge-coupled device (CCD) camera during the XAS measurement. This mass loss with respect to measurement times suggests that the X-ray irradiation might sublime the amino acid, L-Ala powder in vacuum while maintaining the stoichiometric composition. Therefore, assuming the process in which molecules in the irradiation region are simply sublimated by X-ray irradiation, the following model can be considered

to understand this trend and estimate the decay rate of molecule. Here, I_D is defined as the XAS intensity at about 532.5 eV attributable to the π^* . Assuming I_D is decreased with exposure time t , the following formula holds.

$$\frac{dI_D}{dt} = -\lambda I_D, \quad (1)$$

where λ is the decay coefficient of amino acid, as depended on molecular structure and composition, that is $\lambda = 1/\tau$, where τ is the relaxation constant which is related to the decay time of amino acid molecule by the X-ray irradiation. Subsequently, after integrating both sides of Eq. (1), we obtained the following relation:

$$I_D = I_{D0} \exp(-\lambda t) = I_{D0} \exp\left(-\frac{t}{\tau}\right) \quad (2)$$

I_N is the strength of the part not to be destroyed, the total strength I is

$$I = I_N + I_D = I_N + I_{D0} \exp\left(-\frac{t}{\tau}\right) \quad (3)$$

As a result, the overall intensity decreases as the number of exposures increases. Figure 5 summarizes the change in peak intensity around 532.5 eV for (a) Ala, (b) Phe, and (c) Tyr. These intensities were normalized by the intensity at start of the measurement.

The actual fittings in Fig.5 were performed using Eq. (3). As a result, the results of comparing the relaxation constant τ for each amino acid are summarized in Table 1. These values of Ala and Phe were found to be close to each other, while the value of Tyr was smaller than those of the other two. These results suggest the following two mechanisms. First, the relaxation times of Ala and Phe are very close, the decomposition process is basically originated from the scission and transition associated with σ^* (C-OH). Second, for Try, the shorter relaxation constant is considered to be transition process to ketone formation by the recombination as described the above.

The relaxation constant is the smallest for Tyr, besides, the rate of decrease in the intensity as it approaches equilibrium is also the smallest. It is inferred that this is because the process sublimation of Ala and Phe is the main decomposition, while Try is asymptotically approaching the equilibrium state by repeating decomposition and recombination. These results do not deny the previous researches so far. We were able to know the behavior of the decomposition process in a low vacuum state, which was not obtained by the previous findings.

Table 1 Summary of estimated relaxation constant.

	Ala	Phe	Tyr
$\tau(\text{min})$	31.739	30.884	17.957

4. Conclusion

We investigated the decomposition process of Alanine (Ala), Phenylalanine (Phe), and Tyrosine (Tyr) under exposure to soft X-ray radiation in relatively lower vacuum. The decomposition behaviors of Ala and Phe are in good agreement with the previous studies. In contrast, in the case of Try, the novel peak was observed in the X-ray absorption spectroscopy (XAS). This peak structure is presumed to be due to ketone formation derived from the simultaneous progress of decomposition and recombination due to the generation of long-lived Try radicals.

5. Acknowledgement

The synchrotron radiation experiments were carried out at beamline BL17SU of SPring-8 with the approval of RIKEN SPring-8 Center (proposal no. 20190055). The authors would like to thank the members of the Engineering Team, especially for Mr. Atsushi Nishimura, of RIKEN SPring-8 Center for their technical assistance. This work was supported in part by JSPS Grants-in-Aid-for Scientific Research B (No. 17H02755).

6. References

- [1] R. Bouhroum, A. Boulkamh, L. Asia, S. Lebarillier, A. Ter Halle, A. D. Syakti, P. Doumenq, L. Malleret, and P. Wong-Wah-chung, *Regional Studies in Marine Science* **29** (2019), May, 1006.
- [2] W. S. Chow, E. L. Teoh, and J. Karger-Kocsis, *Express Polymer Letters*, **12** (2018) 396.
- [3] T. Morohoshi, K. Ogata, T. Okura, and S. Sato, *Microbes and Environments*, **33** (2018) 19.
- [4] S. Hwang, J. Song, X. Huang, H. Cheng, S. Kang, B. H. Kim, J. H. Kim, S. Yu, Y. Huang, and J. A. Rogers, *Adv. Mater.*, **26** (2014) 3905.
- [5] T. Ponnusamy, L. B. Lawson, L. C. Freytag, D. A. Blake, R. S. Ayyala, and V. T. John, *Biomatter*, **2** (2012) 77.
- [6] H. K. Makadia and S. J. Siegel, *Polymers*, **3** (2011) 1377.
- [7] M. I. Sabir, X. Xu, and L. Li, *J Mater Sci*, **44** (2009) 5713.
- [8] J. Wang, G. A. Botton, M. M. West, and A. P. Hitchcock, *J. Phys. Chem. B*, **113** (2009) 1869 - 1876.
- [9] H. Yamane, M. Oura, K. Sawada, T. Ebisu, T. Ishikawa, N. Yamazaki, K. Hasegawa, K. Takagi, and T. i Hatsui, *J. Electron Spectrosc. Relat. Phenom*, **232** (2019) 11.
- [10] J. Wang, C. Morin, L. Li, A. P. Hitchcock, A. Scholl, and A. Doran, *Journal of Electron Spectroscopy and Related Phenomena*, **170** (2009) 25.
- [11] E. G. Rightor, A. P. Hitchcock, H. Ade, R. D. Leapman, S. G. Urquhart, A. P. Smith, G. Mitchell, D. Fischer, H. J. Shin, and T. Warwick, *J. Phys. Chem. B*, **101** (1997) 1950 -1960.
- [12] T. Beetz and C. Jacobsen, *J. Synchrotron Rad.*, **10** (2002) 280.
- [13] P. Norman and A. Dreuw, *Chem. Rev.*, **118** (2018) 7208.
- [14] J. Goulon, F. Sette, C. Moise, A. Fontaine, D. Perey, P. Rudolf, and F. Baudelet, *Jpn. J. Appl. Phys.*, **32** (1993), 284.
- [15] S. Turchini, N. Zema, S. Zennaro, L. Alagna, B. Stewart, R. D. Peacock, and T. Prospero, *J. Am. Chem. Soc.*, **126** (2004), 4532.
- [16] Y. Izumi, M. Tanabe, A. Imazu, A. Mimoto, M. Tanaka, A. Agui, T. Muro, and K. Nakagawa, *J. Chem. Phys.*, **138** (2013), 074305.
- [17] O. Takahashi, M. Kimoto, and L. G. M. Pettersson, *Chem. Phys.*, **109** (2015), 450.
- [18] Y. Zubavichus, A. Shaporenko, M. Grunze, and M. Zharmikov, *J. Phys. Chem. A*, **109** (2005), 6998.
- [19] L. Yang, O. Plashkevych, O. Vahtras, V. Carravetta, and H. Ågren, *J. Synchrotron Radiation*, **6** (1999), 708.
- [20] Y. Zubavichus, M. Zharmikov, A. Shaporenko, O. Fuchs, L. Weinhardt, C. Heske, E. Umbach, J. D. Denlinger, and Michael Grunze, *J. Phys. Chem. A*, **108** (2004), No. 20.
- [21] M. Tanaka, K. Nakagawa, T. Koketsu, A. Agui,

- and A. Yokoya, *J. Synchrotron Radiation*, **8**(2001), 1009.
- [22] F. Frati, M. O. J. Y. Hunault, and F. M. F. de Groot, *Chem. Rev.* , **120**(2020), 4056.
- [23] S. G. Urquhart and H. Ade, *J. Phys. Chem. B*, **106** (2002) 8531.
- [24] K. Shirasawa, T. Tanaka, T. Seike, A. Hiraya, and H. Kitamura, *AIP Conf. Proc.* , **705**(2004), 203.
- [25] M. Oura, T. Nakamura, T. Takeuchi, Y. Senba, H. Ohashi, K. Shirasawa, T. Tanaka, M. Takeuchi, Y. Furukawa, T. Hirono, T. Ohata, H. Kitamura, and S. Shin, *J. Synchrotron Rad.* , **14**(2007), 483.
- [26] H. Ohashi, Y. Senba, H. Kishimoto, T. Miura, E. Ishiguro, T. Takeuchi, M. Oura, K. Shirasawa, T. Tanaka, M. Takeuchi, K. Takeshita, S. Goto, S. Takahashi, H. Aoyagi, M. Sano, Y. Furukawa, T. Ohta, T. Matsushita, Y. Ishizawa, S. Taniguchi, Y. Asano, Y. Harada, T. Tokushima, K. Horiba, H. Kitamura, T. Ishikawa, and S. Shin, *AIP Conf. Proc.* , **879** (2007) ,523.
- [27] Y. Senba, H. Ohashi, H. Kishimoto, T. Miura, S. Goto, S. Shin, T. Shintake, and T. Ishikawa, *AIP Conf. Proc.* , **879**(2007), 718.
- [28] R. J. Hulsebosch, J. S. van den Brink, S. A. M. Nieuwenhuis, P. Gast, J. Raap, J. Lugtenburg, and A. J. Hoff, *J. Am. Chem. Soc.* , **119** (1997), 8685.
- [29] Chembook, https://www.chemicalbook.com/-ChemicalProductProperty_JP_CB4350297.htm, 2022-03-29.
- [30] Merck, <https://www.merckmillipore.com/JP/en/product/L-Phenylalanine>, MDA_CHEM - 107256, 2022-03-29.
- [31] Merck, <https://www.merckmillipore.com/JP/en/product/L-Tyrosine>, MDA_CHEM-108371, 2022-03-29.

Controlled Sequence Photoresists from Polypeptoids

Florian Kaefer¹, Zoey Meng², Rachel Segalman² and Christopher K. Ober^{*1}

¹*Materials Science and Engineering, Cornell University,
Ithaca 14853, NY, USA*

³*Chemical Engineering and Materials, UC Santa Barbara,
Santa Barbara, CA, 93106-5080*

**cko3@cornell.edu*

Low stochastic, high sensitivity photoresists remain a goal for lithography. Here we present a study of a polymer system, polypeptoids, using a synthetic strategy borrowed from the biomedical community to make improvements to these resist characteristics through control of polymer sequence. We describe peptoid polymers that possess identical molecular size, composition and sequence with higher molecular uniformity than possible by conventional synthetic techniques. We report the results of exposure of these materials to DUV radiation and the chemical changes that occur. In addition, we highlight unexpected observations of the role of sequence on lithographic performance.

Keywords: EUV photolithography, Stochastics, Sequence control, Peptoid, Chemically amplified

1. Introduction

A continuing challenge in the development of EUV photoresists is solving the issue of stochasticity, that is, the random probability distributions of exposure dose, and secondary electron generation that change solubility in a photoresist with its molecular size and molecular composition distribution which ultimately lead to imperfections in pattern formation. For example, in a classical chemically amplified photoresist there is: i) heterogeneity in polymer composition and ii) in the mixing of the photoresist and photoactive additives [1]. The effect of inhomogeneity is believed to contribute to line edge roughness and defect formation among other issues. In most polymer preparation methods in which several building blocks are incorporated, further compositional heterogeneity results from the statistical nature of random copolymerization.

In recent studies, metal organic clusters have been shown to produce high resolution photoresists in which the basic building blocks are so small that molecular homogeneity becomes simpler to achieve [2]. Nevertheless, there remain advantages in working with polymer systems if stochasticity can be

addressed. The chemical versatility of monomer building blocks remain very attractive if the chemical control of synthesis can be implemented. In this report we discuss an approach to chemical control of stochasticity in which solid supported synthetic chemistry is used to prepare peptoid polymer chains [3] that are identical in composition, molecular weight and in sequence.

Peptoids are polyamides that mimic the sequence control of proteins, and are easier to synthesize, yet are different because they lack stereocenters present in proteins since they are not made from amino acids, and they have functional groups attached to nitrogen rather than carbon. This polymer family, prepared using a robot synthesizer system originally developed for protein synthesis, is produced using polymer supported chemistry and can be made in multigram quantities. Attachment to a polymer substrate enables exquisite control of the polymer formation chemistry during synthesis. The number of units in each chain is identical and the average composition is identical, thus minimizing issues of compositional statistics. The greater efficiency of peptoid preparation (compared to peptides) means that resist molecules ranging from 10 to 30 or more

Received April 30, 2022

Accepted June 28, 2022

repeat units are easily produced. Recent simulations by researchers at Lawrence Berkeley Labs have shown very interesting scission behavior of amide bonds under EUV radiation [4]. Both the potential for molecular weight and sequence control and these simulations prompt our studies.

Our expectation is that this approach to the design EUV photoresists will help to limit the defects present in an EUV patterning regime, by minimizing the stochastic nature of light-matter interactions through extreme homogeneity in chemical structure and resulting chemical reactivity [5]. At the same time these strategies take advantage of the inherent flexibility of molecular design afforded by polymer synthesis and do not require completely new processes or entirely new molecular systems.

In our report last year [6], we began by preparing sequences with tyramine as PHOST analogs with t-BOC protecting groups in combination with other hydrophobic comonomers and demonstrated that we could use PAG in combination with the peptoid to prepare chemically amplified photoresist materials. In this report we would like to describe the effect of sequence selection on patterning and development and to update our progress on the study of these new polymer systems. Hydrophobic groups to be described include phenyl ethylene amine and propargyl amine units.

To date our studies are limited to DUV patterning as we begin to understand the effect of composition and sequence on performance. Preliminary studies of the lithographic behavior of these resist systems have been carried out and will be discussed. Our initial observations of peptoid sequence and the versatility of this method will be presented.

2. Experimental

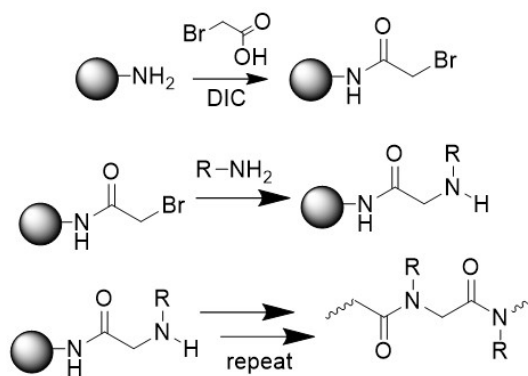


Fig. 1. Synthesis of peptoid polymers. R represents a substituent group chosen for a specific functionality or reactivity.

All reagents were purchased from Sigma Aldrich, Millipore Sigma, TCI America, and Oakwood Products at the highest purity available and used without further purification. Tyramine, benzylamine and propargylamine were purchased from Sigma Aldrich and used as received.

2.1 Synthesis of peptoid photoresists

The peptoid syntheses were conducted using a CSBio Peptide Synthesizer, Model CS336X. For the solid-phase supported synthesis of the peptoids 1g of 2-chlorotrityl chloride resin with a loading of 1.7 mmol g⁻¹ was swollen in dichloroethane (DCE) for 10 minutes and washed with dimethyl-formamide (DMF). The first bromoacetylation step was carried out by adding 10 mL of a 1.3 M bromoacetic acid (BAA) in DMF and 10 mL of a 1.3 M *N,N*-diisopropylethylamine (DIEA) in DMF to the resin and bubbling with nitrogen and shaking for 30 minutes. The resin was then washed repeatedly with DMF. Amination was performed by reacting the acylated resin with 1-2 M of the amine in DMF for 60 minutes constantly bubbling nitrogen and shaking the reactor. Additional bromoacetylation steps were conducted with 1.2 M BAA and 1.4 M *N,N'*-diisopropylcarbodiimide (DIC) in DMF. Cleavage was accomplished by treatment with 20% hexafluoroisopropanol in dichloromethane (DCM). The resin was filtered, and the solution was concentrated via rotary evaporation and lyophilized. The resulting solid was dissolved in 1:1 acetonitrile/water and purified using a preparative HPLC and lyophilized and characterized using a Bruker Matrix Assisted Laser Desorption - Time of Flight (MALDI-TOF) Bruker AutoFlex Max tool. To introduce solubility switching groups the tyramine hydroxyl groups were protected with di-tert-butyl dicarbonate (tBOC). For the 1g peptoid synthesis, it was dissolved in 10 mL acetone and 1.3 equivalents of tBOC and 0.1 mol equivalent 4-dimethylaminopyridine (DMAP), were added and the solution was stirred for 24 hours at room temperature. Afterwards, the sample was concentrated, purified by preparative HPLC and lyophilized. The resulting solid was characterized using MALDI-TOF.

2.2 Lithographic characterization:

For deep-ultraviolet (DUV) exposures the 25 mg peptoid were dissolved in 1ml of propylene glycol methyl ether. To this solution 20 wt% (in respect to peptoid) photoacid generator (TPS-triflate) was added and the solution was sonicated for 5min. The solution was filtered, and spin coated on a UVO cleaned silicon wafer. The coated wafer was post-apply baked for 60s at 110°C.

DUV exposures were conducted on an ASML PAS 5500/300C Wafer Stepper. When carried out, E-beam exposures were performed using a JEOL 6300, 100kV e-beam tool. After exposure, the patterns were post-exposure baked for 60s at 110°C

for 60s and developed in isopropyl alcohol. The resulting patterns were characterized using a Zeiss-Gemini-500-FESEM.

3. Results and discussion

3.1 Controlled length and sequence peptoid photoresists

Resolution in photoresists is controlled by the solubility difference between the exposed and unexposed regions. Similarly, line edge roughness has been correlated to inhomogeneities in regions of the resist possessing both soluble and insoluble components after exposure [7]. These inhomogeneities are partially the result of stochastics in the initial distribution of photoacid generators and solubility change groups [8]. Minimizing such variations via control of the polymer's molecular size is crucial to achieving the lithography performance requirements set by the IEEE IRDS [9]. As resolution and line edge roughness requirements become more demanding, traditional photoresist design or more recent orthogonal methods employing electrochemistry and photochemistry [10] may be inadequate for developing future generations of photoresists.

Peptoids possess repeat units built from *N*-substituted glycines. Compared to peptides, peptoids present numerous advantages including a wider range of functional groups and lower-cost. More efficient synthesis enables production of higher molecular weights with high precision when compared to protein synthesis in molecular weight ranges suitable for photoresists [11]. The most well-developed solid-phase method is the submonomer synthesis (SMS), which combines two types of

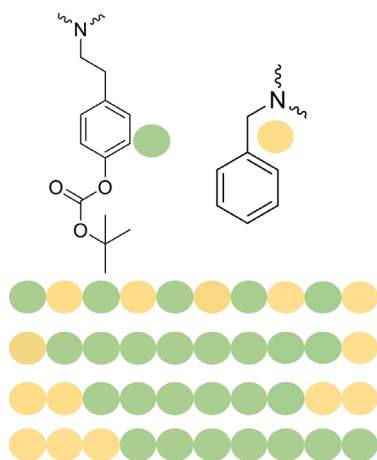


Fig. 2. Sequences of t-BOC protected tyramine (green) and benzyl amine (yellow) in library. Each member of the library consists of segments exactly 10 units long.

repeat units, primary amines and bromoacetic acid, in a stepwise manner (Fig. 1). Following synthesis, preparatory HPLC was used to remove any excess lower molecular weight segments that might have been produced.

The extensive number of commercially available primary amines and the ease of synthesizing novel monomers enable a high degree of molecular complexity to be implemented into peptoids. In this report we describe libraries of two sequence families: one made with tyramine and benzyl amine (Fig. 2), and one made using tyramine with propargyl amine units (Fig. 3). It should be noted

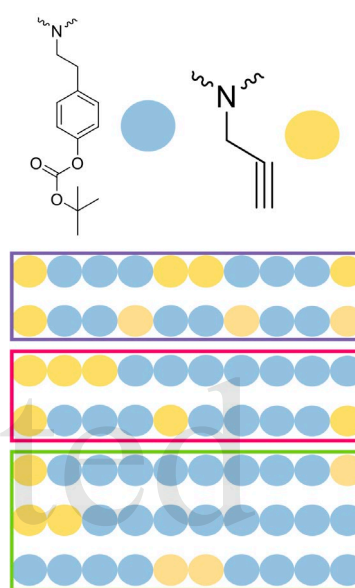


Fig. 3. Sequences of t-BOC protected tyramine (blue) and propargyl amine (yellow) in library. Each member of the library consists of segments exactly 10 units long. Colors of boxes reflect the number of propargyl units in each segment.

that the propargyl amine was included to provide a future point of attachments using click chemistry,

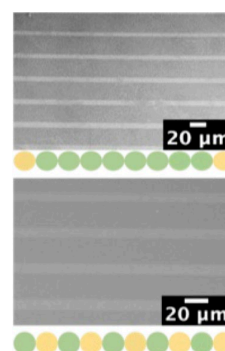


Fig. 4. Patterns produced from tyramine (green) and benzyl amine (yellow) sequences using DUV exposures.

but we elected to study sequences of this material to understand any changes that its incorporation provided. Hydrophobic units are yellow in both sequences.

In these sequences we have attempted to probe the importance of the distribution of the tyramine (PHOST mimic) in the sequence and observe the effect of architecture of lithographic performance using DUV patterning of these materials. Patterning performance can be seen in Fig. 4 and Fig. 5. Generally, a homogenous distribution of both units has better performance than a blocky structure.

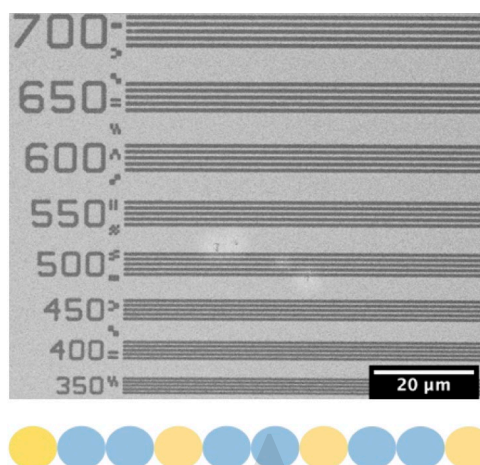


Fig. 5. Patterns produced from tyramine and propargyl amine sequences using DUV exposures. DUV 1:1 line space pattern Dose 100mJ/cm² of a tyramine/propargylamine 10mer. Developed in isopropyl alcohol for 90 sec; film thickness 33nm.

Development conditions were studied using a variety of solvents and can be seen plotted in a 3-coordinate solubility parameter plot (Fig. 6). Fewer

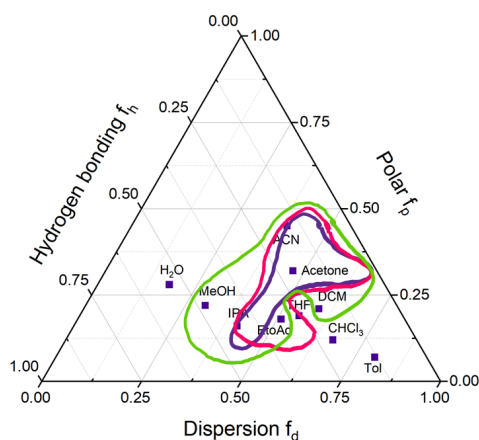


Fig. 6. Solubility plot of tyramine/propargylamine 10mers of different composition and sequence: (purple) 40mol% propargylamine (Pro); (red) 30mol% Pro; (green) 20mol% Pro.

propargyl units gave a polymer with a wider range of solvents. Sequence changes provided very modest changes in solubility.

As shown above for the propargyl amine-tyramine system, chain end caps of the more hydrophobic group were observed to deliver better photoresist performance (e.g., Fig. 5). It should be noted that under e-beam exposure conditions, the unsaturation on the propargyl unit led to crosslinking, but its incorporation does demonstrate a role for hydrophobic end units in a polymer sequence in a chemically amplified resist polymer. Sequence and content play complementary roles in determining the solubility, development, and resolution of these polymers.

Anecdotally, amides have been thought to interfere with the chemical amplification process from experience in its early years, due to vulnerability to poisoning by NMP; yet current resist formulations purposely add tertiary amines to prevent dark losses. Recent research has demonstrated that amides can accelerate deprotonation of radical cations [12] that form along the polymer backbone upon exposure to EUV. This feature helps to prevent recombination with other radicals and increases acid generation, thereby enhancing sensitivity [13].

As the peptoids examined are 10-mers, the structure of the side groups was also carefully chosen to avoid crystallization and tune the glass transition temperature. Other hydrophobic units under exploration include adamantyl amine and phenyl ethyl amine. While these initial results clearly show the potential of peptoids as photoresist materials, the ongoing research remains at an early stage.

4. Conclusion

To summarize, these photopolymers are being investigated to explore methods for producing high resolution, high sensitivity photoresists that minimize stochastic issues through macromolecular design. Recent results of the preparation and lithographic patterning of these materials will be presented. They suggest that the sequence has a clear impact on solubility and development behavior and our initial studies suggest non-polar end monomers lead to better imaging and development.

Acknowledgements

We are grateful to Intel Corp for support of Dr. F. Käfer and Z. Meng through its CINEMA program

on photoresist design.

References

1. A. Lio, *Proc. of SPIE*, **97760V-14** (2016) 9776.
2. H. Xu, K. Sakai, K. Kasahara, V. Kosma, K. Yang, H. C. Herbol, J. Odent, P. Clancy, E. P. Giannelis, C. K. Ober, *Chem. Mater.*, **30** (2018) 4124-4133.
3. M. E. Barry, P. A. Gokturk, A. J. DeStefano, W. v. Zoelen, A. K. Leonardi, C. K. Ober, E. J. Crumlin, R. A. Segalman, *ACS Appl. Mater. Interfaces* **2022**, *14*, *5*, 7340–7349.
4. J. Ma, 2021 *EUVL Workshop Abstract*, Oct. 23-28, 2021
5. D. De Simone, Y. Vesters G. Vandenberghe, *J. Photopolym. Sci. Technol.*, *31*(5), 2018, 651.
6. J. Deng, F. Kaefer, S. Bailey, Y. Otsubo, Z. Meng, R. Segalman and C. K. Ober, *J. Photopol. Sci. Tech.*, *34*(1-6) (2021)
7. T. Kozawa and S. Tagawa, *Jpn. J. Appl. Phys.*, **49** (2010) 030001.
8. P. D. Ashby, D. L. Olynick, D. F. Ogletree and P. P. Naulleau, *Advanced Materials*, **27** (2015) 5813-5819.
9. M. Neisser, H. Levinson, *Proc. SPIE*, **11323**, **XI** (2020).
10. M. J. Supej, B. M. Peterson, B. P. Fors, *Chem.*, **6** (2020) 1794-1803.
11. N. Gangloff, J. Ulbricht, T. Lorson, H. Schlaad, R. Luxenhofer, *Chem. Rev.*, **116** (2016) 1753-1802.
12. T. Susa, K. Okamoto, T. Ishida, H. Yamamoto, T. Kozawa, R. Fujiyoshi, K. Umegaki, *SPIE* (2014) 9051.
13. S. Fujii *et al.* *Jpn. J. Appl. Phys.*, **56** (2017) 06GD01.